TU Delft

Delft University of Technology

Document Version
Final published version

Citation (APA)
Kortman, V. G. (2026). *Intelligence by Design: Exploration of Mechanical Intelligence in Soft Robotics*. [Dissertation (TU Delft), Delft University of Technology]. https://doi.org/10.4233/uuid:3750d551-1f38-4ea1-b3cc-f9e740f53af6

Important note
To cite this publication, please use the final published version (if applicable).
Please check the document version above.

Copyright
In case the licence states “Dutch Copyright Act (Article 25fa)”, this publication was made available Green Open Access via the TU Delft Institutional Repository pursuant to Dutch Copyright Act (Article 25fa, the Taverne amendment). This provision does not affect copyright ownership.
Unless copyright is transferred by contract or statute, it remains with the copyright holder.

Sharing and reuse
Other than for strictly personal use, it is not permitted to download, forward or distribute the text or part of it, without the consent of the author(s) and/or copyright holder(s), unless the work is under an open content license such as Creative Commons.

Takedown policy
Please contact us and provide details if you believe this document breaches copyrights.
We will remove access to the work immediately and investigate your claim.

This work is downloaded from Delft University of Technology.

INTELLIGENCE by DESIGN

Exploration of Mechanical Intelligence in Soft Robotics



Vera G. Kortman

Intelligence by Design

Exploration of Mechanical Intelligence in Soft Robotics

Dissertation

for the purpose of obtaining the degree of doctor
at Delft University of Technology
by the authority of the Rector Magnificus
Prof.dr.ir. H. Bijl,
chair of the Board for Doctorates
to be defended publicly on
Wednesday, 14 October at 10:00

by

Vera Gesina KORTMAN

This dissertation has been approved by the promotors.

Composition of the doctoral committee:

Rector Magnificus	chairperson
Prof. dr. ir. P. Breedveld	Delft University of Technology, promotor
Dr. ir. J. Jovanova	Delft University of Technology, promotor
Dr. ir. A. Sakes	Delft University of Technology, promotor
Independent members:	
Prof. dr. J. Dankelman,	Delft University of Technology
Prof. dr. A. A. Zadpoor,	Delft University of Technology
Dr. H. L. McQuillan,	Delft University of Technology
Prof. dr. J. Paik,	École polytechnique fédérale de Lausanne, Switzerland
Dr. B. Atasoy,	Delft University of Technology, *reserve member*

Keywords: Soft Robotics, Bio-Inspired Design, Mechanical Intelligence
Printed by: Ridderprint, www.ridderpint.nl
Cover by: Vera Kortman

Copyright © 2026 by V. Kortman
ISBN 978-94-6537-933-3

An electronic version of this dissertation is available at: http://repository.tudelft.nl

Table of Contents

Summary ix

Samenvatting xi

1. Introduction **1**
- 1.1. From factory settings to the real world 3
- 1.2. Learning from nature to design for nature 5
- 1.3. Mechanical Intelligence for highly constrained conditions 6
- 1.4. Goal of this thesis 7
- 1.5. Thesis outline 8

2. Perspectives on Intelligence in Soft Robotics **13**
- 2.1. Introduction 15
- 2.2. Peeling the Layers of Intelligence 18
  - 2.2.1. Artificial Intelligence 18
  - 2.2.2. Embodied Intelligence 18
  - 2.2.3. Physical Intelligence 25
  - 2.2.4. Intelligence by Different Computational Systems 28
- 2.3. Environmental Responsive Intelligence 29
  - 2.3.1. Intelligence of Soft Robots 29
  - 2.3.2. Mechanical Intelligence 30
  - 2.3.3. Enablers of Mechanical Intelligence 31
- 2.4. Conclusion 33

Part I: Intelligent Gripping **43**

3. Design of an octopus-inspired suction gripper **45**
- 3.1. Introduction 47
  - 3.1.1. Surgical grippers versus suction grippers 47
  - 3.1.2. State of the art 48
  - 3.1.3. Inspiration from biological suction discs 48
  - 3.1.4. Aim of this study 49
- 3.2. Analysis biological suction disc 50
  - 3.2.1. Decoupling functions 50
  - 3.2.2. Suction generation 50
  - 3.2.3. Seal generation 50
  - 3.2.4. Grip generation 52

3.2.5. Schematic disc design 52
3.3. Prototype development 53
3.3.1. Design constraints 53
3.3.2. Design suction tip 54
3.3.3. Fabrication suction tip 56
3.4. Experimental validation 59
3.4.1. Experimental goal 59
3.4.2. Experimental setup 59
3.4.3. Experimental design 59
3.5. Results 62
3.5.1. Pull-off measurements 62
3.5.2. Slide-off measurements 63
3.5.3. Experiment 2: vacuum pressure 64
3.6. Discussion 66
3.6.1. Main findings 66
3.6.2. Application fields 68
3.6.3. Limitations 68
3.6.4. Design recommendations 69
3.7. Conclusion 70

4. Magnetic shape morphing strategies 77
4.1. Introduction 79
4.1.1. 4D-printing 79
4.1.2. Goal of the study 80
4.2. Methods 81
4.2.1. Search strategy and eligibility criteria 81
4.2.2. Study selection 81
4.2.3. Classification 81
4.3. Single-Stimulus Magnetic-Responsive Structures 83
4.3.1. Random magnetization 83
4.3.2. Programmed magnetization 86
4.4. Multi-Stimuli Magnetic-Responsive Structures 91
4.4.1. Shape change mechanisms of multi-stimuli responsive structures 91
4.4.2. Thermo-magneto responsive structures 93
4.5. Discussion 96
4.5.1. Main findings 96
4.5.2. Limitations 98
4.5.3. Future directions 98
4.6. Conclusion 99

Appendix 4.A 109

5. Design of a magnetic suction gripper 113
5.1. Introduction 115
5.1.1. Challenges in conventional suction gripping 115
5.1.2. Opportunities for advanced magnetic materials 115
5.1.3. Goal 116
5.2. Magnetic Suction Gripper Design 116
5.2.1. Design requirements 116
5.2.2. Design overview 117
5.3. Experimental Validation 121
5.3.1. Attachment performance 121
5.3.2. Deployment performance 127
5.4. Discussion 127
5.4.1. Main findings 127
5.4.2. Limitations 129
5.4.3. Recommendations 130
5.5. Conclusion 130

Part II: Intelligent Movement 133

6. State of the art McKibben Artificial Muscles 135
6.1. Introduction 137
6.2. McKibben Performance Characteristics 138
6.2.1. Force and contraction characteristics 138
6.2.2. Energy Dissipation 142
6.2.3. Fatigue characteristics 145
6.2.4. Experimental Facilities 145
6.3. McKibben Composition Characteristics 145
6.3.1. Outer Sleeve Configuration 145
6.3.2. Inner Bladder Configuration 148
6.4. McKibben Muscle Configurations 149
6.4.1. Natural Muscle Types to McKibben Configurations 149
6.4.2. Individual McKibben Muscles 149
6.4.3. Bundled McKibben Muscles 152
6.5. New Avenues: Smart McKibben Muscles 159
6.5.1. Smart Braided Sleeves and Inner Bladders 159
6.5.2. Alternative Manufacturing Methods 160
6.5.3. Alternative Braided Sleeves 161

6.5.4. Alternative Actuation Methods 161
6.6. Discussion & Conclusions 162
6.6.1. Summary of Main Findings 162
6.6.2. Limitations of this Study 163
6.6.3. Recommendations for Future Research 164

7. Design of adaptive McKibben artificial muscles 177
7.1. Introduction 179
7.2. Braiding for intelligent sleeves 181
7.2.1. Braiding for linear motion 181
7.2.2. Braiding for twisting motion 185
7.3. Experiments 189
7.3.1. Experimental Setup: Linear motion 189
7.3.2. Results: Linear motion 191
7.3.3. Experimental Setup: Twisting motion 191
7.3.4. Results: twisting motion 193
7.4. Discussion 193
7.5. Conclusion 197
Appendix 7.A 200

8. Design of an artificial muscular network 201
8.1. Introduction 202
8.2. Braiding for multi-directional McKibben Muscles 204
8.2.1. Braiding Technique 204
8.2.2. Case Studies 206
8.3. Experiments 211
8.3.1. Experimental Setup: Bending Actuator 212
8.3.2. Results: Bending Actuator 213
8.3.3. Experimental Setup: Convergent Actuator 213
8.3.4. Results: Convergent Actuator 214
8.4. Discussion and Conclusion 214

9. Design of an electro-magnetic kresling actuator 220
9.1. Introduction 222
9.2. Actuator design 223
9.2.1. Design direction 223
9.2.2. Kresling cylinder 223
9.2.3. Electromagnet 225
9.3. Experimental validation 229

9.3.1. Model verification 229
9.3.2. Final prototype 231
9.4. Discussion 232
9.5. Conclusion 233

Part III: Intelligent Transport 236

10. State of the art aspiration catheters 238
10.1. Introduction 240
10.2. Method 241
10.2.1 Patent search method 241
10.2.2 Classification 242
10.3. Improve positioning – passively 244
10.3.1 Tip shape 246
10.3.2 Tip flexibility 246
10.4 Improve suctioning – passively 246
10.4.1 Aspiration port design: sideways oriented 246
10.4.2 Aspiration port design: distal oriented 247
10.5 Improve positioning and suctioning – actively 250
10.5.1 Variable cross-sectional area 250
10.5.2 Targeted suctioning 251
10.5.3 Extending tip reachability 252
10.6 Discussion 252
10.6.1 Summary of main findings 252
10.6.2 Clinical applications and devices 256
10.6.3 Limitations 258
10.6.4 Recommendations for future research 258
10.7 Conclusion 258
Appendix 10.A 263

11. Design of a conveying tubular transport mechanism 264
11.1 Introduction 266
11.2 Material and methods: Design process 267
11.2.1 Compatibility for minimally invasive surgery 267
11.2.2 Final design 268
11.3 Material and methods: Experimental validation 273
11.3.1 Experimental goal 273
11.3.2 Experimental procedure 275
11.3.3 Data analysis 277

11.3.4 Results 277
11.4 Discussion 280
11.4.1 Summary of main findings 280
11.4.2 Limitations 281
11.4.3 Recommendations 281
11.5 Conclusion 282

12. Design of a toroidal transport mechanism 286
12.1. Introduction 288
12.2. Design and prototyping 288
12.1.1 Bio-Inspiration: Peristalsis 288
12.1.2 Design Requirements 289
12.1.3 Design conveying toroid 290
12.1.4 Fabrication 291
12.1.5 Final Prototype 292
12.2 Experimental validation 293
12.3 Discussion 295
12.4 Conclusion 296

13 Discussion 300
13.1 Findings of this thesis 302
13.1.1 Mechanical Intelligence 302
13.1.2 Part I: Intelligent gripping 302
13.1.3 Part II: Intelligent movement 305
13.1.4 Part III: Intelligent transport 307
13.2 Implementation challenges 309
13.2.1 Scalability and robustness 309
13.2.2 Inclusivity, equality and diversity in robotics 310
13.3 Perspective 311
13.4 Scientific contribution 311

Acknowledgements 316

Curriculum Vitae 318

List of publications 322

Summary

As robots increasingly become part of our daily lives, their expected range of abilities continues to grow and the computational demand placed upon them is increasing. Traditional approaches to robotic design have often focused on enhancing control architectures, sensing capabilities and computational intelligence. Yet, simply scaling up computational systems alone might not be sufficiently effective to operate safely and fluidly in the real world. Robots can benefit from forms of intelligence that emerge naturally from their physical embodiment, complementing computational control.

This perspective leads to a growing emphasis on the robot's embodiment as a source of intelligence. Nature offers a powerful source of inspiration for such ideas. Across ecosystems, organisms have evolved body structures that exploit environmental interactions to ease coordination and lower energy demand. This highlights the potential of designing robots whose intelligence emerges not only from computation, but from their physical design. In other words, the mechanical properties and geometry of the body itself mediate interaction and simplify internal processing. In this thesis, we call this perspective on intelligence *mechanical intelligence*. It is defined as the ability of a robot to respond to external conditions through its physical design. **Chapter 2** described how this perspective compares to existing perspectives on intelligence that were found in literature.

It is currently insufficiently understood how soft robots can be designed for mechanical intelligence, rather than by simply adding softness. Building on this, the main goal of this thesis is to investigate mechanical intelligence in soft robots, inspired by nature, with the potential to enhance functionality beyond structured environments. Constrained and hard-to-reach environments are used as representative application domains, as they place strong demands on robotic embodiment, meaning they could benefit from mechanically intelligent designs. To investigate this idea, this thesis focuses on three fundamental robotic interactions: (1) intelligent gripping, (2) intelligent movement and (3) intelligent transport. These are the basic ingredients of almost any higher-order task a robot might perform. In each case, the aim is to design bodies that behave intelligently by design.

In **Part I**, we investigate how mechanical intelligence can be embedded into soft robots to enable gripping in constrained and hard to reach environments. The work focuses on understanding how compliance and geometry can be exploited to reduce dependence on precise sensing and complex control systems. **Chapter 3** addresses this challenge in the context of minimally invasive surgery, where limited access and safety requirements strongly constrain gripper design. Organisms like the octopus are examined to understand how compliant bodies and material properties enable reliable manipulation in unstructured environments. This results into a suction gripper design that emphasizes adaptability and safety. **Chapters 4** and **5** extend this work by exploring magnetic actuation as an embedded shape-change mechanism. Magnetic stimulation allows rapid and remote deformation. **Chapter 4** reviews shape-morphing strategies based on magnetic actuation, providing design insights for soft systems that can be actuated remotely. **Chapter 5** presents a magnetically actuated, passively deployable suction gripper capable of operating across different surrounding media on complex-shaped surfaces.

In **Part II**, we investigate how mechanical intelligence can be embedded into soft robots to enable maneuvering through constrained and narrow environments. In such settings, there is limited space for dense actuator layouts, motivating movement strategies in which simple actuation inputs generate complex motion by design. **Chapter 6** reviews actuators inspired by biological muscular systems. This review identifies their limitations in reproducing complex motion using simple configurations. **Chapters 7** and **8** address this gap by exploring how commercial manufacturing techniques can be adapted to fabricate soft actuators that internally encode complex deformation while preserving simple actuation. **Chapter 9** extends this principle to continuum robots by enabling localized movement through embodied actuation.

In **Part III**, we investigate how mechanical intelligence can be embedded into soft robots to enable reliable transport in narrow and hard-to-reach environments. The work focused on understanding how the robot's body itself can contribute to the transport of objects rather than relying on external grasping or intricate control strategies. To study the challenges of internal transport under severe spatial and safety constraints, the work focused on medical robotics as a representative application domain. **Chapter 10** presents a review of aspiration catheters used for removing blood clots from the body as a representative transport system, highlighting the strong spatial demands placed on robotic embodiment as well as the sensitivity of these systems to clogging and material variability. **Chapter 11** explores an alternative tissue transport strategy based on a cylindrical conveyor mechanism, demonstrating how transport reliability can be improved through mechanical design rather than control. **Chapter 12** advances this trajectory by working towards a soft solution, resulting in a soft conveying toroid that turns itself inside out in a continuous motion. The toroid forms a shape grip, locking onto an object and conveying it forward even when its geometry, stiffness, or surface properties vary widely.

This thesis demonstrates the potential of mechanical intelligence to enable soft robots to function reliably beyond structured environments. This is particularly relevant for constrained and hard-to-reach environments, where limited space, restricted sensing, and unpredictable interaction conditions challenge robotic design. The proposed soft robotic systems illustrate how mechanical intelligence pave the way toward the integration of soft robots into real-world applications.

Samenvatting

Robots spelen een steeds grotere rol in ons dagelijks leven. Daardoor verwachten we ook steeds meer van wat ze kunnen. Om aan die verwachtingen te voldoen, worden robots uitgerust met geavanceerde besturingssystemen, sensoren en 'computationele intelligentie'. Toch zit er een grens aan wat je kunt bereiken door alleen maar meer rekenkracht toe te voegen. Om goed te kunnen functioneren in de complexe en onvoorspelbare wereld om ons heen, kunnen robots ook gebruikmaken van een andere vorm van intelligentie: intelligentie die ontstaat uit de interactie tussen het robotlichaam en de omgeving.

De natuur laat zien hoe krachtig deze aanpak kan zijn. Dieren en andere organismen maken voortdurend gebruik van hun lichaamsvorm en materiaaleigenschappen om efficiënt te bewegen, zich aan te passen aan hun omgeving en energie te besparen. Hierdoor hoeven zij niet elke beweging actief aan te sturen. Ook bij robots kunnen de vorm, structuur en materialen van het lichaam bijdragen aan intelligent gedrag. In dit proefschrift noemen we dit **mechanische intelligentie**: het vermogen van een robot om door zijn fysieke ontwerp op een slimme manier te reageren op de omgeving. In **hoofdstuk 2** wordt beschreven hoe dit perspectief zich verhoudt tot bestaande opvattingen over intelligentie binnen de wetenschappelijke literatuur.

Hoewel zachte robots vaak worden beschouwd als veelbelovende systemen voor mechanische intelligentie, is nog onvoldoende bekend hoe zulke robots doelgericht ontworpen kunnen worden. In veel gevallen worden zachte materialen toegepast zonder expliciet te onderzoeken hoe hun eigenschappen kunnen bijdragen aan intelligent gedrag. Daarom onderzoekt dit proefschrift hoe inzichten uit de natuur kunnen worden ingezet om mechanische intelligentie in zachte robots te integreren. Daarbij ligt de focus op de inzetbaarheid in moeilijk bereikbare omgevingen, omdat juist daar de beperkingen van traditionele robots duidelijk naar voren komen. Om dit te onderzoeken richt dit proefschrift zich op drie fundamentele functies van robots: **grijpen**, **bewegen** en **transporteren**. Deze functies vormen de basis van veel complexere robotische taken.

In **Deel I** onderzoeken we hoe de integratie van mechanische intelligentie in zachte robots kan bijdragen aan het effectief grijpen van objecten in krappe en moeilijk bereikbare omgevingen. Hierbij wordt verondersteld dat materiaaleigenschappen en geometrische ontwerpkeuzes zodanig kunnen worden benut dat minder complexe sensoren en besturingssystemen nodig zijn. **Hoofdstuk 3** richt zich op minimaal invasieve chirurgie, waar beperkte ruimte en hoge veiligheidseisen grote uitdagingen vormen voor het ontwerp van grijpers. Door te kijken naar organismen zoals de octopus wordt onderzocht hoe flexibiliteit en geometrie kunnen bijdragen aan betrouwbaar grijpen. Dit leidt tot een ontwerp voor een veilige weefselgrijper. In **hoofdstukken 4 en 5** wordt vervolgens onderzocht hoe magnetische materialen kunnen worden gebruikt om zachte robots van vorm te laten veranderen. Daardoor kunnen robots op afstand worden aangestuurd zonder complexe interne besturingsmechanismen. **Hoofdstuk 5** presenteert een magnetisch geactiveerde zuiggrijper die zich automatisch kan uitvouwen en zich op verschillende soorten oppervlakken kan vastgrijpen.

In **Deel II** staat beweging centraal. Hier onderzoeken we hoe mechanische intelligentie zachte robots kan helpen om door nauwe en complexe omgevingen te manoeuvreren. Omdat er in zulke omgevingen vaak weinig ruimte is voor motoren en andere aandrijfsystemen, is het belangrijk dat eenvoudige aansturing toch tot complexe bewegingen kan leiden. **Hoofdstuk 6** geeft een overzicht van actuatoren die zijn geïnspireerd op biologische spieren en bespreekt hun huidige beperkingen. **Hoofdstukken 7 en 8** bouwen hierop voort door te laten zien hoe bestaande productietechnieken kunnen worden aangepast om zachte actuatoren te maken die complexe vervormingen kunnen uitvoeren met een eenvoudige aansturing. **Hoofdstuk 9** laat zien hoe beweging lokaal in een robot geïntegreerd kan worden, waardoor veelzijdige bewegingen mogelijk worden.

In **Deel III** onderzoeken we hoe mechanische intelligentie kan bijdragen aan het transporteren van objecten in nauwe en moeilijk bereikbare omgevingen. Hierbij ligt de nadruk op de rol van het robotlichaam zelf, in plaats van op grijpers of complexe regelalgoritmen. Medische robotica wordt gebruikt als voorbeeldtoepassing. **Hoofdstuk 10** bespreekt aspiratiekatheters die worden gebruikt om bloedstolsels uit het lichaam te verwijderen. Deze systemen tonen aan hoe groot de uitdagingen zijn op het gebied van ruimtegebrek, verstoppingen en variatie in biologisch weefsel. **Hoofdstuk 11** presenteert een alternatief transportsysteem gebaseerd op een cilindrisch transportmechanisme en laat zien hoe een doordacht mechanisch ontwerp de betrouwbaarheid van transport kan vergroten. **Hoofdstuk 12** zet een volgende stap richting volledig zachte transportsystemen. Hier wordt een zachte, ringvormige structuur ontwikkeld die zichzelf tijdens het bewegen voortdurend binnenstebuiten keert. Hierdoor kan deze structuur objecten omsluiten, stabiliseren en transporteren, zelfs wanneer deze sterk verschillen in vorm, stijfheid of oppervlakte-eigenschappen.

Dit proefschrift laat zien dat mechanische intelligentie een veelbelovende manier is om zachte robots beter te laten functioneren in complexe en onvoorspelbare omgevingen. Vooral in moeilijk bereikbare situaties, waar ruimte beperkt is en sensoren niet altijd betrouwbaar werken, kan het ontwerp van het robotlichaam zelf een belangrijke bijdrage leveren aan intelligent gedrag. De resultaten van dit onderzoek laten zien hoe mechanische intelligentie kan bijdragen aan de verdere toepassing van zachte robots in de praktijk.

CHAPTER 01

01

INTRODUCTION

1.1 From factory settings to the real-word

For decades, robots have driven major technological progress. Today, however, we are entering a new transition: robots are no longer confined to factory floors, but are increasingly entering our homes, hospitals, and public spaces. This tighter integration within our lives brings clear benefits: robots can take over repetitive or hazardous tasks, improve efficiency and help address growing labor shortages in sectors such as healthcare, agriculture, and logistics. As robots increasingly work alongside humans, rather than replacing them, they must interact safely and respond effectively to human needs. Likewise, operating in real-world settings, such as assisting patients in healthcare, operating in agriculture under changing weather conditions, or navigating crowded warehouses, demands adaptive behavior as a requirement to function effectively in these dynamic and unpredictable environments [1].

Traditional "rigid" robots generally have limited adaptability to environmental deviations. They often rely on intricate control systems and advanced sensors and actuator layouts, which can increase costs and limits scalability. When operating under dynamic conditions, such as changing terrain, variable object properties or unexpected human interaction, failures often require human intervention. Moreover, conventional safety measures such as physical barriers, safety zones, or restricting interaction only to trained operators, further constrain broader use in real-world settings.

The limitations of rigid robots are addressed in the growing field of soft robotics. Soft robots are often defined as systems that incorporate soft materials, such as silicone rubber, allowing them to interact passively with their surroundings [2, 3]. Similar to conventional rigid robots, soft robotic systems generally consist of actuators and/or end effectors. Actuators are components that generate motion, analogous to muscles in biological organisms, whereas end effectors are components that physically interact with the environment, analogous to human hands. However, what precisely qualifies as a "soft" robot remains an open and actively debated question. Must a robot be entirely soft to fall within this category, or is it sufficient for softness to be embedded locally within a rigid structure? Should softness be interpreted as a material property, or also as a behavioral characteristic caused by compliant or flexible structures? Rather than viewing rigid and soft robotics as two distinct and opposing categories, this thesis adopts the perspective that robotic systems exist along a continuum of compliance. Within this continuum, softness is not defined by the absence of rigid components, but by the extent to which a system embeds mechanical compliance to adapt to its environment. Therefore, in this thesis, the definition of a soft robot is as follows:

Soft robot: *A robotic system that leverages the mechanical compliance of its embodiment to passively adapt to environmental variation.*

Here, mechanical compliance can arise from material softness, structural flexibility, geometric design, or a combination thereof. This allows soft robotic systems to adapt to dynamic conditions without relying directly on complex control algorithms [4]. For example, soft robotic grippers are often designed to passively conform to an object's shape, allowing stable grasping without detailed knowledge of the object geometry or extensive sensory

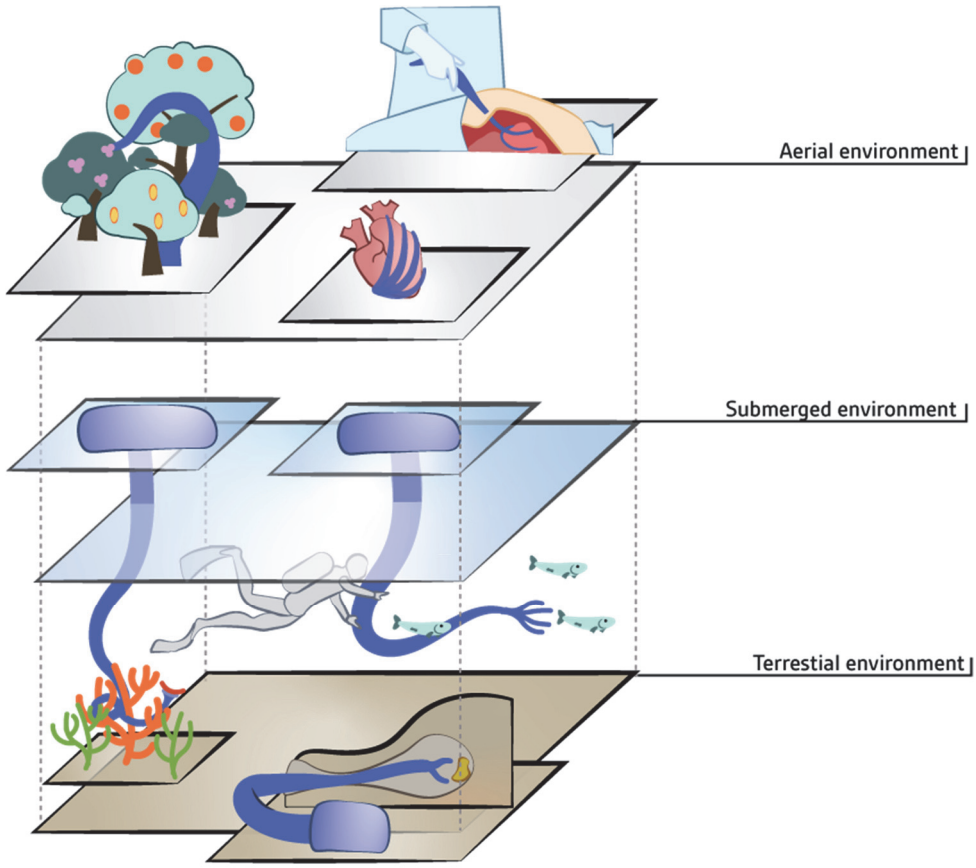


Figure 1.1: **Schematic overview of representative real-world application domains for soft robots.** Across aerial, submerged, and terrestrial environments, robots are increasingly required to operate in unstructured, constrained, and hard-to-reach settings. Variability in geometry, contact conditions, and environmental properties limits the effectiveness of sensing- and actuator-dense approaches, motivating robotic systems whose physical embodiment enables adaptation through safe, reliable interaction. The depicted scenarios illustrate the need for robots capable of maintaining functionality across diverse environments and operating conditions.

feedback. Such embodied adaptation can lead to safer, more reliable interaction as compared to traditional rigid robots, making soft robotics particularly well suited for dynamic, naturally unstructured, and human-centered environments (Figure 1.1) [4]. To understand how such an adaptability emerges, it is helpful to consider the concept "embodied intelligence", which emphasizes that intelligent behavior can emerge from the robot's physical embodiment [5-7]. More specifically, in soft robotics, the coupling between morphology, material properties and their interaction with the environment naturally results in adaptive robotic features [8]. Interaction with the environment can simplify internal processing when coordination is mediated by the mechanical properties and geometry of the physical embodiment itself. In this thesis, the following definition of embodied intelligence is adopted:

***Embodied intelligence**: The investigation of the tight coupling between an agent's body and brain [8].*

1.2 Learning from nature to design for nature

As a relatively young robotic domain, soft-robotic technologies have not yet matured to the point where they can be widely deployed in real-world conditions. While soft robots promise the reduction of computational costs and increased adaptability, their inherent compliancy introduces new challenges such as precision, output force, and robust control in unpredictable environments [9, 10]. For example, a soft robotic gripper's ability to conform to an object's shape comes often with the lack of lifting capacity, its primary functionality. This shortcoming is inherently related to its soft materials properties. Moreover, often the nonlinear behavior of soft robots and their complex contact situations makes their behavior difficult to predict [9]. As softness strongly increases the number of degrees of freedom, theoretically towards infinite, control methods for rigid robots are in their nature less suited for soft robots as they would require too much computational capacity. Therefore, implementation in dynamic real-world environments is still an open challenge.

At the other side, nature shows how organisms thrive in dynamic, unpredictable and unstructured environments. Their bodies have been shaped through millions of years of evolution to match the demands of the habitats they occupy, resulting in morphologies that naturally support effective interaction with their environment [11]. Although soft, continuum structures such as octopus arms, elephant trunks, and earthworms may appear similar at first glance, their forms embed clear environmental specialization [11]. The buoyant underwater habitat of the octopus allows its arms to be large and highly flexible without collapsing under their own weight. In contrast, an elephant trunk must operate in a gravity-dominated environment and therefore incorporates a specialized load-bearing skin that enhances payload capacity [12-14]. Earthworms have evolved in a friction-dominated terrestrial environment, adopting a body plan favorizing soil penetration [11]. These examples illustrate how morphology tunes over long timescales to preserve functionality under environmental constraints**.**

On a much shorter timescale, most organisms with soft, continuum bodies can adapt their morphology in real time, without relying on discrete joints or rigid skeletal elements. The octopus arm provides a clear illustration. Its body contains no bones and consists almost entirely of muscles arranged in multiple layers with different fiber orientations [15]. By selectively activating these layers, the octopus can bend, twist, elongate, and locally stiffen its arm at any point along its length [16, 17]. Coordinating such a large range of possible movements would impose an overwhelming computational burden on the nervous system, but the octopus embeds a clever shortcut: it can temporarily adjust the local softness of its arm. By selectively activating its muscle layers, the octopus forms temporary joints: flexible regions bounded by stiffer segments. These pseudo-joints reduce the degrees of motion and allow the animal to simplify coordination on demand (Figure 1.2) [18-20]. The animal effectively transforms a continuum structure into an articulated, partly rigid, arm whenever the situation requires it. In doing so, the octopus uses its physical embodiment to reduce

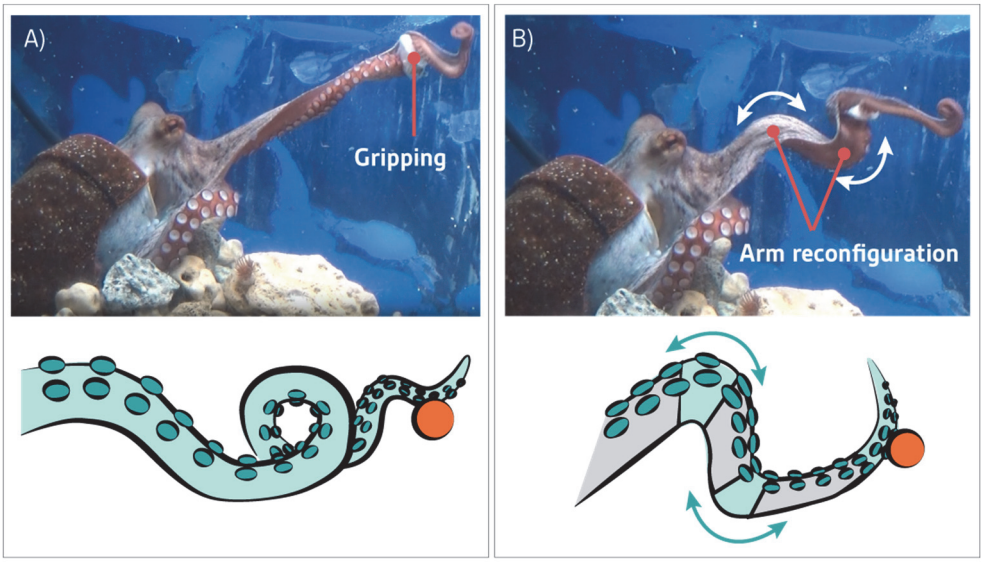


Figure 1.2: Mechanical Intelligence in the octopus arm. a) The octopus arm in fully flexible state gripping a target (reproduced with permission from [19]). b) The octopus arm in articulated state, simplifying coordination by arm reconfiguration (reproduced with permission from [19]). Orange represents prey, such as fish, grey represents stiffened sections and blue represent flexible sections.

neural complexity, relying on the body itself to assist with coordination. These examples highlight an important principle: in nature, adaptability is as much a property of the body as it is of the nervous system. Morphology is shaped over evolutionary timescales to support functional interaction with their environment. Translating these biological principles into engineered systems offers a powerful strategy to reduce control complexity while increasing reliability in uncertain conditions. This design approach in which nature serves as inspiration source for engineering solutions is commonly referred to as bio-inspired design [21].

1.3 Mechanical intelligence for highly constrained conditions

In this thesis, we translate this bio-inspired perspective on adaptability into robotic design by placing the physical body of the robot at the center of adaptation. In such designs, functionality is not preserved solely through sensing or control, but through physical structures deliberately shaped to respond to environmental demands. This perspective motivates a more specific form of embodied intelligence in robotic systems, referred to as mechanical intelligence. While the concept of mechanical intelligence has longer existed in structural engineering, it has not yet been systematically defined or explored in the context of soft robotics [19]. In this thesis, mechanical intelligence is defined as follows:

***Mechanical intelligence**: A robot's ability to respond to external conditions encoded in its body [22].*

Within the scope of this work, external conditions are understood as task-dependent requirements imposed by the operating environment, such as surface properties, load conditions or spatial constraints. A system is considered mechanically intelligent only if its responses preserve or extend its intended functionality. A particularly relevant application domain in which the benefits of mechanical intelligence become apparent is operation in confined and hard-to-reach environments. In such settings, space is limited and environmental geometries are often complex or unknown. Reliable sensing can be difficult and failures costly or dangerous. Such environments could benefit from robots whose bodies themselves contribute to adaptation and coordination. By embedding mechanical intelligence into the robot's body, a single simple input can lead to different behaviors depending on how the robot physically interacts with its surroundings. This makes them potentially well suited for safe, adaptive interaction in situations where precise modeling and explicit control are infeasible. Potential representative application domains include minimally invasive surgical tools navigating inside the human body, continuum robots operating in cluttered or narrow spaces, underwater systems, and grippers functioning in confined or submerged environments (Figure 1.1). Interestingly, these applications differ strongly in scale while sharing similar constraints, making mechanical intelligence an attractive general design strategy.

1.4 Goal of this thesis

While soft robotics and bio-inspired design are well-established fields, there is a clear scientific gap in the understanding of how mechanical intelligence can be integrated into the design process of soft robots. **Therefore, this thesis aims to investigate mechanical intelligence in soft robots, inspired by nature, with the potential to enhance functionality beyond structured environments.** Constrained and hard-to-reach environments are used throughout this thesis as motivating and representative application domains, as they place strong demands on robotic embodiment, meaning they could benefit from mechanically intelligent designs. To reach this goal, robotic interactions are studied around three core robotic functionalities: (1) intelligent gripping, (2) intelligent movement and (3) intelligent transport. Together they form the functional building blocks for higher level functions like assembly, delivery or assistance. The gripping functionality enables direct interaction with the environment by allowing the robot's end effector to manipulate objects. The movement functionality ensures that the robot can position itself accurately, enabling accurate placement and relocation of the end effector within the environment. The transport functionality allows the robot to relocate external objects from one location to another. Each of these functionalities address major challenges in dynamic real-world environments. For gripping, the robot requires interaction with fragile or irregular objects under limited visibility and restricted space for sensing. For movement, the robot requires maneuvering through unpredictable, cluttered, or narrow environments. For transport, the robot has to handle diverse objects safely and efficiently within constrained spaces. Ultimately, combining these functional building blocks results in a versatile multifunctional soft robotic system.

This thesis exploits bio-inspiration to explore design strategies for embedding mechanical intelligence into soft robots. The scientific contribution of this thesis lays in

addressing that gap by investigating what mechanical intelligence means for soft robots and how it can be embedded into their physical embodiment. Specifically, the thesis examines how the three core robotic functionalities can be integrated within the intrinsic architecture of soft robotic systems. The focus is on the following research objectives:

- First, **this thesis investigates how mechanical intelligence can be embedded into soft robotic end effectors to enable gripping beyond structured environments.** The focus is on understanding how compliance and geometry can be exploited to reduce dependence on precise sensing and explicit control, particularly in situations where object properties and interaction conditions are unknown or variable.
- Second, **this thesis investigates how mechanical intelligence can be embedded into soft robotic actuators to enable movement beyond structured environments.** The focus is on understanding how actuator compliance and geometry can enable diverse and coordinated movement patterns to emerge from simple actuation inputs, reducing reliance on explicit control and complex actuator combinations.
- Third, **this thesis investigates how mechanical intelligence can be embedded into soft robotic systems to enable transport beyond structured environments.** The focus is on understanding how the robot's body itself can contribute to the transport of objects through physical interaction rather than relying on external grasping or complex control strategies.

1.5 Thesis outline

The schematic illustration in Figure 1.3 visualizes the outline of this thesis. *Chapter 2* opens by providing a structured overview of different perspectives on intelligence in robotics found in literature. It then presents a detailed discussion and formalization of mechanical intelligence for soft robotics, emphasizing how a robot's responsiveness to real-world conditions can be encoded directly into its physical embodiment.

The remainder of the thesis is subdivided into three parts, corresponding to the three core robotic functionalities: (1) intelligent gripping, (2) intelligent movement and (3) intelligent transport. The first part, **Intelligent Gripping**, focuses on embedding mechanical intelligence into soft robotic end effectors to enable reliable interaction in constrained and hard to reach environments. *Chapter 3* addresses this challenge in the context of minimally-invasive surgery, where limited access and safety requirements strongly constrain gripper design. *Chapters 4* and *5* extend this work by investigating magnetic actuation as an embedded shape-change mechanism. Magnetic stimulation allows rapid, remote deformation. *Chapter 4* reviews shape-morphing strategies based on magnetic actuation, providing design insights for soft systems that can be actuated remotely. *Chapter 5* presents a magnetically actuated, passively deployable suction gripper capable of operating across different surrounding media on complex-shaped surfaces.

The second part, **Intelligent Movement**, focuses on embedding mechanical intelligence into soft robotic actuators to enable maneuvering through constrained and narrow environments. In such settings, there is limited space for dense actuator layouts, motivating movement strategies in which simple actuation inputs generate complex motion by design. *Chapter 6* reviews actuators inspired by biological muscular systems, identifying their

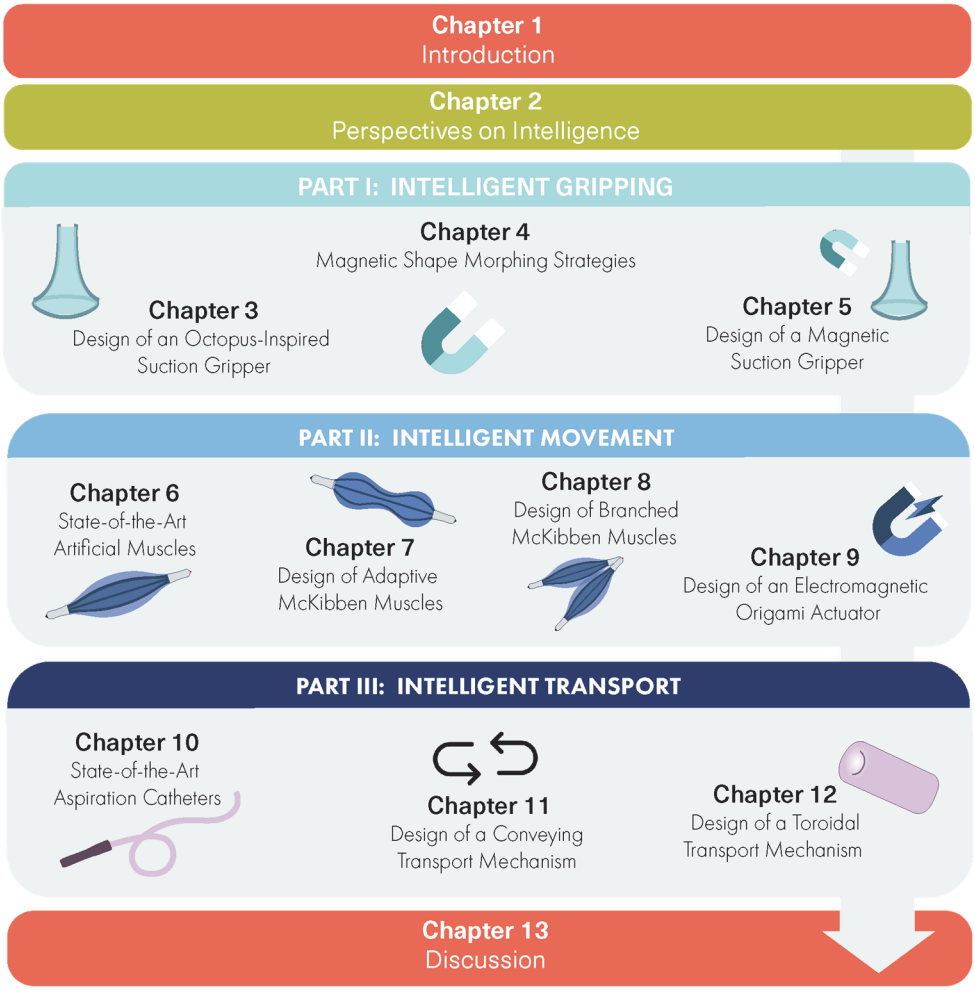


Figure 1.3: Schematic layout of this thesis.

limitations in reproducing complex motion using simple configurations. *Chapters 7* and *8* address this gap by exploring how internal structure and manufacturing strategies can encode complex deformation behaviors within a single actuator while preserving simple actuation. *Chapter 9* extends this principle to continuum robots by enabling localized movement through embodied actuation.

The third part, **Intelligent Transport**, examines how mechanical intelligence can be embedded into soft robotic systems to enable reliable transport in narrow and hard-to-reach environments. This part addresses the challenge in the context of minimally-invasive surgery, where limited access and strict safety requirements have strongly shaped device design. *Chapter 10* presents a review of aspiration catheters used for removing blood clots from the body as a representative transport system, highlighting the strong spatial demands placed on robotic embodiment as well as the sensitivity of these systems to

clogging and material variability. *Chapter 11* explores an alternative tissue transport strategy based on a cylindrical conveyor mechanism, demonstrating how transport reliability can be improved through mechanical design rather than control. *Chapter 12* advances this trajectory by working towards a compliant solution, translating internal tissue transport into a soft robotic system in which adaptive transport functionality is encoded directly into a soft body.

Finally, *Chapter 13* addresses the main findings of this thesis and provides recommendations for future research.

References

[1] S. Aracri *et al.*, "Soft robotics: A route to equality, diversity, and inclusivity in robotics," *Soft robotics,* vol. 11, no. 6, pp. 903-910, 2024, doi: 10.1089/soro.2023.0225.

[2] C. Lee *et al.*, "Soft robot review," *International Journal of Control, Automation and Systems,* vol. 15, no. 1, pp. 3-15, 2017, doi: 10.1007/s12555-016-0462-3.

[3] D. Rus and M. T. Tolley, "Design, fabrication and control of soft robots," *Nature,* vol. 521, no. 7553, pp. 467-475, 2015, doi: 10.1038/nature14543.

[4] B. Mazzolai *et al.*, "Roadmap on soft robotics: multifunctionality, adaptability and growth without borders," *Multifunctional Materials,* vol. 5, no. 3, p. 032001, 2022, doi: 10.1088/2399-7532/ac4c95.

[5] R. Pfeifer and J. Bongard, *How the body shapes the way we think: a new view of intelligence*. MIT press, 2006.

[6] R. Pfeifer, H. G. Marques, and F. Iida, "Soft Robotics: The Next Generation of Intelligent Machines," in *IJCAI*, Beijing, China, 2013, vol. 2013: AAAI Press, pp. 5-11.

[7] D. Zambrano, M. Cianchetti, and C. Laschi, "The morphological computation principles as a new paradigm for robotic design," in *Opinions and outlooks on morphological computation*: University of Zurich, 2014, pp. 214-225.

[8] M. Sitti, "Physical intelligence as a new paradigm," *Extreme Mechanics Letters,* vol. 46, p. 101340, 2021, doi: 10.1016/j.eml.2021.101340.

[9] Y. Zhang, P. Li, J. Quan, L. Li, G. Zhang, and D. Zhou, "Progress, challenges, and prospects of soft robotics for space applications," *Advanced Intelligent Systems,* vol. 5, no. 3, p. 2200071, 2023, doi: 10.1002/aisy.202200071.

[10] K. Ghazi-Zahedi, "Morphological intelligence," *Cham: Springer,* 2019.

[11] B. Mazzolai, E. Del Dottore, T. Speck, N. Rowe, and C. Laschi, "Energy-saving movement strategies in animals and plants for robot design," *Nature Reviews Bioengineering,* vol. 3, no. 11, pp. 921-938, 2025, doi: 10.1038/s44222-025-00344-z.

[12] A. K. Schulz *et al.*, "Elephant trunks use an adaptable prehensile grip," *Bioinspiration & biomimetics,* vol. 18, no. 2, p. 026008, 2023, doi: 10.1088/1748-3190/acb477.

[13] A. K. Schulz *et al.*, "Skin wrinkles and folds enable asymmetric stretch in the elephant trunk," *Proceedings of the National Academy of Sciences,* vol. 119, no. 31, p. e2122563119, 2022, doi: 10.1073/pnas.2122563119.

[14] A. K. Schulz *et al.*, "Second harmonic generation imaging reveals entanglement of collagen fibers in the elephant trunk skin dermis," *Communications Biology,* vol. 8, no. 1, p. 17, 2025, doi: 10.1038/s42003-024-07386-w.

[15] W. M. Kier, "The diversity of hydrostatic skeletons," *Journal of Experimental Biology,* vol. 215, no. 8, pp. 1247-1257, 2012, doi: 10.1242/jeb.056549.

[16] W. M. Kier, "The musculature of coleoid cephalopod arms and tentacles," *Frontiers in cell and developmental biology,* vol. 4, p. 10, 2016, doi: 10.3389/fcell.2016.00010.

[17] W. M. Kier and M. P. Stella, "The arrangement and function of octopus arm musculature and connective tissue," *Journal of morphology,* vol. 268, no. 10, pp. 831-843, 2007, doi: 10.1002/jmor.10548.

[18] D. M. Sivitilli, J. R. Smith, and D. H. Gire, "Lessons for robotics from the control architecture of the octopus," *Frontiers in Robotics and AI,* vol. 9, p. 862391, 2022, doi: 10.3389/frobt.2022.862391.

[19] B. Hochner, L. Zullo, T. Shomrat, G. Levy, and N. Nesher, "Embodied mechanisms of motor control in the octopus," *Current Biology,* vol. 33, no. 20, pp. R1119-R1125, 2023, doi: 10.1016/j.cub.2023.09.008.

[20] G. Sumbre, G. Fiorito, T. Flash, and B. Hochner, "Octopuses use a human-like strategy to control precise point-to-point arm movements," *Current Biology,* vol. 16, no. 8, pp. 767-772, 2006, doi: 10.1016/j.cub.2006.02.069.

[21] M. Helms, S. S. Vattam, and A. K. Goel, "Biologically inspired design: process and products," *Design studies,* vol. 30, no. 5, pp. 606-622, 2009, doi: 10.1016/j.destud.2009.04.003.

[22] V. G. Kortman, B. Mazzolai, A. Sakes, and J. Jovanova, "Perspectives on intelligence in soft robotics," *Advanced Intelligent Systems,* vol. 7, no. 1, p. 2400294, 2025, doi: 10.1002/aisy.202400294.

01

CHAPTER 02

PERSPECTIVES ON INTELLIGENGE IN SOFT ROBOTICS

02

ABSTRACT

Engineers frequently aim to streamline environmental factors to facilitate the effective operation of robots. However, in nature, environmental considerations play a crucial role in shaping the embodiment of organisms. To comply robots with the complexity of real-world environments, embedding similar intelligence is key. In the field of soft robotics, various approaches offer insight into how intelligence can be integrated into artificial agents. A discussed topic is the intricate relationship between the brain and the body at the core of intelligence in robots. The goal of this paper is, therefore, to unravel the strategies to implement different types of intelligence currently adopted in soft robots. A classification is made by making a distinction between agents that adapt to their environment by (1) their adaptive shape, (2) their adaptive functionality and (3) their adaptive mechanics. Additionally, we distinguished the perspectives on intelligence based on their computational approach: centralized computation, decentralized computation or embedded computation. It is concluded that a tailored robotic design approach attuned to specific environmental demands is needed. To unlock the full potential of soft robots, a fresh perspective on embodied intelligence is described, so-called mechanical intelligence, emphasizing the robot's responsiveness to changing external conditions of a real-world environment.

Published as:
Kortman, V. G., Mazzolai, B., Sakes, A., & Jovanova, J. (2025). Perspectives on intelligence in soft robotics. *Advanced Intelligent Systems, 7*(1), 2400294.

2.1 Introduction

The remarkable adaptability and versatility found in various organisms in nature have long captivated the scientific community. Examples include the hyper-redundant arms of cephalopods enabling multi-modal locomotion, the soft bodies of snakes that allow for navigating through tight spaces, and the design of the human hand that allows for precise grasping capabilities. The properties of these natural systems, combining soft and rigid materials, enable them to respond effectively to environmental changes solely through physical interactions.

In contrast, conventional man-made robots typically display limited adaptability due to their rigid design and construction from materials like stainless steel, aluminium, or titanium, with Young's moduli in the order of 10^9–10^{12} Pascal [1, 2]. As a result, conventional rigid robots are generally suitable to perform predefined tasks in controlled and known environments and are generally optimized to perform repetitive tasks. To design robots that are able to perform well in a real-world environment, which is unknown and highly dynamic, the classic approach of robot design should be adapted.

In recent years, a new class of robots started to emerge that incorporate soft materials similar to what is found in nature [3]. Soft robots are typically made of hyper-elastic materials, such as silicone rubbers, with Young's moduli in the range of 10^4–10^9 pascal [2]. Soft robots typically inherent the ability to execute tasks in unknown, dynamic and unpredictable environments. Just like organisms in nature, they exploit their material properties and shape to passively interact with the environment [2, 4]. Researchers have also made significant progress in developing soft robots that possess the unique ability to heal their body structure, akin to the self-recovery mechanisms observed in natural organisms [5, 6]. This makes soft robots suitable for a wide range of applications, from

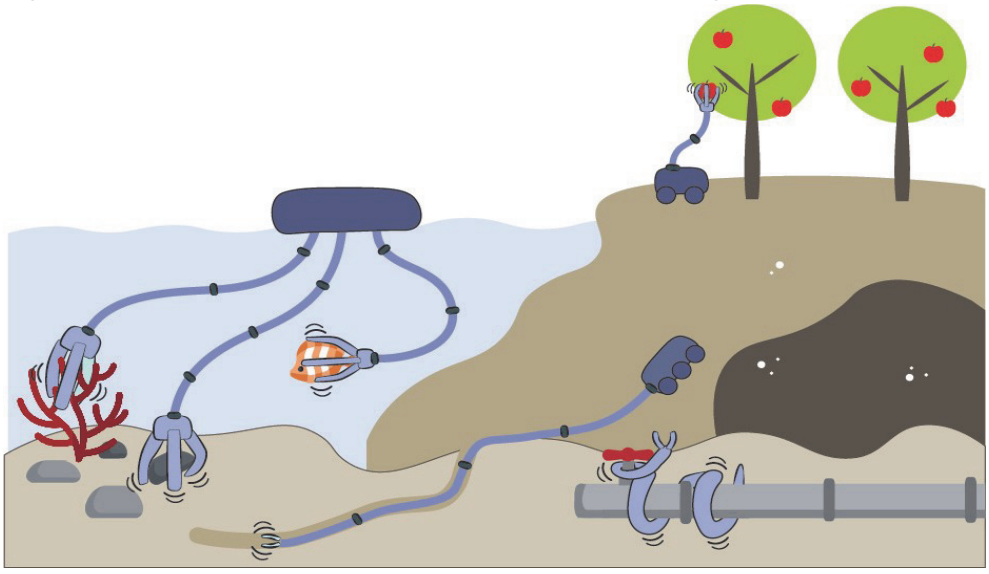


Figure 2.1: Soft robots for deep-sea exploration and terrestrial applications passively adapting to the changing circumstances of the challenging environment.

infrastructure inspection to space applications and deep-sea exploration (Figure 2.1) [3, 7]. Moreover, the material properties of soft robots considerably reduce the risk of harm made during impact [2], which makes them especially suitable for human-machine interaction or interaction with delicate objects, in medical applications or the agro-food industry [2].

Unlike their inspiration sources from nature, soft robots encounter challenges that are inherently associated with their material properties. These challenges currently inhibit their full implementation in real-world applications. Generally, the main challenges these robots encounter are related to their lack of output forces [8] and their unpredictable behavior. The former is mainly related to the properties of the soft actuators embedded in soft robots, which generally generate only low contact forces. The latter is caused by the highly nonlinear behavior of soft robots and their complex contact situations, both a result of their soft material properties. The theoretically unlimited degrees of freedom make standard control methods for rigid robots not applicable, which challenges precise control [7]. Again, the adaptive properties that facilitate the soft robot's intelligent adaptive behavior, simultaneously impede their actual use in real-world applications. Currently, compromises are being made by, for instance, applying moderate softness or only local soft properties, resulting in moderate contact forces or moderate adaptive features.

The ability to integrate intelligence into soft robots without compromising their functionality emerges as a concern. Leg & Hunter [9] define intelligence as '*the ability of an agent to achieve goals in a wide range of environments*'. The adaptive properties of soft robots make them promising candidates for incorporating intelligence, as they can readily respond to a wide range of environmental conditions. By designing soft actuators [10], soft sensors [11], and even soft logic [12, 13] and memory [14, 15], the trend is to develop one monolithic soft structure as an all-in-one system [16, 17], which opens up opportunities for fully autonomous soft robots. Nevertheless, the full realization of this potential depends upon overcoming the existing challenges associated with their soft and highly nonlinear material properties.

In the field of soft robotics, various approaches offer insights into how intelligence can be integrated into artificial agents. A topic of debate is the intricate relationship between the brain and the body at the core of intelligence in robots. Figure 2.2 presents a visual representation of diverse perspectives concerning intelligence embedded within artificial bodies, each emphasizing varying degrees of consideration for the role of the body in the process of incorporating intelligence into robots. These perspectives are defined as follows:

- Artificial intelligence: *'A cognitivist view on intelligence with the focus on brain and central processing. [18]'*
- Embodied Intelligence: *'The investigation of the tight coupling between an agent's body and brain. [19]'*
- Morphological Intelligence: *'The reduction of computational cost for the brain (or controller) resulting from the exploitation of the morphology and its interaction with the environment. [8]'*
- Physical Intelligence: '*Physically encoding sensing, actuation, control, memory, logic, computation, adaptation, learning and decision-making into the body of an agent [19]'.*

- 'Mechanical Intelligence: *'An artificial agent's degree of responsiveness to changing external conditions encoded by the programmed states of its body.'*

The multi-disciplinary landscape of this field of incorporating intelligence in agents led to the adoption of a wide range of technologies. Other reviews describe advances in perceptive intelligence in soft robotics [20], machine learning methods for soft robotics [21], the bio-inspired evolution in soft robotics [22], or summarize the research of (modelling) embodied intelligence in soft robotics [23-25]. This review paper stands out by incorporating and comparing all the major perspectives on intelligence in soft robotics. It not only discusses and compares these perspectives, but also categorizes the strategies typically employed by soft robots. The goal of this paper is, therefore, to unravel the strategies to implement different types of intelligence currently adopted in soft robots. We uniquely center our attention on the design of robots tailored for intricate environments through embodied intelligence. By doing so, we aim to offer valuable insights into state-of-the-art developments and pave the way for future development in this rapidly evolving multidisciplinary field.

The structure of this review is organized as follows: Section 2.2 delves into the various layers of intelligence depicted in Figure 2.2 and listed above, moving from the outermost to the innermost layers. Sections 2.2.1 through 2.2.3 concentrate on the official definitions of the different perspectives, clarified with examples. Section 2.2.4 provides a comparative

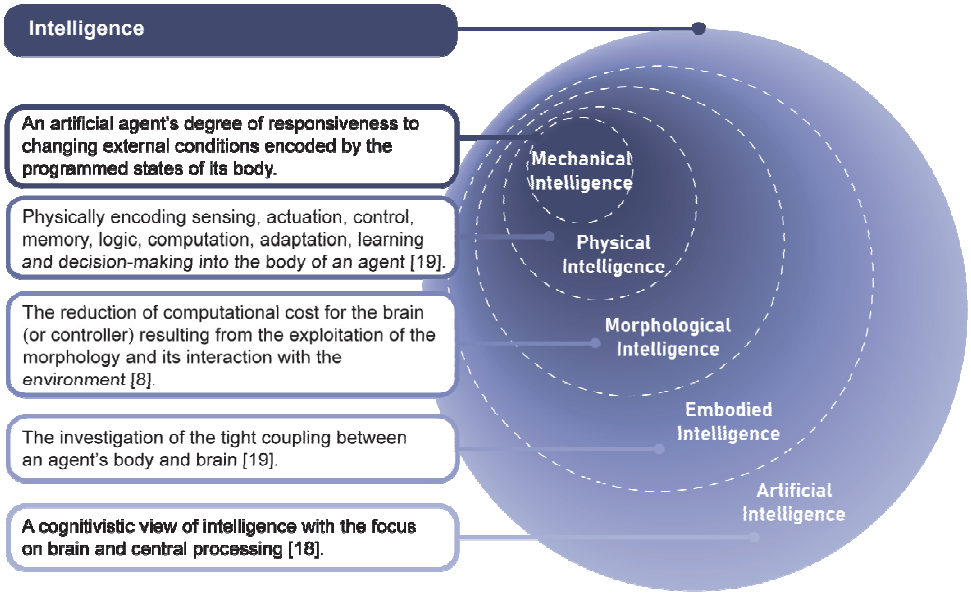


Figure 2.2: Schematic overview of the different perspectives of intelligence in artificial agents. At the left, the official definitions of the different concepts of intelligence are stated. As the core, the concept of mechanical intelligence is presented, which is a fresh perspective on intelligence emphasizing the robot's responsiveness to changing external conditions of a real-world environment. The layers transition from an emphasis on central processing (outermost) to a focus on embedded processing (innermost).

analysis of the computational systems used to embed intelligence in soft robotics. In Section 2.3 we describe a fresh perspective on intelligence, called mechanical intelligence, which emphasizes responsiveness to environmental requirements, see Figure 2.2.

2.2 Peeling the layers of intelligence

2.2.1 Artificial intelligence

Artificial Intelligence (AI) mainly focuses on the computational engine of the robot [18]. This approach is also known as computational intelligence, the classic approach of intelligence, GOFAI (Good Old-Fashioned Artificial Intelligence), or the symbol processing approach [26]. In this approach, the robot's body is usually considered a source of noise that needs to be compensated by its software, whereas the hardware of the robot is usually perceived as the facilitation of the software [18]. Robots based on AI are generally successful in factory environments with controlled conditions, such as situations involving stable movement, constant geometries, constant orientation or known terrain [18]. Examples are industrial robotic arms [27] or humanoid robots such as the humanoid Asimo developed by Honda [4, 28]. Current advancements in AI demonstrate robots that can handle unstructured terrain by, for example, reinforced learning. However, these robots are associated with high computational costs and lack the flexibility to perform different autonomous functionalities in unknown environments [29].

2.2.2 Embodied intelligence

A more modern approach to intelligence was introduced in the mid-1980s, called embodied intelligence, or embodied artificial intelligence. This approach provides a new perspective on intelligence focused on the complex interaction between the robot's embodiment and environment [18]. In this perspective, the robot's physical body is designed in such a way that it eases its internal processing when interacting with the environment. In other words, the robot's control system is mediated by the mechanical properties and geometry of its embodiment [30]. Robots incorporating embodied intelligence are typically more resilient in real-world applications.

Noticeably, organisms in nature master embodied intelligence to respond to real-world situations. Their development is the result of a long evolutionary process. Similarly, the embodied approach emphasizes that the development of robots should focus on their brain-body coevolution, where the brain and body should evolve together. The Embodied Artificial Evolution describes that robots might evolve out of a large pool of genotypes considering materials, components and robot systems [31]. This would result in powerful robots with their material and morphological composition properly exploited for their task-environment performance [31, 32]. Morphological computation is a central concept in the field of embodied intelligence [33], of which Pfeifer *et al*. gave the following definition: '*Morphological computation is based on the processes conducted by the body, that otherwise would be performed by the brain*' [4, 18]. However, the concept of embodied intelligence can be drawn further as, in essence, its focus lies in investigating the tight coupling between an agent body and brain [19].

We identified two approaches for incorporating embodied intelligence into an agent: 1) employing either a decentralized computational system or 2) an embedded computational system. The latter approach is particularly widespread in soft robots. To guide new researchers in the field of embedded computation, we identified three primary strategies currently used to apply embedded computation in soft robots, which will be further discussed below.

2.2.1 Decentralized computation

A way to incorporate embodied intelligence in an agent is by applying decentralized computation, which is in contrast with the centralized computation approach related to AI. Agents using decentralized computation embed conventional controllers locally within their embodiment. A decentralized control system gathers information from local feedback and control signals, with less emphasis on the centralized global state of the agent [34]. An example of an agent that integrates a decentralized control- and feedback system is the octopus. The octopus would be burdened with a highly complex system to control its hyper-redundant arms when its processing would only be performed centrally. The specially arranged anatomy of the octopus' nervous system makes that the majority of its nerve cells are located at the periphery, which is close to the motor and sensory information flow from the arms [35] (Figure 2.3a). This means that the processing of the arm's motor control is partially off-loaded from the central nervous system towards the peripheral nervous system [35], as the neuromuscular system of the arm is able to autonomously execute motor programs [36]. This is emphasized by the octopus' arm which, after being amputated, remains capable of activating motor programs by feedback control due tactile sensory stimulation [37]. In summary, the decentralization of the arm's control system offloads the octopus' overall central control system.

Next to these complex control systems, decentralized computation can also be observed in simple reflexes, such as the patellar reflex. Reflexes showcase a local network of sensory neurons and motor neurons that facilitates a fast response to a stimulus. In the case of the patellar reflex, the stretch of the patellar tendon results in an automatic contraction of the quadriceps muscle. This mechanism, responsible for maintaining balance during walking, functions without interference from the central brain. Reflexes are often useful in situations that require rapid and autonomous responses, for instance during emergencies.

Moreover, a decentralized arrangement of sensory structures could enhance the performance of the feedback system. For example, the non-homogeneous arrangement of the light-sensitive cells in the compound eyes of house flies compensates for the phenomenon of motion parallax [38, 39]. In plants, command centers operate at the level of apexes. This arrangement serves as inspiration for robots that perform lateral motion detection. Another example of space-efficient imaging can be found in the human retina, in which the density of photoreceptors is highest at the center and gradually decreases towards the periphery of the visual field [40] (Figure 2.3a). This results in an optimal balance between resolution and required computational power. By focusing the high-resolution region toward the point of interest, this arrangement ensures an optimal visual information flow [40].

In addition to using decentralized computation, embodied intelligence can be achieved by embedding computation directly into the body of an agent, a process we define as embedded computation. Unlike decentralized computation, which involves integrating conventional controllers or central computation into the embodiment, embedded computation involves embedding intelligence in the embodiment itself. We made a classification of the main strategies that are currently employed to apply embedded computation in soft robots. These soft robots are divided into three distinct groups:

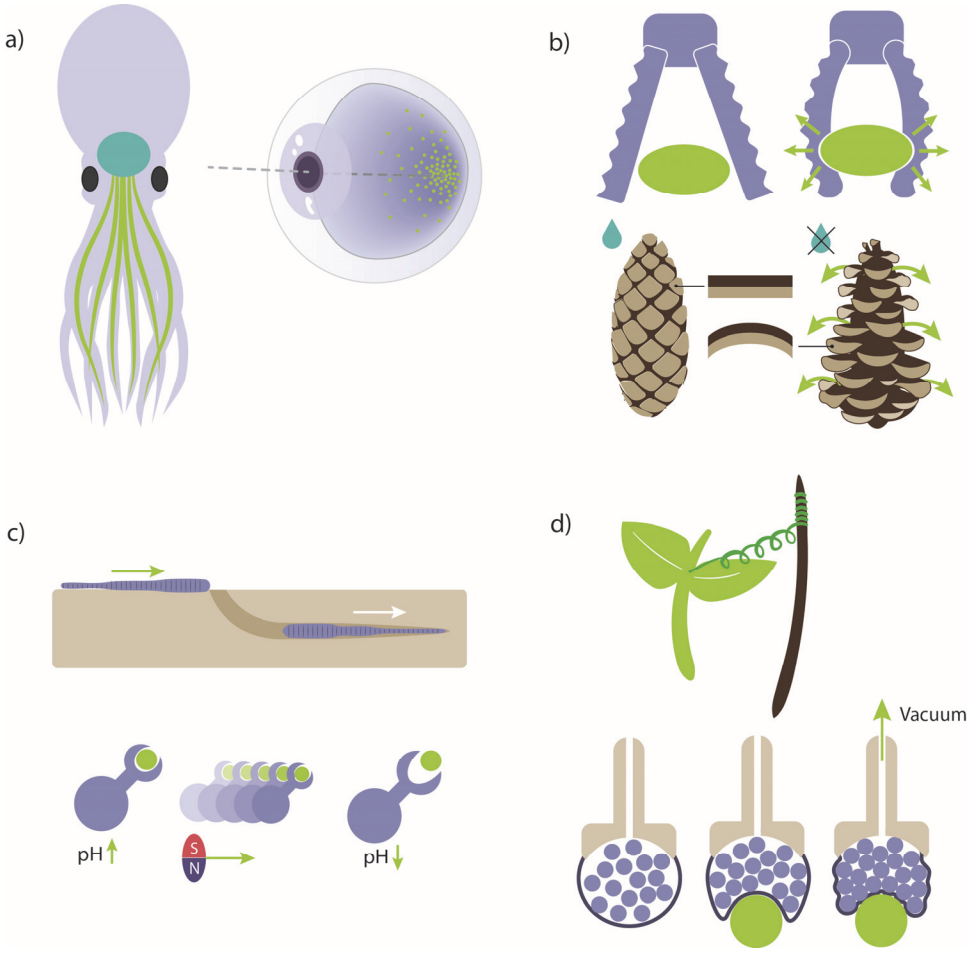


Figure 2.3: Illustration of embodied intelligent agents. a) Left: The decentralized control system of the octopus, in which the central brain and optical lobes are visualized in blue and the peripheral nerve system in green. Right: The decentralized sensing system of the eye, in which the decentral arranged photoreceptors are visualized in green. b) Illustration of embodied intelligence through adaptive shape. Top: The passively adaptive grip of a soft gripper that adapts to different target objects. Bottom: A pine cone opens its scales due to the humidity of the environment. c) Illustration of embodied intelligence through adaptive functionality. Top: Earthworm adapting its shape to optimize its functionality during locomotion in air and locomotion in soil. It has been shown that earthworms only locomote using the first segments in soil. Bottom: Soft microrobot adapting its functionality due to its embedded magnetic particles and pH-sensitive materials. d) Illustration of embodied intelligence through adaptive mechanics. Top: Tendril coil serving as a spring-damper system to support the plant. Bottom: Variable stiff soft gripper which adapts its stiffness when vacuum is applied.

- **Adaptive shape:** Agents in this category embed the ability to adapt their physical configuration in response to environmental cues. Their functionality is facilitated or improved by these adaptive properties.
- **Adaptive functionality:** Agents in this category dynamically adjust their functionality depending on situational demands, which results in multi-functional agents.
- **Adaptive mechanics:** Agents in this category embed the ability to adapt their mechanical properties to the conditions of a new environment.

It must be noted that the groups are not mutually exclusive, as certain agents can exhibit characteristics or features that align with multiple categories concurrently. In such cases, these agents possess attributes or features that place them within the scope of more than one category, indicating an overlap or intersection between the defined groups. Such as a variable stiff soft gripper that both adopts an adaptive shape and adaptive mechanics or an earthworm that both adopts adaptive shape and adaptive functionality, as explained in more detail below. The goal of these groups is not primarily to establish a distinct categorization, but rather to provide inspiration and enhance clarity of the different intelligent approaches found in nature and artificial agents.

Embedded computation by adaptive shape

Generally, soft robots are associated with embodied intelligence due to their soft material properties that adapt to the environment. Soft pneumatic multi-fingered grippers are typical examples of robots that show a control system with embedded computation by passively adapting their shape to the environment. These grippers' behavior is defined by the interaction between their body and the target object. The compliant properties of the individual pneumatic fingers shape the gripper passively around the pressure points of the targeted object, which results in a universal under-actuated gripper [8, 41] (Figure 2.3b). An example of such a gripper making use of contact-driven deformation is the soft gripper developed by Ilievski *et al.* [42], which is able to lift various shaped objects, such as a raw egg and a mouse. Other examples are the multi-fingered robot hand developed by Suzomori *et al.* [43] or the soft pneumatic gripper for delicate surgical manipulation developed by Low *et al.* [44]. These soft pneumatic fingers are also known as Fluidic Elastomer Actuators (FEA), PneuFlex actuators, or Pneumatic Networks (PneuNets) [41]. Next to pneumatic actuation, these soft manipulators can be actuated by tendons, shape-memory materials and other active materials such as hydrogels, or they can be fully contact-driven [41, 45]. Their soft material properties make them passively adaptive to their environment, easing their internal processing. Embedded feedback control is shown in the soft pneumatic fingers developed by Joshi and Paik [46]. These pneumatic fingers estimate their output force and displacement without additional sensors, but by the use of their intrinsic sensing capabilities. Due to their compliant properties, the generated output force and finger displacement result in internal pressure and volume change [46]. This means that the internal properties of the pressure and volume provide feedback regarding the state of the soft pneumatic finger, so the state can be adapted to grasp an object

safely. Another example of a soft gripper that incorporates a feedback system with embedded computation is developed by Gossweiler *et al.* [47]. Due to the embedded mechanochronic polymer, this gripper reacts to stress by changing its color. The color of mechanochronic polymer changes depending on the gripper's level of bending. This enables easy assessment of whether the gripper is currently in a gripping state or a releasing state.

In nature, plants offer a wide variety of inspiration for the integration of embodied intelligence in soft bodies, as plants show intelligent behavior within a brain-less body, which means centralized computation is not available [48, 49]. There is a large variety of plants that react to environmental stimuli by a shape change [49]. An example is the Venus flytrap, which reacts to an external force, e.g. the touch of an insect, by closing its trap due to its bi-stable joint [50]. This mechanism has served as inspiration for a variety of soft robots, such as the compliant shading device Flectofold developed by Korner *et al.* [51], the magnetically actuated bi-stable robot developed by Zhang *et al.* [52], the temperature-actuated snapping hydrogel sheet developed by Fan *et al.* [53], the hygroscopic bilayer structure developed by Lunni *et al.* [54] or the pneumatically actuated bi-stable gripper developed by Pal *et al.* [55]. For a systematic overview of artificial Venus Flytraps, we would like to refer to the study of Esser *et al.* [56]. Many plants deform passively by taking up water from the environment to swell their hygroscopic cells [49]. Depending on the architecture of these hygroscopic cells in combination with non-swelling cells, bi-layered structures are created that show specific deforming behavior. Examples of plants stimulated by humidity are pine cones, which seed scales close when subjected to a humid environment and open when subjected to a dry environment [49] (Figure 2.3b). The direction of deformation of the scales is encoded in the embedded fibers. Non-living agents, such as pine cones or plant seeds [57], are of particular interest as their behavior is completely dependent on their embedded computation. This phenomenon served as inspiration for the development of autonomous soft robots, such as the 4D-printed flap structures that autonomously deform due to changes in environmental humidity [58]. Climbing plants exhibit a similarly remarkable manifestation of embodied intelligence, as they effectively determine their growth direction and attachment points despite the absence of a central nervous system. Similarly, in the apex region of plant roots, the roots display an ability to 'decide' their growth direction. The embedded nature of these decision-making processes, especially in the case of roots lacking visual perception, highlights the intricate and distributed mechanisms at play.

Embedded computation by adaptive functionality

Soft robots possess the unique ability to deform their bodies due to their material properties, enabling them to function differently in varying environments. This principle finds parallels in nature, where certain organisms showcase the capability to deform their bodies to achieve adaptive functionalities. For instance, consider the earthworm, which exhibits remarkable deformable body patterns depending on the desired function, whether it is locomotion or burrowing (Figure 2.3c). When locomoting, the earthworm extends its head while shortening its bottom to avoid slipping [59]. During burrowing, the earthworm anchors its bottom while extending and creating space for its head [60]. These intricate movements are achieved through localized radial extensions or elongations of its body. By

strategically contracting its muscles in various wavelike patterns it can achieve specific deformations that suit the intended functionality. This principle served as inspiration for the earthworm-inspired soft robot developed by Ozkan-Aydin *et al.* [61]. This robot can alternate between anchoring and locomotion by respectively undulating its bottom or peristaltically deforming its full body. An even more drastic example from nature that shows embodied intelligence by adaptive functionality is the caterpillar-to-butterfly metamorphosis, in which a transition is made from locomotion on land to locomotion in the air [62].

An example of a field in which multi-functional bodies proved to be useful is the field of microrobots, as multi-functionality allows for miniaturization. These microrobots respond to different environmental stimuli to actuate different functionalities. Xin *et al.* [63] developed a microrobot for localized cancer cell treatment that opens its gripper in a low pH environment, closes the gripper in a higher pH environment and locomotes using a magnetic field (Figure 2.3c). The robot's response to its environment mediates its control system, which makes the actuation of different functional modes less demanding. Also, the embedded stimuli-responsive materials mediate the robot's feedback system, making the robot independent of an external power source. An example of a multi-functional soft sensor is the fingerprint-inspired e-skin system for sliding detection developed by Chen *et al.* [64]. Four embedded spiral electrodes are patterned in such a way that the amount of skin deformation provides information about both the sliding direction, as well as the displacement and speed. Embedding such a multi-functional sensor in the feedback system would allow a soft robot for further miniaturization.

Other examples showing embodied intelligence by adaptive functionality are the mechanical creatures called 'Strandbeesten' by Theo Jansen. These kinetic machines are designed in such a way that they walk independently powered by the wind. They autonomously change their direction depending on the environment. Some creatures can even change their locomotion mode from walking to flying. These machines' embodiment takes over their control, switching the locomotion mode, embedding an embodied intelligence [19]. They work in cooperation with the environment, instead of working against the disturbances associated with the environment.

Embedded computation by adaptive mechanics

The third category of soft robots that show embedded computation by their adaptive mechanics consists of a group of soft robots that make use of their adaptive properties to adapt the way forces act on their body or are generated by their body in different environments. Nature shows the same principle in, for example, the tendril coils that some plants use to support their weight. These tendrils reach out to detect potential support structures in a straight shape and deform into a coiled shape when they reach the support [65] (Figure 2.3d). The coiled tendril serves as a spring-like and energy-damping structure supporting the plant [49]. This mechanism serves as inspiration for coiling soft robots, which are often built from bi-layered structures with a strain mismatch whose equilibrium state is controlled by certain stimuli, e.g. heat [65, 66], current [67] or pneumatics [68].

Another example found in nature showing embedded computation by its adaptive mechanics is the self-stabilizing feature of the muscle-tendon system in the leg. The elastic properties of the tendon and muscle passively adapt the angulation of the knee during

impact with the ground, corresponding to the irregularities of the terrain [18]. The intrinsic dynamics of a body are exploited to reduce the complexity of its control system [69]. This feature of incorporating self-stabilizing behavior is also referred to as 'intelligence by mechanics' [70]. Holmes *et al.* [71] even hypothesize a feedforward control loop of the muscle activation for legged animal motion by preflexes. An artificial example showing embodied intelligence by self-stabilizing properties is the hexapedal robot developed by Cham *et al.* [72]. This hexapedal robot makes use of the mechanical reflexes of its complaint knee joints to adapt its posture passively to the terrain. This reduces the computational load related to the positioning of the robot's legs.

Soft robots embedding variable stiffness also show embodied intelligence by adaptive mechanics. A classic example is the jammed-based coffee balloon gripper [73]. The gripper deforms passively around the target object in its soft state, adopting embedded computation by an adaptive shape. Where after the application of a vacuum, the coffee particles get packed and the gripper transitions towards its stiffened state (Figure 2.3d). The initial compliant properties of the gripper are exploited to reduce the gripper's controlling load, whereas the stiff properties of the gripper are needed to create sufficient contact forces. Here, the contribution of the gripper's geometry and materials is dominant in reducing its computational load [4]. Another soft robot making use of variable stiffness in a more localized manner is the soft robot arm inspired by the octopus developed by Laschi *et al.* [74]. Similarly to the octopus arm, the arm is divided into muscles, where longitudinal muscles are represented by cables and transversal muscles are represented by Shape Memory Alloys (SMA). Locally activating the SMA actuators and pulling the longitudinal cables results in a local increase in stiffness [74]. The soft properties of the arm provide it with an adaptive shape corresponding to the environment, which is counterbalanced by its local stiffening that increases the output force locally [30]. This is, among others, useful in gripping applications. Cianchetti *et al. [75]* demonstrate that this principle also applies on a smaller scale. They demonstrate a soft arm with dimensions applicable for Minimally Invasive Surgery (MIS), incorporating variable stiffness by granular jamming. In the soft state, the arm is able to move around obstacles, but when needed, the arm transitions into its jammed state to increase its payload. Next to reducing the computational load of an agent, variable stiffness can be used to improve the performance of the feedback system. For example, Yue *et al.* [76] developed a multi-degrees-of-freedom force sensor in which the sensor sensibility can be adjusted by changing the stiffness of its pneumatically actuated variable stiff structure. With this intrinsic range of sensing, the sensor is suitable for a wide range of applications.

An often-cited example of a robot incorporating embodied intelligence is the passive dynamic walker [18, 77, 78]. This two-legged robot walks down a predetermined slope without the need for any control. The mechanical construction of the robot is designed in such a way that the walking behavior is fueled only by gravity. This robot makes optimal use of morphological computation by eliminating the need for any internal processing. There is an ongoing debate surrounding the passive dynamic walker's actual capability to perform morphological computation or whether it is simply a passive mechanical process [79]. To avoid the discussion of the interpretation of the term 'computation', Ghazi-Zahedi [77] proposed an alternative term for morphological computation, which is 'morphological intelligence', defined as '*The reduction of computational cost for the brain (or controller)*

resulting from the exploitation of the morphology and its interaction with the environment' [77]. The term 'computational cost' is applicable in a larger context compared to the definition of embodied computation. It refers not only to the amount of computation encoded in the body but also to the energetic cost [77]. In nature, this kind of intelligent behavior is, for example, shown by fish swimming behind obstacles to optimize their energy expense by resonating upcoming vortices in their body [80]. The vortices excite vibration modes which trigger resonance and motion. They use the dynamics of their flexible body to reduce the energetic cost of swimming, therefore embedding a morphological intelligence in their body. Other examples are V-shaped falling paper systems, which shape can be optimized to minimize the falling speed [81]. The design of a simple piece of paper can impact its interaction with the environment by adapting the drag force generation. This unique quality allows the paper to showcase a form of embedded intelligence resulting from its morphology [81].

2.2.3 Physical intelligence

An approach closely related to embodied intelligence is physical intelligence [19]. Physical intelligence describes the understanding of how a body creates intelligence physically while interacting with the environment. Physical intelligence is defined by Sitti *et al.* [19] as *'physically encoding sensing, actuation, control, memory, logic, computation, adaptation, learning and decision-making into the body of an agent'*. Physical intelligence differs from embodied intelligence by essentially focusing on the intelligence encoded in the body, whereas embodied intelligence focuses on the tight coupling between an agent's body and brain [19].

A physically intelligent example from nature showing improved functionality through its embodiment is the foot of a gecko. The contact surface of the foot is covered by hierarchical microstructures, which gives the gecko the ability to climb vertically [79] (Figure 2.4a). The microstructure creates tight contact between the feet and the underlying terrain, as it adapts to the irregularities of the terrain [79]. This results in sufficiently powerful van der Waals adhesion to walk on vertical surfaces [82]. Geckos would not be able to exhibit this climbing functionality without their specialized morphology, hierarchical arrangement of the setae, orientation of the air and distributed forces (amongst others), which means that the gecko's foot morphology embeds physical intelligence. Examples of physically intelligent soft robots inspired by the gecko are, for instance, the soft unidirectional robot developed by Wang *et al.* [83], the soft adhesive pads developed by Aksak *et al.* [84], or the multi-finger gripper with gecko-inspired adhesives developed by Ruotolo *et al.* [85]. Physical intelligence can also appear among agents if their collective physical interactions create intelligent behavior. In nature, this appears as result of the swarm behavior of ducklings. Here, the ducklings use the vortices generated by the other ducklings to lower the metabolic rate per individual duckling. Examples of soft robots showing physical intelligence through swarm behavior are the microrobots developed by Dekanovsky *et al.* [86, 87]. Their local interaction with each other results in the weaving of spider-like webs that adsorb hormonal pollutants from aqueous environments [86].

An example of a soft robot showing physical intelligence through functionality facilitated by its morphology is the soft kirigami crawling robot developed by Rafsanjani *et*

al. [88]. The skin of this snake-inspired robot contains kirigami cuts, which provides directional frictional properties to the outer surface of the robot (Figure 2.4b) and results in efficient crawling gaits [88, 89]. Without these integrated kirigami structures, the robot could not perform this crawling locomotion mode, which means that the functionality is encoded in the design of the robot's body. These artificially designed structures that show unique properties through their design are also called metastructures [19]. Other unique properties they could include are, for instance, vibration attenuation, electromagnetic behavior, photonic behavior or a negative poison ratio. Embedding metastructures in soft robots provides the body with additional functionalities that it originally would not contain, resulting in a physically intelligent body.

Soft robots could also embed physical intelligence by encoding logic, memory or control in their embodiment. Examples of the former are the circuits developed by Preston *et al.* [12], which exist out of soft pneumatic digital logic gates. By making use of a bistable valve to encode NOT, AND, and OR digital logic, these logic gates have the potential to serve as the base for completely soft autonomous robots. These soft robots could even display their stored memory on a soft bubble display [14]. Other examples of soft robots embedding, logic, memory and control are the soft robots with integrated fluidic circuits developed by Mahon *et al.* [15].

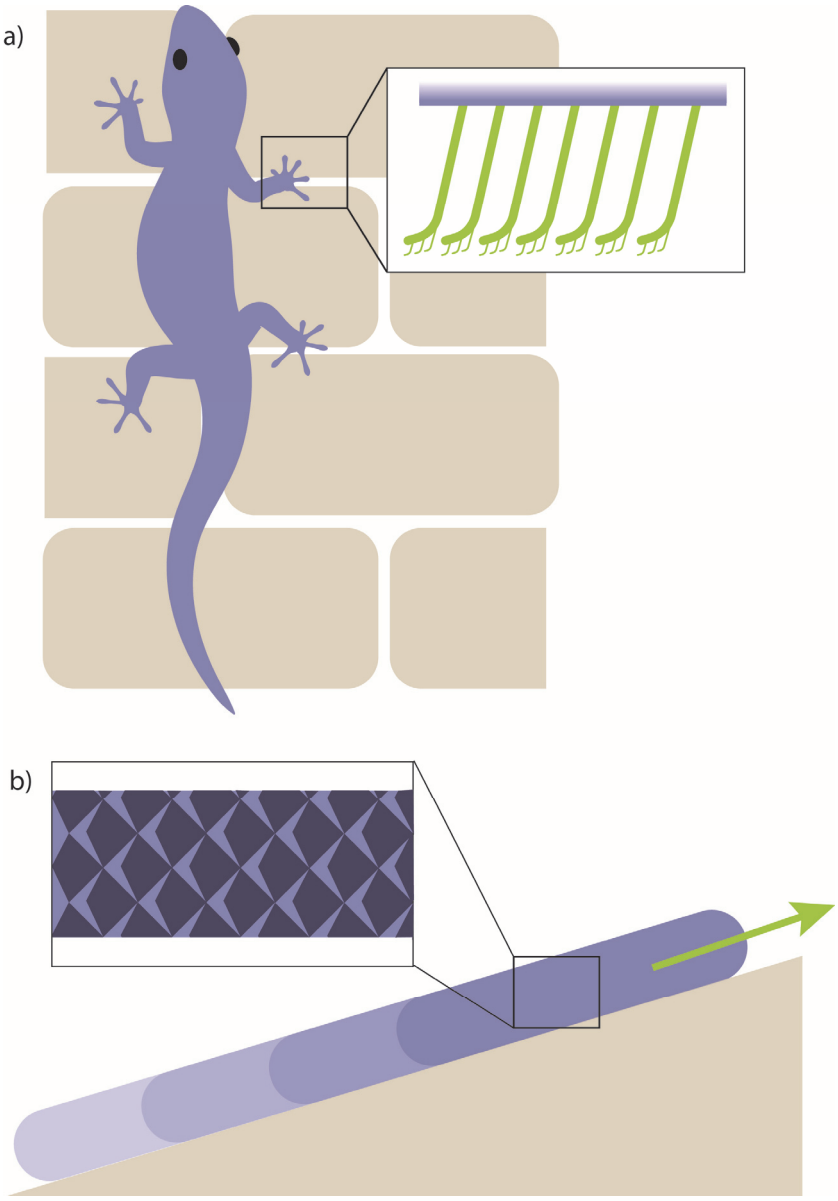


Figure 2.4: Illustration of physical intelligent agents. a) The hierarchical structures consisting of setal arrays, containing setae which terminate in spatulae on the feet of geckos give them the ability to climb vertically. b) The Kirigami soft robot developed by Rafsanjani *et al.* [88] can climb hills due to its kirigami skin.

2.2.4 Intelligence by different computational systems

The overlap and differences between the different perspectives on intelligence can best be understood by their control system architecture. With control or computation, we mean an executive operation that has some steady state and once the initial or boundary conditions change then an algorithm is executed leading to a calculated output based on predetermined rules. A distinction categorizes agents based on the following computational approaches:

- **Centralized computation:**
  In this approach, the control process is centralized, involving a single controller that sends input signals to a corresponding actuator. In a closed-loop system, feedback is provided by a single output signal towards a separate sensor. Centralized computation is associated with the artificial intelligence layer in Figure 2.2.
- **Decentralized computation:**
  An agent that involves decentralized computation distributes some computational load of the central control system across multiple separate controllers. In closed-loop configurations, the feedback system is enhanced by replacing a centralized sensing unit with multiple distributed sensing units. This arrangement can lead to improved agent control, an improved sensory information flow and faster response times. The example of the octopus was given, in which the motor control of the arms is partially offloaded from the central nervous system towards the peripheral nervous system. Decentralized computation is associated with the embodied intelligence layer in Figure 2.2.
- **Embedded computation:**
  Agents employing embedded computation integrate either their control process in the actuator, their sensing mechanism in the actuator, or they embed both within the actuator itself. An agent can incorporate embedded computation by providing the embodiment with an adaptive shape, adaptive functionality and/or adaptive mechanics. Agents are empowered to function autonomously and the opportunity is provided to eliminate the need for an external power source. For this reason, embedded computation is the only computational system that is adopted by non-living organisms that still show adaptive behavior. The example of a pine cone was given, in which both the sensing of the environmental humidity and the control of its bending behavior are embedded in the material of its scales. It must be noted, however, that the cellulose in the scale is not a standalone sensor. Embedded computation is associated with the embodied intelligence layer, the morphological intelligence layer and the physical intelligence layer in Figure 2.2.

Figure 2.5 shows control schemes associated with the different computational systems. Each computational system contributes to various levels of autonomy and control efficiency. It also presents how the types of intelligence shown in Figure 2.2 relate to each other. Artificial intelligence is the only type of intelligence associated with centralized computation whereas the other types of intelligence are associated with embedded computation or decentralized computation. The primary difference between embodied intelligence, morphological intelligence and physical intelligence lies in their emphasis on how embodiment reduces the central processing load. All three perspectives involve embedded computation, integrating

control or sensing within the embodiment. However, an embodied intelligent agent also enhances the coupling between its control system and embodiment by distributing the computational load across multiple locations within the embodiment. This approach offloads the central system or improves the feedback system, aligning with decentralized computation.

2.3 Environmental responsive intelligence

2.3.1 Intelligence of soft robots

Soft robots present an interesting case as they are framed as examples that embody both embodied intelligence as well as physical intelligence. This is often explained by their soft material properties that facilitate embedded computation that makes them suitable for navigating unpredictable and dynamic environments. However, in reality, these soft properties sometimes show inherent challenges to the robot's overall functionality. A typical pneumatically driven soft gripper can be taken as an illustration, which excels in its ability to shape passively to a diverse variety of objects. Although soft grippers demonstrate adaptability, a significant limitation arises in balancing between maintaining sufficient gripping forces and preserving their soft and gentle nature. It can be stated that a balance should be found wherein an intelligent soft robot should not only demonstrate an adaptive behavior but also effectively perform its core functionalities. A soft gripper should possess the capability to respond to changes in the shape of the targeted object while ensuring it sustains sufficient gripping forces. This would, for instance, mean that a soft gripper not only conforms its shape to the targeted object but also modulates its stiffness to maintain optimal load forces under a wide range of conditions.

Environmental considerations play a crucial role in shaping structural adaptations. Fully soft bodies, such as those observed in octopuses, exhibit optimal functionality within

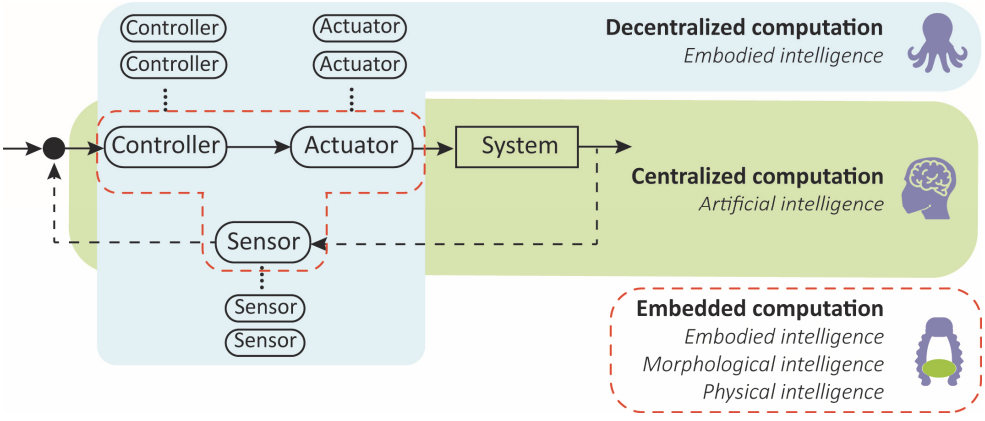


Figure 2.5: Schematic of computational system architectures. Green: Centralized computation associated with an artificial intelligent agent. Blue: Decentralized computation associated with an embodied intelligent agent, distributing computational load of the central control system across multiple separate controllers or a local controller. Red: Embedded computation associated with embodied intelligent, morphological intelligent or physical intelligent agents, driven by an integrated control- and/or sensing system into the body of the agent.

aquatic environments where arm density is equivalent to water, which minimizes energy expenditure. Conversely, in terrestrial settings, rigid skeletal frameworks are indispensable for structural integrity, highlighting the environment-specific requirements in robotic design. Notably, the scale of a robot is contingent upon its environment; fully soft designs, operational in terrestrial environments, adopt smaller sizes to mitigate gravitational impact. The nuanced interplay between structural rigidity, environmental context, and efficiency, advocates for tailored robotic designs attuned to specific environmental demands.

As of now, engineers often seek to streamline environmental factors to facilitate the effective operation of robots. Historically, the simplification of environmental factors was necessitated by the prevailing technologies. However, contemporary advancements in technology present a landscape wherein opportunities have emerged to integrate environmental complexity into the robot design process, which becomes imperative when targeting real-world applications. To develop robots capable of thriving in such diverse and challenging settings, the adoption of embodied intelligence is paramount. This entails the meticulous design of the robot's physical form to harmonize it with its specific operational environment. Consequently, engineers must possess foreknowledge regarding the robot's intended responses to the environment.

2.3.2 Mechanical Intelligence

To achieve responsive behavior, soft robots would need to incorporate so-called mechanical intelligence. We define this term as: *'An artificial agent's degree of responsiveness to changing external conditions encoded by the programmed states of its body'.* Here, the term *external conditions* refers to the set of requirements linked to the agent's working environment for maintaining its functionality. As the working environment changes, the agent needs to adjust and meet new corresponding requirements. In other words, responsive agents can adapt to suit different working environments, ensuring they continue to operate effectively. These adaptations might involve changes in body mechanics, shape, or even functionality. Responsive behavior is embedded in the design of the agent, meaning that various responsive states are intentionally programmed during its design process. This can also be referred to as 'control by design'. The term *programmed states* refers to the agent being designed to respond in predetermined ways to new sets of requirements, ensuring its functionality remains unimpeded. In essence, the agent's degree of responsiveness is encoded through these programmed states. A higher number of states embodying different responses would indicate greater mechanical intelligence in the agent, as it can achieve its goal in a wider range of environments. This perspective on soft robots' responsiveness differs from the embodied intelligence, morphological intelligence and physical intelligence approach, as it primarily focuses on the degree of the agent's responsiveness to the environment and accompanying external stimuli. Therefore, it is important to distinguish this from studies that use the term mechanical intelligence as synonym for embodied intelligence or physical intelligence [90-92]. Mechanical intelligence aligns with an embedded computational system and the various strategies for implementing such a system (adaptive shape, adaptive functionality, and adaptive mechanics), with the addition that the artificial agent actively responds to changes in its environment in a pre-programmed way. Our perspective aligns with the perspective on mechanical intelligence given by Khaheshi & Rajabi [93], and in addition, offers a detailed

definition and view of the implementation field, and focuses specifically on the pre-programmed responsiveness of an artificial agent.

As an example, a regular soft robotic gripper would exhibit mechanical intelligence if it could adapt its shape to different objects without compromising its functional performance. Zhou *et al.* [94] developed such a gripper with soft fingers filled with granular particles that jam at locations where the gripper contacts the target object. This adaptive mechanism allows the gripper to accommodate larger objects and maintain its gripping performance passively. Similarly, another example of mechanical intelligence is demonstrated in the reconfigurable miniature ferrofluidic robot developed by Fan et al. [95]. This soft robot adapts its shape by stretching and splitting into multiple smaller robots, enabling it to navigate through variable spaces effectively, showcasing responsive behavior. Shah et al. [62] created a reconfigurable robot that adapts its locomotion mode based on the terrain, using either rolling or inchworm motion to achieve movement on flat and inclined surfaces, respectively. This responsive functionality exhibits mechanical intelligence, allowing the robot to adapt to changing environmental conditions. The robots developed by Hu *et al.* [96] are yet another example of mechanical intelligence that adapts its locomotion mode depending on the environment. Here, the magnetic field of the environment directly controls the locomotion mode of small-scale soft robots. This way, the robots are able to walk, swim, jump, roll or crawl, depending on the demands of the environment. These examples illustrate how soft robots can embed mechanical intelligence through their responsive mechanics and functionalities, enabling them to adapt and interact effectively with their environments.

2.3.3 Enablers of mechanical intelligence

In order to facilitate an agent with mechanical intelligence, the agent should be able to respond to the environment by its predetermined responsive states. This means it is vital to anticipate the changing demands of the environment. During operation, the soft robot should ideally autonomously gather information from the environment through integrated sensors, subsequently translating this data into appropriate responses. To make optimal use of the agent's embedded intelligence, it should be encouraged to implement a control scheme that is associated with embedded computation in which both the control and sensing system are directly integrated within the agent's body. This type of control system has as advantage that no external power source is needed, thereby enabling the agent to operate fully autonomously.

The soft robots embedding fluidic circuits developed by Laake *et al.* [97] are an example of such an autonomous agent that integrates both its control system and sensing system. These robots' soft actuators are connected to specialized soft valves. These valves transform a continuous inflow of air into cyclic activation, and by connecting the actuators in parallel, the actuators can be stimulated in various sequences. The robot can switch between sequences based on physical cues from the environment, enabling it to autonomously respond to changing conditions. For instance, an impact force could prompt a shift in gait to navigate past obstacles or trigger drug release inside the body.

A strategy to embed mechanical intelligence would be to integrate materials that respond to external stimuli such as heat, light, pH value or magnetism, also called smart materials, into the soft robot. Smart materials are already implemented in commercial

mechatronic applications [98]. Recently published reviews show the upcoming interest and potential of smart materials integrated into soft robots [99-103], microrobots [104], or even smart textiles [105, 106]. Programming soft robots with flexible metamaterials provides additional opportunities to embed soft robots with responsive states [107, 108]. Energy-harvesting soft materials provide the potential for the development of autonomous soft robots without the need for external power sources [109].

An example of a soft robot embedding mechanical intelligence by smart materials is the light-driven artificial flytrap developed by Wani *et al.* [110]. This flytrap integrates a structure consisting of a light-responsive liquid-crystal elastomer. This material detects an object when it enters its field of view and, consecutively, initiates bending due to light-induced rearrangement of its molecular alignment, causing the flytrap to close. This way, this soft device autonomously recognizes objects and initiates closing without the need for an external power source. Other examples of soft robots embedding stimuli-responsive materials are the soft swimming robots developed by Karshalev *et al.* [111]. These swimmers change their color to adapt their visibility in different environments, controlled by environmental stimuli. For instance, glow-in-the-dark swimmers start to emit green and purple light at night in response to solar light charging during the day.

Mechanical metamaterials show great potential for embedding mechanical intelligence

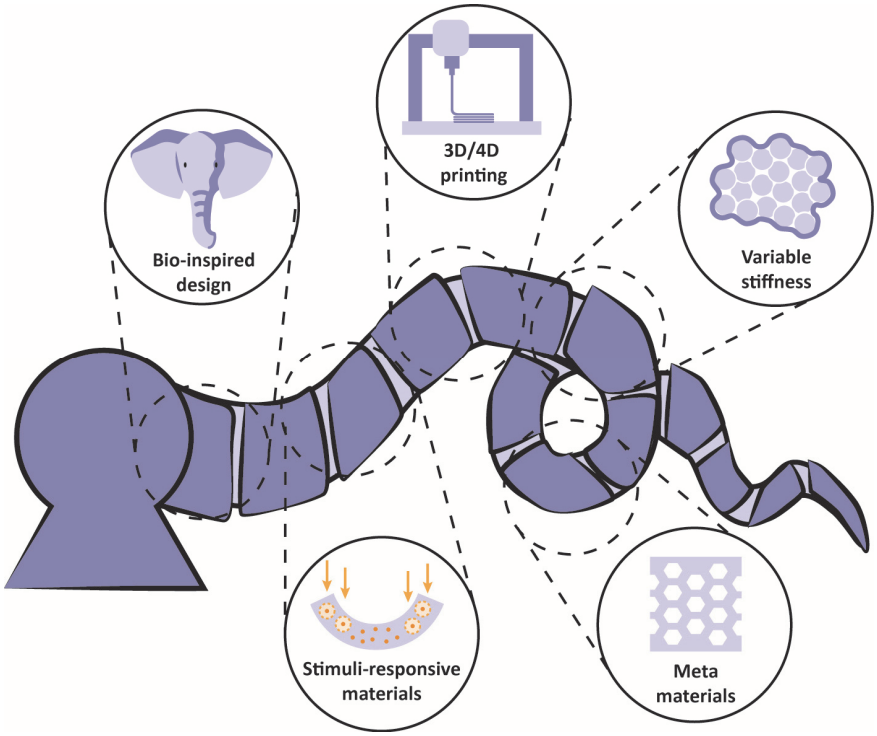


Figure 2.6: Schematic visualization of potential enablers of mechanical intelligent soft robots. Enablers of mechanical intelligent soft robots are diverse and include the use of bio- inspired design methodologies, smart use of stimuli-responsive and meta-materials that can be 3D/4D printed using state-of-the-art manufacturing facilities and can change their stiffness on demand.

into soft robots. Pressure actuation is widely used to actively change the properties of mechanical metamaterials, allowing for easy integration with conventional pneumatically-actuated soft robots. When inflated of deflated, these metamaterials can change their shape, functionality or mechanical properties due to the presence of internal channels or cavities inside a soft matrix [112]. For example, the actuator developed by Pan *et al.* [113] features local auxetic and non-auxetic structures that cause bending upon inflation. Similarly, the metamaterial developed by Chen *et al.* [114] changes stiffness when pneumatically changing the shape of integrated holes. Furthermore, by embedding smart materials in these mechanical metamaterials, these materials can become responsive to external stimuli. Mishra *et al*. [115] demonstrate this with a temperature-responsive soft fluidic finger that bends at low temperatures (<30 °C), and expels fluid at high temperatures (>30 °C), resulting in a gripper capable of mechanically and thermally manipulating heated objects based on the environmental conditions.

The design space for soft robots incorporating mechanical intelligence is characterized by the dynamic interplay between geometry and material properties. By adjusting the geometry of these robots, it becomes possible to provide them with new properties. For instance, designing a body as an airtight membrane with embedded particles allows the stiffness of the entire body to be modified through vacuum application. Model-based designing can provide fast iterations. New possibilities for complex geometries arise with the use of 3D and 4D printing [116]. Furthermore, the incorporation of specific materials can further enhance the capabilities of geometries. For instance, the integration of smart materials enables direct responsiveness to the environment or facilitates adjustable stiffness. Roh *et al.* [117] demonstrate a 4D printed magnetically actuated soft gripper featuring a wavy structure that exhibits complex movements like contracting, grabbing and releasing with a simple input force. These movements are feasible due to the combination of the gripper's wavy geometry and magnetically responsive materials. The potential of the design space for mechanical intelligence integration is immense, bridging various disciplines and offering a unique intersection of cutting-edge technologies. Figure 2.6 shows a schematic visualization of the mentioned potential enablers of mechanically intelligent soft robots.

2.4 Conclusion

The goal of this review paper is to present an overview of the current strategies focused on integrating intelligence into soft robots. Different perspectives on intelligence were explored and we discussed different computational systems that support these different perspectives. Furthermore we classified strategies to provide soft robots with intelligence through their embodiments as follows: (1) intelligence by an agent's adaptive shape, (2) intelligence by an agent's adaptive functionality, and (3) intelligence by an agent's adaptive mechanics. Examples showed in what diverse ways these adaptive properties can be reached, where nature often functions as an excellent source of inspiration. The focus lies on the design of robots tailored for intricate environments through embodied intelligence.

It is important to acknowledge that the definitions of different perspectives on intelligence are subject to change over time, and the boundaries between different approaches tend to overlap. With the continuous growth of the soft robotic community, a diverse range of insights and technologies are being adopted. While this expansion

broadens the horizons of this field, it also introduces challenges in maintaining clarity regarding the distinctions between various perspectives on embedded intelligence. On the other hand, deliberately bringing complementary fields towards each other could yield significant benefits. By drawing from the advancements in the current trend of AI, embodied intelligent soft robotics can enhance its adaptiveness to the environment. Integrating diverse perspectives on intelligence has the potential to facilitate soft robots that adapt to a wide range of environments while functioning optimally.

To bring the intelligence embedded within soft robots to the next level, we described a fresh perspective on embodied intelligence, emphasizing the robot's responsiveness to changing external conditions of a real-world environment. Integrating intelligence into the physical body, contributes to reducing the energy consumption of robots through optimized sensor integration, adaptable locomotion, and collaborative behaviors, ultimately enhancing overall energy efficiency. Research should focus on the integration of fully embedded computational systems in the soft body of the robot, including the control system and sensing system. This opens opportunities towards fully autonomous systems that can operate in a wide range of remote or miniature applications, for example, applications in surgery, underwater applications or applications in disaster areas. Inspiration could be taken from organisms in nature, such as pine cones, which show responsive behavior without an internal power source. As the design space for mechanical intelligence integration is immense, successfully incorporating mechanical intelligence into soft robots requires a strong multi-disciplinary approach, building upon the existing diversity that characterizes the field of soft robotics. In this context, encouraging collaboration and communication between different disciplines, such as designers, engineers, material scientists and biologists, becomes essential in unlocking the full potential of soft robots for various real-world applications.

References

[1] C. Lee *et al.*, "Soft robot review," *International Journal of Control, Automation and Systems,* vol. 15, pp. 3-15, 2017.

[2] D. Rus and M. T. Tolley, "Design, fabrication and control of soft robots," *Nature,* vol. 521, no. 7553, pp. 467-475, 2015.

[3] B. Mazzolai *et al.*, "Roadmap on soft robotics: multifunctionality, adaptability and growth without borders," *Multifunctional Materials,* vol. 5, no. 3, p. 032001, 2022.

[4] R. Pfeifer, H. G. Marques, and F. Iida, "Soft robotics: the next generation of intelligent machines," 2013.

[5] S. Kriegman, S. Walker, D. Shah, M. Levin, R. Kramer-Bottiglio, and J. Bongard, "Automated shapeshifting for function recovery in damaged robots," *arXiv preprint arXiv:1905.09264,* 2019.

[6] S. Terryn *et al.*, "A review on self-healing polymers for soft robotics," *Materials Today,* vol. 47, pp. 187-205, 2021.

[7] Y. Zhang, P. Li, J. Quan, L. Li, G. Zhang, and D. Zhou, "Progress, challenges, and prospects of soft robotics for space applications," *Advanced Intelligent Systems,* vol. 5, no. 3, p. 2200071, 2023.

[8] K. Ghazi-Zahedi, "Morphological Intelligence," *Cham: Springer,* 2019.

[9] S. Legg and M. Hutter, "Universal intelligence: A definition of machine intelligence," *Minds and machines,* vol. 17, pp. 391-444, 2007.

[10] N. El-Atab *et al.*, "Soft actuators for soft robotic applications: A review," *Advanced Intelligent Systems,* vol. 2, no. 10, p. 2000128, 2020.

[11] H. Wang, M. Totaro, and L. Beccai, "Toward perceptive soft robots: Progress and challenges," *Advanced Science,* vol. 5, no. 9, p. 1800541, 2018.

[12] D. J. Preston *et al.*, "Digital logic for soft devices," *Proceedings of the National Academy of Sciences,* vol. 116, no. 16, pp. 7750-7759, 2019.

[13] M. Cianchetti, "Embodied intelligence in soft robotics through hardware multifunctionality," *Frontiers in Robotics and AI,* vol. 8, p. 724056, 2021.

[14] M. P. Nemitz, C. K. Abrahamsson, L. Wille, A. A. Stokes, D. J. Preston, and G. M. Whitesides, "Soft non-volatile memory for non-electronic information storage in soft robots," in *2020 3rd IEEE International Conference on Soft Robotics (RoboSoft)*, 2020: IEEE, pp. 7-12.

[15] S. T. Mahon, A. Buchoux, M. E. Sayed, L. Teng, and A. A. Stokes, "Soft robots for extreme environments: Removing electronic control," in *2019 2nd IEEE international conference on soft robotics (RoboSoft)*, 2019: IEEE, pp. 782-787.

[16] S. Conrad *et al.*, "3D-printed digital pneumatic logic for the control of soft robotic actuators," *Science Robotics,* vol. 9, no. 86, p. eadh4060, 2024.

[17] Y. Zhai *et al.*, "Desktop fabrication of monolithic soft robotic devices with embedded fluidic control circuits," *Science Robotics,* vol. 8, no. 79, p. eadg3792, 2023.

[18] R. Pfeifer and J. Bongard, *How the body shapes the way we think: a new view of intelligence*. MIT press, 2006.

[19] M. Sitti, "Physical intelligence as a new paradigm," *Extreme Mechanics Letters,* vol. 46, p. 101340, 2021.

[20] Z. Lin *et al.*, "Recent advances in perceptive intelligence for soft robotics," *Advanced Intelligent Systems,* vol. 5, no. 5, p. 2200329, 2023.

[21] D. Kim *et al.*, "Review of machine learning methods in soft robotics," *Plos one,* vol. 16, no. 2, p. e0246102, 2021.

[22] S. Kim, C. Laschi, and B. Trimmer, "Soft robotics: a bioinspired evolution in robotics," *Trends in biotechnology,* vol. 31, no. 5, pp. 287-294, 2013.

[23] Z. Zhao, Q. Wu, J. Wang, B. Zhang, C. Zhong, and A. A. Zhilenkov, "Exploring Embodied Intelligence in Soft Robotics: A Review," *Biomimetics,* vol. 9, no. 4, p. 248, 2024.

[24] G. Mengaldo *et al.*, "A concise guide to modelling the physics of embodied intelligence in soft robotics," *Nature Reviews Physics,* vol. 4, no. 9, pp. 595-610, 2022.

[25] Q. Chen, T. Kalpoe, and J. Jovanova, "Design of mechanically intelligent structures: Review of modeling stimuli-responsive materials for adaptive structures," *Heliyon,* 2024.

[26] J. Haugeland, *Artificial intelligence: The very idea*. MIT press, 1989.

[27] Z. Lu, A. Chauhan, F. Silva, and L. S. Lopes, "A brief survey of commercial robotic arms for research on manipulation," in *2012 IEEE Symposium on Robotics and Applications (ISRA)*, 2012: IEEE, pp. 986-991.

[28] Y. Sakagami, R. Watanabe, C. Aoyama, S. Matsunaga, N. Higaki, and K. Fujimura, "The intelligent ASIMO: System overview and integration," in *IEEE/RSJ international conference on intelligent robots and systems*, 2002, vol. 3: IEEE, pp. 2478-2483.

[29] P. Thodoroff, W. Li, and N. D. Lawrence, "Benchmarking real-time reinforcement learning," in *NeurIPS 2021 Workshop on Pre-registration in Machine Learning*, 2022: PMLR, pp. 26-41.

[30] D. Zambrano, M. Cianchetti, and C. Laschi, "The morphological computation principles as a new paradigm for robotic design," in *Opinions and outlooks on morphological computation*: University of Zurich, 2014, pp. 214-225.

[31] D. Howard, A. E. Eiben, D. F. Kennedy, J.-B. Mouret, P. Valencia, and D. Winkler, "Evolving embodied intelligence from materials to machines," *Nature Machine Intelligence,* vol. 1, no. 1, pp. 12-19, 2019.

[32] A. E. Eiben, S. Kernbach, and E. Haasdijk, "Embodied artificial evolution: Artificial evolutionary systems in the 21st Century," *Evolutionary intelligence,* vol. 5, pp. 261-272, 2012.

[33] S. H. Sadati, M. ElDiwiny, S. Nurzaman, F. Iida, and T. Nanayakkara, "Embodied intelligence & morphological computation in soft robotics community: Collaborations, coordination, and perspective," in *IOP Conference Series: Materials Science and Engineering*, 2022, vol. 1261, no. 1: IOP Publishing, p. 012005.

[34] I. D. Neveln, A. Tirumalai, and S. Sponberg, "Information-based centralization of locomotion in animals and robots," *Nature Communications,* vol. 10, no. 1, p. 3655, 2019.

[35] B. Hochner, "An embodied view of octopus neurobiology," *Current biology,* vol. 22, no. 20, pp. R887-R892, 2012.

[36] G. Levy, T. Flash, and B. Hochner, "Arm coordination in octopus crawling involves unique motor control strategies," *Current biology,* vol. 25, no. 9, pp. 1195-1200, 2015.

[37] G. Sumbre, Y. Gutfreund, G. Fiorito, T. Flash, and B. Hochner, "Control of octopus arm extension by a peripheral motor program," *Science,* vol. 293, no. 5536, pp. 1845-1848, 2001.

[38] N. Franceschini, J.-M. Pichon, and C. Blanes, "From insect vision to robot vision," *Philosophical Transactions of The Royal Society Of London. Series B: Biological Sciences,* vol. 337, no. 1281, pp. 283-294, 1992.

[39] R. Pfeifer, F. Iida, and G. Gómez, "Morphological computation for adaptive behavior and cognition," in *International Congress Series*, 2006, vol. 1291: Elsevier, pp. 22-29.

[40] F. Ferrari, J. Nielsen, P. Questa, and G. Sandini, "Space variant imaging," *Sensor Review,* vol. 15, no. 2, pp. 18-20, 1995.

[41] J. Hughes, U. Culha, F. Giardina, F. Guenther, A. Rosendo, and F. Iida, "Soft manipulators and grippers: A review," *Frontiers in Robotics and AI,* vol. 3, p. 69, 2016.

[42] F. Ilievski, A. D. Mazzeo, R. F. Shepherd, X. Chen, and G. M. Whitesides, "Soft robotics for chemists," *Angewandte Chemie International Edition,* vol. 50, no. 8, pp. 1890-1895, 2011.

[43] K. Suzumori, S. Iikura, and H. Tanaka, "Applying a flexible microactuator to robotic mechanisms," *IEEE Control systems magazine,* vol. 12, no. 1, pp. 21-27, 1992.

[44] J.-H. Low, I. Delgado-Martinez, and C.-H. Yeow, "Customizable soft pneumatic chamber–gripper devices for delicate surgical manipulation," *Journal of Medical Devices,* vol. 8, no. 4, p. 044504, 2014.

[45] J. Shintake, V. Cacucciolo, D. Floreano, and H. Shea, "Soft robotic grippers," *Advanced materials,* vol. 30, no. 29, p. 1707035, 2018.

[46] S. Joshi and J. Paik, "Sensorless force and displacement estimation in soft actuators," *Soft matter,* vol. 19, no. 14, pp. 2554-2563, 2023.

[47] G. R. Gossweiler *et al.*, "Mechanochemically active soft robots," *ACS applied materials & interfaces,* vol. 7, no. 40, pp. 22431-22435, 2015.

[48] J. Hughes, A. Abdulali, R. Hashem, and F. Iida, "Embodied artificial intelligence: Enabling the next intelligence revolution," in *IOP Conference Series: Materials Science and Engineering*, 2022, vol. 1261, no. 1: IOP Publishing, p. 012001.

[49] T. Speck *et al.*, "Plants as inspiration for material-based sensing and actuation in soft robots and machines," *MRS Bulletin,* vol. 48, no. 7, pp. 730-745, 2023.

[50] A. S. Westermeier *et al.*, "How the carnivorous waterwheel plant (Aldrovanda vesiculosa) snaps," *Proceedings of the Royal Society B: Biological Sciences,* vol. 285, no. 1878, p. 20180012, 2018.

[51] A. Körner *et al.*, "Flectofold—a biomimetic compliant shading device for complex free form facades," *Smart Materials and Structures,* vol. 27, no. 1, p. 017001, 2017.

[52] Z. Zhang, D. Chen, H. Wu, Y. Bao, and G. Chai, "Non-contact magnetic driving bioinspired Venus flytrap robot based on bistable anti-symmetric CFRP structure," *Composite Structures,* vol. 135, pp. 17-22, 2016.

[53] W. Fan *et al.*, "Dual-gradient enabled ultrafast biomimetic snapping of hydrogel materials," *Science Advances,* vol. 5, no. 4, p. eaav7174, 2019.

[54] D. Lunni, M. Cianchetti, C. Filippeschi, E. Sinibaldi, and B. Mazzolai, "Plant-inspired soft bistable structures based on hygroscopic electrospun nanofibers," *Advanced Materials Interfaces,* vol. 7, no. 4, p. 1901310, 2020.

[55] A. Pal, D. Goswami, and R. V. Martinez, "Elastic energy storage enables rapid and programmable actuation in soft machines," *Advanced Functional Materials,* vol. 30, no. 1, p. 1906603, 2020.

[56] F. J. Esser, P. Auth, and T. Speck, "Artificial venus flytraps: a research review and outlook on their importance for novel bioinspired materials systems," *Frontiers in Robotics and AI,* vol. 7, p. 75, 2020.

[57] L. Cecchini, S. Mariani, M. Ronzan, A. Mondini, N. M. Pugno, and B. Mazzolai, "4D Printing of Humidity-Driven Seed Inspired Soft Robots," *Advanced Science,* vol. 10, no. 9, p. 2205146, 2023.

[58] D. Correa *et al.*, "4D pine scale: biomimetic 4D printed autonomous scale and flap structures capable of multi-phase movement," *Philosophical Transactions of the Royal Society A,* vol. 378, no. 2167, p. 20190445, 2020.

[59] R. Das, S. P. M. Babu, F. Visentin, S. Palagi, and B. Mazzolai, "An earthworm-like modular soft robot for locomotion in multi-terrain environments," *Scientific Reports,* vol. 13, no. 1, p. 1571, 2023.

[60] K. M. Dorgan and K. A. Daltorio, "Fundamentals of burrowing in soft animals and robots," *Frontiers in Robotics and AI,* vol. 10, p. 1057876, 2023.

[61] Y. Ozkan-Aydin, B. Liu, A. C. Ferrero, M. Seidel, F. L. Hammond, and D. I. Goldman, "Lateral bending and buckling aids biological and robotic earthworm anchoring and locomotion," *Bioinspiration & Biomimetics,* vol. 17, no. 1, p. 016001, 2021.

[62] D. S. Shah, J. P. Powers, L. G. Tilton, S. Kriegman, J. Bongard, and R. Kramer-Bottiglio, "A soft robot that adapts to environments through shape change," *Nature Machine Intelligence,* vol. 3, no. 1, pp. 51-59, 2021.

[63] C. Xin *et al.*, "Environmentally adaptive shape-morphing microrobots for localized cancer cell treatment," *ACS nano,* vol. 15, no. 11, pp. 18048-18059, 2021.

[64] H. Chen *et al.*, "Hybrid porous micro structured finger skin inspired self-powered electronic skin system for pressure sensing and sliding detection," *Nano Energy,* vol. 51, pp. 496-503, 2018.

[65] F. Meder, S. P. M. Babu, and B. Mazzolai, "A plant tendril-like soft robot that grasps and anchors by exploiting its material arrangement," *IEEE Robotics and Automation Letters,* vol. 7, no. 2, pp. 5191-5197, 2022.

[66] M. Kanik *et al.*, "Strain-programmable fiber-based artificial muscle," *Science,* vol. 365, no. 6449, pp. 145-150, 2019.

[67] Y. Cheng, R. Wang, K. H. Chan, X. Lu, J. Sun, and G. W. Ho, "A biomimetic conductive tendril for ultrastretchable and integratable electronics, muscles, and sensors," *ACS nano,* vol. 12, no. 4, pp. 3898-3907, 2018.

[68] J. H. Chandler, M. Chauhan, N. Garbin, K. L. Obstein, and P. Valdastri, "Parallel helix actuators for soft robotic applications," *Frontiers in Robotics and AI,* vol. 7, p. 119, 2020.

[69] R. Pfeifer and F. Iida, "Embodied artificial intelligence: Trends and challenges," *Lecture notes in computer science,* pp. 1-26, 2004.

[70] R. Blickhan, A. Seyfarth, H. Geyer, S. Grimmer, H. Wagner, and M. Günther, "Intelligence by mechanics," *Philosophical Transactions of the Royal Society A: Mathematical, Physical and Engineering Sciences,* vol. 365, no. 1850, pp. 199-220, 2007.

[71] P. Holmes, R. J. Full, D. Koditschek, and J. Guckenheimer, "The dynamics of legged locomotion: Models, analyses, and challenges," *SIAM review,* vol. 48, no. 2, pp. 207-304, 2006.

[72] J. G. Cham, S. A. Bailey, J. E. Clark, R. J. Full, and M. R. Cutkosky, "Fast and robust: Hexapedal robots via shape deposition manufacturing," *The International Journal of Robotics Research,* vol. 21, no. 10-11, pp. 869-882, 2002.

[73] E. Brown *et al.*, "Universal robotic gripper based on the jamming of granular material," *Proceedings of the National Academy of Sciences,* vol. 107, no. 44, pp. 18809-18814, 2010.

[74] C. Laschi, M. Cianchetti, B. Mazzolai, L. Margheri, M. Follador, and P. Dario, "Soft robot arm inspired by the octopus," *Advanced robotics,* vol. 26, no. 7, pp. 709-727, 2012.

[75] M. Cianchetti *et al.*, "Soft robotics technologies to address shortcomings in today's minimally invasive surgery: the STIFF-FLOP approach," *Soft robotics,* vol. 1, no. 2, pp. 122-131, 2014.

[76] W. Yue *et al.*, "Origami-inspired structure with pneumatic-induced variable stiffness for multi-DOF force-sensing," *Sensors,* vol. 22, no. 14, p. 5370, 2022.

[77] K. Zahedi and N. Ay, "Quantifying morphological computation," *Entropy,* vol. 15, no. 5, pp. 1887-1915, 2013.

[78] H. Hauser, A. J. Ijspeert, R. M. Füchslin, R. Pfeifer, and W. Maass, "Towards a theoretical foundation for morphological computation with compliant bodies," *Biological cybernetics,* vol. 105, pp. 355-370, 2011.

[79] V. C. Müller and M. Hoffmann, "What is morphological computation? On how the body contributes to cognition and control," *Artificial life,* vol. 23, no. 1, pp. 1-24, 2017.

[80] D. N. Beal, F. S. Hover, M. S. Triantafyllou, J. C. Liao, and G. V. Lauder, "Passive propulsion in vortex wakes," *Journal of fluid mechanics,* vol. 549, pp. 385-402, 2006.

[81] T. Howison, J. Hughes, and F. Iida, "Morphologically programming the interactions of V-shaped falling papers," in *Artificial Life Conference Proceedings 32*, 2020: MIT Press One Rogers Street, Cambridge, MA 02142-1209, USA journals-info …, pp. 359-366.

[82] K. Autumn *et al.*, "Evidence for van der Waals adhesion in gecko setae," *Proceedings of the National Academy of Sciences,* vol. 99, no. 19, pp. 12252-12256, 2002.

[83] X. Wang *et al.*, "Bioinspired footed soft robot with unidirectional all-terrain mobility," *Materials Today,* vol. 35, pp. 42-49, 2020.

[84] B. Aksak, M. P. Murphy, and M. Sitti, "Gecko inspired micro-fibrillar adhesives for wall climbing robots on micro/nanoscale rough surfaces," in *2008 IEEE international conference on robotics and automation*, 2008: IEEE, pp. 3058-3063.

[85] W. Ruotolo, D. Brouwer, and M. R. Cutkosky, "From grasping to manipulation with gecko-inspired adhesives on a multifinger gripper," *Science Robotics,* vol. 6, no. 61, p. eabi9773, 2021.

[86] L. Dekanovsky, B. Khezri, Z. Rottnerova, F. Novotny, J. Plutnar, and M. Pumera, "Chemically programmable microrobots weaving a web from hormones," *Nature Machine Intelligence,* vol. 2, no. 11, pp. 711-718, 2020.

[87] D. Jin and L. Zhang, "Embodied intelligence weaves a better future," *Nature Machine Intelligence,* vol. 2, no. 11, pp. 663-664, 2020.

[88] A. Rafsanjani, Y. Zhang, B. Liu, S. M. Rubinstein, and K. Bertoldi, "Kirigami skins make a simple soft actuator crawl," *Science Robotics,* vol. 3, no. 15, p. eaar7555, 2018.

[89] M. Li, A. Pal, A. Aghakhani, A. Pena-Francesch, and M. Sitti, "Soft actuators for real-world applications," *Nature Reviews Materials,* vol. 7, no. 3, pp. 235-249, 2022.

[90] T. Wang *et al.*, "Mechanical intelligence simplifies control in terrestrial limbless locomotion," *Science Robotics,* vol. 8, no. 85, p. eadi2243, 2023.

[91] Q. Lu, N. Baron, G. Bai, and N. Rojas, "Mechanical intelligence for adaptive precision grasp," in *2021 IEEE International Conference on Robotics and Automation (ICRA)*, 2021: IEEE, pp. 4530-4536.

[92] L. C. Zhao, H. X. Zou, K. X. Wei, S. X. Zhou, G. Meng, and W. M. Zhang, "Mechanical intelligent energy harvesting: from methodology to applications," *Advanced Energy Materials,* vol. 13, no. 29, p. 2300557, 2023.

[93] A. Khaheshi and H. Rajabi, "Mechanical intelligence (MI): a bioinspired concept for transforming engineering design," *Advanced Science,* vol. 9, no. 32, p. 2203783, 2022.

[94] J. Zhou *et al.*, "Adaptive variable stiffness particle phalange for robust and durable robotic grasping," *Soft robotics,* vol. 7, no. 6, pp. 743-757, 2020.

[95] X. Fan *et al.*, "Scale-reconfigurable miniature ferrofluidic robots for negotiating sharply variable spaces," *Science Advances,* vol. 8, no. 37, p. eabq1677, 2022.

[96] W. Hu, G. Z. Lum, M. Mastrangeli, and M. Sitti, "Small-scale soft-bodied robot with multimodal locomotion," *Nature,* vol. 554, no. 7690, pp. 81-85, 2018.

[97] L. C. van Laake, J. de Vries, S. M. Kani, and J. T. Overvelde, "A fluidic relaxation oscillator for reprogrammable sequential actuation in soft robots," *Matter,* vol. 5, no. 9, pp. 2898-2917, 2022.

[98] A. Spaggiari, D. Castagnetti, N. Golinelli, E. Dragoni, and G. Scirè Mammano, "Smart materials: Properties, design and mechatronic applications," *Proceedings of the institution of mechanical engineers, part l: journal of materials: design and applications,* vol. 233, no. 4, pp. 734-762, 2019.

[99] S. Chen, H.-Z. Wang, T.-Y. Liu, and J. Liu, "Liquid metal smart materials toward soft robotics," *Advanced Intelligent Systems,* vol. 5, no. 8, p. 2200375, 2023.

[100] U. Gupta, L. Qin, Y. Wang, H. Godaba, and J. Zhu, "Soft robots based on dielectric elastomer actuators: A review," *Smart Materials and Structures,* vol. 28, no. 10, p. 103002, 2019.

[101] J. G. Kim, J. E. Park, S. Won, J. Jeon, and J. J. Wie, "Contactless manipulation of soft robots," *Materials,* vol. 12, no. 19, p. 3065, 2019.

[102] N. Ebrahimi *et al.*, "Magnetic actuation methods in bio/soft robotics," *Advanced Functional Materials,* vol. 31, no. 11, p. 2005137, 2021.

[103] Z. Shen, F. Chen, X. Zhu, K.-T. Yong, and G. Gu, "Stimuli-responsive functional materials for soft robotics," *Journal of Materials Chemistry B,* vol. 8, no. 39, pp. 8972-8991, 2020.

[104] F. Soto, E. Karshalev, F. Zhang, B. Esteban Fernandez de Avila, A. Nourhani, and J. Wang, "Smart materials for microrobots," *Chemical Reviews,* vol. 122, no. 5, pp. 5365-5403, 2021.

[105] D. Kongahage and J. Foroughi, "Actuator materials: review on recent advances and future outlook for smart textiles," *Fibers,* vol. 7, no. 3, p. 21, 2019.

[106] N. K. Persson, J. G. Martinez, Y. Zhong, A. Maziz, and E. W. Jager, "Actuating textiles: next generation of smart textiles," *Advanced Materials Technologies,* vol. 3, no. 10, p. 1700397, 2018.

[107] A. Rafsanjani, K. Bertoldi, and A. R. Studart, "Programming soft robots with flexible mechanical metamaterials," *Science Robotics,* vol. 4, no. 29, p. eaav7874, 2019.

[108] R. H. Lee, E. A. Mulder, and J. B. Hopkins, "Mechanical neural networks: Architected materials that learn behaviors," *Science Robotics,* vol. 7, no. 71, p. eabq7278, 2022.

[109] V. Vallem, Y. Sargolzaeiaval, M. Ozturk, Y. C. Lai, and M. D. Dickey, "Energy harvesting and storage with soft and stretchable materials," *Advanced Materials,* vol. 33, no. 19, p. 2004832, 2021.

[110] O. M. Wani, H. Zeng, and A. Priimagi, "A light-driven artificial flytrap," *Nature communications,* vol. 8, no. 1, p. 15546, 2017.

[111] E. Karshalev, R. Kumar, I. Jeerapan, R. Castillo, I. Campos, and J. Wang, "Multistimuli-responsive camouflage swimmers," *Chemistry of Materials,* vol. 30, no. 5, pp. 1593-1601, 2018.

[112] J. Qi *et al.*, "Recent progress in active mechanical metamaterials and construction principles," *Advanced Science,* vol. 9, no. 1, p. 2102662, 2022.

[113] Q. Pan, S. Chen, F. Chen, and X. Zhu, "Programmable soft bending actuators with auxetic metamaterials," *Science China Technological Sciences,* vol. 63, no. 12, pp. 2518-2526, 2020.

[114] Y. Chen and L. Jin, "Geometric role in designing pneumatically actuated pattern-transforming metamaterials," *Extreme Mechanics Letters,* vol. 23, pp. 55-66, 2018.

[115] A. K. Mishra *et al.*, "Autonomic perspiration in 3D-printed hydrogel actuators," *Science Robotics,* vol. 5, no. 38, p. eaaz3918, 2020.

[116] Z. Zhang, K. G. Demir, and G. X. Gu, "Developments in 4D-printing: a review on current smart materials, technologies, and applications," *International Journal of Smart and Nano Materials,* vol. 10, no. 3, pp. 205-224, 2019.

[117] S. Roh *et al.*, "3D-printed silicone soft architectures with programmed magneto-capillary reconfiguration," *Advanced Materials Technologies,* vol. 4, no. 4, p. 1800528, 2019.

02

PART 01

INTELLIGENT GRIPPING

CHAPTER 03

DESIGN OF AN OCTOPUS-INSPIRED SUCTION GRIPPER

03

ABSTRACT

Gripping slippery and flexible tissues during Minimal Invasive Surgery is often challenging using a conventional tissue gripper. A force grip has to compensate for the low friction coefficient between the gripper's jaws and the tissue surface. This study focuses on the development of a suction gripper. This device applies a pressure difference to grip the target tissue without the need to enclose it. Inspiration is taken from biological suction discs, as these are able to attach to a wide variety of substrates, varying from soft and slimy surfaces to rigid and rough rocks. Our bio-inspired suction gripper is divided into two main parts: 1) the suction chamber inside the handle where vacuum pressure is generated, and 2) the suction tip that attaches to the target tissue. The suction gripper fits through a 10 mm diameter trocar and unfolds in a larger suction surface when being extracted. The suction tip is structured in a layered manner. The tip integrates five functions in separate layers to allow for safe and effective tissue handling: 1) Foldability, 2) Air-tightness, 3) Slideability, 4) Friction magnification and 5) Seal generation. The contact surface of the tip creates an air-tight seal with the tissue and enhances frictional support. The suction tip's shape grip allows for the gripping of small tissue pieces and enhances its resistance against shear forces. The experiments illustrated that our suction gripper outperforms man-made suction discs, as well as currently described suction grippers in literature in terms of attachment force (5.95 ± 0.52 N on muscle tissue) and substrate versatility. Our bio-inspired suction gripper offers the opportunity for a safer alternative to the conventional tissue gripper in Minimal Invasive Surgery.

Published as:
Kortman, V. G., Sakes, A., Endo, G., & Breedveld, P. (2023). A bio-inspired expandable soft suction gripper for minimal invasive surgery—an explorative design study. *Bioinspiration & Biomimetics, 18*(4), 046004.

3.1 Introduction

3.1.1 Surgical grippers versus suction grippers

Gently but securely gripping and handling of slippery, compliant and irregular tissues remains one of the most challenging procedures during Minimally Invasive Surgery (MIS). In MIS, slender instruments are guided into the abdomen via trocars. These trocars act as portals through small incisions (Figure 3.1a). They typically have a diameter between 5 and 10 mm. Grippers used in current practice commonly use a force grip to manipulate tissues. This force grip is applied by two jaws that grip the tissues sideways and is subsequently translated into a pull force, to relocate or stretch the gripped tissue (Figure 3.1b) [1]. To prevent slip and to compensate for the low friction coefficients between the jaws and tissue, high pinch forces are often applied [2], which in turn can lead to unwanted tissue trauma [1, 3, 4]. Furthermore, force feedback is limited in the currently available MIS grippers, thus creating the risk of excessive force application during surgery and unintended tissue injury.

Tissue trauma due to excessive clamping forces of the gripper can lead to severe implications [1-3, 5]. Bowel perforation is an example of an implication with a high mortality rate due to improper gripper use [6]. Furthermore, Joice *et al.* [7] showed that the largest number of surgical errors during gall bladder removal is associated with gripper jaw induced tearing of the tissue. Next to the bowel and gall bladder, the bile duct, ureters, fallopian tubes and spleen are examples of delicate organs prone to damage by gripping [8].

In order to overcome these challenges, a new type of gripper can be introduced that does not need to enclose the tissue in order to apply high pinch forces for sufficient grip. An interesting direction for this challenge is suction attachment, in which a pressure differential is used to grip different substrates (Figure 3.1b). Suction grippers can exert pull forces directly in line with the instrument shaft, which limits damage caused by compressive pinch forces from the sides. This makes suction technology not only potentially relevant for gripping delicate and slippery tissue, but also for gripping large organs that can not be clamped between the jaws of a grasping forceps.

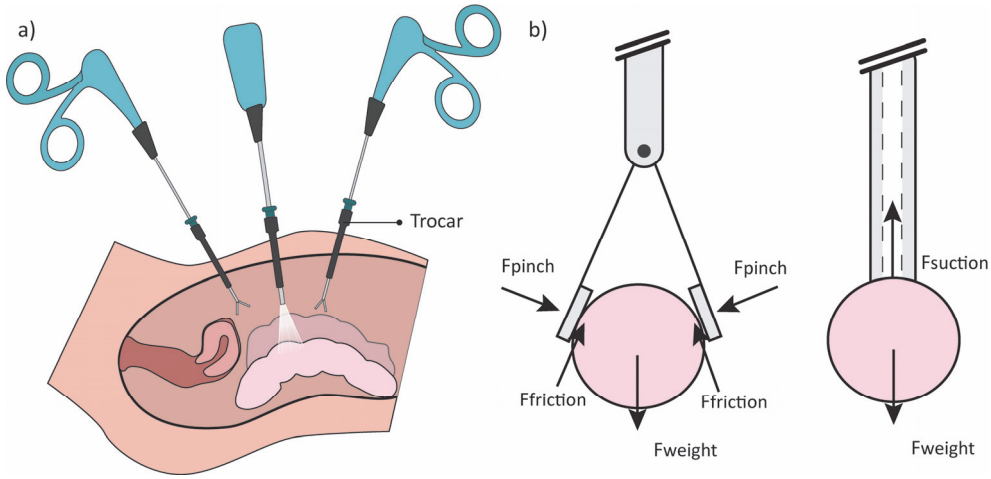


Figure 3.1: a) Schematic overview of a minimally invasive procedure accessing the abdomen. b) Overview of the forces acting on tissue by a grasping forceps (left) and a suction gripper (right).

3.1.2 State of the art

Suction grippers are widely used in industry to grasp a variety of objects, such as cardboard packages, sheet metal, bottles or electronic components. In the medical field, however, commercially available suction stabilizers only exist for (open) cardiac surgery. Examples are the *Octopus Heart Stabilizer* (Medtronic), the *Starfish* (Medtronic) and the *Xpose 3* (Getinge). These devices have been designed to locally stabilize heart tissue during off-pump coronary artery bypass surgery [9-12]. Next to these commercially available devices, suction grippers are described in literature for tissue stabilization, drug delivery and tissue dissection [13-15]. In addition, suction discs have been successfully tested *in-vivo* as a locomotion strategy on heart tissue to perform injections in the heart wall [16, 17].

The devices mentioned above clearly show the potential of suction technology to interact with tissue in MIS. However, the forces that these devices can exert are relatively low, in the range of 1 N, and thus do not allow for tissue lifting or stretching. Only two suction grippers specifically designed for tissue manipulation during MIS have been identified in literature: 1) a laparoscopic suction gripper for bowel manipulation (developed at Delft University of Technology) [18] and 2) a lung positioner for thorascopic surgery (developed at Tokyo institute of technology) [19]. The laparoscopic suction gripper consists of a rigid suction nozzle and was able to generate an attachment force of 5.6 N on bowel tissue using a vacuum pressure of 80 kPa [18]. The lung positioner consists of an array of rigid suction chambers that form a triangular shape inside the body after insertion through a small incision [19]. Even though both devices showed that suction technology is promising for tissue manipulation in a minimally invasive setting, they were challenging to manufacture and vulnerable to air leaks. This vulnerability was substantiated by the lung positioner requiring a continuous vacuum inflow in order to maintain grip on the tissue [19]. Therefore, further development in terms of grip, substrate diversity and manufacturing is needed to bring the concept of vacuum gripping during MIS to the operating room.

3.1.3 Inspiration from biological suction discs

Rubber suction discs are commonplace in our daily environment. Unfortunately, the possibilities of suction attachment of current man-made suction discs are still limited since these discs do not adhere to rough substrates with a roughness greater than 35 μm (where roughness is defined as the average grain size) [20], or remain stationary on slippery substrates when subjected to external forces. This is mainly due to their inability to create a sufficient seal or sufficient friction between the disc and the substrate, making them less suited for attachment to rough surfaces and slippery and soft tissues. Also, the suction attachment of these discs is dependent on deformation due to an initial pressing force, which is undesired for applications on tissues during surgery.

In a number of scientific research groups in the world, research is being carried out unraveling the working mechanisms of suction discs found in nature, as these outperform man-made suction discs in terms of versatility [21]. Many biological suction discs are able to attach to a wide range of substrates, varying from soft and slimy surfaces to rigid and rough rocks [20, 22]. Examples of animals with such powerful suction discs are clingfish, octopods, aquatic insect larvae and starfish [22-27] (Figure 3.2). The process of attachment and detachment can be quite dynamic, with some *gobiidae* fish able to climb the vertical cliffs of waterfalls using a

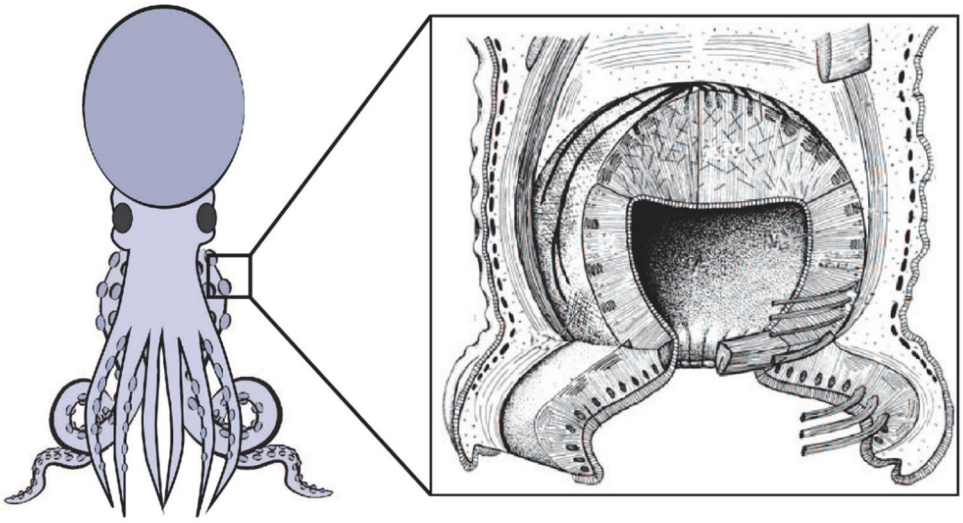


Figure 3.2: Schematic overview of the suction disc of the *Octopod Vulgaris*. (Reproduced with permission from [28]).

pelvic-fin-derived suction disc [29]. Hill-stream loaches even use their entire body as sucker for anchoring in high-speed flows in stream environments [30, 31].

Researchers reported varying ways to design bio-inspired suction discs. The main focus of current research efforts is on mimicking the material characteristics and morphology of the suction disc rim to enable improved attachment performance, for example used for fruit handling in industry. It must be noted that none of these bio-inspired discs has been developed specifically for MIS. Tramacere *et al.* [32] developed octopod inspired suction discs made of soft elastomeric materials and with a network of grooves on their surface. Ditsche *et al.* [20] and Sandoval *et al.* [33] developed suction discs inspired by the Northern Clingfish that featured highly elastic contact surfaces, various types of inclusions, slits and bio-inspired body geometry. Sadeghi *et al.* [34] developed a sucker pad inspired by the tube feet of sea urchins, where multiple individually sealed suction discs are actuated by one vacuum chamber. Designed for the manipulation of fragile, rough or wet objects, these studies evaluated the attachment performance of their bio-inspired suction discs on varying substrates compared to man-made suction discs. The results showed that the bio-inspired suction discs outperformed conventional man-made suction discs in terms of substrate diversity, as they were able to adhere to rough and wet substrates where man-made discs failed [20, 33].

3.1.4 Aim of this study

Even though major strides have been made in the development of bio-inspired suction discs, a number of challenges need to be researched and overcome for tissue manipulation in MIS, such as the generation of sufficient forces for tissue lifting and stretching while incorporating outer dimensions applicable for MIS and maintaining stable sealing. This study uses biological suction discs as inspiration to propose a novel design for a minimally invasive tissue gripper actuated by suction. We will investigate how nature is able to create a strong seal on soft surfaces and how to translate this into a small diameter soft suction disc design for MIS. The goal of our

study is, therefore, to develop and test a bio-inspired suction gripper for manipulating flexible and slippery surfaces during MIS.

3.2 Analysis biological suction disc

3.2.1 Decoupling functions

In order to understand how man-made and biological discs differ from one another, the working principle of a regular man-made suction disc and an octopod suction disc is analyzed. Figure 3.3 visualizes this analysis in a stepwise manner. The first row shows how both suction disc types generally generate suction. An octopod suction disc has a clear distinction between a dedicated suction chamber that generates the vacuum force and an optimized contact surface that maintains the seal and increases grip generation, whereas man-made suction discs generally combine these functions in one single flexible component [21, 25, 28, 35-37].

3.2.2 Suction generation

In the design of regular man-made suction discs, the suction chamber is usually integrated with the contact surface. The deformation of this contact surface generates the suction force. The concave contact surface is pressed towards the substrate (F_i) to expel the air between the two surfaces [38]. The stiffness force of the body of the suction disc (F_0), generated by its internal strain, tends to restore the original shape of the disc (Figure 3.3a), which then generates the vacuum force [39] [38]. This means that a trade-off is made between the required stiffness of the disc to restore its original shape and the required flexibility of the disc to create a seal.

The suction chamber and the contact surface of an octopod suction disc are physically separated. Therefore, they are specialized for their own function, suction generation and seal- and friction generation, respectively. The shape, flexibility and musculature of the suction chamber are optimized for generating powerful volume change. The highly specialized musculature is subdivided into radial, circular and meridional muscles (Figure 3.3b) [35, 37]. As the chamber acts as a muscular hydrostat, muscle contraction in one direction results in the elongation of a muscle in another direction [35, 37]. The suction chamber's wall thins by contraction of the radial muscles, which increases the internal volume of the suction chamber and results in a vacuum force. Cross connective fibers prevent the collapse of the suction chamber when being subjected to vacuum pressure [28]. This form of dimensional stability is also identified in the Northern Clingfish's suction disc, where collagen bundles and flexible rays in the suction chamber's wall add resistance against vacuum pressure [40, 41].

3.2.3 Seal generation

The contact surface of a regular man-made suction disc is usually unable to adapt sufficiently to curved or rough substrates, as the disc as a whole, including the part in contact with the substrate, requires a certain amount of stiffness for sufficient vacuum generation (Figure 3.3c). Due to the physical separation of the suction chamber from the contact surface, the contact surface of an octopod suction disc can be optimized for its sealing properties (Figure 3.3d) [42-44]. The contact surface of an octopod disc contains ridges and grooves that usually mold with the contours of the substrate, thereby closing leakage channels [25, 28]. The surface consists

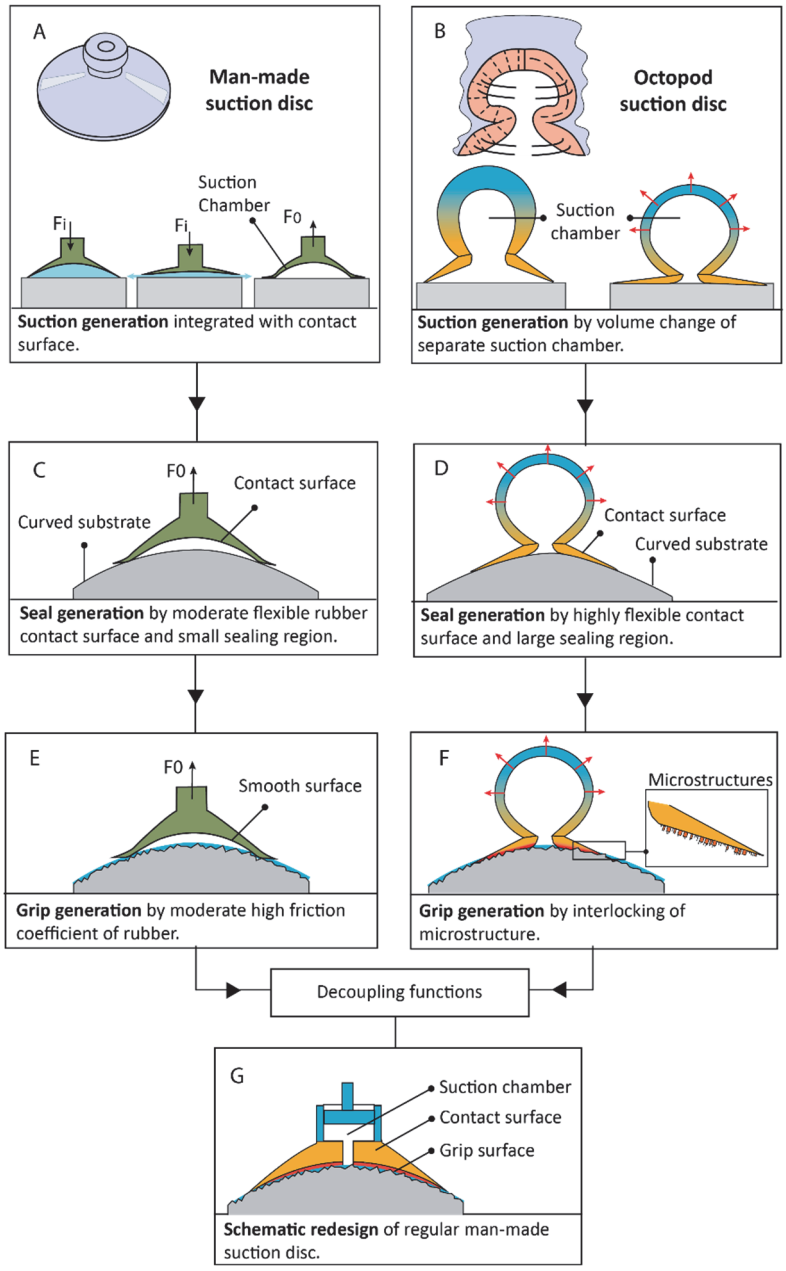


Figure 3.3: Improvement of a regular man-made suction disc by looking at the functionality of the suction disc of an octopus. a) Suction generation of a man-made suction disc. Here, (F_i) represents the initial pressing force and (F_0) the stiffness force of the disc. b) Suction generation of an octopod suction disc. c) Seal generation of the man-made suction disc. d) Seal generation of the octopod suction disc. e) Grip generation of the man-made suction disc. f) Grip generation of the octopod suction disc. g) Schematic redesign of the man-made suction disc by decoupling the functions in separate components. For a more detailed explanation, see text. Color indications: Blue: suction generation, Orange: seal generation, Red: friction generation, Grey: rigid substrate.

of a highly flexible material, allowing it to follow the curves and irregularities of the substrate. Tramacere *et al.* [36] found that the contact surface of an octopod suction disc has a Young's modulus of 7.7 kPa, which is very low as compared to rubber with a Young's modulus between 1-10 MPa [45]. For this reason, an octopod suction disc is able to easily attach to curved and rough substrates. Furthermore, the radial muscles in the disc's contact surface are oriented in such a way that contraction results in flattening and enlargement of the contact surface [28]. This lowers the disc's susceptibility to leakage as it enables the increasing of the sealing region [42]. Tramacere *et al.* [32] tested the influence of suction cup flexibility by mimicking the structured suction disc's contact surface of octopi using Ecoflex 00-30 silicone (Smooth-On Inc., USA). This resulted in approximately 65% higher pull-off forces as compared to a regular suction disc.

3.2.4 Grip generation

Whereas the regular man-made suction disc generally contains a smooth contact surface (Figure 3.3e), the contact surface of an octopod suction disc reveals microstructures (Figure 3f) [21, 32]. These microstructures are also identified on suction discs of a number of other animal classes like decapods [28, 46], clingfish [20, 22, 23, 40], remoras [47, 48], lumpsuckers [41], river loaches [31], catfish [49] [50-52], blepharicerid larvae [24, 53] and parasites [54]. They can appear as rigid hooks that extend from the skeleton, or flexible structures that extend from the epidermis [22, 23, 40, 47, 54]. The rigid hooks interlock with the asperities of the substrate, thereby acting as a ratchet system [48]. The flexible microstructures usually mold over the asperities of the substrate [44]. This increases the contact area between the suction disc and substrate and generates an interlocking effect, which both enhance the disc's grip [23, 31]. Figure 3.4 shows that the suction disc's contact surface of the *Octopus bimaculoides* is covered with grooves and protrusions. The radius of the protrusions is approximately 3-4 μm [46]. The microstructures on the contact surface of the Clingfish is even more hierarchically layered, where the smallest protrusions can adapt to surface asperities of just a few nanometers [20, 23]. These microstructures form a layer on top of the contact surface that magnifies its grip. The magnification of the grip enhances the resistance against shear forces and inward slip. This plays an essential role in the disc's attachment performance, as the man-made suction disc tends to slip inwards when it is pulled off, causing the seal to break rather easily [22, 31]. Also, the interlocking effect results in better grip on slippery surfaces.

3.2.5 Schematic disc design

A schematic redesign of a regular man-made suction disc had been made inspired by the decoupled functions in an octopod suction disc, which are suction generation, seal generation and grip generation (Figure 3.3g). Here, suction generation and seal generation are similarly decoupled in a separate suction chamber that conducts volume change and in a dedicated flexible contact surface that creates a seal. By decoupling these functions, no trade-off has to be made between the required stiffness for the vacuum generation and the required flexibility for the seal generation. The contact surface is optimized to maximize the sealing region, which lowers the disc's susceptibility to leakage. The contact surface is reinforced by a dedicated grip surface optimized on the magnification of grip counteracting shear stresses.

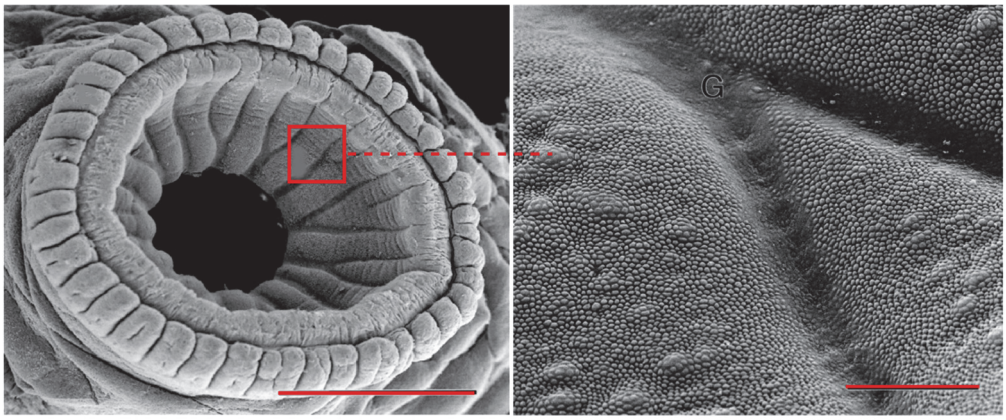


Figure 3.4: Scanning electron micrograph of the rim of the *Octopus Bimaculoides* sucker. Left: The contact surface of the suction disc is covered with grooves. Scale bar: 1.0 mm. Right: The contact surface is additionally covered microstructures to provide frictional support. Scale bar: 100 µm (reproduced with permission from [28]).

3.3 Prototype development

3.3.1 Design constraints

The schematic redesign of the regular man-made suction disc in the previous section acts as base for our suction gripper's design. Some additional design constraints are related to the gripper's use in MIS to ensure safe and reliable handling of slippery tissue. The vacuum force of the disc has a theoretical limit defined by its maximal suction surface and vacuum pressure. Our suction gripper will be actuated by a vacuum pressure of 50 kPa, as the use of this amount of vacuum pressure on human tissue has been extensively tested by the commercially available *Octopus Heart Stabilizer* (Medtronic) [10-12, 55]. Higher vacuum pressures could risk tissue damage. Next to a fixed vacuum pressure, the space available as vacuum surface limits the maximum vacuum force further. The vacuum surface is constrained by the allowed dimensions for surgical instruments during MIS. The vacuum gripper should be guided into the body by a trocar with a maximal diameter of 10 mm, which defines the maximally allowed outer dimensions of the vacuum gripper. The maximum space for the suction surface, a circle 10 mm in diameter, with a maximum vacuum pressure of 50 kPa, results in a theoretical maximum vacuum force of only 3.9 N, assuming that the entire allowed space is used as suction surface, meaning that the wall thickness of the disc equals zero. To place this in perspective, a short literature survey was conducted to list the mass of the different organs inside the human body. Table 3.1 shows an overview of the weight of some of the largest organs, showing the need for roughly 50% higher vacuum forces for tissue lifting, depending on the organ. A strategy for higher vacuum force generation is integrating a folding mechanism into the suction disc, such that it unfolds into a larger suction surface when guided into the abdomen through the trocar.

Table 3.1: The weights of some of the largest organs.

Organ	Weight (g)
Prostate	34.6 ± 13.1 [56]
Pancreas	144 ± 39 [57]
Spleen	156 ± 87 [57]
Kidney	162 ± 39 [57]
Heart	365 ± 71 [57]
Right lung	569 ± 175 [58]

3.3.2 Design suction tip

Layered disc design

The octopod suction disc analysis in the previous section reveals that a regular man-made suction disc can be improved by separating its suction chamber and contact surface and optimizing these for their own function. We will first focus on the design of the suction tip of the suction gripper, which enhances seal generation and grip generation on slippery tissue. The design of the suction chamber is less critical, as there is much design freedom to integrate this chamber in the suction gripper, e.g. in the handle or the shaft of the device. The suction tip's design integrates five functions that it needs to fulfil in order to allow for safe and effective tissue handling:

- Allow the suction tip to expand into a larger suction surface (foldability).
- Create an air-tight suction tip (air-tightness).
- Allow for a smooth transition of the suction tip through the trocar (slideability).
- Magnify the friction coefficient between the suction tip and tissue (friction magnification).
- Allow secure sealing region formation (seal generation).

These functions were translated into separate layers of the suction tip, see Figure 3.5. In order to expand the suction surface of the suction tip, a number of folding mechanisms were considered, varying in their way to transform from an unfolded into a folded state. The challenge was to integrate a mechanism with easy actuation, small required space and the ability to resist high vacuum pressures. A suction tip containing pre-bent rays proved most optimal. These flexible rays return to their natural bent shape after guidance through the trocar. This means that no external actuation is needed to transform the tip into its unfolded state, minimizing usage steps for the surgeon. Additionally, these rays act as a support structure that strengthens the tip's dimensional stability when its subjected to high vacuum pressures. Moreover, the tip maintains its overall flexibility which is needed for folding.

Leakage of the foldable suction tip was prevented by an air-tight layer that covered the folding mechanism. The challenge of this layer's design was to minimize its thickness while maintaining its air-tightness, easy manufacturing and providing a smooth integration with the folding mechanism. A thin layer of silicone turned out to act best considering silicone's

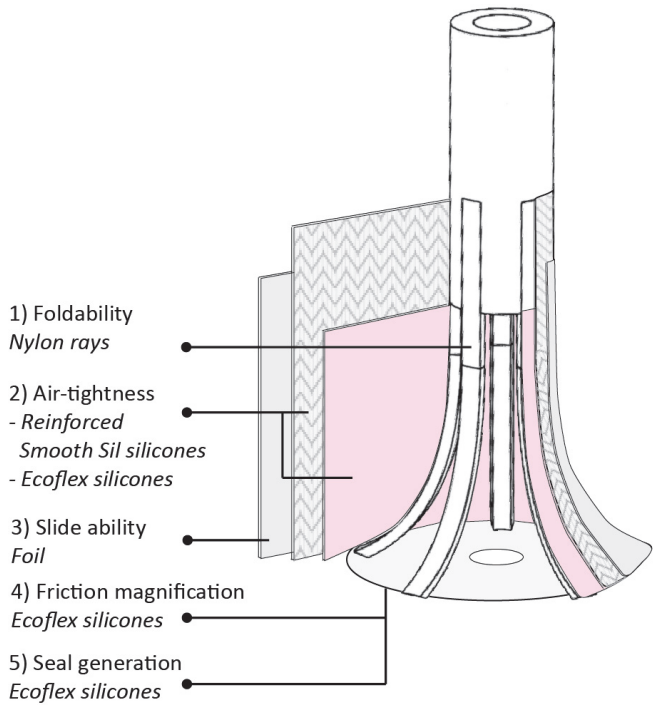


Figure 3.5: Final suction tip design. The final suction tip integrates five functions in separate layers. Pre-bent flat nylons rays act as a folding mechanism. A finely woven mesh serves as reinforcement for the Smooth Sil silicones. Together they provide an air-tight enclosing of the suction tip. A foil eases sliding through the trocar. The footprint layer consists of a membrane fabricated by Ecoflex silicones, which adds high frictional support with the tissue and supports sealing.

high elongation rate, its ability for casting as a thin film and its bio-compatibility. The silicone was reinforced by a finely woven mesh, which acted as a base to cast the silicone film in a three-dimensional shape. The silicon layer interlocks between the mesh fibers after curing to create a secure bond. Also, the mesh provides additional dimensional stability, similar to the collagen fibers of the octopod's suction disc. The silicone enclosure was covered by a thin foil with a low friction coefficient with the trocar.

The design of the footprint of the suction tip was focused on the generation of a secure seal and the magnification of the friction coefficient with the surface of tissue. For the generation of a secure sealing region, the challenge was to lower the risk of the formation of leakage channels between the suction tip's footprint and tissue surface. This is achieved by attaching highly flexible material to the sturdy edge of the suction tip to make the tip better adaptable to the tissue surface. Figure 3.6a shows three possible footprint configurations of this flexible layer. The first configuration shows the suction tip with only its edge covered by flexible material, which creates short leakage channels that can result in failure. In the second configuration, a flexible membrane is attached to the outside of the tip's edge. Because of the membrane, atmospheric air has to intrude a longer distance before causing leakage. The downside of this second footprint configuration is the occupied space of the suction tip. This problem is avoided by placing the flexible membrane at the inside of the tip's edge, as shown in

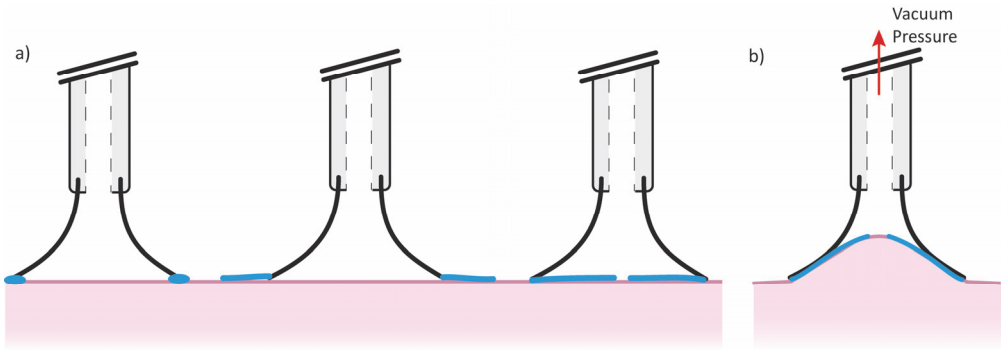


Figure 3.6: Footprint configurations. a) Three footprint configurations with different sealing regions in blue. At the left, the edge of the suction tip covered by a flexible material, resulting in a small sealing region. In the middle, the suction tip with a flexible membrane on the outside, resulting in a large sealing region. At the right, the suction tip with a flexible membrane on the inside, resulting in a large sealing region and small occupied space. b) When vacuum pressure is applied, the tissue is pressed onto the sealing region.

the third configuration. This configuration has the additional benefit that the tissue is pressed onto the footprint of the suction tip when the vacuum pressure pulls the tissue inside the tip (Figure 3.6b). The flexible membrane incorporates a high friction coefficient with tissue to enhance the suction tip's frictional support against shear forces.

Intended use

The intended use of the suction gripper is visualized in Figure 3.7. The gripper's tip unfolds after being guided into the abdomen through the trocar (Figures 3.7a-b). A vacuum pressure is generated to fixate the suction gripper on the tissue surface (Figures 3.7c). The tissue is pulled into the suction tip due to the applied vacuum pressure. The firm grip secures stable tissue lifting and stretching during tissue manipulations (Figure 3.7d). At the end of the procedure, the vacuum pressure is released and the suction tip returns into its folded state when retracted into the trocar (Figure 3.7e).

3.3.3 Fabrication suction tip

A prototype of the suction tip was built to validate its attachment performance. Dimensional stability and foldability of the suction tip were provided by flat nylon rays. The nylon rays were pre-bent into a semi circular shape by heating them while being pressed around a rod. A finely woven mesh was glued between the rays (Universal contact glue, Bison). The air-tight film was fabricated using silicone (Smooth Sil, Smooth-on Inc., USA) with a shore hardness of 40A. This type of silicone has the perfect balance between flexibility, allowing the tip to fold and stiffness to maintain dimensional stability. For the deposition of a thin silicone layer on the mesh, a fabrication method inspired by gravity-based dip-coating was used (Figure 3.8). First, the silicone mixture was poured into the suction tip, creating a silicone basin. Secondly, the suction tip was hung above a drainage platform. Gravitational forces drained the mixture from the silicone basin. During curing, the silicone mechanically interlocked with the mesh. The outer layer of the suction tip was fabricated by revolving a thin polyethylene foil around the suction tip.

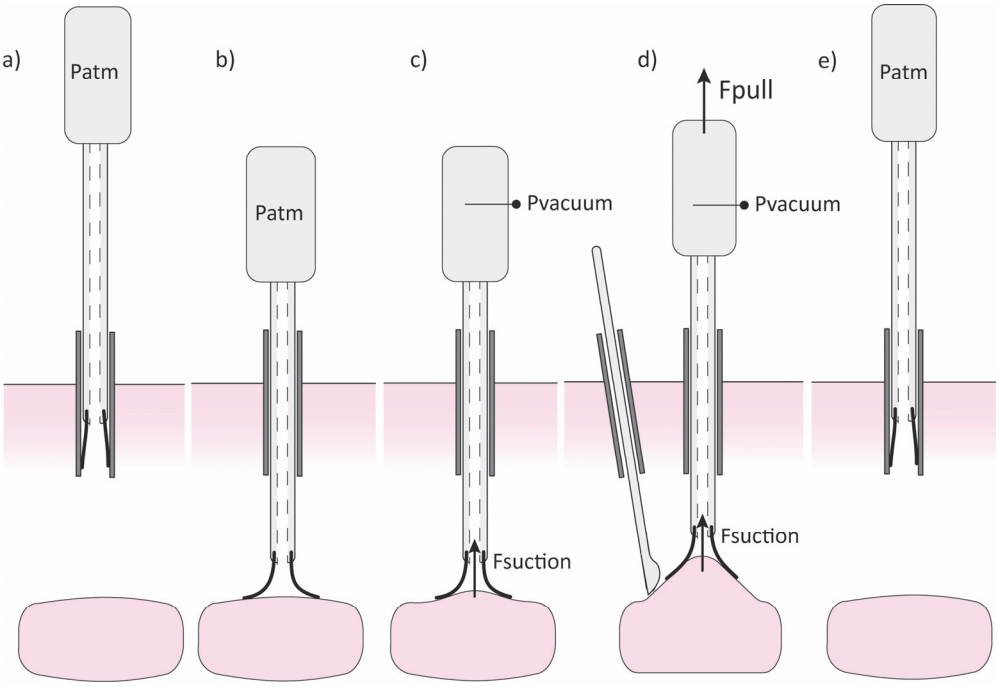


Figure 3.7: Schematic overview of the use scenario of the suction gripper. a) The suction gripper is pushed through the trocar in the folded position. b) The suction tip unfolds and makes contact with the target tissue to ensure a sufficient seal. c) A vacuum pressure is generated to fixate the suction gripper to the target tissue. d) The suction gripper provides stable support for tissue manipulations. e) The target tissue detaches after the vacuum pressure is released. The gripper is pulled back through the trocar.

Ecoflex 00-30 (Smooth-on Inc., USA) was used to fabricate the footprint. This silicone was chosen due to its high elongation rate of 900%, making it suitable to adapt to the shape of the tissue. In order to create the footprint, a thin film of uncured Ecoflex was smeared on a flat plate. The suction tip was placed on this uncured layer to attach the Ecoflex silicone air-tight to the Smooth Sil silicone while curing (Figure 3.9). The suction surface of the suction tip was made as large as possible, while still being able to slide in and out a Ø 10 mm trocar (Figure 3.10). This resulted in a suction surface with a 15 mm diameter in the unfolded state.

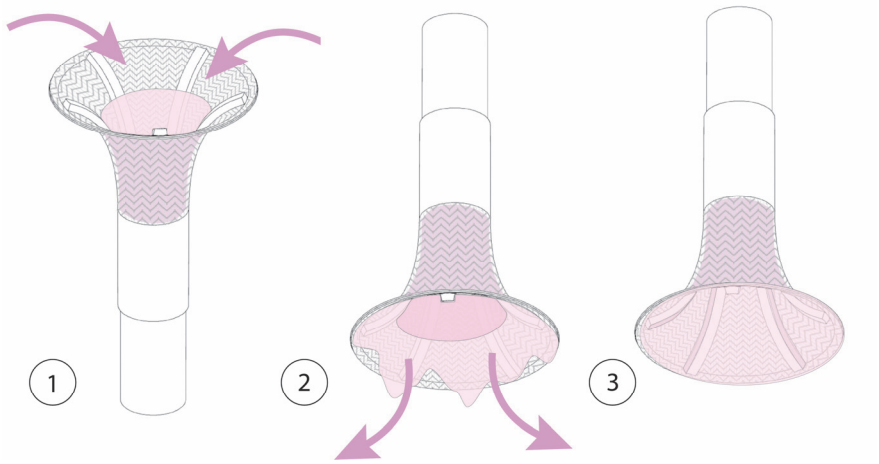


Figure 3.8: Procedure of gravity-based dip coating of the suction tip. A basin of uncured silicones is created inside the tip and gravity forces drain the mixture.

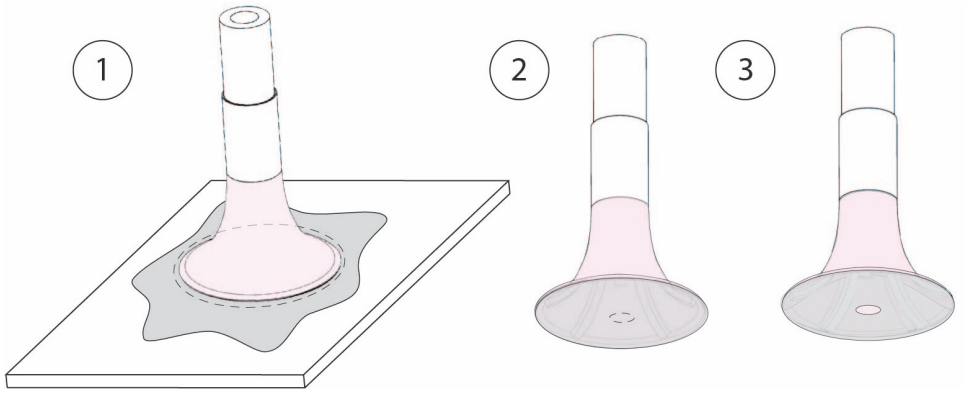


Figure 3.9: Fabrication process of the footprint layer. (1) A thin film of Ecoflex silicone is smeared on a plate. (2) After curing, the footprint is cut around the edge. (3) The closed footprint is cut open.

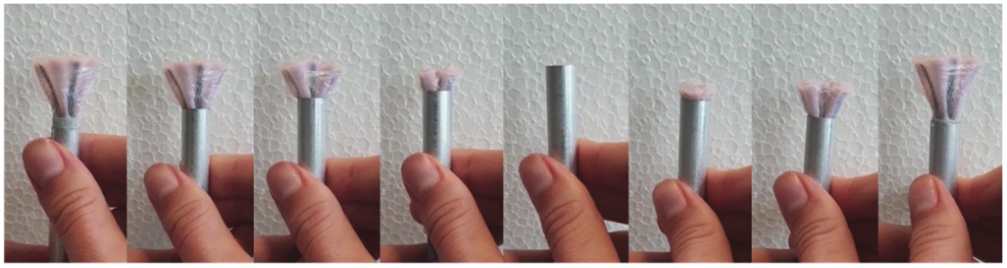


Figure 3.10: Video images of the final tip design extracted and retracted into a Ø 10 mm tube with 0.5 mm wall thickness, representing the trocar.

3.4 Experimental Validation

3.4.1 Experimental goal

The main goal of the experiments was to investigate the performance of the flexible suction tip, by (1) assessing the attachment performance of the suction tip on diverse (phantom) tissues and (2) measuring the effect of the vacuum pressure on the attachment performance.

3.4.2 Experimental setup

The experimental setup is illustrated in Figures 3.11a-d. In this experimental setup, the suction tip was connected to a 30 ml syringe by tubing with high buckling resistance (FESTO PAN-6x1). The suction tip was connected to an s-beam junior load cell (FUTEK, model FLLSB200) via a wire. This wire assured that the suction tip could move freely and, therefore, prevented premature detachment due to peel-off forces. Figure 3.11a shows a closeup of this part of the setup. The load cell, in turn, was connected to a linear stage via a 3D-printed base plate. The linear stage (ALMOTION LT50-TR-G8-200) was connected to a 3D-printed support that functioned as a containment unit for the gelatin tissue phantoms and animal tissues. The linear stage allowed for controlled motion of the load cell with the attached suction tip and thus for measuring the detachment force. Next to pull-off forces, this setup was able to measure slide-off forces exerted on the suction tip by connecting the load cell to the tip using a pulley system (Figure 3.11d). The friction between the pulley and the wire was negligible. The slide-off forces were exerted in line with the contact surface of the suction tip, preventing the generation of a moment that would tilt the suction tip. The vacuum pressure was measured by a vacuum sensor (NXP, model MPX4115AP) that was connected to the tubing of the suction unit using a T-piece connector. Both the load cell and the vacuum sensor were connected to an analogue signal conditioner (CPJ RAIL, SCAIME) and a data acquisition unit set at a sampling rate of 20 Hz (NI USB-6008, National Instruments Corporation).

3.4.3 Experimental design

Experimental variables

The detachment force of the suction tip was the main performance measure of the suction tip. The detachment force was defined as the force required to detach the suction tip from its substrate and could either be orientated perpendicular (pull-off force) or parallel (slide-off force) to the contact surface. The detachment force was tested on a variety of substrates and vacuum pressures. Phantom tissues were manufactured to mimic tissues with varying stiffness, see

Table 3.2: Phantom tissues are made with three different gelatin ratios to mimic three tissues with varying stiffness.

Phantom tissue	Gelatin percentage (wt%)	Stiffness (kPa)	Source
Skeletal muscle tissue	15	31	[58, 59]
Liver tissue	10	17	[59, 60]
Brain tissue	5	5.4	[59, 61]

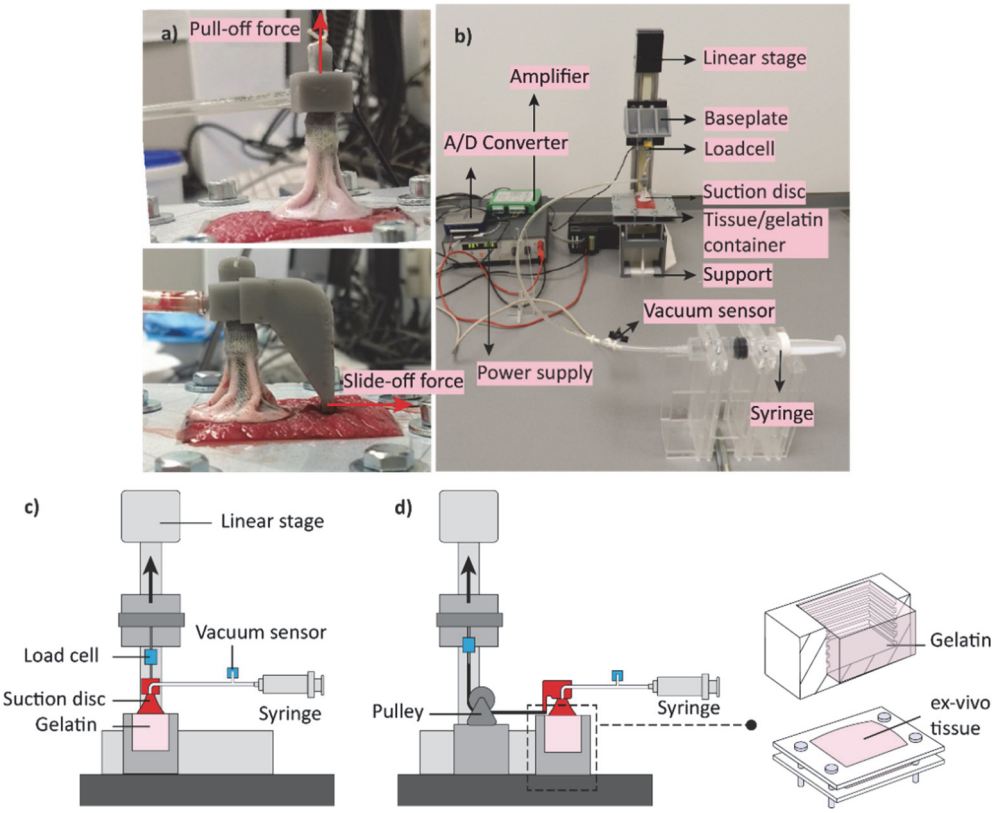


Figure 3.11: Experimental facility. a) The suction tip connected to the linear stage and the syringe, for pull-off measurements and slide-off measurements. b) Overview of the experimental setup to measure the detachment forces. c) Schematic overview of the experimental setup generating pull-off forces. d) Schematic overview of the experimental setup generating slide-off forces.

Table 3.2. A plexiglass plate was used as reference to compare the measurements of the phantom tissues with a fully stiff substrate. All phantoms and the plexiglass substrate were tested in dry and lubricated conditions, as it was expected that the mucus layer of tissues might influence the performance of the suction tip. Vacuum pressures of 30 kPa, 40kPa, 50 kPa, 60 kPa and 70 kPa were used. Additionally, experiments were conducted at the Skillslab in Erasmus Medical Centre (Rotterdam, the Netherlands) using *ex-vivo* chicken liver tissue and *ex-vivo* cow muscle tissue.

Experimental protocol

At the start of each experiment, the load cell was calibrated by subtracting the weight of the suction tip from the measured pull-off force. Next, the suction tip was placed on the substrate and the vacuum pressure was generated by pulling the syringe manually. The syringe was pulled until the desired vacuum pressure was reached, which was monitored in LabVIEW. 3D-printed clamps fixated the syringe at the desired position. The linear stage moved upward with a velocity of 1 mm/s. In order to achieve constant starting conditions, the following two steps

were taken. First, the suction tip was placed on the substrate with an untensioned wire. This ensures that no initial traction was applied to the load cell at the moment of vacuum initiation. Secondly, the tubing connected to the suction base was supported, as its weight could otherwise tilt the suction tip and break the seal. The gelatin was poured into containers with horizontal grooves on the inside to prevent the gelatin from getting lifted during the experiment. As gelatin degrades over time, only gelatin made the same day was used for experiments. The animal tissue samples were fixated between two surfaces of a 3D-printed clamp.

The main experiment was subdivided into two sub-experiments: 1) Experiment 1: Effect of the substrate and 2) Experiment 2: Effect of vacuum pressure. In Experiment 1, the suction tip was tested on different gelatin tissue phantoms, the plexiglass reference substrate and the *ex-vivo* tissue samples. Experiment 1 was further subdivided into five sub-experiments:

- Experiment 1.1. Pull-off measurements on lubricated phantom tissues.
- Experiment 1.2. Pull-off measurements on dry phantom tissues.
- Experiment 1.3. Pull-off measurements on *ex-vivo* tissue samples.
- Experiment 1.4. Slide-off measurements on lubricated phantom tissues.
- Experiment 1.5. Slide-off measurements on *ex-vivo* tissue samples.

The vacuum pressure was set to 50 kPa for all measurements of Experiment 1, based on the vacuum pressure of the commercially used *Octopus heart stabilizer* (Medtronic). The phantom tissues were lubricated with a thin layer of water-based lubricant. The slide-off measurements were performed on lubricated phantom tissues as these generally reassemble the surface properties of tissues closest, being surrounded by a slippery mucus layer. Measurements of Experiment 2 were all performed on lubricated phantom tissue made of 10 wt% gelatin while being subjected to pull-off forces. Vacuum pressures were generated in a range of 30 kPa to 70 kPa. Five trials per condition were executed for all experiments.

- Experiment 2. Pull-off measurements using vacuum pressures in a range of 30 kPa to 70 kPa.

Data analysis

The data of the pressure sensor and load cell was obtained using Labview 2013. From this data, the average detachment force $\pm$ standard deviation was calculated. The data from Experiment 1.1 was analyzed by a one-way ANOVA test to examine if the attachment performance when being subjected to pull-off forces is significantly different for the different substrates. Also, the average detachment force onto lubricated substrates obtained in Experiment 1.1 was compared with the average detachment force onto dry substrates obtained in Experiment 1.2 by an independent two-sided t-test. The data from Experiment 1.3 was analyzed using an independent two-sided t-test to examine if the attachment performance when being subjected to pull-off forces is significantly different for the muscle and liver tissue samples. Furthermore, the data from Experiment 2 was analyzed by a one-way ANOVA test in order to identify if the attachment performance is significantly different for the different vacuum pressures. The statistical significance was set at an α value of less than 0.05. The linearity of the relationship between vacuum pressure and detachment force was analyzed by the correlation coefficient.

3.5 Results

3.5.1 Pull-off measurements

Experiment 1.1 Lubricated phantom tissue

Experiment 1.1 showed that the suction tip induced higher detachment forces to the substrates with a lower stiffness, as illustrated in Figure 3.12. The average detachment force against pull-off forces and its standard deviation on the lubricated plexiglass plate, lubricated 15 wt% gelatin, lubricated 10 wt% gelatin and lubricated 5 wt% gelatin were 2.02 $\pm$ 0.49 N, 2.7 $\pm$ 0.13 N, 3.27 $\pm$ 0.15 N and 3.26 $\pm$ 0.16 N, respectively. A one-way ANOVA test shows that the difference between performance outcomes of the substrates is significant (F(3,16)=23.35, p=4.4×10^{-6}). It was noticeable that the suction tip failed a few times in its initial attachment on the plexiglass plate, while this did not happen with the gelatin phantom tissues. Furthermore, the observation was made that detachment from the rigid substrates (the plexiglass plate and 15 wt% gelatin) was often due to a V-shaped indentation (see Figure 3.13), while the perimeter of the suction tip kept its circular shape during detachment from the flexible substrates.

Experiment 1.2: Dry phantom tissue

The attachment performance of the suction tip against pull-off forces on dry substrates is illustrated in Figure 3.14. The average detachment force and its standard deviation on the dry plexiglass plate, dry 15 wt% gelatin, dry 10 wt% gelatin and dry 5 wt% gelatin were 2.04 $\pm$ 0.12 N, 3.79 N $\pm$ 0.41 N, 4.03 $\pm$ 0.28 N and 3.68 $\pm$ 0.33 N, respectively. One-way ANOVA testing

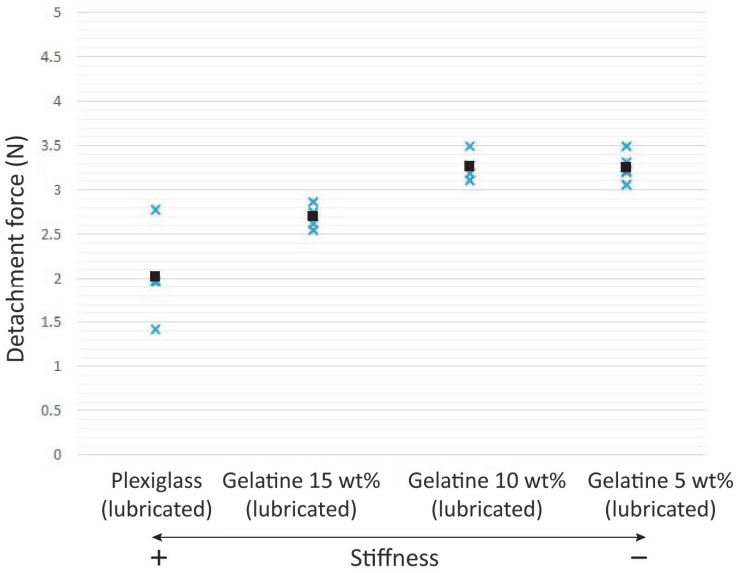


Figure 3.12: Attachment performance against pull-off forces of the suction tip for lubricated substrates that differ in stiffness. The black square represents the average detachment force and the blue crosses represent the individual measurements

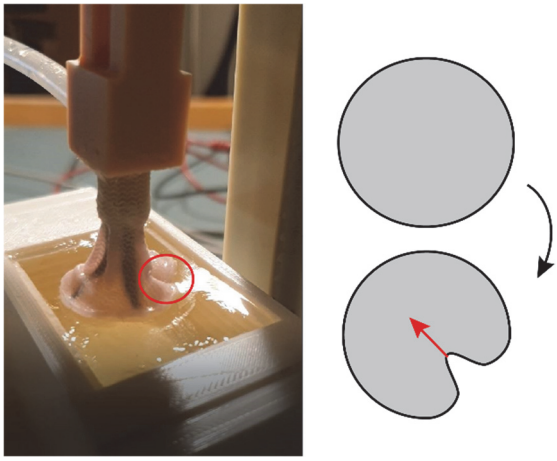


Figure 3.13: Detachment of the suction tip. At the left, a video image of the moment before detachment is shown for a 15 wt% gelatin substrate. The red circle encircles the inward slip of the rim, which causes detachment. At the right, this inward slip is schematically visualized from above.

shows that the difference in performance outcomes between the substrates is significant ($F(3,16)= 17.51$, $p=2.6 \times 10^{-5}$). An independent t-test shows an insignificant effect on the detachment force on the rigid plexiglass plate ($t(8)=0.0816$, $p=0.9369$) between the dry and lubricated state. However, there is a significant effect on the detachment force on the 15 wt% gelatin ($t(8)=5.6733$, $p=4.6861 \times 10^{-4}$), the 10 wt% gelatin ($t(8)=5.3835$, $p=6.5885 \times 10^{-4}$) and the 5 wt% gelatin ($t(8)=2.4758$, $p=0.0384$) between dry and lubricated states. Overall, the suction tip performs better on dry tissue compared to lubricated tissue.

Experiment 1.3: Ex-vivo tissue samples

The attachment performance of the suction tip against pull-off forces on *ex-vivo* animal tissue samples is illustrated in Figure 3.15. The average detachment force and its standard deviation on the liver tissue sample and the muscle tissue sample are 1.98 ± 0.90 N and 5.95 ± 0.52 N, respectively. An independent t-test shows that the difference in performance outcomes between the tissues is significant ($t(8)=8.5783$, $p=2.6333 \times 10^{-5}$). The suction tip performed less well on the liver tissue sample compared to the liver's phantom counterpart, whereas it performed better on the muscle tissue sample compared to the muscle's phantom counterpart.

3.5.2 Slide-off measurements

Experiment 1.4: Lubricated phantom tissues

The average detachment force against slide-off forces and its standard deviation on the lubricated plexiglass plate was 4.61 ± 0.96 N. The suction tip was observed to slide over the plexiglass plate's surface before it detached at once. No detachment force could be measured for the lubricated 15 wt% gelatin and the lubricated 10 wt% gelatin, as the suction tip kept

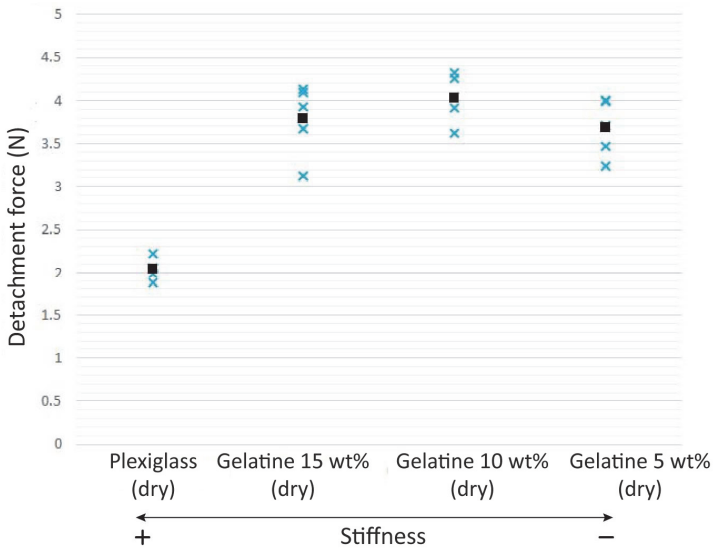


Figure 3.14: Attachment performance of the suction tip against pull-off forces for dry substrates that differ in stiffness. The black square represents the average detachment force and the blue crosses represent the individual measurements.

sliding over the gelatin phantoms without detaching. The average attachment force before the suction tip started sliding for the 15 wt% and 10 wt% gelatin phantoms were 2.06 $\pm$ 0.35N and 1.38 $\pm$ 0.20N, respectively. The suction tip did stop sliding on the lubricated 5 wt% gelatin. However, the gelatin broke before the detachment force could be reached. The reached average attachment force before the 5 wt% gelatin broke was 1.99 $\pm$ 0.35N.

Experiment 1.5: Ex-vivo tissue samples

The slide-off measurements on the *ex-vivo* animal tissue samples showed that the suction tip did not find grip on both surfaces. The suction tip kept sliding over the liver tissue until the end of the sample was reached, or until the tissue slipped out of the suction tip during sliding. The average attachment force during sliding was 1.74 $\pm$ 0.8N. The suction tip kept sliding over the muscle tissue sample until it touched a bump in the tissue surface. The average detachment force of the suction tip on muscle tissue was 6.37 $\pm$ 0.41N.

3.5.3 Experiment 2: Vacuum pressure

Experiment 2 showed that the relationship between the detachment force and the vacuum pressure is non-linear. (Figure 3.16). The relationship between the detachment force and vacuum pressure flattens out for higher vacuum pressures. The correlation coefficient *r* of the relationship is 0.85. The mean detachment force and its standard deviation with a vacuum pressure of 30 kPa, 40 kPa, 50 kPa, 60 kPa and 70 kPa were 1.94 $\pm$ 0.23 N, 2.91 $\pm$ 0.19 N, 3.27 $\pm$ 0.15 N, 3.33 $\pm$ 0.21 N and 3.32 $\pm$ 0.18 N, respectively. One-way ANOVA testing shows that the difference in performance outcomes between the pressures is significant at $p<0.05$ ($F(4,20)=47.62$, $p=6 \times 10^{-10}$). An independent t-test shows no significant difference in the detachment force with a vacuum pressure of 60 kPa and 70 kPa ($t(8)=1.0047$, $p=0.3445$).

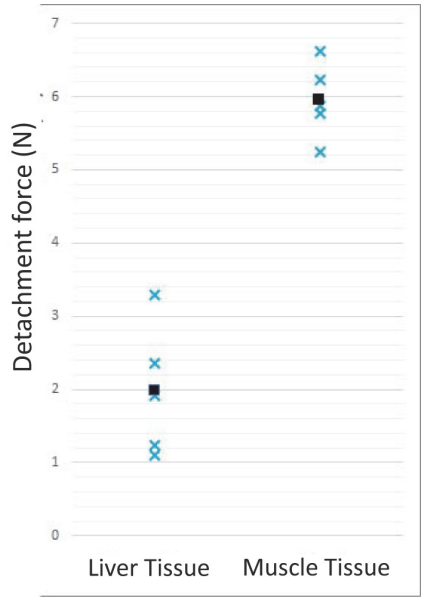


Figure 3.15: Attachment performance against pull-off forces of the suction tip for on *ex-vivo* liver tissue and *ex-vivo* muscle tissue. The black square represents the average detachment force and the blue crosses represent the individual measurements.

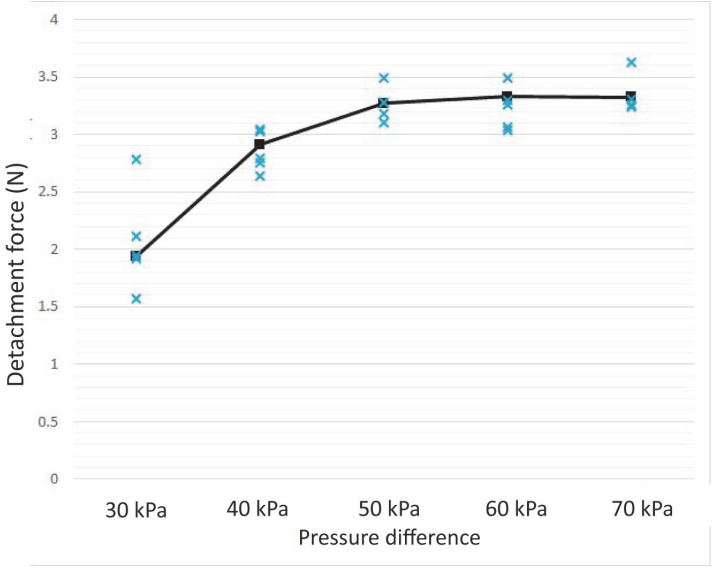


Figure 3.16: Attachment performance against pull-off forces for different vacuum pressure differences on 10 wt% gelatin. The black square represents the average detachment force and the blue crosses represent the individual measurements.

3.6 Discussion

3.6.1 Main findings

In this study, we have developed the first bio-inspired suction disc design for a suction gripper in MIS. A proof-of-principle experiment showed that the developed suction tip was able to successfully and safely grip slippery tissues without enclosing them. Noticeably, the attachment performance of the suction tip was higher on flexible substrates than on rigid substrates. The muscle tissue sample showed clear imprints of the suction tip after a measurement, which reveals that the suction tip is performing a shape grip onto the flexible tissue surface (Figure 3.17a). The tissue is pulled into the suction tip, where the tip's perimeter grasps the flexible tissue, somewhat similar to how a conventional gripper grips tissues (Figure 3.17b). This results in improved sealing and additional grip when attached to flexible substrates. Also, pulling the tissue into the suction tip results in an expansion of the suction surface, as more tissue surface is directly affected by the vacuum pressure. Figure 3.18 shows the force-time graphs and vacuum pressure-time graphs of a trial with the lubricated plexiglass plate and a typical trial with lubricated 10 wt% gelatin, subjected to pull-off forces. It shows that more leakage occurs during the attachment onto the rigid plexiglass plate, whereas less vacuum pressure is lost during attachment on the flexible gelatin. This substantiates that the suction tip seals better on flexible substrates.

When subjected to shear forces, the suction tip's shape grip again enhanced its attachment performance. The highly flexible 5 wt% gelatin was deformed sufficiently into the suction tip to prevent the tip from sliding over the slippery surface. The shape grip was insufficient on the 10 wt% gelatin, the 15 wt% gelatin and the plexiglass plate to prevent the suction tip from sliding. In future research, we propose to look into strategies that increase the grip of the footprint layer to lower the risk of sliding. Nature shows that this could be done by adding a

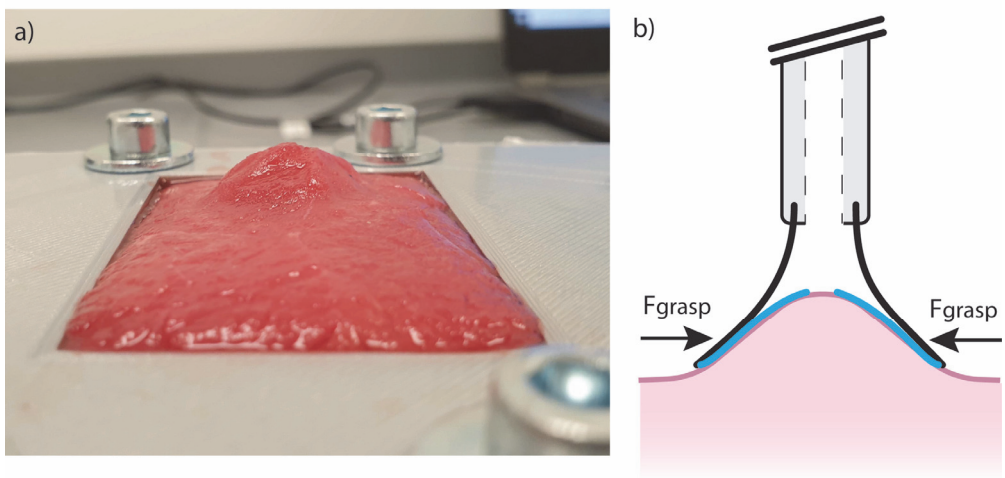


Figure 3.17: a) Imprint of the suction tip on the *ex-vivo* muscle tissue sample. b) Tissue is pulled into the suction tip, resulting in additional grasping forces (F_{grasp}) and an expansion of the suction surface.

microstructure on the footprint's surface [23, 31]. Optionally, the vacuum pressure could be increased when slip is detected, either by eye or an integrated sensing system.

Furthermore, it was observed that the suction tip had more grip on the dry substrates than on the lubricated substrates. This could be caused by the higher friction coefficient between the footprint and the dry substrate, which counteracts inward slip of the rim and thereby results in delayed detachment. This would explain why detachment forces of the suction tip are higher on the muscle tissue sample than the liver tissue sample for both the pull-off measurements and the shear measurements. Although the liver tissue is more flexible than the muscle tissue, its surface is covered by a highly slippery mucus layer. Overall, these results show that the suction tip performs best on flexible and dry tissues.

Increasing the vacuum pressure from 30 kPa to 70 kPa showed a relationship with the attachment force that acted linearly for low vacuum pressures, and flattens out for high vacuum pressures. It could be hypothesized that the substrate is pulled more into the suction tip using high vacuum pressures, increasing the foot print surface and thus the resistance to leakage. At some point, the substrate is maximally deformed and no longer affected by higher vacuum pressures. This would explain why the curve in Figure 3.16 flattens out for higher vacuum pressures. The force-time graphs of a typical measurement (Figure 3.19) indeed show more leakage during attachment at lower actuation pressures.

The developed suction tip was able to exert a maximal detachment force of 3.27 $\pm$ 0.15 N on slippery, flexible phantom tissue, 1.98 $\pm$ 0.90 N on liver tissue and 5.95 $\pm$ 0.52 N on

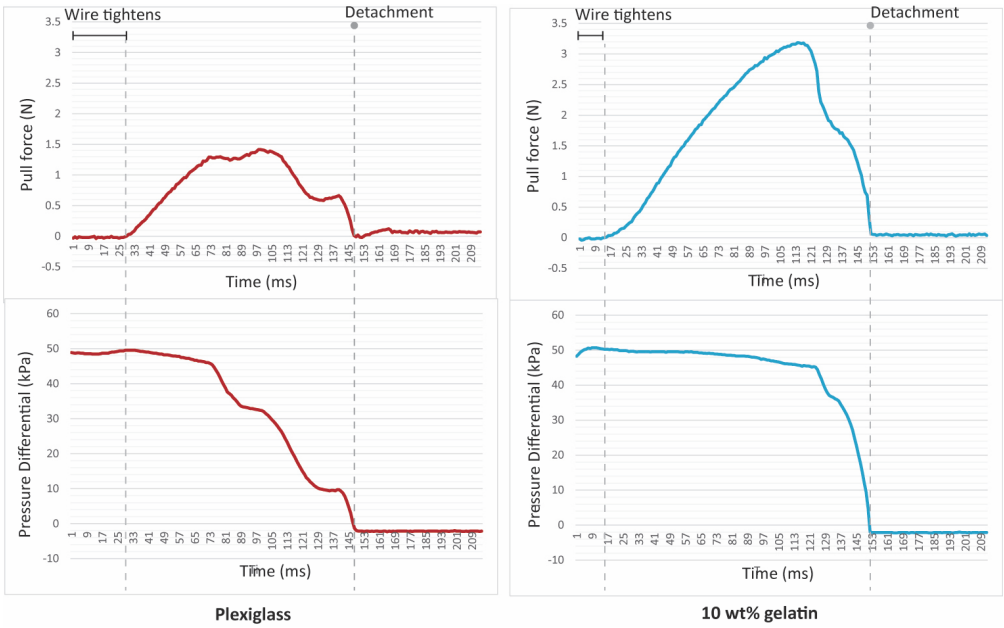


Figure 3.18: Occurrence of leakage on different substrate surfaces when subjected to pull-off forces. Left: Force-time and pressure-time graphs of a measurement with the lubricated plexiglass plate as substrate. Right: Force-time and vacuum pressure-time graphs of a measurement with lubricated 10 wt% gelatin as substrate. More leakage before detachment occurs with the rigid substrate compared to the flexible substrate, which means the suction tip seals better with flexible substrates. Both measurements were performed with an initial pressure difference of 50 kPa.

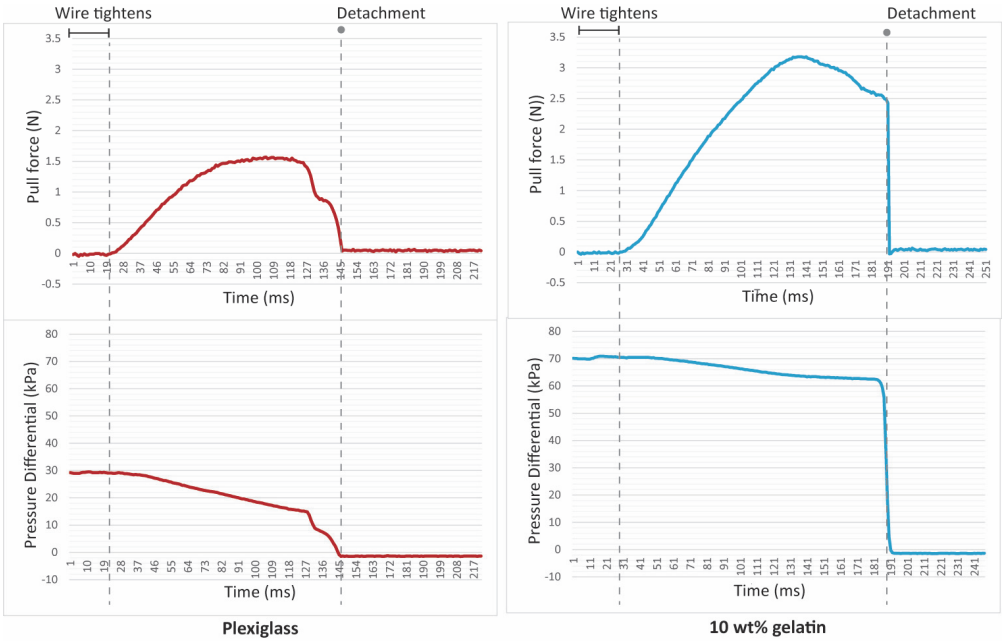


Figure 3.19: Occurrence of leakage using different actuation pressures when being subjected to pull-off forces. Left: Force-time and vacuum pressure-time graphs of a measurement with an initial pressure difference of 30 kPa. Right: Force-time and vacuum pressure-time graphs of a measurement with an initial pressure of 70 kPa. More leakage before detachment occurs using a low initial pressure difference compared to a high initial pressure difference. Both measurements were performed with a lubricated 10 wt% substrate.

muscle tissue. Theoretically, all listed organs in Table 3.1 can be lifted by these attachment forces. It could be argued that heavy organs would be lifted by multiple suction grippers anyway, to prevent local stress accumulation. Figure 3.20 shows the suction tip's ability to lift some arbitrary objects with varying shapes and surface characteristics. The tip is able to grip objects smaller than the suction tip's perimeter by adapting its shape to the object. Figure 3.21 shows how the suction tip is able to lift a slippery chicken heart. During surgery, the vacuum pressure should be monitored and optimized in order to gain sufficient grip on different tissue types, or multiple smaller suction gripper could be used to ensure proper attachment.

3.6.2 Application fields

In some specific applications, it could be favorable to use a suction gripper over a conventional gripper. For example, literature mentions the merit of using suction gripping in bowel and colon manipulations, as these thin membranes are most delicate and easily damaged by squeezing forces of the gripper's jaws [13, 18]. Another application for the suction gripper would be the fixation of voluminous slippery tissue, e.g. liver tissue, during the execution of a biopsy.

.3.6.3 Limitations

This study is subjected to some limitations. The exploratory nature of this study provides only initial insights into the performance behavior of the suction gripper. Future research, including

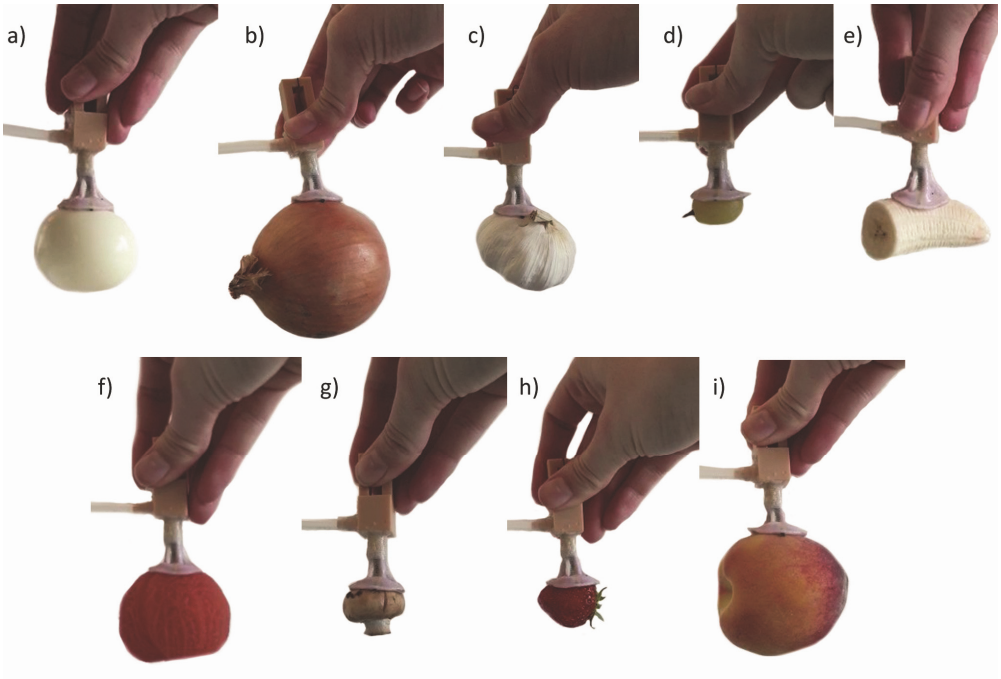


Figure 3.20: Demonstration of gripping objects with varying substrate characteristics, namely; a) peeled egg, b) onion, c) garlic, d) grape, e) banana, f) peeled tomato, g) cooked mushroom, h) strawberry and i) peach.

in-vivo studies, should show in which procedures the use of our suction gripper is favorable over a conventional gripper.

3.6.4 Design recommendations

For the device, some development steps are recommended to increase its potential. First, more research should be focused on optimizing the vacuum actuation, either manually or by a vacuum pump. Figure 3.22 shows a first prototype in which a vacuum chamber is integrated into the suction gripper's handle to facilitate manual actuation. Furthermore, future research should optimize the properties of the footprint layer in terms of grip and flexibility. Future studies should focus on i*n-vivo* experiments to evaluate the performance of the suction gripper in a realistic clinical setting. Biocompatible alternatives should be found for the materials that are currently incorporated in the prototype, before testing on porcine models. Miniaturization of the suction gripper, striving for an outer diameter of 5 mm, is required to function as an equal alternative to the conventional gripper in minimally invasive procedures. Optimization of the folding mechanism could result in a higher gain in the vacuum surface when converting from a folded into an unfolded state. Here, the nylon rays of the current folding mechanism could be replaced by superelastic nitinol wires. These nitinol wires have as an additional advantage that they can be accurately shaped using heat, which increases the shape consistency and durability of the suction grippers. These design recommendations will contribute to increasing the potential of our suction-based tissue gripper.

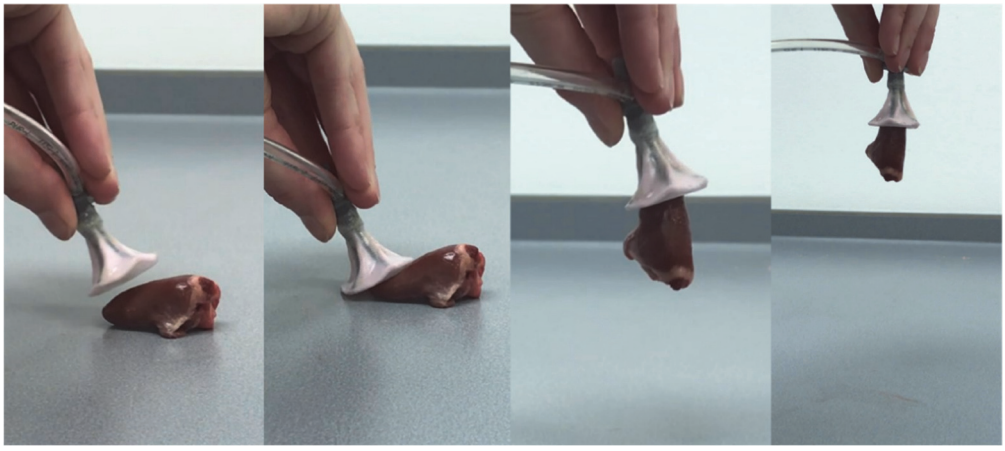


Figure 3.21: Demonstration of the suction tip lifting a chicken heart, where the tip's shape grip enhances its sealing.



Figure 3.22: Vacuum handle (adapted from a *Kiwi* vacuum assisted delivery system) integrated with the bio-inspired suction tip.

3.7 Conclusion

This study presented the development and successful first validation of a bio-inspired suction gripper for MIS. Similar to biological suction discs, our developed gripper is divided into two main parts: 1) the suction chamber inside the handle in which vacuum pressure is generated

and 2) the suction tip that attaches to the target tissue and allows for tissue manipulation during MIS. The suction tip consists of five layers to allow the suction tip to expand into a bigger surface area (foldability), to create an air-tight tip (air-tightness), to allow for a smooth transition of the suction tip through the trocar (slideability) and to create an air-tight seal with the tissue (seal generation) while magnifying frictional support (friction magnification). The experiments illustrated that our suction gripper outperforms man-made suction discs, as well as currently described suction grippers in literature in terms of attachment force (5.61 versus 5.95 N [18]) and substrate versatility (Figures 3.20 and 3.21). The suction tip's shape grip enhances its resistance against slipping during the shear experiments and adapts the tip's shape to grip objects smaller than the suction tip's outer diameter. Our bio-inspired suction gripper offers the opportunity for a safer alternative to the conventional tissue gripper in MIS.

References

[1] H. Visser, E. Heijnsdijk, J. Herder, and P. Pistecky, "Forces and displacements in colon surgery," *Surgical Endoscopy And Other Interventional Techniques,* vol. 16, no. 10, pp. 14263-1430, 2002.

[2] J. Wang, L. Ma, W. Li, and Z. Zhou, "Safety of laparoscopic graspers with different configurations during liver tissue clamping," *Biosurface and Biotribology,* vol. 4, no. 2, pp. 50-57, 2018.

[3] J. A. Cartmill, A. J. Shakeshaft, W. R. Walsh, and C. J. Martin, "High pressures are generated at the tip of laparoscopic graspers," *Australian and New Zealand journal of surgery,* vol. 69, no. 2, pp. 127-130, 1999.

[4] D. D. Marucci, J. A. Cartmill, W. R. Walsh, and C. J. Martin, "Patterns of failure at the instrument–tissue interface," *Journal of Surgical Research,* vol. 93, no. 1, pp. 16-20, 2000.

[5] E. Heijnsdijk, J. Dankelman, and D. Gouma, "Effectiveness of grasping and duration of clamping using laparoscopic graspers," *Surgical Endoscopy and other interventional Techniques,* vol. 16, no. 9, pp. 1329-1331, 2002.

[6] M. van der Voort, E. Heijnsdijk, and D. Gouma, "Bowel injury as a complication of laparoscopy," *Journal of British Surgery,* vol. 91, no. 10, pp. 1253-1258, 2004.

[7] P. Joice, G. Hanna, and A. Cuschieri, "Errors enacted during endoscopic surgery—a human reliability analysis," *Applied ergonomics,* vol. 29, no. 6, pp. 409-414, 1998.

[8] A. F. Khan, M. K. MacDonald, C. Streutker, C. Rowsell, J. Drake, and T. Grantcharov, "Tissue stress from laparoscopic grasper use and bowel injury in humans: establishing intraoperative force boundaries," *BMJ Surgery, Interventions, & Health Technologies,* vol. 3, no. 1, p. e000084, 2021.

[9] N. Scott, J. Knight, B. Bidstrup, H. Wolfenden, R. Linacre, and G. Maddern, "Systematic review of beating heart surgery with the Octopus® Tissue Stabilizer," *European journal of cardio-thoracic surgery,* vol. 21, no. 5, pp. 804-817, 2002.

[10] S. K. Singh, V. Tewarson, S. Gupta, and S. Kumar, "Making octopus tissue stabilizer more effective—a valuable technique," *Indian Journal of Thoracic and Cardiovascular Surgery,* vol. 29, no. 1, pp. 52-54, 2013.

[11] E. L. Jansen, J. Lahpor, C. Borst, P. Gründeman, and J. Bredée, "Off-pump coronary bypass grafting: how to use the Octopus Tissue Stabilizer," *The Annals of thoracic surgery,* vol. 66, no. 2, pp. 576-579, 1998.

[12] E. W. Jansen *et al.*, "Coronary artery bypass grafting without cardiopulmonary bypass using the octopus method: results in the first one hundred patients," *The Journal of thoracic and cardiovascular surgery,* vol. 116, no. 1, pp. 60-67, 1998.

[13] T. Ranzani, S. Russo, C. Walsh, and R. Wood, "A soft suction based end effector for endoluminal tissue manipulation," *in vitro,* vol. 1, p. 1.5, 2016.

[14] S. Becker, T. Ranzani, S. Russo, and R. J. Wood, "Pop-up tissue retraction mechanism for endoscopic surgery," in *2017 IEEE/RSJ International Conference on Intelligent Robots and Systems (IROS)*, 2017: IEEE, pp. 920-927.

[15] T. Horie, S. Sawano, and S. Konishi, "Micro switchable sucker for fixable and mobile mechanism of medical MEMS," in *2007 IEEE 20th International Conference on Micro Electro Mechanical Systems (MEMS)*, 2007: IEEE, pp. 691-694.

[16] N. Patronik, M. Zenati, and C. Riviere, "Preliminary evaluation of a mobile robotic device for navigation and intervention on the beating heart," *Computer Aided Surgery,* vol. 10, no. 4, pp. 225-232, 2005.

[17] N. A. Patronik, T. Ota, M. A. Zenati, and C. N. Riviere, "A miniature mobile robot for navigation and positioning on the beating heart," *IEEE Transactions on Robotics,* vol. 25, no. 5, pp. 1109-1124, 2009.

[18] D. Vonck, J. J. Jakimowicz, H. P. Lopuhaä, and R. H. Goossens, "Grasping soft tissue by means of vacuum technique," *Medical engineering & physics,* vol. 34, no. 8, pp. 1088-1094, 2012.

[19] M. Osaki, T. Omata, T. Takayama, and H. Ohizumi, "Transformable lung positioner for thoracoscopic surgery," in *2011 IEEE/SICE International Symposium on System Integration (SII)*, 2011: IEEE, pp. 138-143.

[20] P. Ditsche and A. Summers, "Learning from Northern clingfish (Gobiesox maeandricus): bioinspired suction cups attach to rough surfaces," *Philosophical Transactions of the Royal Society B: Biological Sciences,* vol. 374, no. 1784, 2019.

[21] F. Tramacere, L. Beccai, F. Mattioli, E. Sinibaldi, and B. Mazzolai, "Artificial adhesion mechanisms inspired by octopus suckers," in *2012 IEEE international conference on robotics and automation*, 2012: IEEE, pp. 3846-3851.

[22] D. K. Wainwright, T. Kleinteich, A. Kleinteich, S. N. Gorb, and A. P. Summers, "Stick tight: suction adhesion on irregular surfaces in the northern clingfish," *Biology letters,* vol. 9, no. 3, 2013.

[23] P. Ditsche, D. K. Wainwright, and A. P. Summers, "Attachment to challenging substrates–fouling, roughness and limits of adhesion in the northern clingfish (Gobiesox maeandricus)," *Journal of Experimental Biology,* vol. 217, no. 14, pp. 2548-2554, 2014.

[24] V. Kang, R. T. White, S. Chen, and W. Federle, "Extreme suction attachment performance from specialised insects living in mountain streams (Diptera: Blephariceridae)," *Elife,* vol. 10, p. e63250, 2021.

[25] F. Tramacere, E. Appel, B. Mazzolai, and S. N. Gorb, "Hairy suckers: the surface microstructure and its possible functional significance in the Octopus vulgaris sucker," *Beilstein journal of nanotechnology,* vol. 5, no. 1, pp. 561-565, 2014.

[26] J. E. Smith, "The Activities of the Tube Feet of Asterias rubens L.: I. The Mechanics of Movement and of Posture," *Journal of Cell Science,* vol. 3, no. 1, pp. 1-14, 1947.

[27] D. Nichols, "The histology and activities of the tube-feet of Echinocyamus pusillus," *Journal of Cell Science,* vol. 3, no. 52, pp. 539-555, 1959.

[28] W. M. Kier and A. M. Smith, "The structure and adhesive mechanism of octopus suckers," *Integrative and comparative biology,* vol. 42, no. 6, pp. 1146-1153, 2002.

[29] T. Maie, H. L. Schoenfuss, and R. W. Blob, "Musculoskeletal determinants of pelvic sucker function in Hawaiian stream gobiid fishes: interspecific comparisons and allometric scaling," *Journal of Morphology,* vol. 274, no. 7, pp. 733-742, 2013.

[30] J. De Meyer and T. Geerinckx, "Using the whole body as a sucker: combining respiration and feeding with an attached lifestyle in hill stream loaches (Balitoridae, Cypriniformes)," *Journal of morphology,* vol. 275, no. 9, pp. 1066-1079, 2014.

[31] Y.-C. Chuang, H.-K. Chang, G.-L. Liu, and P.-Y. Chen, "Climbing upstream: Multi-scale structural characterization and underwater adhesion of the Pulin river loach (Sinogastromyzon puliensis)," *Journal of the mechanical behavior of biomedical materials,* vol. 73, pp. 76-85, 2017.

[32] F. Tramacere, M. Follador, N. Pugno, and B. Mazzolai, "Octopus-like suction cups: from natural to artificial solutions," *Bioinspiration & biomimetics,* vol. 10, no. 3, p. 035004, 2015.

[33] J. A. Sandoval, S. Jadhav, H. Quan, D. D. Deheyn, and M. T. Tolley, "Reversible adhesion to rough surfaces both in and out of water, inspired by the clingfish suction disc," *Bioinspiration & biomimetics,* vol. 14, no. 6, p. 066016, 2019.

[34] A. Sadeghi, L. Beccai, and B. Mazzolai, "Design and development of innovative adhesive suckers inspired by the tube feet of sea urchins," in *2012 4th IEEE RAS & EMBS international conference on biomedical robotics and biomechatronics (Biorob)*, 2012: IEEE, pp. 617-622.

[35] F. Tramacere, N. M. Pugno, M. J. Kuba, and B. Mazzolai, "Unveiling the morphology of the acetabulum in octopus suckers and its role in attachment," *Interface focus,* vol. 5, no. 1, 2015.

[36] F. Tramacere, A. Kovalev, T. Kleinteich, S. N. Gorb, and B. Mazzolai, "Structure and mechanical properties of Octopus vulgaris suckers," *Journal of The Royal Society Interface,* vol. 11, no. 91, 2014.

[37] F. Tramacere, L. Beccai, M. Kuba, A. Gozzi, A. Bifone, and B. Mazzolai, "The morphology and adhesion mechanism of Octopus vulgaris suckers," *PLoS One,* vol. 8, no. 6, p. e65074, 2013.

[38] Z. Max, "Suction cup," Patent Appl. US2055397A, 1936.

[39] A. Tiwari and B. Persson, "Physics of suction cups," *Soft matter,* vol. 15, no. 46, pp. 9482-9499, 2019.

[40] D. M. Green and D. L. Barber, "The ventral adhesive disc of the clingfish Gobiesox maeandricus: integumental structure and adhesive mechanisms," *Canadian journal of zoology,* vol. 66, no. 7, pp. 1610-1619, 1988.

[41] G. S. Arita, "A comparative study of the structure and function of the adhesive apparatus of the Cyclopteridae and Gobiesocidae," University of British Columbia, 1967.

[42] M. Beckert, B. E. Flammang, and J. H. Nadler, "A model of interfacial permeability for soft seals in marine-organism, suction-based adhesion," *Mrs Advances,* vol. 1, no. 36, pp. 2531-2543, 2016.

[43] B. Persson, "On the mechanism of adhesion in biological systems," *Journal of Chemical Physics,* vol. 118, no. 16, pp. 7614-7621, 2003.

[44] B. Persson and S. Gorb, "The effect of surface roughness on the adhesion of elastic plates with application to biological systems," *The Journal of chemical physics,* vol. 119, no. 21, pp. 11437-11444, 2003.

[45] R. Bouaziz *et al.*, "Elastic properties of polychloroprene rubbers in tension and compression during ageing," *Polymers,* vol. 12, no. 10, p. 2354, 2020.

[46] W. M. Kier and A. M. Smith, "The morphology and mechanics of octopus suckers," *The Biological Bulletin,* vol. 178, no. 2, pp. 126-136, 1990.

[47] B. Fulcher and P. Motta, "Suction disk performance of echeneid fishes," *Canadian journal of zoology,* vol. 84, no. 1, pp. 42-50, 2006.

[48] M. Beckert, B. E. Flammang, and J. H. Nadler, "Remora fish suction pad attachment is enhanced by spinule friction," *Journal of Experimental Biology,* vol. 218, no. 22, pp. 3551-3558, 2015.

[49] B. Bhatia, "Adaptive modifications in a hill-stream catfish, Glyptothorax telchitta (Hamilton)," in *Proc Natl Inst Sci India*, 1950, vol. 16, no. 4, pp. 271-285.

[50] N. Singh and N. Agarwal, "The SEM surface structure of the adhesive organ of Pseudoecheneis sulcatus McClelland (Teleostei: Sisoridae), from Garhwal Himalayan Hillstreams," *Acta Ichthyologica et Piscatoria,* vol. 21, no. 2, 1991.

[51] A. K. Sinha and I. Singh, "The morphology of the adhesive organ of the sisorid fish, Glyptothorax pectinopterus," *Japanese Journal of Ichthyology,* vol. 36, no. 4, pp. 427-431, 1990.

[52] K. W. Conway, N. K. Lujan, J. G. Lundberg, R. L. Mayden, and D. S. Siegel, "Microanatomy of the paired-fin pads of ostariophysan fishes (Teleostei: Ostariophysi)," *Journal of Morphology,* vol. 273, no. 10, pp. 1127-1149, 2012.

[53] V. Kang, R. Johnston, T. van de Kamp, T. Faragó, and W. Federle, "Morphology of powerful suction organs from blephariceridlarvae living in raging torrents," *BMC zoology,* vol. 4, no. 1, p. 10, 2019.

[54] A. L. Ingram and A. R. Parker, "The anatomy and attachment mechanism of the haptor of a Capsala sp.(Platyhelminthes: Monogenea: Capsalidae) on the blue marlin, Makaira nigricans (Istiophoridae)," *Journal of Natural History,* vol. 39, no. 42, pp. 3633-3647, 2005.

[55] C. Borst *et al.*, "Coronary artery bypass grafting without cardiopulmonary bypass and without interruption of native coronary flow using a novel anastomosis site restraining device ("Octopus")," *Journal of the American College of Cardiology,* vol. 27, no. 6, pp. 1356-1364, 1996.

[56] G. L. de la Grandmaison, I. Clairand, and M. Durigon, "Organ weight in 684 adult autopsies: new tables for a Caucasoid population," *Forensic science international,* vol. 119, no. 2, pp. 149-154, 2001.

[57] D. Singh, Y. Bansal, S. M, A. N. Pandey, and S. Tyagi, "Weights of human organs at autopsy in Chandigarh zone of north-west India," *Journal of Indian Academy of Forensic Medicine,* vol. 26, no. 3, pp. 97-99, 2004.

[58] B. C. W. Kot, Z. J. Zhang, A. W. C. Lee, V. Y. F. Leung, and S. N. Fu, "Elastic modulus of muscle and tendon with shear wave ultrasound elastography: variations with different technical settings," 2012.

[59] M. Scali, P. Breedveld, and D. Dodou, "Experimental evaluation of a self-propelling bio-inspired needle in single-and multi-layered phantoms," *Scientific reports,* vol. 9, no. 1, p. 19988, 2019.
[60] S. Mueller and L. Sandrin, "Liver stiffness: a novel parameter for the diagnosis of liver disease," *Hepatic medicine: evidence and research,* pp. 49-67, 2010.
[61] S. Chatelin, A. Constantinesco, and R. Willinger, "Fifty years of brain tissue mechanical testing: from in vitro to in vivo investigations," *Biorheology,* vol. 47, no. 5-6, pp. 255-276, 2010.

03

CHAPTER 04

MAGNETIC SHAPE MORPHING STRATEGIES

04

ABSTRACT

In the field of Additive Manufacturing (AM), four-dimensional (4D) printing has emerged as a promising technique to fabricate smart structures capable of undergoing shape morphing in response to specific stimuli. Magnetic stimulation offers a safe, remote, and rapid actuation mechanism for magnetically responsive structures. This review provides a comprehensive overview of the various strategies and manufacturing approaches employed in the development of magnetically stimulated shape morphing 4D printed structures, based on an extensive literature search. The review explores the use of magnetic stimulation either individually or in combination with other stimuli. While most of the literature focuses on single-stimulus responsive structures, a few examples of multi-stimuli responsive structures are also presented. We investigate the influence of the orientation of magnetic particles in smart material composites, which can be either random or programmed during or after printing. Finally, the similarities and differences among the different strategies and their impact on the resulting shape-morphing behavior are analyzed. This systematic overview functions as a guide for readers in selecting a manufacturing approach to achieve a specific magnetically actuated shape-morphing effect.

Published as:
Kortman, V. G., De Vries, E., Jovanova, J., & Sakes, A. (2024). Magnetic Stimulation for Programmed Shape Morphing: Review of Four-Dimensional Printing, Challenges and Opportunities. *3D Printing and Additive Manufacturing, 11*(3), 977-993.

4.1 Introduction

4.1.1 4D printing

Additive Manufacturing (AM), also known as three-dimensional (3D) printing, is a layer-by-layer manufacturing technique following a digital design to produce a 3D object [1, 2]. Recent developments in 3D printing techniques enabled the development of printable stimuli-responsive materials, also called smart materials, resulting in printed structures that can transform their geometry, properties or functionality after printing under the influence of external stimuli [3]. This is now often referred to as four-dimensional (4D) printing [4]. In 4D printing, conventional 3D printing techniques are used, where smart materials add an extra dimension by enabling a transformation of the fabricated structure over time (Figure 4.1). It should be noted that 4D printing is not a standalone technology but adds an extra feature to conventional 3D printing techniques. Originally, Tibbits [4] defined 4D printing as a process that enables multi-material printed objects that can transform over time, or material structures that change from one shape to another, with a fourth dimension as time. Recent advances show that this definition might not be complete, since structures are developed that do not change their shape, but rather change properties like stiffness or colour under external stimuli [5, 6]. More recent definitions of 4D printing take this possibility into account together with the predictability and programmability of the response [7, 8]. This is a crucial aspect to enable the use of 4D printed materials outside the test laboratories in real-world applications. As of now, no consensus has been reached for a standard definition of 4D printing.

Smart 4D printed structures can respond to stimuli like temperature [9, 10], pH [11, 12], humidity [13, 14], light [15, 16], electric field [17, 18] or magnetic field [19-21]. Compared to other stimulation methods, magnetic actuation is an effective actuation method as it allows for non-contact stimulation and precise control by managing the intensity of the magnetic field. Additionally, magnetic particles can immediately respond to a changing magnetic field, resulting in a fast actuation of the shape change. In, for instance, thermal actuation, heat needs to be transferred in the material to enable shape change, which is not instantaneous [22]. Furthermore, this immediate magnetic interaction also provides the opportunity for reversible shape change. After removing the actuating magnetic field, the permanent shape can be restored. Another advantage of magnetic stimulation is the broad possibility of material selection. Where stimulation by light requires materials with responsiveness to specific wavelengths, for magnetic stimulation the smart material can be developed, for instance, by combining magnetic particles with different types of polymer materials. Some types of magnetic particles are even biocompatible [23]. Finally, magnetically responsive structures can be manufactured using 3D printing techniques. This enables the complex orientation of magnetic particles, resulting in precisely programmable shape morphing.

With the advantages of magnetic actuation, these structures offer numerous potential applications, including soft robotics [24], biomedical engineering [25] and flexible electronics [26]. There are several reviews published focusing on various aspects of 4D printing and the wide range of applications of soft smart materials [11, 27-32]. For instance, Hu [33] describes the possibilities of different materials, 3D printing fabrication techniques and applications. The review from Lui *et al.* [22] focuses especially on 4D printing directed at biomedical aspects.

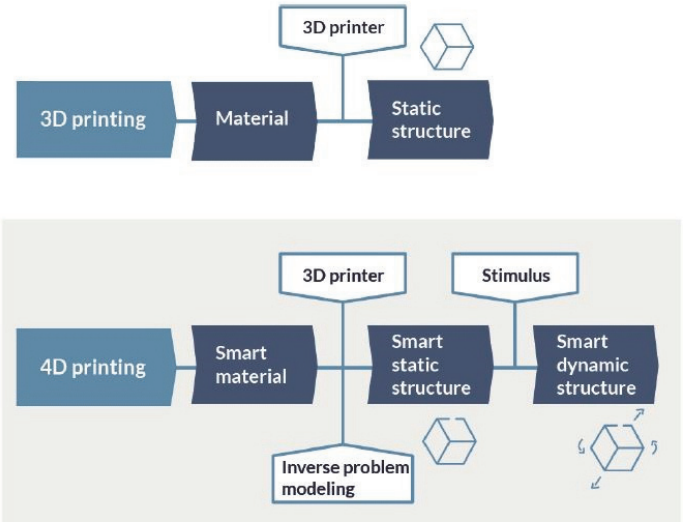


Figure 4.1: Process steps of 3D printing and 4D printing. Top: process steps of 3D printing methods. Bottom: process steps of 4D printing methods. 4D printing of structures enables change of shape or property in a predictable or programmable manner after the printing process under the application of an external stimulus.

Other reviews address material types used for 4D printing, like general composite materials [34], polymers [35-38], hydrogels [39], or even specifically the opportunities of PolyLactic Acid (PLA) [40]. None of these reviews focuses specifically on magnetic stimulation, but rather on all stimulation types used for 4D printing. Besides 4D printing, magnetic responsive material structures could be fabricated using conventional manufacturing methods. Bastola and Hossain [41] present a review of the shape morphing performance of magnetic soft materials, manufactured either by conventional manufacturing techniques or 3D printing. Also, Wu *et al.* [42] and Nguyen *et al.* [43] present reviews on soft magnetic composites and shape morphing. However, no review is found extensively discussing 4D printing strategies of magnetic responsive structures specifically focused on shape morphing. This review aims to fill this gap.

4.1.2 Goal of the study

This review focuses specifically on the 4D printing of magnetic-stimuli responsive structures, including structures that respond to a magnetic field alone, as well as structures with multi-stimuli responsiveness to a magnetic field and other stimuli. This literature review aims to provide an overview of different shape morphing strategies adopted in the field of 4D-printing of magnetic stimuli-responsive structures. Examples of different manufacturing techniques will be provided, as well as material combinations and application fields. This overview creates clarity on the possibilities and potential gaps in current developments. The overview could also inspire and guide readers in selecting a shape morphing strategy to achieve a specific function. The scope of this review does not contain an in-depth elaboration on the synthesis of magneto-active materials, for which we would like to refer to the study by Bastola & Hossain [44].

4.2 Methods

4.2.1 Search strategy and eligibility criteria

A systematic literature search was performed using the Scopus database and following PRISMA2020 guidelines [45]. The full search queries and search strategies are provided in Appendix 4.A1. The search was limited to articles in English and was performed on June 2, 2023, in the Scopus database. A two-step screening process was performed, comprising title and abstract screening and full-text assessment using the predefined eligibility criteria:

- The content of the study should provide technical information about the manufacturing process of the magnetic 4D-printed structure.
- The study should address structures fabricated by a 3D printing technique.
- The study should provide information about structures actuated by the magnetic field.
- The study should involve a structure that can change shape under the influence of a magnetic field. Structures that are only guided or navigated using a magnetic field are excluded.
- Studies only presenting theoretical modelling are excluded.
- Only full papers were included; conference proceedings were excluded.

4.2.2 Study selection

The search yielded 1591 records. Figure 4.A1 shows the search results in a PRISMA flow diagram. Duplicates were removed, resulting in a total of 1566 articles of which the title and abstract were screened. This resulted in 129 articles for full-text screening. Documents not available online were excluded, resulting in 121 documents for eligibility assessment. Finally, backward citation searching of the included studies resulted in the addition of 16 additional documents. Based on the eligibility criteria, 85 studies were selected for inclusion.

4.2.3 Classification

The literature included in this review describes different magnetically induced shape morphing strategies. A classification is presented based on the strategy used to enable shape morphing of the structures. A visual overview of this classification is presented in Figure 4.2. In all classes, different 3D printing processes are adopted, as well as different material composites, particle orientations and actuation methods. Whereas most studies addressed single-stimulus responsive structures for which a magnetic field activates the shape change (57), few developed multi-stimuli responsive shape morphing structures (28) in which a magnetic field in combination with another stimulus actuates shape morphing. To create flexible magnetic responsive structures, often a composite material is used consisting of a matrix material (i.e., polymers or fluids) and a functional magnetic filler. The matrix material is the component holding the functional filler together and forming the bulk of the composite. Magnetic particles are used as functional fillers to enable the magnetic responsive character of the composite material.

For the class of single-stimulus responsive structures, the orientation or distribution of the magnetic particles influences the shape morphing induced by an external magnetic field.

Random magnetisation can be achieved by homogeneously distributing magnetic particles with random magnetic orientation in the matrix material. This results in shape morphing dependent on the design and shape of the structure, as well as the type, strength and direction of the external magnetic field used to activate the shape morphing mechanism. On the other hand, the orientation or distribution of the magnetic particles can also be specifically programmed, thereby designing the resulting shape morphing under the influence of an external magnetic field. This programming of the magnetic particles can either be done during or after the 3D printing process and curing of the composite material.

Multi-stimuli responsive structures, on the other hand, are composed of a matrix material selected as a smart material that is already responsive to external stimuli. By adding a functional filler to this smart material, the composite's responsiveness to another stimulus is added. Shape Memory Polymers (SMP), which can respond to light or heat, are a class of materials that could be used. By adding a magnetic filler to, for example, a thermal sensitive SMP, both a temperature change and an external magnetic field could activate shape morphing of the structure. Combinations of other smart materials and magnetic fillers could lead to activation by the magnetic field and pH-value, light, humidity, ultrasound or electric field.

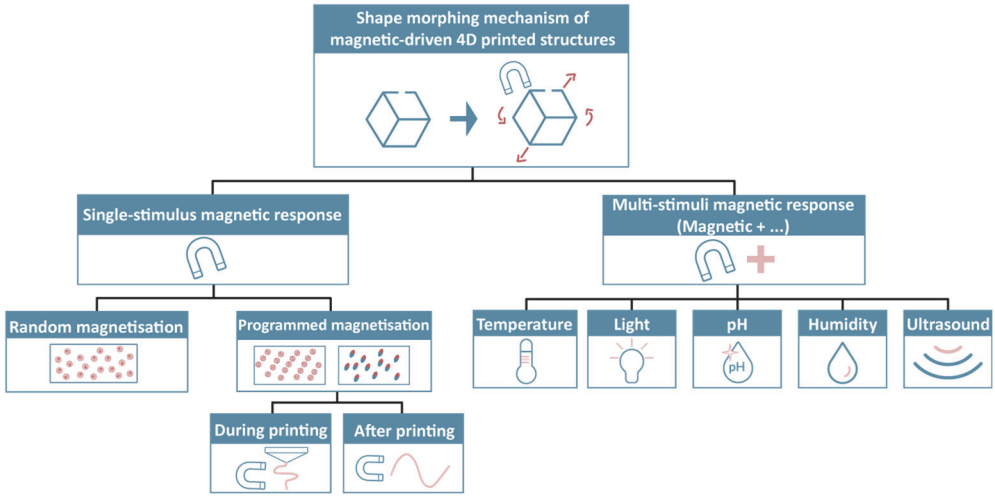


Figure 4.2: **Schematic classification of shape morphing strategies of magnetically responsive structures.** A subdivision is made between single-stimulus and multi-stimuli structures.

4.3 Single-stimulus magnetic responsive structures

4.3.1 Random magnetisation

Random orientation and homogeneous distribution

The use of a random magnetisation strategy to create magnetic responsive structures is done by printing a structure with a composite material consisting of homogeneously dispersed magnetic particles with random orientation in a matrix material. The literature included in this class makes use of soft magnetic nanoparticles. Compared to hard magnetic particles, soft single-domain magnetic nanoparticles do not require magnetisation to react to an external magnetic field. Hard magnetic particles need to be magnetised, which results in the particles obtaining a specific magnetisation orientation. Soft single-domain magnetic nanoparticles obtain immediate high magnetisation when a magnetic field is actuated. This results in the alignment of the magnetic particles with the external magnetic field causing the formation of particle chains. The resulting bulk deformation of the matrix material occurs due to the magnetic interaction force between the magnetic nanoparticle chains and the magnetic field (Figure 4.3) [46, 47]. The final shape change of the structure is the result of an equilibrium between the magnetic force (of the magnetic nanoparticles with the external magnetic field) and the elastic interaction force (of the matrix material). Since the soft magnetic nanoparticles exhibit no magnetic remanence, they lose the magnetisation upon removal of a magnetic field. They return to a random orientation and the permanent shape of the structure is restored due to the elastic force. Soft magnetic particles of carbonyl iron or iron oxide (Fe_3O_4) are commonly used as magnetic fillers in combination with a matrix material consisting of a fluid, a hydrogel or an elastomer.

Ferrofluid injection in hollow structures

When magnetic nanoparticles are dispersed in a fluid (the so-called carrier fluid), this is called a ferrofluid. This ferrofluid can be injected in a 3D printed, hollow structure. A hollow structure can be partially filled with ferrofluid so that the fluid itself can also still flow (Figure 4.4a), or completely so that only the magnetic particles in the fluid can move (Figure 4.4b). Partially

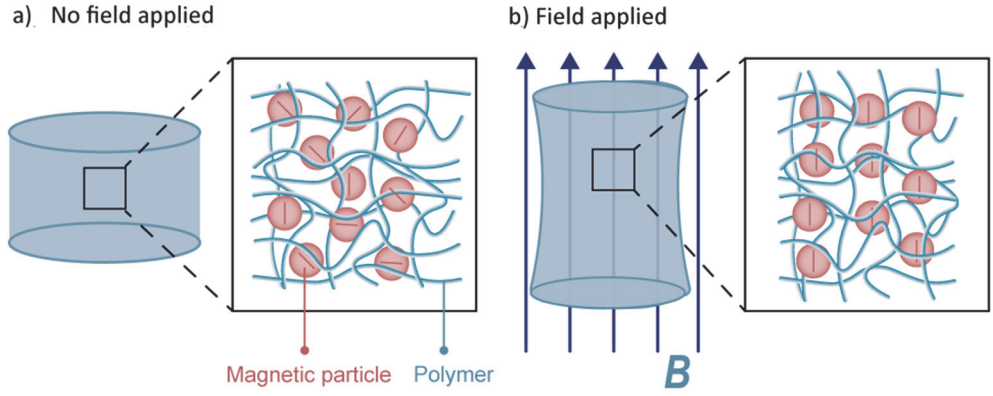


Figure 4.3: Random magnetisation of soft single-domain magnetic particles. a) Homogeneous distribution of the magnetic particles (red) with random magnetic orientation in the material matrix (blue) when there is no external magnetic field. b) The magnetic particles (red) align in the direction of the external magnetic field and cause bulk deformation of the matrix (blue).

filling the structure with fluid will result in a flow of fluid upon an external magnetic field. The magnetic force will then bend specific parts of a structure towards the external magnetic field [48]. Completely filling a structure with ferrofluid lets an external magnetic field control both the shape and stiffness of the printed structures [49]. Due to the random distribution of the magnetic nanoparticles in a ferrofluid, it has no net magnetisation when no external magnetic field is applied [50]. In the presence of an external magnetic field, the magnetic nanoparticles align with the applied field. The shape change of the structure depends on the magnitude of the magnetic force and the material properties of the printed hollow structure. The stiffness of the ferrofluid can be adapted due to its ability to change its rheological behaviour when a magnetic field is applied. In the presence of a magnetic field, the ferrofluid behaves like a semi-solid [51]. The magnetic particles align with the magnetic field and form chain structures (Figure 4.4b). These chains oppose the motion of the fluid due to the magnetic force, influencing the viscosity of the fluid and the properties of the complete structure.

Different 3D printing methods are adopted for printing hollow structures, for instance, stereolithography [49] or Fused Deposition Modelling (FDM) [52]. However, in all examples in the included literature, the ferrofluid is injected manually with a syringe after printing the hollow structure [48, 49, 52, 53]. The design of the hollow structure defines the shape change actuated by the magnetic responsive ferrofluid. By designing this with care even multi-modal shape change can be achieved. For instance, Han *et al*. [52] developed a stent structure that can elongate or contract under an applied uniform or gradient magnetic field, respectively [52]. In a uniform magnetic field, the magnetic particles align along the straight magnetic field lines which causes elongation of the structure, whereas a gradient magnetic field results in compression of the structure. This multi-modal shape change provides interesting possibilities, for example for creating temporary stents that transport to a desired location and expand to reopen the vessel.

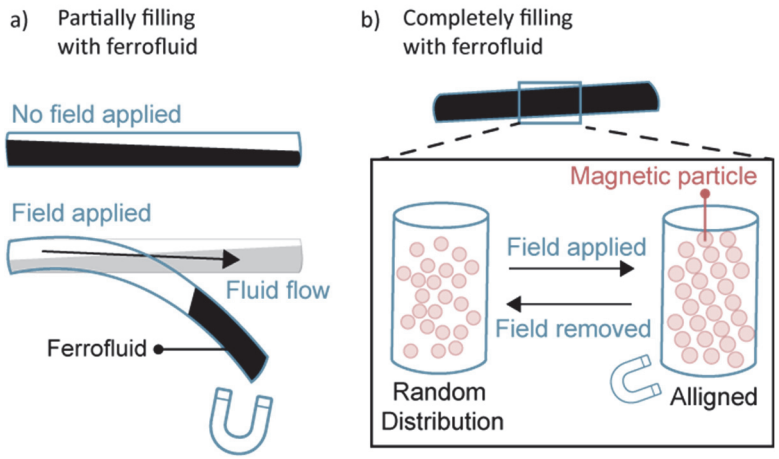


Figure 4.4: Ferrofluid in hollow structures. a) Partially filling a structure with ferrofluid allows the fluid to flow when attracted by an external magnetic field. b) Completely filling a structure with ferrofluid changes the order of the magnetic particles in the ferrofluid, since they align with the applied magnetic field. Here, the magnetic particles are visualized in red and the matrix in blue.

Magnetic particles in hydrogels

Another option is to homogeneously disperse magnetic particles in a polymer, for instance, a hydrogel or an elastomer. The advantage of this is that the structure can be 3D printed with magnetic particles embedded in the polymer matrix. Compared to ferrofluids, these structures can be single processing structures, where there is no need to assemble separate parts or inject magnetic particles. Another difference is that the magnetic particles are attached to the polymer chain during the curing process, and thus rigidly fixed in the matrix, instead of being able to move freely in the carrier fluid [54]. The orientation and direction of the magnetic particles can, also in this case, be influenced by an external magnetic field.

Hydrogels are usually composed of large amounts of water and cross-linked polymer networks. The biocompatibility of hydrogels makes it an interesting material, for instance in bio-engineering. By adding magnetic particles to a hydrogel network, magnetic responsive structures can be printed via extrusion-based 3D printing methods. These structures can be attracted to an external magnetic field, exhibit self-healing, or the magnetic field can control the swelling degree [55, 56]. The latter is of interest for applications in on-demand drug release [55]. However, in the literature, only rather simple shape change is shown in hydrogels with randomly distributed magnetic particles.

Magnetic particles in flexible elastomers

Magnetic particles can also be added to, for instance, PLA [57], PolyDiMethylSiloxane (PDMS) [47, 58], ThermoPlastic Rubber (TPR) [46, 59], PolyVinyl Alcohol (PVA) [60], or photocurable resins [61]. As said, the final shape morphing under the influence of a magnetic field is based on the equilibrium between the magnetic force and the elastic interaction force. Besides the properties of the matrix material, other aspects influence the shape morphing of structures with random magnetisation profiles of the magnetic particles. By varying the concentration of magnetic particles, the responsiveness to the external magnetic field is adapted. Here, a higher concentration results in higher magnetic responsiveness [57]. Also, the thickness and length of the structure influence the responsiveness. A thinner structure with fewer printed layers is easier to bend and deform. An explanation for this could be that during printing, some materials in the previous layer could be melted and fill voids [46]. For the length of a structure, experiments with a 3D printed magnetic beam show that a longer beam is more sensitive to a magnetic field and shows a larger bending movement [46]. Therefore, by combining different parameters in the design, the deformation under a magnetic field could be tuned.

Fabrication of magnetic flexible elastomer structures

Just like different materials, also a wide range of 3D printing methods could be used for the fabrication of magnetic flexible elastomer structures. For instance, FDM [46, 62, 63], Direct Ink Writing (DIW) [47, 58, 60] or Digital Light Processing (DLP) [61].

For FDM, the basic principles are based on extruding material in a semisolid state. The material must solidify while remaining in the printed shape and bond to the previously extruded material. Most FDM printers are based on temperature to control the material state. To print magnetic responsive structures using FDM, magnetic filament is fabricated by melting the polymer particles, adding the magnetic particles, stirring this mixture to ensure a homogeneous distribution, and finally using a twin-screw to extrude the filament [46, 57]. This filament is then used in the FDM printer to print the desired structure. DIW is similar to FDM

in that the material is extruded via a nozzle, however, for DIW the material needs to be cured after extrusion. The magnetic particles are stirred in the ink before extrusion via a syringe. The concentration of magnetic particles influences the resulting magnetic responsiveness. However, the concentration should not be too high, since adding magnetic particles to a matrix material influences the rheological behaviour of the melted filament or ink. This influences the flow through a nozzle under applied shear stress and the resulting printing resolution [58]. Mixing, for instance, thermoplastic rubber with carbonyl iron particles results in ink that can be extruded using FDM.

Different structures can be printed, exhibiting shape morphing under the influence of an external magnetic field. Cao *et al.* [46] showcase this using their 3D printed flower structure that opens its petals depending on the length and position of the individual petals when placed on a magnet. When using random magnetisation with homogeneous magnetic particle distribution, other design characteristics can additionally influence the shape change. Roh *et al.* [47] showed the influence of the outer shape of different parts of a printed elastin mesh from a mixture of PDMS and carbonyl iron particles. By printing the mesh with wavy and straight segments, different shape morphing results could be shown actuated by a magnetic field. The wavy parts bend more towards the external magnet placed underneath the structure, deforming the structure and enabling the grabbing of an object. It is also shown that these structures present opportunities for applications that require a fast response [46, 58]. Furthermore, the properties of the external magnetic field can influence the shape change of the structures. A printed butterfly structure from PDMS with magnetic particles is used to show that the flapping speed of the butterfly depends on the varying speed of the external magnetic field. Zhu *et al*. [58] showed that a faster varying magnetic field results in a faster flapping speed of their structure. Therefore, by modulating the intensity, distribution and varying speed of the external magnetic field, the shape change of the structure can be influenced [58].

A 3D printing technique not based on the extrusion of material is DLP, where a projector light source is used to cure an entire layer of photopolymer. A vat contains a liquid photopolymer in which magnetic particles are dispersed. Similar to DIW, when using photopolymerisation-based techniques, the concentration of magnetic particles should be chosen with care. The particle concentration should not be too high, since the magnetic particles are competing with the photo-initiator for light absorption. The particles are black, exhibiting poor optical transmission and absorbing part of the light, diminishing the ultraviolet (UV) energy available for curing the photopolymer [61]. However, by carefully selecting the materials and printing parameters, it is still possible to fabricate flexible magnetic responsive structures exhibiting shape changes like bending and stretching [64].

4.3.2 Programmed magnetisation

Programming magnetic particles

Instead of homogeneously dispersing magnetic particles with random orientations in a matrix material, the distribution of soft magnetic particles or the orientation of magnetised hard magnetic particles in the matrix material can be programmed. This influences the shape morphing of magnetic responsive structures. The anisotropy or magnetisation direction in the structure improves responsiveness to an external magnetic field. Without programming, the magnetic moments and directions of all particles have random orientations and directions

(Figure 4.5a). By programming the magnetic moments of all particles in a specific direction, the magnetic attraction force of the structure is optimised (Figure 4.5b). When an external magnetic field is applied, the direction and programming of the magnetic domains define the shape morphing (Figure 4.5c).

Hard magnetic particles require magnetisation to give them magnetic properties and retain magnetic remanence. Therefore, upon the magnetisation of the particles, a specific direction of the magnetic dipoles is programmed, resulting in a programmed magnetic moment when interacting with an external magnetic field takes place. However, to enable a programmed magnetic moment with soft magnetic nanoparticles, another strategy is needed, since they have a single magnetic domain. This can be achieved by creating anisotropy in the distribution of the particles in the matrix. This can be done by patterning the soft magnetic particles with an external magnetic field before the material is cured. The soft magnetic particles align in the direction of the magnetic field and form particle chains. These chains are locked in the matrix when the material is cured.

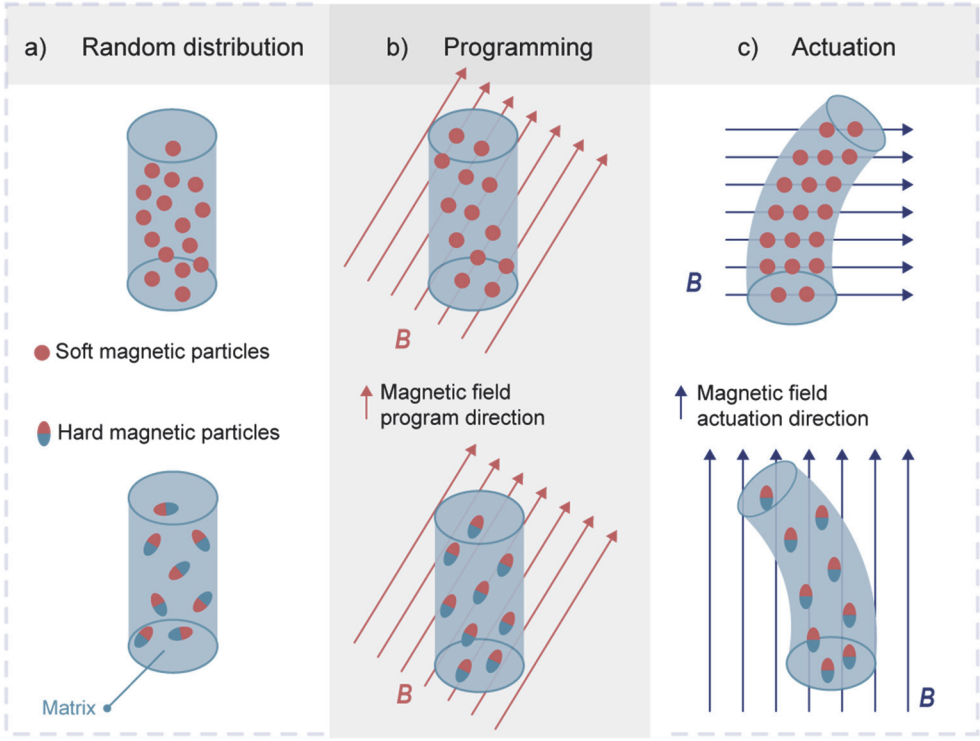


Figure 4.5: **Shape morphing mechanism of programmed magnetic responsive structures.** a) Before programming, the particles are randomly distributed (for soft magnetic particles) or randomly oriented (for hard magnetic particles) in the matrix (blue). b) During (soft and hard magnetic particles) or after (only hard magnetic particles) the fabrication process, the particles are programmed in a specific pattern (soft) or magnetisation direction (hard) defined by the magnetic field direction. c) Upon activation with an external magnetic field, the particles align with the magnetic field, resulting in a shape change of the flexible structure.

Two strategies are adopted to program the magnetisation of these structures: the programming of the orientation or patterning of the magnetic particles can be done *during* or *after* the 3D printing manufacturing process. The programming of magnetic particles during printing can be accomplished with both soft and hard magnetic particles. Another option is to print structural elements of magnetic composite material in a multi-material structure. By planning the location of the magnetic composite material, the magnetic response is tuned. When adopting the strategy of programming the magnetic particles after printing, hard magnetic particles should be used. The magnetic particles are first fixed in the fabricated structure during printing. After printing, this structure is deformed in the desired shape, followed by the magnetisation of a strong external magnetic field, resulting in the reorientation of the magnetic particles. The high remanence of hard magnetic particles is necessary to program the magnetisation profile in the matrix.

Programming during printing

The shape morphing of magnetic responsive structures can be programmed by designing structural elements of magnetic material in a non-magnetic material. By using a material with and without magnetic filler, the interaction between the two creates different shape morphing results under an external magnetic field [20, 65-69]. The resulting shape morphing of a structure could be programmed based on the magnetic moment of the magnetic structural elements, which depends on the element orientation and size, the external actuation magnetic field, and the shape of the complete structure [65, 70]. Figure 4.6a shows how to design such a structure. First, the desired magnetic moments are determined which define the orientation of the structural elements. After this, the structure is fabricated by printing the magnetic structural element in a flexible material. This way, a wide variety of movements can be programmed and actuated, including walking, swimming and grabbing [65-68]. The programmed structural magnetic elements permit the predesigned shape transformation of the structure induced by an external magnetic field.

Alternatively, magnetic elements could be printed and sealed in a flexible matrix [65], part of the structure could be filled with magnetic fluid [66], or both the magnetic and nonmagnetic material could be 3D printed using multi-material printing. For instance, Ji *et al.* [67] used two material vats, one filled with magnetic particles and one filled with nonmagnetic photocurable resin, and switched the vats once the material was cured. For this purpose, extrusion-based methods, like FDM, could also be used. By incorporating multiple printing heads with different materials, both materials can be printed in a predefined path [20, 68, 69].

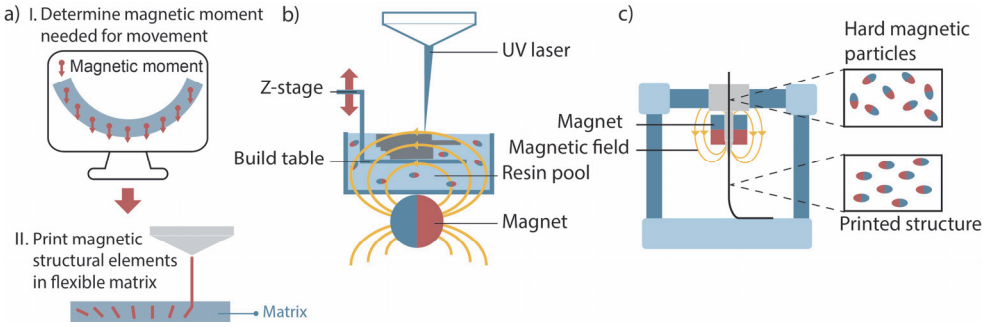


Figure 4.6: **Fabrication techniques for magnetic programming during printing.** a) Design and manufacturing of structural elements in the material matrix (blue) [18]. b) Simplified schematic of vat photopolymerisation technique. The resin vat contains a photopolymer mixed with magnetic particles. By the external magnet placed underneath the vat, the alignment of the particles can be programmed. [68-72] c) Simplified schematic of direct ink writing technique with a magnetic field around the printing nozzle [73-76].

Instead of using multi-material systems, the magnetic particles inside the magnetic material can be designed in a specific direction or orientation to achieve programmed shape morphing. Reorientation of hard magnetic particle domains or alignment of soft magnetic particles can be achieved during the printing process by applying an external magnetic field to the structure before the magnetic particles are fixed in the flexible matrix material. This allows for more complex and defined shape changes, as the magnetic particles can be programmed in different orientations in a single structure. It should be noted that the magnetic particles are usually magnetized before printing, whereas reorientation of the particles is achieved during printing.

In the included literature, several examples are found in which 3D printing is used only to print a mould [71, 72, 77]; the magnetic responsive structures are fabricated using more conventional techniques. The advantage of a mould is the repeated use for the fabrication of the magnetic responsive structure. The material mixture is poured into the mould, and by placing an external magnet underneath the mould while curing the material, the magnetic particles are aligned and fixed in the matrix material [71]. However, the advantages of using 3D printing as the primary fabrication method are not only fewer fabrication steps but also more specific control over the programming of different orientations or alignments in different layers of the structure. By selectively curing the matrix material, different magnetisation profiles or particle alignments could be programmed in one structure by switching the orientation of the magnetic field or printing direction. Literature shows examples of both vat photopolymerization processes [71, 73-76, 78-81] or extrusion-based methods [82-87] for the fabrication of 3D printed magnetic structures while orienting or aligning the magnetic particles during the printing process.

For the magnetically-actuated photopolymerization process, an external magnet is placed underneath the resin vat (Figure 4.6b). The resin consists of a photopolymer mixed with magnetic particles. While selectively curing the resin and controlling the direction of the magnetic field from the external magnet, different magnetisation domains can be programmed in the structure. The curing can be done with an ultraviolet laser [78, 80] or a digital light projector [73, 74, 76, 79]. Before solidifying the resin, the magnetic particles can

freely move in the resin. When using soft magnetic particles like carbonyl iron, upon application of an external magnetic field, the particles align with the magnetic field to form chain-like clusters [74, 80]. These clusters are fixed in the polymer matrix after curing, which enables the shape morphing actuated by an external magnetic field. By controlling the location of the external magnet, it is possible to direct the magnetic particles to a specific location in the structure [73]. Using soft magnetic particles, cilia-like surfaces can be developed that can serve as micro-pumping systems [80]. Also, hard magnetic particles as neodymium (NdFeB) particles or strontium ferrite particles, can be used. However, these need to be pre-magnetised in a uniform magnetic field to obtain magnetisation [78, 79]. The orientation of the hard magnetic particles is adjusted by the external magnet underneath the resin vat. This orientation is fixed upon the curing of the photopolymer. Compared to soft magnetic particles, a less intense magnetic field is needed for the actuation of the shape morphing of a structure with hard magnetic particles. A disadvantage is the risk of agglomeration of the hard magnetic particles due to the magnetic attraction force of the magnetised particles [78]. Xu *et al*. [79] present planar micro-robots fabricated with hard NdFeB particles in a photocurable resin without agglomeration of the particles. The robots can show complex shape morphing according to the designed magnetisation profiles. This gives possibilities for multiple applications, for instance in creating magnetic grippers or walking robots [79].

Where in vat photopolymerization methods the magnetic particles are homogeneously distributed in the resin vat, for DIW, the magnetic particles are distributed in the filament or ink. For this, hard magnetic particles are used. The non-magnetised hard magnetic particles are added to the uncured elastomer matrix with silica nanoparticles. The resulting composite ink is then magnetised under an impulse magnetic field. The silica nanoparticles are added to ensure the right rheological properties required for DIW. Similar to vat photopolymerization methods, a magnet can be placed under or beside the building platform to orient the particles before curing [82, 83]. Another option is to place a magnet around the extrusion nozzle, orienting hard magnetic particles as they are extruded (Figure 4.6c) [84-86]. The hard magnetic particles in the extruded material are magnetised before printing, and the magnetic field around the nozzle orients the magnetic polarities. This allows programming different magnetic polarities during the printing in separate layers and locations, either by reversing the magnetic field around the nozzle or by changing the printing direction [85, 87]. To avoid interference with the magnetic polarities of the printed structure, a shield is attached to the nozzle to attenuate the magnetic field strength. After printing, the structure is cured in an oven, maintaining the printed magnetic domains.

Programming after printing

The second strategy for the orientation of magnetic particles is to program the magnetic domains after the printing of the structure is finished [19, 88, 89]. This strategy can only be adopted when hard magnetic particles are incorporated into the structure since the high remanence of these particles is needed to program the magnetisation domain. Figure 4.7 presents a schematic of the programming strategy. First, a structure is printed with a homogeneous distribution of non-magnetised hard magnetic particles, using for instance DIW [19, 89] or Selective Laser Sintering (SLS) [88]. The flexible structure could then be deformed in the desired transformation shape [19, 89]. By using a strong external magnetic field, the

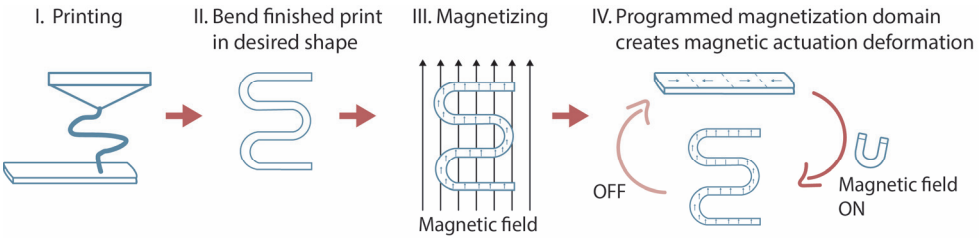


Figure 4.7: Schematic of the programming process after the printing is finalised. I. 3D printing of the magnetic structure. II. Bend the finished structure in the desired shape. III. Magnetize the structure using a high-intensity external magnetic field. IV. Actuate the structure using a low-intensity external magnetic field.

hard magnetic particles are then magnetised in this specific magnetisation configuration. The particles align their polarities with the external magnetic field. Due to their remanence, this magnetisation configuration remains after the strong external magnetic field is removed. The unconstrained structure transforms to the original shape due to the elasticity. Upon application of a smaller actuating magnetic field, the magnetic domains are aligned with the external field and the programmed shape is formed. Multi-functional magnetic actuation can be realised by reprogramming the magnetic configuration. By reapplying a strong external magnetic field, which should be higher than the coercive strength of the magnetic material, the previous configuration is erased and the new magnetisation profile can be re-magnetised. Zhang *et al*. [19] showcased a magnetic responsive hand, fabricated from PDMS with hard NdFeB particles, printed using injection printing. The hand was first printed, after which it was manually folded in a shape (rock, paper or scissor), in which it was magnetised by a strong magnetic field. To switch between the different shapes, manual reprogramming is required. Wu *et al.* [88] show an example of printing a structure in Thermoplastic PolyUrethane (TPU) using SLS. SLS is a powder-based 3D printing method that enables the printing of polymeric composites with high mechanical strength [88]. Hard non-magnetized NdFeB particles are mixed with the TPU powder. A laser draws thin lines in the powder mixture, thereby melting and bonding the powder together and forming layers [90].

4.4 Multi-stimuli magnetic responsive structures

4.4.1 Shape change mechanisms of multi-stimuli responsive structures

Strategies

To gain full advantages of environmental stimuli and broaden the practical application of printed structures in different environments, it could be interesting to develop structures responsive to multiple stimuli. A common strategy to achieve this is to add magnetic particles to a specific type of smart material [35, 91, 92]. Another strategy is to create bilayer structures, consisting of two layers of materials that are both responsive to a specific stimulus [93]. Current developments often focus on thermal stimulation as the basic stimulation mode in combination with magnetism. This could be either by direct heating of the material in combination with magnetic actuation or by indirect heating of an SMP caused by the magnetic particles. Stimuli other than thermal can also be used in combination with magnetic

actuation, for instance, the pH-value of the environment [94] or light [95]. Some developments even focus on structures responsive to more than two stimuli, combining magnetic actuation with temperature and pH-value of the environment [96, 97], or combining responsiveness to magnetism, light, humidity and ultrasound [98]. In all multi-stimuli responsive structures found in literature, magnetic particles are introduced in the structures to enable magnetic control of the mobility and transport of the structures.

Several examples found in the included literature use stimuli-sensitive hydrogel as a smart material. These are water-filled polymer networks that can swell and shrink depending on the amount of water flowing in (resulting in swelling) or out (resulting in shrinkage) of the network, which is dependent on the temperature or pH-value of the environment. For temperature-responsive hydrogels, higher temperatures result in weaker bonds between the polymer and water molecules in that hydrogel [99]. Responsiveness to the pH-value of the environment is due to the exchange of positively charged ions between the hydrogel and the solution. For this responsiveness, the hydrogel structures must be placed in an aqueous solution [96].

pH-responsiveness

Literature shows examples of hydrogels combined with magnetic particles to create structures that are both influenced by an external magnetic field and the pH-value of the environment. Important players for this responsiveness are the carboxylic acid (-COOH) groups, which can deprotonate when they are in a water solution with a pH value above the acidity constant, thereby creating negatively charged -COO^- groups [94, 96]. These negatively charged chains can absorb more water. This absorption of water in the hydrogel material results in the expansion of the structure. In reverse, when the structure is placed in a solution with a pH-value lower than the acidity constant, the polymer chains protonate again, forming -COOH groups. The water molecules are repelled, and thus the hydrogel network shrinks. By embedding magnetic particles in the structure, the structure is not only responsive to the pH-value of the environment but also to an external magnetic field. Lee *et al.* [94, 96] show an example of a micro-robot made of a temperature- and pH-sensitive hydrogel with embedded magnetic particles. Both the temperature and the pH value influence the swelling degree of the structure, making the robot adapt to the environment. Magnetic responsiveness is used to control the position of the micro-robot. Combining the different stimuli, allows the robot to pass through smaller channels or block channels if necessary. These micro-robots could be used in the biomedical research field, for in vitro research, but also create possibilities for cell transportation and on-demand disease treatment. They can be printed using photon polymerisation-based 3D printing techniques. In this technique, two laser beams are used to scan a vat. At the intersection of these laser beams, photo-polymerisation occurs [90]. The magnetic particles could be introduced into the structure after printing, by placing the printed structure in a suspension with iron oxide particles [94]. Another example shows the fabrication of a magnetic responsive hydrogel using DLW. Here, the magnetic particles are introduced in the hydrogel precursor before printing [96].

Light responsiveness

Another example in literature shows the possibility of creating a hydrogel structure, whose shape can be controlled by light. A photo-thermal mechanism is used, which allows the

structure to convert light into heat, which drives the shape morphing of the hydrogel structure. This shape morphing is only shown underwater, and the light is used to heat the water in which the structure is placed. As the higher temperature of the surrounding water results in the breakage of the bonds between the polymer chains of the hydrogel and the water in the hydrogel, this leads to volume shrinkage of the hydrogel [100]. By combining this thermal-sensitive hydrogel with a layer of a hydrogel containing magnetic particles, which is not thermal-sensitive, upon light stimulation and thus heating, the stress between the two layers results in the bending of the structure (Figure 4.8a). Furthermore, the magnetic layer allows position control of the structure by using an external magnetic field. This bilayer structure can be printed using a two-headed extrusion printing system. In this example, the hard magnetic particles are magnetised and oriented by an external magnet placed underneath the build plate before curing the structure with UV-light [100].

4.4.2 Thermo-magneto responsive structures

We identified two strategies that combine thermal and magnetic actuation: 1) using direct heating and magnetic actuation [101, 102], or 2) by indirect heating of the material using magnetic actuation of magnetic particles [103-109].

Shape memory polymers

In both strategies, SMPs can be used. These are smart materials that can return from a transformed state (the temporary state) into their original shape (the permanent shape) under the influence of an external stimulus. The external stimulus used in this case is thermal stimulation. When an SMP is heated above the so-called glass transition temperature (*Tg*), it transfers from a stiff "glassy" state to a soft flexible state. Upon cooling, this temporarily deformed shape is locked in the structure. The original shape can be restored by reheating the material. The 3D manufacturing and programming of a thermal SMP is shown in Figure 4.8b. After printing, the structure is heated above the transition temperature of the SMP used and the structure can be easily deformed with external force. It is then shaped in the "temporary shape". By cooling down the structure, this temporary shape is locked. The structure recovers to a permanent shape upon heating once the transition temperature is reached.

Direct heating

Direct actuation of both a magnetic field and thermal heating, is shown in a structure created by a multi-material extrusion system [102]. Two types of materials are extruded: a Magnetic Soft Material (MSM), only responsive to an external magnetic field, and a Magnetic Shape Memory Polymer (M-SMP). The M-SMP consists of a composite material of hard magnetic particles and an SMP. Both MSM and M-SMP are separately extruded via a multi-head DIW system. The hard magnetic particles are reoriented due to two permanent magnets around each of the printing nozzles. When the M-SMP is heated above *Tg*, it transfers from a stiff "glassy" state to a soft flexible state. Whenever the material is in the soft flexible state, it can respond to an external magnetic field due to the incorporated hard magnetic particles. By combining these two materials in one structure, more complex shape changes are achieved compared to single magnetic responsive structures [25].

Indirect heating

Applications often do not allow external heating of a structure. The addition of magnetic particles in an SMP provides the opportunity to indirectly heat a structure from the inside, enabling remote actuation by an external magnetic field [3]. The magnetic nanoparticles act as inductive heaters in an alternating magnetic field that heats the SMP [8, 110]. The magnetic nanoparticles heat due to the rotating magnetic moment inside the particles (Néel effect) and the rotation of the particle itself, along with its magnetic moment (Brownian motion) [111]. This heat transfers from the magnetic nanoparticles to the matrix, triggering the shape memory response of the matrix material. Compared to the shape memory process presented in Figure 4.8b, the only difference occurs in step *VI. Recovery upon heating*, which is caused by the magnetic particles in an alternating magnetic field. As the printed structure defines the permanent shape, all geometric freedom of 3D printing methods can be exploited. Examples found in the literature are applied in the biomedical field, showing a self-expandable stent [106], an occlusion device [104, 112], a bone tissue repair device [107] and a tracheal scaffold [108].

Different 3D print methods are used to print M-SMP structures, which are DLP [103], DIW [105, 106, 113] and FDM [104, 107-109, 112, 114]. The most commonly used SMPs are PolyCaproLactone (PCL) and PolyLactic Acid (PLA). The magnetic particles used are iron oxide particles. The concentration of magnetic nanoparticles is of great importance when designing a structure with good shape morphing effects. There should be enough magnetic nanoparticles in the structure to enable heating of the structure to activate the shape memory effect. If the right magnetic nanoparticle concentration is used, a structure can show great shape memory capabilities with recovery rates of more than 90% [103, 106]. Yue *et al.* [109] measured temperature inside a rectangular structure morphing to its permanent shape under the alternating magnetic field. At the edge of the structure, the temperature is lower than on the inside, since on the outside heat dissipation occurs more easily. This could be of advantage in, for example, biomedical applications, where the surface temperature could be a critical factor. The surface temperature is measured for a PLA structure with iron oxide magnetic nanoparticles [107]. The temperature was around 40 °C, which is within the temperature tolerance of the body. A higher surface temperature of (part of) the structure could be desirable, since for example, cancer cells can be killed at temperatures higher than 50 °C [90]. Therefore, the heating of the structure by the magnetic nanoparticles could not only induce shape change of a structure but can also be used to ablate specific cancer cells. Tang *et al*. [105] showed this through a structure of two hydrogels, one with and one without magnetic nanoparticles.

The concentration of magnetic nanoparticles has a great influence on the time needed for shape recovery. A higher concentration leads to a shorter recovery time since a higher heating efficiency is reached [108]. The recovery time is also highly dependent on the complexity of the shape and size of the structure [107]. Where the magnetically expandable stent developed by Wei *et al.* [106] needs 23 seconds for full recovery, the more complex geometric design of the bone repair structure developed by Zhang *et al.* [107] needs 100 seconds for full recovery to the permanent shape. When comparing the recovery upon outside heating of a structure and the magnetic inductive heating, contradictory results are found in the recovery time, showing a shorter time for the conventional heating [112] or no significant difference [107].

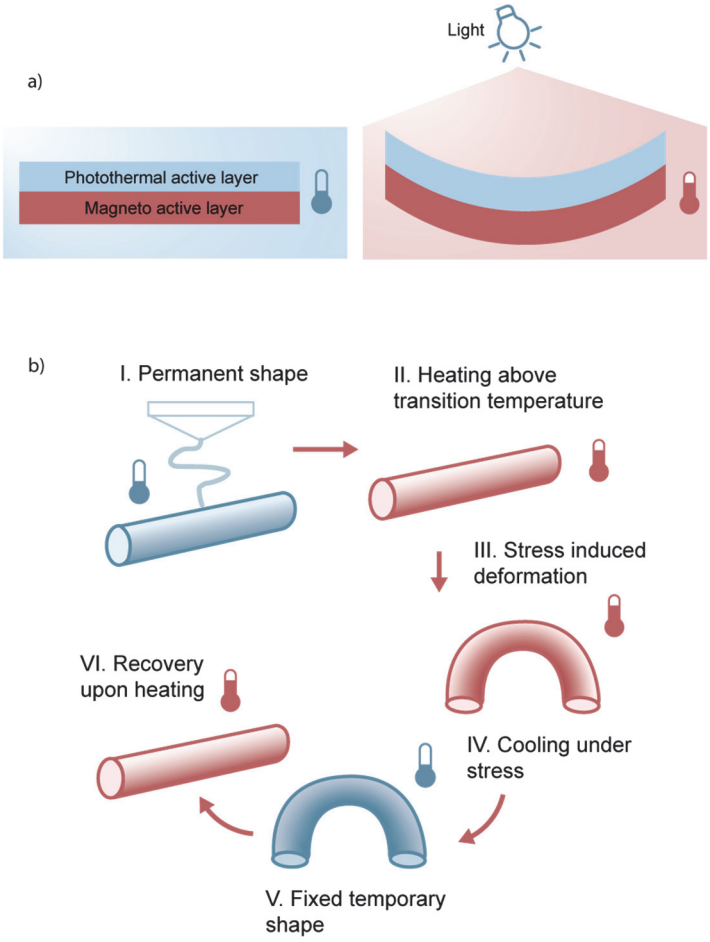


Figure 4.8: Multi-stimuli magnetic responsive structures. a) Actuation of a bilayer structure with a photothermal active layer and a magneto active layer. b) Strategy of 3D printing and programming of Shape Memory Polymers (SMP). I. SMP printed in the permanent shape. II. Heating the SMP above the transition temperature. III. Deform the SMP structure with external force. IV. Cool the structure below its transition temperature. V. The temporary shape is fixed. VI. The permanent shape is recovered upon heating.

No differences were found in the shape recovery percentage of both heating methods [107, 112].

4.5 Discussion

4.5.1 Main findings

The goal of this review was to provide an overview of shape morphing strategies in the 4D printing of magnetic responsive structures. To structure these strategies, a classification is presented showing a division in single and multi-stimuli magnetic responsive structures. For the single-stimulus responsive structures, the distribution and orientation of the magnetic

particles in the matrix material are important factors influencing shape morphing. Soft magnetic nanoparticles can be homogeneously distributed in a matrix material without any programming of the magnetic particles. Furthermore, both soft and hard magnetic particles can be programmed to have a specific distribution and orientation throughout the structure. This way, with a lower concentration of magnetic particles or a lower intensity of the actuating magnetic field, the same shape morphing effect can be accomplished. The manufacturing processes for programmed magnetic structures are more complex compared to structures with random magnetisation.

Programming the orientation and alignment of the magnetic particles can be achieved either during or after the 3D printing process and curing of the material. Reorientation of magnetic particles during the printing process provides the opportunity to program multi-modal shape changes in the structure. To program the magnetic particles, an external magnetic field is used during printing, oriented around the build plate or resin vat, or around the printing nozzle. This can be done with both soft and hard magnetic particles, where the latter require magnetisation before printing. For methods that place a magnet around a printing nozzle, more complex adjustments are needed compared to using a separate external magnet. An external magnet and special shield must be installed on a conventional extrusion-based 3D printer. The magnetisation domain of structures printed with hard magnetic particles can also be programmed after printing. For this, the particles do not require magnetisation before printing, which decreases the risk of agglomeration of the magnetic particles. However, there is less freedom and precise control in the programming of the particle orientations compared to the programming during printing, possibly resulting in less accurate shape morphing results. The advantage of hard magnetic particles, independent of the programming strategy, is that they allow for reprogramming. Table 4.1 shows an overview of the different shape morphing strategies in the 4D printing of magnetic responsive structures together with the corresponding references and the 3D printing techniques that are used in those included studies. With the use of the provided overview and classification, a manufacturing approach can be chosen for selected case studies. For instance, in the case that a structure with an omnidirectional magnetic profile is required, the embedded magnetic particles need to be programmed. This could be done during printing using a resin-based 3D printing technique, such as SLA, as this setup provides the possibility to reorientate a magnet during the printing process. In case the structure only requires a bi-directional magnetic profile, the magnetic particles can be programmed during printing using an extrusion-based 3D printing technique, such as FDM, utilizing an electromagnet around the nozzle. When a lab lacks advanced 3D printing resources but wants to experiment with simple magnetic actuated structures, a ferrofluid injected 3D printed structure could be the optimal choice. Park et al. [115] showed that ferrofluid encapsulating structures can be made with the use of a conventional FDM printer, which is paused during the print to fill the gaps with ferrofluid.

Table 4.1: Overview of shape-morphing strategies and manufacturing approaches of magnetically actuated 3D printed structures.

Strategy	3D-printing technique	References	Behaviour
Random magnetisation – Ferrofluid	Extrusion-based: [52, 115] Resin-based: [48, 49] Powder-based: -	**[48, 49, 52, 53, 115]**	1) Uniform magnetic response 2) Stiffness change
Random magnetisation – Hydrogel	Extrusion-based: [55, 56] Resin-based: - Powder-based: -	**[39, 54-56]**	1) Uniform magnetic response
Random magnetisation – Elastomer	Extrusion-based: [46, 47, 57-60, 63] Resin-based: [61] Powder-based: -	**[34-36, 41, 46, 47, 56-64]**	1) Uniform magnetic response
Programmed magnetisation – During printing, elements	Extrusion-based: [20, 65, 68, 69] Resin-based: [67, 70] Powder-based: -	**[20, 65-70]**	1) Uniform magnetic response 2) Multi-directional magnetic response
Programmed magnetisation – During printing, orientation	Extrusion-based: [82-87] Resin-based: [71, 73-76, 78-81] Powder-based: -	**[22, 27, 29, 30, 33, 35, 41, 71-87]**	1) Uniform magnetic response 2)Multi-directional magnetic response
Programmed magnetisation – After printing, orientation	Extrusion-based: [19, 89] Resin-based: - Powder-based: [88]	**[19, 88, 89]**	1) Uniform magnetic response 2)Multi-directional magnetic response

To fully use the advantages of all stimuli present in an environment, multi-stimuli responsive structures could be created. Examples are identified of combinations of magnetic field responsiveness with the pH-value of the environment, light, or temperature. To achieve this, a composite material is used consisting of magnetic particles in a smart matrix material, or a bilayer structure of two separate responsive materials. It should be noted that in most examples of multi-stimuli responsive magnetic structures, the magnetic particles are used to control the transport of the structure, whereas the other stimuli are responsive to the shape morphing of the structure. Depending on the desired application, multi-stimuli responsive structures made from different smart materials could benefit from the possibility of adding magnetic-induced shape change.

Magneto-active shape morphing structures can be found in a wide range of applications. In the field of soft robotics, the advancement of magnetically actuated soft robots brings unique advantages [116]. Magnetic actuation serves as an alternative for conventional actuation methods, such as pneumatics or hydraulics. Soft robots could be remotely actuated through their environment by a change of their surrounding magnetic field. This provides opportunities for miniaturization or autonomous behavior. Biomedical applications of small-scale soft robots may include the placement of stents [52, 106] or delivery of medicines [117]. Other applications of magneto-active shape morphing structures may include smart grippers [118] or smart electronics [85].

4.5.2 Limitations

This literature review has several limitations. First, relevant literature not presented by the search query could have provided additional information, which is of importance related to the goal of providing an overview of the current developments in the 4D printing of magnetic responsive structures. 4D printing is a relatively new concept, and the name is not commonly used yet. This led to the need to describe the process in the search query, to include literature targeting the concept of 4D printing. Secondly, to delimit the scope of this review, it was chosen to focus only on shape morphing structures fabricated by 3D printing methods. However, using conventional manufacturing techniques, other shape morphing strategies could be adopted, which could also present new opportunities in 3D printing.

4.5.3 Future directions

The advantage of using 3D printing techniques over conventional manufacturing techniques is that they allow for the fabrication of more complex geometries. However, the majority of the literature presents mostly 2–2.5D structures. Only a few examples present complex structures benefiting the possibilities of 3D printing. This is possibly due to the exploratory state of the research area. Often an example of a simple structure is presented to exhibit the shape morphing opportunity of the material combination, design or printing method. Furthermore, often 1D shape morphing is shown, like bending, rotating, elongating or compressing. So far, only a few examples show multi-modal, complex shape transformations. This area could be interesting to reach different actuation modes of an actuator, for example in invasive micro-robots or on-demand drug delivery, to achieve more precise control of the shape morphing. By creating more sophisticated designs, with for example varying magnetic particle contents in different parts of material or using different external magnetic fields for the actuation of a single structure, more complex and possibly multi-modal shape changes

could be achieved. Another option to achieve multiple deformation modes is by using multi-stimuli responsive structures. Also, the advantages of bilayer structures, combining two independent responsive materials, could result in multiple deformation modes.

4.6 Conclusion

This literature review presents an overview of different strategies adopted for creating magnetic responsive 4D printed structures and their shape morphing characteristics. As different 3D printing techniques could result in similar shape morphing structures, a classification is presented based on the strategy of orienting the magnetic particles in the matrix material. The included literature showed either single-stimuli magnetic responsive structures or multi-stimuli responsive structures. For the single-stimulus magnetic responsive structures, the shape morphing could be achieved by random or programmed magnetisation of the magnetic particles in the composite material. Programming of the magnetic particles can either be done during or after the 3D printing process. The multi-stimuli responsive structures could either combine magnetic actuation with temperature changes, pH-value of the environment, humidity or light. Examples in this review show that it is possible to fabricate and apply magnetic stimulated 4D printed structures in different shapes, sizes and application fields. A high interest is shown in applications in the biomedical field due to the advantages of (remote) magnetic-driven actuation. 3D printing techniques allow for complex structures compared to conventional manufacturing. To continue the development and implementation of magnetic responsive 4D printed structures, it is important to fully benefit from the possibilities of 3D printing methods, discover multi-modal transformation options, research different material combinations, and develop methodologies that help designers and engineers navigate in the, what looks like, endless possibilities.

References

[1] Z. U. Arif, M. Y. Khalid, R. Noroozi, A. Sadeghianmaryan, M. Jalalvand, and M. Hossain, "Recent advances in 3D-printed polylactide and polycaprolactone-based biomaterials for tissue engineering applications," *International Journal of Biological Macromolecules,* 2022, doi: 10.1016/j.ijbiomac.2022.07.140.

[2] Z. U. Arif *et al.*, "Additive manufacturing of sustainable biomaterials for biomedical applications," *Asian Journal of Pharmaceutical Sciences,* p. 100812, 2023, doi: 10.1016/j.ajps.2023.100812.

[3] M. Bengisu and M. Ferrara, *Materials that move: smart materials, intelligent design*. Springer, 2018.

[4] S. Tibbits, "4D printing: multi-material shape change," *Architectural Design,* vol. 84, no. 1, pp. 116-121, 2014, doi: 10.1002/ad.1710.

[5] C. Yang *et al.*, "4D printing reconfigurable, deployable and mechanically tunable metamaterials," *Materials Horizons,* vol. 6, no. 6, pp. 1244-1250, 2019, doi: 10.1039/C9MH00302A.

[6] J. Wang, Z. Wang, Z. Song, L. Ren, Q. Liu, and L. Ren, "Biomimetic shape−color double-responsive 4D printing," *Advanced Materials Technologies,* vol. 4, no. 9, p. 1900293, 2019, doi: 10.1002/admt.201900293.

[7] P. Imrie and J. Jin, "Polymer 4D printing: Advanced shape-change and beyond,"

Journal of Polymer Science, vol. 60, no. 2, pp. 149-174, 2022, doi: 10.1002/pol.20210718.

[8] X. Kuang *et al.*, "Advances in 4D printing: materials and applications," *Advanced Functional Materials,* vol. 29, no. 2, p. 1805290, 2019, doi: 10.1002/adfm.201805290.

[9] B. Goo, C.-H. Hong, and K. Park, "4D printing using anisotropic thermal deformation of 3D-printed thermoplastic parts," *Materials & Design,* vol. 188, p. 108485, 2020, doi: 10.1016/j.matdes.2020.108485.

[10] A. Kotikian, R. L. Truby, J. W. Boley, T. J. White, and J. A. Lewis, "3D printing of liquid crystal elastomeric actuators with spatially programed nematic order," *Advanced materials,* vol. 30, no. 10, p. 1706164, 2018, doi: 10.1002/adma.201706164.

[11] M. Nadgorny, Z. Xiao, C. Chen, and L. A. Connal, "Three-dimensional printing of pH-responsive and functional polymers on an affordable desktop printer," *ACS applied materials & interfaces,* vol. 8, no. 42, pp. 28946-28954, 2016, doi: 10.1021/acsami.6b07388.

[12] H. He, J. Guan, and J. L. Lee, "An oral delivery device based on self-folding hydrogels," *Journal of Controlled Release,* vol. 110, no. 2, pp. 339-346, 2006, doi: 10.1016/j.jconrel.2005.10.017.

[13] K. Kim *et al.*, "4D printing of hygroscopic liquid crystal elastomer actuators," *Small,* vol. 17, no. 23, p. 2100910, 2021, doi: 10.1002/smll.202100910.

[14] L. Ionov, "Hydrogel-based actuators: possibilities and limitations," *Materials Today,* vol. 17, no. 10, pp. 494-503, 2014, doi: 10.1016/j.mattod.2014.07.002.

[15] O. Kuksenok and A. C. Balazs, "Stimuli-responsive behavior of composites integrating thermo-responsive gels with photo-responsive fibers," *Materials Horizons,* vol. 3, no. 1, pp. 53-62, 2016, doi: 10.1039/C5MH00212E.

[16] H. Yang *et al.*, "3D printed photoresponsive devices based on shape memory composites," *Advanced Materials,* vol. 29, no. 33, p. 1701627, 2017, doi: 10.1002/adma.201701627.

[17] L. Hines, K. Petersen, and M. Sitti, "Inflated soft actuators with reversible stable deformations," *Advanced Materials,* vol. 28, no. 19, pp. 3690-3696, 2016, doi: 10.1002/adma.201600107.

[18] S. L. Dong, L. Han, C. X. Du, X. Y. Wang, L. H. Li, and Y. Wei, "3D printing of aniline tetramer-grafted-polyethylenimine and pluronic F127 composites for electroactive scaffolds," *Macromolecular rapid communications,* vol. 38, no. 4, p. 1600551, 2017, doi: 10.1002/marc.201600551.

[19] Y. Zhang *et al.*, "4D printing of magnetoactive soft materials for on-demand magnetic actuation transformation," *ACS applied materials & interfaces,* vol. 13, no. 3, pp. 4174-4184, 2021, doi: 10.1021/acsami.0c19280.

[20] J. Simińska-Stanny *et al.*, "4D printing of patterned multimaterial magnetic hydrogel actuators," *Additive Manufacturing,* vol. 49, no. 102506, 2022, doi: 10.1016/j.addma.2021.102506.

[21] M. A. Moreno-Mateos, M. Hossain, P. Steinmann, and D. Garcia-Gonzalez, "Hybrid magnetorheological elastomers enable versatile soft actuators," *npj Computational Materials,* vol. 8, no. 1, p. 162, 2022, doi: 10.1038/s41524-022-00844-1

[22] Y. S. Lui, W. T. Sow, L. P. Tan, Y. Wu, Y. Lai, and H. Li, "4D printing and stimuli-

responsive materials in biomedical aspects," *Acta biomaterialia,* vol. 92, pp. 19-36, 2019, doi: 10.1016/j.actbio.2019.05.005.

[23] D. D. Stueber, J. Villanova, I. Aponte, Z. Xiao, and V. L. Colvin, "Magnetic Nanoparticles in Biology and Medicine: Past, Present, and Future Trends," *Pharmaceutics,* vol. 13, no. 7, p. 943, 2021, doi: 10.3390/pharmaceutics13070943.

[24] A. Zolfagharian, A. Kaynak, and A. Kouzani, "Closed-loop 4D-printed soft robots," *Materials & Design,* vol. 188, p. 108411, 2020, doi: 10.1016/j.matdes.2019.108411.

[25] S. Y. Hann, H. Cui, M. Nowicki, and L. G. Zhang, "4D printing soft robotics for biomedical applications," *Additive Manufacturing,* vol. 36, p. 101567, 2020, doi: 10.1016/j.addma.2020.101567.

[26] J. Lee, H.-C. Kim, J.-W. Choi, and I. H. Lee, "A review on 3D printed smart devices for 4D printing," *International Journal of Precision Engineering and Manufacturing-Green Technology,* vol. 4, pp. 373-383, 2017, doi: 10.1007/s40684-017-0042-x.

[27] S. M. Montgomery, X. Kuang, C. D. Armstrong, and H. J. Qi, "Recent advances in additive manufacturing of active mechanical metamaterials," *Current Opinion in Solid State and Materials Science,* vol. 24, no. 5, p. 100869, 2020, doi: 10.1016/j.cossms.2020.100869.

[28] P. Morouço *et al.*, "Four-dimensional (Bio-) printing: a review on stimuli-responsive mechanisms and their biomedical suitability," *Applied Sciences,* vol. 10, no. 24, p. 9143, 2020, doi: 10.3390/app10249143.

[29] P. Rastogi and B. Kandasubramanian, "Breakthrough in the printing tactics for stimuli-responsive materials: 4D printing," *Chemical Engineering Journal,* vol. 366, pp. 264-304, 2019, doi: 10.1016/j.cej.2019.02.085.

[30] D. Valiulis and E. Jurkonis, "Additive manufacturing by 3D and 4D printing methods: a review of materials, methods and applications," *Journal of Chemical Technology and Metallurgy,* vol. 55, no. 6, pp. 2094-2104, 2020, doi: 10.1007/s42452-024-05999-8.

[31] M. Q. Zafar and H. Zhao, "4D printing: future insight in additive manufacturing," *Metals and Materials International,* vol. 26, pp. 564-585, 2020, doi: 10.1007/s12540-019-00441-w.

[32] A. Tariq *et al.*, "Recent advances in the additive manufacturing of stimuli-responsive soft polymers," *Advanced Engineering Materials,* vol. 25, no. 21, 2023, doi: 10.1002/adem.202301074

[33] Y. Hu, "Recent progress in field-assisted additive manufacturing: materials, methodologies, and applications," *Materials Horizons,* vol. 8, no. 3, pp. 885-911, 2021, doi: 10.1039/D0MH01322F.

[34] A. Rayate and P. K. Jain, "A review on 4D printing material composites and their applications," *Materials Today: Proceedings,* vol. 5, no. 9, pp. 20474-20484, 2018, doi: 10.1016/j.matpr.2018.06.424.

[35] M. Falahati *et al.*, "Smart polymers and nanocomposites for 3D and 4D printing," *Materials today,* vol. 40, pp. 215-245, 2020, doi: 10.1016/j.mattod.2020.06.001.

[36] N. Xia, D. Jin, V. Iacovacci, and L. Zhang, "3D printing of functional polymers for miniature machines," *Multifunctional Materials,* Review vol. 5, no. 1, 2022, Art no. 012001, doi: 10.1088/2399-7532/ac4836.

[37] M. Y. Khalid, Z. U. Arif, R. Noroozi, M. Hossain, S. Ramakrishna, and R. Umer, "3D/4D

printing of cellulose nanocrystals-based biomaterials: Additives for sustainable applications," *International Journal of Biological Macromolecules,* p. 126287, 2023.

[38] Z. U. Arif, M. Y. Khalid, W. Ahmed, and H. Arshad, "A review on four-dimensional (4D) bioprinting in pursuit of advanced tissue engineering applications," *Bioprinting,* vol. 27, p. e00203, 2022, doi: 10.1016/j.bprint.2022.e00203.

[39] S. Malekmohammadi *et al.*, "Smart and biomimetic 3D and 4D printed composite hydrogels: opportunities for different biomedical applications," *Biomedicines,* vol. 9, no. 11, p. 1537, 2021, doi: 10.3390/biomedicines9111537.

[40] M. Mehrpouya, H. Vahabi, S. Janbaz, A. Darafsheh, T. R. Mazur, and S. Ramakrishna, "4D printing of shape memory polylactic acid (PLA)," *Polymer,* vol. 230, p. 124080, 2021, doi: 10.1016/j.polymer.2021.124080.

[41] A. K. Bastola and M. Hossain, "The shape–morphing performance of magnetoactive soft materials," *Materials & Design,* vol. 211, p. 110172, 2021, doi: 10.1016/j.matdes.2021.110172.

[42] S. Wu, W. Hu, Q. Ze, M. Sitti, and R. Zhao, "Multifunctional magnetic soft composites: A review," *Multifunctional materials,* vol. 3, no. 4, p. 042003, 2020, doi: 10.1088/2399-7532/abcb0c.

[43] V. Q. Nguyen, A. S. Ahmed, and R. V. Ramanujan, "Morphing soft magnetic composites," *Advanced Materials,* vol. 24, no. 30, pp. 4041-4054, 2012, doi: 10.1002/adma.201104994.

[44] A. K. Bastola and M. Hossain, "A review on magneto-mechanical characterizations of magnetorheological elastomers," *Composites Part B: Engineering,* vol. 200, p. 108348, 2020, doi: 10.1016/j.compositesb.2020.108348.

[45] M. J. Page *et al.*, "PRISMA 2020 explanation and elaboration: updated guidance and exemplars for reporting systematic reviews," *bmj,* vol. 372, 2021, doi: 10.1136/bmj.n160

[46] X. Cao, S. Xuan, S. Sun, Z. Xu, J. Li, and X. Gong, "3D printing magnetic actuators for biomimetic applications," *ACS applied materials & interfaces,* vol. 13, no. 25, pp. 30127-30136, 2021, doi: 10.1021/acsami.1c08252.

[47] S. Roh *et al.*, "3D-printed silicone soft architectures with programmed magneto-capillary reconfiguration," *Advanced Materials Technologies,* vol. 4, no. 4, p. 1800528, 2019, doi: 10.1002/admt.201800528.

[48] E. S. Keneth, A. R. Epstein, M. S. Harari, R. S. Pierre, S. Magdassi, and S. Bergbreiter, "3D printed ferrofluid based soft actuators," in *2019 International Conference on Robotics and Automation (ICRA)*, 2019: IEEE, pp. 7569-7574, doi: 10.1109/ICRA.2019.8793998.

[49] J. A. Jackson *et al.*, "Field responsive mechanical metamaterials," *Science advances,* vol. 4, no. 12, p. eaau6419, 2018, doi: 10.1126/sciadv.aau6419.

[50] R. E. Rosensweig, "Magnetic fluids," *Annual review of fluid mechanics,* vol. 19, no. 1, pp. 437-461, 1987, doi: 10.1146/annurev.fl.19.010187.002253.

[51] M. Dassisti and G. Brunetti, "Introduction to magnetorheological fluids," *Encyclopedia of Smart Materials,* vol. 5, pp. 187-202, 2022, doi: 10.1016/B978-0-12-803581-8.11744-8.

[52] W. Han, W. Gao, and X. Wang, "A novel magneto-mechanical metamaterial cell structure with large, reversible and rapid two-way shape alteration," *Smart Materials*

and Structures, vol. 30, no. 3, p. 035018, 2021, doi: 10.1088/1361-665X/abdcfe.

[53] H. Pang, L. Pei, J. Xu, S. Cao, Y. Wang, and X. Gong, "Magnetically tunable adhesion of composite pads with magnetorheological polymer gel cores," *Composites Science and Technology,* vol. 192, p. 108115, 2020, doi: 10.1016/j.compscitech.2020.108115.

[54] G. Filipcsei, Csetneki, I., Szilágyi, A., Zrínyi, M., *Magnetic field-responsive smart polymer composites* (Oligomers-polymer composites-molecular imprinting). Berlin, Heidelberg: Springer, 2007, pp. 137-189.

[55] D. Podstawczyk, M. Nizioł, P. Szymczyk, P. Wiśniewski, and A. Guiseppi-Elie, "3D printed stimuli-responsive magnetic nanoparticle embedded alginate-methylcellulose hydrogel actuators," *Additive Manufacturing,* vol. 34, p. 101275, 2020, doi: 10.1016/j.addma.2020.101275.

[56] E. S. Ko, C. Kim, Y. Choi, and K. Y. Lee, "3D printing of self-healing ferrogel prepared from glycol chitosan, oxidized hyaluronate, and iron oxide nanoparticles," *Carbohydrate polymers,* vol. 245, p. 116496, 2020, doi: 10.1016/j.carbpol.2020.116496.

[57] S. Kumar, R. Singh, A. Batish, and T. Singh, "Additive manufacturing of smart materials exhibiting 4-D properties: a state of art review," *Journal of Thermoplastic Composite Materials,* vol. 35, no. 9, pp. 1358-1381, 2022, doi: 10.1177/0892705719895052.

[58] P. Zhu, W. Yang, R. Wang, S. Gao, B. Li, and Q. Li, "4D printing of complex structures with a fast response time to magnetic stimulus," *ACS applied materials & interfaces,* vol. 10, no. 42, pp. 36435-36442, 2018, doi: 10.1021/acsami.8b12853.

[59] X. Cao, S. Xuan, Y. Gao, C. Lou, H. Deng, and X. Gong, "3D Printing Ultraflexible Magnetic Actuators via Screw Extrusion Method," *Advanced Science,* Article vol. 9, no. 16, 2022, doi: 10.1002/advs.202200898.

[60] S. Chuayprakong, A. Wanamonkol, and M. Khayandee, "Programmable 4D-Printed Responsive Structures," in *Key Engineering Materials*, 2020, vol. 856: Trans Tech Publ, pp. 317-322, doi: 10.4028/www.scientific.net/KEM.856.317.

[61] S. Lantean, Barrera, G., Pirri, C. F., Tiberto, P., Sangermano, M., Roppolo, I., & Rizza, G., " 3D printing of magnetoresponsive polymeric materials with tunable mechanical and magnetic properties by digital light processing. ," *Advanced Materials Technologies,* vol. 4, no. 11, 2019, doi: 10.1002/admt.201900505.

[62] S. Kumar, R. Singh, A. Batish, and T. P. Singh, "Additive manufacturing of smart materials exhibiting 4-D properties: A state of art review," *Journal of Thermoplastic Composite Materials,* Review vol. 35, no. 9, pp. 1358-1381, 2022, doi: 10.1177/0892705719895052.

[63] M. Lalegani Dezaki and M. Bodaghi, "Sustainable 4D printing of magneto-electroactive shape memory polymer composites," *International Journal of Advanced Manufacturing Technology,* Article vol. 126, no. 1-2, pp. 35-48, 2023, doi: 10.1007/s00170-023-11101-0.

[64] A. A. Mohammed, J. Miao, I. Ragaisyte, A. E. Porter, C. W. Myant, and A. Pinna, "3D printed superparamagnetic stimuli-responsive starfish-shaped hydrogels," *Heliyon,* Article vol. 9, no. 4, 2023, Art no. e14682, doi: 10.1016/j.heliyon.2023.e14682.

[65] S. Qi, H. Guo, J. Fu, Y. Xie, M. Zhu, and M. Yu, "3D printed shape-programmable magneto-active soft matter for biomimetic applications," *Composites Science and*

Technology, vol. 188, p. 107973, 2020, doi: 10.1016/j.compscitech.2019.107973.
[66] H. Lee *et al.*, "3D-printed programmable tensegrity for soft robotics," *Science Robotics,* vol. 5, no. 45, p. eaay9024, 2020, doi: 10.1126/scirobotics.aay9024.
[67] Z. Ji, C. Yan, B. Yu, X. Wang, and F. Zhou, "Multimaterials 3D printing for free assembly manufacturing of magnetic driving soft actuator," *Advanced Materials Interfaces,* vol. 4, no. 22, p. 1700629, 2017, doi: 10.1002/admi.201700629.
[68] R. Tognato *et al.*, "A stimuli-responsive nanocomposite for 3D anisotropic cell-guidance and magnetic soft robotics," *Advanced Functional Materials,* vol. 29, no. 9, p. 1804647, 2019, doi: 10.1002/adfm.201804647.
[69] A. K. Bastola, M. Paudel, and L. Li, "Development of hybrid magnetorheological elastomers by 3D printing," *Polymer,* vol. 149, pp. 213-228, 2018, doi: 10.1016/j.polymer.2018.06.076.
[70] S. Zhang *et al.*, "3D-printed micrometer-scale wireless magnetic cilia with metachronal programmability," *Science Advances,* Article vol. 9, no. 12, 2023, Art no. eadf9462, doi: 10.1126/sciadv.adf9462.
[71] A. Al-Azawi *et al.*, "Slippery and magnetically responsive micropillared surfaces for manipulation of droplets and beads," *AIP Advances,* vol. 10, no. 8, p. 085021, 2020, doi: 10.1063/5.0012852.
[72] Z. Yang, J. K. Park, and S. Kim, "Magnetically responsive elastomer–silicon hybrid surfaces for fluid and light manipulation," *Small,* vol. 14, no. 2, p. 1702839, 2018, doi: 10.1002/smll.201702839.
[73] L. Lu, P. Guo, and Y. Pan, "Magnetic-field-assisted projection stereolithography for three-dimensional printing of smart structures," *Journal of Manufacturing Science and Engineering,* vol. 139, no. 7, 2017, doi: 10.1115/1.4035964.
[74] L. Lu, E. Baynojir Joyee, and Y. Pan, "Correlation between microscale magnetic particle distribution and magnetic-field-responsive performance of three-dimensional printed composites," *Journal of Micro and Nano-Manufacturing,* vol. 6, no. 1, 2018, doi: 10.1115/1.4038574.
[75] J. Kim, S. E. Chung, S.-E. Choi, H. Lee, J. Kim, and S. Kwon, "Programming magnetic anisotropy in polymeric microactuators," *Nature materials,* vol. 10, no. 10, pp. 747-752, 2011, doi: 10.1038/nmat3090.
[76] S. Lantean *et al.*, "Magnetoresponsive Devices with Programmable Behavior Using a Customized Commercial Stereolithographic 3D Printer," *Advanced Materials Technologies,* Article vol. 7, no. 11, 2022, Art no. 2200288, doi: 10.1002/admt.202200288.
[77] Z. Wang *et al.*, "Hybrid magnetic micropillar arrays for programmable actuation," *Advanced Materials,* vol. 32, no. 25, p. 2001879, 2020, doi: 0.1002/adma.202001879.
[78] H. Shinoda, S. Azukizawa, K. Maeda, and F. Tsumori, "Bio-mimic motion of 3D-printed gel structures dispersed with magnetic particles," *Journal of The Electrochemical Society,* vol. 166, no. 9, pp. B3235-B3239, 2019, doi: 10.1149/2.0361909jes.
[79] T. Xu, J. Zhang, M. Salehizadeh, O. Onaizah, and E. Diller, "Millimeter-scale flexible robots with programmable three-dimensional magnetization and motions," *Science Robotics,* vol. 4, no. 29, p. eaav4494, 2019, doi: 10.1126/scirobotics.aav4494.
[80] S. Azukizawa, H. Shinoda, K. Tokumaru, and F. Tsumori, "3D printing system of

magnetic anisotropy for artificial cilia," *Journal of Photopolymer Science and Technology,* vol. 31, no. 1, pp. 139-144, 2018, doi: 10.2494/photopolymer.31.139.

[81] T. Kuhnt *et al.*, "4D Printed Shape Morphing Biocompatible Materials Based on Anisotropic Ferromagnetic Nanoparticles," *Advanced Functional Materials,* Article vol. 32, no. 50, 2022, Art no. 2202539, doi: 10.1002/adfm.202202539.

[82] H. Deng, K. Sattari, Y. Xie, P. Liao, Z. Yan, and J. Lin, "Laser reprogramming magnetic anisotropy in soft composites for reconfigurable 3D shaping," *Nature communications,* vol. 11, no. 1, p. 6325, 2020, doi: 10.1038/s41467-020-20229-6.

[83] D. Kokkinis, M. Schaffner, and A. R. Studart, "Multimaterial magnetically assisted 3D printing of composite materials," *Nature communications,* vol. 6, no. 1, p. 8643, 2015, doi: 10.1038/ncomms9643.

[84] Z. Wang, Y. Wu, D. Wu, and Z. Hai, "3D printing of magnetically actuated miniature soft robots," in *2021 IEEE 16th International Conference on Nano/Micro Engineered and Molecular Systems (NEMS)*, 2021: IEEE, pp. 804-808, doi: 10.1109/NEMS51815.2021.9451386.

[85] Y. Kim, H. Yuk, R. Zhao, S. A. Chester, and X. Zhao, "Printing ferromagnetic domains for untethered fast-transforming soft materials," *Nature,* vol. 558, no. 7709, pp. 274-279, 2018, doi: 10.1038/s41586-018-0185-0.

[86] M. H. D. Ansari *et al.*, "3D Printing of Small-Scale Soft Robots with Programmable Magnetization," *Advanced Functional Materials,* Article vol. 33, no. 15, 2023, Art no. 2211918, doi: 10.1002/adfm.202211918.

[87] W. Han, W. Gao, and X. Wang, "Implementation of printability for magneto-active soft materials based on programmed 3D printing technique," *Smart Materials and Structures,* Article vol. 31, no. 11, 2022, Art no. 115015, doi: 10.1088/1361-665X/ac976a.

[88] H. Wu *et al.*, "Selective laser sintering-based 4D printing of magnetism-responsive grippers," *ACS applied materials & interfaces,* vol. 13, no. 11, pp. 12679-12688, 2020, doi: 10.1021/acsami.0c17429.

[89] J. Tang, B. Sun, Q. Yin, M. Yang, J. Hu, and T. Wang, "3D printable, tough, magnetic hydrogels with programmed magnetization for fast actuation," *Journal of Materials Chemistry B,* vol. 9, no. 44, pp. 9183-9190, 2021, doi: 10.1039/D1TB01694F.

[90] I. Gibson *et al.*, *Additive manufacturing technologies*. Springer, 2021.

[91] S. Jang and S. Park, "4D printed untethered milli-gripper fabricated using a biodegradable and biocompatible electro- and magneto-active hydrogel," *Sensors and Actuators B: Chemical,* Article vol. 384, 2023, Art no. 133654, doi: 10.1016/j.snb.2023.133654.

[92] J. Bai and G. Bu, "Progress in 4D printing technology," *Journal of Advanced Manufacturing Science and Technology,* Article vol. 2, no. 1, 2022, doi: 10.51393/j.jamst.2022001.

[93] L. Ren *et al.*, "4D printing dual stimuli-responsive bilayer structure toward multiple shape-shifting," *Frontiers in Materials,* vol. 8, p. 655160, 2021, doi: 10.3389/fmats.2021.655160.

[94] C. Xin *et al.*, "Environmentally adaptive shape-morphing microrobots for localized cancer cell treatment," *ACS nano,* vol. 15, no. 11, pp. 18048-18059, 2021, doi: 10.1021/acsnano.1c06651.

[95] X. Hu, Z. Ge, X. Wang, N. Jiao, S. Tung, and L. Liu, "Multifunctional thermo-magnetically actuated hybrid soft millirobot based on 4D printing," *Composites Part B: Engineering,* vol. 228, p. 109451, 2022, doi: 10.1016/j.compositesb.2021.109451.

[96] Y.-W. Lee, H. Ceylan, I. C. Yasa, U. Kilic, and M. Sitti, "3D-printed multi-stimuli-responsive mobile micromachines," *ACS applied materials & interfaces,* vol. 13, no. 11, pp. 12759-12766, 2020, doi: 10.1021/acsami.0c18221.

[97] Y. W. Lee *et al.*, "Multifunctional 3D-Printed Pollen Grain-Inspired Hydrogel Microrobots for On-Demand Anchoring and Cargo Delivery," *Advanced Materials,* Article vol. 35, no. 10, 2023, Art no. 2209812, doi: 10.1002/adma.202209812.

[98] B. Han *et al.*, "Multi-field-coupling energy conversion for flexible manipulation of graphene-based soft robots," *Nano Energy,* vol. 71, p. 104578, 2020, doi: 0.1016/j.nanoen.2020.104578.

[99] H. van der Linden and J. Westerweel, "Temperature-sensitive hydrogels," in *Encyclopedia of Microfluidics and Nanofluidics*. Boston: Springer, 2014.

[100] X. Hu, Z. Ge, X. Wang, N. Jiao, S. Tung, and L. Liu, "Multifunctional thermo-magnetically actuated hybrid soft millirobot based on 4D printing," *Composites Part B: Engineering,* Article vol. 228, 2022, doi: 10.1016/j.compositesb.2021.109451.

[101] H.-W. Huang, M. S. Sakar, A. J. Petruska, S. Pané, and B. J. Nelson, "Soft micromachines with programmable motility and morphology," *Nature communications,* vol. 7, no. 1, p. 12263, 2016, doi: 10.1038/ncomms12263.

[102] C. Ma *et al.*, "Magnetic multimaterial printing for multimodal shape transformation with tunable properties and shiftable mechanical behaviors," *ACS Applied Materials & Interfaces,* vol. 13, no. 11, pp. 12639-12648, 2020, doi: 10.1021/acsami.0c13863.

[103] D. Cohn, M. Zarek, A. Elyashiv, M. A. Sbitan, V. Sharma, and R. V. Ramanujan, "Remotely triggered morphing behavior of additively manufactured thermoset polymer-magnetic nanoparticle composite structures," *Smart Materials and Structures,* vol. 30, no. 4, p. 045022, 2021, doi: 10.1088/1361-665X/abeaeb.

[104] C. Lin, L. Liu, Y. Liu, and J. Leng, "4D printing of bioinspired absorbable left atrial appendage occluders: a proof-of-concept study," *ACS Applied Materials & Interfaces,* vol. 13, no. 11, pp. 12668-12678, 2021, doi: 10.1021/acsami.0c17192.

[105] J. Tang *et al.*, "Programmable shape transformation of 3D printed magnetic hydrogel composite for hyperthermia cancer therapy," *Extreme Mechanics Letters,* vol. 46, p. 101305, 2021, doi: 10.1016/j.eml.2021.101305.

[106] H. Wei, Q. Zhang, Y. Yao, L. Liu, Y. Liu, and J. Leng, "Direct-write fabrication of 4D active shape-changing structures based on a shape memory polymer and its nanocomposite," *ACS applied materials & interfaces,* vol. 9, no. 1, pp. 876-883, 2017, doi: 10.1021/acsami.6b12824.

[107] F. Zhang, L. Wang, Z. Zheng, Y. Liu, and J. Leng, "Magnetic programming of 4D printed shape memory composite structures," *Composites Part A: Applied Science and Manufacturing,* vol. 125, p. 105571, 2019, doi: 10.1016/j.compositesa.2019.105571.

[108] W. Zhao, F. Zhang, J. Leng, and Y. Liu, "Personalized 4D printing of bioinspired tracheal scaffold concept based on magnetic stimulated shape memory composites," *Composites Science and Technology,* vol. 184, p. 107866, 2019, doi: 10.1016/j.compscitech.2019.107866.

[109] C. Yue *et al.*, "Three-dimensional printing of cellulose nanofibers reinforced PHB/PCL/Fe3O4 magneto-responsive shape memory polymer composites with

excellent mechanical properties," *Additive Manufacturing,* vol. 46, p. 102146, 2021, doi: 10.1016/j.addma.2021.102146.

[110] Q. Zhao, H. J. Qi, and T. Xie, "Recent progress in shape memory polymer: New behavior, enabling materials, and mechanistic understanding," *Progress in Polymer Science,* vol. 49, pp. 79-120, 2015, doi: 10.1016/j.progpolymsci.2015.04.001.

[111] K. Wu, J. Liu, D. Su, R. Saha, and J.-P. Wang, "Magnetic nanoparticle relaxation dynamics-based magnetic particle spectroscopy for rapid and wash-free molecular sensing," *ACS applied materials & interfaces,* vol. 11, no. 26, pp. 22979-22986, 2019, doi: 10.1021/acsami.9b05233.

[112] C. Lin *et al.*, "4D-printed biodegradable and remotely controllable shape memory occlusion devices," *Advanced Functional Materials,* vol. 29, no. 51, p. 1906569, 2019, doi: 10.1002/adfm.201906569.

[113] X. Wan, Y. He, Y. Liu, and J. Leng, "4D printing of multiple shape memory polymer and nanocomposites with biocompatible, programmable and selectively actuated properties," *Additive Manufacturing,* Article vol. 53, 2022, Art no. 102689, doi: 10.1016/j.addma.2022.102689.

[114] H. Liu, F. Wang, W. Wu, X. Dong, and L. Sang, "4D printing of mechanically robust PLA/TPU/Fe3O4 magneto-responsive shape memory polymers for smart structures," *Composites Part B: Engineering,* Article vol. 248, 2023, doi: 10.1016/j.compositesb.2022.110382.

[115] J. Park, Y. T. Choi, A. B. Flatau, and N. M. Wereley, "Encapsulations of magnetorheological fluids within 3-D printed elastomeric cellular structures," *IEEE Transactions on Magnetics,* vol. 58, no. 8, pp. 1-5, 2021, doi: 10.1109/TMAG.2021.3137838.

[116] Y. Kim and X. Zhao, "Magnetic soft materials and robots," *Chemical reviews,* vol. 122, no. 5, pp. 5317-5364, 2022, doi: 10.1021/acs.chemrev.1c00481.

[117] J. Zhang *et al.*, "Voxelated three-dimensional miniature magnetic soft machines via multimaterial heterogeneous assembly," *Science robotics,* vol. 6, no. 53, p. eabf0112, 2021, doi: 10.1126/scirobotics.abf0112.

[118] Q. Ze *et al.*, "Magnetic shape memory polymers with integrated multifunctional shape manipulation," *Advanced Materials,* vol. 32, no. 4, p. 1906657, 2020, doi: 10.1002/adma.201906657.

04

Appendix 4.A

4.A1 Search strategy

A systematic literature search was performed using the Scopus database and following PRISMA2020 guidelines. The search query consisted of three categories to describe the 4D printing of magnetic responsive shape morphing structures. The first part of the search string included keywords related to the fabrication method, both the general terms for 3D printing and the specific 3D printing methods. The second category consists of the general magnetic aspect. In the third category, the keywords are related to the fourth dimension, focusing on changing the shape of materials, the use of smart materials, and materials that respond to stimulus or could be programmed. Finally, keywords were used to exclude papers from the search that did comply with the categories but fell out of the scope of this study.

The full search string is as follows:

TITLE-ABS-KEY((print* OR "additive manufact*" OR "rapid prototyp*" OR "selective laser sintering" OR "direct ink writ*" OR "binder jet*" OR "stereolithography" OR "fused deposition model*" OR "electron beam melting" OR "powder bed" OR "Ultraviolet-lithography") AND(*magnet*) AND (shape OR smart OR stimul* OR programm*)) AND NOT (assays OR circuit OR "energy harvesting" OR antenna OR "nuclear magnetic Resonance Imag*") AND (LIMIT-TO (LANGUAGE, "English"))

The search was limited to articles in English and was performed on June 2, 2023, in the Scopus database.

4.A2 Bibliometric Analysis

Figure 4.A2 and 4.A3 shows the results of the bibliometric analysis of the 85 studies resulting from the search string.

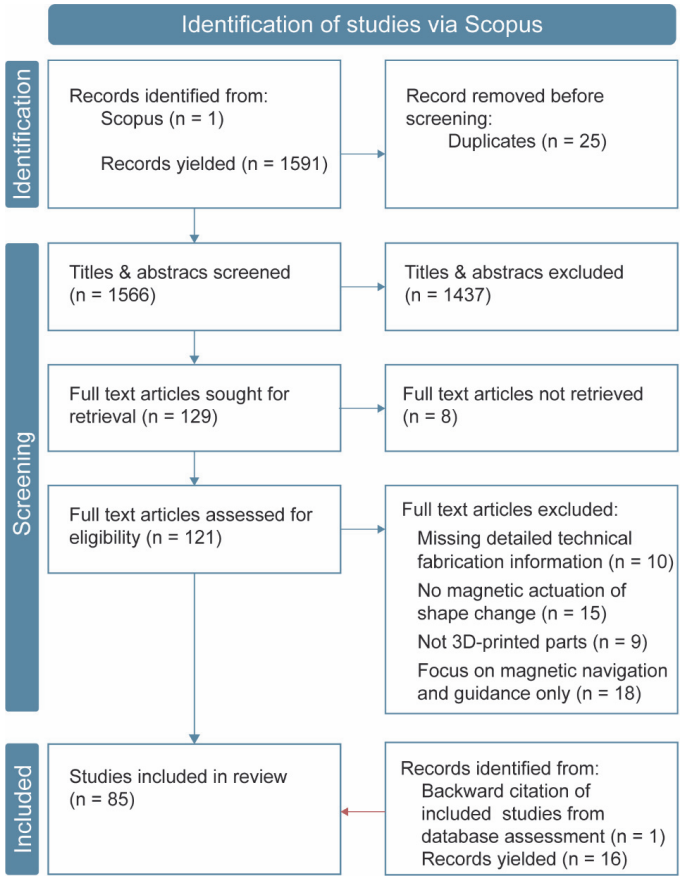


Figure 4.A1: Flow diagram showing the search results. Following PRISMA2020 guidelines

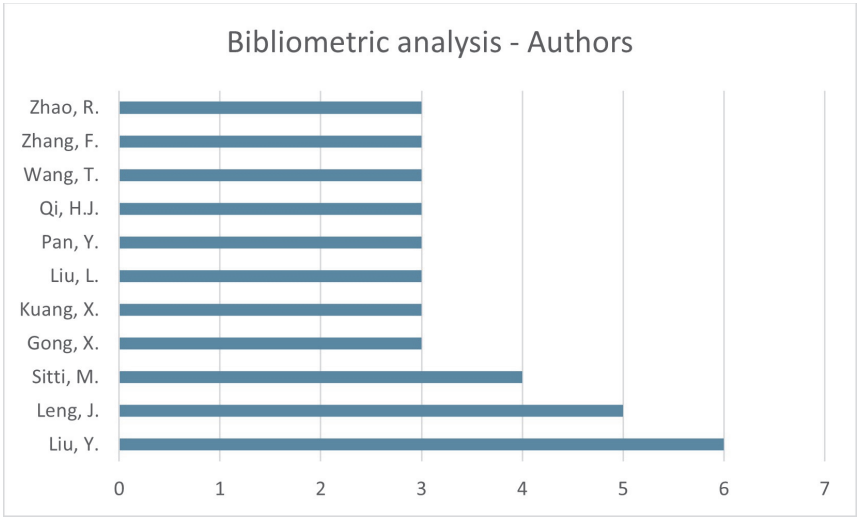


Figure 4.A2: An overview of the most occurring authors of the included studies.

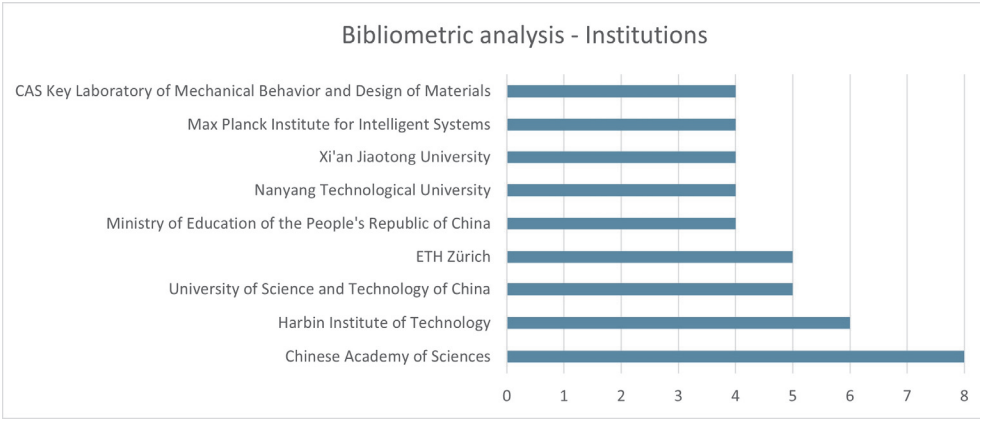


Figure 4.A3: An overview of the most occurring institutions of the included studies.

04

CHAPTER 05

DESIGN OF A MAGNETIC SUCTION GRIPPER

ABSTRACT

Suction grippers offer a distinct advantage in their ability to handle a wide range of items. However, attaching these grippers to irregular and rough surfaces presents an ongoing challenge. To address this obstacle, this study explores the integration of magnetic intelligence into a soft suction gripper design, enabling fast external magnetic actuation of the attachment process. Additionally, miniaturization options are enhanced by implementing a compliant deploying mechanism. The resulting design is the first-of-its-kind magnetic actuated deployable suction gripper featuring a thin magnetic membrane (Ø 50 mm) composed of carbonyl iron particles embedded in a silicone matrix. This membrane is supported by a frame made of superelastic nitinol wires that facilitate deployment. During experiments, the proof-of-principle prototype demonstrates successful attachment on a diverse range of curved surfaces in both dry and wet environments. The gripper achieves attachment on curved surfaces with radii of 50–75 mm, exerting a maximum attachment force of 2.89±0.54 N. The current gripper design achieves a folding percentage of 75%, enabling it to fit into a Ø 12.5 mm tube and access hard-to-reach areas while maintaining sufficient surface area for attachment forces. The proposed prototype serves as a foundational steppingstone for further research in the development of reliable and effective magnetic-actuated suction grippers across various configurations. By addressing the limitations of attachment to irregular surfaces and exploring possibilities for miniaturization and precise control, this study opens new avenues for the practical application of suction grippers in diverse industries and scenarios.

Published as:
Kortman, V. G., de Vries, E., Jovanova, J., & Sakes, A. (2024). Unlocking versatility: magnetic-actuated deployable suction gripper for complex surface handling. *Soft Robotics, 11*(6), 1020-1031.

5.1 Introduction

5.1.1 Challenges in Conventional Suction Gripping

Attachment to rough, wet, and irregular surfaces and shapes poses a challenge across a wide range of applications spanning the medical field, robotic manipulation, and industrial sectors. Suction grippers have emerged as prevalent tools for grasping and manipulating diverse objects and surfaces, including large sheet materials such as glass and metal, as well as various types of packaging boxes. In comparison to mechanical grippers, suction grippers offer the advantage of accommodating different object types and sizes, unconstrained by gripper dimensions. Moreover, suction grippers enable the secure handling of delicate objects without compromising their structural integrity, a crucial aspect in industries like the food sector.

The primary obstacle faced by conventional suction grippers lies in their inability to adhere to surfaces that are rough, irregularly shaped, and porous. Establishing an airtight seal between the suction disc and these surfaces proves challenging, as even the slightest gap can lead to leakage channels, resulting in the gradual reduction of the pressure difference between the disc and the surrounding environment [1]. Sandoval *et al.* [2] showed that the adhesion of a commercially available suction cup drastically drops with increasing surface convexity and concavity. To enable the adaptation of suction grippers in applications that would greatly benefit from this gripping mechanism, ongoing research focuses on developing suction grippers that can effectively adhere to rough, irregularly shaped, and soft surfaces.

Despite progress in attaching to rough and irregular-shaped surfaces by researchers such as Ditsche *et al.* [3], Sandoval *et al.* [2], and Koivikko *et al.* [4], significant challenges remain. These challenges include the miniaturization of suction grippers, precise control over gripper actuation, reducing energy consumption, and the development of universal grippers for diverse surfaces and shapes [5]. The miniaturization of suction grippers is hindered by the inherent relationship between attachment forces and the size of the vacuum chamber [5]. Fine control over gripper actuation is crucial for delicate objects and versatile applications, especially in fields like minimally invasive surgery [6]. The use of smart soft materials responsive to magnetic fields holds promise for advancing these developments [7].

5.1.2 Opportunities for Advanced Magnetic Materials

Adding magnetic intelligence to suction grippers enables external control of its attachment using a magnetic field instead of a vacuum pump. This magnetic actuation offers precise control over the attachment's intensity and without the need for complex tubing systems or multiple vacuum pumps. Additionally, magnetic fields possess the ability to travel through various mediums like air, human tissue, and water, opening interesting external operation possibilities. Remote control of the gripper becomes achievable, improving system miniaturization by eliminating the need for a direct connection between the actuation mechanism and the gripper. Finally, magnetic interaction is fast and reversible, enabling swift attachment and detachment of the suction gripper.

Few and limited implementations of magnetically actuated suction grippers have been reported in literature. Zhang *et al.* [8] presented a suction disc using Magneto-Rheological Elastomer (MRE) and a permanent magnet for wall-climbing robots. In a subsequent study, a softer actuation system with a silicone edge and electro-permanent magnet was introduced

[9]. Koivikko *et al.* [10] developed a suction gripper capable of switching between soft and hard modes using Magneto-Rheological (MR) fluid to improve structural integrity. Iwasaki *et al.* [11] designed an elastomeric suction disc controlled by a magnetic field for medical treatments and Hu *et al.* [12] proposed a magnetic suction disc with a deformable magnetic polymer membrane. However, attachment of most of these magnetic suction cups was limited to smooth surfaces.

5.1.3 Goal

This study aims to develop a suction gripper utilizing advanced magnetic materials for actuation by an external magnetic field. The objective is to design a versatile gripper that can attach to irregular-shaped objects by incorporating magnetic responsiveness into a soft matrix to enhance the sealing capability. To allow for use in tight spaces and improve the load carrying capacity, we propose to explore deploying mechanisms, similar to the one proposed in our previous study [13].

5.2 Magnetic Suction Gripper Design

5.2.1 Design Requirements

To ensure attachment to a wide range of complex-shaped objects, this study should present a suction gripper design that accommodates surfaces with single and double curvatures, and varying radii (Figure 5.1). The gripper design should incorporate the basic components such as the gripper body, rim (outer edge of the gripper), and footprint (bottom part of the gripper in contact with the substrate) while integrating soft and rigid materials. Soft materials facilitate adaptation to non-flat surfaces, while rigid components maintain structural integrity and provide the necessary pressure for a secure seal. Furthermore, sufficient friction at the gripper-object interface is vital for successful attachment and lifting. The gripper surface should, therefore, be designed to provide adequate friction, enhancing gripping performance while delaying failure. Safety measures regarding the use of magnetic fields are crucial, therefore, a maximum flux density of 400mT is set for actuation, which is in accordance with the International Commission on Non-Ionizing Radiation Protection (ICNIRP).

For some applications, the suction gripper is required to lift an object instead of just attaching to a surface. Taking examples from applications in the fruit industry, different fruits and vegetables have different weights, requiring different lifting forces. Most current developments in this industry focus on the harvesting of strawberries, tomatoes and apples, as they are harvested in large quantities [14, 15]. For instance, strawberries typically weigh between 15 and 20 grams, while large tomatoes and apples range between 125-220 grams and 177-235 grams, respectively [16, 17]. This would require a suction force of, approximately, 2.3 N. The attachment force of the suction gripper F_s is determined by the pressure difference (ΔP) and the suction surface area (A_s), as shown in Equation 5.1. Theoretical limits for the attachment force of a suction gripper are, therefore, determined by the maximum suction surface area and maximum vacuum pressure that can safely be applied. Unfortunately, the maximum surface area is often restricted by the entry point into the human body or the available space inside marine or space vehicles. A foldable structure can mitigate these challenges as this would allow the usage in hard-to-reach environments and provide more miniaturisation options, for example for usage in the medical field to perform attachment

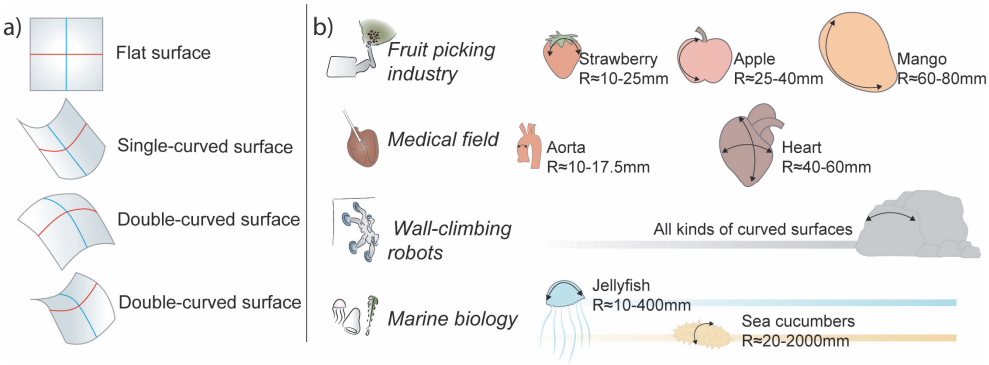


Figure 5.1: Complex-shaped object examples. a) Different curved surfaces, from a flat surface to a single and double curved surface. b) Objects for attachment in different potential use applications, with their corresponding dimensions.

inside the body, or in marine biology, for deep-sea attachment. The smaller the gripper dimensions can be in a folded state, the smaller entrances could be used while maintaining equal suction forces.

$$F_s = \Delta P \cdot A_s \tag{5.1}$$

5.2.2 Design Overview

The final design of the magnetic suction gripper consists of a magnetic responsive suction mechanism, a deployable frame, and a handle, see Figure 5.2a-b. The magnetic gripper is connected to a tube and handle for comfortable two-finger grasping, while the thumb controls the position of the permanent magnet attached to a spring-positioned rod. The small permanent magnet actuates the suction gripper. Figure 5.2c shows the three phases when operating the magnetic suction gripper.

a) **Folded state of the magnetic actuated gripper:** In this phase, the magnetic gripper is folded in a smaller tube to enable the insertion of the gripper into hard-to-reach places.
b) **Deployed and deactivated magnetic gripper mode:** When the gripper arrives at the target location, it is extracted from the tube. Due to the superelasticity of the nitinol wires, the gripper deploys. When there is no magnetic field near the gripper membrane, the magnetic membrane will remain in its flat resting state.
c) **Activated magnetic gripper mode:** When a magnetic field is brought in close contact to the magnetic membrane, the membrane is attracted to the magnet, creating a cavity. Due to the negative pressure difference between this cavity and the surrounding environment, the gripper attaches to the substrate. By removing the magnetic field from the proximity of the magnetic membrane, the membrane will return to its original resting state.

Magnetic Responsive Membrane

An advanced magnetic material, composed of silicone and magnetic particles, was designed to respond to magnetic actuation. The magnetic composite material contains magnetic particles randomly distributed within the silicone matrix. During the curing process, no

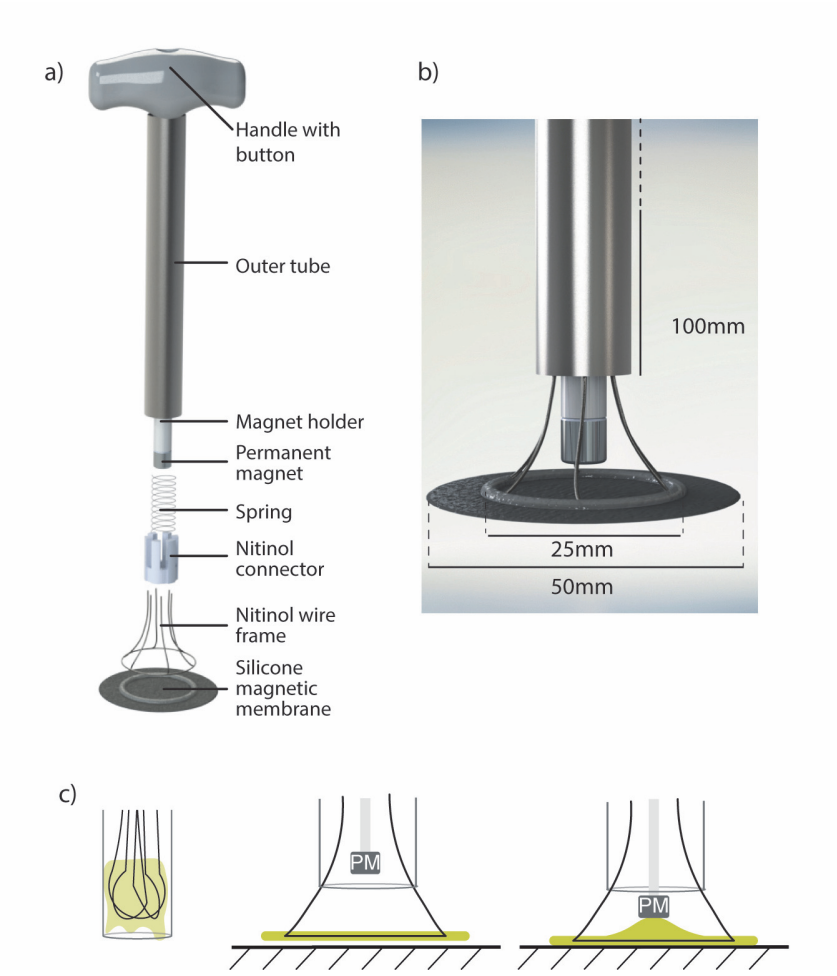


Figure 5.2: Final Design Magnetic Suction Gripper. a) Exploded view of the developed magnetically actuated suction gripper. b) Dimensions of the gripper design. The nitinol wires have a diameter of 0.5 mm. The magnet has a diameter of 6 mm and a height of 10 mm. The tube has an inner lumen of 12.5 mm. c) Operation modes of the magnetic suction gripper, consisting of: (1) Folded state inside a tube. (2) Deployed state upon attachment to a substrate. (3) Attachment state upon magnetic actuation by the permanent magnet (PM) of the shape change of the membrane resulting in attachment forces to the substrate.

external magnetic field was present. As a result, the magnetic particles dispersed uniformly in the material, yielding an isotropic magnetic composite that can be attracted by an external magnetic field. This material was employed to create a thin membrane, designed to be attracted by an external magnetic field.

The magnetic actuation force must be capable of overcoming both the suction force in the gripper cavity and the elastic forces in the magnetic membrane. The elastic force of the membrane opposes the magnetic force interacting with the membrane and should be

minimized to enhance the effect of the magnetic force. The design challenge lies in finding the right balance between the magnetic particle content and the material's elasticity, ensuring sufficient deformation of the volume cavity can occur. In the final design, the magnetic membrane is made of silicone-type Dragon Skin (Smooth-on, USA), with a shore hardness of 20A. This silicone is mixed with 70 wt% carbonyl iron microparticles of 5-9 µm (Sigma-Aldrich, USA) in an isotropic configuration. Research by Hu *et al.* [12] and Zhang *et al.* [8, 9] have found that a weight ratio of iron powder exceeding 75% causes a loss of elasticity in the material. Although the stretching ratio drops with higher particle content, the material with 70 wt% particles still performed well [12]. The selected thickness for the membrane is approximately 0.5 mm, which provides strong magnetic attraction, sufficient strength to prevent tearing, and flexibility to adapt to curved surfaces.

To enable magnetic actuation in the final design, a permanent magnet was used. The shape of the permanent magnet affects the shape and strength of the magnetic field. Therefore, an optimal size and capacity magnet is crucial for a successful functional design. The magnetic force between two nearby surfaces usually depends on the flux density, the magnetic surface area and the permeability of space. This underscores a crucial point: the size of the magnet imposes constraints on the maximum magnetic force. This limitation arises because the maximum flux density and permeability of space are predetermined. A larger magnet creates a stronger magnetic field but also attracts a larger portion of the magnetic membrane, leaving less membrane attached to the substrate, potentially affecting the seal. A smaller magnet can lift less of the magnetic membrane, but might be more beneficial as it allows for a larger portion of the membrane to contribute to the seal. Furthermore, a smaller magnet improves the ability to attach to objects smaller than the nitinol wire frame diameter, as the inner magnetic membrane can create a seal around the object. The current proof-of-principle prototype, therefore, uses a 6 mm cylindrical Neodymium grade 45 magnet (Supermagnete, Germany). The magnetic membrane has an outer diameter of 50 mm.

Deployable Frame

When combining the smart magnetic material in a suction configuration, a gripper body is required. To include opportunities for miniaturisation, a deploying frame should be implemented. This frame expands the suction surface when it reaches the target location and provides sufficient pressure to create a seal with irregular surfaces. It should also serve as a base to attach to the magnetic membrane.

Different deploying mechanisms were explored for the frame of the suction gripper, such as joint mechanisms, origami mechanisms, umbrella mechanisms, rotational deploying mechanisms, and compliant mechanisms. Although each mechanism has its advantages, with further miniaturisation in mind, it was chosen to adopt pre-bent ultrathin superelastic nitinol wires as a deployable frame. The superelastic nitinol wire frame allows for passive folding and deploying of the suction gripper and provides stability for the magnetic membrane. To suffice the double functionality of the nitinol wires, various designs for the nitinol folding frame were created and evaluated for their level of deployability and ability to exert sufficient pressure onto the magnetic membrane, see Figure 5.3. It was found that the outer dimensions of the

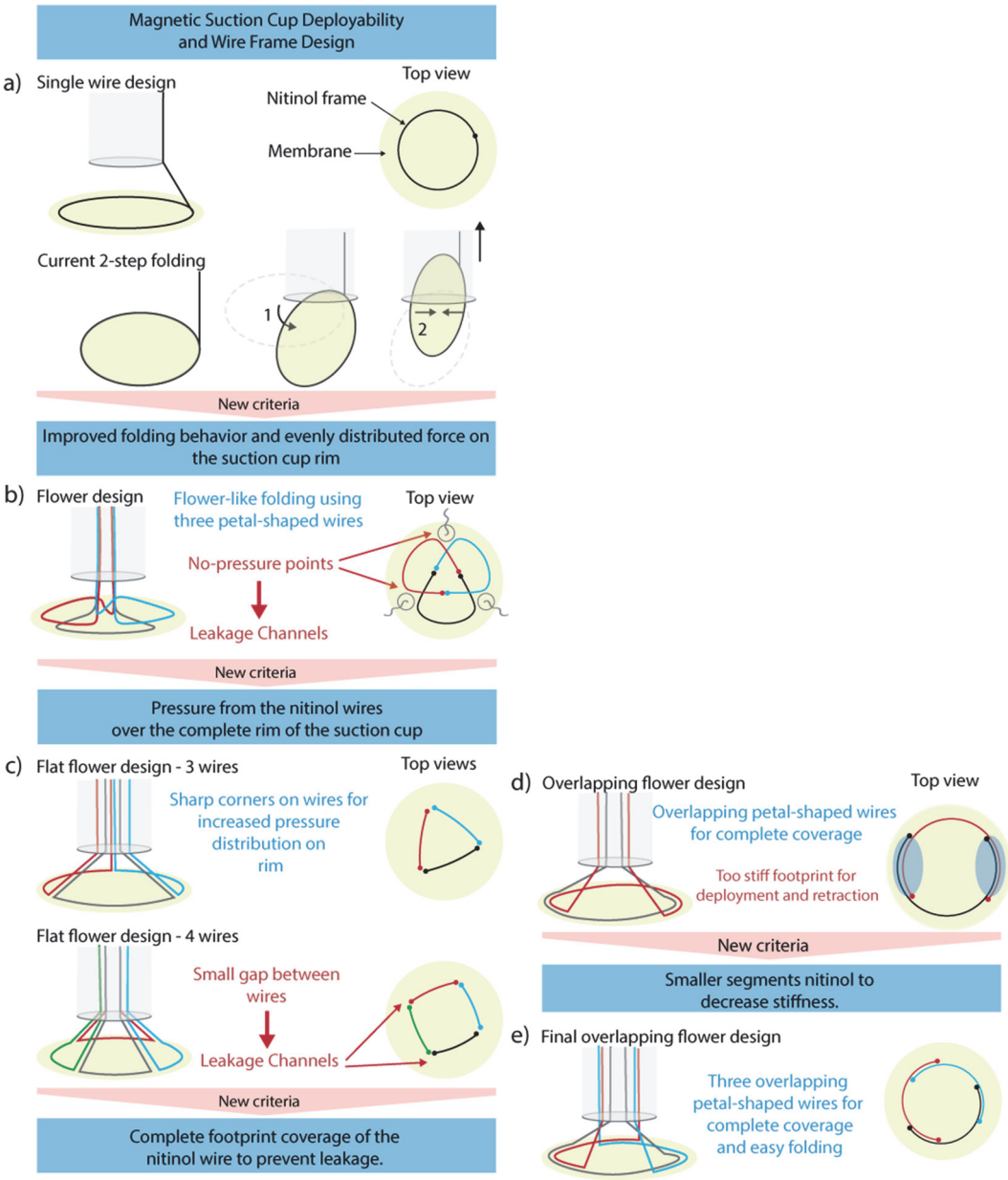


Figure 5.3: Iterations of Nitinol Frame Configurations. a) Single wire structure with a two-step bending sequence. b) Flower-like structure with too little pressure on the rim. c) Flower structure with sharper angles and steeper incline, where leakage channels still resulted in failure of attachment. d) Structure with overlapping wires for pressure on the complete rim. e) Final design of the nitinol frame.

suction disc in folded state were determined by three elements: the nitinol wire frame, the silicone magnetic membrane, and the permanent magnet. To minimize the folded state dimensions, the diameter and quantity of nitinol wires are minimised while still ensuring sufficient stability and pressure on the membrane for a secure seal formation.

Leakage of the suction disc is prevented by the formation of a stable rim. By overlapping the nitinol wires and creating a flat ring of these wires on the footprint, it is expected that leakage channels can be minimised so that a pressure difference can be created upon magnetic actuation, see Figure 5.3d. Using two wires in this configuration creates a stiff, flat frame that is suitable for sealing on flat surfaces but not on irregular shapes. Besides, the two-wire structure was difficult to fold into a smaller tube due to its stiffness. To address this issue, a structure with three nitinol wires was developed, see Figure 5.3e. The nitinol wire used in the final design is a super-elastic nitinol wire (55% Ni, 45% Ti) (Titaniumshop, the Netherlands) with a diameter of 0.5 mm, and the heat treatment temperature is set to 500 °C. The nitinol wire is encapsulated in silicone and cured onto the magnetic membrane. The silicone membrane protrudes the nitinol frame to improve the sealing of the gripper.

The final prototype is illustrated in Figure 5.4. The handle and nitinol connector were 3D-printed with an SLA printer (Formlabs, Form 3B) in clear resin. The magnet holder with a button was printed in clear PLA on an FDM printer (Ultimaker 3). The outer tube (stainless steel) has an inner lumen of 12.5 mm. In the proof-of-principle prototype, the magnetic membrane has a total diameter of 50 mm, and the nitinol frame rim a diameter of 25 mm.

5.3 Experimental Validation

5.3.1 Attachment Performance

Goal of the Experiment

To ensure the gripper's versatility across various applications, it must successfully attach to an array of complex-shaped objects. By combining single and double curvatures, concave or convex surfaces with different radii are formed. Demonstrating the gripper's adeptness with complex-shaped objects involves showcasing its attachment capabilities to different single and double-curved surfaces separately. Furthermore, to allow for its use in different application fields, the gripper must exhibit attachment capabilities in diverse environmental settings. These settings include airborne scenarios and liquid mediums like water or blood. Showcasing its adaptability in these environments necessitates the evaluation of its capacity for attachment both in air and when submerged in water. The objective of the attachment experiment was twofold: 1) to examine the magnetic suction gripper's capacity to adhere to different surfaces and 2) to measure the lifting force achieved by the gripper during attachment.

Two dependent variables were measured:

1. **The attachment force**: which was measured as the maximum force required to detach the suction gripper from the substrate.
2. **The pressure difference underneath the suction gripper**.

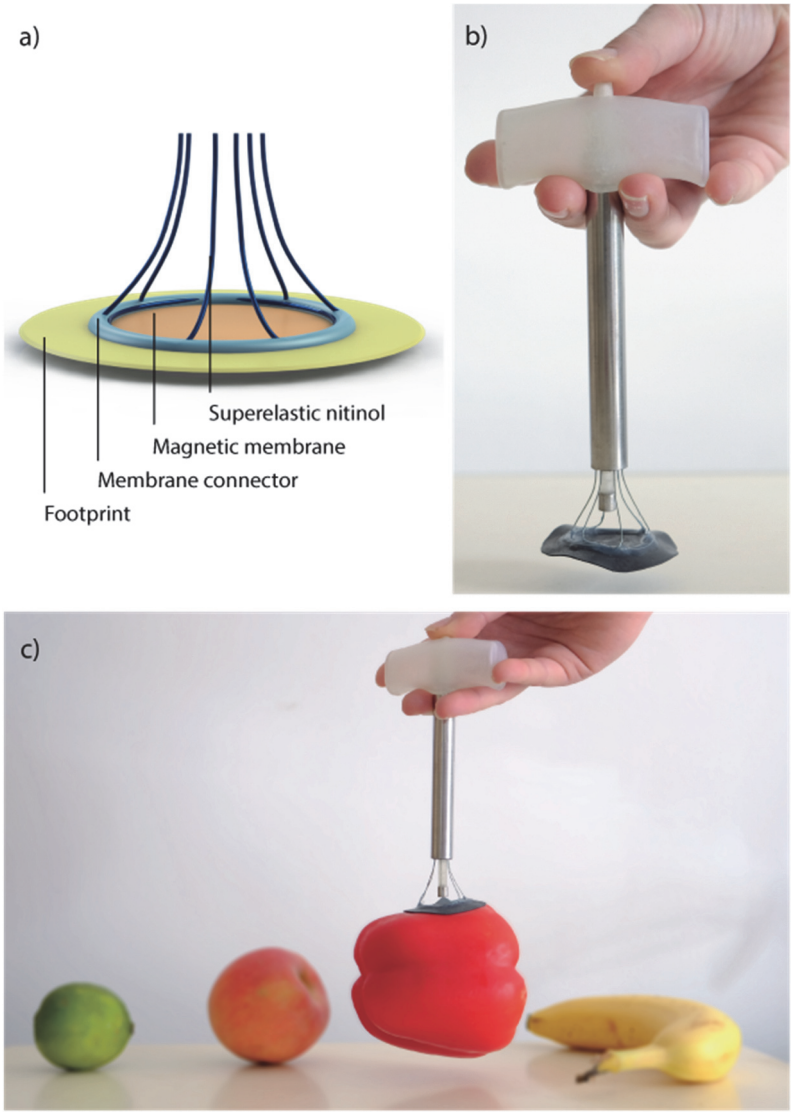


Figure 5.4: Final Proof-of-Principle Prototype Magnetic Suction Gripper. a) Illustration of the components included in the final design. b) Instrument configuration of the magnetic suction gripper. c) The instrument gripper lifting of a bell pepper.

Three independent variables were considered:

1. **The shape of the curved substrate**: ten different surfaces were tested, varying from a flat surface to a maximum curvature of 25 mm, both convex and concave (Figure 5.5).
2. **The environmental condition**: air or submerged in water.
3. **The presence or absence of a magnetic field**.

Each condition was repeated five times.

Experiment setup

The magnetic suction gripper was affixed to a holder to ensure consistent magnetic actuation during the validation process (Figure 5.6). To control the actuation, a permanent magnet (Ø6 mm) was employed. The gripper's attachment was accomplished by moving the magnet downward and then lifting it to a designated reference point on the holder, which pulled the membrane upwards and created a suction chamber underneath it. At this position, the magnet was securely fixed using butterfly screws. The holder was connected to a linear stage, which, in turn, was connected to a load cell (Futek, model LSB205) to measure the gripper's attachment force. The linear stage was controlled using ControlDesk (dSPACE). To integrate the load cell with the linear stage, a custom-made aluminium block was manufactured. The load cell was then connected to a computer via an amplifier module (Futek, model CGS110). For the test surfaces, 3D-printed PLA surfaces were manufactured. These surfaces featured a hole connected to a silicone tube, which, in turn, was linked to a pressure sensor (NXP, model

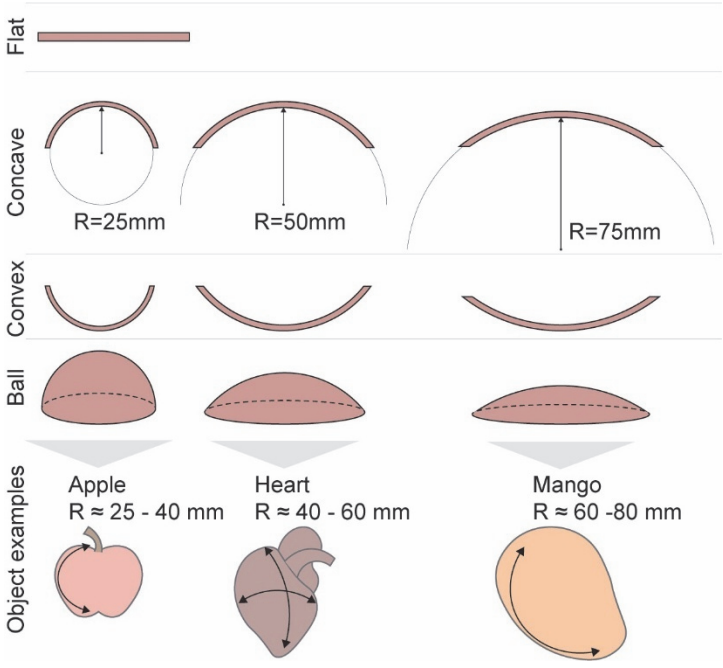


Figure 5.5: Test Surface Illustrations with Reference Objects.

MPX4115AP) for vacuum measurements. To facilitate the experiments conducted in the air environment, the surfaces were mounted on top of a plastic box, providing space for the vacuum tubing. For the experiments conducted in the submerged environment, the surfaces were positioned inside a plastic container, which was filled with water. In these experiments, no pressure tests were conducted.

Experiment Protocol

Before commencing the experiment, the load cell underwent calibration to account for the weight of the suction gripper. To initiate the experiment, the linear stage was carefully adjusted to lower the gripper until its magnetic membrane made contact with the test surface. The gripper was then affixed perpendicularly to the linear stage, positioned at the centre of each test surface. To achieve magnetic attachment, the butterfly screws securing the magnet were loosened, allowing the magnet to descend towards the magnetic membrane. Once the magnetic attraction occurred, the magnet was raised to the desired position and securely fixed. For measurements taken without magnetic actuation, the magnet was positioned at the top of the holder, ensuring no magnetic attraction influenced the membrane. Subsequently, the linear stage was elevated at a steady speed of 5 mm/s over a distance of 100 mm. This sequence of steps was repeated five times for each experimental condition.

Data Analysis

The data of the load cell was collected via ControlDesk. The data from the pressure sensor was collected via LabVIEW 2013. The data was analysed by a one-way ANOVA test to examine if significant differences in attachment force were found for the different surfaces in both environments separately. Consistent performance between conditions is favourited for a highly versatile magnetic gripper. To analyse the influence of the environment on the attachment performance in air or water, an independent two-sided t-test for each of the test surfaces was performed (α= 0.05).

Attachment Performance Results

The experiments illustrated that the gripper illustrates higher attachment forces for curved surfaces with larger radii (see Table 5.1). The measurements are visualized in Figures 5.7 and 5.8. One-way ANOVA tests revealed that there was a statistically significant difference in the attachment force of at least one concave surface in air ($F(2,12)=41.73$, $p=3.9 \times 10^{-6}$) and in water ($F(2,12)=60.56$, $p=5.4 \times 10^{-7}$), at least one convex surface in air ($F(2,12)=7.86$, $p=0.007$) and in water ($F(2,12)=32.62$, $p=1.4 \times 10^{-5}$) and at least one ball-shaped surface in air ($F(2,12)=44.21$, $p=2.9 \times 10^{-6}$) and in water ($F(2,12)=22.56$, $p=8.6 \times 10^{-5}$). Independent t-tests showed no significant difference between concave 50 mm and 75 mm radius surfaces in air ($t(8)=1.803$, $p=0.11$) and in water ($t(8)=2.241$, $p=0.055$), no significant difference between convex 50 mm and 75 mm radius surfaces in air ($t(8)=1.086$, $p=0.309$) and in water ($t(8)=1.167$, $p=0.277$) and a significant difference between 50 mm and 75 mm radius ball in air ($t(8)=3.354$, $p=0.010$) and water ($t(8)=3.200$, $p=0.0126$). Independent t-tests showed a significant difference between air and water tests for the concave 75 mm radius surface ($t(8)=2.8207$, $p=0.0225$) and the convex 25 mm radius surface ($t(8)=4.4622$, $p=0.0021$). For

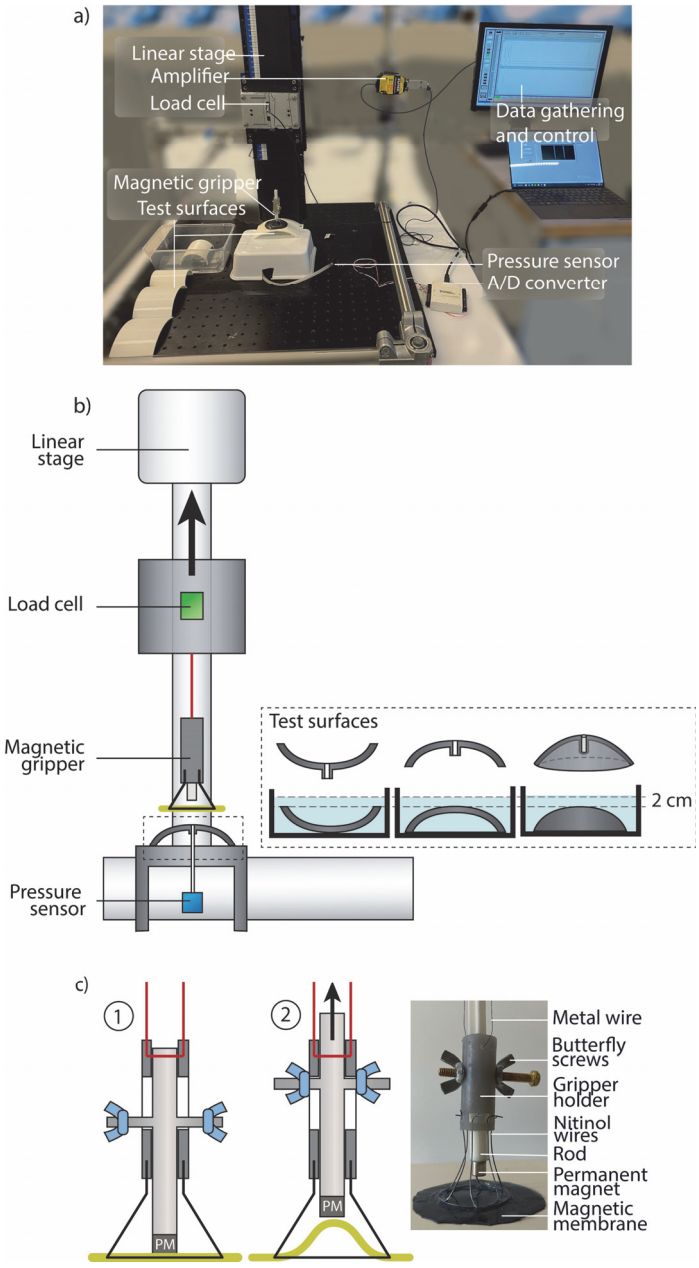


Figure 5.6: Test Setup for the Attachment Performance Experiment. a) The magnetic gripper assembly with magnetic actuation mechanism for the experimental validation. b) Schematic overview of the experimental setup. c) Two-step procedure to apply a constant actuation force. (1) Loosening the screws and lowering the magnet. (2) Raising the magnet to top position and tightening the screws.

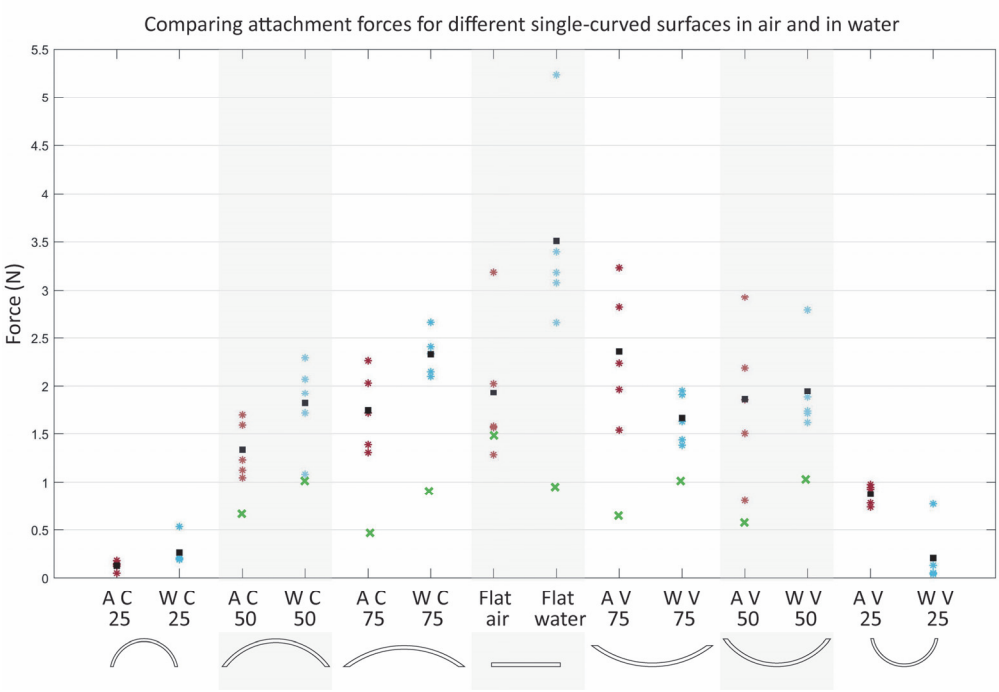


Figure 5.7: Attachment Forces of the Magnetic Suction Gripper on the Single Curved Surfaces and Environments. The stars in red and blue represent the individual maximum attachment force for the experiments, for respectively the measurements in air and in water. The black boxes represent the mean values of the attachment force. The green crosses show the average maximum attachment force without magnetic actuation for the surfaces where the attachment was achieved. A = Air, C = Concave, V = Convex, W = Water. The numbers indicate the radii of the surfaces.

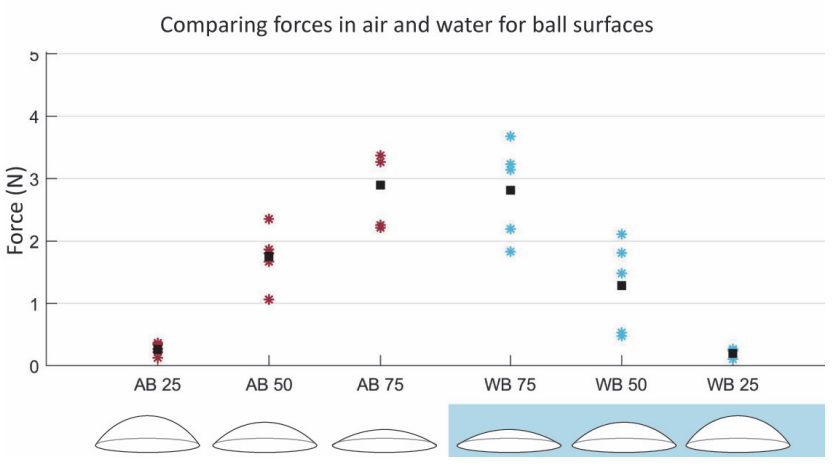


Figure 5.8: Attachment Force of the Magnetic Suction Gripper on the Double-Curved "Ball" Surfaces. The red stars represent the results of the measurements in air, and the blue stars from the measurements in water. A = Air, B = Ball, W = Water. The numbers indicate the radii of the surfaces.

the other types of curved surfaces where the attachment was achieved, no significant difference between the air or water environment was found. For the experiments where no magnetic actuation was used, the attachment was possible on all surfaces except the 25 mm curved surfaces, although this force was always smaller compared to the attachment with magnetic actuation.

5.3.2 Deployment Performance

The prototype underwent evaluation regarding its deployability. Tests were conducted using a nitinol wire frame connected to the magnetic membrane, mirroring the final design's dimensions. 3D-printed tubes with inner diameters of 20 mm, 17.5 mm, 15 mm, 12.5 mm, and 10 mm were utilized for testing purposes. The results, depicted in Figure 5.9, indicate that the nitinol wire frame could fit and stretch inside the smallest tube with a diameter of 10 mm. However, the silicone membrane connection between the nitinol wire and the magnetic membrane did not fit within the smallest-diameter tube. The magnetic gripper design could be fully folded within the 12.5 mm tube, achieving a deployment percentage of 75%. The nitinol deployment mechanism increases the theoretically achievable suction force of the magnetic gripper, with the current rim and suction surface dimension ratio, by 75%.

5.4 Discussion

5.4.1 Main Findings

The exploratory design study has resulted in a concept for a magnetically actuated and deployable suction gripper. The prototype demonstrated successful magnetic actuation and attachment to curved surfaces in various environments. Figure 5.10 shows initial trials that demonstrate attachment to a diverse collection of objects. The design incorporates an advanced isotropic magnetic material composed of carbonyl iron particles and silicone. This combination results in significant shape changes of the membrane when subjected to magnetic actuation. The high friction coefficient of the silicone matrix material enhances the gripper's frictional support against shear stresses. By combining the thin magnetic membrane with a nitinol frame, the gripper creates vacuum attachment forces. The nitinol frame provides stability, allowing the membrane to be placed on a substrate, forming a low-pressure cavity underneath the membrane. The superelastic properties of nitinol enable the gripper to be folded into a smaller tube, facilitating downsizing and increasing the suction area when deployed.

The prototype gripper demonstrated secure attachment to both single-curved and double-curved surfaces with a radius of 50 mm or higher in air and water. Attachment performance was similar between curved surfaces and flat surfaces, indicating effectiveness across different shapes. The maximum lifting forces achieved in air was 2.89 ± 0.54 N, allowing for lifting objects to approximately 350 grams with a single gripper, such as strawberries, large tomatoes and large apples. A mean maximum pressure difference of 3.38 ± 0.77 kPa was reached, which complies with the relatively small cavity formed underneath the membrane upon magnetic actuation. Attachment to a curved surface with a radius of 25mm was unsuccessful, as the gripper was not able to create a seal. However, attachment

Table 5.1: Experiment Results of the Attachment Experiment with Magnetic Actuation (n = 5).

Type of Surface	Radius	Attachment Force Air	Pressure Difference in Air	Attachment Force Water
Flat	Infinite	1.93±0.75N	2.57±0.30kPa	3.51±1.0N
Concave	25 mm	0.13±0.05N	0.99±0.34 kPa	0.27±0.15N
	50 mm	1.34±0.32N	3.38±0.77 kPa	1.82±0.53N
	75 mm	1.74±0.33N	1.49±0.20 kPa	2.33±0.25N
Convex	25 mm	0.87±0.09N	0.86±0.63 kPa	0.21±0.04N
	50 mm	1.85±0.91N	3.30±1.13 kPa	1.95±0.53N
	75 mm	2.36±0.74N	2.48±0.93 kPa	1.66±0.24N
Ball	25 mm	0.26±0.07N	0.63±0.46 kPa	0.20±0.07N
	50 mm	1.75±0.53N	2.62±0.76 kPa	1.28±0.85N
	75 mm	2.89±0.54N	1.98±0.74 kPa	2.82±0.85N

Table 5.2: Experiment Results of the Attachment Experiment without Magnetic Actuation (n = 2).

Type of Surface	Radius	Attachment Force Air	Attachment Force Water
Flat	Infinite	1.54±2.09N	0.91±1.04N
Concave	25 mm	-	-
	50 mm	0.68±0.70N	1.01±1.15N
	75 mm	0.48±0.47N	0.87±0.92N
Convex	25 mm	-	-
	50 mm	0.61±0.77N	1.06±1.41N
	75 mm	0.67±0.62N	1.01±1.16N
Ball	25 mm	-	-
	50 mm	0.18±0.00N	0.22±0.05N
	75 mm	0.11±0.01N	1.15±1.36N

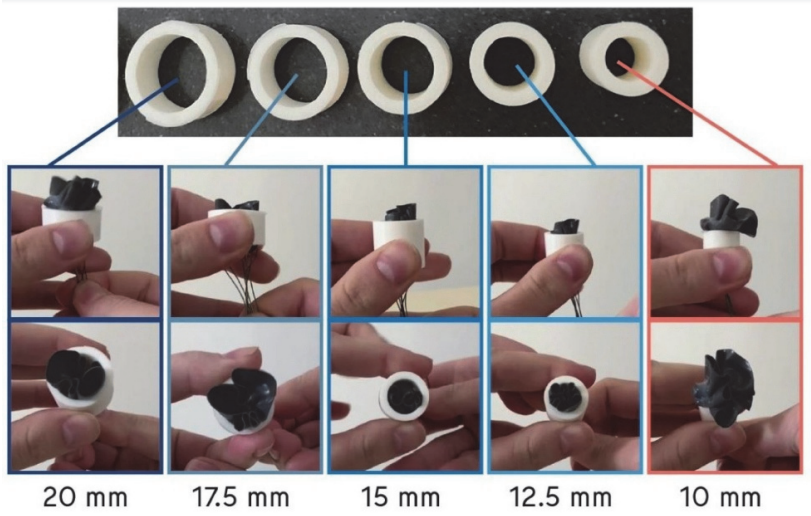


Figure 5.9: Proof-of-Principle Prototype Folded Configuration. For the tube diameter of 10mm, the silicone membrane connector limits the withdrawal of the gripper.

to curved surfaces with a radius less than 25 mm was achieved by sealing the inner part of the magnetic membrane onto the substrate while the nitinol wire frame surrounded the object without making contact, see Figure 5.10a-b. These observations indicate that attachment is challenging for surfaces where the curvature aligns with the gripper rim. The ability of the gripper to attach to substrates without actuation could indicate that adhesive forces of the membrane itself also play a role in providing attachment.

5.4.2 Limitations

The experiments performed in this study rest on the constancy of attachment conditions across various measurements. The assumption was made that any deviations in attachment performance were solely attributed to the distinct shapes of the test surfaces and their environmental conditions. Also, a uniform distribution of magnetic particles in the membrane was assumed. A larger sample size is required to draw definite conclusions on the attachment performance. As stated within the goal of this research, the proof-of-principle prototype focuses on attaching to differently shaped surfaces. However, it should be noted that for a wide range of objects, the surface roughness should also be incorporated. The gripper is shown to attach to rougher surfaces, as shown in Figure 5.10e, where it is attached to sandpaper with a coarse grid, as well as to the surface texture of a strawberry. Even so, attachment to those objects was more prone to failure when compared to the smoother surface of a grape or a glass lightbulb. Future experiments should discover the effect surface roughness on attachment performance further.

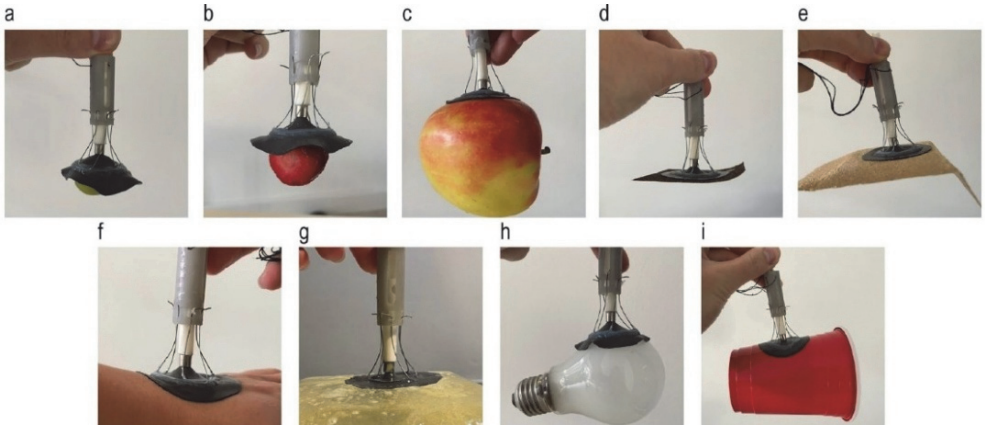


Figure 5.10: Attachment of the Magnetic Suction Gripper to Various Objects. a) Lifting a grape b) Lifting a strawberry c) Lifting a larger apple d) Attach to fine sandpaper with a grid of 600 K e) Attach to coarse sandpaper with a grid of 40 K. f) Attach to human skin. g) Attach to soft gelatine sample. h) Lifting a delicate lightbulb. i) Lifting a delicate soft plastic cup, and performing attachment without substrate deformation.

5.4.3 Recommendations

The suitability of the gripper in specific applications, such as the medical field, should be further evaluated. The gripper's foldability and attachment to small configurations, like heart tissue, need to be assessed. Initial trials demonstrated attachment to a gelatine phantom representing the stiffness of heart tissue, suggesting potential feasibility (Figure 5.10g). For future research, the magnetic interaction could be improved by programming the magnetic particles in the soft matrix material in a specific orientation. This will enhance the magnetic force and provide the possibility of a more controlled detachment process. To comprehensively understand the gripper's performance, further evaluations are recommended including a wider range of surface characteristics, such as roughness, and different strategies for magnetic actuation. The dimensions of the membrane and magnet should be optimized for effective sealing and miniaturization by modelling the magnetoactive membrane and its deformation and actuation force, comparable to the analytical model developed by Pan *et al.* [18]. Possibilities for the integration of multi-stimuli behavior could be discovered by embedding the shape memory effect into the nitinol frame.

5.5 Conclusion

In this study, we introduced a magnetic actuated suction gripper and examined its ability to grasp a wide range of objects. The proposed gripper relies on a small external magnetic field to induce a shape change in a soft magnetic membrane, generating a vacuum on diverse surfaces and shapes. The membrane was manufactured from a mix of silicone and carbonyl iron microparticles. To enhance stability and flexibility, we incorporated three superelastic Nitinol wires in the suction gripper, enabling the gripper to fold up to 25% of its original outer diameter. The magnetic gripper showcased remarkable success in grasping various objects of different shapes and sizes, showcasing its versatility and adaptability. Experiments were performed on single-curved surfaces, double-curved surfaces and flat surfaces, both in air and

in water environments. Maximal mean attachment forces of 2.89 ± 0.54 N and 3.51 ± 1.0 N were found in respectively air and water. This force proved adequate to lift objects weighing around 350 grams, considering the current gripper dimensions and magnetic actuation strength. These results indicate the promising potential of the magnetically actuated gripper for implementation in diverse applications from medical to marine exploration. Further research and development in this domain could lead to enhanced gripping capabilities, particularly on challenging substrates and difficult-to-reach areas.

References

[1] A. Tiwari and B. Persson, "Physics of suction cups," *Soft matter,* vol. 15, no. 46, pp. 9482-9499, 2019.

[2] J. A. Sandoval, S. Jadhav, H. Quan, D. D. Deheyn, and M. T. Tolley, "Reversible adhesion to rough surfaces both in and out of water, inspired by the clingfish suction disc," *Bioinspiration & biomimetics,* vol. 14, no. 6, p. 066016, 2019.

[3] P. Ditsche and A. Summers, "Learning from Northern clingfish (Gobiesox maeandricus): bioinspired suction cups attach to rough surfaces," *Philosophical Transactions of the Royal Society B,* vol. 374, no. 1784, p. 20190204, 2019.

[4] A. Koivikko, D.-M. Drotlef, C. B. Dayan, V. Sariola, and M. Sitti, "3D-Printed Pneumatically Controlled Soft Suction Cups for Gripping Fragile, Small, and Rough Objects," *Advanced Intelligent Systems,* vol. 3, no. 9, p. 2100034, 2021.

[5] J. Shintake, V. Cacucciolo, D. Floreano, and H. Shea, "Soft robotic grippers," *Advanced materials,* vol. 30, no. 29, p. 1707035, 2018.

[6] D. F. Gruber and R. J. Wood, "Advances and future outlooks in soft robotics for minimally invasive marine biology," *Science Robotics,* vol. 7, no. 66, p. eabm6807, 2022.

[7] M. V. Gandhi and B. Thompson, *Smart materials and structures*. Springer Science & Business Media, 1992.

[8] P. Zhang, M. Kamezaki, K. Otsuki, Z. He, H. Sakamoto, and S. Sugano, "Development of a vacuum suction cup by applying magnetorheological elastomers for objects with flat surfaces," in *2020 IEEE/ASME International Conference on Advanced Intelligent Mechatronics (AIM)*, 2020: IEEE, pp. 777-782.

[9] P. Zhang, M. Kamezaki, Z. He, H. Sakamoto, and S. Sugano, "EPM–MRE: electropermanent magnet–magnetorheological elastomer for soft actuation system and its application to robotic grasping," *IEEE Robotics and Automation Letters,* vol. 6, no. 4, pp. 8181-8188, 2021.

[10] A. Koivikko, D.-M. Drotlef, M. Sitti, and V. Sariola, "Magnetically switchable soft suction grippers," *Extreme Mechanics Letters,* vol. 44, p. 101263, 2021.

[11] H. Iwasaki, F. Lefevre, D. D. Damian, E. Iwase, and S. Miyashita, "Autonomous and reversible adhesion using elastomeric suction cups for in-vivo medical treatments," *IEEE Robotics and Automation Letters,* vol. 5, no. 2, pp. 2015-2022, 2020.

[12] X. Hu, Y. Fu, Y. Liu, B. Liu, and S. Qu, "Acarid Suction Cup-Inspired Rapid and Tunable Magnetic Adhesion," *Advanced Materials Technologies,* vol. 6, no. 8, p. 2100004, 2021.

[13] V. G. Kortman, A. Sakes, G. Endo, and P. Breedveld, "A bio-inspired expandable soft suction gripper for minimal invasive surgery—an explorative design study," *Bioinspiration & Biomimetics,* vol. 18, no. 4, p. 046004, 2023.

[14] H. Zhou, X. Wang, W. Au, H. Kang, and C. Chen, "Intelligent robots for fruit harvesting: Recent developments and future challenges," *Precision Agriculture,* vol. 23, no. 5, pp. 1856-1907, 2022.

[15] R. Bogue, "Fruit picking robots: has their time come?," *Industrial Robot: the international journal of robotics research and application,* vol. 47, no. 2, pp. 141-145, 2020.

[16] M. A. F. Falah, H. i. Husna, A. Dewi, and J. Jumeri, "Quality evaluation of fresh strawberry (Fragaria sp. cv. Earlybrite) during storage in a tropical environment," in *AIP Conference Proceedings*, 2016, vol. 1755, no. 1: AIP Publishing.

[17] F. s. A. N. Zealand. "Fruits and vegetable measures program." https://www.foodstandards.gov.au/science-data/monitoringnutrients/ausnut/foodmeasures/fruits-and-vegetable-measures-program (accessed 12 March, 2024).

[18] T. Pan, R. Leng, O. Uitz, C. Seepersad, Z. Ounaies, and M. Frecker, "Analytical modeling of a magnetoactive elastomer unimorph," *Smart Materials and Structures,* vol. 32, no. 9, p. 095021, 2023.

PART 02

INTELLIGENT MOVEMENT

CHAPTER 06

STATE-OF-THE-ART MCKIBBEN ARTIFICIAL MUSCLES

ABSTRACT

McKibben Artificial Muscles (AMs) are known as a prominent class of pneumatic actuators in soft robotics and biomechanical engineering, due to their unique structure and multifunctionality. This paper presents a comprehensive review of recent advancements in McKibben AMs, focusing on their performance, structural variations, and operational principles. A systematic literature search on Scopus identified 146 relevant articles, which were analyzed for both performance metrics and design characteristics. Inspired by natural muscle behavior, McKibben AMs enable complex motions such as bending, linear extension, and twisting. These actuators can be organized as individual or bundled systems: individual units are typically arranged in linear or circular patterns, while bundled systems occur in serial, parallel, braided, convergent, or pennate configurations. Recent innovations in smart actuation methods, braided sleeves and internal bladders have expanded their capabilities, enabling embedded sensing, environmental adaptability and untethered operation. Additionally, alternative manufacturing methods offer promising solutions for developing McKibben muscles with enhanced functionality and tailored properties.

Published as:
Kortman, V. G., Jovanova, J., Nabae H., Endo G., Suzumori K., & Sakes, A. (2026). Designing High Performance McKibben Muscles: A Critical Guide for Implementation. *Bioinspiration & Biomimetics, 21*(3), 031002.

6.1 Introduction

In the domain of soft robotics and biomechanical engineering, McKibben Artificial Muscles (AMs) have emerged as a notable class of pneumatic actuators, characterized by their unique structural composition and versatile functionality. Positioned at the intersection of engineering and biology, McKibben AMs are conceived as a means to imitate natural musculature. Developed by J.L. McKibben in the late 1950s, these AMs illustrate inherent compliance, low mass, and controllability which render them particularly suitable to a spectrum of applications, such as wearables, robotics, prosthetics, and rehabilitation engineering.

The typical composition of a McKibben AM involves a flexible outer sleeve, usually a braid or textile, commonly crafted from materials such as nylon or polyethylene, providing the necessary structural integrity. Enveloped within this outer sleeve is an inner pneumatic bladder, typically composed of a compliant material, such as latex, rubber, or silicone, see Figure 6.1. At the distal tip of the McKibben AM, an end cap is placed to close off the pneumatic bladder. The synergy between the flexible outer sleeve and the inflatable inner bladder enables controlled, biomimetic motion of the McKibben AM, similar to natural muscles. To activate the muscle, pressurized fluid is normally injected into the open end of the inner pneumatic bladder using a connection cap. Once the inner bladder is fully pressurized, the volume of the inner bladder increases and produces a force in the radial direction against the braided sleeve. The braided sleeve subsequently transforms the generated radial force into the length direction along the braid axis [1].

McKibben AMs exist in a large size-range from approximately 1 mm to 50 mm in diameter and variable lengths. For example, a McKibben AM with a diameter of 1.5 mm was developed by de Volder *et al.* [2] that could achieve contraction forces of 6 N, an axial strain of 15%, and a maximal actuation speed of 350 mm/s, whereas a much larger hydraulic AM was developed by Mori *et al.* [3], with a diameter of 40 mm that could achieve up to 28 kN. State-of-the art McKibben AMs can generate axial strains of up to 30-35% [4].

McKibben AMs have recently regained significant attention as soft robotic systems increasingly demand lightweight, high compliance, and high force actuators. At the same time, research on McKibben AMs has become widely scattered across biomechanics, robotics, materials science, and rehabilitation engineering journals, making it difficult for new researchers to navigate the field. Therefore, this paper undertakes a comprehensive review to illustrate the intricate mechanical principles governing McKibben AMs and explores their diverse configurations across disciplines. By summarizing how key design and performance parameters influence actuator behavior, this work aims to provide clear, implementation oriented guidance and fill a gap in literature for researchers who seek an overview. For this purpose, we have conducted a literature review in Scopus (05-02-2024) using "McKibben" as the single keyword, which yielded 838 results. Papers focusing on analytical and experimental studies involving McKibben AM were included in this study, resulting in a total of 146 included articles. Review papers and papers solely focusing on control, finite element analysis, the application of McKibben AMs in other structures, and artificial intelligence, as well as non-English papers were excluded from this review. Generally, closed loop PID based force or position control remains the most commonly applied approach for McKibben actuators [5, 6].

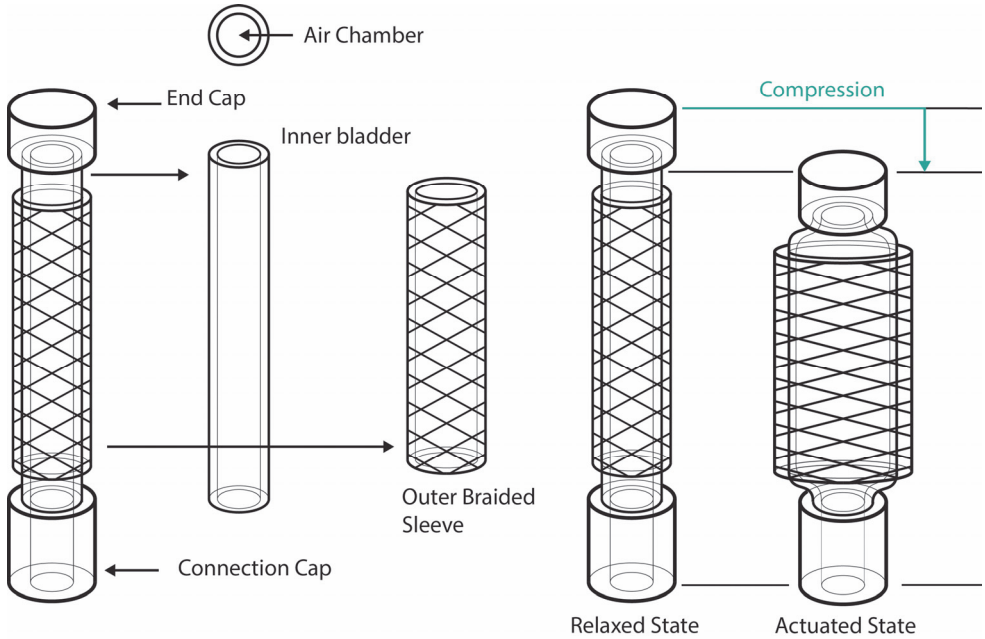


Figure 6.1: Structural Composition of McKibben Artificial Muscles (AMs). McKibben AMs comprise of a flexible outer braided sleeve, an inner air chamber, an end cap, and a connection cap. By inflating the inner pneumatic bladder, the McKibben AM will either expand or compress, depending on the braiding angle.

For comprehensive treatments of control design and system dynamics, we refer readers to Tondu & Lopez [5], Caldwell et al. [6], and De Volder et al. [2].

We focus on classical McKibben AMs as their architecture, fabrication methods and design parameters form a distinct class of pneumatic artificial muscles with well-defined characteristics and industrially scalable fabrication. Including other pneumatic artificial actuators, such as fiber reinforced elastomer actuators, would substantially broaden the scope and reduce the focus of the study.

6.2 McKibben Performance Characteristics

6.2.1 Force and contraction characteristics

Figure 6.2 shows the composition and geomertic variables of McKibben AMs. McKibben AMs are often characterized based on their tension force, contraction force, and blocking force. The tension force is the force generated along the wires in the outer sleeve when the McKibben is pressurized, whereas the contraction force is the force produced during muscle contraction. The contraction force is highest when the axial strain is lowest and varies with the initial braid angle, see Figure 6.3. The blocking force is the resisting force against further contraction when the muscle is pressurized but prevented from shortening. The blocking force opposes the contraction force and, therefore, benefits from friction, whereas the contraction force is negatively affected by friction.

McKibben AMs generate an axial contraction force that can be expressed by the classical Chou & Hannaford model, shown in Equation (6.1), which assumes inextensible fibers and

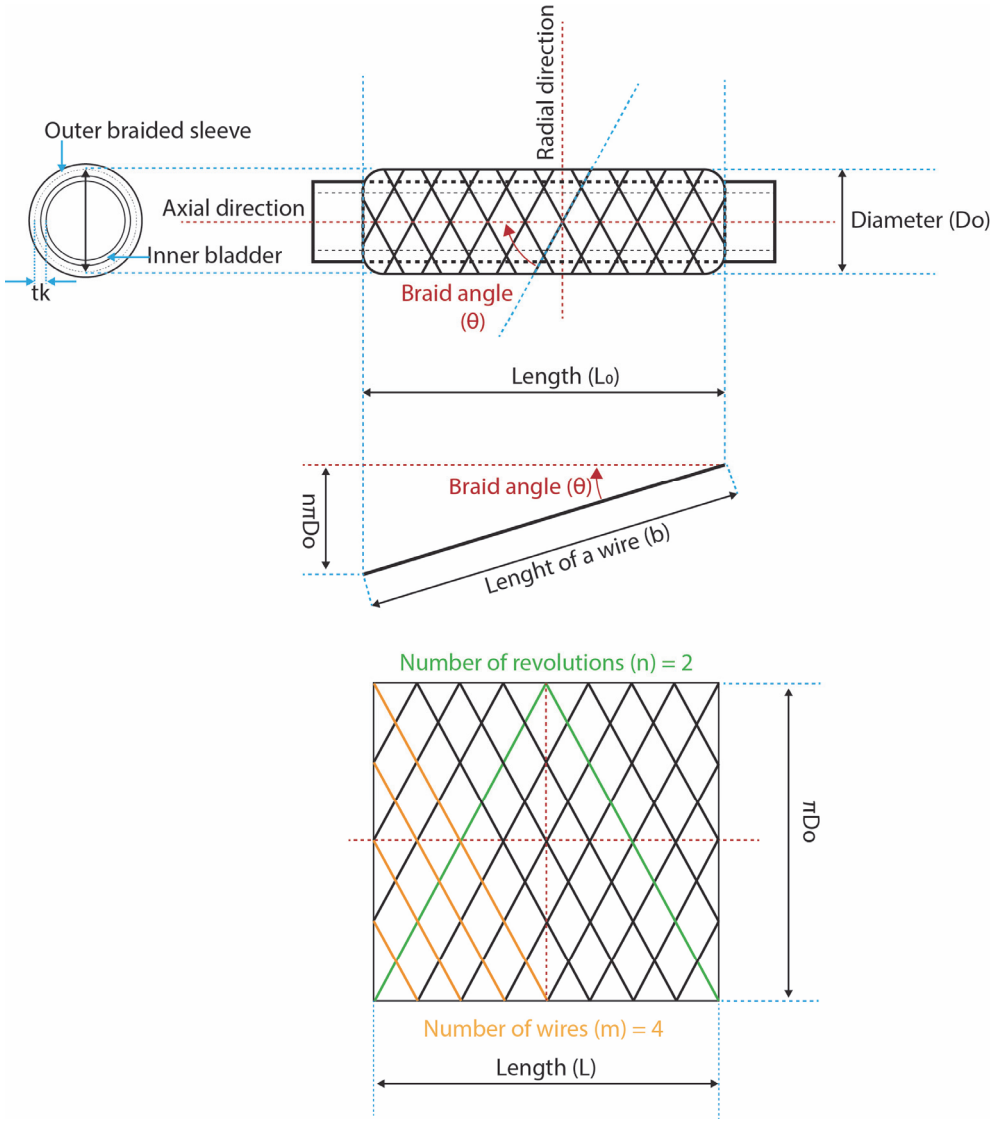


Figure 6.2: Composition and Geometric Variables of McKibben Artificial Muscles (AMs). McKibben AMs composition indicating the sum of the thickness of the bladder with half of the sleeve width (t_k), the braid angle (θ), the initial length of the muscle (L_0), the length of an individual wire (b), the diameter of the McKibben AM (D_0), the number of full rotations per wire (n), and the number of wires in the outer braided sleeve (m).

relates the force to the geometry of the actuator [7]. This formulation is widely used in analytical and experimental studies of pneumatic artificial muscles. The same model can also be rearranged into strain-based forms, in which the geometry is expressed as a function of axial strain (ε) [4, 5, 8].

$$F_c = \frac{\pi}{4} P D_0^2 (3\cos^2\theta - 1) \quad (6.1)$$

D_0, P and θ denote the diametric constant of the AM [mm], the applied pressure [Pa] and the braid angle (defined as the angle between any wire of the outer braid and the axial axis, see Figure 6.2) [°], respectively. Using the inextensible fiber assumption, the diameter of the AM is defined as:

$$D = \frac{b \sin\theta}{n\pi} \quad (6.2)$$

Where b is the length of an individual wire [mm] in the outer braided sleeve and n is the number of full rotations per wire [-], see Figure 6.2. The axial strain ε is defined as (3), with L_0 the initial length of the McKibben AM [mm] and L the contracted length [mm].

$$\varepsilon = \frac{L_0 - L}{L_0} \quad (6.3)$$

The generated contraction force is proportional to the applied pressure, substantiating that McKibben AMs using liquids instead of air, can generate larger amounts of force than those actuated by air [9-15]. Iwata *et al.* [9] developed a hydraulic McKibben AM (Ø 21 mm) capable of generating a contraction force of 8 kN. Mori *et al.* [3] developed a similar McKibben AM (Ø 40 mm) that could achieve a contraction force of 28 kN by applying high tensile force sleeve wires, optimizing the weaving pattern of the outer braided sleeve, and increasing the strength of the connection and end caps. In the study of Thomalla *et al.* [8], a new model was developed for hydraulic McKibben AMs that tracked the generated axial force of the actuator while considering the change in actuator wall thickness. This new model showed increased accuracy of approximately 1% over the state-of-the-art (elastic) force models.

The contraction force is proportional to the outer diameter of the McKibben AM, with larger McKibben AMs able to achieve higher contraction forces, as can be observed from Equation (6.1). The effect of scaling on the performance of McKibben AMs was investigated in more detail in an experimental study by Peel *et al.* [14]. It was found that a longer actuator resulted in a larger contraction stroke and lower contraction force. Though contraction forces decreased as the diameter and length decreased, which is in line with Equation (6.1), the force per unit AM volume was shown to increase with decreasing diameter. However, the relative work per actuation volume was decreased by roughly 35% in smaller AMs [14].

McKibben AMs are commonly modelled or characterized as actuators, but their second role as support structure introduces strain–pressure combinations outside of normal actuation regions. This occurs, for example, when the McKibben AMs are placed in an antagonistic configuration. In the study by Olson *et al.* [16] a more complete set of possible strain–pressure combinations for McKibben AMs was investigated, including those of passive or unpressurized actuators, as well as pressurized extension and compression beyond the maximum actuation

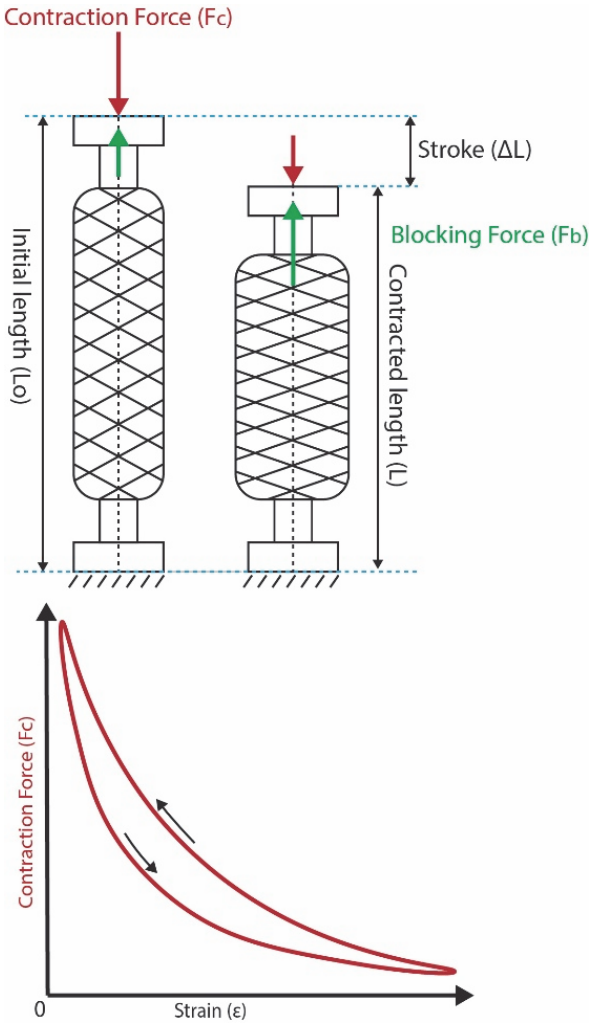


Figure 6.3: McKibben Artificial Muscles (AM) Performance Variables. McKibben AM performance variables indicating the initial length (L_0), contracted length (L), strain (ΔL), axial strain (ε), contraction force (F_c) and blocking force (F_b) of the artificial muscle. The contraction force scales with the contraction ratio, with the maximum contraction force at zero contraction, whereas the blocking force is maximum and full contraction. Hysteresis in the system creates the distinct force loop during inflation and deflation.

strain. They demonstrate a trade-off between the maximum axial strain and force required to passively extend the AM, and that stiffer elastomers inner bladders require an increase in actuation pressure without a compensatory increase in maximum achieved force.

Different studies describe the dynamic responses of McKibben AMs for different pressures and frequencies [7, 17, 18]. Wenlin *et al.* [19] report that the driving frequency across various applications is generally concentrated within 0.3 Hz. They mention that when the driving frequency exceeds 1 Hz, their AMs cannot be fully inflated and deflated anymore due to the viscoelasticity of the bladder. Experiments show that with increasing driving frequency, the

amount of hysteresis of the AM increases. Davis *et al.* [18] show that major constraining elements on the AM dynamics is the supply pipe and valve resistance, favouring a minimal amount of pipe connectors and large orifice valves.

A large number of papers describes physical, empirical or experimental models of McKibben AMs [5, 20-33]. In these studies, slight alterations are made to the state-of-the-art in terms of the implementation of a more sophisticated friction modulation, noncylindrical shape, and more accurate braiding representations. These studies will not be discussed in detail.

6.2.2 Energy Dissipation

Although the theoretical contraction force can be calculated by Equation (6.1), it does not consider the hardness of the inner bladder and the frictional forces experienced in the McKibben AM. Whilst these properties are neglectable at larger scales, when downsizing the McKibben AMs, these factors need to be considered. Considering the effect of the bladder thickness and the frictional forces in the sleeve, Chou and Hannaford [7, 34] proposed an improved formula for the relationship between the contraction force F_c and the pressure difference P, including a correction for the bladder thickness:

$$F_c = \frac{\pi}{4} P\left[{D_0}^2\{3cos^2\theta - 1\}\right] + \pi P t_k \left[D_0\left(2sin\theta - \frac{1}{sin\theta}\right) - t_k\right] \qquad (6.4)$$

Where t_k is the sum of the thickness of the bladder with half of the sleeve width. However, even though Equation (6.4) represents the characteristics of McKibben AMs more closely than Equation (6.1), there is a substantial gap between experimental data and the predictions due to the lack of considering energy losses in the AM. One of the major energy losses in McKibben AMs is due to frictional resistance and appears as the wires rotate during contraction or extension, see Figure 6.4 [35]. These resistances can be subdivided into:

(1) rotational resistance due to the frictional forces between wires

During axial contraction or extension, the braiding angle changes as the wires slide over each other. This causes friction, reducing efficiency and increasing hysteresis of the McKibben AM. Efficiency refers to the ratio between the mechanical work delivered during contraction and the pneumatic/hydraulic energy supplied [12]. Surface texture is a key factor influencing wire-to-wire friction. To minimize this friction, a smoother wire surface is more desirable [22], which correlates with the findings of Hoque *et al.* [36], as well as less contact points between the wires. If the thickness of the wires or the number of wires is reduced, the maximum axial strain could potentially be improved since the rotational resistance of the threads decreases [35]. Furthermore, to reduce friction further, in some outer sleeves not every wire is woven consistently, with some weaves that are intentionally skipped, thus minimizing the rotational resistance of the wires. The number of contact points between the wires can be calculated using the following equation [37]:

$$N_{contact} = \frac{2b^2 sin^2\theta cos^2\theta}{n{w_y}^2} \qquad (6.5)$$

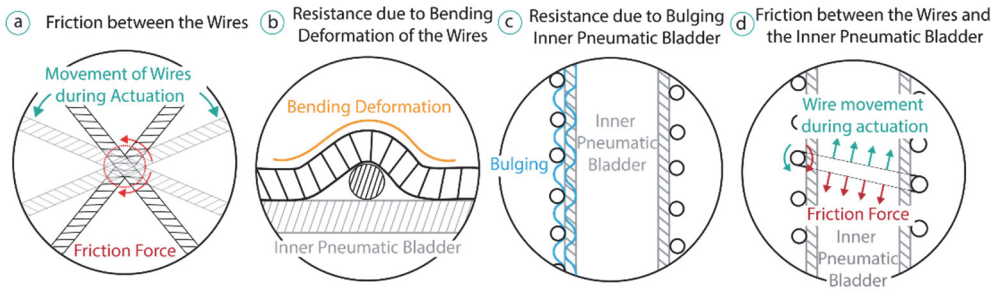


Figure 6.4: Energy Losses in McKibben Artificial Muscles. a) rotational resistance due to the frictional forces between the wires, b) resistance due to bending deformation of wires, c) resistance due to bulging of the inner bladder through the sleeve, d) resistance due to the frictional force between wires and the bladder.

With w_y the wire width [mm].

(2) resistance due to bending deformation of wires

Energy is dissipated in order to produce bending deformation of the wires during movement. Therefore, wires that exhibit lower bending stiffness, such as braided wires or wires out of a more flexible material, can potentially decrease this type of energy loss in the AM.

(3) resistance due to bulging of the inner bladder through the sleeve

During inflation, the inner bladder will start to expand until it reaches the outer braided sleeve, where the radial expansion is halted and converted into the axial direction. By increasing the applied pressure to the bladder, the bladder can start to bulge through the holes in the outer sleeve, which causes frictional and energy losses, and can lead to rupture. Therefore, there is an interplay between the compliance of the bladder, the elasticity of the bladder material, and the cover factor of the outer braided sleeve.

(4) resistance due to the frictional force between wires and the bladder.

During actuation of the McKibben AMs relative motion between the wires and the bladder ensues. This relative motion results in frictional losses and therefore a loss in efficiency of the McKibben AM. Taking these factors into account leads to the following equation [35]:

$$F_c = \frac{\pi}{4} P {D_0}^2 \{3cos^2\theta_0 - 1\} - \frac{4m^2 n}{bsin\theta_0} (M_f + M_d + M_r + M_{tr}) \qquad (6.6)$$

With m is the number of wires in the outer sleeve [-], M_f the resistant moment due to friction between wires [Nmm], M_d the rotational resistant moment due to the bending deformation of wires [Nmm], M_r the rotational resistant moment due to the bulging of the rubber [Nmm], and M_{tr} the resistant moment due to the frictional force between wires and the bladder [Nmm].

As can be seen from Equation (6.6), an increase in the number of wires m in the outer sleeve, reduces the contraction force of the McKibben AM. This is substantiated by the experimental

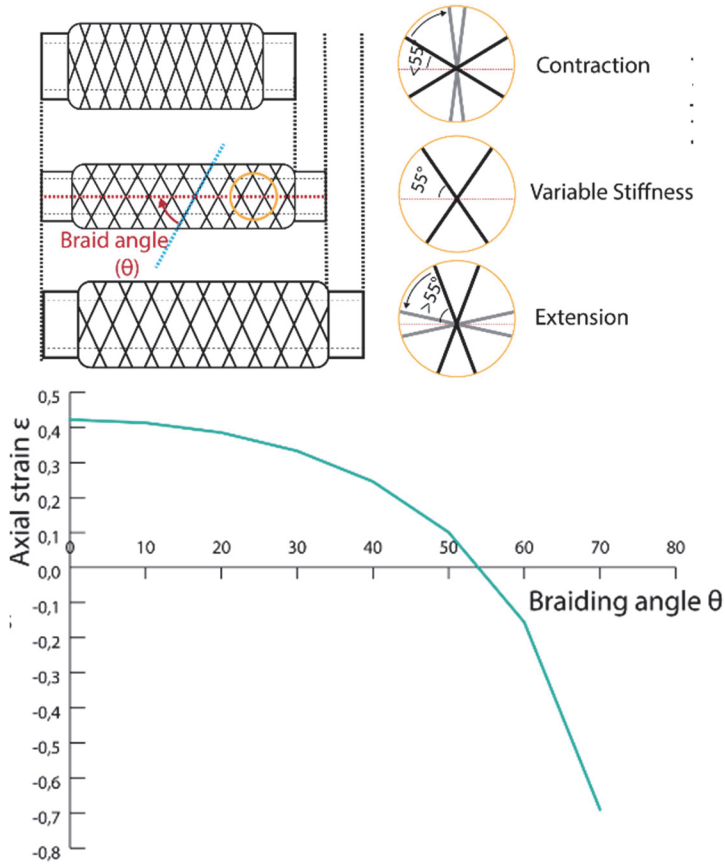


Figure 6.5: McKibben Artificial Muscle (AM) Braid Angle Contribution to Functionality. The braid angle is defined as the angle between the wires of the outer sleeve and the axial axis of the muscle. The braid angle determines the performance of the McKibben AM. Braid angles under 54.7° will result in contraction, braid angles at 54.7° will cause variable stiffness, and braid angles over 54.7° cause extension of the McKibben AM. The effect of the braid angle on the contraction ratio is schematically presented in the graph on the bottom.

study of Kurumaya *et al.* [38], in which they investigated the effect of the inner bladder hardness and number of wires in the outer sleeve on the blocking force and the axial strain of thin McKibben muscles (Ø 1.8 mm). It was found that when the number of outer wires increases, the blocking force also increases due to an increase in friction between the wires, as well as between the wires and the inner pneumatic bladder, at the cost of the axial strain. Additionally, it was found that the number of outer wires need to be at least 24 with a braiding angle of at least 18°, to reduce the risk of rupture. The hardness of the bladder was also found to be an important factor for design because it determines the ease of tube deformation, axial strain, and amount of air pressure required to achieve a given contraction. Davis and Caldwell [39] showed that to determine the number of wires necessary to prevent braid failure of the McKibben AM, the following equation can be used:

$$m = \frac{P{D_0}^2 \pi \cos\theta \sin\theta}{2 s A_{wire}} \quad (6.7)$$

With s representing the ultimate tensile strength of the wire [Pa] and A_{wire} representing the cross-sectional area of the wire [mm^2].

6.2.3 Fatigue characteristics

When applying McKibben AMs in robotic applications, fatigue life is a major challenge. McKibben AMs exhibit fatigue characteristics influenced by the materials used and the cyclic nature of their operation. Over time, repeated inflation and deflation cycles can lead to wear and tear, particularly in the inner bladder and outer braided sleeve, which may result in reduced performance and eventual failure due to material fatigue. In a study of Klute *et al.* [40], a model was developed that predicts the maximum number of life cycles of a McKibben AM based on available uniaxial tensile properties of the actuator's inner bladder. Experimental results revealed that McKibben AMs fabricated with natural latex rubber bladders have a fatigue limit 24 times greater than actuators fabricated with synthetic silicone rubber at large axial strains. In a study by Wenlin *et al.* [19], they found that air leakage in the middle was the most common fatigue phenomenon in their McKibben AM.

6.2.4 Experimental Facilities

Isotonic and isometric testing methods are pivotal in evaluating the performance of McKibben AM. Isotonic testing involves assessing the AM under constant loading conditions, allowing for the measurement of contraction length, contraction force, and speed as the AM performs work against a fixed resistance. This method provides insights into the strain, response time, and mechanical efficiency under dynamic loading scenarios. Conversely, isometric testing measures the AM's force output while maintaining a constant length, thereby evaluating its static force generation capabilities. Together, these methods comprehensively characterize the mechanical properties and functional performance of McKibben AMs.

In a study of Salahuddin *et al.* [41], an integrated characterization method is proposed that combines isometric and isotonic testing. This test set-up allows for simultaneously measuring the free stroke of a McKibben AM, the stroke while operating against an externally applied force (isotonic), the blocked force while keeping the muscle at constant length (isometric); and the force and displacement change when the McKibben AM operates against a return spring (variable force, pressure).

6.3 McKibben Composition Characteristics

6.3.1 Outer Sleeve Configuration

The outer sleeve of McKibben AMs is normally manufactured using several wires interwoven with each other in a biaxial braiding pattern and fabricated around a mandrel [39, 42]. In biaxial-braided sleeves, a single wire set (generally orientated at an angle in the + and - directions) is interlaced with each other to form the braided fabric surface. Simulations reveal that loads are sustained mostly by the outer braided sleeve, whereas the inner bladder stores the majority of the external work as elastic energy [43]. Geometric variables that affect the final mechanical performance of the outer braided sleeve include the braid angle q [°], helical

length L_h of one pitch of wire [mm], mandrel or braid diameter d_b [mm], wire width w_y [mm], and cover factor C [-].

One might argue that the pleated muscles are a kind of McKibben AMs using only parallel wires as the outer braided sleeve. These types of actuators outperform traditional McKibben AMs in terms of axial strain but exhibit drastically higher radial expansion due to the lack of radial-oriented wires in the sleeve. Due to the substantial differences between the pleated and biaxially braided McKibben AMs, we will not include these types of muscles in our review.

Braid Angle

The ability of McKibben AMs to contract or extend depends on the initial braid angle θ [°] of the outer sheath, see Figure 6.5. Both the axial strain and hysteretic behaviour of McKibben AMs are governed by the initial braid angle [39, 44, 45]. At the fully contracted position, the braid angle is set by the energetics of the operation of the AM at 54.7° [39]. The axial strain can be calculated using Equation (6.3) and (6.8):

$$\varepsilon_{max} = 1 - \frac{1}{\sqrt{3}\cos\theta} \tag{6.8}$$

Equation (6.8) assumes the actuator is under zero external load, with inextensible braid and fully pressurized [46]. From Equation (6.8), the maximum theoretical axial strain can be determined when the contraction force nears zero [47]. From this, it is found that when θ is approximately 54.7°, the maximum axial strain becomes 0. Theoretically this means that McKibben AM with braiding angle of 54.7° generates no motion even if high pressure is applied, which makes them into a types of variable stiffness actuator. If the wires of the braid cross at an angle less than 54.7°, the radial expansion of the inner bladder will be transferred into axial compression and the McKibben AM will generate tension force at its ends. Braid angles over 54.7° result in axial extension.

The effect of the braid angle was experimentally investigated in a study by Gentry *et al.* [48]. They show that variations of the braid angle has a significant effect on the axial strain and the blocked force. It was found that contractile McKibben AM subjected to a pre-strained cyclic displacement test generated over 13 times the absolute blocking force and about 34% larger stroke than extensile AMs.

The minimum braid angle is limited by adjacent braid wires being forced against each other, assuming the inner bladder has a diameter small enough to allow for full braid dilation [39]. This minimum braid angle can, therefore, vary depending on the braid pattern, the wire material, and the diameter of the wire. Typically, the minimum braid angle is around 20° [6]. However, using a mathematical approach, Davis and Caldwell [39] showed that by halving the number of wires in the outer braided sleeve, the minimum braid angle can be reduced by 50% (from 19° to 9°) which results in an increase in the contractile range of the AM of approximately 7%, with a simultaneous peak contraction force increase of over 16% [39]. The minimum braid angle that can be obtained depends on the cover factor and can be calculated as follows [39].

$$\theta_{min} = \frac{sin^{-1}(\frac{2w_y m}{\pi D_0})}{2} \tag{6.9}$$

Wire Elasticity

To prevent energy consumption during actuation, inextensible wires are preferred for the outer braided sleeve, such as high-stiffness aramid (Kevlar®) and Ultra-High Molecular Weight Polyethylene (UHMWPE) (Dyneema® and Spectra®) [49-51]. In the study of Krishnan *et al.* [52] even silk is proposed as a braid material due to its higher stiffness than nylon and steel.

As can be observed in Equation (6.1), the effect on wire elasticity on the contraction force and ratio is not considered. The inelastic braid assumption suggests that the outer braided sleeve of the McKibben AMs is inextensible to effectively convert the radial expansion of the bladder into axial contraction or extension of the muscle overall [53]. Although this assumption has often been cited as a likely source of model error, it keeps being used due to researchers' inability to directly measure the effects of braid elasticity [54]. However, a reduction in efficiency, both in terms of contraction force and axial strain, will be observed by the axial deformation of the wires. This is substantiated by the static model by Davis *et al.* [29].

The effect of the wire stiffness, wire diameter, and wire structure on the blocking force was also investigated experimentally in a study by Hoque *et al.* [36]. It was found that the stiffness of the wire was directly proportional to the AMs blocking force and axial strain. Furthermore, it was found that wire diameter governs the blocking force, with smaller wire dimension resulting in a reduced blocking force. Braided wires illustrated higher friction and, therefore, slightly lower free axial strains.

Cover Ratio

The number and geometry of the wires that make up the outer braided sleeve can be expressed as the cover factor and is an essential property of a McKibben AM. The cover factor is defined as the ratio of area occupied by the wires within a periodic pore unit to the total

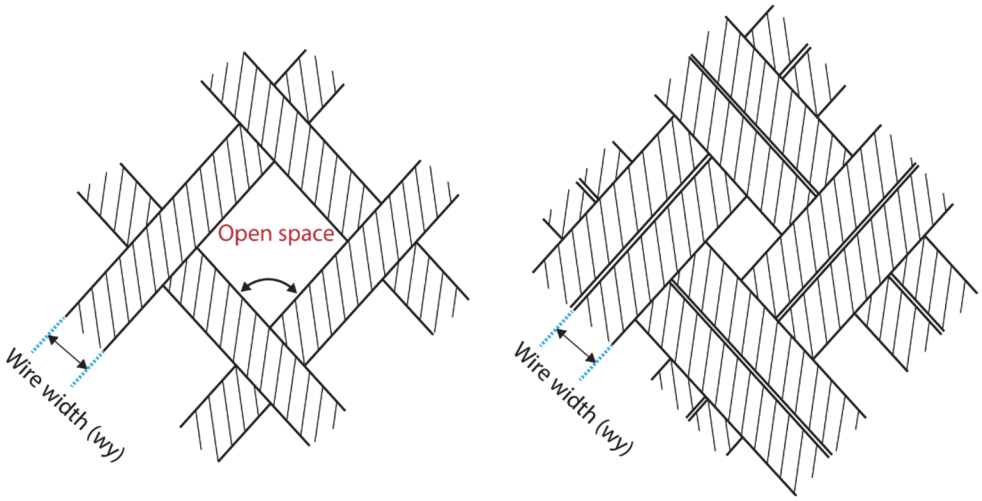


Figure 6.6: Outer Braided Sleeve Cover Factor of McKibben Artificial Muscles (AMs). The cover factor is defined as the ratio of area occupied by the wires within a periodic pore unit to the total area of the pore unit. A cover factor of at least 0.7 for McKibben AMs is preferred to prevent bulging of the bladder through the outer braided sleeve. Using multiple wires or flat wires with increased wire width can be used to increase the cover factor (right).

area of the pore unit, as shown in Figure 6.6. As derived by Sangian *et al.* [55], the cover factor is described by Equation (6.10) and is a function of the braid diameter D_0 [mm], the initial braid angle θ [°], the wire width w_y [mm], and the number of wires m [-].

$$C = \frac{w_y m}{\pi D_0 cos(\frac{\theta}{2})} - \left[\frac{w_y m}{2\pi D_0 \cos(\frac{\theta}{2})}\right]^2 \quad (6.10)$$

Braided outer sleeves with high cover factors are normally required in manufacturing McKibben AMs due to the working conditions at high pressures. When fewer wires are used in manufacturing of the braided sleeve this results in wider gaps between the wires and consequently may result in rupture due to the internal bladder passing through the gaps at high pressures [1, 39]. In an effort to increase the cover factor, and thus the durability of the AM, on some occasions, multiple wires per direction or flat wires are used. Generally, a high cover factor of at least 0.7 is desired for proper functioning of the McKibben AMs, although examples of McKibben AMs exist with lower cover factors, such as 0.47 [1, 44]

6.3.2 Inner Bladder Configuration

An important geometrical property in determining the performance of a McKibben AM is the wire-to-bladder distance at the resting length. When the inner side of the braid structure is not in contact with the outer wall of the elastomeric bladder, the actuator's dead-band pressure increases dramatically since, when the bladder begins to expand, it is unable to transfer the force to the braiding structure and the actuator will remain inactive until the elastomeric bladder comes into contact with the braided sheath [53]. In Equation (6.1), this distance is considered 0. Although friction decreases the efficiency of the muscles, as well as the contraction force, static friction between the wires themselves, as well the static friction between the inner bladder and wires, can increase the blocking force of the McKibben AM. Therefore, a trade-off remains.

By reducing the dead volume within the inner pneumatic bladder, the bandwidth of the McKibben AM can be increased by up to 400%, with a similar increase in stiffness [18]. To reduce the dead volume, different filler materials can be used, such as elastic particles, solid particles and liquids, with the added benefits of increased stiffness. At the same time, the air volume used to actuate the AM can be reduced by up to 80-90% [18].

Strain energy losses could be reduced by preventing stretching of the inner pneumatic bladder, maximizing the energy stored in the braids and the efficiency of the McKibben AM. In a study of Cavallaro *et al.* [56], an oversized bladder containing radial folds was used. In the study by Meller *et al.* [12], an inelastic LDPE bag was used as the inner bladder that unfolded during actuation. It was shown that this actuator had an efficiency of almost 80% and could achieve a blocking force of up to 500 N.

The Young's Modulus of the inner pneumatic bladder also plays an important role in determining the performance of McKibben AMs. In an experimental study by Hoque *et al.* [36], it was found that a softer bladder, with a lower Young's Modulus, was able to generate higher free axial strains, with the risk of destructive failure. In addition, a larger diameter bladder was able to generate significantly higher blocking force but a lower axial strain on average due to the increased friction between the wires and the bladder [36]. In the study of Ball *et al.* [57,

58], a model was presented that allows prediction of the effect of bladder pre- stretch, showing bladder pre-stretch results in higher actuator force and longer stroke length.

Modeling the inner pneumatic bladder is often challenging due to their complex non-linear deformations [59]. The literature on McKibben AM modeling mostly focuses on contractile AMs. However, Garbulinski *et al.* [60] presents new hyper-elastic constitutive models and revalidate methods for extensile McKibben AMs that were previously studied for contractile McKibben AMs. The effect of hemi-spherical deformation of the inner pneumatic bladder near the end caps was investigated in the study by Kadowaki *et al.* [61]. In their study, the inner pneumatic bladder was modeled as hemi-spherical, resulting in improved accuracy in the predication of the force-contraction profiles of McKibben AM.

6.4 McKibben Muscle Configurations

6.4.1 Natural Muscle Types to McKibben Configurations

McKibben muscles were originally designed to mimic natural muscles. Compared to natural muscles, McKibben AMs exhibit similar performance in terms of contraction strain at 20-35%, as well as a higher tension intensity of 88-144 N/cm^2 (versus 35 N/cm^2), higher work density of 0.13-0.20 J/cm^3 (versus 0.13 J/cm^3), higher energy efficiency 0.32-0.49 (versus 0.2-0.25), and higher peak power density of 2.65 W/cm^3 (versus 0.70 W/cm^3) [7, 62]. However, McKibben AMs lack the ability to be arranged as freely as natural muscles. McKibben AMs can approach the dynamic behaviour of skeletal muscles by carefully choosing an adequate outer braided sleeve [63]. To achieve the required force production, axial strain, and motion, for the intended application a specific type of muscle architecture might be required.

There are several muscle architectures that can be found in the natural world. Muscles are usually arranged in *parallel* or *pennate architectures*. In *parallel muscles*, the fascicles (motor-units of the muscles) run parallel to the axis of force generation. There are several parallel muscle architectures, such as *fusiform*, *convergent*, and *circular muscles*. A *convergent muscle* has a triangular or fan-shape as the fibres converge at its insertion and are fanned out broadly at the origin. A less common example of a parallel muscle is a *circular muscle* such as the *orbicularis oculi* in the eyelids, in which the muscle fibres are longitudinally arranged, but create a circle from origin to insertion. *Pennate muscles* differ from parallel muscles in that the fascicles attach obliquely (in a slanting position) to the tendon. This type of muscle generally allows higher force production but a smaller range of motion than *parallel muscles*.

6.4.2 Individual McKibben Muscles

Individual McKibben Muscles take the shape of parallel natural muscles and can be found in a linear and circular configuration, see Figure 6.7.

McKibben - Linear

Bladder Alterations

Whereas natural muscles can only contract to create moments and forces on their surroundings, McKibben AMs can also enable active extension depending on the braid angle. However, McKibben AMs differ from natural skeletal muscles in that they cannot perform passive elongation movements, in which the muscle is stretched by an external force from its

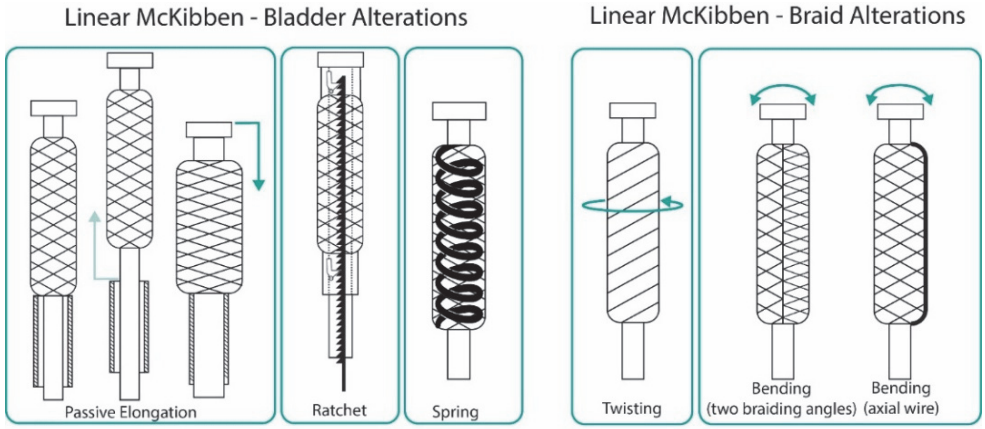


Figure 6.7: Individual McKibben Artificial Muscles (AMs) mimicking the functionality of parallel natural muscles. Linear McKibben AMs can either extend, contract, or illustrate variable stiffness during inflation. Circular McKibben AMs can be used to increase or decrease in diameter, similar to how a sphincter muscle operates.

natural length while deactivated. Since contractile McKibben AMs can only generate tensile force, they are often deployed in an antagonistic setup: two acting on opposite sides of a pulley, similar to the configuration of the triceps and biceps muscles controlling movement of the upper arm and elbow, respectively.

In studies by Tanaka *et al.* [64] and Kobayashi *et al.* [65], back-stretchable McKibben muscles are proposed that contract like a conventional McKibben AM when air pressure is applied and back-stretches like a natural skeletal muscle with no applied pressure (see Figure 6.8). In the design by Tanaka *et al.* [64], the inner bladder of the McKibben AM is extended and placed inside an inextensible flexible tube that is slightly bigger in diameter. In this set-up, when the muscle is not actuated, the inner bladder provides passive elongation when subjected to extension forces. However, whilst actuated, the inner bladder locks into position inside the inextensible flexible tube. In comparative experiments on a robotic arm, they achieved a 22% increase in the antagonist muscle driving range compared with conventional McKibben AMs without causing the muscles to sag significantly. Another difference between McKibben AMs and their natural counterpart can be found in the way the sarcomere, the basic unit of a skeletal muscle, generates contraction. In the cross-bridge model of a sarcomere, the muscle accumulates nanoscale strokes of myosin head motors to generate larger strokes, similar to a ratchet-type mechanism, which makes the muscle more robust against mechanical disturbances and able to produce larger strokes. Taking inspiration from the nanoscale stroke method, the spring-like behaviour of McKibben AMs could potentially be negated, and large strokes could be generated that are independent from the applied load. Cho *et al.* [66] developed a McKibben AM utilizing two pawls integrated at both ends and a flexible rack inserted in the lumen, see Figure 6.8. The ratchet-integrated McKibben AM was able to achieve a large stroke length of 250 mm (20 cycles) by accumulating displacements from multiple small strokes by repeating the cycle of pressurization and depressurization. In comparison, a similar-sized regular McKibben AM was able to achieve a stroke length of approximately 30 mm. Cullinan *et al.* [71] proposes a similar design that integrates a pulley system, resulting in a robust McKibben AM with simplified control [72].

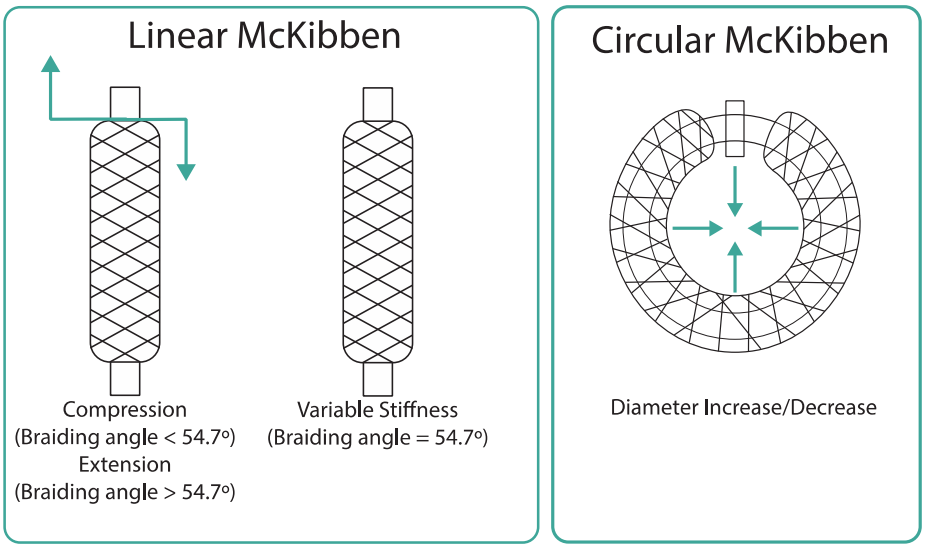


Figure 6.8: Linear McKibben Artificial Muscles Configurations found in Literature. Left: Linear McKibben Artificial Muscles (AMs) with different bladder alterations. Passive elongation is seen in the back-stretchable McKibben developed by Tanaka *et al.* [64], a ratchet mechanism is utilized in the McKibben AM developed by Cho *et al.* [66], and a compression spring was added by Kim *et al.* [67]. Right: Linear McKibben AMs with different braid alterations. A twisting McKibben AM was developed by Tian *et al.* [68], a bendable McKibben AM using two distinct braiding angles was developed by Faudzi *et al.* [69], and another bendable McKibben AM using an inextensible wire was developed by Feifei *et al.* [70].

Another bladder alteration is proposed by Kim *et al.* [67], in which a low stiffness compression spring is added to the bladder to prevent buckling of the McKibben AM, see Figure 6.8. By adding a compression spring to the McKibben AM, the effect of the axial strain on the contraction force is reduced, which makes this AM more suitable for use in large range of motion structures. Furthermore, a 31% greater contraction force and 26% higher contraction speed could be achieved in comparison to a conventional McKibben AMs, as well as a 21.5% increase in actuator efficiency. Finally, in a study by Legrand *et al.* [73], a McKibben AM is proposed containing a working channel that can be used to guide other tools through during operation of the McKibben AM.

Braid Alterations

Next to extension and compression, individual linear McKibben AMs can also be used as variable stiffness actuators when the braid angle is set to 54.7°, resulting in an axial strain of 0. An example of such a variable stiffness McKibben AM is the one developed by Iwata *et al.* [72].

Additionally, by removing one direction of the braid, the linear McKibben AM can be transformed into a twisting AM. In a study by Tian *et al.* [68], a new fabrication process is proposed to realize twisting McKibben AMs by utilizing braiding technology and water-soluble fibers, see Figure 6.8. In the braiding process, half of the sleeve fibers of the artificial muscle is substituted with water-soluble fibers. Using this method, McKibben AMs with maximum twist angles of up to 160° could be obtained. Similarly, in the study of Olson *et al.* [74], a

McKibben AM was helically wound around a compliant foam core to create a combined twisting and contraction motion with twist angles of up to 60°. In the study of Connolly *et al.* [51] another twisting McKibben AM is illustrated.

Another braid alteration, in which two different braids are present on either side of the McKibben AM, can result in a bending motion. In the study by Faudzi *et al.* [69], a McKibben AM (Ø 14 mm) was developed that contains two braids with different braiding angles (52° and 73°) on either side of the AM, which enable bending angles of up to 32°, see Figure 6.8. The McKibben AM was manufactured by first embedding two separate braids into silicone, cutting these in half in the length direction, and finally attaching the two braided halves with a different braid angles to each other. In a follow-up study [75], the effect of the different weave pattern combination on the bending characteristics was researched using the Finite Element Method (FEM). It was found that the highest bending angles were obtained with braiding angle combinations of 32/90°, 32/70°, and 32/62° (in descending order of bending angle). Additionally, it was found that the braided layer needs to be placed close to the outer surface of the AM and the air chamber of the bladder needs to be large in order to increase bending performance [76].

Bendable McKibben AMs can also be obtained by partly restricting the movement of the braid in the axial direction. In the design proposed by Feifei *et al.* [70], an inextensible wire is guided through the braid in the axial direction, which limits axial expansion of the McKibben AM at this side, see Figure 6.8. Du *et al.* [77] proposes a similar design in which an elastic support is connected to the braid to restrict unilateral axial displacement of the McKibben AM. It was show that bending angles of up to 90° were achieved in an experimental prototype. Finally, in the design by Xiang *et al.* [78] a Shape Memory Alloy (SMA) wire was placed in parallel to an extending McKibben AM to initiate bending motions and in the study of Maeda *et al.* [79] an Shape Memory Polymer (SMP) was integrated into the braided sleeve of a McKibben AM to create bending and torsional motions.

McKibben – Circular

No singular circular McKibben configurations have been identified.

6.4.3 Bundled McKibben Muscles

In Figure 6.9, the potential parallel McKibben AM configurations are indicated.

McKibben – In Series

By placing multiple contracting or extending McKibben AMs in series, the stroke can be increased, whilst maintaining the contraction force of a single McKibben AM. However, the system as a whole can only apply as much force as the weakest McKibben AM allows. Otherwise, the weakest AM would rupture or overstretch. The amount of contraction or extension of the full system (ΔL_{total}) is a summation of the individual stroke lengths (ΔL_k) pertaining to the McKibben AMs within the system, Equation (6.11). The total axial strain is a length-weighted average of the axial strains of the individual AMs (ε_k), as shown in Equation (6.12). This means that single McKibben AMs with longer initial length have more influence on the overall axial strain.

$$\Delta L_{total} = \sum \Delta L_k \tag{6.11}$$

$$\varepsilon_{total} = \frac{\sum \epsilon_k \cdot L_{0k}}{\sum L_{0k}} \quad (6.12)$$

Placing an extensible McKibben AM in series with a contractile McKibben AM can initiate movement of a spacer that is placed in between the two AMs, as is seen in the study of Lathrop *et al.* [80]. In this study, a contracting and extending McKibben AM were connected to each other via a cylindrical ring which was connected to a cable that actuated a steerable tip of a medical instrument.

Next to contraction or extension, a serial muscle arrangement can be used for creating locomotion motions, similar to the movement of an earthworm (Figure 6.10). An example of this is given by the mono-line drive design by Tsukagoshi *et al.* [81]. In this McKibben AM (Ø 2.6 mm deflated, Ø 6.1 mm inflated), a travelling wave is generated using a single input

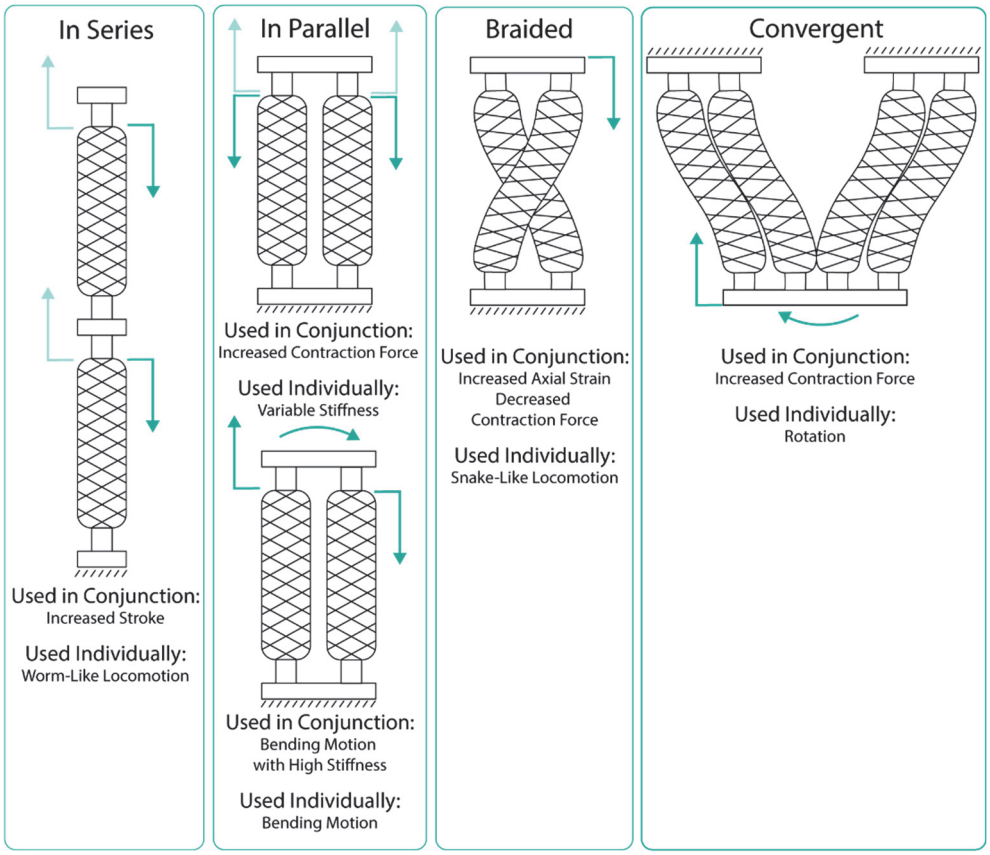


Figure 6.9: McKibben Artificial Muscle (AM) configurations mimicking the functionality of natural muscles. McKibben AMs can be placed in series, in parallel, can be braided or be placed in a convergent configuration. McKibben AMs placed in series can be used to increase the stroke or create worm-like locomotion. McKibben AMs placed in parallel can be used to increase the contraction force or to create bending motions (with high stiffness). Braided McKibben AMs have been shown to increase the contraction ratio, whilst simultaneously decreasing the contraction force. Furthermore, they can be used to create locomotion motions. Finally, convergent McKibben AMs can be used to increase the contraction force or create a rotation.

pressure. For this purpose, the inner bladder of this McKibben AM contains a plurality of holes of different sizes to cause a time delay in chamber inflation and the outer braided sleeve is subdivided into multiple sections (chambers) using three tangential wires. This set-up makes it possible to induce a worm-like propulsion motion, as well as a bending motion, using a single input tube. The prototype was successfully tested in a lung model, illustrating its ability to successfully propel and steer through variable diameter branches. One might argue that this is a single McKibben AM, however, due to the use of different chambers, the McKibben AM functions as multiple AMs in series.

McKibben – In Parallel

By placing McKibben muscles in parallel, the total contraction force of the McKibben AM can be increased without affecting the axial strain or stroke length. The total contraction force (F_{total}) is expressed mathematically as the summation (Σ) of individual contraction forces (F_c) pertaining to the McKibben AMs within the system:

$$F_{total} = \sum_k F_c \tag{6.13}$$

Here, F_c signifies the contraction force of the *k-th* McKibben AM. A similar strategy is seen in short parallel muscles, such as in the *biceps brachii*, located in the upper arm of the human body. The challenge with using multiple McKibben AMs in parallel is to attach the muscles in a space efficient way. In the study of Zhang *et al.* [82], an improved multi-connector is proposed. Due to its detachable nature, the multi-connector can change contraction force and outer shape based on demand, meaning it can be applied to a wider range of fields.

In an experimental study of Kurumaya *et al.* [38], it was shown that the axial strain of McKibben AMs can be increased by bundling, owing to its flexibility. The developed multifilament muscle comprised bundles of thin McKibben AMs and exhibited high deformability in comparison to conventional McKibben AMs of the same diameter. Furthermore, the interaction between the muscle fibres due to their radial expansion (similar to how a pleated AM functions), resulted in an 26% increase in the axial strain in comparison to a single McKibben AM. A design that takes advantage of this is illustrated by Bruder and Wood [83], in which two McKibben AMs are placed in parallel in a "chain-link" actuator structure to achieve axial strains of over 50%. A parallel McKibben AM muscle bundle can also function much like our skeletal muscle organs that selectively recruit a different number of motor fibers depending on the load demand [84]. A variable recruitment McKibben AM bundle can adaptively activate the minimum number of AMs to increase its overall efficiency.

The parallel McKibben AM configuration can also be used to generate bending motions. Typically, McKibben AMs do not allow for bending motions, as in their natural state they either contract or extend and do not allow for passive extension. Therefore, in order to achieve bending motions, in general at least two McKibben AMs should be used in parallel for planar motions and three McKibben AMs for spatial motions, similar to how muscles attach to our bones to initiate the movement of our joints. In a study by Iwata et al. [72], bendable and variable stiffness McKibben AMs were manufactured consisting of an extensible McKibben AM connected to a compressible McKibben AM. This way, both bending and variable stiffness could be achieved. Using two McKibben AMs with a diameter of Ø 21 mm, they were able to achieve a bending angle of 290°. Another bending configuration is proposed by Suzumori *et*

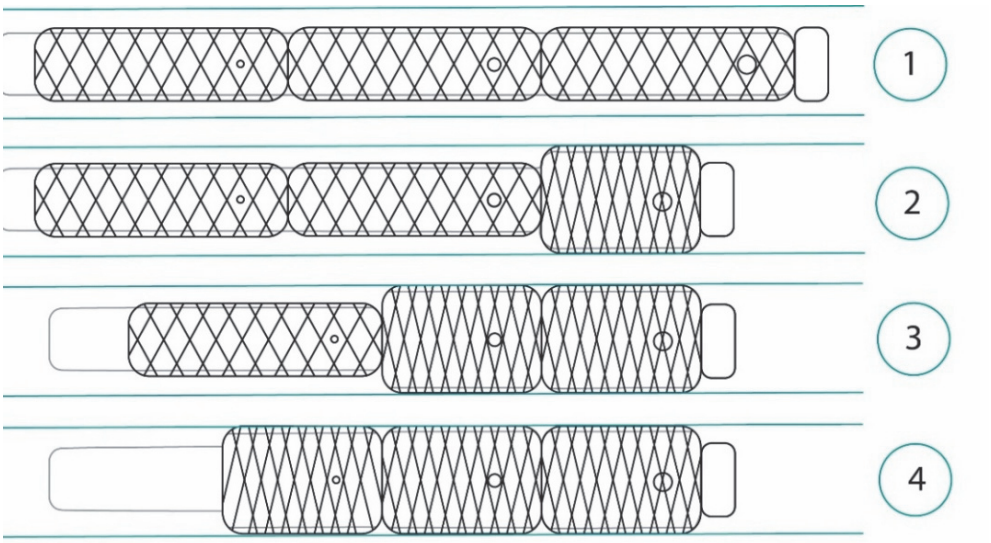


Figure 6.10: Mono-Line Drive McKibben Artificial Muscle (AM) Design by Tsukagoshi *et al.* [81]. In the mono-line drive design, three McKibben AMs are placed in series. In the pneumatic inner bladder of the designs, three holes of different diameter are present that cause sequential inflation of the McKibben AMs. Step 1 indicates the resting position of the design. In Step 2, the distal McKibben AMs is inflated, causing it to anchor to the luminal wall. Step 3 and 4 indicates the sequential inflation of the middle and proximal McKibben AM.

al. [85]. In this multi-filamented McKibben AM (Ø 21 mm), one central contracting McKibben AM and five surrounding extending McKibben AMs were bundled using non-elastic bands. Bending angles of up to 360° were reached in a 1.5m long prototype. Similar bundled McKibben AM configurations are found in [86-91]. In the study of Lathrop *et al.* [91], a slightly different approach was taken in which four contracting McKibben AMs were placed inside an outer slotted tube, that enabled bending motions of the structure.

Since McKibben AMs cannot passively lengthen, the performance of an antagonistic AMs configuration is decreased, similar what was previously described. In the study of Vocke III *et al.* [92], the performance of an antagonistic McKibben AM system was increased by decreasing the passive parasitic force caused by the opposing AM. It was found that with the proper selection of design parameters, including mechanism geometry and McKibben geometry, an ideal McKibben AM configuration can be chosen that maximizes deflection for a given arbitrary loading. In a study of Kang *et al.* [17], flow dynamics of a pneumatic valve and thermodynamics of the inflating and deflating process are included to formulate the pressure variance of the antagonistic Mckibben AMs to yield better accuracy in high frequency motions.

McKibben – Braided

Next to parallel arrangements, the McKibben AMs can be braided together to form one bigger braided AM. Braided McKibben AMs have been shown to increase the axial strain [93, 94]. In a study by Koizumi *et al.* [93], it was substantiated that the axial strain of a biaxially braided McKibben AMs is larger than the axial strain of a single McKibben muscle. In this experimental study, the axial strain of braided McKibben AMs consisting of 8, 12, or 16 strands were compared with an individual McKibben AM and eight McKibben AMs placed in parallel, all with a length of 200 mm. The braided McKibben muscles showcased a contracting ratio of 0.37; a

9% increase compared to that of an individual McKibben AM. In addition, the contracting force per muscle was reduced by approximately 10% to 40% depending on the braiding angle, due to the increase in friction between the muscles. A similar result was observed in the study of Kadir *et al.* [95], in which the axial strain significantly increased in a braided architecture, at the cost of the contraction force.

In a follow-up study, Koizumi *et al.* [94] developed a double-braided structure increasing the axial strain even further towards 0.41. It was found that there is a positive correlation between the number of braid cycles and the maximum axial strain, which allowed for achieving axial strains of up to 0.41 with a double-braided muscle, versus 0.36 in a single-braided muscle. However, the axial strain was approximately 11% lower than what was found in the analytical model, which is hypothesized due to the increase of friction as the number of braiding cycles increases, which in turn is due to the increase in the number of contact points between the muscles [94].

Another major advantage of using a braided structure is its ability to be elongated by applying an external force. Current parallel McKibben AMs cannot passively or actively extend like natural muscles, which make their use in antagonistic set-ups challenging, as previously discussed. In the study of Na *et al.* [96], they investigated the ability of the double-braided structure proposed by Koizumi *et al.* [94] to be actively stretched for use in an antagonistic set-up. They demonstrated that the driving range of joint angle actuated by braided McKibben AMs (joint angle of 73°) was larger than that of the unbraided McKibben AMs (joint angle of 88°).

A different braid pattern was proposed by Abe *et al*. [97]. In this study, the '18 Weave' pattern is proposed in which one McKibben AMs is guided through wefted McKibben AMs, see Figure 6.11. Whilst the axial strain is significantly lower than the braided structure developed by Koizumi *et al.* [94], an advantage of this structure is its flat configuration, which is advantageous in, for example, exosuits or garments. Kurumaya *et al*. [49] developed yet another flat and flexible braided McKibben structure consisting of three braided strands that are interlaced by exchanging a single muscle strand with each other at specific positions along the length of the muscle. This braided structure showed exceptional flexibility in comparison to the ones developed by Abe and Koizumi et al. [93, 94, 97]. The experimental results demonstrated that the initial braiding pitch influences both the contraction force and the axial strain. A maximum contraction force of 14.8 N and maximum axial strain of 0.34 was found using these braided muscles [49].

By integrating McKibben AMs into external structures or matrices through weaving or braiding, a wider range of movement patterns, such as twisting and bending motions, can be achieved. In a study conducted by Funabora *et al.* [98], 18 McKibben AMs were arranged in a 5 x 4 grid structure with thin plastic plates between layers, square clamps at intersections, and each muscle folded back on itself to double the output force. This setup was integrated into a garment to induce bending and twisting motions of the back of the user. Subsequently, Funabora *et al.* [99] developed an active textile where 12 McKibben AMs were woven through a flexible rubber structure in a cross-shaped pattern to enable in-plane and out-of-plane bending, as well as twisting motions. Similar cross-shaped pathways are observed in an active textile developed by Nakagawa *et al.* [102], where 28 McKibben AMs were embroidered onto a flexible textile, enabling in- and out-of-plane bending, as well as twisting motions, similar to the design by Funabora *et al.* [99].

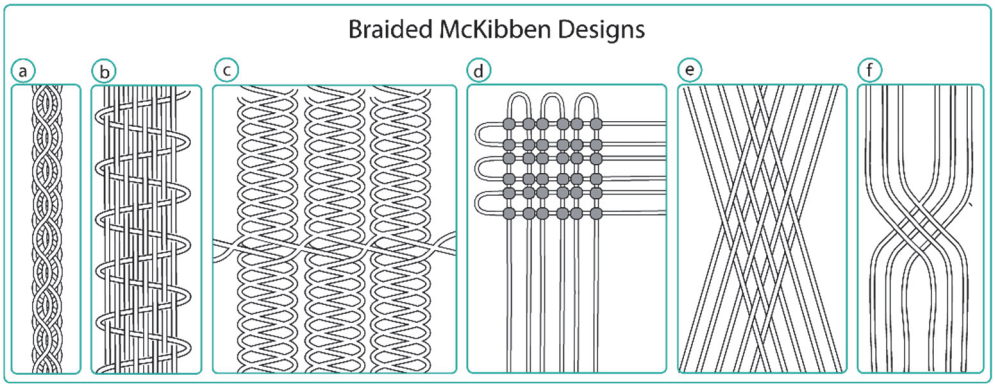


Figure 6.11: **Braided McKibben Artificial Muscle (AM) Designs found in Literature.** a) Multi-braided structure, as proposed by Koizumi *et al.* [93, 94], Kadir *et al.* [95] and Na *et al.* [96]. b) Wefted McKibben AM structure, proposed by Abe *et al.* [94], Hiramitsu [100] and Marshall *et al.* [101]. c) Interlaced braiding pattern in which one McKibben AM is interchanged between the braids at certain instances, as proposed by Kurumaya *et al.* [49]. d) McKibben AM configured in a grid-like pattern with thin plastic plates between layers, square clamps at intersections, and each McKibben AM folded back on itself to double the output force, as proposed by Funabora *et al.* [98]. e) Cross-shaped braiding pattern, as proposed by Funabora *et al.* [5, 99]. f) Cross-shaped braiding pattern of an active textile developed by Nakagawa *et al.* [102].

In the research conducted by Hiramitsu *et al.* [100], McKibben AM were integrated into textile structures, comprising fabric strings or strips arranged in a plain weave pattern. Within this pattern, one McKibben AM was intricately woven through the structure, serving as the thin warps, while the wefts consisted of strings or strips constituting the textile. Through this configuration, a contractile active textile was realized. A similar architectural approach was observed in the study conducted by Marshall *et al.* [101]. Their findings revealed that lower muscle density corresponded to increased thickness during expansion and reduced axial strain of the active textile.

A further iteration was made by Hiramitsu *et al.* [103], in which active textiles were proposed that can achieve bending motions. In addition to a plain weave, in this study a twill weave and sateen weave pattern, in which a different amount of McKibben AM run on the front and back of the textile, were used to initiate bending motions. It was found that the characteristics of the wefts (AMs that run horizontally) and warps (AMs that run in vertically), such as cross-sectional shape, bending stiffness and elasticity, determine the characteristic of the active textile.

McKibben – Convergent

Multifilament muscles can have various shapes and can mimic the shape of human muscles, including convergent configurations [38]. The advantages of multifilament muscles are that the points of force application are easily altered and the output force increases in proportion to the number of bundled muscles [38]. A convergent muscle configuration was found in the study of Kurumaya *et al.* [104]. In this study, two different types of convergent muscle configurations were developed: 1) using two bundles of 60 McKibben AMs divided by an angle of 30° similar to the biceps muscle and 2) using 16 McKibben AMs that fan out, resulting in a flat muscle similar to the deltoid muscle. A axial strain of approximately 0.2 was found for each set-up.

McKibben – Pennate

Studies focusing on McKibben AMs often focus solely on the contractile elements and rarely address the contribution of flexible connective tissue that forms an integral part of the morphology of biological muscle. A fundamental feature of pennate muscles is that muscle fibers are oriented at an angle to the line of action and rotate as they shorten, becoming more oblique throughout a contraction (Figure 10.12). This change in fiber orientation (pennation angle) can amplify the shortening velocity of a fiber and increase output velocity, output force and work output capacity of the muscle [105, 106].

The velocity advantage resulting from dynamic changes in the pennation angle can be characterized as a gear ratio or amplification factor (muscle velocity/fiber velocity). A pennate muscle's gear ratio varies automatically depending on the load such that a muscle operates with a high amplification during rapid contractions and low amplification during forceful contractions. Muscle force is attenuated by the cosine of the pennation angle and a change in fiber displacement is amplified by the secant of the pennation angle [107]. For a contractile pennate actuator at a constant pressure, the initial configuration represents the maximum force because it is the minimum pennation angle [107]. The transmission ratio TR_{force} of the input to the output force can be found using the following equation [107]:

$$TR_{force} = \frac{F_m}{xF_c} = cos\,\alpha \qquad (6.14)$$

With F_m the muscle force exerted by the pennate architecture set-up, x the number of individual McKibben AMs in the set-up, F_c the contraction force per muscle in line with the axial axis of each individual McKibben AM in the set-up, and α the pennation angle, which is defined as the angle between the McKibben AMs and the vertical attachment point. The muscle force F_m of a bipennate architecture can be calculated using the following equation:

$$F_m = cos\,\alpha\, x\, F_c \qquad (6.15)$$

Azizi *et al.* [105] showed that a pennate-like McKibben AM array can mimic the variable gearing mechanism of natural pennate muscles. When the array contracts against light loads, the individual McKibben AMs undergo changes in pennation angle, the array increases in thickness and produces a large displacement. Conversely, when the array contracts against heavy loads, the individual McKibben AMs rotate less, the array increases less in thickness, produces a smaller amount of displacement and a higher contraction force. As a result, the actuator is automatically adapted to the specific task.

In the study by Wang *et al.* [108], McKibben-type AMs were integrated into a flexible matrix in a pennate architecture. The developed actuators demonstrate that the material properties of both the contractile units and connective tissue play a crucial role in force generation, force transmission and deformation.

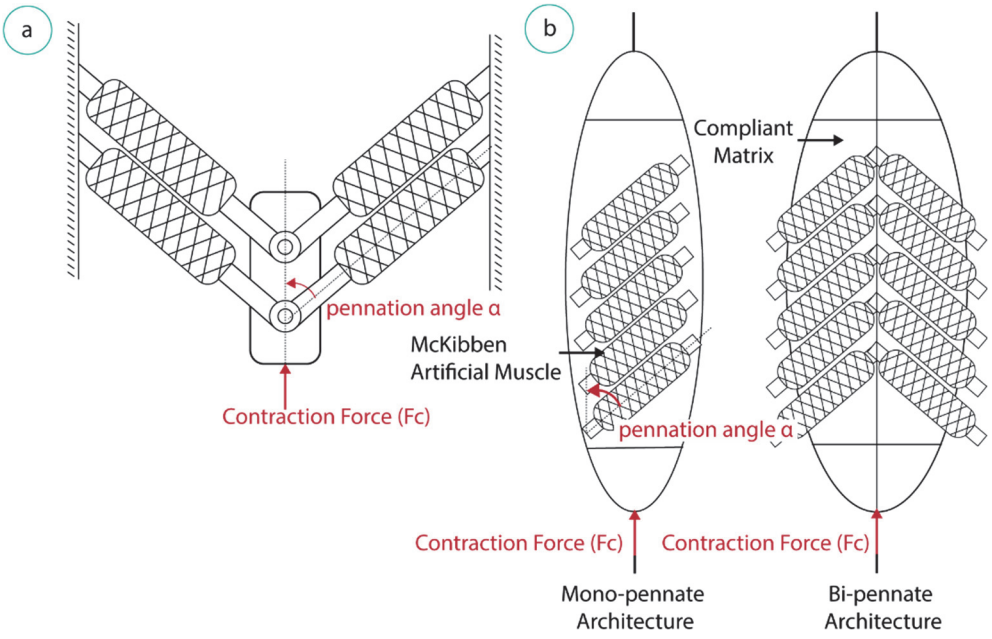


Figure 6.12: Pennate McKibben Artificial Muscle Designs found in Literature: a) Bi-pennate muscle architecture proposed by Duan *et al.* [106] and Azizi et al. [105] and b) Pennate and bi-pennate architecture embedded in a compliant matrix proposed by Wang *et al.* [108].

6.5 New Avenues: Smart McKibben Muscles

6.5.1 Smart Braided Sleeves and Inner Bladders

The braided outer sleeves of McKibben AMs are crucial for their performance. The main function of the braided sleeve is to convert the radial expansion of the inner bladder to axial compression or extension. However, the outer braided sleeve could be used to alter the performance of the McKibben AM or add extra functionalities, including sensing capabilities [75, 109-123]. The braided sleeve of the McKibben AMs could be sensorized by using smart wire materials.

Conductive wires are able to sense contraction and force by measuring the changes in coil inductance [109, 110, 112, 114, 116, 117, 120, 124]. In a study by Wakimoto *et al.* [120], a McKibben AM with an internal pressure-sensing function was proposed by using one conductive wire in the sleeve. The applied pressure on the McKibben AM was estimated by observing the electrical resistance of the conductive fibre. Furthermore, research by Felt and Remy [125] has shown that measuring the axial strain and force is possible by interlacing conductive, insulated wires through the braided sleeve. These wires act as a solenoid-like circuit with an inductance that more than doubles when the McKibben AM contracts. A similar design was proposed by Erin *et al.* [109]. In this study, an inductive coil was wrapped around the outer braided sleeve, which allowed for measuring the contraction force and the displacement through the changes in coil inductance.

Conductive materials and mechanisms can also be added to the McKibben AM to enable displacement sensing. Wakimoto *et al.* [121, 126] proposed a sensor made out of rubber and a conductive film integrated into the inner pneumatic bladder. The dielectric elastomer sensor designed by Kanno *et al.* [113] consisted of thin, highly compliant dielectric and conductive membranes, which allowed the length of the actuator to be detected by reading the capacitance. The sensor directly wrapped around the inner tube of the McKibben AM. Other studies proposed conductive rings placed concentric to the outer braided sleeve of the McKibben AM to enable radial expansion sensing. Zhong *et al.* [123] proposed a soft radial sensor placed around the McKibben AM composed of liquid metal (gallium-indium-stannum) and a silicone substrate, whereas Kuriyama *et al.* [127] proposed an electroconductive rubber ring. Additionally, piezo-resistive sensor placed in parallel to the McKibben AM [115], a flexible strain sensor [111], a nylon string coated sensor attached to the braid [128], and a telescopic capacitive length transducer inside the lumen [129], were proposed.

Optical fibres for contraction and shape sensing were proposed by [118, 119, 122]. In the studies of Tian *et al.* [118] and Yoshimoto *et al.* [122] a step-index multimode optical fibre was integrated in the McKibben AM, and the length was estimated based on the change in the amount of light propagating in the optical fibre. Akagi *et al.* [130] proposed another optical method to measure displacement in which a photoflector was placed in the inner lumen of the McKibben AM to measure the distance to the inner pneumatic bladder during inflation.

Other designs incorporate a piezo-resistive sensor placed in parallel to the McKibben AM [115], a soft radial sensor placed around the McKibben AM composed of liquid metal (gallium-indium-stannum) and a silicone substrate [123], a dielectric elastomer sensor integrated into the inner pneumatic bladder [113, 131], a flexible strain sensor [111], a nylon string coated sensor attached to the braid [128], a photoflector placed in the inner lumen [130], a telescopic capacitive length transducer inside the lumen [129], and an electroconductive rubber ring placed concentric to the actuator [127]. The dielectric elastomer sensor designed by Kanno *et al.* [113] consisted of thin, highly compliant dielectric and conductive membranes, which allow the length of the actuator to be detected by reading the capacitance. In the study of Kumar *et al.* [37], a hybrid McKibben AM was proposed containing a dielectric bladder. A mathematical model for this type of actuator is given by Goulbourne [132].

In a study by Yahara *et al.* [133], a smart outer sleeve was developed containing helical Shape Memory Polymer (SMP) fibres. The SMP wires allowed for changing the braiding angle after fabrication, which in turn allowed for active alteration of the performance of the McKibben AM. In the study by Takashima *et al.* [134], the outer sleeve of a commercially available McKibben AM was impregnated with SMP resin. By actuating this McKibben AM over the glass temperature (T_g), it functions as a regular McKibben AM. However, the McKibben AM can be cooled down below T_g to fix the AM in this rigid, actuated, state. Smart materials were also used in the study of Lopez-Diaz *et al.* [135], in which a self-healing hydrogel polymer was used as the inner pneumatic bladder of the McKibben AM. The developed self-healing hydrogel was able to self-heal without the need for an external stimulus, which could be beneficial to improve the durability of the AM in the future.

6.5.2 Alternative Manufacturing Methods

Current McKibben AMs are mainly manufactured using lab-scale braiding machines [1]. Although these machines offer high precision, they suffer from several essential

disadvantages. Firstly, the braiding machines are limited in generating only a narrow range of braid angles. Secondly, producing a consistent cover factor is limited due to the friction between fibres. Third, long fibre lengths are needed to operate braiding machines, which limit the introduction of novel fibre materials for research-scale production especially when only short lengths of experimental fibres are available [1].

An alternative way to manufacture braided sleeves is by using additive manufacturing or 3D-printing [1]. 3D-printing allows for improved versatility in controlling the materials, geometry and the structure of the braids, as well as allow for direct printing of the end connectors of the AM. In a study by Sangian *et al.* [136], an extrusion style 3D-printing machine was used to manufacture a smart braided sleeve with a cover factor of 0.47. Each individual printed wire was made of PolyCaproLactone (PCL) and was precisely printed around a rotating cylindrical steel rod. The right to left printing direction was first performed and then the entire mandrel with the printed helix was dip-coated in alginate solution and dried. Subsequently, the left to right printing direction was performed to form the second helical fibre on top of the dry alginate film. The mandrel was then immersed in the water bath to dissolve the alginate interlayer.

6.5.3 Alternative Braided Sleeves

The majority of the McKibben AMs use a biaxial braiding pattern. Alternative braiding patterns are rarely explored. Furthermore, other braiding methods, including triaxial braids could be explored. In triaxial-braided fabric three sets of wires are used and intertwined with each other around straight wires at about a 45° angle. In this method, braiding very dense structure patterns is less feasible compared to biaxial-braided fabrics, but the axial directional properties are improved in this method. A major downside of this braiding method is the presence of the axial braiding wires, which will counteract the compression or extension in the muscle. Therefore, if this type of braiding technique is considered, either elastic or free-moving axial wires should be used. A knitted McKibben AM was developed by Ball *et al.* [137] in which the sleeve expands by letting the loops of fibre slide past each other, changing the dimensions of the rectangular cells in the stitch pattern. Preliminary tests showed that free contraction greater than 50% is achievable using this knitting pattern. However, the motion relied on using fibres with low coefficient of friction in order to reduce hysteresis.

In a study by Bennington *et al.* [138], a viscoelastic sheath was added to the outer sleeve. It was shown that different polymeric sheaths could augment the shape of a standard McKibben AM's force-velocity curve. Another alternative outer sleeve was presented by Naclerio *et al.* [139] in which a thin, single layer of woven, bias-cut fabric was used that was foldable when depressurized. The airtight fabric was adhered together with a flexible adhesive, negating the need for an inner bladder. Experiments showed less than 1% hysteresis. Similarly, a bellows-shaped outer sleeve was proposed by Risangtuni *et al.* [140] achieving an elongation ratio of almost 70%.

6.5.4 Alternative Actuation Methods

A major failure mode of McKibben AMs is rupture of the inner pneumatic bladder. In an effort to overcome this, research has been conducted to manufacture bladderless McKibben AMs. A bladderless McKibben muscles was developed by Sangian [55], in which a thermally expanding paraffin wax was used to replace the bladder. This paraffin wax was contained within an

electrically conductive braid which allowed for Joule heating of the paraffin. Using this method, Sangian [55] was able to manufacture a lightweight muscle of 0.14 g with a diameter of 1.4 mm which was capable of generating a tensile stress of 50 kPa (0.039 N) in 20 s. The maximum axial strain of 0.1 was achieved in 60 s. In the study by Salahuddin *et al.* [141], a hydrogel-filled McKibben AM was proposed. In this design, the inner pneumatic bladder was replaced by thermo-responsive hydrogel beads that can swell in the presence of water. The hydrogel McKibben AMs were able to achieve a blocking force of 5-6 N and an axial strain of 0.07-0.08, although the response time was very low (>1 hour).

One of the challenges for McKibben AMs is that they generally need air hoses and air sources like compressors for actuation, which can lead to bulky systems overall. Chemo-mechanical transformations can be used to produce a mechanical force from a reversible chemical reaction to generate muscle contraction. Nabae *et al.* [142] propose an electrically driven McKibben AM (Ø 4 mm) using a tube-shaped Polymer Electrolyte Fuel Cell (PEFC) using platinum electrodes. In this design, the tube-shaped PEFC was used to initiate a reversible gas/liquid chemical reaction inside the McKibben AM to initiate expansion, generating an axial strain of 0.047. In a follow-up study by Kodaira *et al.* [143], the axial strain (0.22), response time (35 s) and durability of the PEFC was improved by using an Au/Pt double-layer electrode which decreased the appearance of cracks in the electrode. In the study of Vial *et al.* [144], another chemo-mechanical reaction was proposed to actuate a McKibben AM (Ø 15 mm) in which a granular ion-exchange polymer was placed inside the inner pneumatic bladder. The addition of acidic (NaOH) or alkaline (HCl) solutions provoked a swelling-deswelling cycle, respectively, resulting in an axial strain of 0.2, a blocking force of 332 N, and a response time of 1313s. A similar approach was proposed by Tondu *et al.* [45].

Creating fully untethered McKibben AMs involves integrating self-contained pneumatic or other actuation system within the muscle structure to provide on-board actuation, eliminating the need for external tethers. An untethered McKibben AMs was proposed by Mirvakili *et al.* [145], in which a magnetically induced liquid-to-gas phase transition of a liquid created a volumetric expansion (steam) and thus developed sufficient pressure inside the McKibben AM for mechanical operations. The untethered McKibben AM was able to generate actuation strains of up to 20% (in 10 seconds). A stretchable electrically-driven driven pump for McKibben AMs was proposed by Cacucciolo *et al.* [146]. This pump was able to directly accelerate liquid molecules by means of an electric field, requiring no moving parts, obtaining a blocking force of 0.84N and a maximum axial strain of 0.02. In the paper by Sangian *et al.* [46], a small-size, fully enclosed, hydraulic McKibben muscle powered by a low voltage pump connected to a 25 mL water tank was investigated. These muscles were able to generate a blocking force up to 26 N and strains up to 23% at a water pressure of 2.5 bar.

6.6 Discussion & Conclusions

6.6.1 Summary of Main Findings

This review paper summarizes the latest advancements in the development of McKibben AMs, highlighting their performance and unique configurations. Innovations in McKibben AM design have led to enhanced performance characteristics, including increased force output, improved efficiency, and greater durability. By mimicking natural muscle configurations, intricate motions can be created, including bending motions, linear motions and twisting

motions. Smartly placing McKibben AMs in flexible or soft structures can lead to intricate motions overall. Different architectures provide distinct performance advantages. Series configurations increase overall stroke and enable worm like or peristaltic locomotion. Parallel configurations enhance force output and can provide variable stiffness, bending, twisting, or antagonistic behavior. Braided configurations can increase achievable strain and facilitate flat or textile integrated actuator geometries. Convergent assemblies improve force density by combining multiple actuators into a shared output node, while pennate configurations offer a tunable trade-off between force and shortening velocity by adjusting the pennation angle.

Current McKibben actuators still exhibit several inherent limitations. Efficiency remains constrained by elastomer viscoelastic losses [12]. Hysteresis and friction, originating from bladder viscoelasticity, braid elasticity and strand on strand interactions, impede precision [39, 53, 54]. Environmental sensitivity also remains significant as material durability is affected by temperature fluctuations and humidity [147]. In addition, scaling effects become dominant as actuators shrink, altering pressure–flow relationships and mechanical response [14].

Recent developments offer promising avenues to mitigate some of these limitations. Additive manufacturing and textile based architectures improve customization and achievable strain. For example, 3D printed braided sleeves enable precise control over braid angle and cover factor, offering more versatile geometry tuning than traditional McKibben AMs [1, 136]. Similarly, knitted sleeves [137] and multifilament braided designs [93, 97] enable flat or textile integrated actuators, and can increase attainable contraction stroke. However, these approaches still face material fatigue and hysteresis constraints inherited from elastomeric bladders and fiber friction [93, 97, 137].

Smart material based approaches further expand design possibilities. Shape memory polymer (SMP) braids can tune contraction characteristics [133] and stiffness [134] during operation, while self-healing hydrogel based McKibben actuators provide autonomous damage mitigation that may improve durability [135]. In parallel, bladder free or non-fluidic McKibben type actuators eliminate the need for compressors or pumps and avoid leakage, trading untethered integration for slow response times or thermal constraints [55, 141, 145]. Overall, these material innovations address long standing challenges such as fatigue resistance, leakage, and system integration, but hysteresis and bandwidth limitations remain challenges that these new designs alone do not fully overcome.

Although the present review focuses on the design and performance characteristics of McKibben AMs, it is important to acknowledge the main application domains that have shaped their development. Broadly, McKibben AMs are often employed in wearables and prosthetics, where they assist or restore human motion through exoskeletons, orthotic devices, prostheses, and rehabilitation systems. Depending on the required wearability and compliance, they are either mounted on rigid frames or integrated into garments or soft matrix structures. A second major domain is robotics and manipulation, including humanoid platforms, soft and continuum manipulators, and a variety of locomotion systems. These application areas highlight the versatility of McKibben actuators and proves the importance of understanding design parameters in the context of practical deployment.

6.6.2 Limitations of this Study

One limitation of this study arises from the exclusive focus on papers that specifically include the word "McKibben" in their title or abstract. This approach inherently restricts the breadth of the literature reviewed, potentially overlooking relevant studies that examine McKibben AMs under alternative terminologies or broader categories of pneumatic artificial muscles. Our scope is limited to actuators explicitly described as McKibben muscles with external braided sleeves. We acknowledge that this excludes certain fiber-reinforced elastomer actuators and McKibben-like designs. Consequently, important insights, comparative analyses, and advancements documented in research that uses different nomenclature or focuses on similar AM technologies may be excluded, leading to a narrower understanding of the current state of knowledge and development in the field. For example, fiber-reinforced elastomeric enclosures (FREEs) fall outside our formal search results due to terminology differences, but their related studies present interesting architecture-level design strategies using nested series configurations to amplify stroke [148] and pennate arrangements to trade force and contraction [149]. Future reviews could benefit from a more inclusive search strategy that encompasses a wider array of related terms and research contexts to capture a more comprehensive picture of the advancements and challenges associated with McKibben AMs. Additionally, for comparison of performance characteristic of different muscle like actuators (e.g. electroactive polymers, shape-memory alloys, carbon-nanotube actuators, and other fluidic artificial muscles), we would like to refer the reader to existing comprehensive reviews [150].

6.6.3 Recommendations for Future Research

Future research on McKibben AMs should prioritize several critical areas to enhance their performance and expand their applicability. Innovations in material science are essential, focusing on developing new composites and elastomers that improve durability, flexibility, and responsiveness of the inner pneumatic bladder, thereby addressing issues like fatigue resistance and operational lifespan. Efforts to improve energy efficiency will make McKibben AMs more viable for portable and long-duration uses, potentially involving optimized pneumatic systems or alternative actuation methods. Miniaturization of these actuators is another key area, particularly for expanding their use in medical devices such as minimally invasive surgical tools and wearable technologies, which requires maintaining strength and efficiency at smaller scales. Existing studies indicate that miniaturization can significantly alter pressure–force behavior and maximum stroke, but a unified scaling framework is still lacking [14]. We therefore highlight the development of such scaling laws as an important direction for future research. Finally, developing application-specific designs tailored to the unique demands of different fields can maximize the effectiveness and versatility of McKibben AMs.

References

[1] D. Sangian, "From Traditional Braiding Methods to Additive Manufacturing for Fabricating Mckibben Artificial Muscles," *Biomed. J. Sci. Tech. Res,* vol. 38, pp. 30728-30735, 2021.

[2] M. De Volder, A. J. M. Moers, and D. Reynaerts, "Fabrication and control of miniature McKibben actuators," *Sensors and Actuators, A: Physical,* Article vol. 166, no. 1, pp. 111-116, 2011.

[3] M. Mori, K. Suzumori, M. Takahashi, and T. Hosoya, "Very high force hydraulic McKibben artificial muscle with a p-phenylene-2, 6-benzobisoxazole cord sleeve," *Advanced Robotics,* vol. 24, no. 1-2, pp. 233-254, 2010.

[4] H. Schulte, "The characteristics of the McKibben artificial muscle," *The application of external power in prosthetics and orthotics,* pp. 94-115, 1961.

[5] B. Tondu and P. Lopez, "Modeling and Control of McKibben Artificial Muscle Robot Actuators," *IEEE Control Systems,* Article vol. 20, no. 2, pp. 15-38, 2000.

[6] D. G. Caldwell, G. A. Medrano-Cerda, and M. Goodwin, "Control of pneumatic muscle actuators," *IEEE Control Systems Magazine,* vol. 15, no. 1, pp. 40-48, 1995.

[7] C.-P. Chou and B. Hannaford, "Measurement and modeling of McKibben pneumatic artificial muscles," *IEEE Transactions on robotics and automation,* vol. 12, no. 1, pp. 90-102, 1996.

[8] S. D. Thomalla and J. D. Van De Ven, "Modeling and Implementation of the McKibben Actuator in Hydraulic Systems," *IEEE Transactions on Robotics,* Article vol. 34, no. 6, pp. 1593-1602, 2018, Art no. 8454729.

[9] K. Iwata, K. Suzumori, and S. Wakimoto, "A method of designing and fabricating McKibben muscles driven by 7 MPa hydraulics," *International Journal of Automation Technology,* vol. 6, no. 4, pp. 482-487, 2012.

[10] S. Yokota and T. Komatsu, "Flexible hydraulic actuator for space manipulators," *JSME international journal. Ser. C, Dynamics, control, robotics, design and manufacturing,* vol. 37, no. 1, pp. 179-184, 1994.

[11] Z. Zhang, J. Hou, D. Ning, X. Gong, and Y. Gong, "Modeling and experiments on the drive characteristics of high-strength water hydraulic artificial muscles," *Smart Materials and Structures,* Article vol. 26, no. 5, 2017, Art no. 055023.

[12] M. A. Meller, M. Bryant, and E. Garcia, "Reconsidering the McKibben muscle: Energetics, operating fluid, and bladder material," *Journal of Intelligent Material Systems and Structures,* Article vol. 25, no. 18, pp. 2276-2293, 2014.

[13] B. Solano and C. Rotinat-Libersa, "Compact and lightweight hydraulic actuation system for high performance millimeter scale robotic applications: Modeling and experiments," in *Journal of Intelligent Material Systems and Structures*, 2011, vol. 22, 13 ed., pp. 1479-1487.

[14] L. D. Peel, L. Muratalla, J. Baur, and D. Foster, "The effect of scale on fluid-filled flexible composite actuators," in *ASME 2011 Conference on Smart Materials, Adaptive Structures and Intelligent Systems, SMASIS 2011*, 2011, vol. 2, pp. 581-590.

[15] W. Kobayashi and K. Ito, "Displacement estimation of tap-water driven McKibben muscles," in *Proceedings of 2015 International Conference on Fluid Power and Mechatronics, FPM 2015*, 2015, pp. 672-676.

[16] G. Olson, H. Manjarrez, J. A. Adams, and Y. Menguc, "Experimentally Identified Models of McKibben Soft Actuators as Primary Movers and Passive Structures," *Journal of Mechanisms and Robotics,* Article vol. 14, no. 1, 2022, Art no. 011006.

[17] B. S. Kang, C. S. Kothera, B. K. S. Woods, and N. M. Wereley, "Dynamic modeling of mckibben pneumatic artificial muscles for antagonistic actuation," in *Proceedings - IEEE International Conference on Robotics and Automation*, 2009, pp. 182-187.

[18] S. Davis, J. Canderle, P. Artrit, N. Tsagarakis, and D. G. Caldwell, "Enhanced dynamic performance in pneumatic muscle actuators," in *Proceedings - IEEE International Conference on Robotics and Automation*, 2002, vol. 3, pp. 2836-2841.

[19] C. Wenlin *et al.*, "Experimental study on dynamic characteristics and fatigue of mckibben pneumatic artificial muscles," in *2021 IEEE International Conference on Real-Time Computing and Robotics, RCAR 2021*, 2021, pp. 223-226.

[20] A. Al-Ibadi, S. Nefti-Meziani, and S. Davis, "Valuable experimental model of contraction pneumatic muscle actuator," in *2016 21st International Conference on Methods and Models in Automation and Robotics, MMAR 2016*, 2016, pp. 744-749.

[21] G. Belforte, T. Raparelli, and S. A. Sirolli, "A novel geometric formula for predicting contractile force in McKibben pneumatic muscles," *International Journal of Automation Technology,* Article vol. 11, no. 3, pp. 368-377, 2017.

[22] E. G. Hocking and N. M. Wereley, "Analysis of nonlinear elastic behavior in miniature pneumatic artificial muscles," *Smart Materials and Structures,* vol. 22, no. 1, p. 014016, 2012.

[23] C. S. Kothera, M. Jangid, J. Sirohi, and N. M. Wereley, "Experimental characterization and static modeling of McKibben actuators," *Journal of Mechanical Design,* Article vol. 131, no. 9, pp. 0910101-09101010, 2009.

[24] N. Tsagarakis and D. G. Caldwell, "Improved modelling and assessment of pneumatic muscle actuators," in *Proceedings - IEEE International Conference on Robotics and Automation*, 2000, vol. 4, pp. 3641-3646.

[25] K. Zang, Y. Wang, X. Fu, and X. Hu, "Study on modeling of Mckibben pneumatic artificial muscle," in *Proceedings - International Conference on Intelligent Computation Technology and Automation, ICICTA 2008*, 2008, vol. 1, pp. 721-725.

[26] D. Nakanishi, Y. Sugimoto, H. Honda, and K. Osuka, "Experiments and analysis for modeling of mckibben pneumatic actuator," *Journal of Robotics and Mechatronics,* Article vol. 28, no. 6, pp. 830-836, 2016.

[27] J. Bishop-Moser and S. Kota, "Design and Modeling of Generalized Fiber-Reinforced Pneumatic Soft Actuators," *IEEE Transactions on Robotics,* Article vol. 31, no. 3, pp. 536-545, 2015, Art no. 7114309.

[28] J. Bishop-Moser, G. Krishnan, and S. Kota, "Force and moment generation of fiber-reinforced pneumatic soft actuators," in *IEEE International Conference on Intelligent Robots and Systems*, 2013, pp. 4460-4465.

[29] S. Davis, N. Tsagarakis, J. Canderle, and D. G. Caldwell, "Enhanced modelling and performance in braided pneumatic muscle actuators," *The International Journal of Robotics Research,* vol. 22, no. 3-4, pp. 213-227, 2003.

[30] W. Shen and G. L. Shi, "An enhanced static mathematical model of braided fibre-reinforced pneumatic artificial muscles," *Proceedings of the Institution of Mechanical Engineers. Part I: Journal of Systems and Control Engineering,* Article vol. 225, no. 3, pp. 212-225, 2011.

[31] A. Sanchez, V. Mahout, and B. Tondu, "Nonlinear parametric identification of a McKibben artificial pneumatic muscle using flatness property of the system," in *IEEE Conference on Control Applications - Proceedings*, 1998, vol. 1, pp. 70-74.

[32] R. Tang and D. Liu, "An enhanced dynamic model for McKibben pneumatic muscle actuators," in *Australasian Conference on Robotics and Automation, ACRA*, 2012.

[33] R. Soleymani and H. Khajehsaeid, "A mechanical model for McKibben pneumatic artificial muscles based on limiting chain extensibility and 3D application of the network alteration theories," *International Journal of Solids and Structures,* Article vol. 202, pp. 620-630, 2020.

[34] C.-P. Chou and B. Hannaford, "Static and dynamic characteristics of McKibben pneumatic artificial muscles," in *Proceedings - IEEE International Conference on Robotics and Automation*, 1994, pt 1 ed., pp. 281-286.

[35] D. Chen and K. Ushijima, "Prediction of the mechanical performance of McKibben artificial muscle actuator," *International Journal of Mechanical Sciences,* vol. 78, pp. 183-192, 2014.

[36] M. A. Hoque, E. Petersen, and X. Fang, "Effect of Material Properties on Fiber-Shaped Pneumatic Actuators Performance," in *Actuators*, 2023, vol. 12, no. 3: MDPI, p. 129.

[37] D. Kumar, S. Ghosh, S. Roy, and S. Santapuri, "Modeling and analysis of an electro-pneumatic braided muscle actuator," *Journal of Intelligent Material Systems and Structures,* Article vol. 32, no. 4, pp. 399-409, 2021.

[38] S. Kurumaya, H. Nabae, G. Endo, and K. Suzumori, "Design of thin McKibben muscle and multifilament structure," *Sensors and Actuators A: Physical,* vol. 261, pp. 66-74, 2017.

[39] S. Davis and D. G. Caldwell, "Braid effects on contractile range and friction modeling in pneumatic muscle actuators," *The International Journal of Robotics Research,* vol. 25, no. 4, pp. 359-369, 2006.

[40] G. K. Klute and B. Hannaford, "Fatigue characteristics of McKibben artificial muscle actuators," in *IEEE International Conference on Intelligent Robots and Systems*, 1998, vol. 3, pp. 1776-1781.

[41] B. Salahuddin, H. Warren, and G. M. Spinks, "A comprehensive test method for measuring actuation performance of McKibben artificial muscles," *Smart Materials and Structures,* Article vol. 30, no. 4, 2021, Art no. 045016.

[42] Q. Zhang, D. Beale, S. Adanur, R. M. Broughton, and R. P. Walker, "Structural analysis of a two-dimensional braided fabric," *Journal of the Textile Institute,* vol. 88, no. 1, pp. 41-52, 1997.

[43] J. Quaglierini, M. Arroyo, and A. Desimone, "Mechanics of tubular meshes made of helical fibers and application to modeling McKibben artificial muscles," in *2023 IEEE International Conference on Soft Robotics, RoboSoft 2023*, 2023.

[44] D. Sangian, "New types of McKibben artificial muscles," 2016.

[45] B. Tondu, R. Emirkhanian, S. Mathé, and A. Ricard, "A pH-activated artificial muscle using the McKibben-type braided structure," *Sensors and Actuators A: Physical,* vol. 150, no. 1, pp. 124-130, 2009.

[46] D. Sangian, S. Naficy, G. M. Spinks, and B. Tondu, "The effect of geometry and material properties on the performance of a small hydraulic McKibben muscle system," *Sensors and Actuators, A: Physical,* Article vol. 234, pp. 150-157, 2015.

[47] W. Liu and C. R. Rahn, "Fiber-Reinforced Membrane Models of McKibben Actuators," *Journal of Applied Mechanics, Transactions ASME,* Article vol. 70, no. 6, pp. 853-859, 2003.

[48] M. F. Gentry and N. M. Wereley, "Effects of braid angle on pneumatic artificial muscle actuator performance," in *Smart Materials, Adaptive Structures and Intelligent Systems*, 2008, vol. 43321, pp. 617-623.

[49] S. Kurumaya, H. Nabae, G. Endo, and K. Suzumori, "Active textile braided in three strands with thin McKibben muscle," *Soft Robotics,* vol. 6, no. 2, pp. 250-262, 2019.

[50] P. H. Nguyen and W. Zhang, "Design and computational modeling of fabric soft pneumatic actuators for wearable assistive devices," *Scientific reports,* vol. 10, no. 1, p. 9638, 2020.

[51] F. Connolly, C. J. Walsh, and K. Bertoldi, "Automatic design of fiber-reinforced soft actuators for trajectory matching," *Proceedings of the National Academy of Sciences,* vol. 114, no. 1, pp. 51-56, 2017.

[52] S. Krishnan, T. Nagarajan, A. M. A. Rani, and T. Rao, "Silk Pneumatic Artificial Muscle (SPAM) construction for bio-medical engineering application," in *BEIAC 2012 - 2012 IEEE Business, Engineering and Industrial Applications Colloquium*, 2012, pp. 302-306

[53] B. Tondu, "Modelling of the McKibben artificial muscle: A review," *Journal of Intelligent Material Systems and Structures,* vol. 23, no. 3, pp. 225-253, 2012.

[54] J. M. Chambers and N. M. Wereley, "Analysis of Pneumatic Artificial Muscles and the Inelastic Braid Assumption," *Actuators,* Article vol. 11, no. 8, 2022, Art no. 219.

[55] D. Sangian, J. Foroughi, S. Farajikhah, S. Naficy, and G. M. Spinks, "A bladder-free, non-fluidic, conductive McKibben artificial muscle operated electro-thermally," *Smart Materials and Structures,* Article vol. 26, no. 1, 2017, Art no. 015011.

[56] P. V. Cavallaro, M. P. Smith, J. D. O'Donnell, A. Redington, and E. Warner, "SOFT ARTIFICIAL MUSCLE ACTUATORS FOR UNDERSEA LAUNCH & RECOVERY SYSTEMS," in *ASME International Mechanical Engineering Congress and Exposition, Proceedings (IMECE)*, 2022, vol. 9.

[57] E. Ball, Y. Lin, and E. Garcia, "Characterization and modeling of geometric variations in McKibben pneumatic artificial muscles," in *Proceedings of SPIE - The International Society for Optical Engineering*, 2013, vol. 8686.

[58] E. Ball and E. Garcia, "Effects of bladder geometry in pneumatic artificial muscles," *Journal of Medical Devices, Transactions of the ASME,* Article vol. 10, no. 4, 2016, Art no. 041001.

[59] G. Wang, N. M. Wereley, and T. Pillsbury, "Non-linear quasi-static model of pneumatic artificial muscle actuators," *Journal of Intelligent Material Systems and Structures,* Article vol. 26, no. 5, pp. 541-553, 2015.

[60] J. Garbulinski, S. C. Balasankula, and N. M. Wereley, "Characterization and analysis of extensile fluidic artificial muscles," *Actuators,* Article vol. 10, no. 2, pp. 1-26, 2021, Art no. 26.

[61] J. Kadowaki, D. Sasaki, H. Yase, and R. Kusaka, "Improvement of McKibben type artificial rubber muscle model based on end shape deformation," in *2021 IEEE International Conference on Mechatronics, ICM 2021*, 2021.

[62] G. K. Klute, J. M. Czerniecki, and B. Hannaford, "McKibben artificial muscles: Pneumatic actuators with biomechanical intelligence," *IEEE/ASME International Conference on Advanced Intelligent Mechatronics, AIM,* Article pp. 221-226, 1999..

[63] B. Tondu and S. D. Zagal, "McKibben artificial muscle can be adapted to be in accordance with the Hill skeletal muscle model," in *Proceedings of the First IEEE/RAS-EMBS International Conference on Biomedical Robotics and Biomechatronics, 2006, BioRob 2006*, 2006, vol. 2006, pp. 714-720.

[64] S. Tanaka, H. Nabae, and K. Suzumori, "Back-stretchable McKibben muscles: Expanding the range of antagonistic muscle driven joints," *IEEE Robotics and Automation Letters,* 2023.

[65] R. Kobayashi, S. Tanaka, H. Nabae, G. Endo, and K. Suzumori, "McKibben Muscle With Elastic Thread Embedded in Parallel Extending Range of Motion of Muscle-Driven Robots," *IEEE Robotics and Automation Letters,* 2025.

[66] H. S. Cho, T. H. Kim, T. H. Hong, and Y. L. Park, "Ratchet-integrated pneumatic actuator (RIPA): A large-stroke soft linear actuator inspired by sarcomere muscle contraction," *Bioinspiration and Biomimetics,* Article vol. 15, no. 3, 2020, Art no. 036011.

[67] S. Kim, S. R. Lee, S. Lee, D. Lee, and D. Shin, "Power-Efficient Soft Pneumatic Actuator Using Spring-Frame Collateral Compression Mechanism," *Actuators,* Article vol. 11, no. 3, 2022, Art no. 76.

[68] W. Tian, S. Wakimoto, D. Yamaguchi, and T. Kanda, "Fabrication Process for Twisting Artificial Muscles
by Utilizing Braiding Technology and
Water-Soluble Fibers," *IEEE Robotics and Automation Letters,* 2024.

[69] A. A. M. Faudzi, M. R. M. Razif, I. N. A. M. Nordin, K. Suzumori, S. Wakimoto, and D. Hirooka, "Development of bending soft actuator with different braided angles," in *2012 IEEE/ASME International Conference on Advanced Intelligent Mechatronics (AIM)*, 2012: IEEE, pp. 1093-1098.

[70] Z. Feifei, S. Dohta, T. Akagi, and H. Matsushita, "Development of a bending actuator using a rubber artificial muscle and its application to a robot hand," in *2006 SICE-ICASE International Joint Conference*, 2006, pp. 381-384.

[71] M. F. Cullinan, E. Bourke, K. Kelly, and C. McGinn, "A mckibben type sleeve pneumatic muscle and integrated mechanism for improved stroke length," *Journal of Mechanisms and Robotics,* Article vol. 9, no. 1, 2017, Art no. 011013.

[72] K. Iwata, K. Suzumori, and S. Wakimoto, "Development of contraction and extension artificial muscles with different braid angles and their application to stiffness changeable bending rubber mechanism by their combination," *Journal of Robotics and Mechatronics,* vol. 23, no. 4, pp. 582-588, 2011.

[73] L. Julie, O. Mouloud, and V. P. Emmanuel, "Concentric muscles-miniature pneumatic actuator with integrated channel for surgical instruments," in *GMM-Fachberichte*, 2021, vol. 2021-February, 98 ed., pp. 105-108.

[74] G. Olson and Y. Menguc, "Helically wound soft actuators for torsion control," in *2018 IEEE International Conference on Soft Robotics, RoboSoft 2018*, 2018, pp. 214-221.

[75] I. Nordin, A. Faudzi, M. Razif, E. Natarajan, S. Wakimoto, and K. Suzumori, "Simulations of two patterns fiber weaves reinforced in rubber actuator," *Jurnal Teknologi,* vol. 69, no. 3, pp. 133-138, 2014.

[76] I. N. A. M. Nordin, S. Wakimoto, and K. Suzumori, "Simulations of fiber braided bending actuator: Investigation on position of fiber layer placement and air chamber diameter," in *2015 10th Asian Control Conference (ASCC)*, 2015: IEEE, pp. 1-5.

[77] H. Du, R. Shao, X. Xu, and W. Xiong, "Design and validation of a pneumatic bending actuator," in *Proceedings - 2022 7th International Conference on Automation, Control and Robotics Engineering, CACRE 2022*, 2022, pp. 121-125.

[78] C. Xiang, J. Guo, Y. Chen, L. Hao, and S. Davis, "Development of a SMA-Fishing-Line-McKibben Bending Actuator," *IEEE Access,* Article vol. 6, pp. 27183-27189, 2018.

[79] S. Maeda, S. Wakimoto, and S. Yahara, "Proposal of pneumatic rubber muscles with Shape-Memory Polymer reinforcement fibers realizing desirable motion," in *2016 IEEE International Conference on Robotics and Biomimetics, ROBIO 2016*, 2016, pp. 1221-1226.

[80] R. Lathrop, M. Ourak, J. Deprest, and E. V. Poorten, "Concentric Dual-Chamber Pneumatic Artificial Muscles: Miniature Actuators Designed for Use in Minimally Invasive Surgical Instruments," *Journal of Medical Robotics Research,* Article vol. 7, no. 2-3, 2022, Art no. 2241007.

[81] H. Tsukagoshi, K. Terashima, and Y. Takai, "A self-propelled catheter capable of generating travelling waves with steering function by mono-line drive," in *2018 IEEE International Conference on Robotics and Automation (ICRA)*, 2018: IEEE, pp. 38-43.

[82] S. Zhang, D. Gong, and J. Yu, "Design of a Multi-connection Pneumatic Artificial Muscle," in *2022 12th International Conference on CYBER Technology in Automation, Control, and Intelligent Systems, CYBER 2022*, 2022, pp. 301-306.

[83] D. Bruder and R. J. Wood, "The Chain-Link Actuator: Exploiting the Bending Stiffness of McKibben Artificial Muscles to Achieve Larger Contraction Ratios," *IEEE Robotics and Automation Letters,* Article vol. 7, no. 1, pp. 542-548, 2022.

[84] J. Y. Kim, N. Mazzoleni, and M. Bryant, "Free strain gradient reversal of a variable recruitment fluidic artificial muscle bundle," in *Proceedings of SPIE - The International Society for Optical Engineering*, 2021, vol. 11586.

[85] K. Suzumori, S. Wakimoto, K. Miyoshi, and K. Iwata, "Long bending rubber mechanism combined contracting and extending tluidic actuators," in *2013 IEEE/RSJ international conference on intelligent robots and systems*, 2013: Ieee, pp. 4454-4459.

[86] J. Bishop-Moser, G. Krishnan, C. Kim, and S. Kota, "Design of soft robotic actuators using fluid-filled fiber-reinforced elastomeric enclosures in parallel combinations," in *IEEE International Conference on Intelligent Robots and Systems*, 2012, pp. 4264-4269

[87] S. Kawamura, M. Sudani, M. Deng, Y. Noge, and S. Wakimoto, "Modeling and system integration for a thin pneumatic rubber 3-DOF actuator," *Actuators,* Article vol. 8, no. 2, 2019, Art no. 32.

[88] Y. Toyama and S. Wakimoto, "Development of a thin pneumatic rubber actuator generating 3-DOF motion," in *2016 IEEE International Conference on Robotics and Biomimetics, ROBIO 2016*, 2016, pp. 1215-1220.

[89] S. Wakimoto, K. Suzumori, and J. Takeda, "Flexible artificial muscle by bundle of McKibben fiber actuators," in *IEEE/ASME International Conference on Advanced Intelligent Mechatronics, AIM*, 2011, pp. 457-462.

[90] M. Yuzaki, K. Iwata, S. Wakimoto, and T. Kanda, "Development of a thin pneumatic rubber actuator generating 3DOF motion - Design using FEM analysis and fabrication of the actuator," in *ACTUATOR 2018 - 16th International Conference and Exhibition on New Actuators and Drive Systems, Conference Proceedings*, 2018, pp. 563-566.

[91] B. Lathrop, M. Ourak, and E. Vander Poorten, "Miniature Pneumatic Artificial Muscles for Use in Surgical Devices," in *GMM-Fachberichte*, 2022, pp. 4-7.

[92] R. D. Vocke, C. S. Kothera, A. Chaudhuri, B. K. S. Woods, and N. M. Wereley, "Design and testing of a high-specific work actuator using miniature pneumatic artificial muscles," *Journal of Intelligent Material Systems and Structures,* Article vol. 23, no. 3, pp. 365-378, 2012.

[93] S. Koizumi, S. Kurumaya, H. Nabae, G. Endo, and K. Suzumori, "Braiding thin McKibben muscles to enhance their contracting abilities," *IEEE Robotics and Automation Letters,* vol. 3, no. 4, pp. 3240-3246, 2018.

[94] S. Koizumi, S. Kurumaya, H. Nabae, G. Endo, and K. Suzumori, "Recurrent braiding of thin McKibben muscles to overcome their limitation of contraction," *Soft robotics,* vol. 7, no. 2, pp. 251-258, 2020.

[95] M. R. A. Kadir, A. A. M. Faudzi, and M. A. A. Rahman, "Performance Evaluation for Braided McKibben Pneumatic Actuators in Telescopic Nested Structure," *IEEE Robotics and Automation Letters,* Article vol. 7, no. 4, pp. 10906-10913, 2022.

[96] G. Na, H. Nabae, and K. Suzumori, "Braided thin mckibben muscles for musculoskeletal robots," *Sensors and Actuators A: Physical,* Article vol. 357, 2023, Art no. 114381.

[97] T. Abe *et al.*, "Fabrication of "18 weave" muscles and their application to soft power support suit for upper limbs using thin mckibben muscle," *IEEE Robotics and Automation Letters,* vol. 4, no. 3, pp. 2532-2538, 2019.

[98] Y. Funabora, "Prototype of a fabric actuator with multiple thin artificial muscles for wearable assistive devices," in *SII 2017 - 2017 IEEE/SICE International Symposium on System Integration*, 2017, vol. 2018-January, pp. 356-361.

[99] Y. Funabora, "Flexible Fabric Actuator Realizing 3D Movements Like Human Body Surface for Wearable Devices," in *IEEE International Conference on Intelligent Robots and Systems*, 2018, pp. 6992-6997.

[100] T. Hiramitsu, K. Suzumori, H. Nabae, and G. Endo, "Experimental evaluation of textile mechanisms made of artificial muscles," in *RoboSoft 2019 - 2019 IEEE International Conference on Soft Robotics*, 2019, pp. 1-6.

[101] R. Marshall *et al.*, "Mechanical Characterisation of Woven Pneumatic Active Textile," *IEEE Robotics and Automation Letters,* Article vol. 8, no. 5, pp. 2804-2811, 2023.

[102] K. Nakagawa, Y. Sakai, Y. Funabora, and S. Doki, "Turning a Functional Cloth Into an Actuator by Combining Thread-Like Thin Artificial Muscles and Embroidery Techniques," *IEEE Robotics and Automation Letters,* Article vol. 7, no. 3, pp. 5827-5833, 2022.

[103] T. Hiramitsu, K. Suzumori, H. Nabae, and G. Endo, "Active textile: woven-cloth-like mechanisms consist of thin McKibben actuators," *Advanced Robotics,* Article vol. 37, no. 7, pp. 480-494, 2023.
[104] S. Kurumaya, K. Suzumori, H. Nabae, and S. Wakimoto, "Musculoskeletal lower-limb robot driven by multifilament muscles," *ROBOMECH Journal,* Article vol. 3, no. 1, 2016, Art no. 18.
[105] E. Azizi and T. J. Roberts, "Variable gearing in a biologically inspired pneumatic actuator array," *Bioinspiration and Biomimetics,* Article vol. 8, no. 2, 2013, Art no. 026002.
[106] E. Duan and M. Bryant, "Implications of Spatially Constrained Bipennate Topology on Fluidic Artificial Muscle Bundle Actuation," *Actuators,* Article vol. 11, no. 3, 2022, Art no. 82.
[107] T. Jenkins and M. Bryant, "Pennate actuators: Force, contraction and stiffness," *Bioinspiration and Biomimetics,* Article vol. 15, no. 4, 2020, Art no. 046005.
[108] Y. Wang, C. Liu, L. Ren, and L. Ren, "Bioinspired soft actuators with highly ordered skeletal muscle structures," *Bio-Design and Manufacturing,* Article vol. 5, no. 1, pp. 174-188, 2022.
[109] O. Erin, N. Pol, L. Valle, and Y.-L. Park, "Design of a bio-inspired pneumatic artificial muscle with self-contained sensing," in *2016 38th Annual International Conference of the IEEE Engineering in Medicine and Biology Society (EMBC)*, 2016: IEEE, pp. 2115-2119.
[110] W. Felt, K. Y. Chin, and C. D. Remy, "Contraction Sensing with Smart Braid McKibben Muscles," *IEEE/ASME Transactions on Mechatronics,* Article vol. 21, no. 3, pp. 1201-1209, 2016, Art no. 7302589.
[111] H. Hagihara, S. Wakimoto, T. Kanda, and S. Furukawa, "Operation of a pneumatic soft manipulator using a wearable interface with flexible strain sensors," in *IEEE International Conference on Intelligent Robots and Systems*, 2019, pp. 4949-4954.
[112] V. A. Ho and S. Hirai, "Measuring McKibben actuator shrinkage using fiber sensor," in *Proceedings - IEEE International Workshop on Robot and Human Interactive Communication*, 2015, vol. 2015-November, pp. 628-633.
[113] R. Kanno, S. Watanabe, K. Shimizu, and J. Shintake, "Self-Sensing McKibben Artificial Muscles Embedded with Dielectric Elastomer Sensor," *IEEE Robotics and Automation Letters,* Article vol. 6, no. 4, pp. 6274-6280, 2021, Art no. 9468315.
[114] J. Legrand, B. Loenders, A. Vos, L. Schoevaerdts, and E. Vander Poorten, "Integrated Capacitance Sensing for Miniature Artificial Muscle Actuators," *IEEE Sensors Journal,* Article vol. 20, no. 3, pp. 1363-1372, 2020, Art no. 8862955.
[115] M. Maselli, D. Zrinscak, V. Magliola, and M. Cianchetti, "A piezoresistive flexible sensor to detect soft actuator deformation," in *RoboSoft 2019 - 2019 IEEE International Conference on Soft Robotics*, 2019, pp. 372-377.
[116] J. Misumi, S. Wakimoto, and K. Suzumori, "Experimental investigation of conductive fibers for a smart pneumatic artificial muscle," in *2015 IEEE International Conference on Robotics and Biomimetics, IEEE-ROBIO 2015*, 2015, pp. 2335-2340.
[117] K. Omura, K. Goto, S. Wakimoto, and T. Kanda, "Development of pneumatic valves and a fiber sensor for a smart artificial muscle," in *ACTUATOR 2018 - 16th*

International Conference and Exhibition on New Actuators and Drive Systems, Conference Proceedings, 2018, pp. 567-570.

[118] W. Tian, S. Wakimoto, T. Kanda, and D. Yamaguchi, "Displacement Sensing of an Active String Actuator Using a Step-Index Multimode Optical Fiber Sensor†," *Sensors,* Article vol. 22, no. 9, 2022, Art no. 3232.

[119] S. Wakimoto, S. Kogawa, H. Matsuda, K. Nagaoka, and T. Kanda, "Comparison of smart artificial muscles with different functional fibers," in *GMM-Fachberichte*, 2021, vol. 2021-February, 98 ed., pp. 124-126.

[120] S. Wakimoto, J. Misumi, and K. Suzumori, "New concept and fundamental experiments of a smart pneumatic artificial muscle with a conductive fiber," *Sensors and Actuators A: Physical,* vol. 250, pp. 48-54, 2016.

[121] S. Wakimoto, K. Suzumori, T. Kanda, and K. Kure, "Soft pressure sensor embedded in McKibben actuator," in *IEEE/ASME International Conference on Advanced Intelligent Mechatronics, AIM*, 2007.

[122] Y. Yoshimoto, S. Wakimoto, W. Tian, K. Inoue, D. Yamaguchi, and T. Kanda, "Combination Process of a Pneumatic Artificial Muscle and a Fiber Optical Sensor System †," *Engineering Proceedings,* Article vol. 27, no. 1, 2022, Art no. 86.

[123] S. Zhong *et al.*, "A contraction length feedback method for the McKibben pneumatic artificial muscle," *Sensors and Actuators A: Physical,* Article vol. 334, 2022, Art no. 113321.

[124] A. Hitzmann, Y. Wang, T. Kessler, and K. Hosoda, "Using conductive fabrics as inflation sensors for pneumatic artificial muscles," *Advanced Robotics,* Article vol. 35, no. 16, pp. 995-1011, 2021.

[125] W. Felt and C. D. Remy, "Smart braid: Air muscles that measure force and displacement," in *2014 IEEE/RSJ International Conference on Intelligent Robots and Systems*, 2014: IEEE, pp. 2821-2826.

[126] S. Wakimoto, K. Suzumori, and T. Kanda, "Development of intelligent McKibben actuator," in *2005 IEEE/RSJ International Conference on Intelligent Robots and Systems, IROS*, 2005, pp. 487-492.

[127] S. Kuriyama, M. Ding, Y. Kurita, J. Ueda, and T. Ogasawara, "Flexible Sensor for McKibben Pneumatic Artificial Muscle Actuator," *International Journal of Automation Technology,* Article vol. 3, no. 6, pp. 731-740, 2009.

[128] I. Hamamoto, T. Akagi, S. Dohta, and H. Matsushita, "Development of a flexible displacement sensor using nylon string coated with carbon and its application for McKibben actuator," in *2006 SICE-ICASE International Joint Conference*, 2006, pp. 1943-1946.

[129] M. G. Antonelli, P. Beomonte Zobel, A. De Marcellis, and E. Palange, "Design and Characterization of a Mckibben Pneumatic Muscle Prototype with an Embedded Capacitive Length Transducer," *Machines,* Article vol. 10, no. 12, 2022, Art no. 1156.

[130] T. Akagi, S. Dohta, Y. Kenmotsu, F. Zhao, and M. Yoneda, "Development of smart inner diameter sensor for position control of Mckibben artificial muscle," in *Procedia Engineering*, 2012, vol. 41, pp. 105-112.

[131] N. C. Goulbourne and S. Son, "Numerical and experimental analysis of McKibben actuators and dielectric elastomer sensors," in *ASME International Mechanical Engineering Congress and Exposition, Proceedings*, 2008, vol. 10 PART A, pp. 175-186

[132] N. C. Goulbourne, "A mathematical model for cylindrical, fiber reinforced electro-pneumatic actuators," *International Journal of Solids and Structures,* Article vol. 46, no. 5, pp. 1043-1052, 2009.

[133] S. Yahara, S. Wakimoto, T. Kanda, and K. Matsushita, "McKibben artificial muscle realizing variable contraction characteristics using helical shape-memory polymer fibers," *Sensors and Actuators A: Physical,* vol. 295, pp. 637-642, 2019.

[134] K. Takashima, J. Rossiter, and T. Mukai, "McKibben artificial muscle using shape-memory polymer," *Sensors and Actuators, A: Physical,* Article vol. 164, no. 1-2, pp. 116-124, 2010.

[135] A. Lopez-Diaz *et al.*, "Autonomous self-healing pneumatic McKibben muscle based on a new hydrogel material," in *2020 3rd IEEE International Conference on Soft Robotics, RoboSoft 2020*, 2020, pp. 13-18.

[136] D. Sangian, A. Jeiranikhameneh, S. Naficy, S. Beirne, and G. M. Spinks, "Three-dimensional printed braided sleeves for manufacturing mckibben artificial muscles," *3D Printing and Additive Manufacturing,* vol. 6, no. 1, pp. 57-62, 2019.

[137] E. J. Ball, M. A. Meller, J. B. Chipka, and E. Garcia, "Modeling and testing of a knitted-sleeve fluidic artificial muscle," *Smart Materials and Structures,* Article vol. 25, no. 11, 2016, Art no. 115024.

[138] M. J. Bennington, T. Wang, J. Yin, S. Bergbreiter, C. Majidi, and V. A. Webster-Wood, "Design and Characterization of Viscoelastic McKibben Actuators with Tunable Force-Velocity Curves," in *2023 IEEE International Conference on Soft Robotics, RoboSoft 2023*, 2023.

[139] N. D. Naclerio and E. W. Hawkes, "Simple, low-hysteresis, foldable, fabric pneumatic artificial muscle," *IEEE Robotics and Automation Letters,* Article vol. 5, no. 2, pp. 3406-3413, 2020, Art no. 9013028.

[140] A. G. Risangtuni, S. Suprijanto, and Y. Y. Nazaruddin, "Markerless Video Motion Analysis of A Modified McKibben Muscle Soft Pneumatic Actuator," in *Proceedings of the 2021 International Conference on Instrumentation, Control, and Automation, ICA 2021*, 2021, pp. 28-32.

[141] B. Salahuddin, H. Warren, and G. M. Spinks, "Thermally actuated hydrogel bead based braided artificial muscle," *Smart Materials and Structures,* Article vol. 29, no. 5, 2020, Art no. 055042.

[142] H. Nabae, A. Kodaira, T. Horiuchi, K. Asaka, G. Endo, and K. Suzumori, "Soft Polymer-Electrolyte-Fuel-Cell Tube Realizing Air-Hose-Free Thin McKibben Muscles," in *IEEE International Conference on Intelligent Robots and Systems*, 2019, pp. 8287-8293.

[143] A. Kodaira, H. Nabae, T. Horiuchi, K. Asaka, G. Endo, and K. Suzumori, "Au/Pt double-layer electrodes and expanding internal chamber for improving air-hose-free thin mckibben muscles," in *2021 IEEE 4th International Conference on Soft Robotics, RoboSoft 2021*, 2021, pp. 419-426.

[144] D. Vial, B. Tondu, P. Lopez, Y. Aurelle, and A. Ricard, "Ion-exchange polymer artificial muscle and actuating system," *Proceedings of SPIE - The International Society for Optical Engineering,* Conference paper vol. 2779, pp. 359-364, 1996.

[145] S. M. Mirvakili, D. Sim, I. W. Hunter, and R. Langer, "Actuation of untethered pneumatic artificial muscles and soft robots using magnetically induced liquid-to-gas phase transitions," *Science Robotics,* Article vol. 5, no. 41, 2020, Art no. aaz4239

[146] V. Cacucciolo, H. Nabae, K. Suzumori, and H. Shea, "Electrically-Driven Soft Fluidic Actuators Combining Stretchable Pumps With Thin McKibben Muscles," *Frontiers in Robotics and AI,* Article vol. 6, 2020, Art no. 146.

[147] A. Zhagiparova, V. Golubev, and D. Kim, "Recent Developments in Pneumatic Artificial Muscle Actuators," in *Actuators*, 2025, vol. 14, no. 12: MDPI, p. 582.

[148] X. Zhang and G. Krishnan, "A nested pneumatic muscle arrangement for amplified stroke and force behavior," *Journal of intelligent material systems and structures,* vol. 29, no. 6, pp. 1139-1156, 2018.

[149] S. Satheeshbabu, N. Thompson, C. Xiao, and G. Krishnan, "Architectures of soft pneumatic actuators inspired by muscle fiber arrangements," in *2019 2nd IEEE International Conference on Soft Robotics (RoboSoft)*, 2019: IEEE, pp. 271-276.

[150] M. Shi and E. M. Yeatman, "A comparative review of artificial muscles for microsystem applications," *Microsystems & Nanoengineering,* vol. 7, no. 1, p. 95, 2021.

06

CHAPTER 07

DESIGN OF ADAPTIVE MCKIBBEN ARTIFICIAL MUSCLES

ABSTRACT

The octopus achieves intricate arm deformations through local muscle interactions rather than centralized coordination. Inspired by this principle, this study aims to develop embodied intelligent McKibben Artificial Muscles (AMs), in which global deformation is encoded directly into their physical structure. The key design parameter explored is the braiding angle, which governs the type and magnitude of motion. By spatially varying this angle along the actuator, we demonstrate embedded capabilities for local extension and contraction within a single AM. Additionally, a mismatch in braiding angles between opposing wire sets generates a twisting motion. To implement these variations, traditional braiding techniques were adapted for localized angle control. Within a single McKibben AM, a maximum strain of +0.06 and minimum strain of -0.19 was measured. A twist angle of 100° was achieved using a 50.4° angle difference at 50 kPa actuation pressure. A final modular prototype demonstrated the integration of multiple motion modes within a single actuator body. These results highlight the potential of mechanically intelligent AMs to simplify actuation systems in soft robotics. Applications include wearable technologies such as exoskeletons and prosthetics, as well as bioinspired systems like artificial hearts or continuum robotic arms, where compact and adaptive actuation is essential.

Published as:
Kortman, V. G., Jovanova, J., & Sakes, A. (2025). Adaptable by design: encoding complex deformation profiles in mckibben artificial muscles. *Materials & Design*, 115188.

7.1 Introduction

Nature demonstrates that complex motion does not always require complex control. For example, the octopus achieves intricate arm deformations through local muscle interactions without requiring centralized control. Here, main motions as contraction, extension, bending and twisting are driven by the interplay of longitudinal, circular, and helical muscles. Similar fiber-reinforced architectures are found across a wide range of biological systems, including other muscular hydrostats like squid tentacles and elephant trunks, as well as plant structures. This highlights the widespread relevance of this principle.

In the field of soft robotics, McKibben Artificial Muscles (AMs) are commonly used to achieve similar adaptive characteristics as found in biological systems. These actuators are valued for their compliance, large blocked forces, high contraction ratios and fast response time. McKibben AMs stand out by their design simplicity, consisting of a simple inner bladder wrapped in a braided sleeve, as shown in Figure 7.1a. The distal end of the muscle is closed off by an end cap, while the proximal end is connected to a pressure source. The McKibben AM can be either pneumatically or hydraulically actuated by pressurizing the inner bladder. Comparable to the octopus, the motion of the AM is defined by the constraints of directional fibers. Upon pressurization, the inner bladder increases volume, resulting in a diameter expansion. The braided sleeve constrains this radial deformation. Consequently, due to the rotation of its wires, the sleeve transforms the AM's radial deformation into either a contraction or an extension movement. Their similarity to muscles in nature makes these AMs particularly suitable in cases where adaptivity and safety are needed for interaction with humans, such as prosthetics, soft wearables or robotic rehabilitation. They are also advantageous in scenarios that require simple and lightweight control, including continuum robotics.

The design of the braided sleeve is key in determining the McKibben AMs deformation profile. Equation 7.1 shows how the generated force of the McKibben AM (F_{muscle}) relates to its diameter D, applied pressure P, strain ε and braiding angle θ_B [1, 2]. The braiding angle between the wires of the braided sleeve defines whether F_{muscle} is positive or negative, resulting in either contraction or extension of the AM. These AMs are typically employed as linear actuators.

$$F_{muscle} = \frac{\pi}{4} D^2 P \left(\frac{1}{sin\theta_B}\right)^2 \{3(1-\varepsilon)^2 \, cos^2\theta_B - 1\} \qquad (7.1)$$

However, to achieve more complex motions such as bending [3-5], twisting [6-8] or caterpillar-like locomotion [9, 10], multiple AM's need to be combined (Figure 7.1b). Unlike their counterparts in nature, these combined McKibben AMs have the disadvantage that their implementation often require complex control algorithms or intricate actuation systems to achieve desired complex shape changes. Every individual AM requires a cumbersome system of compressors/pumps, tubing and water/gas containers. The added weight and volume to the robotic system make these McKibben AMs impractical for use in constrained situations and reduce comfort during human interaction. Additionally, this complex actuation system

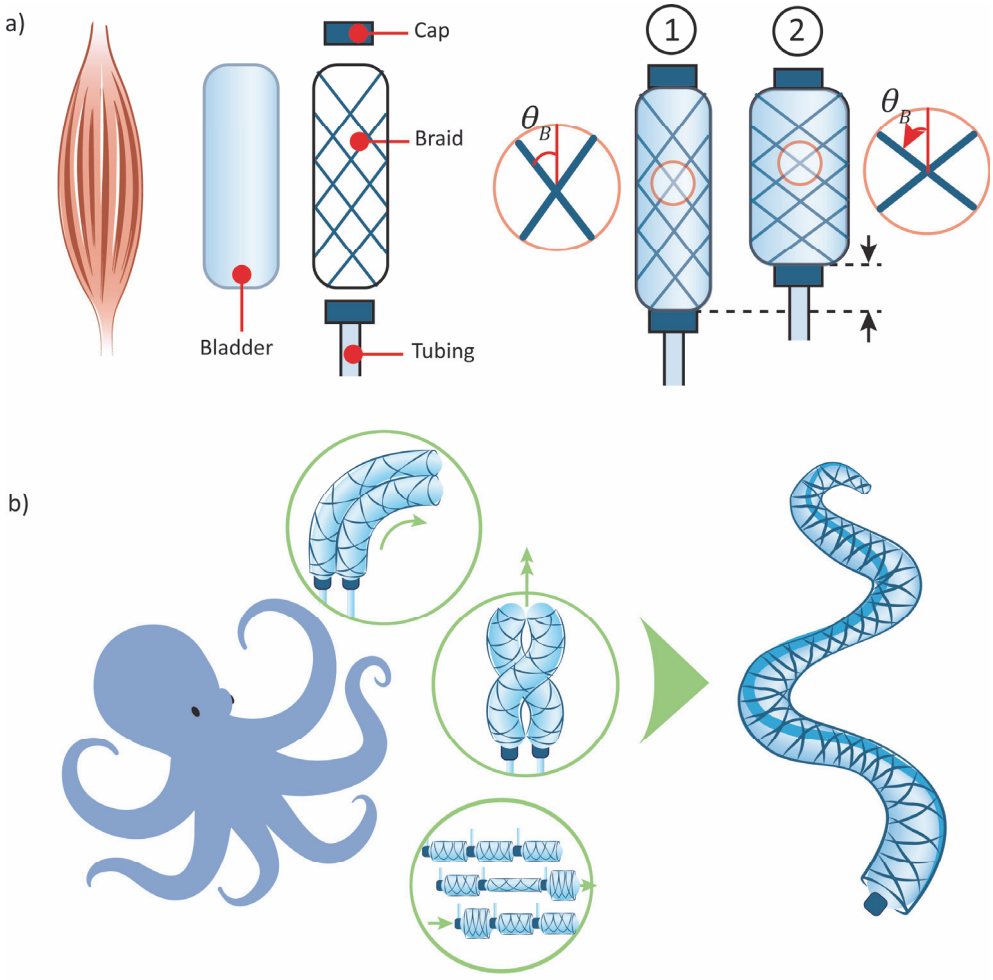


Figure 7.1: McKibben Artificial Muscles (AMs). a) Schematic representation of a McKibben Artificial Muscle (AM). Expansion of the inner bladder results in contraction or extension of the actuator, depending on the braiding angle θ_B. b) Soft robots that embed complex motions, such as bending, twisting and advanced linear deformation, usually require a complex system of multiple McKibben AMs. To simplify robotic systems, complex motions need to be embedded in the design of a single McKibben AM.

impacts reliability by increasing the vulnerability to leakages. These disadvantages limits their ability to replicate the complex, distributed deformations seen in natural muscles.

Therefore, a simplified AM system architecture is needed, which can be achieved by encoding complex deformation behavior into the actuator's embodiment. This approach aligns with the embodied intelligence (EI) framework, which emphasizes that intelligent behavior can emerge from the coupling between morphology, material properties and their interaction with the environment [11-14]. Therefore reducing the required computational load. By tailoring local interactions between the McKibben AM's braided sleeve and inner bladder, we achieve global shape change through passive, geometry-encoded actuation. In the present

work, the local interaction between the braided sleeve and the compliant bladder will be employed to define the global deformation of the McKibben AM. This results in complex motions like bending or twisting emerging from a single, simple input like inflation. Currently, different strategies have been used to manufacture McKibben AMs embedding a locally adapted sleeve. These usually entail alternative manufacturing techniques, such as 3D printing or molding [15-17]. These techniques involve advanced manufacturing facilities, custom-made instruments, high material costs, low production scalability or time-consuming processes, which reduce their applicability. Alternatively, Connolly *et al.* [18] demonstrated a related approach using fiber-reinforced pneumatic actuators that embed complex motions by locally varying fiber orientations within a molded silicone body. While they show comparable motions as McKibben AMs, their underlying working principle differs. In the design by Connolly *et al.* [18], the deformation is governed by locally varying stiffness and material anisotropy, whereas McKibben AMs rely on sliding and rotation of fibers within an external braided sleeve. The McKibben architecture outstand molding-based embedding of fibers in terms of manufacturing scalability. The use of commercially available braiding machines enables efficient fabrication of actuators with greater lengths, diameters, and production throughput. To our knowledge, no McKibben AMs with locally adaptable sleeves have yet been developed while maintaining the simplicity and scalability of conventional braiding techniques.

The goal of this study is to develop embodied intelligent McKibben AMs, whose global behavior is physically programmed into their embodiment. While maintaining compatibility with regular braiding techniques, this study analyzes the relevant design parameters for functionally encoded sleeves, develops novel braiding strategies for manufacturing and evaluates the deformation behavior of prototyped mechanically encoded McKibben AMs.

7.2 Braiding for Intelligent Sleeves

7.2.1 Braiding for Linear Motion

Relevant Design Parameters

Depending on the design parameters of the braided sleeve, the interaction between the sleeve and the inflated bladder results in a specific linear motion. Therefore, knowing which parameters are relevant is essential to embed a complex linear deformation profile into the braid. This way, a singular McKibben AM can be created showing locally different contraction or extension behavior. The single AM could, for example, be implemented to exhibit complex linear locomotion [9, 10] or might be wrapped such that its deformation resembles a human heart [19].

To understand how to adjust these design parameters, we look closely into the interaction between the bladder and the braided sleeve during inflation. As shown in Figure 7.2a, the inflation pressure P applied to the inner bladder of the McKibben AM results in a longitudinal force (F_L) and a circumferential force (also known as the hoop force) (F_H). They depend on the diameter D and the length L of the bladder, as elaborated in Appendix 7.A.

In the case of an equilibrium condition, which means no linear motion, the resultant force (F_R) caused by the hoop force and longitudinal force is in line with the tension force (T) applied to the braid wires. Here, the angle of the resultant force (θ_R) is similar to the braid angle of the

wires (θ_B), called the neutral angle. As described in classical hose theory [20], this neutral angle has a theoretical value of 54.7^0, with its derivation provided in Appendix 7.A.

As shown in Figure 7.2b, a braid angle smaller than the neutral angle will force the wires to rotate inwards, resulting in the contraction of the McKibben AM. Similarly, a braid angle larger than the neutral angle will force the wires to rotate outwards, resulting in the extension of the McKibben AM. The amount of extension or contraction (ε) can be determined by (7.2), depending on stroke length (ΔL), the initial length (L_0) and the initial braiding angle (θ_{B0}). Here, a positive value indicates extension and a negative value indicates contraction.

$$\varepsilon = \frac{\Delta L}{L_0} = 1 - \frac{\cos(\theta_B)}{\cos(\theta_{B_0})} \tag{7.2}$$

To conclude, the linear deformation profile of the McKibben AM can be directly adapted by adjusting the braiding angle locally ($\theta_{B,i}$). The overall strain of the AM (ε_{tot}) is the result of the combined strain contributions from each local segment (ε_i), as shown in (7.3), (7.4) and (7.5). It should be noted that the final braiding angle after linear deformation is not solely determined by geometry, but is also influenced by external factors such as load, fiber pre-tension and actuation pressure.

$$\varepsilon_i(\theta_{B_i}) = \begin{cases} < 0, & \theta_{B,i} < 54.7° \\ = 0, & \theta_{B,i} = 54.7° \\ > 0, & \theta_{B,i} > 54.7° \end{cases} \tag{7.3}$$

$$\Delta L_{tot} = \sum \Delta L_i = \sum \varepsilon_i \cdot L_{0i} \tag{7.4}$$

$$\varepsilon_{tot} = \frac{\Delta L_{tot}}{L_{0,tot}} = \frac{\sum \varepsilon_i \cdot L_{0,i}}{\sum L_{0,i}} \tag{7.5}$$

Manufacturing Technique

To embed a complex linear motion in a McKibben AM, a manufacturing technique had to be developed to adapt the braiding angle of the braided sleeve locally. A key objective was to retain the use of conventional braiding technology to preserve manufacturing simplicity, which can be achieved in several ways. Conventional braiding the sleeve of the McKibben AM often involves an industrial braiding machine, also known as a *Maypole braider*. This machine manufactures the braided sleeve by interlacing a set of wires around a cylindrically shaped braiding mandrel. Normally, this mandrel has a constant diameter and is pulled at a constant speed (Figure 7.3a). Interestingly, the design of the mandrel offers many opportunities to customize the braiding angle of the sleeve locally. Specifically, a locally adjustable braiding angle can be achieved by either locally adjusting the pulling speed or the diameter of the mandrel. Here, increasing the speed or increasing the mandrel diameter reduces the final braiding angle, while decreasing the speed or decreasing the mandrel diameter enlarges the final braiding angle.

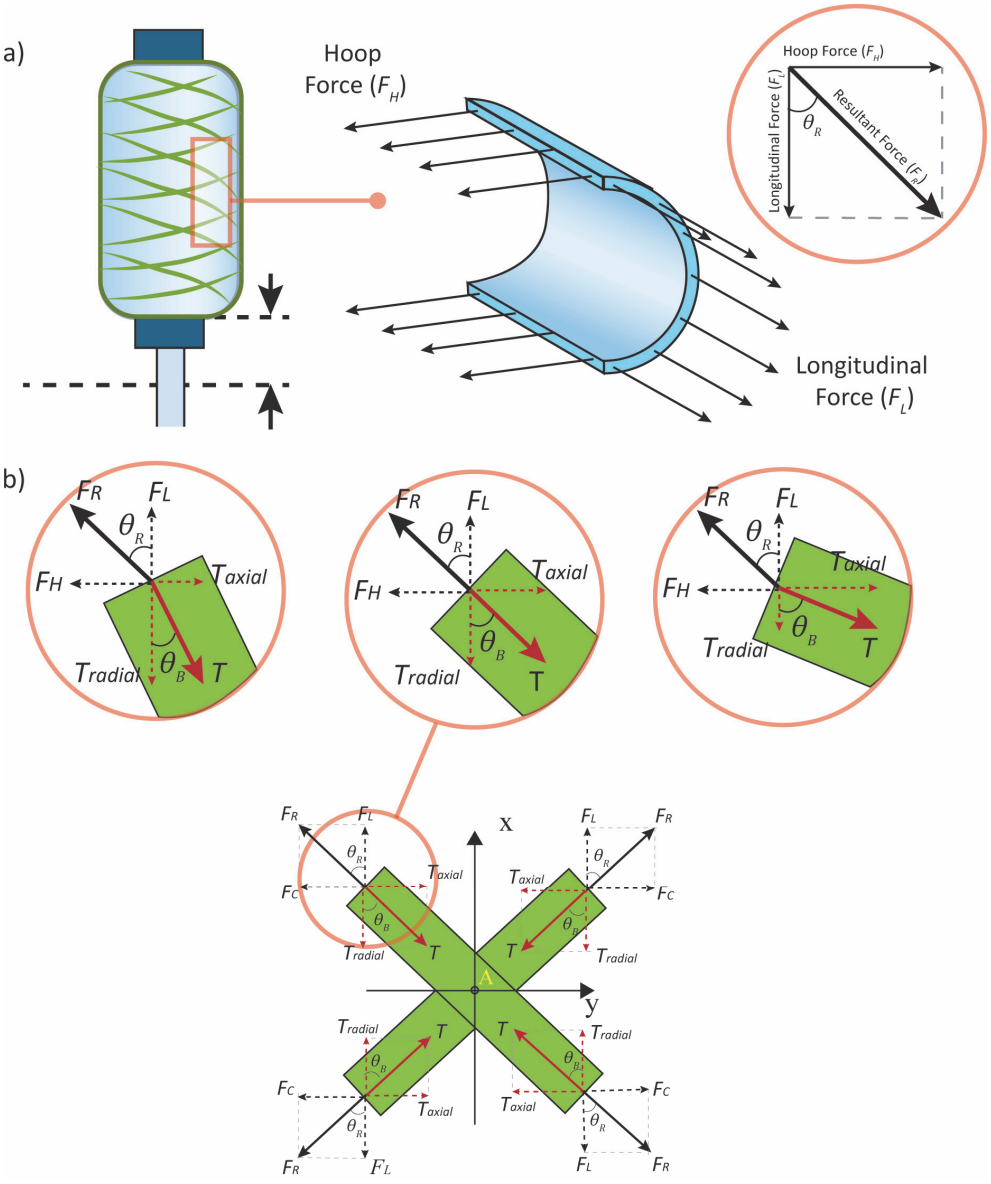


Figure 7.2: How the braid angle (θ_B) determines linear motion. a) A hoop force (F_H) and longitudinal force (F_L) are applied to the bladder during inflation, of which the resultant force (F_R) affects the braid wires, with angle θ_R. b) Left: A braiding angle (θ_B) smaller than the resultant angle (θ_R) leads to inwards rotation of the braid wires, meaning contraction. Middle: A braiding angle (θ_B) similar to the resultant angle (θ_R) leads to no linear motion. Right: A braiding angle (θ_B) larger than the resultant angle (θ_R) leads to outward rotation of the braid wires, meaning extension.

Table 7.1: Fabrication parameters of the linear actuators.

		Actuator 1	Actuator 2	Actuator 3
Top segment	Mandrel length [mm]	50	50	50
	Mandrel diameter [mm]	11	26.5	11
Middle segment	Mandrel length [mm]	50	50	50
	Mandrel diameter [mm]	26.5	11	11
Bottom segment	Mandrel length [mm]	50	50	50
	Mandrel diameter [mm]	11	26.5	11

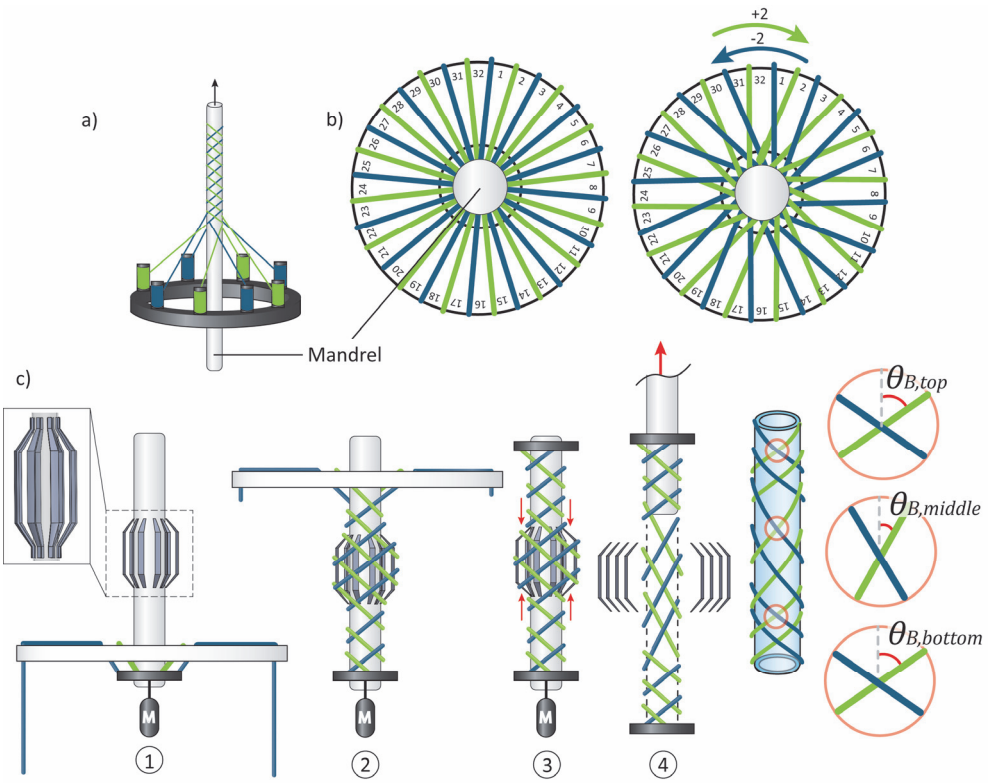


Figure 7.3: Manufacturing process of a braided sleeve with a locally adaptive braiding angle. a) A hollow round braid created around a mandrel using a conventional braiding machine. The mandrel is pulled at a constant speed for consistent braid parameters. b) Braiding pattern using a Kumihimo braiding disc to create a hollow round braid around a mandrel. c) Final manufacturing process. (1) Setting up the braiding disc with 32 wires attached to a cap (black) and a mandrel with sets of compliant rods (grey) to increase its diameter locally. A weight, indicated by M, introduces a constant pulling speed. (2) The wires are consistently braided around the mandrel. (3) The compliant rods are detached from the mandrel and removed from the braid by pushing them inwards. (4) The mandrel is removed from the braid, resulting in a braided sleeve with a locally adjusted braiding angle.

Three prototypes were made to demonstrate the effect of different braiding angles over the length of a single McKibben muscle. To ease prototyping, a traditional Japanese *Kumihimo* braiding disc was used as an alternative to an industrial braiding machine. This braiding disc functions as a perfect tool to quickly iterate with the design parameters of the braided sleeve. The braiding pattern for a hollow round braid, also known as *Naiki Gumi*, was used to manufacture the braided sleeve. Figure 7.3b illustrates the steps of this braiding pattern, which results in a similar braid as produced by an industrial braiding machine.

In this study, we chose to adapt the braiding angle of the sleeve by employing a mandrel with customized diameter, as this gave more consistent results in combination with the manual braiding process. The manufacturing process is shown in Figure 7.3c. The mandrel was 3D-printed (*Ultimaker S5, Polylactic Acid (PLA)*) with sets of compliant rods to increase the diameter locally. The rods were attached to the mandrel by sliding their ends into circularly arranged slots embedded in the mandrel. After braiding, these rods were easily disassembled by pushing them inwards, after which the mandrel was easily removed from the braided sleeve. The diameter of the large mandrel sections was 26.5 mm, while the diameter of the small mandrel sections was 11 mm. The braid consisted of 32 polyethylene (PE) wires with a 0.3 mm diameter (*Grappler 8, Shimano*). To finish the McKibben AM, the mandrel was replaced by a silicone bladder (*Ecoflex 0030, Smooth-On*) with a similar diameter. The silicone bladder was covered by talcum powder (*Zwitsal*) to reduce the friction between the bladder and the braided sleeve, optimizing the deformation of the sleeve. Three prototypes were manufactured, each divided into three segments meaning three customized mandrels were used. This allowed for deformation profiles with three distinct configurations. Table 7.I shows the fabrication parameters of the three actuators. Note that the large mandrel sections include transition lengths of 10 mm to transition from a small diameter (11 mm) to a large diameter (26.5 mm), and the other way around. The braiding angles of the individual segments were measured using a digital microscope (*Dino-Lite Edge AM73915MZTL*), providing high magnification and resolution. The angle was determined by digitally marking the individual wires and calculating the angle between them using the DinoCapture 3.0 software. The first prototype consists of a contracting middle segment surrounded by two extending segments (Figure 7.4a). The braiding angles of the top, middle and bottom segments are 57.1^0, 22.5^0 and 57.0^0, respectively. The second prototype consists of an extending middle segment surrounded by two contracting segments (Figure 7.4b). The braiding angles of the top, middle and bottom segments are 35.0^0, 55.8^0 and 34.0^0, respectively. The third prototype acts as a reference, with three contracting segments (Figure 7.4c). The braiding angles of the top, middle and bottom segments are 35.6^0, 43.8^0 and 29.7^0, respectively. Here, it is important to remember that braiding angles below 54.7^0 result in contraction and braiding angles above 54.7^0 result in extension. The prototypes demonstrate that locally varying braiding angles can be implemented using a customized mandrel with varying diameters.

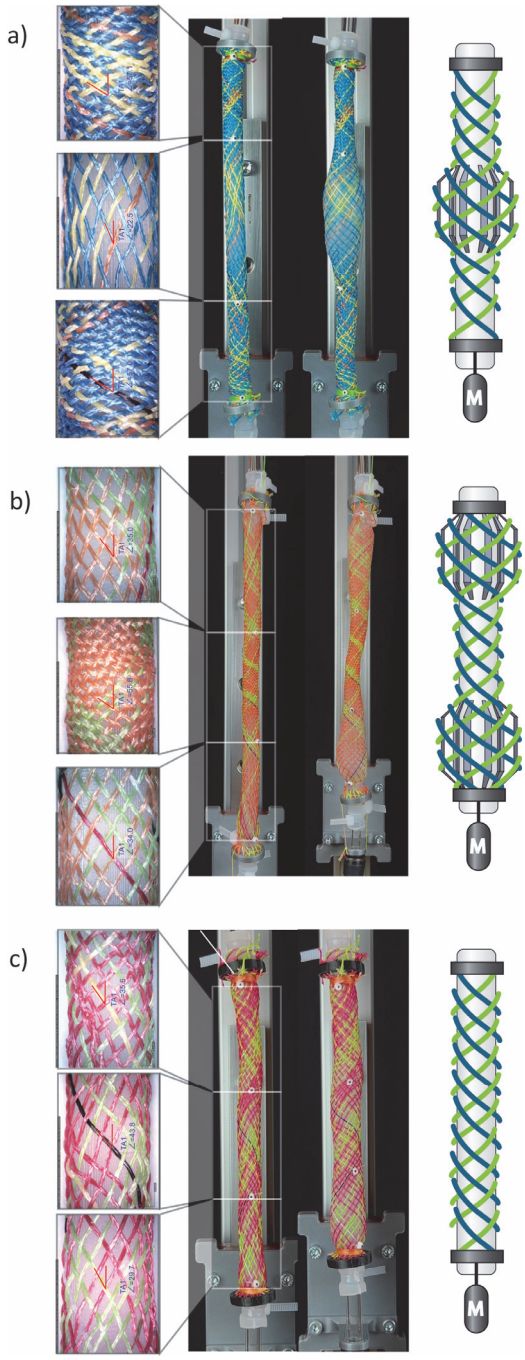


Figure 7.4: Final prototypes. a) Actuator 1 consisting of contracting middle segment surrounded by two extending segments. Right: Customized mandrel design. b) Actuator 2 consisting of an extending middle segment surrounded by two contracting segments. Right: Customized mandrel design. c) Actuator 3 consisting of three contracting segments, functioning as reference. Right: Customized mandrel design.

7.2.2 Braiding for Twisting Motion

Relevant Design Parameters

Currently, a single McKibben muscle can only exhibit a twisting motion in combination with other McKibben muscles or by wrapping the AM into a space-inefficient configuration. A space-efficient twisting McKibben AM would be beneficial in, for example, biomedical applications or unstructured environments [21]. To develop a McKibben artificial muscle capable of twisting, it is necessary to create an imbalance between the forces generated by the opposing helical families in the braided sleeve. The braided wires are arranged in both clockwise and counterclockwise helical patterns around the inner bladder. By altering the mechanical influence of one family relative to the other, a net torque is produced, causing the actuator to twist. For simplification, Figure 7.5a illustrates how single-directional helices induce a twisting motion. When the bladder inflates, the helices expand in diameter. Because the helix wire is inelastic, this expansion is compensated by reducing the number of turns of the helix, resulting in a twisting motion. However, in traditional McKibben AMs, the clockwise and counterclockwise helices generate opposing torques that cancel each other out. Therefore, to achieve a net twisting effect, the helices must be designed asymmetrically, meaning they should have a different number of turns.

Suppose we have two helical families, Helix 1 with N_1 turns and Helix 2 with N_2 turns. The total length of each helix before expansion (S_i) and after expansion (S_i') is determined using (7.6)-(7.7). Here, p_i is the helix pitch length before expansion, p_i' is the helix pitch length after expansion, D is the diameter, D' is the diameter after expansion and N_i' is the helix number of turns after expansion (Figure 7.5b).

$$S_i = N_i\sqrt{p_i^2 + (\pi D)^2} \tag{7.6}$$

$$S_i' = N_i'\sqrt{p'^2_i + (\pi D')^2} \tag{7.7}$$

Due to the inelasticity of the helices, the total helix length remains unchanged after expansion. The net twisting effect in turns (ΔN) is given by (7.8). The twisting angle θ_{twist} is given by (7.9). Here, N_i' denotes the effective continuous number of turns of each helical family after inflation. The helical number of turns after expansion is further derived in Appendix A.

$$\Delta N = N_1' - N_2' \tag{7.8}$$

$$\theta_{twist} = 360° \cdot \Delta N \tag{7.9}$$

In conclusion, a single twisting McKibben AM can be created by adapting the opposing helices' number of turns (N). This means, at the same time, that the braiding angle of the clockwise helices ($\theta_{B,1}$) differs from the braiding angle of the counterclockwise helices ($\theta_{B,2}$) (Figure 7.5c).

$$\theta_{twist} = \begin{cases} \neq 0, & N_1 \neq N_2 \text{ and } \theta_{B,1} \neq \theta_{B,2} \\ = 0, & N_1 = N_2 \text{ and } \theta_{B,1} = \theta_{B,2} \end{cases} \tag{7.10}$$

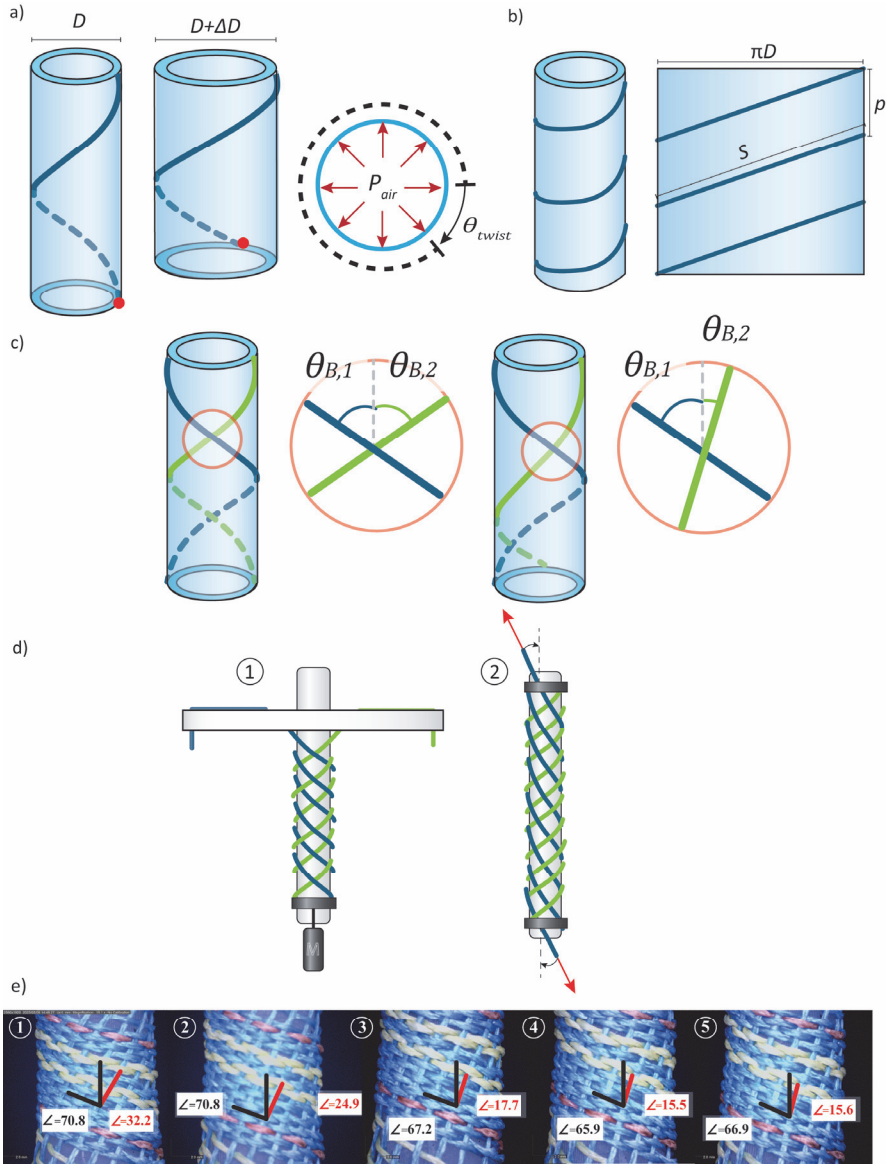


Figure 7.5: Inducing a twist angle θ_{twist} by unbalanced helical families. a) Schematic representation of twist by a single helical family. Here, D is the diameter and P_{air} is the internal pressure. b) Helical design parameters, here p is the helical pitch length and S is the length of one helical turn. c) Left: Balanced helical families, with similar number of turns (N) and braiding angle (θ_B), resulting in no net twisting motion. Right: Unbalanced helical families, with different number of turns (N) and braiding angle (θ_B), resulting in a net twisting motion. d) Schematic manufacturing process. (1) Braiding the sleeve with a Kumihimo braiding disc around a regular mandrel, (2) Tensioning the wires of one helical family, resulting in a braiding angle difference between the opposing helical families. e) Final prototype. (1) Non-stretched, with a braiding angle difference of 38.6^0, (2) stretched by a 50 g weight, resulting in a braiding angle difference of 45.9^0, (3) stretched by a 100 g weight, resulting in a braiding angle difference of 47.2^0, (4) stretched by a 150 g weight, resulting in a braiding angle difference of 50.4^0 and (5) stretched by a 200 g weight, resulting in a braiding angle difference of 51.3^0.

With this minor adaptation of its sleeve design, a McKibben AM can embed torque during its motion. It should be noted that Equation (7.9) provides the geometric relation between the current braid configuration and the actuator twist. However, the braid geometry itself is pressure-dependent. This means the helical number of turns N_i' evolves with actuator deformation, which is governed by the internal pressure. Consequently, the twist develops continuously during inflation. The two helical families are mechanically coupled and the actuator reaches a stable twist angle when the torques from both helical families balance.

Manufacturing Technique

A manufacturing strategy was implemented to create a disbalance in the number of turns between the opposing helices of a braided sleeve, as shown in Figure 7.5d. Again, the *Kumihimo* braiding disc was employed to manufacture the braided sleeve. This time, the sleeve was braided around a regular mandrel with a constant diameter. After finalizing the sleeve and assembling the silicone bladder (*Ecoflex 0030, Smooth-On*), one helical family is tensioned. Tensioning the clockwise turning helices results in a clockwise twisting McKibben AM when pressurized. Vice versa, if the counterclockwise helices are tensioned, this results in a counterclockwise twisting McKibben AM. Introducing a difference in the number of turns (*N*) between the helices simultaneously means that the helices employ a different braiding angle. Table 7.2 shows the geometric fabrication parameters of the twisting AM.

Figure 7.5e shows the final prototype with a difference in the number of turns (*N*), and thus a braiding angle difference. The difference in the braiding angle of the opposing helices was measured using a digital microscope (*Dino-Lite Edge AM73915MZTL*). The angle was determined by digitally marking the individual wires and calculating the angle between them using the DinoCapture 3.0 software. The disbalance was introduced by tensioning one set of helices of the prototype. To demonstrate the effect of asymmetry in the helical structure on the twisting effect, the prototype was adapted to embed a range of braiding angle differences. Using a single prototype ensured that all other design parameters of the McKibben AM remained constant, isolating the effect of the braiding angle difference. This variation was achieved by stretching the prototype, thereby decreasing the braiding angles of both helical sets. Because the helices start with different angles, their change in angle during stretch is not uniform, resulting in an increased braiding angle difference as the prototype is stretched. The McKibben AM is stretched by applying a weight of 50 grams, 100 grams, 150 grams and 200 grams. This resulted in a difference in the braiding angle ($\Delta\theta_B$) of 45.9^0, 47.2^0, 50.4^0 and 51.3^0, respectively. The difference in braiding angle without using a weight was measured as 38.6^0. The prototype demonstrates that by tensioning helices, their braiding angle can be adjusted compared to the opposing-turning helices.

7.3 Experiments

The main goal of the experiments was to investigate the effect of an adjustable braiding angle on the (1) linear motion and (2) twisting motion of McKibben AMs. Therefore, two experiments were performed, the first focusing on the linear motion and the second focusing on the twisting motion. The aim was to investigate the overall actuation behavior of the prototyped McKibben artificial muscles, to verify whether local modifications in braid parameters lead to the expected deformation responses.

Table 7.2: Geometric fabrication parameters unloaded twisting actuator.

	Helical family 1	Helical family 2
Mandrel length [mm]	70	70
Mandrel diameter [mm]	10	10
Amount of turns [-]	1	3.5

7.3.1 Experimental Setup: Linear Motion

The setup for demonstrating the linear AMs is illustrated in Figure 7.6. In this setup, the three prototypes described in Section 7.2.1 were investigated. Each prototype consisted of three segments, namely top, middle, and bottom, distinguished by their braiding angles. Four polystyrene markers were stitched onto each McKibben AM to indicate the transition between these segments. The McKibben AM was positioned vertically by clamping the proximal end onto the main frame. The distal end was attached to a vertical miniature ball runner guide (Rexroth, MWA-020-SNS-C0-H-3) by a 3D-printed support, constraining the actuator to a 2D plane and preventing out-of-plane motion. The McKibben AM was connected to a manual pump with a pressure sensor in between (IFM electronic, PU5404). The motion of the AM was recorded by a camera on a tripod, positioned approximately 40 cm in front of the actuator. The pressure sensor was connected to an analogue signal conditioner (CPJ RAIL, SCAIME) and a data acquisition unit set at a sampling rate of 20 Hz (NI USB-6008, National Instruments Corporation). A millimeter scale bar was placed next to the McKibben AM for calibration purposes.

The deformation of the top, middle, and bottom segments of every McKibben AM was the main performance measure. The deformation is presented as stroke length (ΔL) and strain (ε), computed by (7.5), meaning a positive value indicates extension and a negative value contraction. The stroke length was defined as the change in length between the markers that

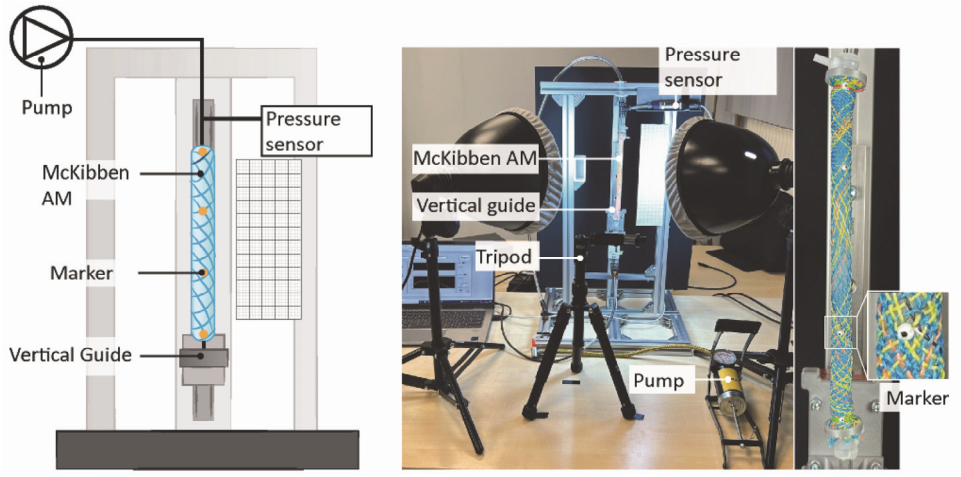


Figure 7.6: Linear motion. Overview of the experimental setup.

indicated the start and end of a specific segment. The deformation was measured for different actuation pressures, ranging from 10 kPa to 50 kPa.

At the start of each measurement, the McKibben AM was positioned with the markers facing the camera. The pressure was increased in steps of 10 kPa, 20 kPa, 30 kPa, 40 kPa and 50 kPa, which was monitored in LabVIEW 2018. The subsequent pressure steps were indicated on the video footage by an auditory signal. Ten trials per condition were performed for all three prototypes. The video footage was analyzed using *Tracker (6.1.7)* software (Open Source Physics). Here, the motion of the segments was extracted by tracking the four markers. An XY axis was plotted in the software with the origin positioned at the stationary proximal end of the McKibben AM. The videos were calibrated using the millimeter graph paper. Comparing the X-t plots of the separate markers resulted in the relative deformation of the intermediate segments. The videos were recorded in 4K resolution (3840 × 2160 pixels) at 30 fps with the camera plane perpendicular to the actuator to avoid parallax effects. The rigid scale bar was placed in the same plane as the actuator to ensure accurate pixel-to-length calibration. The small, high-contrast markers were attached to the braided sleeve with minimal contact area to reduce marker deformation. Uniform, diffuse lighting created by light boxes and a high-contrast background were used to enhance marker visibility during tracking.

7.3.2 Results: Linear Motion

Figure 7.7a-c shows the strain (ε) of the top, middle, and bottom segments of the three McKibben AMs. The first prototype has a maximum mean stroke length (ΔL) of +2.8 mm (top), -18.1 mm (middle) and +5.4 mm (bottom), corresponding to a strain of +0.06, -0.19, and +0.10, respectively. This clearly demonstrates that the middle segment, with a braiding angle of 22.5^0, is contracting. Contrarily, the top and bottom segments, with braiding angles of 57.1^0 and 57.0^0, are extending. The second prototype has a maximum mean stroke length (ΔL) of -12.2mm (top), +2.6 mm (middle) and -15.5 (bottom), corresponding to a strain of -0.15, 0.04, and -0.21, respectively. This demonstrates that the middle segment, with a braiding angle of 55.8^0 is extending. Contrarily, the top and bottom segments, with braiding angles of 35.0^0 and 34.0^0, are contracting. The third prototype has a maximum mean stroke length of -4.4 mm (top), -7.1 mm (middle) and -5.5 mm (bottom), corresponding to a strain of -0.09, -0.14, and -0.13, respectively. All three segments, with a braiding angle of 35.6^0, 43.8^0 and 29.7^0, are contracting. The actuator exhibited a full inflation–deflation cycle within approximately 0.5 s, corresponding to an estimated response time of a few hundred milliseconds. The observed dynamics are primarily governed by the compliance of the silicone bladder and the low operating pressure range used in this study.

Applying (7.2) to predict segment strain revealed discrepancies between theoretical and experimental values. While the model correctly predicted the direction of motion, elongation or contraction, it fell short in estimating the strain magnitude. This may be due to gradual transitions between segments, which lack sharp boundaries and introduce intermediate braiding angles not captured by the model. Additionally, the assumption of isolated segments does not reflect the mechanical interaction between adjacent segments. Despite these limitations, the theoretical framework remains valuable for understanding how braiding angles influence motion and for guiding actuator design.

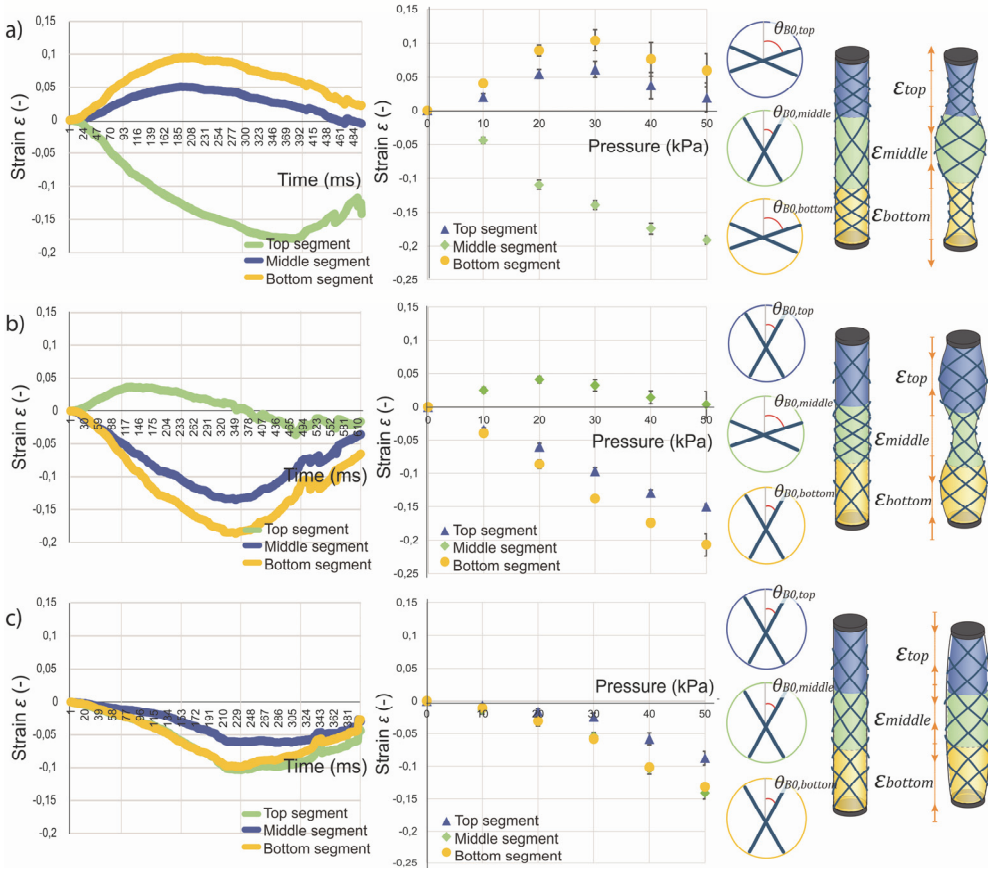


Figure 7.7: Results: Linear motion. a) Deformation profile of the first prototype, embedding an extending top and bottom segment and a contracting middle segment. Left: The average strain (ε) of the individual segments over time. Here, a positive strain indicates extension and a negative strain indicates contraction, showing one full actuation cycle. Right: The average strain (ε) of the individual segments for different actuation pressures. Data represent mean ± standard deviation from 10 repeated measurements (n = 10). b) Deformation profile of the second prototype, embedding a contracting top and bottom segment and an extending middle segment. Left: The average strain (ε) of the individual segments over time, showing one full actuation cycle. Right: The average strain (ε) of the individual segments for different actuation pressures. Data represent mean ± standard deviation from 10 repeated measurements (n = 10). c) Deformation profile of the reference prototype, embedding a contracting top, middle and bottom segment. Left: The average strain (ε) of the individual segments over time, showing one full actuation cycle. Right: The average strain (ε) of the individual segments for different actuation pressures. Data represent mean ± standard deviation from 10 repeated measurements (n = 10).

3.7.3 Experimental Setup: Twisting Motion

The setup for demonstrating the twisting AMs is illustrated in Figure 7.8. In this setup, the five prototype configurations described in Section 7.2.2 were investigated. Each configuration was created by tensioning the McKibben AM with a specific weight, inducing a corresponding braiding angle difference between the opposing helices. A nylon strap was attached to the

distal end of the AM to function as a pointer. Similar to the linear motion setup, the McKibben AM was positioned vertically by clamping the proximal end onto the main frame. The McKibben AM was, again, connected to a pump with a pressure sensor in between (IFM electronic, PU5404). The rotation of the AM was recorded by a camera on a tripod positioned approximately 60 cm above the actuator. The camera was aligned with the actuator's rotation axis and fixed in position and orientation perpendicular to the measurement plane. A circular protractor was placed beneath the McKibben AM to measure the rotation. The videos were recorded in 4K resolution (3840 × 2160 pixels) at 30 fps. Uniform, diffuse lighting created by light boxes and a high-contrast background were used to enhance pointer visibility.

The twisting angle (θ_{twist}) of the McKibben AM configurations was the main performance measure. The angle was measured for different actuation pressures, ranging from 10 kPa to 50 kPa. At the start of each measurement, the McKibben AM was positioned with the pointer facing 0 degrees on the circular protractor. The pressure was increased in steps between 10 kPa, 20 kPa, 30 kPa, 40 kPa and 50 kPa, which was monitored in LabVIEW 2018. The subsequent pressure steps were indicated on the video footage by an auditory signal. Five measurements per condition were performed for all five prototype configurations. The twisting angle was extracted from the video footage by analyzing the final position of the pointer on the circular protractor.

7.3.4 Results: Twisting Motion

Figure 7.8b shows the twisting angle for the different prototype configurations, depending on the actuation pressure. The maximum mean twisting angle was 29°, 64°, 82°, 100° and 100° for the prototype stretched by 0 grams, 50 grams, 100 grams, 150 grams and 200 grams, respectively. A saturation in twisting angle seems to be reached when being stretched by a weight of 150 grams, which resembles a braiding angle difference of 50.4°.

7.4 Discussion

The goal of this study was to develop embodied intelligent McKibben AMs by designing for encoded interactions between the braided sleeve and the inner bladder. In this McKibben AM design, the local interaction between the braid and bladder defines the global, complex shape transformation. This concept is inspired organisms embedding fiber-reinforced architecture, such as the octopus. The octopus controls the shape of its arms through distributed motions such as contraction, extension, twisting, and bending. In the octopus, contraction, extension, and twisting are driven by longitudinal, circular, and helical muscles, respectively. Bending arises from the coordinated interaction of these muscles. Similarly, in the McKibben AM, linear motion and twisting were directly programmed, and bending can emerge from a combination of these linear motions. As the design parameters of the braided sleeve are key for shaping the deformation profile of the McKibben AM, the braided sleeve was designed such that its local adaptations caused complex motions. The braiding angle between the wires was identified as the core parameter to embed multiple motions in the sleeve. First, the braiding angle defines whether the AM is contracting or extending upon inflation, and additionally the

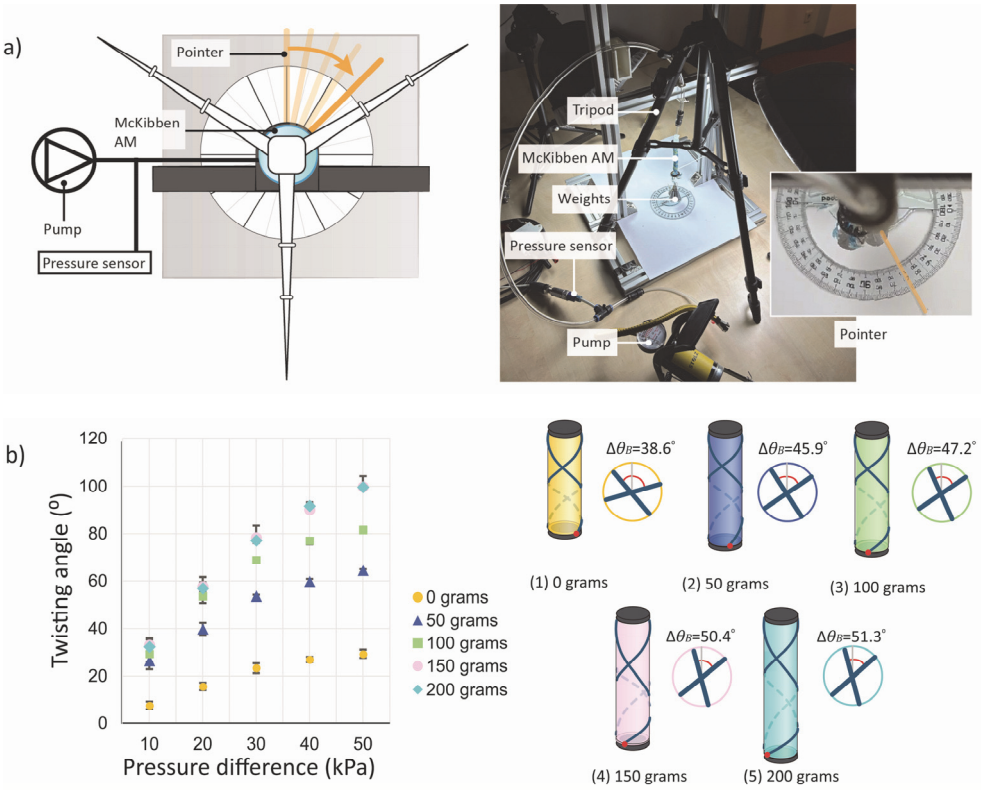


Figure 7.8: Results: Twisting motion. a) Overview of the experimental setup. b) Twisting angle measured for different internal pressures. Data represent mean ± standard deviation from 5 repeated measurements (n = 5). Here, the final prototype is evaluated in a configuration that is (1) Non-stretched, with a braiding angle difference ($\Delta\theta_B$) of 38.6^0, (2) stretched by a 50 g weight, resulting in a braiding angle difference ($\Delta\theta_B$) of 45.9^0, (3) stretched by a 100 g weight, resulting in a braiding angle difference($\Delta\Theta_B$) of 47.2^0, (4) stretched by a 150 g weight, resulting in a braiding angle difference ($\Delta\theta_B$) of 50.4^0 and (5) stretched by a 200 g weight, resulting in a braiding angle difference ($\Delta\theta_B$) of 51.3^0.

range of extension or contraction. Lowering the braiding angle beyond 54.7° results in local contraction, whereas increasing the braiding angle beyond 54.7° results in local extension. A controlled change in braiding angle along the length of the braided sleeve was achieved by introducing a customized mandrel in the braiding process. Here, a mandrel with increased diameter results in a reduced braiding angle, and a decreased mandrel diameter results in an increased braiding angle. Secondly, a twisting motion can be embedded into the braided sleeve by introducing a differential in the number of turns between the opposing helical families. This results in a braiding angle difference between those wires. This disbalance was achieved by simply tensioning one helical family.

Experiments showed that the local adaptation of a McKibben AM's braiding angle successfully resulted in complex deformation profiles. McKibben AMs were prototyped using the beforementioned strategies for local braiding angle adjustment. The segments with braiding angles larger than 54.7° effectively caused local extension, whereas segments with smaller braiding angles caused local contraction. Since 54.7° represents the neutral angle, the

available range for extension is inherently smaller than that for contraction. This was also reflected in the experiments, where the mean length shifts of the extending segments were consistently lower than those of the contracting segments. The largest measured difference within a single McKibben AM was found between segments with a braiding angle of 57.1^0 and 22.5^0, with a relative maximum strain (ε) of +0.06 and minimum strain of -0.19. Interestingly, the strain of the extending segments decreased at higher pressure levels. This reduction may be attributed to the curvature observed in the McKibben muscle under high pressure, likely caused by internal structural irregularities, or by the static friction of the linear guide. While the exact mechanism was not investigated in this study, these effects highlight areas for further systematic investigation in future work. Additionally, a difference between inflation and deflation cycles was observed, indicating the presence of mechanical hysteresis. This is a well-known characteristic of McKibben actuators and other soft pneumatic systems. The hysteresis primarily arises from the viscoelastic behavior of the silicone bladder and frictional energy losses between the internal bladder and the braided sleeve.

A twist motion was successfully induced by creating a disbalance between the braiding angle of the opposing helical families. A braiding angle difference of 50.4° resulted in the largest twist angle, 100 degrees, using an actuation pressure of 50 kPa. The experiments showed that the twisting angle of the actuator saturates at a certain pressure, depending on the braiding angle difference. This behavior is expected, as the actuator continues to twist until the torque generated by the opposing helical family is balanced, effectively aligning toward a braiding angle difference of 0 degrees. Theoretically, the maximum possible braiding angle difference approaches 90°, with one set of helices nearing a braiding angle of 0° and the other approaching 90°. However, in the prototyped actuator, saturation occurred at a difference of 50.4°, likely due to geometric constraints and internal friction.

Bending in the McKibben AM can be locally encoded into the braid by combining contraction and extension patterns. A McKibben AM incorporating an extending leg and a contracting leg was prototyped as a proof of concept. This segment was built into a modular AM to showcase different local motion modules can be embedded along the length of the actuator, including contraction/extension sequences, a bending module, and a twisting module. This modular composition highlights the potential of how complex, global shape changes arise from local braid-bladder interactions. Figure 7.9 provides an overview of guidelines for the design of a modular McKibben AM embedding a complex deformation profile along its length. Future work will look into strategies to combine complex linear motion, bending and twisting into a monolithic non-assembly actuator, thereby focusing on a technique to tension the helical wires in a localized manner.

Future research should further explore the potential of these embodied intelligent AMs by investigating a wider range of actuation pressures, braiding angles, and wire types. The use of automated braiding machines could enable precise local adjustments while avoiding unintended structural irregularities, and also allow for more accurate measurements through synchronized data acquisition. Although care was taken to minimize camera distortion, the optical tracking measurements may still be subject to parallax errors. Future work will employ higher-precision measurement methods to further reduce uncertainty.

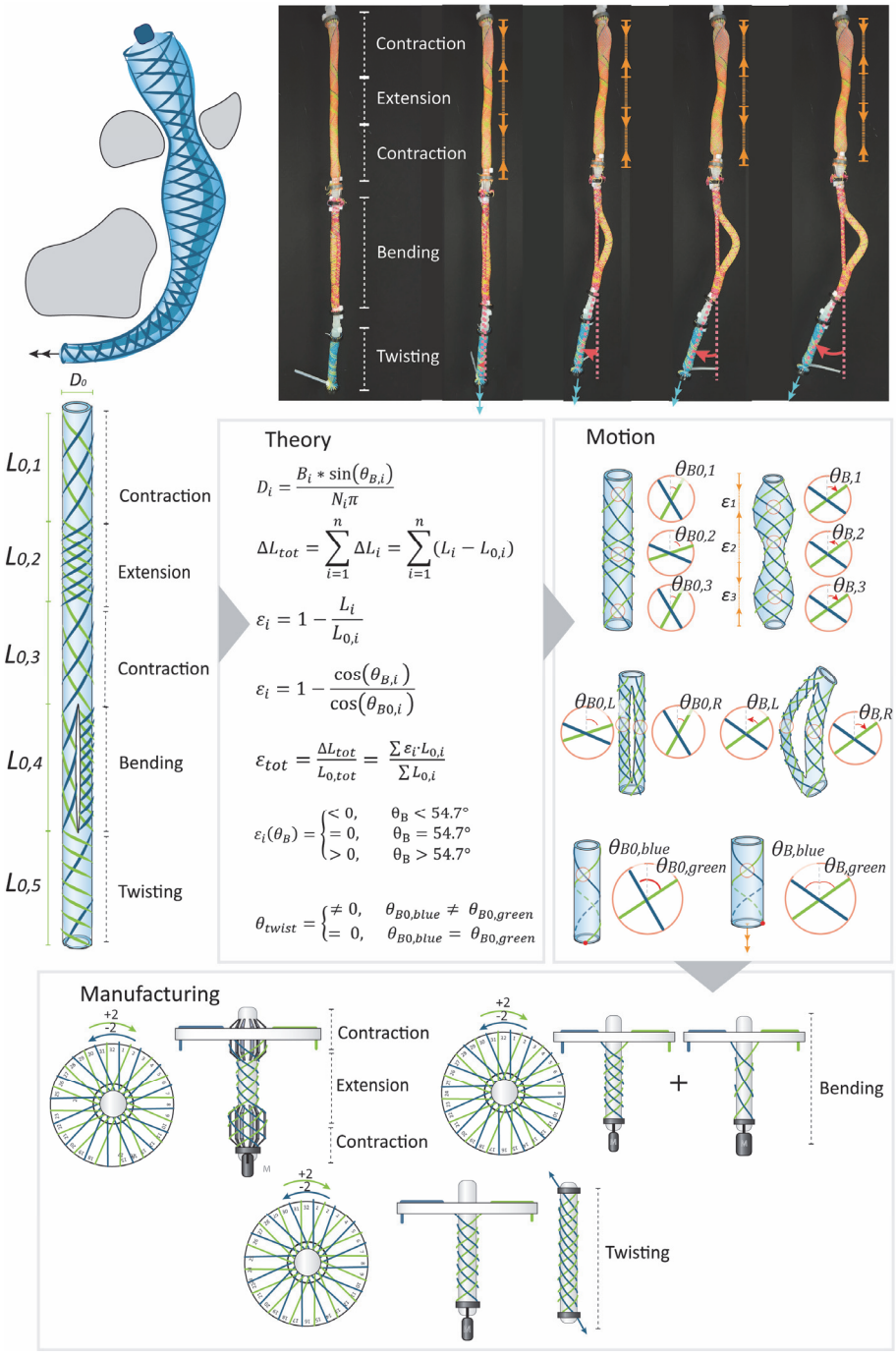


Figure 7.9: Proof of concept of a modular McKibben Artificial Muscle. Top: Prototyped McKibben AM including contraction/extension sequences, a bending module, and a twisting module. Bottom: Guideline overview for the design of a modular McKibben AM for complex motion.

Nevertheless, the current setup was sufficient to capture consistent and repeatable results, clearly illustrating the overall deformation trends.

Force characterization was not included in this study, as the focus was on deformation behavior rather than maximizing force output. Since the fundamental configuration of McKibben actuators remains unchanged, the local braid adaptations introduced here are not expected to significantly affect their intrinsic force-generation behavior. Future work will include quantitative testing under load to verify this.

No degradation was observed during the experimental period, the variability between cycles remained low (see Figure 7.6 and 7.7), but long-term cyclic testing will be required to evaluate durability. Applying adhesives at wire crossover points may prevent fiber sliding and extend actuator lifetime, as demonstrated by Kobayashi *et al.* [22].

Alternative actuation methods, such as (electro)magnetism or temperature-driven mechanisms, could enhance the responsiveness of intelligent McKibben AMs to their environment. This opens opportunities for untethered and energy-efficient actuators. In addition, the effects of both downscaling and upscaling on the deformation profile of the AM should be assessed. The current design provides a strong foundation for scalability, as the global behavior of the McKibben AM is inherently defined by its physical structure, reducing the need for complex control systems.

Embodied intelligent AMs offer strong potential for integration into soft robotic arms that require complex deformation profiles while maintaining simple control schemes. This is particularly valuable in applications involving constrained or hard-to-reach environments. Additionally, these mechanically encoded AMs can simplify the design of soft exoskeletons and prosthetics by enabling complex movements through lightweight and low-complexity actuation. Beyond wearable robotics, the developed AMs may also be applied in bioinspired systems such as artificial organs and continuum robotic arms, where they can generate complex motions using simple inputs within a compact, space-efficient structure.

7.5 Conclusion

This study demonstrated that complex motion in McKibben artificial muscles (AMs) can be adaptable by design, without complex control systems. Inspired by the decentralized actuation strategies of biological systems such as the octopus, we developed embodied intelligent AMs whose global deformation behavior is embedded by local interactions between the braided sleeve and the inner bladder. This highly reduces the complexity of both their actuation and system architecture, just by designing the actuator for a pre-defined motion. By tailoring the braiding angle along the actuator's length, a modular design approach within a singular McKibben AM can be deployed. Different motion types are locally embedded, such as contraction, extension, twisting and bending. This creates opportunities for the implementation of McKibben AMs in complex environments which require advanced motions and space-efficient systems, such as bioinspired artificial organs, continuum robotic arms, wearable exoskeleton, prosthetics or surgical robotics.

Manufacturing strategies were developed that preserve the simplicity of conventional braiding techniques used in commercial McKibben AMs. As a result, material costs remain low and the production process is highly scalable. While the study used manual braiding, an industrial braiding machine (such as maypole braiders) can easily execute a similar process to

reduce production time. Popular braided sleeve suppliers list product lines covering diameters ranging between 1-100mm with lengths of several meters, showcasing the potential for scaling. Further advancements in automated braiding machines could enable precise spatial control of the braiding angle along the McKibben AM, increasing its deformation accuracy and repeatability for large-scale manufacturing. This scalability increases the potential to transfer mechanically encoded McKibben AMs from a laboratory setting into commercially implementation in real-world systems. Additionally, embedding alternative actuation methods, such as (electro)magnetism or temperature-driven mechanisms, would enhance the responsiveness of intelligent McKibben AMs even further. This enables untethered operation in mobile and wearable applications.

Implementation of these embodied intelligent AMs reduces their reliance on complex controllers or bulky multi-actuator setups. In the long term, these actuators could serve as building blocks for fully soft robotic systems with embedded intelligence, capable of responding to their environments through physical programming.

References

[1] H. Tomori and T. Nakamura, "Theoretical comparison of McKibben-type artificial muscle and novel straight-fiber-type artificial muscle," *International Journal of Automation Technology,* vol. 5, no. 4, pp. 544-550, 2011, doi: 10.20965/ijat.2011.p0544.

[2] H. F. Schulte and J. R. Pearson, "Characteristics of the braided fluid actuator," 1961.

[3] R. Kang, D. T. Branson, T. Zheng, E. Guglielmino, and D. G. Caldwell, "Design, modeling and control of a pneumatically actuated manipulator inspired by biological continuum structures," *Bioinspiration & biomimetics,* vol. 8, no. 3, p. 036008, 2013, doi: 10.1088/1748-3182/8/3/036008.

[4] E. Papadakis, D. P. Tsakiris, and M. Sfakiotakis, "An Octopus-Inspired Soft Pneumatic Robotic Arm," *Biomimetics,* vol. 9, no. 12, p. 773, 2024, doi: 10.3390/biomimetics9120773.

[5] K. Suzumori, S. Wakimoto, K. Miyoshi, and K. Iwata, "Long bending rubber mechanism combined contracting and extending tluidic actuators," in *2013 IEEE/RSJ international conference on intelligent robots and systems*, 2013: Ieee, pp. 4454-4459, doi: 10.1109/IROS.2013.6696996.

[6] J. Zou *et al.*, "Muscle-fiber array inspired, multiple-mode, pneumatic artificial muscles through planar design and one-step rolling fabrication," *National Science Review,* vol. 8, no. 10, p. nwab048, 2021, doi: 10.1093/nsr/nwab048.

[7] Z. Lin, Q. Shao, X.-J. Liu, and H. Zhao, "An anthropomorphic musculoskeletal system with soft joint and multifilament pneumatic artificial muscles," *Advanced Intelligent Systems,* vol. 4, no. 10, p. 2200126, 2022, doi: 10.1002/aisy.202200126.

[8] T. Doi, S. Wakimoto, K. Suzumori, and K. Mori, "Proposal of flexible robotic arm with thin McKibben actuators mimicking octopus arm structure," in *2016 IEEE/RSJ International Conference on Intelligent Robots and Systems (IROS)*, 2016: IEEE, pp. 5503-5508, doi: 10.1109/IROS.2016.7759809.

[9] H. Sato *et al.*, "Development of a compact pneumatic valve using rotational motion for a pneumatically driven mobile robot with periodic motion in a pipe," *IEEE Access,* vol. 9, pp. 165271-165285, 2021, doi:10.1109/ACCESS.2021.3135035.

[10] Y. Mano, R. Ishikawa, Y. Yamada, and T. Nakamura, "Development of high-speed type peristaltic crawling robot for long-distance and complex-line sewer pipe inspection," in *2018 IEEE/RSJ International Conference on Intelligent Robots and Systems (IROS)*, 2018: IEEE, pp. 8177-8183, doi: 10.1109/IROS.2018.8593436.

[11] R. Pfeifer and J. Bongard, *How the body shapes the way we think: a new view of intelligence*. MIT press, 2006.

[12] C. Laschi and M. Cianchetti, "Soft robotics: new perspectives for robot bodyware and control," *Frontiers in bioengineering and biotechnology,* vol. 2, p. 3, 2014.

[13] D. Zambrano, M. Cianchetti, and C. Laschi, "The morphological computation principles as a new paradigm for robotic design," in *Opinions and outlooks on morphological computation*: University of Zurich, 2014, pp. 214-225.

[14] D. Howard, A. E. Eiben, D. F. Kennedy, J.-B. Mouret, P. Valencia, and D. Winkler, "Evolving embodied intelligence from materials to machines," *Nature Machine Intelligence,* vol. 1, no. 1, pp. 12-19, 2019, doi: 10.1038/s42256-018-0009-9.

[15] D. Sangian, "From Traditional Braiding Methods to Additive Manufacturing for Fabricating Mckibben Artificial Muscles," *Biomed. J. Sci. Tech. Res,* vol. 38, no. 5, 2021, doi: 10.26717/BJSTR.2021.38.006211.

[16] W. Tian, S. Wakimoto, D. Yamaguchi, and T. Kanda, "Fabrication process for twisting artificial muscles by utilizing braiding technology and water-soluble fibers," *IEEE Robotics and Automation Letters,* vol. 9, no. 4, pp. 3147-3154, 2024, doi: 10.1109/LRA.2024.3360817.

[17] S. Yahara, S. Wakimoto, T. Kanda, and K. Matsushita, "McKibben artificial muscle realizing variable contraction characteristics using helical shape-memory polymer fibers," *Sensors and Actuators A: Physical,* vol. 295, pp. 637-642, 2019, doi: 10.1016/j.sna.2019.06.012.

[18] F. Connolly, C. J. Walsh, and K. Bertoldi, "Automatic design of fiber-reinforced soft actuators for trajectory matching," *Proceedings of the National Academy of Sciences,* vol. 114, no. 1, pp. 51-56, 2017, doi: 10.1073/pnas.1615140114.

[19] M. A. Horvath *et al.*, "Towards alternative approaches for coupling of a soft robotic sleeve to the heart," *Annals of biomedical engineering,* vol. 46, pp. 1534-1547, 2018, doi: 10.1007/s10439-018-2046-2.

[20] Society of Automotive Engineers Fluid Conductors and Connectors Technical Committee, "Wire Braid Angle Response Characteristics in Hydraulic Hose," *SAE Transactions,* vol. 106, pp. 107-26, 1997, doi: 10.4271/972706.

[21] E. T. Roche *et al.*, "Soft robotic sleeve supports heart function," *Science translational medicine,* vol. 9, no. 373, p. eaaf3925, 2017, doi: 10.1126/scitranslmed.aaf3925.

[22] R. Kobayashi, H. Nabae, Z. Mao, G. Endo, and K. Suzumori, "Enhancement of Thin McKibben Muscle Durability Under Repetitive Actuation in a Bent State," *IEEE Robotics and Automation Letters,* 2024, doi: 10.1109/LRA.2024.3455890.

Appendix 7.A

The neutral angle is well-defined in classical hose theory and can be derived as follows [1]:

$$F_H = \frac{PDL}{2} \tag{A.1}$$

$$F_L = \frac{PD^2\pi}{4} \tag{A.2}$$

$$\tan(\theta_R) = \frac{F_L}{F_H} = \frac{2L}{D\pi} \tag{A.3}$$

$$L = \frac{D\pi}{\tan(\theta_R)} \tag{A.4}$$

$$\tan(\theta_R) = \frac{2}{\tan(\theta_R)} \tag{A.5}$$

$$\tan^2(\theta_R) = 2 \tag{A.6}$$

$$\theta_R = \theta_B = \tan^{-1}\sqrt{2} = 54.7° \tag{A.7}$$

$$S_1 = N_1\sqrt{p_1^2 + (\pi D)^2} \tag{A.8}$$

$$S_2 = N_2\sqrt{p_2^2 + (\pi D)^2} \tag{A.9}$$

$$S_1' = N_1'\sqrt{p'^2_1 + (\pi D')^2} \tag{A.10}$$

$$S_2' = N_2'\sqrt{p'^2_2 + (\pi D')^2} \tag{A.11}$$

$$N_1' = N_1\frac{\sqrt{p_1^2+(\pi D)^2}}{\sqrt{p'^2_1+(\pi D')^2}} \tag{A.12}$$

$$N_2' = N_2\frac{\sqrt{p_2^2+(\pi D)^2}}{\sqrt{p'^2_2+(\pi D')^2}} \tag{A.13}$$

$$\Delta N = N_1' - N_2' \tag{A.14}$$

$$\theta_{twist} = 360° \cdot \Delta N \tag{A.15}$$

[1] Society of Automotive Engineers Fluid Conductors and Connectors Technical Committee, "Wire Braid Angle Response Characteristics in Hydraulic Hose," *SAE Transactions*, vol. 106, pp. 107-26, 1997, doi: 10.4271/972706.

CHAPTER 08

DESIGN OF AN ARTIFICIAL MUSCULAR NETWORK

ABSTRACT

McKibben Artificial Muscles (AMs) are widely used in soft robotics as actuators due to their compliance and high force output. However, achieving complex motions with multiple AMs in different orientations remains challenging, as each requires a bulky pneumatic or hydraulic system, complicating assembly and increasing the risk of leaks. These limitations restrict their use in compact or lightweight applications. Inspired by natural muscle architectures that optimize force distribution and enable multidirectional motion, this study aims to integrate complex fiber arrangements into a single McKibben AM. A novel fabrication technique was developed using an interplay between multiple traditional Japanese Kumihimo braiding discs to create multi-directional AMs. Two case studies demonstrate the approach: (1) a bending actuator capable of achieving programmed bending angles depending on actuation pressure, and (2) a convergent actuator whose combined branches reconfigured output force direction to extend motion range. The resulting branched AMs locally encode complex motion within their structure, eliminating the need for complex actuator systems. This manufacturing strategy advances McKibben AM design towards more compact, adaptive, and versatile systems for advanced soft robotic applications.

Published as:
Kortman, V. G., Sakes, A., & Jovanova, J. (2026). Advancing McKibben Artificial Muscles: Bio-Inspired Design for Complex Motion. *Journal of Intelligent Material Systems and Structures*, 1045389X261484720.

8.1 Introduction

Biological muscle tissues have long captivated the scientific community, acting as exceptional actuators. They are capable of generating large contraction forces, rapid movements and they finely tune movements through the coordinated action of millions of microscopic fibers. These muscles acted as inspiration source for the development of McKibben Artificial Muscles (AMs). Their compliance, large blocked forces, high contraction ratios and fast response time make them popular for a wide range of applications. McKibben AMs have a relatively simple structure, consisting of an inner bladder wrapped in a braided sleeve (Figure 8.1). When pressurizing the inner bladder, it expands in volume, increasing its diameter. This radial expansion causes the surrounding braided sleeve to deform. As the braid's wires shift and rotate around their contact points, the sleeve shortens or elongates due to its geometry. This way, the sleeve converts the actuator's radial deformation into either a contraction or an extension. These actuators are frequently embedded in cases where adaptivity and safety are needed for interaction with humans, such as prosthetics or robotic rehabilitation, due to their soft material characteristics. Or in cases that require lightweight systems, including continuum robotics. Their simple design allows them to be produced using standard industrial manufacturing methods, making them commercially available. A large body of literature exists on their behavior, control and applications [1-3]. To provide new readers with a practical overview of this field, Kortman *et al.* [4] systematically analyzed working principles, performance characteristics and emerging configurations of McKibben AMs.

While traditional McKibben AMs are effective soft actuators, they fall short in matching the complex architecture of biological muscle tissue. In nature, muscle architecture is not solely cylindrical and muscle movement is not solely axial. Muscle fibers act as a system that optimizes performance through intelligent force distribution, redirection, and navigation [5]. In parallel muscles, such as the *biceps brachii*, fibers run along the muscle's line of action, producing long contractions and rapid movement [6]. Pennate muscles, like the *deltoid*, arrange their fibers at an angle to the tendon, allowing more fibers to pack into a given volume and thereby increasing force [6]. Convergent muscles, such as the *pectoralis major*, distribute fibers across multiple origins (mounting points) while converging to a single insertion (output point), enabling complex directional control and adaptable force output depending on which fibers are activated [7]. Even more complex arrangements, like the interwoven fibers of the tongue, the bypassing flexor tendons of the fingers or the interconnected fibers of cardiac tissue, allow for highly localized and precise control of movement.

Current research focused on McKibben muscular architecture has explored multiple strategies to enhance performance. One approach arranged multiple McKibben AMs in an angular, pennate configuration, resulting in adaptive pull forces and contraction rates [8]. Kurumaya *et al*. [9] bundled thin McKibben AMs into multi-filament systems, mimicking skeletal muscles with parallel fiber arrangements and achieving increased contraction rates. Other efforts to expand the range of motion of McKibben AMs have mainly focused on embedding bending capabilities. These systems typically assemble multiple McKibben AMs that are individually actuated, producing asymmetric motion [10-13]. While these examples of McKibben AM systems with advanced architectures proved effective in generating

multidirectional movement, these designs require complex actuator systems, including a cumbersome tubing system, connectors, and compressors/pumps. This results in an increase in weight, volume, and rigid components, which limits their practicality in constrained spaces and reduces comfort during human interaction. Consequently, current McKibben designs remain restricted in their ability to vary force direction or produce multidimensional motion while maintaining their design simplicity. Additionally, Kortman *et al.* [14] developed a novel manufacturing technique to fabricate McKibben artificial muscles (AMs) with locally varying braiding angles. This enables the creation of actuators with advanced deformation profiles along their length, such as localized contraction, extension or twisting. However, these actuators remain limited to standard single cylindrical architectures and are therefore unable to replicate the complex structural organization found in biological muscle tissue. Advanced silicone-based soft actuators have been developed while showcasing rich deformation capabilities, fabricated with specialized fabrication methods such as bubble casting [15]. However, these approaches lack the fabrication simplicity and industrial scalability characteristic of McKibben AMs.

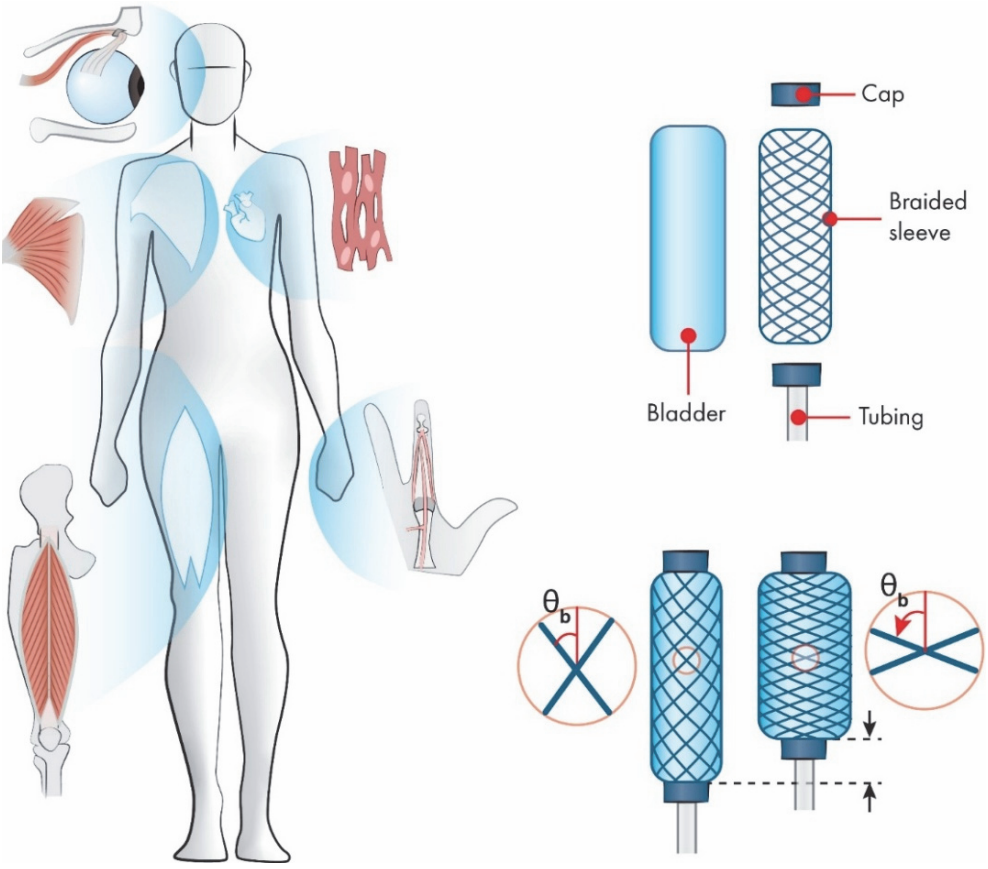


Figure 8.1: From muscular tissue to artificial muscles. Left: The complex architecture of human muscles. Right: Schematic representation of a McKibben Artificial Muscle (AM). Expansion of the inner bladder results in contraction or extension of the actuator, depending on the braiding angle θ_B.

Therefore, the goal of this study is to embed complex muscle architecture into the embodiment of a monolithically braided McKibben Artificial Muscle to advance its range of motion.

8.2 Braiding for multi-directional McKibben Muscles

8.2.1 Braiding Technique

To embed complex muscle architecture within a monolithic McKibben AM, a novel manufacturing method had to be developed. The focus lays on adapting the braiding technique of the AM's braided sleeve such that is allows to diverge into multiple output points and/or converge into a single mounting point. A key objective was to stick to conventional braiding technology to preserve the outstanding design simplicity of current McKibben AMs. Conventionally, braiding the McKibben AM's sleeve involves an industrial braiding machine, also known as a *Maypole braider* (Figure 8.2a). This machine manufactures the braided sleeve by interlacing a set of wires around a cylindrically shaped braiding mandrel. In the study by Kortman *et al.* [14], a traditional Japanese Kumihimo braiding disc was instead employed to produce braids with a similar braiding pattern, while offering greater flexibility to rapidly explore and iterate design parameters. This approach retains key constraints of the Maypole braider while enabling increased geometric freedom. The Naiki Gumi pattern, a hollow round braid, was used to manufacture the braided sleeve. Figure 8.2b illustrates the steps of this braiding pattern, replicating a similar braid as produced by an industrial braiding machine. In the present work, this manual braiding strategy is extended to enable the fabrication of more complex architectures, requiring modifications to support branched and multi-directional actuator designs. For multi-directional McKibben AMs two structural configurations are required:

(1) A diverging shape, where a main branch splits into sub-branches
(2) A converging shape, where sub-branches merge into a main branch

To create multiple sub-branches, a smart interplay between multiple braiding discs was employed. Figure 8.2c shows the developed manufacturing strategy for a braid with a main branch that splits into two sub-branches. The shape of the adopted mandrel corresponds to the shape of the desired McKibben AM, which is in this example an Y-shape. The braiding process starts with a single braiding disc that manufactures the main branch. At the junction, the wires are divided over two separate braiding discs. Afterwards, both sub-branches are braided separately with individual braiding discs. As visualized in Figure 8.2c, it is essential to interchange a few wires from both braiding discs at the junction, such that the cover ratio at the division lines at the junction remains constant. Otherwise the inner bladder of the AM will bulge through these gaps during pressurization. The mandrel can either be directly constructed using the inner bladder of the McKibben AM, or by a temporary structure that is replaced by the inner bladder after the braiding process.

The design parameters of the braided sleeve characterizes the performance of the McKibben AM. As shown in Equation (8.1), the muscle force (F_{muscle}) depends on design parameters such as the braiding angle θ_B [°], axial strain ε [-], muscle diameter D [mm] and

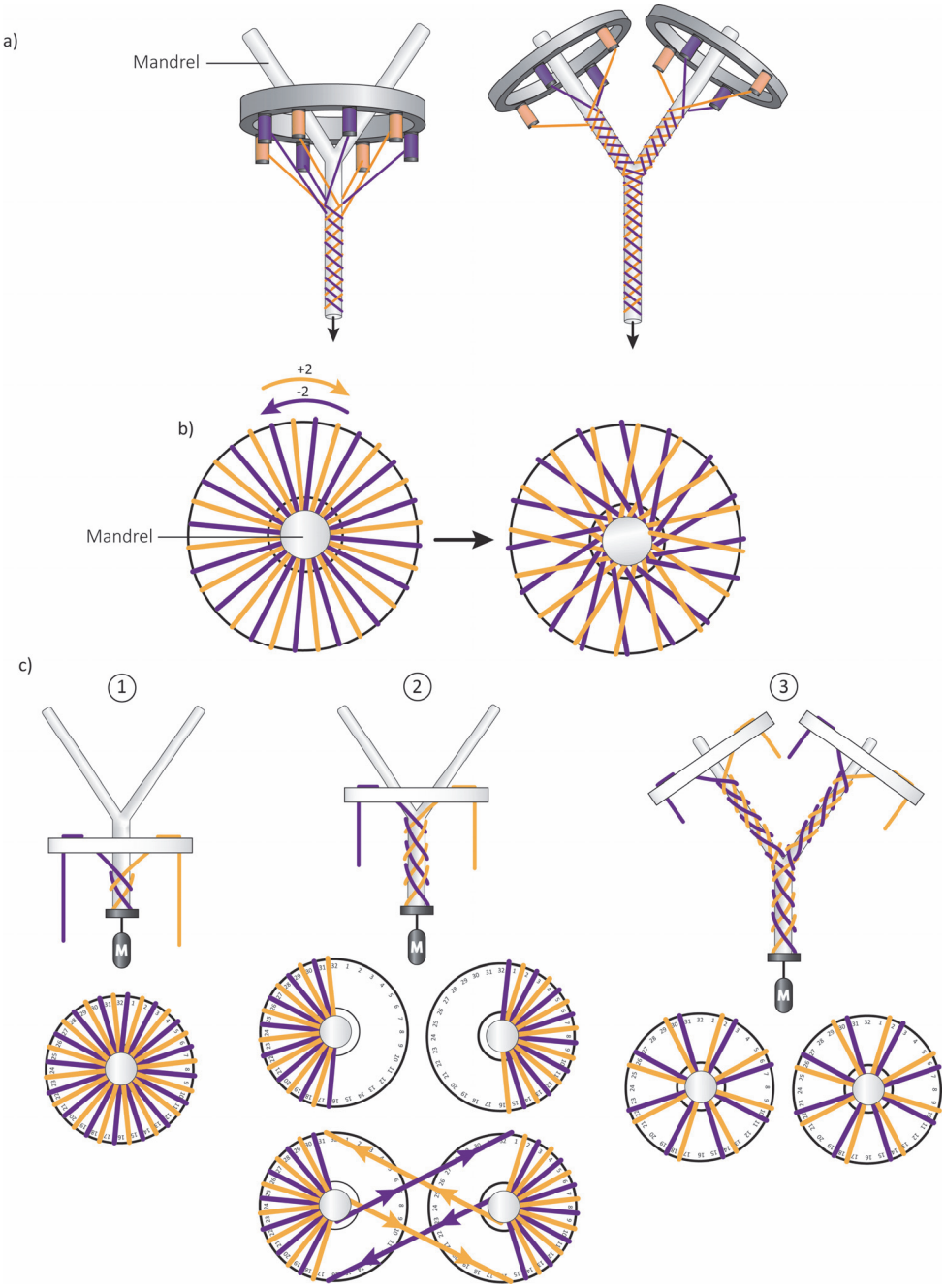


Figure 8.2: Manufacturing process of a braided sleeve with multi-directional architecture. a) Hollow round braid created around a mandrel using a conventional braiding machine. The mandrel is pulled at a constant speed for consistent braid parameters. b) Braiding pattern using a Kumihimo braiding disc to create a hollow round braid around a mandrel. c) Final manufacturing process. (1) Braiding the main branch with one braiding disc. (2) Dividing the wires over two braiding discs as the junction. (3) Braiding the sub-branches using separate braiding discs.

actuation pressure P [MPa]. The braiding angle θ_B defines the amount of maximum contraction or extension of the AM. The axial strain ε is defined as Equation (8.2), where L_0 [mm] is the initial length and L [mm] is the length of the AM after pressurization. The cover factor of the McKibben AM expresses number and geometry of the wires that make up the outer braided sleeve. It is defined as the ratio of area occupied by the wires within an area unit compared to the total area unit. As derived by Sangian *et al.* [16], the cover factor (C) is described by Equation (8.3) and depends on the braid diameter D [mm], the braiding angle θ_B [°], the wire width w_y [mm], and the number of wires m [-]. Together, these are the main parameters defining the output motion of the McKibben AM, making them essential in embedding the range of motion into an AM design. Additionally, the braiding angle θ_B on itself governs the deformation mode of the McKibben AM. A more detailed description of the underlying mechanisms can be found in the study by [14]. In summary, the braid angle defines the kinematic constraint imposed by the braid: low braid angles favor contraction, high braid angles favor extension, and a disbalance between braiding angles of opposing helical families induces twist. These relationships arise directly from the interaction between the braid and the inflating bladder.

$$F = \frac{\pi}{4} D^2 P \left(\frac{1}{sin\theta_B}\right)^2 \{3(1-\varepsilon)^2 \, cos^2\theta_B - 1\} \tag{8.1}$$

$$\varepsilon = \frac{L_0 - L}{L_0} \tag{8.2}$$

$$C = \frac{w_y m}{\pi D cos(\frac{\theta_B}{2})} - \left[\frac{w_y m}{2\pi D \cos(\frac{\theta_B}{2})}\right]^2 \tag{8.3}$$

7.2.2 Case Studies

To demonstrate the potential of monolithic McKibben AMs embedding a complex architecture, two case studies are conducted. The resulting actuator designs are intended as illustrative case studies to demonstrate the design flexibility enabled by the proposed manufacturing approach. The first one focuses on redirecting the contraction force of the McKibben AM to convert its linear movement into a bending motion. The second one focuses on distributing the contraction force of the McKibben AM over multiple attachment points to expand its range of motion.

Bending McKibben AM

A bending actuator composed of a monolithic McKibben AM is particularly interesting, as current bending actuators typically rely on a complex assembly of connected McKibben AMs. This requires a bulky pneumatic/hydraulic supply network, complex control systems and results in increased weight and volume. Single-unit bending McKibben AMs have been demonstrated by incorporating a constraining tendon to induce a curvature. However, this requires additional manual intervention during the manufacturing process as this step can not be integrated into the braiding procedure, making it impractical for large-scale production.

The architecture of a McKibben AM has to introduce an asymmetry into the structure to generate a bending motion. This asymmetry can be enforced by an architecture with

multiple sub-branches with different motion characteristics. This can, for example, be achieved by implementing a different braiding angle for both sub-branches. A braiding angle larger than 54 degrees results in an extending motion and a braiding angle smaller than 54 degrees results in a contracting motion. Shifting the braiding angle away from this transition point of 54 degrees results in either a larger contraction or a larger extension. Also, a difference in cover ratio induces a difference in contraction or extension, due to geometric constraints between the wires.

For this case study, a prototype was built that consists of a main branch that diverges into two sub-branches and along its length converges back towards its main branch. Figure 8.3 shows how the braiding procedure of this bending McKibben AM proceeds, as an extension of Figure 8.2c. It should be noted that the mandrel is initially Y-shaped, meaning both sub-branches are braided separately, after which the branches are brought together to converge them back into the main branch. The braid parameters are kept constant over the length of the AM by attaching a weight onto the mandrel to pull the mandrel with constant speed through the braiding disc. At the first junction, the wires are divided over two braiding discs. Afterwards, both sub-branches are braided separately with individual braid parameters, such as different braiding angles. As showcased by Kortman et al. [14], different braiding angles can be achieved manually by adapting the weight that pulls the mandrel through the braiding disc. Arrived at the second junction, the wires from both braiding discs are merged on one braiding disc, continuing braiding the main branch. As mentioned in Subsection 8.2.1, it is essential to interchange a few wires from both braiding discs at the junction, such that the cover ratio at the division lines of this points remains constant. For the prototype, the braid consisted of 32 polyethylene (PE) wires with a 0.3 mm diameter (*Grappler 8, Shimano*). The initial braiding angles of the sub-branches were measured using a digital microscope (*Dino-Lite Edge AM73915MZTL*). One sub-branch is constructed of wires with a braiding angle of 64 degrees, which means this branch acts as an extending element. The other sub-branch is constructed by a double-wired braid around a small diameter mandrel, resulting in a dense configuration. Due to its high cover ratio, this sub-branch acts as a semi-static element. After braiding, the mandrel was replaced by a silicone bladder with a similar diameter. The semi-static sub-branch embedded a silicone bladder of 5 mm in diameter (*Netproshop*) and the large-diameter sub-branch embedded a silicone bladder of 10 mm in diameter (*Ecoflex 0030, Smooth-On*). The silicone bladder was covered by talcum powder (*Zwitsal*) to reduce the friction between the bladder and the braided sleeve, optimizing the deformation of the sleeve. As shown in Figure 8.4, the prototype demonstrates that asymmetric motion characteristics can be embedded into a multi-directional McKibben AM architecture.

Figure 8.3b illustrates the geometric schematic of the bending McKibben muscle system. The system consists of a main muscle branch that is fixed at its proximal end and splits into two subbranches at a distance (w) apart. After diverging, the subbranches converge back into a single distal branch terminating at point P. Equation (8.4) describes the relationship between the braiding angles of the individual branches (θ_{bi}) and their resulting lengths (L_i), which ultimately determines the bending motion of the actuator. Each branch behaves like a classical McKibben muscle. In the branched configuration, if two parallel subbranches have different braiding angles, pressurization creates a length

difference. Because the subbranches are connected at a fixed distance w, this length difference forces the structure to bend by bending angle (φ_P), determined by (8.5). The position of endpoint P in the plane (with the origin at the fixed base and the actuator initially aligned along the y-axis) can then be computed as (8.6) and (8.7). Equations (8.6) and (8.7) indicate that the overall range of motion can be easily tuned through simple adjustments of the main branch length. Specifically, adjusting the length of the first main branch (L_{m1}) shifts the rotation point *M*, while increasing the length of the second main branch (L_{m2}) acts as an amplification factor for the induced bending motion. This illustrates the versatility of branched actuator architectures, where small geometric modifications can produce substantial changes in the achievable range of motion.

$$L_i = L_i^0 \cdot \frac{\cos(\theta_{bi,0})}{\cos(\theta_{bi})} \tag{8.4}$$

$$\varphi_p = \arctan\left(\frac{L_2 - L_1}{w}\right) \tag{8.5}$$

$$y_M = L_{m1} + \frac{L1+L2}{2} \tag{8.6}$$

$$P = \left(x_M + L_{m2}\sin(\varphi_p), y_M + L_{m2}\cos(\varphi_p)\right) \tag{8.7}$$

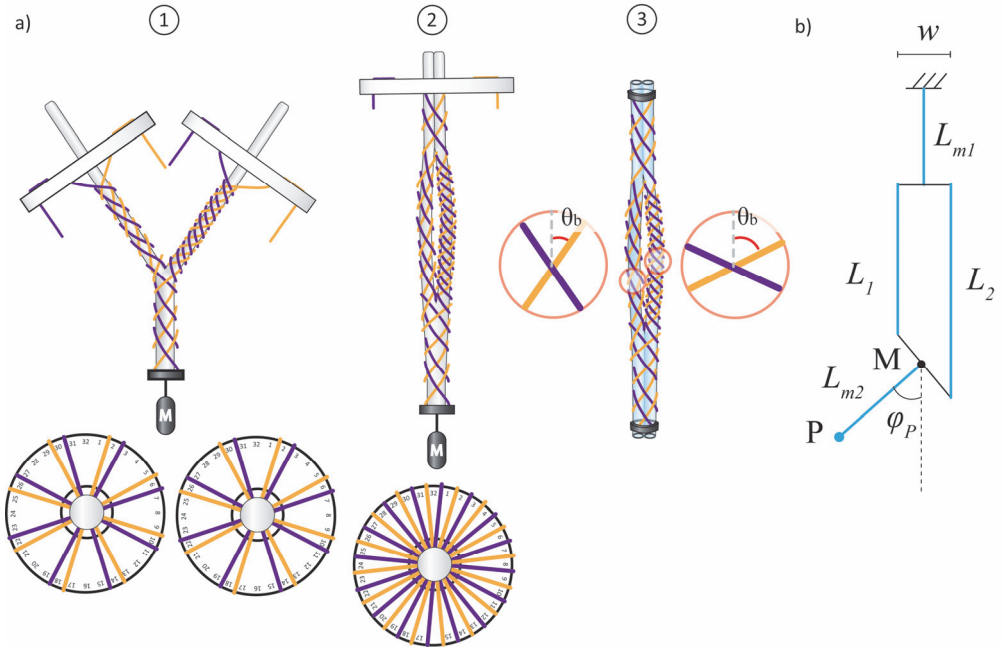


Figure 8.3: Manufacturing process of a bending McKibben AM. a) (1) The sub-branches are braided with different braid parameters to induce different motion characteristics. (2) At the second junction, the sub-branches are merged on one braiding disc and brought into the main branch. (3) The mandrel is replaced by the inner bladder, creating the McKibben AM. b) Geometric schematic of the bending actuator showing the lengths of the individual branches (L_i), the width between the branches (w) and the bending angle of endpoint P (φ_P).

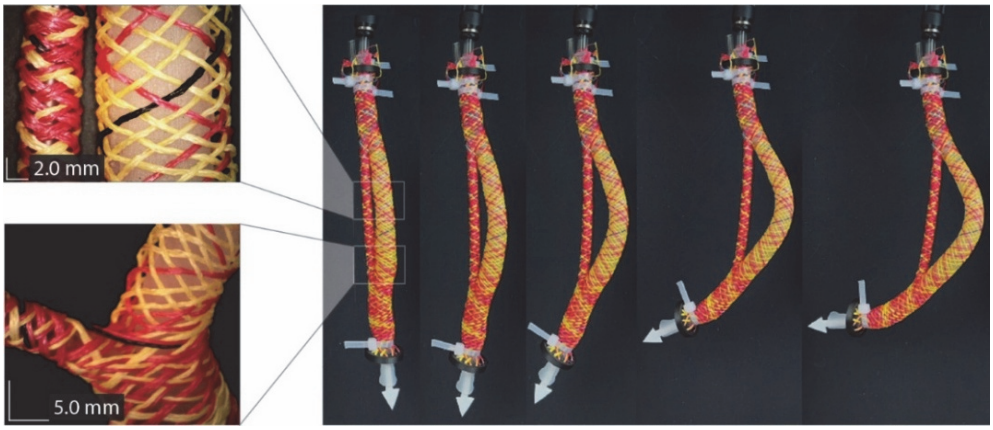


Figure 8.4: Final prototype of the bending McKibben AM. Left: Close-up of the sub-branches and the junction point. The initial braiding angle of both sub-branches is 64 degrees, with the small-diameter sub-branch having a larger cover ratio. Right: The asymmetric motion characteristics convert the linear deformation into a bending motion.

Convergent McKibben AM

The main skeletal muscle architectures in the human body consist of parallel, pennate (or angulated), convergent and circular fiber configurations. Convergent muscles have multiple origins (attachment points) with fibers that converge to a single tendon. These muscles are particularly interesting, as they can pull in different directions depending on which fibers are active. The branching fiber architecture lets the muscle act over a larger motion area. An example of a convergent muscle is the *Pectoralis Major*. This muscle originates from different points on the chest and converges to the upper arm. Contraction of the muscle's upper fibers results in and upward-forward motion of the arm, whereas contraction of its lower fibers results in inward-downward motion of the arm. Together, these fiber regions continuously reconfigure the output force, where the interplay between activated fibers determines both direction and magnitude of the resultant motion [7]. This principle of distributed force control for an extended range of motion is interesting for new AM geometries.

The multifilament McKibben AMs developed by Kurumaya *et al.* [9, 17] demonstrate the design freedom to imitate convergent muscle architectures such as the *Pectoralis Major*. They highlight the advantage of multifilament AMs in altering their point of force application and output force range through the number of bundled muscles. However, these multifilament systems still rely on the assembly of multiple individual McKibben AMs. A monolithic convergent McKibben AM would greatly simply the actuation system and fabrication process by adopting a non-assembly convergent braid. Additionally, bonding individual McKibben AMs together may exhibit similar motions, but the mechanics are distinctly different compared to monolithic braided McKibben AMs. The braids of bonded actuators remain independent and therefore tend to bend asymmetrically when only one unit is pressurized, often producing unintended curvature. In a monolithically braided design, the branches share a continuous braid, which suppresses this bending and results in a straight motion of the main branch when only one sub-branch is actuated.

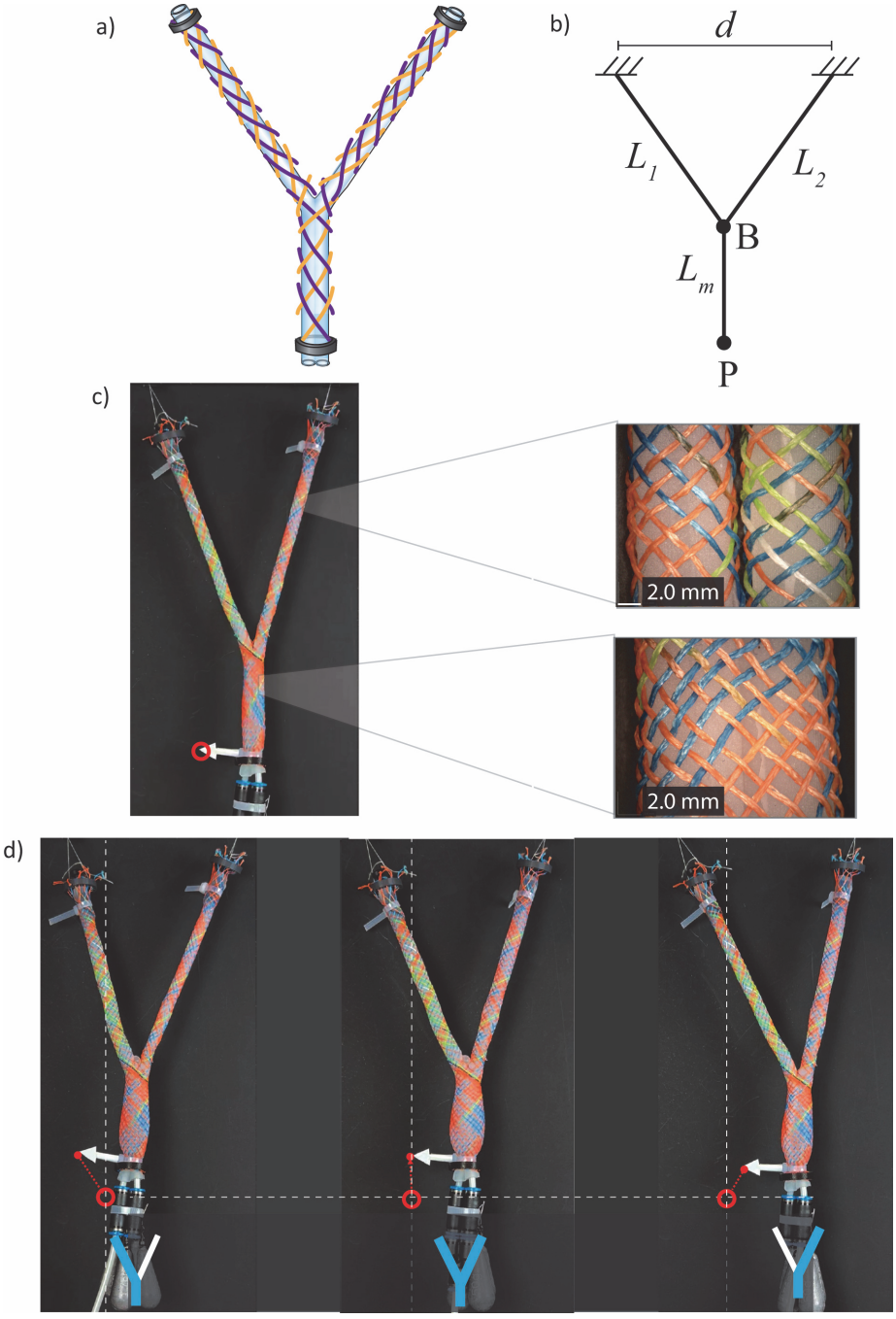


Figure 8.5: Final prototype of the convergent McKibben AM. a) Schematic representation of the Y-shaped convergent AM. b) Geometric schematic of the convergent AM showing the individual branch lengths (L_i) and the distance between the branches (d). c) The unpressurized McKibben AM, where the red circle highlight the start position. d) The AMs range of motion when the sub-branches are separately and simultaneously actuated.

To demonstrate the potential of a convergent McKibben AM, in this case study, a prototype was built that consists of a main branch that converges into two sub-branches. The braiding procedure illustrated in Figure 8.2c was followed to manufacture the required convergent McKibben AM, resulting in the prototype shown in Figure 8.5. Here, both sub-branches can be actuated separately, but can also be actuated as a co-working unit. The McKibben AM is divided into a lower part that exhibits linear movement and an upper part that exhibit an extended range of motion by the interplay between the actuated sub-branches. The braiding angles of the sub-branches were measured using a digital microscope (*Dino-Lite Edge AM73915MZTL*). In this prototype, the initial braiding angle of both sub-branches are kept approximately similar, namely 46 and 50 degrees. The main branch has an initial braiding angle of 49 degrees. The prototype demonstrates that a non-assembly convergent braid can be created using multiple braiding discs, to be integrated in a convergent McKibben AM.

Figure 8.5b illustrates the geometric schematic of the convergent McKibben muscle system. The system consists two subbranches that are fixed at their proximal ends at a distance (d) and merge into a single main branch at point B, which terminates at point P. Equation (8.8) describes the relationship between the braiding angles of the individual branches (θ_{bi}) and their resulting lengths (L_i), which ultimately determines the range of motion of the actuator. Again, each branch behaves like a classical McKibben muscle. The position of branch point B in the plane (with the origin at the fixed base and the actuator initially aligned along the y-axis) can then be computed as (8.9) and (8.10). Consequently, the position of endpoint P is described by (8.11). Importantly, the model demonstrates that varying contraction of the two subbranches shifts the location of the junction point B, thereby redirecting the orientation of the main branch. As a result, relatively small changes in branch geometry can produce substantial variations in the actuator's reachable workspace, further highlighting the versatility of branched McKibben architectures for generating diverse motions through simple geometric design modifications.

$$L_i = L_i^0 \cdot \frac{\cos(\theta_{bi,0})}{\cos(\theta_{bi})} \quad (8.8)$$

$$x_B = \frac{d^2 + L_1^2 - L_2^2}{2d} \quad (8.9)$$

$$y_B = \sqrt{L_1^2 - x_B^2} \quad (8.10)$$

$$P = (x_B, y_B + L_m) \quad (8.11)$$

8.3 Experiments

The main goal of the experiments was to investigate the potential of multi-directional McKibben AMs by measuring (1) the range of motion of the bending McKibben AM and (2) the range of motion of the convergent McKibben AM. Therefore, two experiments were performed, the first focusing on the bending motion and the second focusing on the convergent motion. Building on the study by Kortman *et al*. [14], these experiments demonstrate that McKibben AMs are not only capable of embedding complex deformation profiles through advanced braiding strategies, but can also be manufactured in branched

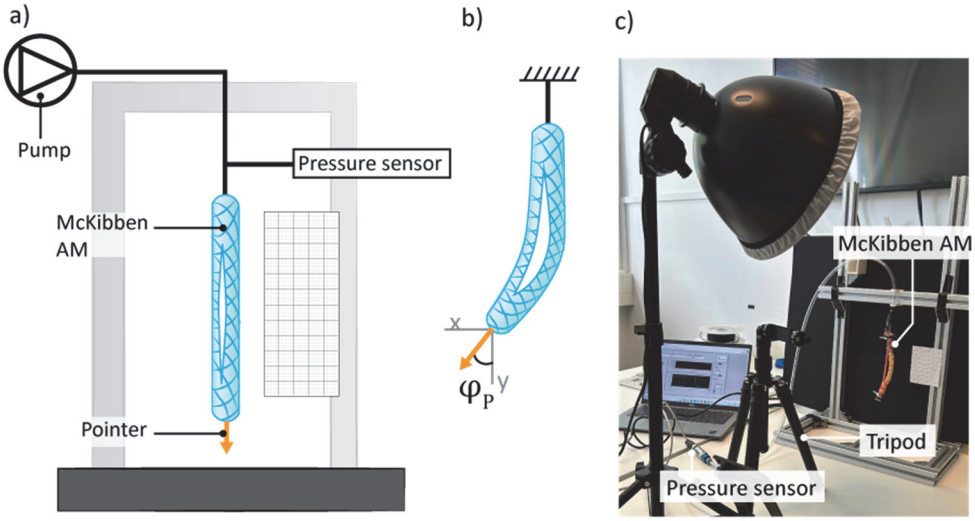


Figure 8.6: Overview of the experimental setup to evaluate the bending AM. a) Schematic Setup to track the motion of the bending AM. b) The bending angle (φ_P) is measured relative to the vertical axis moving along with the tip. c) Overview of the setup.

topologies inspired by biological systems. Such branched architectures substantially expand the attainable workspace compared with conventional McKibben designs.

8.3.1 Experimental Setup: Bending Actuator

The setup for demonstrating the bending AM is illustrated in Figure 8.6a. In this setup, the bending prototype was evaluated. A pointer was attached to the distal end of the AM as tracking point of the AM's tip during the bending motion. The McKibben AM was mounted vertically by clamping the proximal end to the main frame. The McKibben AM was connected to a manual pump with a pressure sensor in between (IFM electronic, PU5404). The motion of the AM was recorded by a camera positioned on a tripod in front of the main frame. The pressure sensor was connected to an analogue signal conditioner (CPJ RAIL, SCAIME) and a data acquisition unit set at a sampling rate of 20 Hz (NI USB-6008, National Instruments Corporation). Millimeter graph paper was placed next to the McKibben AM for calibration purposes.

The rotation angle of the McKibben AM's distal end was the main performance measure during this experiment. The bending angle was measured relative to the vertical axis moving along with the tip (Figure 8.6b). The bending angle was measured for different actuation pressures, ranging from 10 kPa to 50 kPa.

At the start of each measurement, the McKibben AM was positioned in a relaxed positioned. The pressure was increased in steps of 10 kPa till a maximum of 50 kPa was reached, which was monitored in LabVIEW 2018. The subsequent pressure steps were indicated on the video footage by an auditory signal. Five trials per condition were performed. The video footage was analyzed using *Tracker (6.1.7)* software (Open Source

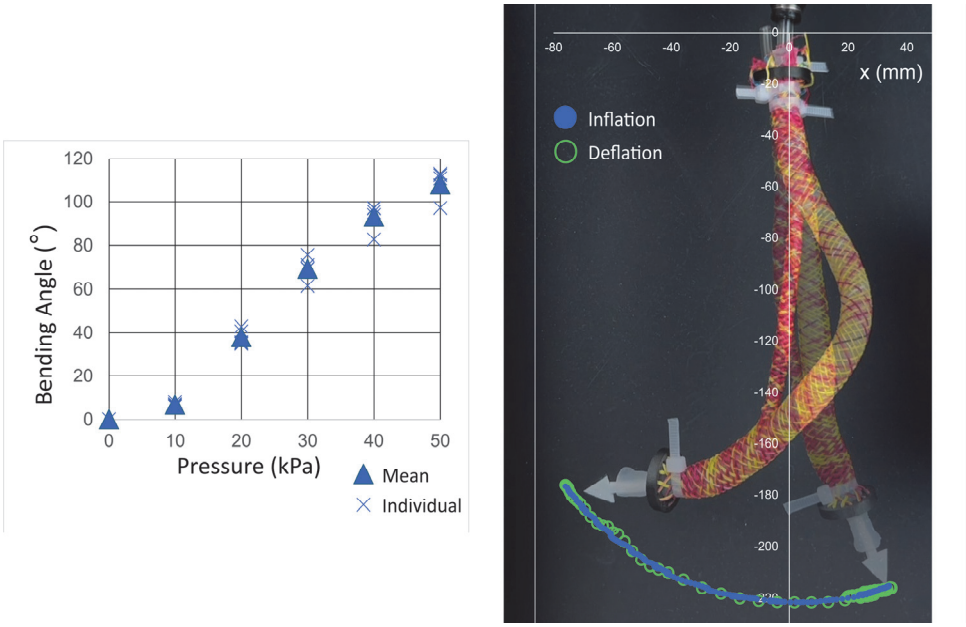


Figure 8.7: Results: Bending McKibben AM. Left: The bending angle (φ_P) for different actuation pressures. The solid triangles indicate the mean rotation angles, where the crosses indicate the individual measurements (n=5). Right: The tracked motion of the AMs tip. The blue and green tracking points indicate the inflation and deflation cycles, respectively.

Physics). Here, the bending angle of the tip was extracted by tracking the tip of the arrow. The videos were calibrated using the millimeter graph paper.

8.3.2 Results: Bending Actuator

Figure 8.7 shows the bending angle and tracked bending motion of the McKibben AM's tip. It has a mean rotation angle of 6.8°, 37.8°, 69.5°, 93.3° and 108.2° for an actuation pressure of respectively 10 kPa, 20 kPa, 30 kPa, 40 kPa and 50 kPa. The maximum measured bending angle is 112.9°.

8.3.3 Experimental Setup: Convergent Actuator

The setup for demonstrating the convergent AM is illustrated in Figure 8.8. In this setup, the convergent prototype was evaluated. A horizontal arrow was attached to the distal end of the AM as tracking point of the AM's tip during its motion. The McKibben AM was mounted vertically by clamping the sub-branched ends to the main frame with 50 mm distance in between. The McKibben AM was connected to a manual pump with a pressure sensor in between (IFM electronic, PU5404). The motion of the AM was recorded by a camera positioned on a tripod in front of the main frame. The pressure sensor was connected to an analogue signal conditioner (CPJ RAIL, SCAIME) and a data acquisition unit set at a sampling rate of 20 Hz (NI USB-6008, National Instruments Corporation). Millimeter graph paper was placed next to the McKibben AM for calibration purposes. A 200 grams

load was attached to the main branch of the AM. The motion of the AM was tracked for three different conditions:

- Left sub-branch pressurized
- Right sub-branch pressurized
- Both sub-branches pressurized

At the start of each measurement, the McKibben AM was positioned in a relaxed positioned. The pressure was increased to 40 kPa, which was monitored in LabVIEW 2018. The video footage was analyzed using *Tracker (6.1.7)* software (Open Source Physics). Here, the coordinates of the tip were extracted by tracking the tip of the arrow. The videos were calibrated using the millimeter graph paper. Additionally preliminary force measurements were done to provide an indication of the load-bearing capacity of the prototype in its current form. The tip of the AM was fixated and the generated force measured using a loadcell (Futek), while being inflated by a pressure of 40 kPa. In total, five measurements were conducted.

8.3.4 Results: Convergent Actuator

Figure 8.9 presents the tracked coordinates of the convergent McKibben artificial muscle (AM) over the course of the experiment. The plot illustrates how the actuator's position changes during inflation and deflation. The system produces an average maximum force of 7.4 ± 0.007 N. This value reflects the peak performance achieved consistently across five trials.

8.4 Discussion and Conclusion

The goal of this study was to embed complex muscle architectures into a monolithically braided McKibben Artificial Muscle (AM) to enhance its range of motion. While traditional McKibben AMs are effective soft actuators, they fall short in replicating the intricate architecture of biological muscle tissue. In biological systems, muscle fibers form well-tuned arrangements that optimize performance through intelligent force distribution, redirection, and navigation. This allows them to vary their force direction and, therefore, produce multidimensional motion.

To translate these principles into artificial muscle design, a novel manufacturing method was developed. The focus lay on adapting the braiding technique of the AM's outer sleeve so that it could diverge into multiple output branches and/or converge into a single mounting point. This approach results in a non-assembly, multi-directional braid. A key objective was to retain compatibility with conventional braiding technology to preserve the outstanding simplicity of McKibben AMs. To create a braid with complex architecture, a smart interplay between multiple braiding discs was employed, which resulted in a multi-directional braid. Together with playing the braid parameters, an extended range of motion was embedded in the AM design.

Two case studies were conducted to demonstrate the benefits of multi-directional McKibben AMs: (1) a bending actuator, and (2) a convergent actuator. The bending actuator was created by introducing an asymmetry into the architecture. It consisted of a

monolithically braided McKibben AM featuring a main branch that diverged into two sub-branches and subsequently reconverged. Each sub-branch embedded different motion characteristics by braiding with different cover ratios, enforcing the motion asymmetry. Experiments showed that this configuration achieved a maximum bending angle of 113°, with the bending–pressure curve exhibiting an initial slow-rising phase followed by an

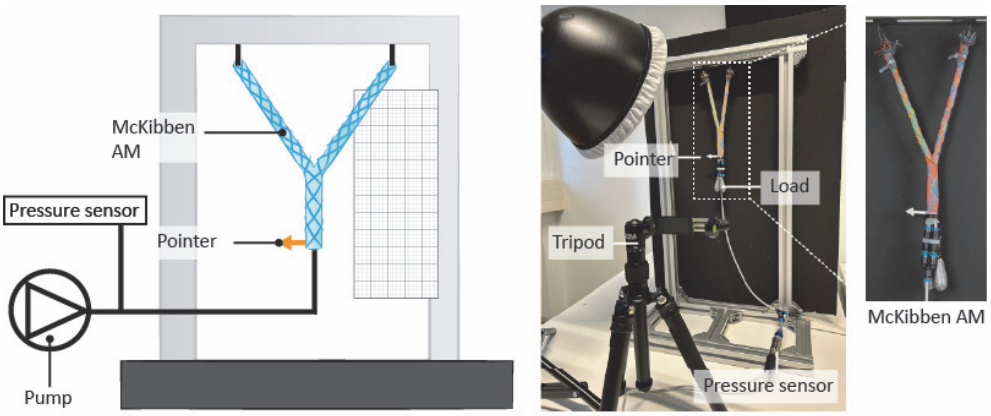


Figure 8.8: **Experimental setup to evaluate the range of motion of the convergent AM.**

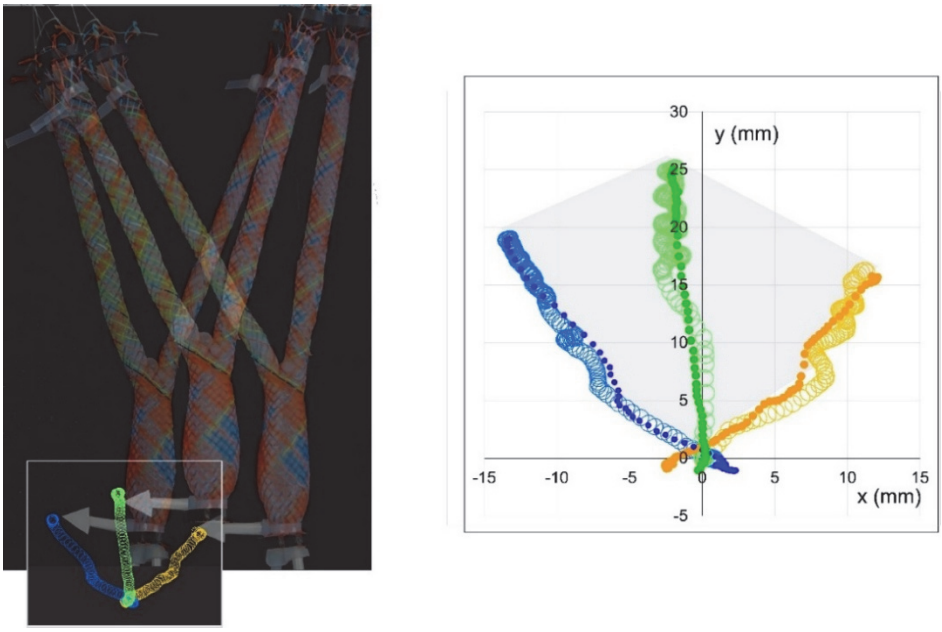


Figure 8.9: Results: Convergent McKibben AM. The tracked motion of the tip of the convergent AM. The blue circles indicate the left sub-branch pressurized condition, the yellow circles indicate the right sub-branch pressurized condition and the green circles indicate the condition in which both sub-branches are pressurized. Open circles indicate the inflation cycle and solid circles the deflation cycle. The range of motion is indicated in grey.

approximately linear increase. The early nonlinearity is hypothesized to result from dead volume between the braid and the unpressurized bladder that fills before the braid begins to deform. This highlights the importance of accurately matching the diameters of the inner bladder and the braid for both the main branch and the sub-branches. The results show that a range of bending angles were programmed into the AM's embodiment, depending on the actuation pressure. The tracked motion followed a smooth, continuous curvature, confirming that a linear contraction can be transformed into a bending motion to increase the AM's motion range.

The convergent actuator extended the AM's motion range by embedding a convergent braid structure. In nature, convergent muscles can pull in different directions depending on which fiber regions are active, allowing operation across a larger motion space. A prototype was built consisting of a main branch converging into two convergent sub-branches, which could be actuated independently or simultaneously. Results showed that the range of motion was extended when both branches worked together, as the interplay between them reconfigured the output force direction. The tracking data indicate a difference between the inflation and deflation trajectories. This behavior may arise from hysteresis effects associated with viscoelasticity of the silicone bladder and frictional interactions between the braid and bladder. Also, video footage shows slight displacement due the lateral velocity during deflation from an angled configuration, which may further contribute to the observed differences between inflation and deflation paths. Minor inconsistencies, such as uneven bladder expansion and variations in manual braiding, may have influenced the motion symmetry, but overall, the prototypes successfully demonstrated the advantages of McKibben AMs with complex architectures.

Overall, braiding monolithic McKibben structures enables the creation of continuous muscular networks that are difficult to achieve with casting-based approaches. By splitting and re-joining the braid, branches are integrated directly into a single actuator, expanding the design space beyond local contraction, extension, or twist [14]. Within each branch, the local braid parameters define its deformation mode, while the overall architecture allows these branches to mechanically interact. This interaction between branches creates advanced motions such as bending or multi-axis curvature, providing new multimodal actuation possibilities.

Force characterization was not included in this study, as the focus was on motion behavior instead of maximizing force output. However, the presence of a junction

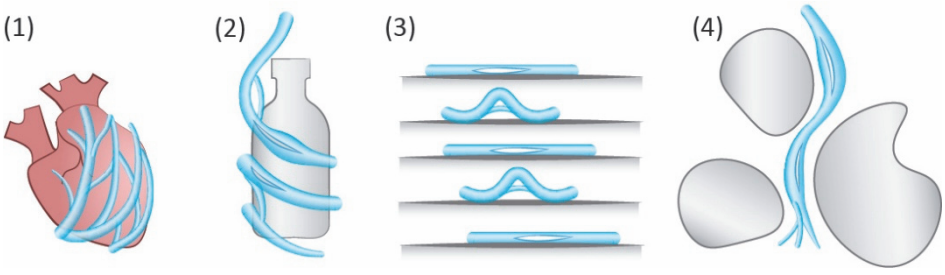


Figure 8.10: Potential applications for multi-directional McKibben AMs. (1) Muscular network acting compressing over surface. (2) Continuum gripper adapting to target object. (3) Actuator with complex locomotion sequence. (4) Continuum arm maneuvering obstacles environment.

inherently alters the load path, and future systematic blocked-force testing are required to quantify how much force is redirected through each branch. Importantly, compatibility with high-strength bladders and higher operating pressures makes that the force capacity of branched designs could approach that of conventional McKibben muscles when fabricated with optimized materials. Nevertheless, the mechanical behavior of the junction region remains an open challenge, which makes failure analysis will be essential to determine the practical limits the branched McKibben AM structure. Interestingly, [18] demonstrated in their study that bifurcated braided structures with controlled wire interchanges can maintain structural integrity under load.

Future research should focus on extending the proposed multi-directional AM architecture. Convergent muscles with a greater number of sub-branches could further expand the range of motion and enable more uniform force distribution over the contact surface. Braid parameters should be optimized for force output and range of motion. Predictive models should be developed to systematically explore the expanded design space introduced by branched McKibben architectures. These can be used to tailor the actuator design to specific performance requirements and applications. Increasing the number of sub-branches could promotes consistent contraction across a surface, analogous to cardiac tissue. Combining convergent and divergent sub-branches could enable localized bending, suitable for applications such as soft pumping systems. Figure 8.10 illustrates potential applications of these multi-directional AMs, including soft continuum arms that can navigate or wrap around objects, achieving multiple degrees of freedom in one integrated actuator.

Sub-branching introduces a geometric constraint: at each junction, the total number of reinforcing wires must be divided among the sub-branches, requiring smaller diameters to maintain a constant cover ratio, comparable to how blood vessels decrease in diameter as they branch. This should be accounted for in the design process. Despite this, the non-assembly braid structure enables easy fabrication with minimal assembly, reducing leakage risk and maintaining low material cost.

Manufacturing strategies were developed which underlying braiding principle is conceptually compatible with industrial braiding machines, ensuring scalability. While this study employed manual braiding, industrial maypole braiders can reproduce similar geometries with reduced production time. Commercial braided sleeves are already available in diameters ranging from 1–100 mm and lengths of several meters, indicating strong scalability potential. Advances in automated braiding could allow spatial control of braid angles, improving deformation accuracy and repeatability for large-scale production. However, direct scalability to conventional Maypole braiders is limited by the continuous nature of those machines. Implementing branched structures would require specialized automation, such as controlled bobbin transfers or modular braiding units capable of introducing branches without pausing the procedure. Nevertheless, similar automated systems exist already in cable manufacturing and textile engineering, where splicing and branching are achieved through adapted braiding machines, known for their use in 3D braiding [18-22]. These systems are commercially available for application fields such as medical devices [23, 24]. This demonstrates the potential for automation of branched McKibben muscles in future developments and could accelerate the transition of intelligent McKibben AMs from laboratory prototypes to commercial systems. Furthermore,

integrating alternative actuation methods, such as magnetic or thermally driven mechanisms, may enhance responsiveness and enable untethered operation in mobile and wearable applications, as shown in earlier work [25, 26]. Also, further integration of strategically designed braid parameters would advance the actuator's adaptability by design [14, 27]. Altogether, the novel manufacturing strategy expands the potential applications of McKibben AMs in more advanced and complex systems.

References

[1] B. Tondu, "Modelling of the McKibben artificial muscle: A review," *Journal of Intelligent Material Systems and Structures,* vol. 23, no. 3, pp. 225-253, 2012.

[2] Z. Zhang and M. Philen, "Pressurized artificial muscles," *Journal of Intelligent Material Systems and Structures,* vol. 23, no. 3, pp. 255-268, 2012.

[3] B. Kalita, A. Leonessa, and S. K. Dwivedy, "A review on the development of pneumatic artificial muscle actuators: Force model and application," in *Actuators*, 2022, vol. 11, no. 10: MDPI, p. 288.

[4] V. G. Kortman, J. Jovanova, H. Nabae, G. Endo, K. Suzumori, and A. Sakes, "Designing McKibben muscles: a critical review for practical implementation," *Bioinspiration & biomimetics,* vol. 21, no. 3, p. 031002, 2026.

[5] R. L. Lieber and J. Fridén, "Functional and clinical significance of skeletal muscle architecture," *Muscle & Nerve: Official Journal of the American Association of Electrodiagnostic Medicine,* vol. 23, no. 11, pp. 1647-1666, 2000.

[6] E. Duan and M. Bryant, "Design of Pennate Topology Fluidic Artificial Muscle Bundles Under Spatial Constraints," in *Smart Materials, Adaptive Structures and Intelligent Systems*, 2021, vol. 85499: American Society of Mechanical Engineers, p. V001T01A011.

[7] T. Lulic-Kuryllo, F. Negro, N. Jiang, and C. R. Dickerson, "Differential regional pectoralis major activation indicates functional diversity in healthy females," *Journal of Biomechanics,* vol. 133, p. 110966, 2022.

[8] T. Jenkins and M. Bryant, "Pennate actuators: force, contraction and stiffness," *Bioinspiration & Biomimetics,* vol. 15, no. 4, p. 046005, 2020.

[9] S. Kurumaya, H. Nabae, G. Endo, and K. Suzumori, "Design of thin McKibben muscle and multifilament structure," *Sensors and Actuators A: Physical,* vol. 261, pp. 66-74, 2017.

[10] J. Zou *et al.*, "Muscle-fiber array inspired, multiple-mode, pneumatic artificial muscles through planar design and one-step rolling fabrication," *National science review,* vol. 8, no. 10, p. nwab048, 2021.

[11] R. Kang, D. T. Branson, T. Zheng, E. Guglielmino, and D. G. Caldwell, "Design, modeling and control of a pneumatically actuated manipulator inspired by biological continuum structures," *Bioinspiration & biomimetics,* vol. 8, no. 3, p. 036008, 2013.

[12] E. Papadakis, D. P. Tsakiris, and M. Sfakiotakis, "An Octopus-Inspired Soft Pneumatic Robotic Arm," *Biomimetics,* vol. 9, no. 12, p. 773, 2024.

[13] K. Suzumori, S. Wakimoto, K. Miyoshi, and K. Iwata, "Long bending rubber mechanism combined contracting and extending tluidic actuators," in *2013 IEEE/RSJ international conference on intelligent robots and systems*, 2013: Ieee, pp. 4454-4459.

[14] V. G. Kortman, J. Jovanova, and A. Sakes, "Adaptable by design: encoding complex deformation profiles in mckibben artificial muscles," *Materials & Design,* p. 115188, 2025.

[15] T. J. Jones, E. Jambon-Puillet, J. Marthelot, and P.-T. Brun, "Bubble casting soft robotics," *Nature,* vol. 599, no. 7884, pp. 229-233, 2021.

[16] D. Sangian, J. Foroughi, S. Farajikhah, S. Naficy, and G. M. Spinks, "A bladder-free, non-fluidic, conductive McKibben artificial muscle operated electro-thermally," *Smart Materials and Structures,* Article vol. 26, no. 1, 2017, Art no. 015011

[17] S. Kurumaya, K. Suzumori, H. Nabae, and S. Wakimoto, "Musculoskeletal lower-limb robot driven by multifilament muscles," *Robomech Journal,* vol. 3, no. 1, p. 18, 2016.

[18] R. Miksch and F. Ficker, "Multi Bifurcation Branch Braided Structures on a Herzog Variation Braiding Machine," in *Recent Developments in Braiding and Narrow Weaving*: Springer, 2016, pp. 15-20.

[19] X. Yang *et al.*, "Rotary Three-Dimensional Braider Design Method Based on the Average Cutting Circle Strategy," *Engineering,* 2025.

[20] C. Emonts *et al.*, "Innovation in 3D braiding technology and its applications," *Textiles,* vol. 1, no. 2, pp. 185-205, 2021.

[21] A. Bogdanovich, "An overview of three-dimensional braiding technologies," *Advances in braiding technology,* pp. 3-78, 2016.

[22] M. Lengersdorf and T. Gries, "Three-dimensional (3D)-maypole braiding," in *Advances in braiding technology*: Elsevier, 2016, pp. 89-105.

[23] Teleflex Incorporated. "Bi/tri/quad-furcated braided structures." https://www.teleflexmedicaloem.com/suture-and-fiber-technologies-2/bifurcated-braids/ (accessed 21-01, 2026).

[24] Cortland Biomedical. "3D and Branch Braiding." https://www.cortlandbiomedical.com/braided-biomedical-textiles/ (accessed 21/01, 2026).

[25] V. G. Kortman, E. de Vries, J. Jovanova, and A. Sakes, "Unlocking Versatility: Magnetic-Actuated Deployable Suction Gripper for Complex Surface Handling," *Soft Robotics,* vol. 11, no. 6, pp. 1020-1031, 2024.

[26] V. G. Kortman, J. T. Hompes, A. Sakes, and J. Jovanova, "Kresling origami actuator with embedded electromagnetic actuation," *Smart Materials and Structures,* vol. 34, no. 6, p. 065018, 2025.

[27] V. G. Kortman, B. Mazzolai, A. Sakes, and J. Jovanova, "Perspectives on intelligence in soft robotics," *Advanced Intelligent Systems,* vol. 7, no. 1, p. 2400294, 2025.

CHAPTER 09

DESIGN OF AN ELECTRO-MAGNETIC KRESLING ACTUATOR

ABSTRACT

In nature, organisms such as the octopus and earthworm exhibit remarkable adaptability by dynamically reconfiguring their bodies into contracting and extending segments. Drawing inspiration from this flexibility, origami-inspired designs in robotics have proven effective in creating adaptable, deployable, and lightweight building blocks for modular robotic arms. The Kresling cylinder, a bistable cylindrical origami structure, exemplifies this approach by functioning as both a contracting and extending actuator. In this study, a standalone electromagnetically-actuated Kresling actuator was developed, consisting of a Kresling cylinder positioned between two electromagnets, each composed of a copper coil and a ferromagnetic core. The challenge lies in bridging the relatively large gap between the two ends of the Kresling cylinder, since the magnetic field strength decreases rapidly over length. A Finite Element Analysis (FEA) was employed to optimize the electromagnets' dimensions for effective contraction and extension. The electromagnets were optimized for low mass and high magnetic attraction, resulting in a weight-efficient actuator. A prototype was successfully manufactured, demonstrating rapid contraction and extension in both horizontal and vertical orientation. Unlike existing solutions, the developed soft linear actuator does not suffer from bulky pneumatic components, vulnerable airtight systems or slow operational speed. Therefore, the Kresling actuator is particularly well-suited for use in dynamic, remote or restricted environments. The simple design of the manufactured prototype shows the potential for both large-scale and small-scale applications.

Published as:
Kortman, V. G., Hompes, J. T., Sakes, A., & Jovanova, J. (2025). Kresling origami actuator with embedded electromagnetic actuation. *Smart Materials and Structures*, *34*(6), 065018.

9.1 Introduction

In nature, organisms with soft bodies, such as the octopus or the earthworm, exhibit remarkable adaptability in response to their environment. The octopus, for example, can change the shape of its arms by individually controlling different segments, creating local contracting, extending or bending segments. This ability allows the octopus to actively alter the shape of its arms to reach or fetch targets effectively.

This inherent flexibility and modularity contrasts with traditional robotic arms, which are typically constructed from rigid materials and have limited adaptability. This rigidity presents significant challenges when these robotic arms are employed in confined or narrow spaces. Applications such as logistical pick-and-place operations, vehicle manufacturing and inspection, or the cleaning and maintenance of restricted areas encounter difficulties due to the inflexibility of conventional robotic designs [1]. Consequently, dividing a robotic arm into flexible segments that can both extend or retract, depending on the environment, holds considerable potential for advancing robotic technology in these demanding environments.

Typical soft modular robotic arms integrate pneumatic linear actuators, such as bellows or McKibben muscles, to adapt their configuration in response to environmental demands [2-4]. However, the bulky nature of these pneumatic components, including the necessary pumps, limits the compactness of the arm, thereby affecting its manoeuvrability. Additionally, the need for an airtight system imposes constraints on the design freedom of the arm and increases its risk of operational vulnerabilities caused by leakages. Soft linear actuators that operate through alternative mechanisms, such as temperature-based actuation, encounter challenges related to lengthy cooling times, which can hinder their efficiency in dynamic applications. Furthermore, soft robotic arms often experience deflection due to loading, sometimes even from their own body weight, as they lack bearing capacity [5].

In the field of robotics, origami-inspired designs have demonstrated significant benefits in creating lightweight, deployable and tunable robots [6, 7]. Origami patterns that form thin-walled cylinders can fold into a compact shape while maintaining lateral stiffness during deployment. One notable example is the Kresling cylinder, a bistable and cylindrical-shaped origami structure. A Kresling cylinder can be described as a triangulated cylindrical origami composed of repeated triangular surfaces, with each unit cell consisting of one valley and one mountain crease line (Figure 9.1) [8]. This configuration allows the cylinder to have two stable states: (1) a folded (contracted) disc-shaped state and (2) an unfolded (extended) cylindrical-shaped state [9]. The transformation between these states occurs through linear motion, showcasing the potential of the volume-efficient Kresling cylinder to act as a soft linear actuator. The Kresling cylinder is of particular interest because of its bending resistance when fully unfolded. In this state, the folding lines become tensioned, locking the structure into a more rigid form. This enhances its load-bearing capacity while still allowing smooth transitions between the folded and unfolded states.

Origami-inspired structures currently employ various actuation methods, including pneumatic, mechanical and stimuli-responsive actuation. These actuation strategies often result in bulky actuators, scaling issues, delicate components, slow speed, or inability to provide local actuation [6, 9-12]. The latter hinders the development of a modular robotic arm where, like an octopus arm, individual segments can effectively and independently contract or extend. Alternatively, Novelino *et al.* [6] developed a magnetically-actuated Kresling system demonstrating precise and rapid elongation and contraction. Although this design negates

many of the challenges currently faced with alternative actuation methods, these magnetically-actuated structures require generating a large magnetic field by surrounding coils. This requirement prevents the Kresling structure from acting as a standalone system, limiting its use in applications where external coils cannot be placed, such as in remote or restricted environments. It would be beneficial to embed the coils into the design of the Kresling actuator to initiate contraction or extension locally. The goal of this study is, therefore, to develop a standalone electromagnetically-actuated linear Kresling actuator, suitable for integration in a robotic arm.

9.2 Actuator Design

9.2.1 Design Direction

A schematic of the developed electromagnetic Kresling actuator is shown in Figure 9.1. This actuator consists of a Kresling cylinder positioned between two electromagnets, each comprising a copper coil and a ferromagnetic core. The copper coils are connected to a power source with the electric current running in opposite directions, resulting in coils with opposite polarities. By alternating the electric current, the Kresling actuator can either contract or extend. The most challenging operational orientation of the Kresling actuator is vertical, as it must generate sufficient electromagnetic force to overcome its own weight during contraction. To ensure optimal performance, the produced electromagnetic force must exceed the combined weight of the actuator and the folding resistance of the Kresling cylinder. This underscores the importance of designing weight-efficient electromagnets to effectively actuate the Kresling cylinder. In the remainder of this study, the performance of the Kresling actuator is evaluated by its contraction efficiency (η). This efficiency is defined as the difference between the generated electromagnetic force (F_m) and the opposing forces, where the opposing forces are identified as the gravitational force of the actuator (F_g) and the folding resistance of the Kresling cylinder ($F_{kresling}$), as in (9.1). Here, the electromagnetic force is defined as the net magnetic interaction between the two electromagnets, arising from the force exerted on each magnet by the magnetic field of the other. In this study, the electromagnetic force is evaluated with the electromagnets positioned at their maximum separation, as this is the most critical case during the actuator's motion.

$$\eta = \frac{F_m - F_g - F_{kresling}}{F_g + F_{kresling}} \tag{9.1}$$

9.2.2 Kresling Cylinder

The folding pattern of a Kresling cylinder is shown in Figure 9.1. Two parameters can be used to characterize the Kresling cylinder, namely the polygon side length (a) and the stroke length (S). The polygon side length depends on the radius of the polygon (R) and the number

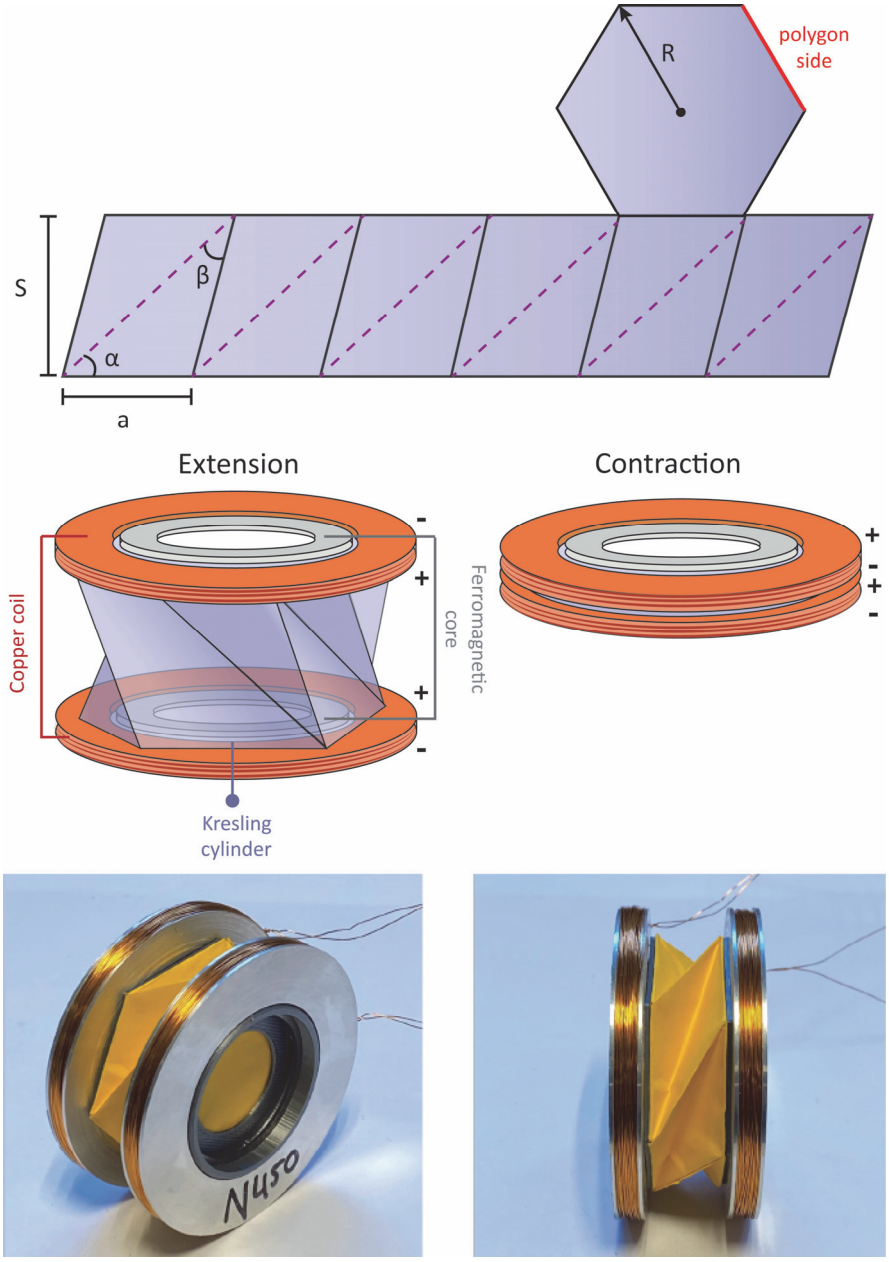


Figure 9.1: Overview of the electromagnetic Kresling actuator. Top: Folding pattern of the Kresling cylinder indicating the stroke length S, polygon side length a, triangle angles α and β and polygon radius R. The purple dotted lines resemble the valley crease lines, while the black solid lines resemble mountain lines. Middle: Schematic overview of the actuator in extension and contraction. Bottom: Prototyped actuator.

of polygon sides (m), see (9.2). Consequently, the stroke length of the Kresling cylinder (S) can be determined by the polygon side length and angles α and β, as in (9.3).

$$a = 2Rsin(\frac{\pi}{m}) \quad (9.2)$$

$$S = a(\sin(\alpha)\cos(\alpha) + \frac{\sin^2(\alpha)}{\tan(\beta)}) \quad (9.3)$$

For an optimized contraction efficiency (η), it is key to minimalize the folding resistance of the cylinder. To achieve this, the main dimensions of the Kresling cylinder are designed to minimize energy dissipation during folding. Wang *et al.* [13] found that a Kresling configuration with angles α=30^0 and β=30^0 exhibits minimal folding resistance. Additionally, Moshtaghzadeh *et al.* [14] found that the stability of the Kresling cylinder increases with a higher number of polygon sides (m). However, an increased number of polygon sides also reduces the stroke length, as described by (9.2) and (9.3), resulting in a less efficient linear motion. Thus, a trade-off should be made between stroke length and stability of the Kresling cylinder. To act as proof-of-concept during this study, a Kresling cylinder with a six-sided polygon and a radius (R) of 30 mm is selected as the base, resulting in a stroke length (S) of 26 mm.

The stroke length of the Kresling cylinder can be divided into three states: (1) the folded state, (2) the low-energy unfolded state and (3) the high-energy unfolded state. The Kresling cylinder dissipates minimal energy during deployment between the folded state and the low-energy unfolded state. However, a clear energy jump occurs between the low-energy unfolded state and the high-energy unfolded state, attributed to the outward bending of the valley crease lines. To develop a weight-effective electromagnetic Kresling actuator, the Kresling cylinder should be unfolded towards the stroke length corresponding to the low-energy stable state (S'). A proof-of-concept Kresling cylinder was folded using 80 g/m2 paper. Using this cylinder, a resistance increase was noted at ¾ of the original stroke length (S). This 'low-resisting' stroke length will be considered as the effective stroke length (S') for the remainder of this study.

To determine the contraction efficiency (η) of the electromagnetic Kresling actuator, the folding resistance of the Kresling cylinder ($F_{kresling}$) should be determined. This was measured by manually compressing the proof-of-concept Kresling cylinder with a load cell (Futek), while the Kresling cylinder was oriented horizontally to avoid gravitational influence. This procedure was repeated 50 times, with the peak forces recorded. The average peak resistance force ($F_{kresling}$) was determined as 0.33 N.

9.2.3 Electromagnet

Generally, an electromagnetic coil is created by winding a conducting wire around a ferromagnetic core. This enhances the magnetic flux density compared to what would be achieved without the core [15]. The ferromagnetic core channels the magnetic flux, magnetizing the core, whereafter the field of the magnetized core adds to the field produced by the coil. In the case of the electromagnetic Kresling actuator, it is crucial to add limited height to the Kresling cylinder to obtain a high folding ratio. To keep the electromagnets as flat as possible, multilayer solenoidal coils were used, in which multiple layers of wires were wound around a straight cylindrical shape. Multilayer coils generate a higher magnetic field

for a given current compared to a single-layer coil [15]. Equation (9.4) shows how the magnetic field strength (B) of a coil depends on the number of windings (N), the current (I), the coil length (L_{coil}) and the permeability of free space (μ_0). The number of windings (N) is related to the length (L_{coil}) and width (W_{coil}) of the coil and can be determined using the packing density (φ) of the wires inside the coil, see (9.5). The packing density (φ) indicates the portion of the coil's cross-section covered by the wires.

$$\boldsymbol{B} = \left(\frac{\mu_0 NI}{L_{coil}}\right)\hat{\boldsymbol{n}} \tag{9.4}$$

$$\varphi = \frac{A_{wires}}{A_{total}} \cdot 100\% = \frac{\pi(0.5D_{wire})^2 N}{L_{coil}W_{coil}} \cdot 100\% \tag{9.5}$$

The challenge of designing the electromagnets to actuate the Kresling cylinder lies in bridging the relatively large gap between the two cylinder ends, since the magnetic field strength decreases rapidly with distance. This causes counteractive design choices, as larger electromagnets generate stronger electromagnetic forces, but add more weight that should be lifted during contraction. Therefore, insight into the effect of the dimensions of the separate parts of the electromagnet should be studied. The Finite Element Analysis (FEA) was employed to simulate the electromagnetic forces between the two opposing electromagnets. In this analysis, the electromagnetic system is described by the Maxwell's equations. The material behavior is defined by the constitutive relations accounting for the macroscopic properties of the materials, considering the material permittivity ε, the material permeability μ, the material conductivity σ and the external current density J_e. A quasi-static system was

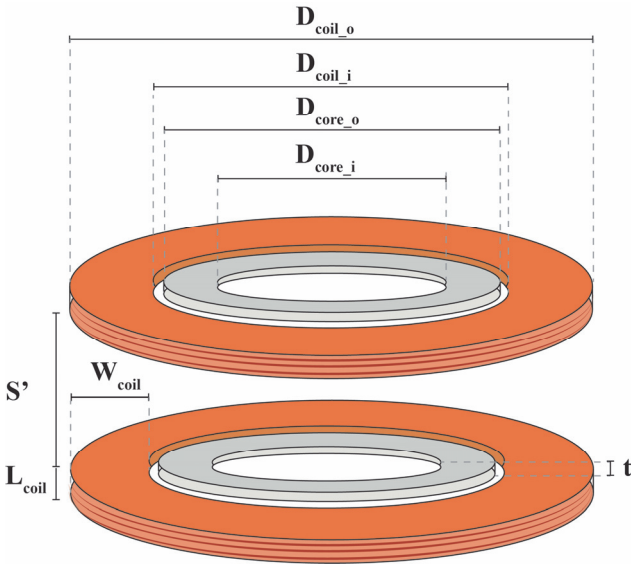


Figure 9.2: Geometrical setup of the electromagnets. Indicating stroke length S', coil length L_{coil}, coil width $W_{coil,}$ core thickness t, outer coil diameter D_{coil_o}, inner coil diameter D_{coil_i}, outer core diameter D_{core_o} and inner core diameter D_{core_i}.

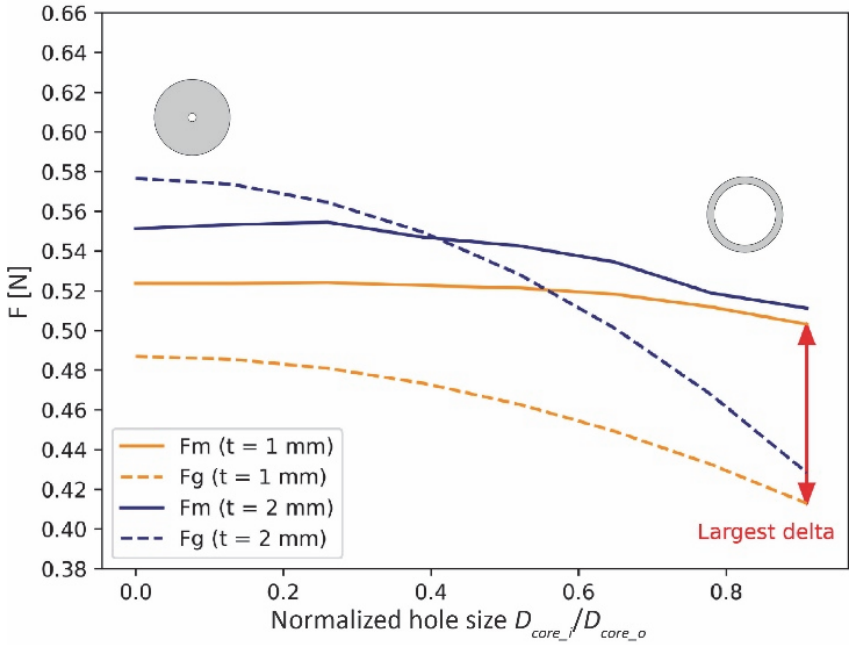


Figure 9.3: Effect of the inner core diameter on the electromagnetic attraction (F_m) and gravitational force (F_g) of the electromagnet. The solid lines represent the electromagnetic force, the dashed lines represent the gravitational force, the yellow lines represent a core with 1 mm thickness (t), and the blue lines represent a core with 2 mm thickness (t).

assumed. The model was used to compute the electromagnetic force generated between the electromagnets as a function of their geometric and electrical parameters. The commercial finite element software Comsol Multiphysics 6.2 was employed, combined with the AC/DC module. The model consists of 65477 elements with mesh refinement on the cores.

Figure 9.2 shows the geometric setup with corresponding parameters, in which the electromagnets are represented as two identical circular, multiturn, copper coils combined with two similar iron cores. The coil is excited by a current I with a coil wire conductivity of 6×10^7 S/m and N windings. The model computes the attracting electromagnetic forces F_{m1} and F_{m2} that affect coil 1 and coil 2, respectively.

To create weight-effective electromagnets, they are designed for low mass and high magnetic attraction. The cores are modelled with varying thicknesses (t) and inner diameters (D_{core_i}) to evaluate their effect on the magnetic attraction of the electromagnets, specifically the contribution of core magnetization towards the center of the core. For consistency with the proof-of-concept Kresling cylinder, the inner diameter of the coil (D_{coil_i}) is set at 46 mm, while the outer diameter of the core (D_{core_o}) is set at 38.5 mm to allow sufficient space for a connection mechanism between the coil and the core. The coil dimensions are standardized to isolate the effects of the core, using an 8 mm coil width (W_{coil}), a 5 mm coil length (L_{coil}), 220 windings (N) and a current (I) of 3 A. The coil weighs 36 grams. The inner diameter of the cores varies from 0 mm to 35 mm in 5 mm increments, considering cores with 1 mm and 2 mm thickness. As a result, Figure 9.3 illustrates the relationship between the generated electromagnetic force (F_m) and the inner diameter of the core, and how this correlates with

the gravitational force that must be overcome for full contraction. The figure shows that the electromagnetic force remains relatively stable with increasing inner diameter. This suggests that the electromagnetic force is concentrated near the coil. Conversely, an increased inner diameter significantly impacts the weight of the electromagnet. Thus, it is advantageous to employ cores with a relatively large inner diameter and low thickness, as this configuration maximizes the difference between F_m and F_g, resulting in the largest contraction efficiency (η).

To assess the impact of the coil dimensions on the contraction performance (η), different values for the coil length (L_{coil}) and coil width (W_{coil}) are considered. The influence of coil dimensions on the generated electromagnetic field requires a relationship between the number of wire windings (N), coil length (L_{coil}) and coil width (W_{coil}). To determine this, the general packing density (φ) for a coil with a 0.3 mm diameter wire is determined by counting the number of windings (N) for a manufactured coil with a 3.1 mm length (L_{coil}), 9.5 mm width (W_{coil}) and an inner radius of 23 mm. This results in 220 wire windings and a general packing density (φ) of 52.8%, following (9.5). It is assumed that the packing density remains constant for other coil dimensions.

The number of windings and the coil dimensions affect the total weight of the electromagnets, and consequently, the total gravitational force (F_g) that the electromagnets need to overcome (9.1). Figure 9.4 shows the effect of the coil length (L_{coil}) and the coil width (W_{coil}) on the contraction efficiency (η) of the electromagnetic Kresling actuator. In this model, the cores are represented as discs with a 38.5 mm outer diameter, a 35 mm inner diameter

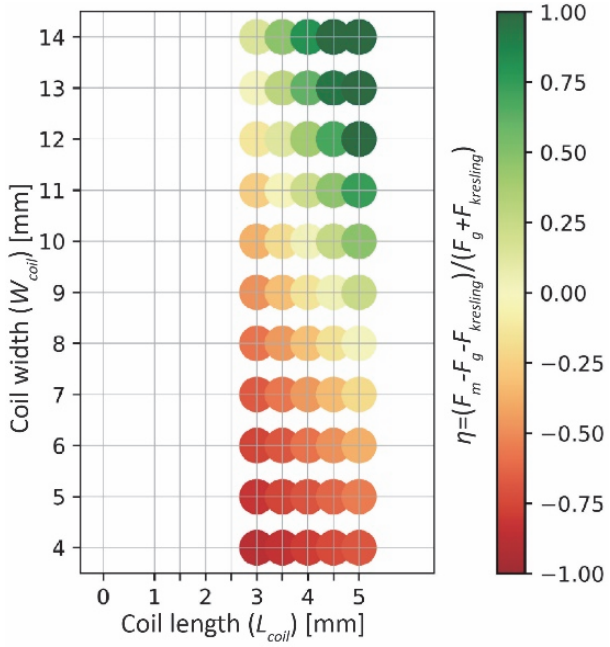


Figure 9.4: Effect of the coil length (L_{coil}) and coil width (W_{coil}) on the contraction efficiency (η) of the electromagnetic actuator. The color coding dictates the boundary between dimensional combinations that produce insufficient (bottom left) and sufficient (top right) contraction efficiency, the latter with a positive contraction efficiency value. F_m is the generated electromagnetic force, F_g is the associated gravitational force and $F_{kresling}$ is the folding resistance of the Kresling cylinder.

and a thickness of 1 mm. The inner diameter of the coil is set at 46 mm. The wires, with a diameter of 0.3 mm, are excited with a current of 3A. The folding resistance of the Kresling cylinder was included to determine the contraction efficiency (η). The figure indicates that the coils must be designed with a specific combination of length (L_{coil}) and width (W_{coil}) within the green area to generate sufficient contraction efficiency (η). The FEA shows that an increased coil height and width enhances the electromagnetic force effectively offsetting the added weight during contraction.

9.3 Experimental Validation

9.3.1 Model verification

The main goal of the experiments was to verify the results of the FEA model and the associated indicative design trends of the electromagnets. The performance measure was the electromagnetic force generated by sets of electromagnets with varying coil and core geometries. These measurements were compared with the expected electromagnetic force from the FEA model for those specific geometries. Six electromagnets with varying coil and

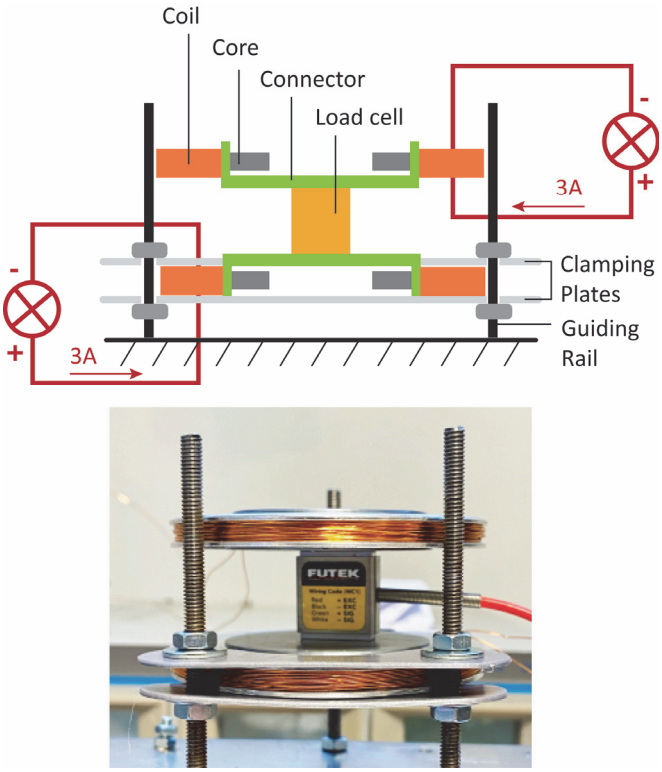


Figure 9.5: Experimental setup. Sets of electromagnets with varying dimensions are positioned vertically with a load cell in between to measure the generated electromagnetic force.

Table 9.1: The measured electromagnetic force (F_{meas}) and expected electromagnetic force (F_{exp}) for different electromagnet configurations.

N [-]	t [mm]	$D_{core\ i}$ [mm]	$D_{core\ o}$ [mm]	L_{coil} [mm]	H_{coil} [mm]	F_{meas} [N]	F_{exp} [N]
200	1	35	38.5	4.9	5.5	0.26	0.40
200	2	20	38.5	4.9	5.5	0.29	0.44
220	1	35	38.5	3.2	9.2	0.38	0.51
220	2	20	38.5	3.2	9.2	0.40	0.55
260	1	35	38.5	3.7	9.5	0.49	0.71
260	2	20	38.5	3.7	9.5	0.53	0.77

Table 9.2: Details of the final prototype.

Parameter	Value	Unit	Description
L_{coil}	4.5	mm	Coil length
W_{coil}	13.5	mm	Coil width
N	450	-	Number of windings
$D_{coil\ i}$	46	mm	Coil inner diameter
a	30	mm	Polygon side length
S'	20	mm	Effective stroke length
$D_{core\ o}$	38.5	mm	Core outer diameter
$D_{core\ i}$	35	mm	Core inner diameter
t	1	mm	Core thickness
m_{coil}	172.2	g	Coil weight
$m_{kresling}$	12	g	Kresling cylinder weight
$m_{connection}$	37	g	Connection weight
m_{core}	17	g	Core weight

core dimensions were manufactured for this purpose. The multilayer solenoidal coils were produced by winding a 0.3 mm diameter coated copper wire (Velleman) around a machined aluminium holder. The ferromagnetic cores were manufactured by laser cutting a steel plate of the desired thickness. A 3D-printed connector made from PolyLactic Acid (PLA) was used to connect the coil and core, with the coil clamped around the cap and the core inserted into it.

The experimental setup, illustrated in Figure 9.5, consists of two electromagnets positioned vertically with a 20 mm gap in between them. A load cell (Futek) was placed between the electromagnets to measure the generated electromagnetic force that pulls the electromagnets towards each other. The lower electromagnet was secured between two 3D-printed plates (PLA), while the upper electromagnet was positioned using three guiding rails for stability and alignment. The two electromagnets were connected to two individual power supplies (VoltCraft PS-403D) with electrical clamps, using a current of 3A. The data of the load cell was obtained using Labview. From this data, the electromagnetic force (F_m) was determined by subtracting the weight of the electromagnet (F_g) from the measured force (F_{meas}). Table 9.1 shows the experimental results, comparing the measured electromagnetic forces (F_{meas}) to those expected from the FEA (F_{exp}). The experimental results allign with the performance trends identified using the model, even though there was a 30% error identified between the expected values from the FEA and the measured values from the experiments.

This discrepancy might be caused by the imperfect packing density of the hand-wound coils, which leads to an overestimation of the electromagnetic forces. Additionally, the friction between the guiding rails and the upper electromagnet could have caused deviations. Nevertheless, the FEA still suffices for revealing general trends for electromagnet design and providing indicative estimations of how changing the core and coil dimensions affects the actuator's performance.

9.3.2 Final Prototype

The FEA explored how variations on geometric parameters of the electromagnets affect the actuator performance, which resulted in trends regarding the coil and core dimensions. Following these trends from the FEA and the measured average error, a prototype of the electromagnetic Kresling actuator was manufactured within a performance-effective region to evaluate its ability to successfully contract and extend. The Kresling cylinder was constructed using 80 g/m2 paper. The coils and the cores were connected by the 3D-printed connector (PLA). The Kresling cylinder was attached to the connector using glue (Pattex). The dimensions and characteristics of the final prototype are shown in Table 9.2. The video footage in Figure 9.6 demonstrates that the configuration of this electromagnetic Kresling actuator is able to successfully contract and extend in both horizontal orientation and vertical orientation, bearing its own weight. The prototype showcases contraction and extension within 0.2 seconds for both a hanging position as well as a standing position.

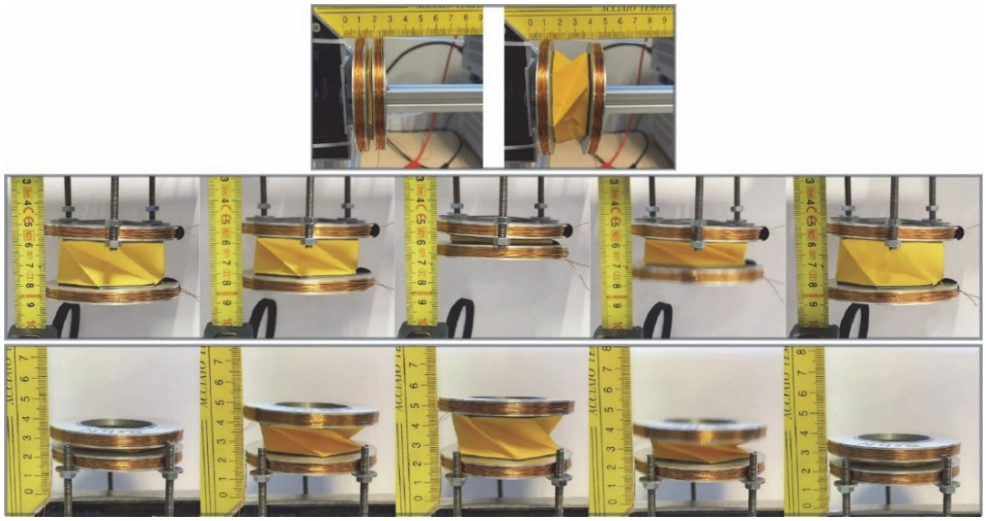


Figure 9.6: Contraction and extension of the prototype. Top: Linear motion in horizontal orientation. Middle: Linear motion in vertical orientation and hanging position. Bottom: Linear motion in vertical orientation and standing position.

9.4 Discussion

This study presents the idea of a standalone electromagnetically-actuated Kresling actuator. The actuator consists of a Kresling cylinder positioned between two electromagnets, each composed of a copper coil and a ferromagnetic core. The embedded Kresling cylinder is of particular interest because of its bending resistance when fully unfolded, which enhances its load-bearing capacity while still allowing smooth transitions between the folded and unfolded states. An FEA was employed to analyse trends towards the dimensions of the electromagnets to effectively contract or extend the Kresling cylinder. The primary design challenge of the electromagnets lies in bridging the relatively large gap between the two ends of the Kresling cylinder, since the magnetic field strength decreases rapidly over length. Counteractive design choices need to be made, as larger electromagnets generate stronger electromagnetic forces, but add weight that should be lifted during contraction. Therefore, the main components of the electromagnets, the coil and the core, are analysed for low mass and high magnetic attraction to create weight-effective electromagnets. The electromagnets were designed as multilayer solenoidal coils to maintain a flat profile for easier integration into the actuator's embodiment. The observations led to a set of practical design guidelines that inform the effective design of electromagnets specifically for use in the Kresling actuator. Regarding the ferromagnetic core, the FEA indicated that increasing its inner diameter and reducing its thickness maximises the difference between generated electromagnetic forces and the opposing weight, resulting in the largest contraction efficiency. This insight led to the design trend that reducing the core's mass, by decreasing its area and thickness, enhances contraction efficiency, with only a minimal trade-off in magnetic performance. Additionally, regarding the multilayer solenoid coil, the FEA indicated that an increased coil height and width enhance the electromagnetic force, effectively offsetting its added weight during contraction. This insight led to the design trend that increasing the coil density enhances contraction efficiency, despite the increase in weight. Following these trends regarding the main components of the electromagnet, a prototype of the electromagnetically-actuated Kresling actuator was manufactured within a performance-effective region. The prototype successfully demonstrated contraction and extension in both horizontal and vertical directions.

Interestingly, these design guidelines for flat, weight-effective electromagnets could be employed more broadly for the implementation of embedded electromagnetic actuation into soft robots in general. Specifically, they could be valuable for incorporating embodied actuation into functional soft robotic designs.

The Kresling actuator differentiates from other electromagnetic linear actuators, such as those developed by Mohamed *et al.* [16] and Yin *et al.* [17], by transforming its entire outer shape from a flat configuration to an extended one. This makes it specifically suitable for integration into a continuum robotic arm (Figure 9.7). The actuator's ability to locally contract or extend based on its polarity makes it an ideal modular component, supporting a modular approach for manufacturing robotic arms. Moreover, as demonstrated by Wu *et al.* [18], the Kresling cylinder has the potential to function as an omnidirectional bending actuator. Incorporating this bending capability into the electromagnetic Kresling actuator could enable the development of a modular robotic arm with precise local control over bending, contraction, and extension. It would be valuable to study the possibilities of more complex movements by simulating the actuator's full deformation, as demonstrated by Jin et al. [19].

Additionally, the impact of scaling on the performance of the electromagnetic Kresling actuator should be examined. When the actuator is upscaled or downscaled, both the electromagnetic force and its relationship to the actuator's weight are altered. For instance, an upscaled Kresling actuator could be advantageous in logistical pick-and-place operations, where greater force and reach are needed. A downscaled version could be effective in restricted settings, such as during Minimally Invasive Surgery, where it could be attached to the tip of a catheter to enable precise needle deployment through the actuation of the electromagnets. Moreover, future research should focus on exploring the potential of the actuator's open internal lumen, which could be utilized for transporting objects or integrating tools.

9.5 Conclusion

In this study, we introduced a novel solution for a soft linear actuator. An electromagnetic Kresling actuator was manufactured capable of extending and contracting based on its polarity. Unlike existing solutions, the developed soft linear actuator does not suffer from bulky pneumatic components, vulnerable airtight systems or slow operational speed. Therefore, the Kresling actuator is particularly well-suited for use in dynamic, remote or restricted environments.

Future research will focus on integrating the developed actuator into a modular robotic arm and studying the effect of scaling. These additional functionalities contribute to revealing the full potential of the electromagnetic Kresling actuator, where the simple design of the manufactured prototype shows the potential for incorporating embodied actuation into functional soft robotic designs.

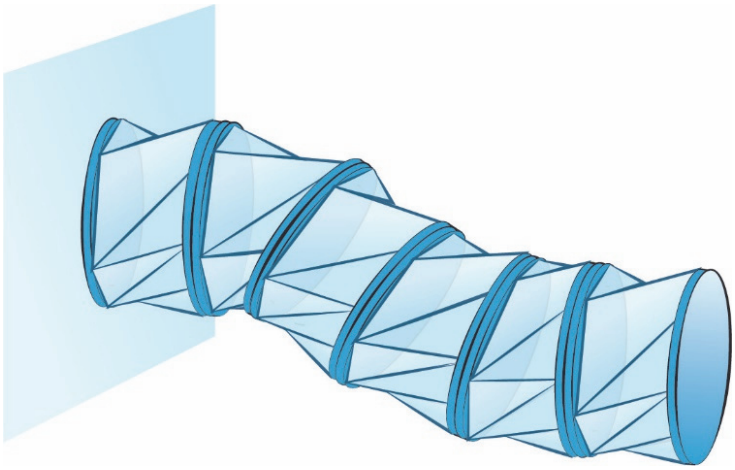


Figure 9.7: Impression of the electromagnetic Kresling actuator integrated into a continuum arm.

References

[1] L. Botti, E. Ferrari, and C. Mora, "Automated entry technologies for confined space work activities: A survey," *Journal of occupational and environmental hygiene,* vol. 14, no. 4, pp. 271-284, 2017.

[2] L. Hongwei, X. Yan, C. Zhang, and Y. Huxiao, "Kinematic modeling and control of a novel pneumatic soft robotic arm," *Chinese Journal of Aeronautics,* vol. 35, no. 7, pp. 310-319, 2022.

[3] X. Chen, D. Duanmu, and Z. Wang, "Model-based control and external load estimation of an extensible soft robotic arm," *Frontiers in Robotics and AI,* vol. 7, p. 586490, 2021.

[4] W. Wang, Y. Zhu, S. Cai, and G. Bao, "Ultralong stretchable soft actuator (US2A): Design, modeling and application," *Chinese Journal of Mechanical Engineering,* vol. 36, no. 1, p. 13, 2023.

[5] J. Santoso and C. D. Onal, "An origami continuum robot capable of precise motion through torsionally stiff body and smooth inverse kinematics," *Soft Robotics,* vol. 8, no. 4, pp. 371-386, 2021.

[6] L. S. Novelino, Q. Ze, S. Wu, G. H. Paulino, and R. Zhao, "Untethered control of functional origami microrobots with distributed actuation," *Proceedings of the National Academy of Sciences,* vol. 117, no. 39, pp. 24096-24101, 2020.

[7] Z. Li, N. Kidambi, L. Wang, and K.-W. Wang, "Uncovering rotational multifunctionalities of coupled Kresling modular structures," *Extreme Mechanics Letters,* vol. 39, p. 100795, 2020.

[8] X. Wang, H. Qu, and S. Guo, "Tristable property and the high stiffness analysis of Kresling pattern origami," *International Journal of Mechanical Sciences,* vol. 256, p. 108515, 2023.

[9] J. Kaufmann, P. Bhovad, and S. Li, "Harnessing the multistability of kresling origami for reconfigurable articulation in soft robotic arms," *Soft Robotics,* vol. 9, no. 2, pp. 212-223, 2022.

[10] C. Zhang *et al.*, "Plug & play origami modules with all-purpose deformation modes," *Nature Communications,* vol. 14, no. 1, p. 4329, 2023.

[11] J. Kim, D.-Y. Lee, S.-R. Kim, and K.-J. Cho, "A self-deployable origami structure with locking mechanism induced by buckling effect," in *2015 IEEE International Conference on Robotics and Automation (ICRA)*, 2015: IEEE, pp. 3166-3171.

[12] N. Nayakanti, S. H. Tawfick, and A. J. Hart, "Twist-coupled kirigami cells and mechanisms," *Extreme Mechanics Letters,* vol. 21, pp. 17-24, 2018.

[13] X. Wang, H. Qu, X. Li, Y. Kuang, H. Wang, and S. Guo, "Multi-triangles cylindrical origami and inspired metamaterials with tunable stiffness and stretchable robotic arm," *PNAS nexus,* vol. 2, no. 4, p. pgad098, 2023.

[14] M. Moshtaghzadeh, E. Izadpanahi, and P. Mardanpour, "Stability analysis of an origami helical antenna using geometrically exact fully intrinsic nonlinear composite beam theory," *Engineering Structures,* vol. 234, p. 111894, 2021.

[15] M. Feliziani, T. Campi, S. Cruciani, and F. Maradei, *Wireless Power Transfer for E-Mobility: Fundamentals and Design Guidelines for Wireless Charging of Electric Vehicles*. Elsevier, 2023.

[16] S. Mohamed, Y. Im, H. Shin, Y. Kim, and B. Shin, "Design, modeling, and simulation of a novel electromagnetic linear actuator for linear motion," *IEEE Access,* 2024.

[17] P. Yin *et al.*, "Kresling origami-inspired electromagnetic energy harvester with reversible nonlinearity," *Smart Materials and Structures,* vol. 33, no. 3, p. 035043, 2024.

[18] S. Wu, Q. Ze, J. Dai, N. Udipi, G. H. Paulino, and R. Zhao, "Stretchable origami robotic arm with omnidirectional bending and twisting," *Proceedings of the National Academy of Sciences,* vol. 118, no. 36, p. e2110023118, 2021.

[19] Y. Jin, S. Liu, J. Li, G. Cao, and J. Liu, "Mechanical responses of soft magnetic robots with various geometric shapes: locomotion and deformation," *Robotica,* vol. 41, no. 4, pp. 1203-1220, 2023.

PART 03

INTELLIGENT TRANSPORT

CHAPTER 10

STATE-OF-THE-ART ASPIRATION CATHETERS

ABSTRACT

Thrombus removal from the human body is facilitated through the utilization of aspiration catheters during minimally invasive thrombectomy procedures, where a pressure differential guides the targeted tissue through a flexible tubular medical instrument. In this paper, we present a patent analysis of thrombectomy aspiration catheter tip designs sourced from the EspaceNet database. Our findings reveal that enhancing the operability of aspiration catheters can be achieved by improving ease of positioning or suction capacity, whether through active or passive means. In terms of the former, both tip shape and flexibility play pivotal roles in maneuvering the distal end effectively. Variations in aspiration port characteristics, either distal-oriented or sideways-oriented, have the potential to enhance suction efficiency. In the active approach, aspects of positioning and suctioning are integrated into a single design, allowing for seamless transitions between configurations. While numerous design characteristics can coexist in a thrombectomy aspiration tip, a balance between flexibility and buckling resistance, as well as between maximizing aspiration lumen diameter and minimizing tip diameter, must be struck. This paper offers an insightful overview of existing thrombectomy aspiration tip designs, providing valuable inspiration for future innovations in this field.

Published as:
Kortman, V. G., Verberne, Y., Atalla, M. A., & Sakes, A. (2024). Advancements in aspiration catheter tip design for thrombectomy: A comprehensive patent review. *Frontiers in Medical Technology, 6*, 1388638.

10.1 Introduction

Mechanical thrombectomy is a minimally invasive medical procedure that plays a crucial role in the treatment of various vascular conditions, particularly those involving locoregionally formed vascular clots or thromboembolisms [1]. This minimally invasive technique involves the introduction of special mechanical devices through catheters to remove potentially life-threatening occlusions from blood vessels, most commonly in the brain for ischemic stroke or the peripheral arteries. Thrombectomy can rapidly restore blood flow to endangered tissue, thereby minimizing the risk of long-term damage or disability [2]. Within the realm of minimally invasive mechanical thrombectomy, aspiration, or suction, is one of the most widely used techniques to extract extraneous entities like vascular clots or thromboembolisms.

Aspiration catheters, also referred to as suction catheters, are one of the key instruments utilized for mechanical thrombectomy using aspiration. They are characterized by a slender suction lumen housing with an aspiration port at the distal end. In a typical aspiration procedure, the catheter's aspiration port is initially positioned in close proximity to the intended target site, followed by the application of negative pressure through a suction device affixed to the proximal end of the catheter. Consequently, thromboembolisms or liquids, situated in front of the aspiration port are conveyed through the catheter lumen, out of the body. The magnitude of the suction force exerted by an aspiration catheter is directly related to both the suction pressure applied and the surface area of the aspiration port.

When designing an aspiration catheter, a balance in stiffness and size is required to attain a properly functioning catheter. Firstly, the catheter needs to be flexible enough to traverse the tortuous curved vessels while remaining sufficiently stiff to transfer the suction force from one end to the other and prevent buckling. Secondly, a larger catheter opening is required to increase the suction power and reduce blockages, however, this makes catheter insertion more complicated. The compromise in stiffness and size differs depending on the surgical application; specifically, the size of the target vessels and their anatomy. A critical component that defines the requirement of both factors is the aspiration catheter tip. To fulfil the application-specific design requirements, different aspiration catheters with specific tip design features have been developed. The three most commonly used thrombectomy aspiration catheters are *Export XT* from Medtronic, *Pronto V3* from Vascular Solutions, and *QuickCat* from Volcano Therapeutics (currently Philips) [3-5]. Corresponding specifications of these catheters are summarized in Table 10.1.

This paper aims to provide a comprehensive overview of aspiration tip designs documented in patent literature, with a focus on improving the operability of these devices. Clear classification of existing approaches within the literature can serve as inspiration for the design of future innovations in aspiration catheter technology. Notably, the overview focuses on thrombi removal through aspiration catheters, a particularly challenging task due to the higher density of solids compared to fluids and gases. According to the described goal, the following definitions will be used within this paper.

Table 10.1: Specifications most commonly used thrombectomy aspiration catheters in 2018 [1-3]

Catheter Name	Extraction Lumen Area [mm2]	Working length [cm]	Unique Selling Points
Export XT	0.937	140	Deliverability Kink Resistance Aspiration Power
Pronto V3	0.929	140	Deliverability Vessel Wall Adhesion Prevention
QuickCat	0.858	145	Deliverability Extraction Performance

Thrombectomy aspiration catheter: *a flexible tubular medical device for insertion into the human body that withdraws solid tissue through air pressure differential.*

Catheter tip: *the distal end of the catheter which consists of an aspiration lumen and an aspiration port.*

In the upcoming section, we present our criteria to find and classify relevant patents. Subsequently, we describe in more detail the different categories of our classification, explaining the innovative aspects of the corresponding patents within Sections 10.3, 10.4 and 10.5. Afterwards, we discuss our findings in Section 10.6 in which we compare the findings of the selected patents and the currently commercially available thrombectomy aspiration catheters, followed by a conclusion in Section 10.7.

10.2 Method

10.2.1 Patent search method

In order to get a comprehensive overview of the previously formulated problem definition, a patent search was executed on the worldwide version of Espacenet. The following search query was performed: *(ti = "Aspiration" OR ti = "Suction") AND ctxt = "Catheter" AND cpc = "A61" AND (claims = "Tip" OR claims = "Distal end") AND desc = "Thromb*"*. The resulting patents include either one of the synonyms 'aspiration or suction' within their title and the word 'catheter' in either the title, abstract or claims. This way, innovations concerning aspiration and applicability for catheters are included. Further, the cooperative patent classification (CPC) code A61 filters on patents within the category 'medical or veterinary science and hygiene'. In order to ensure all patents include specifications about the tip design, one of the synonym search terms 'tip or distal end' should be existent within the claims. Lastly, since it was chosen to focus on the removal of solid tissue, the truncation 'thromb' should be mentioned within the description of the patent to ensure suitability for this application.

The patents incorporated into the literature overview resulting from the search term were selected based on the eligibility criteria. Primarily, the inclusion criteria necessitated that a patent focuses on the enhancement of the design of the catheter tip. This enhancement was required to be distinct and independent of any modifications made to other segments of the catheter, such as the shaft or proximal end. Additionally, patents

featuring supplementary components other than the catheter itself in their main embodiment, such as a movable rod, were excluded from consideration. The exclusion criteria encompassed devices and technologies such as balloon catheters, stent catheters, distal ends equipped with fluid jets, designs involving active clot-busting mechanisms, innovations related to tip visibility, suction syringes, and embolic filters. It should be noted that only patents documented in the English language were considered for inclusion in this study.

The patent selection method is visualized in the Supplementary Materials. The search query, executed in August 2023, resulted in a list of 234 patents after which a manual selection was made. After eliminating duplicate entries (38), the initial patent pool was reduced to 196 records. Next, a careful examination of the abstracts, claims, and drawings was conducted to identify patents specifically related to the design of the tip. As a result, 123 patents were excluded from consideration. The remaining 73 patents underwent a more comprehensive evaluation, scanning the full text to determine if they met the eligibility criteria. After this thorough assessment, a final selection of 41 patents was chosen for further analysis.

10.2.2 Classification

The selected patents all aim to improve the operability of the aspiration catheter (Figure 10.1). This is claimed to be achieved by either 1) enhancing the ease of positioning or 2) improving the suction capacity. Both goals can be attained through a passive or active tip design. The active tip designs are beneficial for enhancing the ease of positioning as well as improving the suction capacity. For improving the positioning of the catheter passively, two subcategories were identified: 1) tip shape and 2) tip flexibility. The former addresses the shape of the distal end and the potential implementation of a guidewire to improve the ability to position the catheter in close proximity to the occlusion. The latter enhances the flexibility of the tip, subsequently improving the manoeuvrability of the catheter through the vasculature and close to the occlusion. Modifying the design of the aspiration port, and thus the cross-sectional area, directly influences the suction capacity of the catheter. A distinction can be made between patents that proposed innovative aspiration port designs that are located at the side of the catheter shaft (aspiration port design: sideways oriented) and patents proposing aspiration port designs located at the distal end (aspiration port design: distal oriented). Figure 10.1 gives an overview of the resulting categories, including snapshots of the corresponding 41 patents included in this review. Two patents, [6, 7], occur twice within different categories.

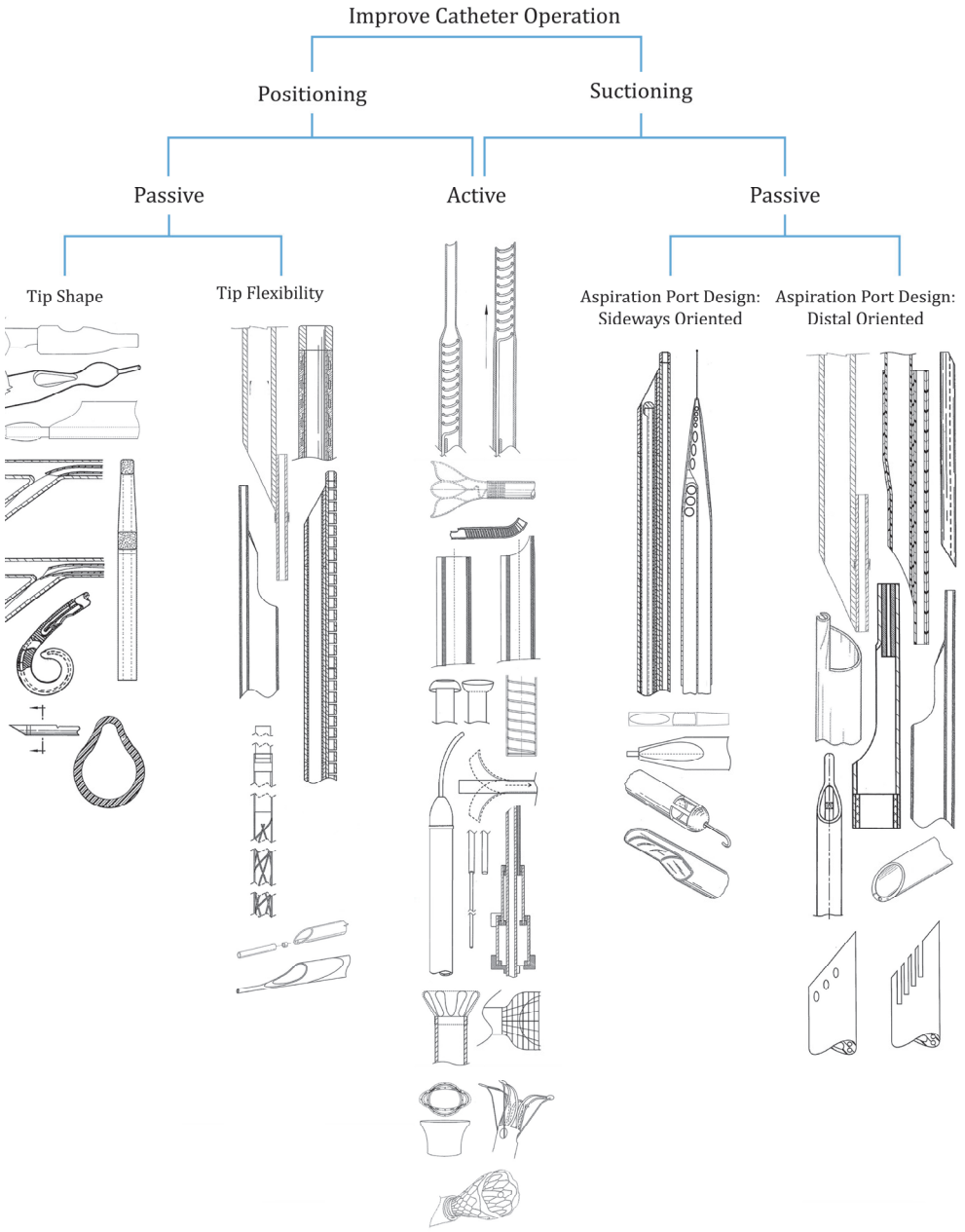


Figure 10.1: Categories of patents addressing the design of thrombectomy aspiration catheter tips.

10.3 Improve positioning – Passively

Prior to the aspiration of the thromboembolism, the catheter is advanced through the body towards the target location. Within this chapter, multiple patents improving the ease of positioning through the design or flexibility of the tip will be discussed.

10.3.1 Tip shape

The patents shown in Figure 10.2 improve the ease of positioning due to the design of the tip of the catheter. Within Cremascoli *et al.* [8] (Figure 10.2.1), a catheter is introduced consisting of a tapered portion between the tubular body and distal end. The drop-shaped aspiration port is located behind the tip within the tapered portion of the tubular body. Ease of positioning is improved since the guidewire is centered at the tip. The tapered portion also improves the maneuverability of the distal end and the catheter operates a-traumatically due to its blunt tapered shape and softness of its tip. The patent described by Mori [9] (Figure 10.2.2), achieves excellent positioning over the thromboembolism through a similar configuration. Again, the aspiration port is located within the sidewall of the distal end and the guidewire is positioned co-axially at the tip. The patent emphasizes the importance of locating the aspiration port and guidewire insertion port on opposite sides with the latter longitudinally shifted in the proximal direction. Reekers [10] (Figure 10.2.3) introduces a preformed, curved, and pliable, pigtail-type tip improving positioning. The preformed curvature is made in the direction of the aspiration port to ensure a certain distance between the port and vessel wall to prevent potential damage to the vessel wall. The distal end of the design by Chou *et al.* [11] (Figure 10.2.4) has a tapered portion, enhancing the ease of positioning.

In the case of an obliquely cut tip, Auth *et al.* [12] (Figure 10.2.5) emphasize the importance of positioning the guidewire at the side of the aspiration port where the tip angles back. Contradictory to this, Provost-Tine *et al.* [13] (Figure 10.2.6) introduce a design in which the guidewire does not have a fixed location with respect to the aspiration port. The guidewire is located within the aspiration lumen and is free to move within this area. Both lumens are thus not separated which is claimed to be beneficial for both positioning and extraction of the catheter, as it allows for a low-profile catheter. Furthermore, the design according to Izawa *et al.* [14] (Figure 10.2.7) is characterized by the design of the protruding guidewire. The distal end of this wire is encapsulated with a tapered leading end tip member, separated from the main tube with a larger diameter than the diameter of the guidewire lumen. Due to this increase in diameter, the guidewire is bent towards the center of the distal end, minimizing interference between the suction catheter and the blood vessel during positioning.

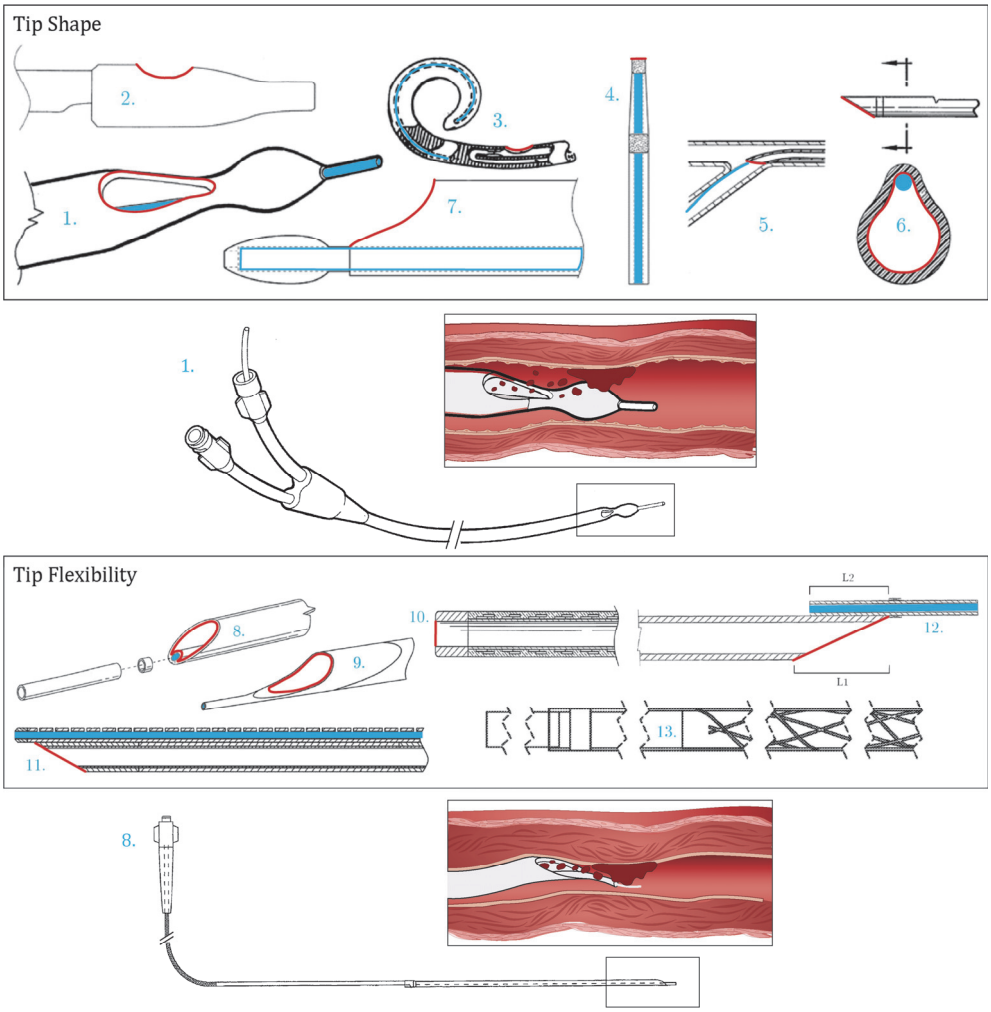


Figure 10.2: Patents concerning tip shape (1 [8], 2 [9], 3 [10], 4 [11], 5 [12], 6 [13], 7 [14]) and tip flexibility (8 [15], 9 [16], 10 [17], 11 [18], 12 [6], 13 [19]). Color indications: Red: Aspiration port, Blue: Guidewire lumen and placement.

10.3.2 Tip flexibility

Tip flexibility contributes to the bendability of the distal end and therefore improves the ease of positioning. The patents shown in Figure 10.2 address this matter in various ways. In order to improve the ease of positioning, Le *et al.* [15] (Figure 10.2.8) and Tanikawa *et al.* [16] (Figure 10.2.9) include an obliquely cut distal end in combination with a protruding flexible tip. This tip is preferably made from the thermoplastic elastomer Pebax and has a durometer varying between 25-55 and 55-72 within the former and latter, respectively. The design also reduces the risk of damaging the vessel. The hardness of the tip is decreased towards the distal end in a stepwise manner in order to prevent kinking. Within the design by Itou *et al.* [17] (Figure 10.2.10), kinking is avoided by introducing a stainless-steel reinforcing member within the soft and flexible tip. This additionally enables a thin wall-thickness of the tip. Kataishi *et al.* [7] (Figure 10.3.22) and Chou *et al.* [11] (Figure 10.2.4) include a homogeneously flexible tip. Within Kusakabe [18] (Figure 10.2.11), the bendability of the tip is achieved by composing the guidewire lumen of segments, each positioned side by side with an interruption in between.

Within the patent described by Miki *et al.* [6] (Figure 10.2.12), the trade-off between tip flexibility and sufficient stiffness is addressed. Even though flexibility is beneficial for positioning, sufficient stiffness is required to prevent buckling and to transmit mechanical power from the proximal side to the distal end of the catheter. Attaching the aspiration lumen to a large portion of the main shaft diminishes flexibility but increases stability. According to this patent, the ideal design satisfies the following constraints: $0.5 \leq L2/L1$ and $L2 - L1 \leq 5$ mm. As shown in Figure 10.2.12, L1 represents the horizontal distance of the obliquely cut tip and L2 represents the portion of the aspiration lumen attached to the main shaft. Lastly, it should be noted that all patents within this section mention a hydrophilic lubricative coating applied to the distal end of the catheter to further improve the ease of positioning. Corvese [19] (Figure 10.2.13) describes an improved catheter system that leverages PTFE tubes and liners with gaps and spaces for flexures to enable navigation through tortuous and highly constrained neurovasculature.

10.4 Improve suctioning – Passively

Subsequent to positioning the catheter tip in front of the thromboembolism, the aspiration is actuated. Within this chapter, the patents including a tip design improving the suction capacity through the aspiration port design are discussed.

10.4.1 Aspiration port design: Sideways oriented

The patents shown in Figure 10.3, all have a unique aspiration port design with varying characteristics such as shape, size, location, and the number of ports. Li *et al.* [20] (Figure 10.3.14) describe the implementation of an asymmetrical aspiration port along the virtual line A. As a result of this asymmetry, the suction pressure distribution varies over the aspiration port. The increase in suction pressure at the most proximal end of the aspiration port enhances removal. Within the design of Tanaka [21] (Figure 10.3.15), the aspiration port is formed as a long hole at the side of the catheter. The open area of this port is

adjustable through the usage of an axially slidable inner tube. The catheter tip in this design is closed off.

Smalling [22] (Figure 10.3.16) claims that a plurality of aspiration ports in variable shapes and sizes enhances thrombus removal. The ports are arranged in groups along the tapered distal end of the catheter. The port size of each group gradually increases towards the proximal side of the catheter. The variability in ports results in differing aspiration vectors, increasing the effective aspiration area. Also, due to the tapered shape of the distal end, the contact between the thromboembolism and the aspiration port is enhanced. Whenever a thromboembolism is not aspirated by one of the initial ports, the thromboembolism is gradually trapped by the tip and aspirated by one of the subsequent ports. Within catheters with a constant diameter, the distance between the aspiration port and non-aspirated thromboembolism increases as the catheter advances through the vessel, therefore reducing the likelihood of removal.

Within the patents described by Wu *et al.* [23] (Figure 10.3.17) and Ruggio [24] (Figure 10.3.18), again a plurality of aspiration ports is incorporated within the design. Within the former, in addition to an opening at the distal end, six elliptical side holes are positioned along the tip extending to the shaft of the catheter, enhancing the removal of large thromboembolisms. The tapered shape of the distal end and rounded edges prevent tissue damage. Concerning Ruggio [24], the apertures are located along the sidewall of the hemispherical and closed catheter tip. The extending guidewire, protruding from the center of the tip, is designed to pulverize occlusions. Another advantage of multiple aspiration ports is the maintenance of functionality whenever one of the openings is blocked.

10.4.2 Aspiration port design: Distal oriented

In the case of one single aspiration port at the distal end of the catheter, the configuration of the tip greatly influences the suction capacity. Within this subcategory, two approaches are discussed: 1) enhancing the suction capacity and 2) preventing disruption of the aspiration through the configuration of the distal end.

The patents shown in Figure 10.3.19-3.23 are designed to enhance the suction capacity of the catheter. Miki *et al.* [6] (Figure 10.2.12), Fojtik [25] (Figure 10.3.19), and Bagaoisan *et al.* [26] (Figure 10.3.20) all recommend an obliquely cut tip. By obliquely cutting the tip, the surface area of the aspiration port is increased whilst maintaining a suitable diameter of the aspiration lumen. Furthermore, this simultaneously increases the suction force and reduces the risk of clogging due to the enlarged port. Additionally, the angled opening can be beneficial for aspirating thromboembolisms positioned closer to the vessel wall and enables reduced stiffness towards the distal end. Miki *et al.* [6] additionally claim that the ideal length of the horizontal distance of the obliquely cut tip lies between two and ten millimeters. A smaller length is more likely to cause damage within the vessel whilst a longer length complicates removal.

The design according to Fojtik [25] optimizes the implementation of the guidewire lumen and the wall thickness of the tip. The guidewire lumen is incorporated within the walls of the aspiration lumen. The thickness of the walls is minimized in order to maximize the aspiration lumen within the given constraints. This resulted in an unevenly distributed

wall thickness in which the thicker part consists of the guidewire lumen. The overall stiffness remains sufficient in order to prevent kinking.

Within the patent by Mori [27] (Figure 10.3.21), the distal end is not only cut obliquely but also in a concavely curved manner. The curved and rounded edges increase the cross-sectional area of the aspiration lumen and are beneficial for the positioning of the catheter within the blood vessel. The same applies to the designs according to Kataishi *et al.* [7] (Figure 10.3.22) and Li *et al.* [28] (Figure 10.3.23) in which the distal end is cut in a combination of curved and angled parts. Within the latter, the ease of manufacturing is taken into account as well.

The suction force required for thromboembolism removal can be disrupted in multiple manners. The aspiration port can be blocked by the thromboembolism or the aspiration lumen can collapse due to kinking. Both phenomena prevent airflow through the device, which is required for aspiration. The patents shown in Figures 3.24-3.26 focus on an approach to prevent this loss of functionality. The distal end of the catheter described by Gülcher *et al.* [29] (Figure 10.3.24) has a nose-shaped element that penetrates the thromboembolism before contacting the aspiration port. Subsequently, only fragmented pieces are aspirated, preventing blockage of the port. Comparable with the previously discussed design of Ruggio [24] (Figure 10.3.18), the extending guidewire is used to pulverize the occlusions. Within the patent by Consigny [30] (Figure 10.3.25), the distal end compromises a cutting edge, spirally tapered along the oblique tip. Through this configuration, obstacles adhered to the vessel wall are removed whilst advancing the catheter through the body. Additionally, it is possible to rotate the device in the direction of the spiral during positioning to further enhance the removal. Goff *et al.* [31] (Figure 10.3.26) introduce multiple designs of the distal end which disrupt potential sealing between the aspiration port and thromboembolism. This can be done through axial slots or additional ports complicating the complete sealing of the lumen. Within these designs, the desired effect is achieved through the passive design of the distal end. Alternatively, the patent introduces active manners or a combination of both. For example, potential sealing between the aspiration port and thromboembolism can be disrupted by introducing a vibrating wire.

There is a trade-off between maintaining sufficient flexibility of the tip of the catheter to enhance positioning and prevent damage to surrounding tissue and maintaining sufficient structural rigidity to prevent buckling through which the aspiration lumen is sealed and suctioning is hindered. Within the before-mentioned patent introduced by Gülcher *et al.* [29] (Figure 10.3.24), a stabilization wire is led through the tip, limiting the folding tendency. Alternatively, a reinforcing member within the distal end can be implemented [16, 17, 21] or a stiffness gradient can be added [16].

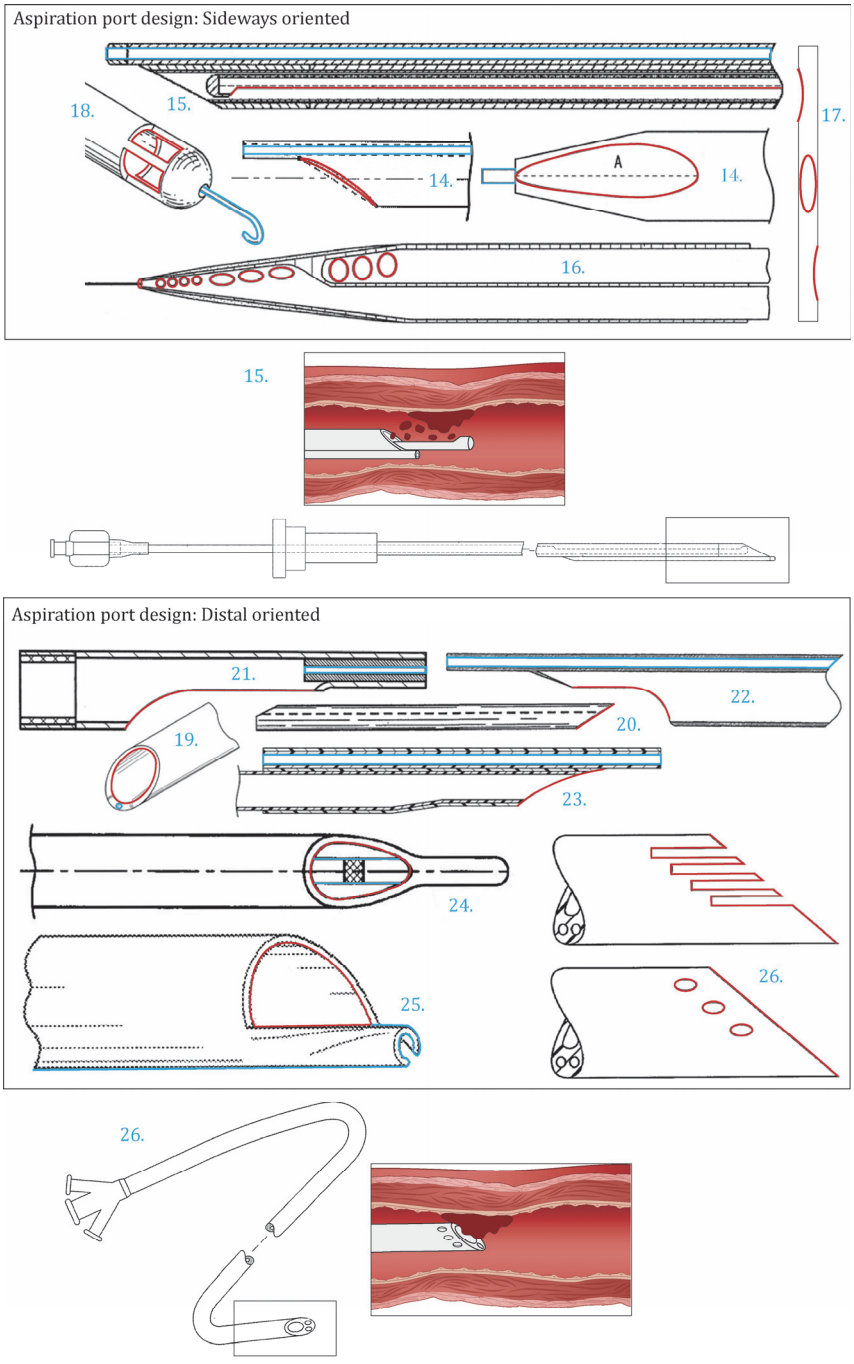


Figure 10.3: Patents concerning aspiration port design. Top: Aspiration port design: sideways oriented (14 [20], 15 [32], 16 [22], 17 [23], 18 [24]). Bottom: Aspiration port design: distal oriented (19 [25], 20 [26], 21 [27], 22 [7], 23 [28], 24 [29], 25 [30], 26 [31]). Color indications: Red: Aspiration port, Blue: Guidewire lumen and placement.

10.5 Improve positioning and suctioning – Actively

The patents within this category focus on improving positioning or suction capabilities of the catheter tip in an active manner by switching between states, varying the cross-sectional area of the aspiration lumen, enabling more targeted suctioning, or extending the reachability of the tip, see Figure 10.4.

10.5.1 Variable cross-sectional area

The patents shown in Figure 10.4.27-4.35 increase the surface area of the aspiration lumen after positioning the distal end at the target location. Within Vale *et al.* [33] (Figure 10.4.27) an expandable tip is introduced. In the collapsed state, the cross-sectional area of the tip is equal to the catheter shaft, making the catheter low in profile, flexible, and thus suitable for positioning. After reaching the target location, the distal end is expanded radially, increasing the suction port diameter, and enabling the aspiration of the thromboembolism. The enlarged, funnel-shaped, port makes it possible to remove larger thromboembolisms from the blood vessel. Within this example, the expandable tip compromises a strutted framework, supplying mechanical support, encapsulated with a flexible cover. The expandable state of the cloth retrieval catheter is actuated by pulling the outer tubing backwards, also known as reversibly driven. A similar device is described by Mintz [34] (Figure 10.4.28) in which the expandable member includes a plurality of tensile-actuated axial prongs and/or a basket comprising struts that are configured to be expanded radially outwards in response to a tensile force applied to the pull members. Alternatively, a self-expanding structure can be introduced. Similar expandable distal ends are introduced within Li *et al.* [35] (Figure 10.4.29), Nguyen *et al.* [36] (Figure 10.4.30) and Baron *et al.* [37] (Figure 10.4.31), although slightly different in shape. Furthermore, the design described by Casey *et al.* [38] (Figure 10.4.32) utilizes the environment to switch between configurations. The tip inverts whenever retracted, creating a funnel-shaped tip with an enlarged distal end diameter compared to the transition phase.

Von Hoffmann [39] (Figure 10.4.33) and Li *et al.* [40] (Figure 10.4.34) both uniformly increase the diameter of the distal end prior to suctioning. Within the former, this is enabled by an axially movable support coil. The aspiration lumen is made from a stretchable material or a tubular wall that is folded within the preferred configuration. After delivery to the target location, the movable support is translated to the distal end of the catheter, subsequently enlarging the diameter of the aspiration lumen. The recommended length of the support is 5-15 cm. Within Li *et al.* [40], a spring component is implemented in the catheter wall which can be stretched or compressed. This way, the stiffness and diameter of the distal end can be altered simultaneously by pulling one of the two pulling members attached to the proximal or the distal end of the spring, subsequently stretching or compressing the spring, respectively. The low stiffness and small diameter state is beneficial for positioning, whilst the opposite is desired during the aspiration phase. Desai *et al.* [41] (Figure 10.4.35) describe a catheter with a customizable size and shape of the distal lumen using pull wires.

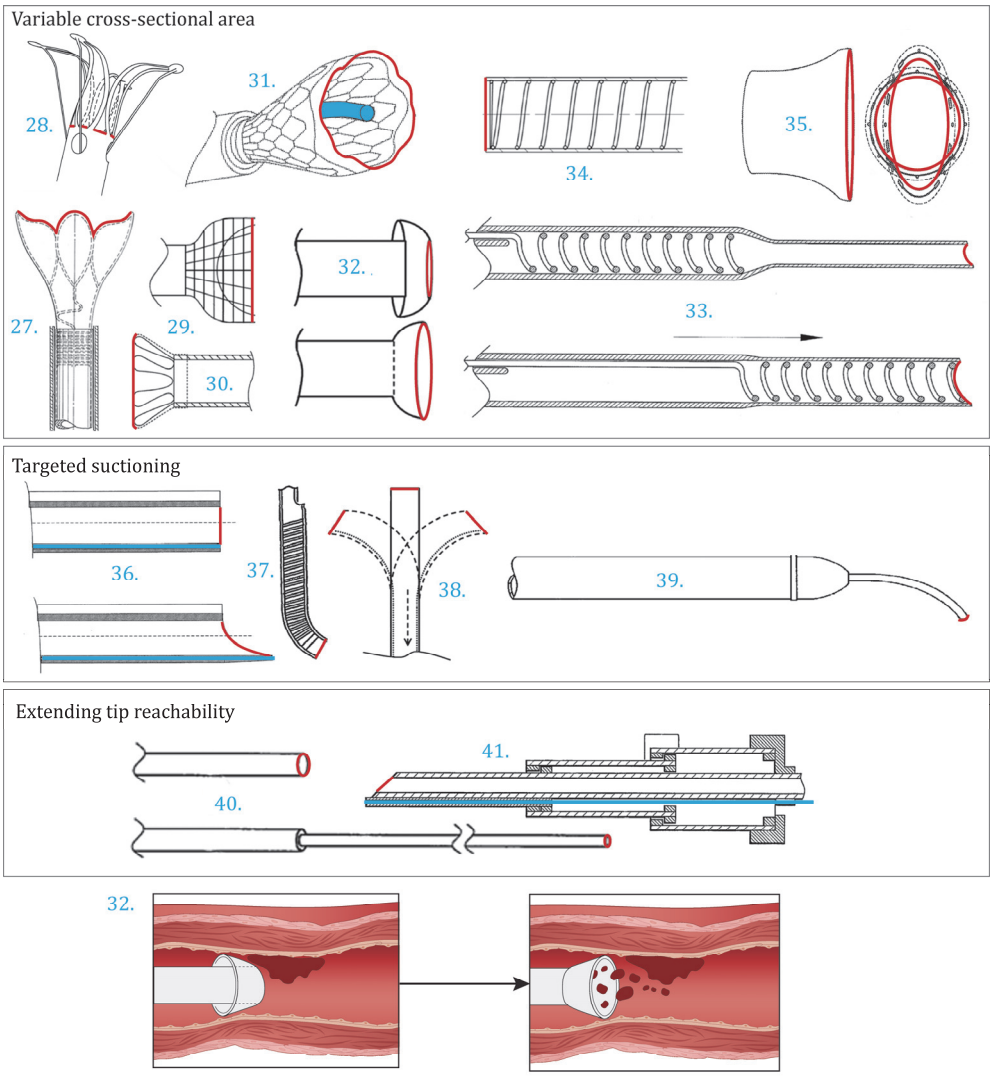


Figure 10.4: Patents improving suctioning and positioning by actively increasing the cross-sectional area of the aspiration lumen (27 [33], 28 [34], 29 [35], 30 [36], 31 [37], 32 [38], 33 [39], 34 [40], 35 [41]), by actively enabling targeted suctioning (36 [42], 37 [43], 38 [44], 39 [45]), or by actively extending the reachability of the tip (40 [46], 41 [47]). Color indications: Red: Aspiration port, Blue: Guidewire lumen and placement.

10.5.2 Targeted suctioning

Instead of enlarging the aspiration port for suctioning, the second collection of patents within Figure 10.4 focuses on the more targeted aspiration of the thromboembolism. During delivery, the distal ends described by Spurchise *et al.* [42] (Figure 10.4.36) and Ogle *et al.* [43] (Figure 10.4.37) are both cylindrically shaped with an orthogonal distal end. When positioned, the tip changes in shape, beneficial for aspiration. Within Spurchise *et al.* [42]

this is done by switching between an orthogonal and oblique tip shape using a core wire. The oblique configuration enlarges the aspiration port surface area and allows bending the tip towards the thromboembolism. The distal end shown in the design described by Ogle *et al.* [43] consists of at least three segments, enabling a curved state in the direction of the thromboembolism for targeted removal. The distal end introduced by Laub [44] (Figure 10.4.38) includes a steerable tip that can be operated by the surgeon using one or more steering wires. Within Phelps *et al.* [45] (Figure 10.4.39), the tip is steerable as well. However, the diameter of this tip is sufficiently smaller, focusing on the removal of plaque. Also, rotational movement is enabled.

10.5.3 Extending tip reachability

Depending on the area of application, the diameter of the vessel can vary. For example, thromboembolism removal within the brain requires catheters with a smaller diameter when compared to removal within other parts of the body. The patents shown in Figure 10.4.40 and 4.41 anticipate to these scenarios, by introducing a smaller diameter tip that can be extended to enhance the reachability of the catheter. Yang *et al.* [46] (Figure 10.4.40) and Douk *et al.* [47](Figure 10.4.41) both introduce a catheter with a telescoping structure. Whenever constraint, the smaller diameter, low-profile, distal end can be axially extended to further advance through the vessel to the target location for removal. Within Douk *et al.* [47], this structure is incorporated within the catheter shaft as well. The design consists of three telescoping segments in total.

10.6 Discussion

10.6.1 Summary of main findings

In this study, we give an overview of patent literature addressing thrombectomy aspiration catheter tip designs. In total, 41 patents are incorporated within this study, presenting innovations on the distal end of the catheter without introducing add-ons. It was found that the designs can be categorized into three groups, all improving the overall operability of the catheter. Namely, by improving the ease of positioning passively (13), improving the suction capacity passively (13), or by addressing both elements simultaneously in an active manner (15). The designs introduced by Miki *et al.* [6] (Figure 10.4.12) and Kataishi *et al.* [7] (Figure 10.6.23) are incorporated twice in two categories, as shown in Figure 10.2. These innovations enhance both positioning and suctioning passively, by increasing tip flexibility and the effective cross-sectional area of the aspiration lumen through the distal end configuration.

Improving positioning passively includes innovations concerning tip shape (7) and tip flexibility (6). The former group mainly addresses the shape of the tip and the guidewire implementation. The flexibility of the tip can either be implemented in a stepwise manner towards the distal end or homogeneously. Within the category of patents passively improving the suction capacity of the catheter, both the sideways aspiration port design (5) and distal end aspiration port design (8) are influential factors. Concerning the former, aspiration port characteristics can vary in shape, size, location, and number of ports. The

configuration of the distal end can enhance suction capacity by maximizing the surface area of the aspiration port through a non-orthogonal cut. Additionally, suction disruptions, such as sealing of the aspiration lumen and aspiration port blockage should be prevented. Within an active tip design, both goals, improving positioning and suctioning, can be achieved simultaneously by switching states. The collapsed state is low in profile and flexible, therefore maneuverable. Subsequently, the expanded state increases the cross-sectional area of the aspiration lumen, enabling more targeted suctioning of the thromboembolism, extending the reachability of the tip, and preventing kinking of the tip to enhance removal. Therefore, by implementing these key areas for improvement in aspiration catheter design, safer and more efficient thrombectomy procedures are envisioned in the future.

The distribution of patents over the last three decades, Figure 10.5, shows a shift from research focused on optimizing the tip design, towards increased interest in variable cross-section catheter designs. This observation implies a trend towards improving active positioning and suctioning of catheter tips and might be fueled by recent research involving advanced actuation mechanisms using shape memory and superelastic materials like Nitinol, as well as magnetic actuation. The opposite trend is seen for patents focusing on distally orientated aspiration port designs. Furthermore, we see patents focusing on extending the tip reachability from 2010 onwards, which might allow for transferring through smaller blood vessels in the future.

Atraumatic tip

The three discussed categories were drawn up based on the main goals addressed within the selected patents. However, many patents additionally include improvements to the catheter tip in order to prevent trauma to surrounding tissue. Three different approaches can be found in the identified patents. Firstly, by applying a coating to the distal end, friction

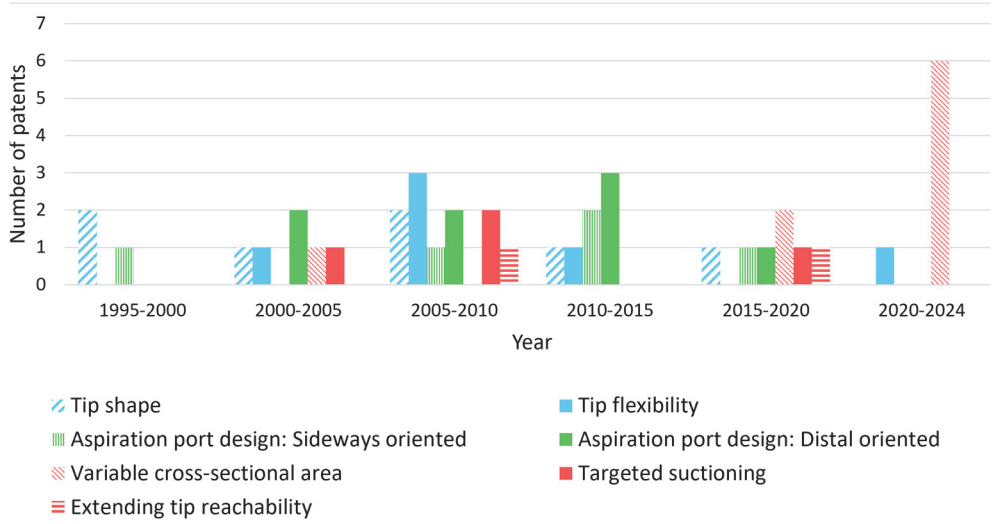


Figure 10.5: Distribution of the included patents, classified on catheter tip designs that improve the operability of the aspiration catheter by (1) passively enhancing positioning (blue), (2) passively improving suctioning (green) or (3) actively improving the positioning and suctioning (red).

between the catheter and vessel wall is decreased. This simultaneously makes it easier to reach the target location and minimizes harm (Approach A). Additionally, it is possible to apply the low friction coating on the inside of the aspiration lumen, to reduce the possibility of the thromboembolism sticking to the inside. Other patents mention softened or rounded tips to prevent damage (Approach B). Furthermore, hindering suctioning between the vessel wall and the aspiration port is beneficial for an atraumatic treatment (Approach C). Table 10.2 summarizes which improvements are implemented in the selected patents, categorized according to the three mentioned approaches. Note that design specifications may overlap in resulting improvements. For example, when the ease of positioning is improved, the risk of damage is potentially reduced as well. Therefore, only patents explicitly mentioning making the catheter less traumatic are included within the table. Experiments should be executed to evaluate the effectiveness of the elements summarized in Table 10.2.

Guidewire implementation

A guidewire can be implemented within the catheter tip. This wire is advanced to the target

Table 10.2: Patents addressing atraumatic tip design. A: reduce friction between the catheter and vessel wall, B: through the configuration of the distal end, and C: prevent suctioning of the vessel wall.

Patent	A	B	C	Specifications
[6]	X			Hydrophilic coating
[12]	X			Lubricious coating (polyvinylpyrrolidone hydrogel), the usage of an antithrombogenic material (heparin complex or hirudin), and a low friction coating on the inside of the aspiration lumen
[16]	X			Lubricious coating
[22]	X			Formed or coated with smooth or low-friction and soft material (Teflon)
[27]	X			Hydrophilic coating
[30]	X			Lubricious coating (Teflon) or hydrophobic coating (silicone lubricant dispersion PN 4097 or hydrogel)
[34]	X			Flexible material or coating
[37]	X			ePTFE (Teflon) coating
[39]	X			Lubricous coating (Paralene, Teflon, silicone rubber, or polyimidepolytetrafluoroethylene composite materials)
[8]	X	X		Blood compatible coating and soft and flexible tip with tapered portion
[17]	X	X		Hydrophilic lubricous coating and a soft and flexible tip
[35]	X	X		Lubricous coating (PTFE), hydrophilic or hydrophobic, and a reduced cross-section and compliant tip
[33]	X	X		Lubricous coating (hydrogel or flexible fluoropolymer) and a funnel-shaped tip with a soft distal ridge
[15]		X		Convex edge and a flexible tip tube
[23]		X		Tapered tip with fillet shape and a rounded structure of tip
[25]		X		Rounded and smoothed distal end
[28]		X		Curved surface of the distal end (combination of concave and convex parts)
[38]		X		Low-profile, curved tip
[40]		X		Smaller and flexible distal end
[29]			X	Pressure balancing hole opposite to aspiration hole to prevent the aspiration hole to attach to the vessel
[9]			X	Additional side hole to prevent the aspiration port to get stuck to the blood vessel wall.
[10]			X	Preformed curved tip in the direction of the aspiration port ensures distance between suction inlet and vessel
[29]			X	Pressure balancing hole opposite to aspiration hole to prevent the aspiration hole to attach to the vessel

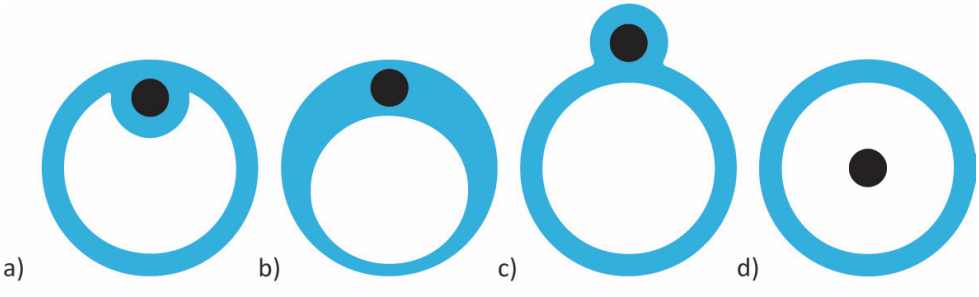


Figure 10.6: Distal end cross-sections visualizing guidewire (black dot) implementation: a) fixed location within aspiration lumen, b) fixed location within enlarged catheter wall, c) fixed location outside aspiration lumen, d) fixed or variable location within the aspiration lumen.

location first, after which the rest of the catheter body follows, potentially easing the positioning. Within Figure 10.6, several configurations are shown to emphasize the variability of the guidewire implementation within the selected patents. The figures visualize the distal end cross-section, in which the black dot represents the guidewire.

Within the first three configurations, the guidewires have an off-center fixed location within the distal end. Auth *et al.* [12] claim that in the case of an obliquely cut tip, it is beneficial for the ease of positioning to fix the guidewire on the side where the tip angles backwards. A trade-off exists between the cross-sectional area of the aspiration lumen and the overall size of the tip, since enlarging the former improves the suction capacity whilst a larger diameter of the tip complicates positioning. Also, the wall thickness and force distribution should be sufficient to prevent buckling. Within the last configuration, see Figure 10.6d, the guidewire is positioned within the aspiration lumen, at either a fixed or variable location. In the case of the former, the distal end of the tip is closed, and the guidewire protrudes through this surface. Concerning the latter, dependent on the surroundings and curvatures in the vessel wall, the guidewire can move to a suitable location within the aspiration lumen. This design is introduced within the patent by Li [20]. Although, configuration (d) is the easiest to manufacture, the guidewire might hinder thromboembolism removal. Note that the implementation of the guidewire does not have to be constant along the entire length of the distal end. For example, within the design described by Ruggio [24] (Figure 10.3.18), configuration (a) is followed by the fixed version of configuration (d). Changing the guidewire configuration along the catheter body will allow for the optimization of the mechanical properties of the catheter but complicates manufacturing. In future, research could be conducted to determine the most optimal guidewire guidance to improve the trackability of the catheter, as well as look into innovative ways to manufacture a variable guidewire lumen along the catheter body, for example by using state-of-the-art extrusion and additive manufacturing technologies.

State of the art

Within Table 10.3, the design specifications of the instruments shown in Table 10.1 are evaluated based on the innovations mentioned in the patent review. It is shown which design features of the included patents are present within currently clinically available

Table 10.3: Similar features between the state-of-the-art thrombectomy catheters (A: Export XT, B: Pronto V3, and C: QuickCat) and selected patents with corresponding categories.

Improve Catheter Operability				
	Improve Positioning		Improve Suctioning	
Feature	**Tip Design**	**Tip Flexibility**	**Aspiration Port Design: Sideways Oriented**	**Aspiration Port Design: Distal Oriented**
Fixed guidewire position at the side where the tip angles back [12]	A			
Tapered portion between body and tip [8]	B			
Centered guided [8, 9]	B, C			
Enlarged guidewire tip [14]	B			
Variable guidewire position within aspiration lumen [13]	B, C			
Lubricous hydrophilic coating [6, 12, 16, 22, 27, 30, 39]	A, B, C			
Soft tip [17]		A		
Obliquely cut aspiration lumen [6, 25, 26]				A, B, C
Prevent vessel wall adhesion [9, 29]				B

aspiration catheters. It can be noted that none of the designs implements an alternative sideways oriented aspiration port design to improve the suction capacity. All three instruments consist of one single and symmetrical aperture located at the tip of the catheter. Also, all designs implement an obliquely cut tip, maximizing the cross-sectional area of the aspiration lumen, and have a lubricious hydrophilic coating. Information regarding tip flexibility was not found for all three instruments. The Pronto V3 is shown to include the most features introduced within the selected patents. In terms of real-world outcomes, Table 10.3 highlights the potential for enhancing current commercial aspiration catheters to better navigate towards thromboembolisms and enhance their suction capabilities without encountering issues of clogging by incorporating the strategies identified in the patent review.

10.6.2 Clinical applications and devices

To assess the translational aspect of the patented aspiration catheter designs, we traced the companies to which patents were assigned, and we evaluated the similarities between the patented design and their commercially available instruments. Upon examining the patents, we found several examples of commercially available catheters that are based on the reviewed patent designs. One example is the *TransVascular Aspiration Catheter* (Nipro, Osaka, Japan), which features a flexible catheter tip with an oblique, concave distal end, easing catheter positioning inside the blood vessel. This tip design is described in patents by Kataishi *et al.* [7], Kusakabe *et al.* [18], and Mori *et al.* [27]. Similarly, the *Thrombuster PRO* (Kaneka Medical Products, Tokyo, Japan) achieves tip flexibility through an oblique, asymmetrical catheter tip, as described in patents by Miki *et al.* [6], Li [20], and Li and Kurose [28]. The *Eliminate aspiration catheter* (Terumo, Tokyo, Japan) incorporates a flexible,

obliquely cut catheter tip reinforced with a braid to prevent buckling, as described by Itou and Fukuoka [17]. The *Tensing 7 delivery catheter* (Route 92 Medical, San Mateo, CA) features a tapered, atraumatic tip that facilitates positioning within the blood vessel, as described in the patent by Chou *et al.* [11]. Additionally, the *Helo PE thrombectomy catheter* (Endovascular Engineering, Menlo Park, CA) embeds a self-expanding catheter tip that ensures a wide opening for large clot removal, as described by Baron *et al.* [37]. The safety and feasibility of this catheter design are currently evaluated in a clinical trial [48].

A common trend observed in the patents was the use of polymeric materials like PEBAX, which allows for varying hardness levels in specific areas of the shaft [13, 15, 16]. In particular, one patent [16] detailed a PEBAX catheter shaft with a Shore hardness ranging from 63D to 72D at the proximal end, tapering to a Shore hardness of 40D to 55D at the distal tip. Another patent [15] described a flexible tip made from a softer 25-44D PEBAX. Additionally, several patents highlighted the advantages of incorporating a radiopaque material at the distal tip of the aspiration catheter [8, 13, 17, 38] or applying a coating with an anti-thrombogenic agent [12].

It should be noted that the patents often do not specify particular application areas or target regions. Furthermore, the overall functioning of the catheter is the sum of all parts of the device, including the shaft design and handle. However, one can infer the intended working environments of the patented catheters by looking at their tip and shaft design. Some catheters are optimized for navigating narrowed and tortuous portions of blood vessels during peripheral interventions, such as the saphenous veins [8] or the carotid and cerebral arteries [38], while others are designed for use in larger blood vessels, such as the pulmonary artery. The former category emphasizes methods to enhance tip flexibility and foldability to reach smaller blood vessels and target thromboembolisms locally [8, 17, 38], whereas the latter focuses on precise tip positioning within larger vessels [9, 10]. It must also be noted that the removal of chronic or acute thromboembolisms poses different challenges, with the former being more resistant to removal. For example, in a study of Madjidyar *et al.* [49], it was found that the thrombus composition can affect the efficacy of thrombectomy. In their study, they were unable to aspirate fibrin-rich clots using the *ADAPT catheter* (SOFIA 5F, Microvention, USA), whereas the removal of “softer” erythrocyte-rich clots was also unsuccessful in one third of the cases. Even though the authors do not offer an explanation as to why the clots could not be aspirated, we hypothesize that an insufficient pressure differential and the clot composition, with strong connections to the blood vessel wall, are the main contributors. Therefore, using an aspiration port with an increased suction diameter in these cases might be beneficial. Additionally, optimal catheter design depends on the type of aspiration technique employed. Aspiration catheters can either remove the thromboembolisms through the catheter via continuous flow or trap it at the tip using vacuum force. The latter benefits from strong vacuum forces that dislodge and remove the thromboembolisms effectively. Larger diameter catheters, like those used for large vessel occlusions in cerebral thrombectomy, or those with tip designs that enhance suction are advantageous. The latter includes sideways-positioned aspiration ports [20-24], multiple aspiration ports [22-24] or tips with a variable cross-sectional area [33-41]. These designs allow for greater vacuum forces using similar vacuum pressures. An increased vacuum pressure would require higher kink resistance by, for

example, reinforcing the shaft with a braid [17]. For peripheral applications with continuous flow aspiration catheters, flexibility is key to navigating tortuous vessels. These catheters might embed steerable tips [42-45], tapered tips for improved manoeuvrability [8, 9, 11] or a gradually lower durometer towards their distal end [16]. Gradually adapting the durometer lowers the risk of buckling over the length of the catheter. Additionally, an extended guidewire can be used to break up occlusions before suction [24].

10.6.3 Limitations

The selected patents within this study are gathered from one database only, namely the worldwide version of Espacenet. Potentially, the results can be expanded by making use of additional databases. Specific eligibility criteria were drawn up to select a demarcated number of patents. Due to the search query, only patents mentioning the truncation 'thromb' within the description were selected. Innovations mentioning this aspect only elsewhere or concerning the aspiration of other solid tissues might have been unjustly excluded. Furthermore, since the study focuses on the distal end of the catheter, improvements made in the shaft or proximal end are not incorporated in this review, although these enhancements might prove crucial for overall device operability. Additionally, some patents simultaneously address multiple design goals. In these cases, the main goal was leading for the development of the categories. Potentially, the categorization can be expanded by including the sub-goals. Finally, to overcome current limitations in aspiration catheter design, it is a necessity to establish close collaborations between the biomedical engineers designing the innovative catheters and clinicians that will utilize these devices to ensure easy integration and adoption of the improved technology into the interventions.

10.6.4 Recommendations for future research

This study gives an overview of thrombectomy aspiration catheter tip design variables, structured in different categories based on the patent design goal. This study can form the basis for future development in aspiration catheter tip designs with improved operability. For this purpose, additional research is required to assess contradictory design specifications or variables that cannot be combined. Even though not specifically described as a category, it is of importance to develop an atraumatic tip to ensure safety during navigation and operation of the catheters. In future, we envision aspiration catheters to utilize active positioning, using magnetic- or wire-actuation, to optimize efficiency and safety, with an increase in aspiration lumen size, using shape memory and superelastic materials such as Nitinol, to prevent kinking and improve thromboembolism dislodgement. We also envision additional means of thromboembolism removal to be used as an add on to aspiration, such as the wasp-inspired transport means [50, 51].

10.7 Conclusion

In this study, we give a comprehensive overview of thrombectomy aspiration catheter tip designs available in patent literature. Overall, 41 patents were included and divided over

five subcategories. It was found that the overall operability of the aspiration catheters can be improved by enhancing the ease of positioning or the suction capacity, either actively or passively. Whenever the active approach is chosen, both functionalities can be addressed simultaneously by switching states, which is advantageous for an efficient and safe procedure. The overview given within this paper might serve as a source of inspiration for future innovations concerning thrombectomy aspiration catheter tip designs.

References

[1] Miloro P, Sinibaldi E, Menciassi A, Dario P. Removing vascular obstructions: a challenge, yet an opportunity for interventional microdevices. *Biomed Microdevices.* (2012) 14(3):511–32. doi: 10.1007/s10544-011-9627-2

[2] Evans MRB, White P, Cowley P, Werring DJ. Revolution in acute ischaemic stroke care: a practical guide to mechanical thrombectomy. *Pract Neurol.* (2017) 17:1–14. doi: 10.1136/practneurol-2017-001685

[3] Medtronic. Export AP aspiration catheter. Available online at: https://europe.medtronic.com/xden/healthcareprofessionals/products/cardiovascular/catheter/export-ap.html (accessed 2023-12-21, 2023).

[4] Teleflex. Pronto extraction catheters. Available online at: https://teleflex.com/usa/en/product-areas/interventional/peripheral-interventions/pronto-extraction-catheters/index.html (accessed 2023-12-21, 2023).

[5] Philips. Quickcath extraction catheter. Available online at: https://www.usa.philips.com/healthcare/product/HCIGTDQKCTEXCT/quickcat-extraction-catheter (accessed 2023-12-21, 2023).

[6] Miki S, Nishide T, Takatera M, Hanita S, inventor; Kaneka CORP, assignee. *Suction catheter.* European Patent EP1543779A1; EP1543779A4; EP1543779B1. (2004).

[7] Kataishi Y, Mori S, Sano Y, Kikuchi T, Isshiki T, inventor; Nipro CORP, assignee. *Thrombus suction catheter with improved suction and crossing.* European Patent EP1440663A1; EP1440663B1. (2004).

[8] Cremascoli P, Silva Orrego P, inventor; NGC Medical SPA, assignee. *Two-lumen suction catheter for distal protection in a percutaneous intervention*. European Patent EP1430924A1; EP1430924B1. (2004).

[9] Mori S, inventor; Nipro CORP, assignee. *Thrombus suction catheter with excellent passableness*. European Patent EP1820531A1; EP1820531A4. (2006).

[10] Reekers JA, inventor; Cordis Europ, assignee. *Suction catheter with preformed tip*. European Patent EP0810002A1; EP0810002B1. (1997).

[11] Chou TM, Wilson SD, Shinsky V, inventor; Route 91 Medical INC, assignee. *Aspiration catheter systems and methods of use*. World Patent WO2019222518A2; WO2019222518A3. (2019).

[12] Auth DC, Gordon LS, Devore LJ, inventor; Boston Scient Corp Northwest T, assignee. *Percutaneous aspiration thrombectomy catheter system.* United States Patent US5827229A. (1998).

[13] Provost-Tine M, Papa B, and Riopel M, inventor; Medtronic Vascular INC, Provost-Tine M, Papa B, and Riopel M, assignee. *Aspiration catheter with tracking portion*. World Patent WO2006023329A2; WO2006023329A3. (2006).

[14] Izawa K and Hiwa H, inventor; Goodman CO LTD, assignee. *Suction catheter*. World Patent WO2014091881A1. (2014).

[15] Le HV *et al.*, inventor; Possis Medical INC, Le HV, Schrom MP, Wong DL; Matson KR, Swanson DA, Grant KC, Klee JT, assignee. *Dual lumen aspiration catheter system.* World Patent WO2007100585A2; WO2007100585A3. (2007).

[16] Tanikawa M, Umegaki R, and Nishimura Y, inventor; Nipro CORP, Tanikawa M, Umegaki R, and Nishimura Y, assignee. *Thrombus-aspiration catheter.* World Patent WO2008123521A1. (2008).

[17] Itou T and Fukuoka T, inventor; Terumo CORP, assignee. *Intravascular foreign matter suction assembly.* European Patent EP1639951A1; EP1639951B1. (2006).

[18] Kusakabe S, inventor; Terumo Clinical Supply CO LTD, assignee. *Intravascular foreign matter suctioning catheter*. World Patent WO2014155489A1. (2014).

[19] Corvese R, inventor; Infinity Neuro LLC, assignee. *Improved aspiration catheter systems and methods of manufacture of the same.* World Patent WO2022087060A1. (2022).

[20] Li C, inventor; Kaneka CORP, assignee. *Suction catheter.* World Patent WO2019012819A1. (2019).

[21] Tanaka S, inventor; Terumo Clinical Supply CO LTD, assignee. *Catheter for aspiration of foreign matter in blood vessel*. World Patent WO2014147815A1. (2014).

[22] Smalling R and Smalling RG, inventor; Smalling Medical Ventures LLC, assignee. *Aspiration thrombectomy catheter system, and associated methods*. United States Patent US10188409B2; US2015080853A1. (2007).

[23] Wu Z, Liang D, and Li T, inventor; WU ZHIQUN, assignee. *Thrombus aspiration system*. China Patent CN203802532U. (2014).

[24] Ruggio JM, inventor; RUGGIO JOSEPH M, assignee. *Apparatus and method for aspirating intravascular, pulmonary and cardiac obstructions*. World Patent WO9512421A1. (1995).

[25] Fojtik SP, inventor; Control Medical Technology LLC, assignee. *Rapid exchange aspiration catheters with lumens configured for optimized flow*. World Patent WO2012040507A1; WO2012040507A9. (2012).

[26] Bagaoisan CJ, Ha HV, Patel MR, Lam S, Muni KR, and Zadno-Azizi G-R, inventor; Medtronic Percusurge INC, assignee. *Aspiration catheters and method of use*. World Patent WO02083229A2; WO02083229A3. (2002).

[27] Mori S, inventor; NIPRO CORP, assignee. *Thrombus suction catheter*. European Patent EP1728531A1; EP1728531B1. (2006).

[28] Li C and Kurose Y, inventor; Kaneka CORP, assignee. *Suction catheter, and method for manufacturing suction catheter*. World Patent WO2018025865A1. (2018).

[29] Gülcher M and Schmitt MM, inventor; Gülcher M and Schmitt MM, Qualimed Innovative Medizinprodukte GMBH, assignee. *Aspiration catheter*. United States Patent US2014214048A1; US9878076B2. (2013).

[30] Consigny P, inventor; Consigny P, assignee. *Spiral thrombectomy catheter*. United States Patent. (2013).
[31] Goff TG, Orth MJ, Yang MC, and Ha H, inventor; Fox Hollow Technologies INC Goff TG, Orth MJ, Yang MC, and Ha H, assignee. *Methods and apparatus for assisted aspiration*. World Patent WO2007030388A2; WO2007030388A3. (2007).
[32] Luther RB, inventor; Luther Medical Products INC, assignee. *Dual lumen infusion/aspiration catheter*. United States Patent US5554136A. (1996).
[33] Vale D, Kelly R, Casey B, and Keating K, inventor; Neuravi LTD, assignee. *Aspirating clot retrieval catheter with expandable mouth.* European Patent EP3875046A1. (2021).
[34] Mintz E, inventor; COVIDIEN LP, assignee. *Aspiration systems and methods, and expanding-mouth catheters*. United States Patent US2022061870A1. (2022).
[35] Li L, Wang A, and Zhu G, inventor; Guangzhou Maijing Medicine Tech Development CO LTD, assignee. *Suction catheter with adjusTable 10.suction cavity opening caliber.* China Patent CN110623705A; CN110623705B. (2019).
[36] Nguyen K *et al.*, inventor; Elixir Medical CORP , Nguyen K, Yan J, assignee. *Devices and methods for aspiration of thrombus.* World Patent WO2021016213A1. (2021).
[37] Baron SJ , Rosenthal M, Snow D, Domecus B, and Le T, inventor; Endovascular Eng INC, assignee. *Aspiration devices for treatment of thrombosis including expandable distal ends and systems and methods thereof*. Canada Patent CA3210625A1. (2022).
[38] Casey B, Kelly R, Keating K, and Vale D, inventor; Neuravi LTD, assignee. *An aspiration catheter, systems, and methods thereof*. European Patent EP3827765A1. (2021).
[39] Von Hoffmann G, inventor; Von Hoffmann G, Onset Medical CORP, assignee. *Intracranial aspiration catheter.* United States Patent US2008065045A1; US8231600B2. (2004).
[40] Li L, Wang A, and Zhu G, inventor; Guangzhou Maijing Medical Tech Development CO LTD, assignee. *Suction catheter device*. China Patent CN110584744A; CN110584744B. (2019).
[41] Desai SM , Jadhav AP , and Atchaneeyasakul K, inventor; Gravity Medical Tech INC ; Desai SM , Jadhav AP , and Atchaneeyasakul K, assignee. *Aspiration catheter*. World Patent WO2023122026A2; WO2023122026A3. (2023).
[42] Spurchise M and Nowak Jr T, inventor; Medtronic Vascular INC, assignee. *Aspiration catheter having selectively deformable tip.* United States Patent US2009270800A1; US7947012B2. (2009).
[43] Ogle MF , Webster MWI, Galdonik JA, Boldenow GA, and Anderson E, inventor; Lumen Biomedical INC, Ogle MF, Webster MWI, Galdonik JA, Boldenow GA, and Anderson E, assignee. *Thrombectomy catheters and other aspiration catheters*. World Patent WO2007022383A2; WO2007022383A3. (2007).
[44] Laub GW, inventor; TDL Innovations LLC, assignee. *Steerable aspiration catheter system*. Canada Patent CA2995193A1; CA2995193C. (2017).
[45] Phelps DY and Furnish G, inventor; assignee. *Lipid pool aspiration arrangement for the treatment of vulnerable atherosclerosis plaque*. United States Patent US2003073975A1. (2002).

[46] Yang Y, Yourgenlow AS, Young LM, and Yee B, inventor; Imperative Care INC, assignee. *Neurovascular aspiration catheter with elliptical aspiration port*. United States Patent US10786270B2; US2020155181A1. (2019).

[47] Douk N, inventor; Medtronic Vascular INC, assignee. *Aspiration catheter having a variable over-the-wire length and methods of use*. World Patent WO2005011786A1. (2005).

[48] Kobayashi T, Secemsky EA, Klein AJ, Faintuch S, Bulman JC, Weinstein JL *et al.* A safety and feasibility single-arm study of a novel catheter thrombectomy device for the treatment of pulmonary embolism (ENGULF). J*J Soc Cardiovasc Angiogr Interv*. (2024) 3(6):102049. doi: 10.1016/j.jscai.2024.102049

[49] Madjidyar J, Vidal LP, Larsen N, Jansen O. Influence of thrombus composition on thrombectomy: ADAPT vs. Balloon guide catheter and stent retriever in a flow model. *Fortschr Röntgenstr.* (2020) 192; p. 257-263

[50] De Kater EP, Sakes A, Bloemberg A, Jager DJ, and Breedveld P. Design of a flexible wasp-inspired tissue transport mechanism. *Front Bioeng Biotechnol*. (2021) 9; p. 782037. doi: 10.3389/fbioe.2021.782037

[51] Sakes A, Van De Steeg IA, De Kater EP, Posthoorn P, Scali M, and Breedveld P. Development of a novel wasp-inspired friction-based tissue transportation device. *Front Bioeng Biotechnol.* (2020) 8: p. 575007. doi: 10.3389/fbioe.2020.575007

Appendix 10.A

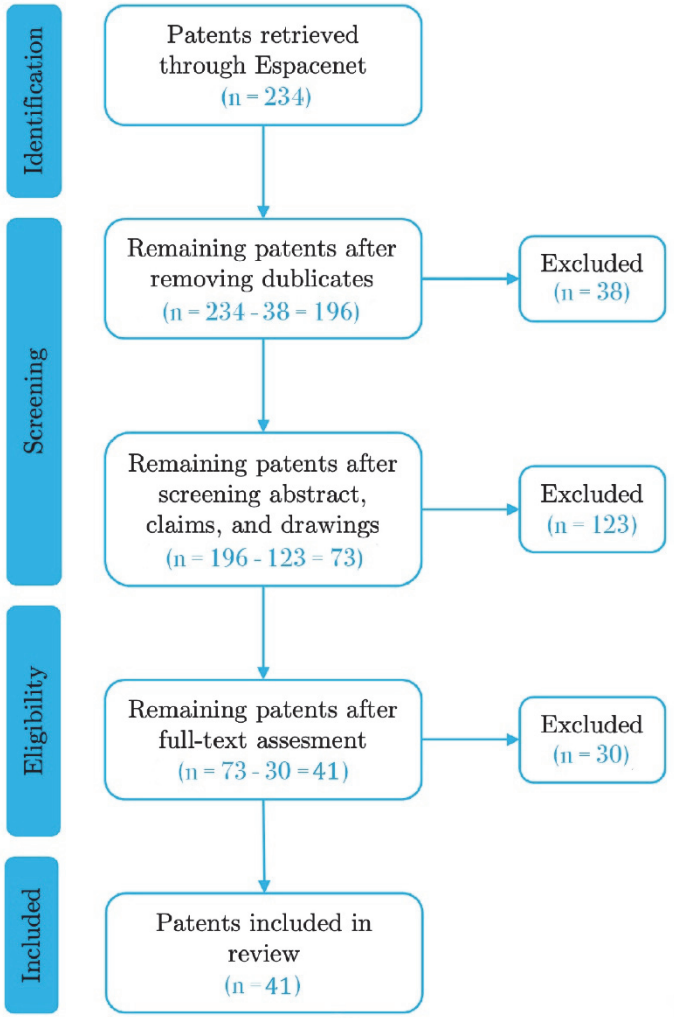


Figure 10.A.1: Flow diagram showing the search results. Following PRISMA2020 guidelines

CHAPTER 11

DESIGN OF A CONVEYING TUBULAR TRANSPORT MECHANISM

ABSTRACT

Tissue extraction plays a crucial role in various medical disciplines, with aspiration catheters serving as the prevailing method. Unfortunately, these catheters face limitations such as clogging and dependence on tissue properties and device dimensions. Therefore, there is a pressing need for an improved tissue extraction device that enables efficient and reliable tissue removal during Minimally Invasive Surgery (MIS). In this study, we present a novel tissue transport system that utilizes a cylindrical conveyor belt mechanism for reliable tissue transportation. We conducted experiments using a proof-of-principle prototype to explore the influence of tissue elasticity, rotational velocity, instrument orientation, and tissue shape on the transportation rate, efficiency, and reliability. Tissue phantoms with gelatine concentrations of 3, 9, and 12 wt% were employed to simulate a range of Young's moduli from 1 to 110 kPa. The mean transportation rates for these phantoms were 7.75 ± 0.48, 8.43 ± 1.50, and 8.90 ± 0.56 g/min, respectively. Notably, all phantoms were transported successfully. The perfect reliability exhibited underscores the potential of our instrument as an alternative to aspiration catheters. This research presents a significant step forward in the field of tissue extraction, offering a promising approach for MIS with enhanced efficiency and reliability.

Published as:
Kortman, V. G., Verberne, Y., Jovanova, J., & Sakes, A. (2023). Advancing minimally invasive surgery: a cutting-edge cable-actuated conveying mechanism for reliable tissue transportation. *Plos one, 18(*12), e0295585.

11.1 Introduction

In a large variety of medical specialities, including cardiology [1], gynaecology [2], neurology [3] and critical care [4], tissues are extracted as a preventative or therapeutic measure [5]. In preventative procedures, (suspicious) tissue is obtained for diagnostic purposes and adequate sample quality is required for accurate analysis. Alternately, unhealthy or obstructive tissue, such as thrombus or tumorous tissue, is removed in therapeutic procedures. Robotic surgery provides safe access to hard-to-reach places to remove tumorous or inflamed tissue [6]. Tissue extraction during surgery is enabled by transportation mechanisms integrated into slender medical instruments, including flexible graspers and aspiration lumens. Medical equipment including bioptomes, stent-retrievers, laparoscopic devices, and catheters all operate using these operating principles [7]. For the elimination of thrombus, for instance, percutaneous aspiration catheters are frequently used. As shorter surgery times are beneficial in order to reduce both anaesthesia time and operation costs [7], continuous transportation mechanisms, such as aspiration, are advantageous over non-continuous methods, such as graspers.

Aspiration catheters are currently one of the most frequently utilized medical devices in Minimally Invasive Surgery (MIS) for tissue removal and are consequently referred to as the golden standard [7]. Aspiration catheters consist of a flexible tubular body with a suction channel. The tissue in front of the catheter's tip is transported through the lumen and towards the handle using a negative pressure differential. Unfortunately, clogging is a common problem with aspiration catheters [7], especially in longer and narrower devices. This phenomenon occurs whenever the friction force between the extracted tissue and the shaft exceeds the suction force (Figure 11.1). Achieving sufficient pressure differential to transport tissues is challenging due to energy losses that occur over the length of the shaft, which makes them unsuitable for further downsizing or increasing the length [8]. This subsequently also emphasizes the dependency of the reliability of aspiration-based transportation on tissue composition. Stiffer clots are less likely to adjust their shape and, therefore, experience a higher risk of getting clamped within the shaft of the device [9]. Furthermore, the suction force can lead to damage to both the surrounding and transported tissue [7]. The latter is especially a drawback in the case of tissue extraction for diagnostic purposes.

Sakes *et al.* [7] propose an alternative mechanism for aspiration-based devices, in which tissue is transported using a friction differential between the device and the tissue. Inspired by the egg-laying structure of the wasp, the device consists of six reciprocating semi-cylindrical blades, which move forwards or backwards in a specific motion sequence and enclose the tissue transportation lumen. Assuming that all blades contribute equally to the total friction with the tissue, the tissue will translate in the direction of the majority of the blades. Transportation in the opposite direction can be prevented by limiting the number of blades retreating simultaneously, whilst keeping the remaining blades stationary or moving these forwards. Experimental validation showed that the device is able to reliably transport tissues with an average transportation rate of 0.25 ± 0.04 g/min for tissue with a Young's modulus of approximately 55 kPa. Using a friction-based transport mechanism will decrease the dependency on tissue elasticity and allow for further downsizing of tissue transportation mechanisms without loss of functionality. However, even though the mechanism shows promising results, the transportation rate of the tissue is still dependent on tissue elasticity, although clogging is no longer an issue [7]. It is hypothesized that soft incoherent tissues

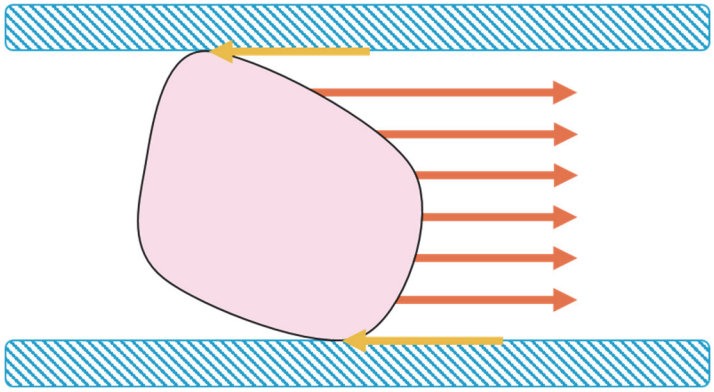


Figure 11.1: Schematic representation of the forces within an aspiration catheter. The orange lines represent the suction force in the desired direction of translation whilst the yellow lines resemble friction between the transported tissue and the shaft of the device. The effect of gravity is neglected.

potentially deform or shear near the blade surface, resulting in lower transportation efficiencies. Whereas on the other extreme, stiff, incompressible, tissues lack tissue deformation, which results in insufficient contact points between the tissue and reciprocating blades for friction-based extraction. Furthermore, due to the movement sequence, in which at least one blade moves always in the opposite direction of the desired transport direction, the overall transportation rate is relatively low. Instead of using a reciprocating motion, an alternative would be to use a mechanism that solely moves in the desired transport direction, such as a conveying mechanism. This would decrease the dependency on tissue properties and improve the transportation rate.

Based on the challenges of current tissue transportation mechanisms, the main objective of this research is to design a novel continuous tissue transportation mechanism compatible with MIS using friction with the tissue to its advantage and in which the transportation reliability is independent of tissue elasticity. The transportation reliability, transportation velocity and transportation efficiency are measured to compare the transportation performance of the novel tissue transport mechanism with commercial tissue transportation devices. The effects of tissue stiffness, tissue shape, instrument angle and rotational velocity are analyzed. With these experiments, we show that the reliability of this novel mechanism remains unaffected by factors such as tissue elasticity, tissue shape and device orientation. Note that the scope of this study does not include the procedure of tissue manipulation and resection.

11.2 Material and methods: Design process

11.2.1 Compatibility for minimally invasive surgery

Compatibility for MIS relates to multiple aspects of the device such as dimensions, material selection, and design decisions considering safety. All elements can be decisive in whether the instrument can be utilized for tissue removal within the human body and inserted through a small incision. In order to enable insertion through a small incision, we set a maximum outer diameter (Øouter) of 10 mm and a minimum inner diameter (Øinner) of 5 mm. Aspiration catheters' outer diameters typically range from 3-6 F [10], which corresponds to a diameter of

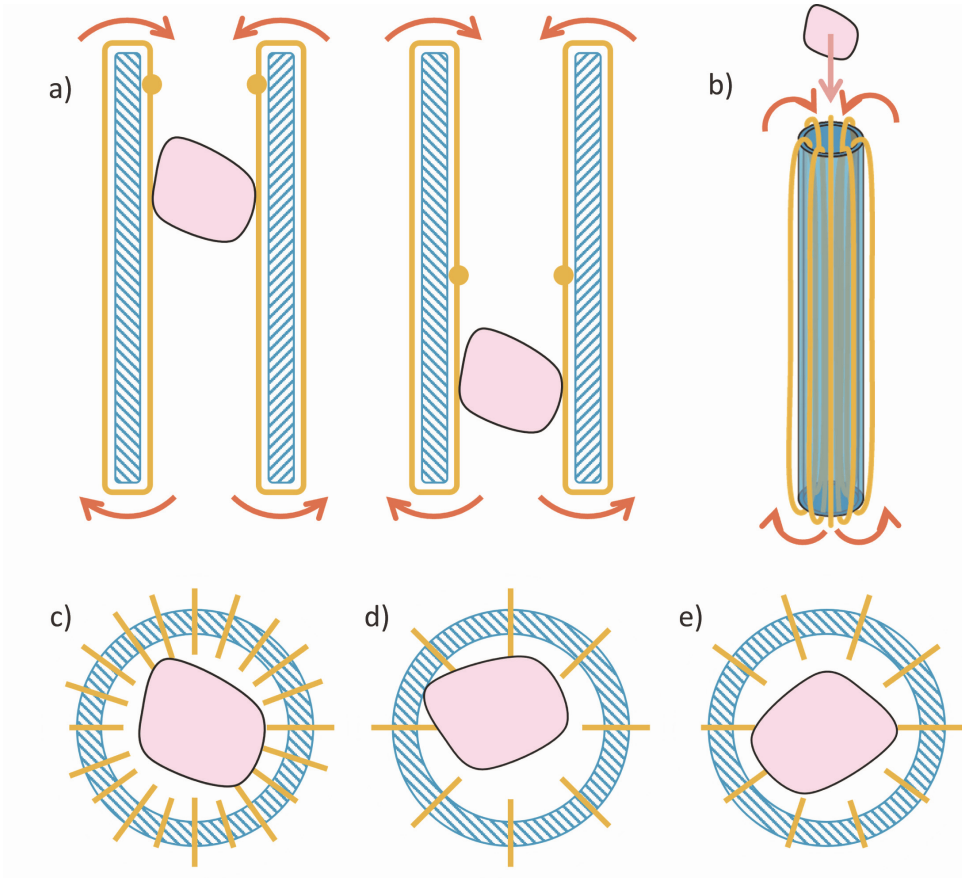


Figure 11.2: Schematic longitudinal and radial cross-sectional visualisations of the tubular body of the transportation concept. a) Conveying movement of the wire shown by the yellow dot. b) Transportation concept in which the continuously rotating cables take the tissue along the tubular body due to the friction between the cables and the tissue. c) Maximizing points of contact between the cables and piece of tissue requires large actuation force. d) Minimizing points of contact between the cables and piece of tissue causes risk of sticking to tubular wall, and e) Final cable design in which one cable is wrapped ten times around the tubular wall. The yellow lines represent the rotating cables and the pink shape the tissue.

1-2 mm. However, depending on the type of MIS, other dimensions apply. For example, the average diameter of commercially available colonoscopes is 13 mm [11]. Furthermore, the ability to transport tissue should be independent of the diameter and length of the device, to allow for further downscaling in the future.

In order to enable fast and reliable tissue transport, the device should transport a wide range of tissues. The mechanical properties of tissue both vary amongst different types and change when diseased. For example, Yu *et al.* [12] found that the Young's modulus of a tumor within a kidney is approximately 20 kPa higher compared to healthy kidney tissue. Furthermore, strain rates non-linearly influence the measured tissue elasticity [13]. Based on data on the biomechanical properties of soft tissue [13-15], the working range for the to-be-developed transportation mechanism is set to 1–110 kPa. This represents a large range of

tissues and organs, from brain tissue and adipose tissue at low strain rates (±1 kPa [13]) to fibrous tissue such as tendons (51.5 ± 25.1 kPa [14]) to cancellous prostate tissue (30-110 kPa [15]), which can be encountered during MIS. Aspiration catheters are assumed to be suitable for the removal of liquids. Therefore, this form of matter is excluded.

In order to enable fast and reliable tissue removal, the transportation rates of the proposed instrument should be comparable to currently clinically available instruments. Transportation rates of commercially available catheters vary between 1.03 and 4.93 mL/s [10]. These velocities are achieved when aspirating liquids and are thus not representative of the removal of solid tissue. More indicative are the transportation rates of clinically available morcellators. These vary between 6.2 to 40.4 g/min during laparoscopic surgery [16]. Therefore we aim to have a similar transportation rate to what is achieved in currently clinically available morcellators.

11.2.2 Final design

Enable cable-driven transport

The proposed mechanism enables tissue transportation by mimicking the working principle of a conveyor belt. Instead of a rotating planar surface, a cable is spanned along the inner tube of the instrument, which is subsequently actuated to generate a translational motion. Similar to the design of Sakes *et al.* [7], friction between the tissue and the body of the medical instrument is used as an advantage. Due to friction between the cable(s) and tissue, the latter is transported whenever continuously rotating the cable(s) in the direction of removal (Figure 11.2a-b). Effective tissue transportation of this novel mechanism depends on the cable configuration, the cable guiding through the instrument, the friction regulation between the cables and the instrument and efficient actuation of the cables.

Different cable configurations were validated for the suitability of tissue transportation. Increasing the number of loops wrapped around the tube decreases gaps between the cables, further enclosing the transported tissue and maximizing the potential points of contact between the tissue and cable, see Figure 11.2c. The latter is beneficial since friction between the tissue and cable is desirable within the implemented working principle. However, increasing the number of loops of cable simultaneously increases the friction between the cable and the instrument, requiring a larger force for actuation and potentially increasing the chance of wear. As illustrated in Figure 11.2d, if the device contains too few loops, the tissue is at risk of sticking to the tubular wall. In the final design, it was decided to use one cable wrapped around the tubular body a total of ten times, see Figure 11.2e. The loops are evenly distributed resulting in a spacing of approximately 1.4 millimeters. Continuous tissue transportation is achieved by clamping each loop of cable along a revolving axis. Whilst it might be favorable to actuate all loops separately, this simultaneously demands more space to position all ten rotating mechanisms. Within the final design, a total of five points of actuation, distributed equally along a circular path was chosen. Figure 11.3 shows a schematic overview of the cable-driven transport mechanism.

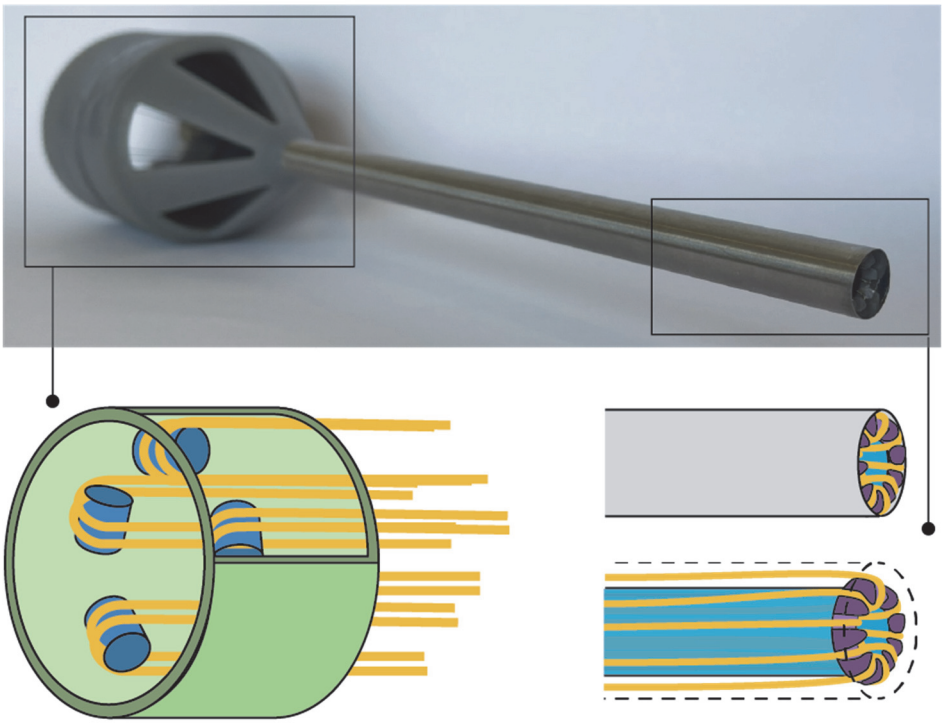


Figure 11.3: Schematic view of the actuation side of the device and the distal end of the cone. Viewed with and without the outer tube.

Enable low-friction cable movement

Within the designed mechanism, the physical phenomenon of friction is used as an advantage to transport tissue. However, even though high friction is desired between the tissue and cable, there are also regions in which friction is experienced as an obstacle, see Figure 11.4. Also, note that specific regions of friction within the device are dependent on the amount of cable tension. Namely, whenever the cable is completely stretched, the contact area between the cable and both the tip and actuation axes is increased. Since it is not beneficial for the former but is desired for the latter, a trade-off remains. High friction between the cable and the shaft of the device is unwanted, as it will result in a higher force that is required to actuate the mechanism, as well as wear. To minimize this hindrance, the cable is spanned with an offset of approximately 0.6 mm with respect to the shaft, as illustrated in Figure 11.3. However, at the tip of the device, the cable is required to be guided, automatically resulting in a point of contact. In order to prevent kinking and wear of the cable, a grooved tip guides the cable loops through slots resulting in a curvature with a diameter of 1 mm. Furthermore, this tip ensures proper positioning of the cables throughout actuation. Within the handle, the cable is guided over a larger diameter to allow for easy tissue removal and to generate space for the actuation mechanism. The cable is spanned with an offset with respect to the handle

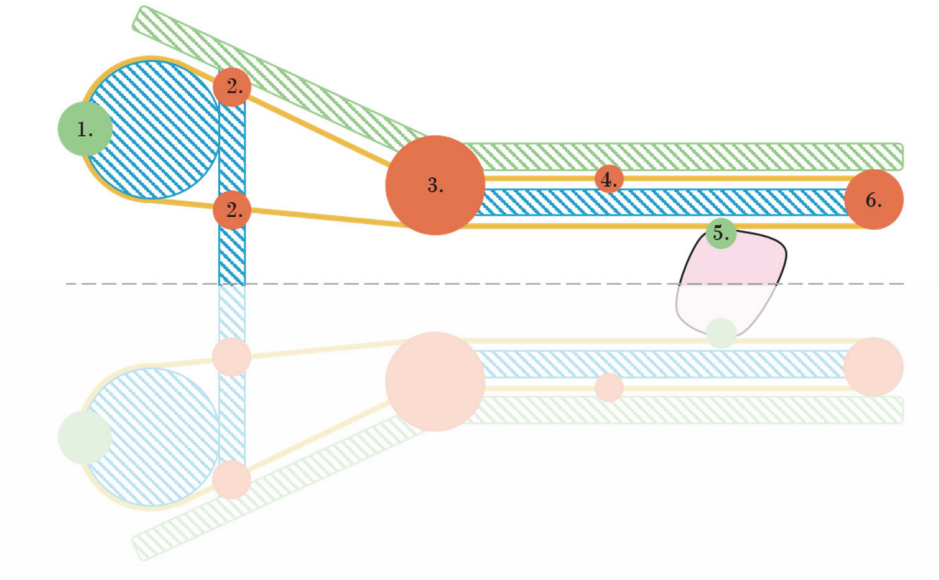


Figure 11.4: Schematic overview of the device. Green and orange dots resemble areas in which friction is either desired or not, respectively.

body, to avoid undesired friction. At the actuation axes (see Figure 11.3), however, high friction is needed in order to propel the cable in the specified direction.

Prototype development

The final proof of principle prototype is illustrated in Figure 11.5. Additionally, a selection of usage steps is visualized in Figure 11.6. The final prototype consists of 24 parts. All elements, excluding the axes, shafts, and cables, were manufactured through Additive Manufacturing (Form 3B, Formlabs, Somerville, MA, USA). The cone includes the cable tensioning mechanism, form lock, gaps for tissue extrusion, and guiding apertures for all loops of the cable. The cable tensioning mechanism consists of a screw thread that increases the distance between the tubular body and gears, which subsequently tensions the cables.

The design of the actuation mechanism is optimized to enable the passing of the cable, provides sufficient stiffness for the forces on the actuation axes and provides attachment to the cone. Since all five actuation points have a differently orientated axis of rotation, bevel gears were implemented, see Figure 11.5c. The rotation of the integrated internal gear results in the rotation of all other gears, subsequently rotating all cables simultaneously. In order to increase the friction with the cable, the actuation axes contain two V-slots, both narrowing towards the center of the axis. Due to this decline in width, the cable is clamped within, and whenever the axis rotates, the cable is pulled in the same direction. The shaft is made from two Stainless Steel capillary tubes with a length of 150 mm through which the cable runs. The outer tube has an outer diameter of Ø10 mm and a wall thickness of 0.2 mm. The inner tube has an outer diameter of Ø7 mm and a wall thickness of 0.4 mm. The shaft is kept in place using a spacer that also serves as a cable guide and is press-fitted on the cone. At the distal end of the shaft, a 3D-printed tip was press-fitted to maintain cable positioning and prevent

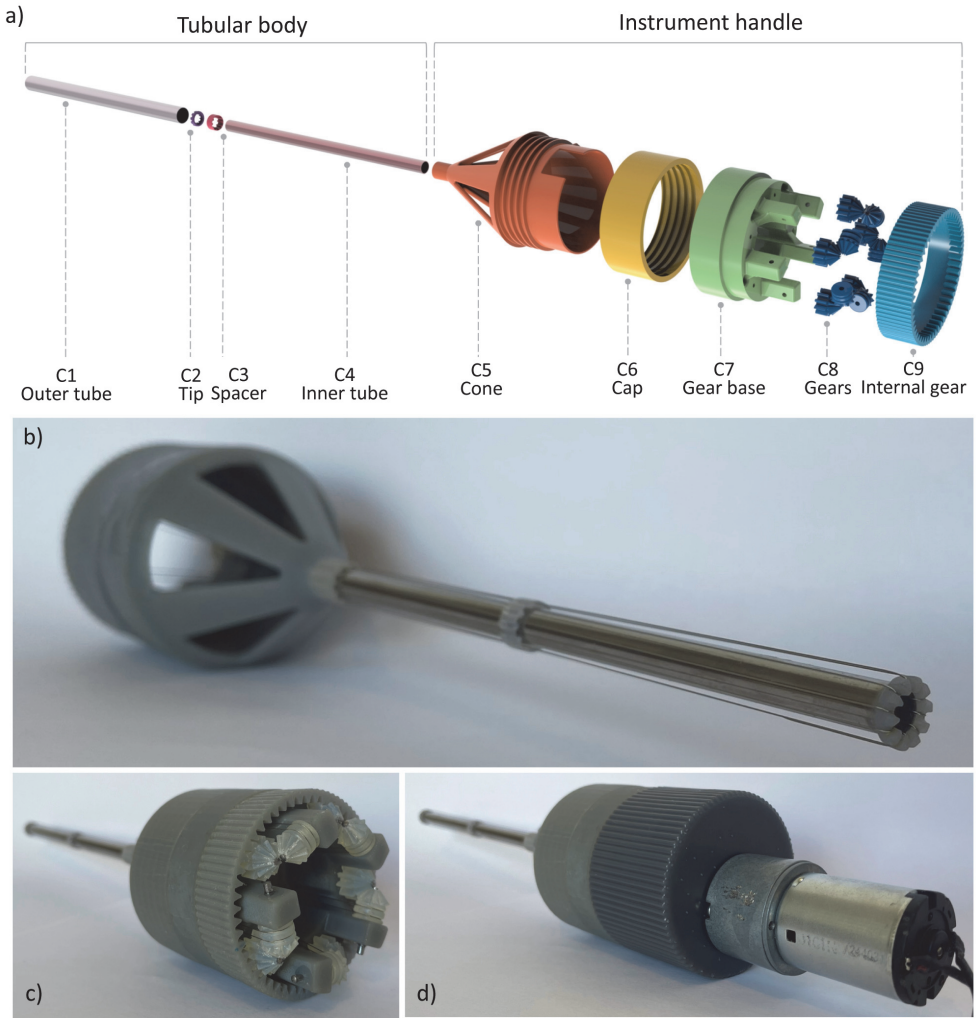


Figure 11.5: Final design. a) Exploded view of the proof of principle prototype with its components (C). b) Device excluding the outer tube. c) Gearbox of device, and d) Device configuration for motorized actuation.

kinking. The cable within the final prototype is made from stainless steel and consists of nineteen Ø0.2 mm intertwined smaller cables (1x19). This dimension is selected in a trade-off between minimizing size whilst maintaining sufficient mechanical properties. After wrapping the cable around the shaft, both ends were connected to each other using a flat knot.

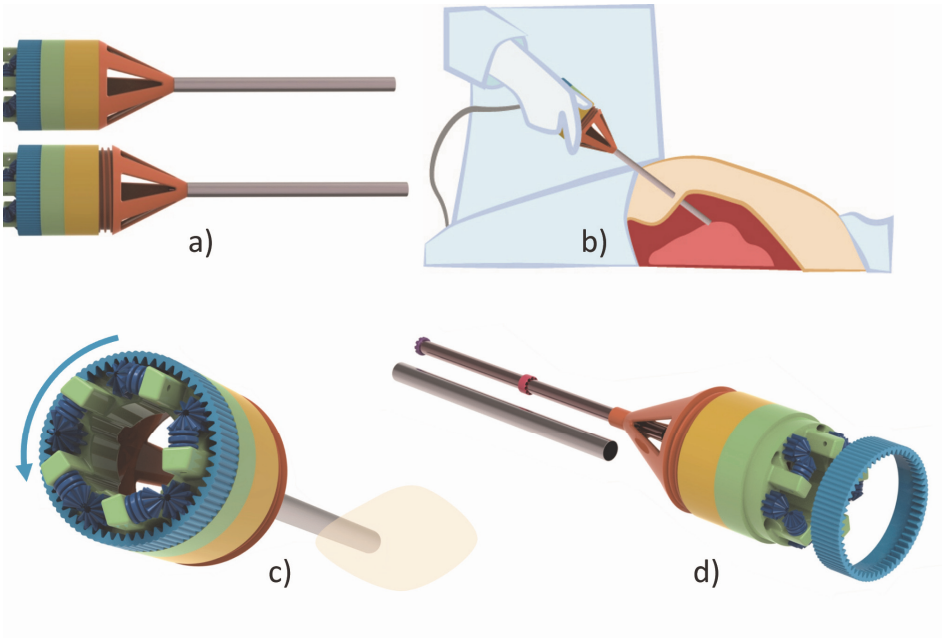


Figure 11.6: Usage steps. a) Tensioning of cable, b) Instrument insertion in the human body through a 10 mm diameter incision, (c) Tissue removal through motorized rotation of the internal gear, and d) Potential device disassembly for complete or partial re-usage.

11.3 Material and methods: Experimental validation

11.3.1 Experimental goal

The main goal of the experiments is to determine the transport reliability of the designed transportation mechanism for a range of rotational velocities of the internal gear and the elasticity of the tissue (Experiments 1-9), the angle at which the device is operated (Experiments 10-12), and sample shape of the transported tissue (Experiment 13). The secondary outcomes of the experiments are the transportation velocity and the transportation efficiency, such that the performance of the developed transportation mechanism can be compared to currently clinically available tissue transport devices.

The independent variables are:

- Tissue elasticity. The transportation mechanism ought to be suitable for tissues within the elasticity range of 1–110 kPa. This represents a large range of tissues and organs which can be encountered during MIS. To mimic the mechanical characteristics of these tissues, tissue phantoms were manufactured using a gelatine-water mixture. The implemented samples have a gelatine weight percentage (wt%) of 3, 9, and 12, representing a tissue elasticity of approximately 1-10, 55, and 100-110 kPa, respectively [17]. Red food colouring was added to enhance the visibility of the tissue phantoms.

- Rotational velocity. The developed mechanism is actuated by the rotation of the internal gear. Increasing the velocity of this motion subsequently increases the translation rate of the cables and, therefore, the tissue transportation velocity. However, it might be hypothesized that high velocities of the cable can potentially result in slip with the tissue. Therefore, this aspect is varied within the experiments to indicate its influence. To guarantee consistent rotation of the proof of principle prototype, actuation is facilitated through an electromotor. Experiments are executed with three different actuation velocities, resulting in a voltage of 8.5, 11, and 13.5 V. The lower extremity is the minimum required voltage in order to set the internal gear in motion. The subsequent rotational velocity is expressed in Rotations Per Minute (RPM). Note that identical power supply voltages do not directly imply equivalent rotational velocities. This is due to different friction forces between the cable and instrument between the experiments as a result of varying cable tension. Therefore, no absolute values can be retrieved from the comparison between tissue elasticity groups, the relative outcomes are merely indicative.
- Instrument orientation. Within MIS, the tubular body of the device is advanced through the human body until correctly positioned for removal. In order to access these target locations, the orientation of the instrument is varied gradually, which impacts the effect of gravity. For example, a more upright position of the tubular body with the tip pointed downwards results in a force on the tissue opposite to the direction of removal. Whenever the gravitational force is higher than the friction between the cable and tissue, removal is obstructed. Within the experimental setup, the operation of the proof of principle prototype is tested horizontally and by pointing the tip of the instrument downwards at an angle of 20°.
- Tissue phantom shape. Transportation within the designed mechanism is enabled through friction between the cable and tissue. These loops of cable are evenly distributed along a circular path, subsequently spanning a tubular body. Whenever this body is completely filled with tissue, all cables contribute to the transportation of the tissue, maximizing the positively experienced friction between both. Whenever this is not the case, fewer cables affect this motion. To map this influence, tests are executed with cylindrical and half-cylindrical tissue phantoms. The diameter and height of each sample are 5 and 15 mm, respectively.

The dependent variables are:

- Transportation velocity. All previously mentioned independent variables potentially influence the transportation velocity of the tissue phantoms. Minimizing the required time for removal is desired within MIS, reducing anaesthesia time and operational costs [7]. Therefore, it is desired to maximize this variable, matching or exceeding the flow rates of currently used devices. The transportation velocity is expressed in [mm/s], calculated by dividing the travelled distance of the tissue phantom within the tubular body by the required time. Additionally, to enable comparison to commercially available devices, an estimation is made of the corresponding transportation rate in [g/min], calculated by dividing the average tissue phantom

weight by the average time required for the concerning to travel through the tubular body.

- Transportation efficiency. Transportation efficiency comprises whether the travelled distance of the cables corresponds with the translation of the tissue. Within an ideal scenario, these values are identical. However, whenever friction between the cable and tissue is insufficient, slip occurs, decreasing the translation of the latter with respect to the former. This can for example be caused by inadequate contact points between both, due to larger experienced friction between the tissue and tubular wall of the device, or due to gravity forces adverse to the direction of removal. Since *time* [s] is measured within the experiments, the transportation efficiency is calculated as indicated in Equation (11.1) and Equation (11.2). Within this equation, $\eta_{transportation}$ represents the transportation efficiency in [%] and $t_{theoretical}$ [s] and $t_{measured}$ [s] the theoretical and measured translation time, respectively. The rotational velocity of the motor, RPM_{motor}, is converted to the corresponding rotational velocity of the spur and bevel gears, by multiplying this variable with the teeth ratio of the internal and spur gear, $teeth_{internal}$ and $teeth_{spur}$, respectively. The fraction of the travelled tissue distance, Δx_{tissue} [mm], divided by the circumference of the pulley directly attached to the bevel gear, c_{pulley} [mm], determines the theoretically required number of rotations for this translation. Dividing the second element by the first and multiplying with a factor of sixty results in the theoretical translation time. Note that a perfect transmission between gears and between the clamping axes and cable is assumed.

$$\eta_{transportation} = \frac{t_{theoretical}}{t_{measured}} \cdot 100\% \quad (11.1)$$

$$t_{theoretical} = \frac{\frac{\Delta x_{tissue}}{c_{pulley}}}{RPM_{motor} \cdot \frac{teeth_{internal}}{teeth_{spur}}} \cdot 60 \quad (11.2)$$

- Transportation reliability. Lastly, the variable transportation reliability indicates whether all tissue phantoms are successfully transported within the executed experiments. Phenomena such as clogging or malfunctioning of the device are unacceptable within medical procedures. The transportation reliability *r*, expressed as a percentage [%], is calculated as indicated within Equation (11.3). $n_{successful}$ represents the number of times in which the tissue phantom is successfully transported through the tubular body of the device and n_{total} is the total amount of experiments executed. This variable is aimed to be as high as possible.

$$r = \frac{n_{successful}}{n_{total}} \cdot 100\% \quad (11.3)$$

11.3.2 Experimental Procedure

The experimental setup is illustrated in Figure 11.7a. The transport system is mounted in a PMMA standard and supported at three fixed locations. One of the five holes within the cone is orientated perfectly towards the point of vision, allowing for clear detection of the transported tissue phantoms. Behind the gearbox, an electromotor (Igarashi 33GN2738-132-

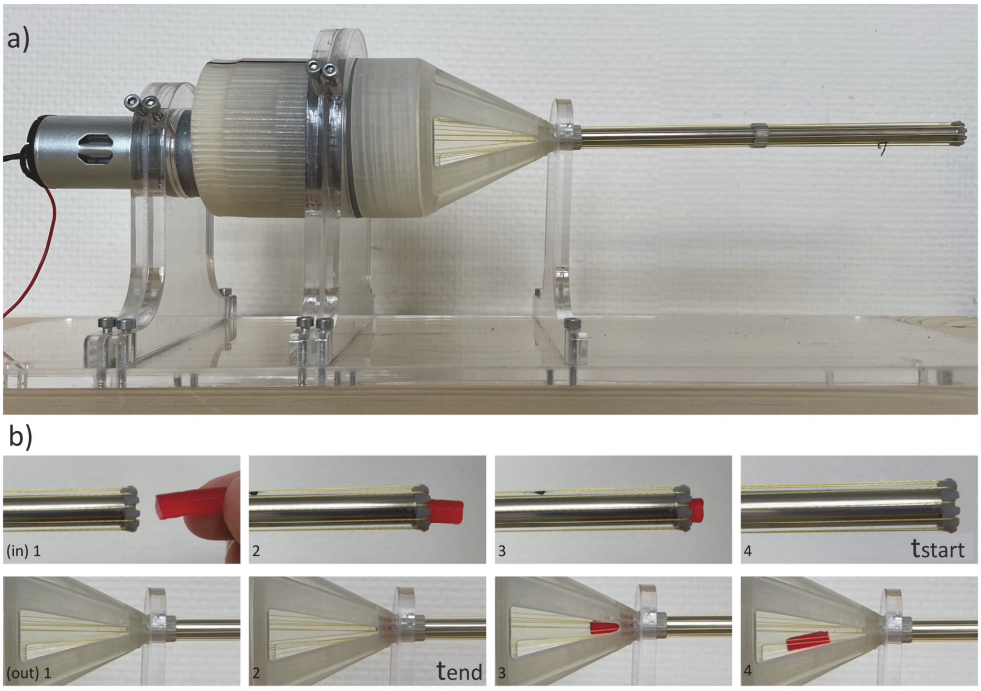


Figure 11.7: Experimental setup. a) Proof of principle prototype mounted in a PMMA standard. b) Snapshots of a tissue phantom entering and exiting the tubular body of the device, indicating the configuration in which the start and end times are determined, used to calculate the transportation velocity.

GV-5 50:1, 12V) is placed to actuate the prototype. This is facilitated by attaching the axis of the electromotor by means of a shape lock to the internal gear. A power supply is attached to the electromotor. Furthermore, a black line was drawn on the outside of the internal gear to determine the rotational velocity of the prototype, which is expressed in RPM. Also, the knot used to tie both ends of the cable to one another was marked black and was used as a reference to determine the rotational velocity of the cable. The outer tube is removed throughout the experiments. To ensure identical tissue phantom sample sizes, the different gelatine mixtures were poured into molds, containing cylindrical cut-outs with a diameter of 5 mm and height of 15 mm. The half-cylindrical tissue phantoms were cut manually by splitting the cylindrical shapes in half.

In total, 13 experiments were carried out, see Table 11.1. Each individual experiment was performed with ten tissue phantoms. The prototype was mounted in the experimental setup, after which the electromotor was turned on. Subsequently, the tissue phantom was inserted manually at the tip of the device. Once the tissue phantom travelled the entire distance through the tubular body and was visible within the handle, the measurement was terminated. After this, the process was repeated with a new tissue phantom for a total of ten times. Each experiment was recorded using a camera.

11.3.3 Data analysis

The video footage obtained during the experiments is evaluated manually by systematically freezing the video frames to extract the RPM of the internal gear and the required time for each tissue phantom to travel through the tubular body of the device. Within Figure 11.7b, several snapshots are displayed of a tissue phantom entering and exiting the tubular body. The rotational velocity of the cable is approximated by counting the number of times the black line on the outside of the internal gear passes by throughout all ten measurements, divided by the total experiment time. The retrieved information is processed within Matlab, whereby Boxplots and statistical analysis are utilized to gain insights. One-way ANOVA and independent two-sample t-tests are performed for data analysis.

11.3.4 Results

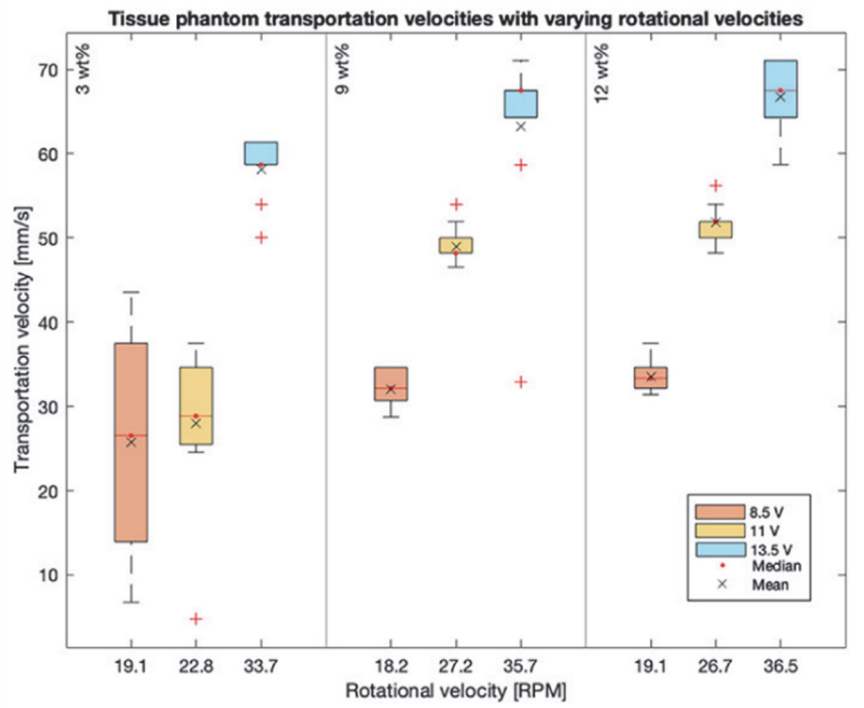
The data extracted from Experiments 1–9 (see Table 11.1) is displayed in Figure 11.8a. Within these experiments, the goal was to gain insights into the dependency of the transportation velocities of tissue phantoms with differing elasticity properties on the rotational velocity of actuation. It can be seen that an increase in rotational velocity subsequently increases the transportation rates for all three categories. A statistically significant difference in the transportation velocity caused by deviating power supply is established through one-way ANOVA analysis, for the 3 wt% ($F(2, 27) = 33.13$, $p = 5.40\ 10^{-8}$), 9 wt% ($F(2, 27) = 53.55$, $p = 4.01\ 10^{-10}$) and 12 wt% ($F(2, 27) = 316.82$, $p = 1.80\ 10^{-19}$) gelatine tissue phantoms. With the current set-up, the highest transportation rates are attained through a 13.5 V power supply for all three groups, resulting in a mean velocity of 58.16 ± 3.59 mm/s, 63.23 ± 11.24 mm/s, and 66.75 ± 4.19 mm/s for the 3, 9, and 12 wt% gelatine tissue phantoms, respectively. This resembles a mean transportation rate of 7.75 ± 0.48 g/min, 8.43 ± 1.50 g/min, and 8.90 ± 0.56 g/min accordingly, assuming a tissue phantom mass of 0.3 gram. The highest variance is measured whilst transporting 3 wt% gelatine tissue phantoms with a power supply of 8.5 V, resulting in a mean velocity of 25.80 ± 13.88 mm/s.

Within Figure 11.8b, data extracted from Experiments 4–6 and 10–12 (see Table 11.1) are graphically displayed. In these experiments, the transportation velocity is measured with varying instrument orientations for all three weight percentage gelatine tissue phantoms. For the 9 and 12 wt% gelatine tissue phantom categories, higher transportation velocities were attained whenever the device was oriented horizontally when compared to the tip pointing downwards at an angle of 20°. This is confirmed by the independent two-sample t-tests, indicating significantly different transportation velocities for the 9 ($h = 1$, $p = 5.38\ 10^{-4}$) and 12 wt% ($h = 1$, $p = 3.47\ 10^{-7}$) gelatine tissue phantoms. Within the 3 wt% gelatine phantoms, no significant difference is found between the transportation velocities within varying instrument orientations according to an independent two-sample t-test ($h = 0$, $p = 0.3511$). Lastly, different shapes of tissue phantoms were transported within the proof of principle prototype. This experiment was only executed for 9 wt% gelatine tissue phantoms with a corresponding power supply of 11 V. The results are graphically summarized in Figure 11.9. Both the half-cylindrical and cylindrical tissue phantoms were reliably transported with a transportation rate of 100%.

Table 11.1: Overview of the executed experiments using the proof of principle prototype. Each experiment was executed with ten tissue phantoms, resulting in a total of 130 measurements.

Experiment number	**1**	**2**	**3**	**4**	**5**	**6**	**7**	**8**	**9**	**10**	**11**	**12**	**13**
Power supply (V)	8.5	8.5	8.5	11	11	11	13.5	13.5	13.5	11	11	11	11
Tissue phantom (wt%)	12	9	3	12	9	3	12	9	3	12	9	3	9
Device orientation (°)	0	0	0	0	0	0	0	0	0	-20	-20	-20	0
Tissue Phantom Shape	cylinder	cylinder	cylinder	cylinder	cylinder	cylinder	cylinder	cylinder	cylinder	cylinder	cylinder	cylinder	½ cylinder
Transportation Efficiency (%)	91	91	47	100	91	44	95	89	90	92	84	75	91
Reliability (%)	100	100	100	100	100	100	100	100	100	100	100	100	100

a)



b)

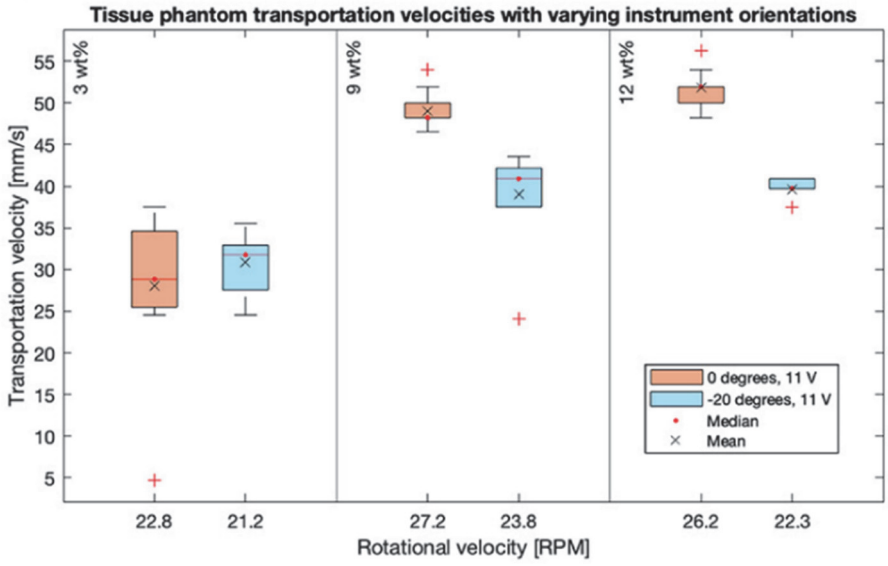


Figure 11.8: Results illustrated in boxplot graphs. Outliers are plotted individually using the red '+' marker symbol. a) The transportation velocities of all three weight percentage gelatine tissue phantom categories as a result of varying rotational velocities. b) The transportation velocities of all three weight-percentage gelatine tissue phantom categories as a result of varying instrument orientations, all actuated with a power supply of 11 V.

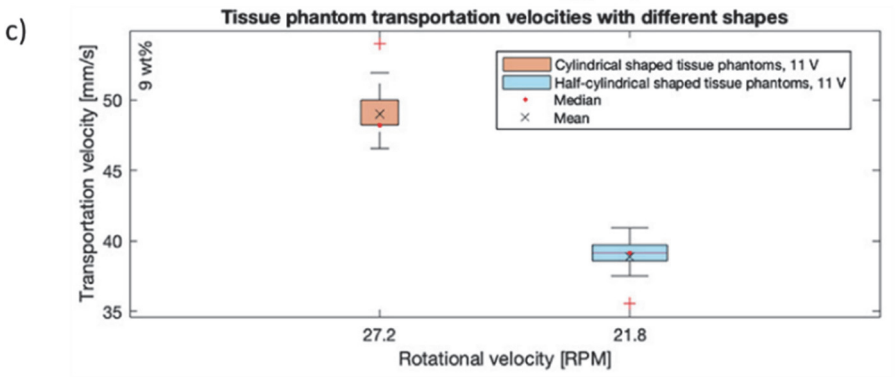


Figure 11.9: Results illustrated in boxplot graphs. The transportation velocities of all three weight-percentage gelatine tissue phantom categories as a result of varying tissue phantom shapes, all actuated with a power supply of 11 V. Outliers are plotted individually using the red '+' marker symbol.

The transportation efficiency of the device was determined, as indicated by Equation 11.1. The results, based on the mean tissue transportation time and rotational velocity of the internal gear of each experiment, are displayed in Table 11.1. It was found that the transportation efficiency decreases whenever the tip is pointed downwards at an angle of 20° with the 9 and 12 wt% gelatine tissue phantoms. Efficiency remains identical in the case where the tissue phantoms are halved and thus adjusted in shape. In Experiments 3 and 6, efficiency is significantly lower at 47% and 44%, respectively.

11.4 Discussion

11.4.1 Summary of main findings

The proof of principle prototype enables continuous transportation of tissue within a Young's modulus range of 1–110 kPa, mimicked using 3, 9, and 12 wt% gelatine tissue phantoms with a transportation reliability of 100%. The maximum mean mass transportation rate of these categories is measured to be 7.75 ± 0.48, 8.43 ± 1.50, and 8.90 ± 0.56 g/min, respectively. This lies within the range of transportation rates of clinically available morcellators operated during laparoscopic surgery , such as the Steiner morcellator (Karl Storz). This morcellator has a mean transportation rate of 6.3 g/min [16]. However, laparoscopic morcellators such as the Gynecare Morcellex (Ethicon) reach higher transportation rates of around 28 g/min [18]. Similar transportation rates could potentially be reached by an increase in the rotational velocity of the developed transport mechanism, as the experiments showed that this significantly increases transportation rates for all three phantom tissues. During the experiments, no stagnation and corresponding equilibrium were retrieved which means that the maximum transportation velocity of the developed transportation mechanism was not reached yet. Transportation efficiency increases for tissue phantoms with higher elasticity properties. It is hypothesized that soft tissues are more likely to deform or shear near the cable surface, being more sensitive to slip. At the other extreme, stiffer tissues clamp within the cable loops and therefore experience high friction between both, which is beneficial for the

developed transportation mechanism. Concerning shaft orientation, an efficiency loss of approximately 8 and 7% was found when pointing the tip of the device downwards when compared to horizontal operation, for transportation of the 9 and 12 wt% gelatine tissue phantoms, respectively. Efficiency remained identical in the case where the tissue phantoms were halved, and thus adjusted in shape. It is expected that the decrease in tissue phantom volume and weight measures up to the decrease in contact points between the concerning and cable. Alternatively, it can be hypothesized that not all contact points are required for friction-based transport of the tissue. The mechanism's independence on tissue volume is, for instance, beneficial for the removal of tissue during laser surgery, which is associated with variable shrinkage of the tissue specimen [19]. With the current advancements in exoscope-based surgery, it becomes even more evident to remove irregular tissue from hard-to-reach surgical sides [20]. Throughout the experiments, all tissue phantoms were transported successfully through the tubular body of the device, resulting in a reliability of 100%. The developed conveying transport mechanism outperforms other tissue transport devices, such as aspiration-based devices or the friction-based transportation device developed by Sakes *et al.* [7], in the ability to transport tissue independently of their elasticity or shape. Moreover, unlike aspiration-based devices, surrounding tissue is unaffected by the transportation mechanism and the conveying transportation principle allows for miniaturization without compromising on performance.

11.4.2 Limitations

The proof of principle prototype showcased the working principle of using a conveying mechanism for tissue transportation. However, as expected, undesired friction occurs between the spanned cable and the tip of the instrument, resulting in excessive wear. Subsequently, the bending radius of the cable decreased, which increased the experienced friction. Furthermore, whenever the tissue reached the proximal end of the tubular body, the translation velocity of the tissue rapidly decreased due to the gradual loss in contact area with the cable. Due to this occurrence, the tissue often remained partially trapped within the tubular body. Although this might not be an issue during continuous operation, a slight redesign of the cable guidance in the handle can help prevent this in future. Additionally, the rotational velocity of the actuation is varied between experiments by altering the power supply of the electromotor, expressed in voltage. Dependent on the, at that time, experienced resistance, this resulted in a specific rotational velocity of the internal gear, which is thus not identical within each experiment powered with the same voltage. Finally, future research should include *ex-vivo* and *in-vivo* studies to gather more insight into the performance of the developed tissue transportation mechanism. Although the gelatine phantom tissues mimic the stiffness of a wide range of tissues, these phantom tissues are unable to fully resemble all tissue properties accurately, such as their heterogeneous composition and friction coefficient. These properties could affect the interplay between the transported tissues and cables.

11.4.3 Recommendations

In the future, the device should be redesigned to tailor the desired friction to its function and prevent excessive wear. More rubber-like materials in the gears might be advantageous to enhance the clamping functionality, whilst a wear-resistive material could be applied for the bevel gears. To prevent excessive wear of the tip due to cable sliding, it is recommended to

make use of an alternative material, such as stainless steel, for this component. Excessive cable tension resulted in slight bending of the gear base and play between the electromotor and the housing caused a slightly jolty motion of the device. In order to prevent play between the components, the gear base and electromotor connection should be fortified and redesigned, for instance by supporting the bevel gear's axes at both sides to ensure the alignment of the bevel gears. With these adaptations, the durability of the transportation device should be demonstrated in fatigue studies. In order to increase access to different clinical application areas of the device, the shaft could be made flexible or steerable to enable the circumnavigation of delicate structures and bones. However, when positioning the device within a curvature, a length difference occurs between paths along the tube. To maintain tension along all loops of cable, the corresponding tensioning mechanism and cable implementation ought to be adjusted. Additionally, the ability of the device to grip tissues could be investigated, as only a small area of contact resulted in the device pulling the tissue into the shaft. The developed transportation mechanism could be integrated into existing devices used in, for instance, Natural Orifice Transluminal Endoscopic Surgery (NOTES), endoluminal surgery or laparoscopic surgery. The inner lumen provides space for the insertion of other instruments used during these procedures, such as scalpels and graspers, or imaging tools, such as an endoscope. Integrating such instruments with the transportation mechanism eliminates the need for additional incisions. Also, future studies should validate the performance of the device in *ex-vivo* and *in-vivo* (animal) studies and should encompass a wide range of tissues, such as uterine, bowel or muscle tissue, featuring different tissue shapes and volumes. This would not only provide valuable insights into the mechanism's versatility, but the transported tissue samples can additionally be analyzed for superficial and histological damage. Damage could be caused by tissue heating (due to friction forces) or tissue fragmentation (due to shear forces generated by the cables). Lastly, future research should focus on sterilizability to make the device applicable for clinical use.

11.5 Conclusion

The goal of this study was to design a continuous tissue transportation mechanism compatible with MIS in which the transportation reliability is independent of tissue elasticity. The designed instrument enables tissue removal using friction between a continuously rotating conveying cables mechanism. The proof of principle prototype demonstrated the feasibility of the mechanism in successfully transporting 3, 9, and 12 wt% gelatine tissue phantoms, resulting in the reliability of the instrument of 100%. The maximum mean mass transportation rate of these categories was measured to be 7.75 ± 0.48, 8.43 ± 1.50, and 8.90 ± 0.56 g/min, respectively, illustrating the achieved transportation velocities lay within the rates of clinically available morcellator operated during laparoscopic surgery. Furthermore, potential barriers of the currently golden standard aspiration catheter are overcome, such as the risk of clogging, damage hazard to surrounding tissue, and the dependency of the force of removal on the diameter of the tubular body. All these elements contribute to the potency of the designed mechanism to become a viable tissue transportation mechanism for MIS in future.

References

[1] S. Pornratanarangsi *et al.*, "Extraction of challenging intracoronary thrombi: multi-device strategies using guide catheters, distal vascular protection devices and aspiration catheters," *The Journal of invasive cardiology,* vol. 20, no. 9, pp. 455-462, 2008.

[2] S. Cohen and J. A. Greenberg, "Hysteroscopic morcellation for treating intrauterine pathology," *Reviews in Obstetrics and Gynecology,* vol. 4, no. 2, p. 73, 2011.

[3] A. J. Yoo and T. Andersson, "Thrombectomy in acute ischemic stroke: challenges to procedural success," *Journal of stroke,* vol. 19, no. 2, p. 121, 2017.

[4] M. Zawadka *et al.*, "Real-time ultrasound guidance as compared with landmark technique for subclavian central venous cannulation: a systematic review and meta-analysis with trial sequential analysis," *Critical Care Medicine,* vol. 51, no. 5, pp. 642-652, 2023.

[5] W. W. Spurbeck, A. M. Davidoff, T. E. Lobe, B. N. Rao, K. P. Schropp, and S. J. Shochat, "Minimally invasive surgery in pediatric cancer patients," *Annals of Surgical Oncology,* vol. 11, no. 3, pp. 340-343, 2004.

[6] M. Di Luca *et al.*, "Use of the transoral robotic surgery to treat patients with recurrent lingual tonsillitis," *The International Journal of Medical Robotics and Computer Assisted Surgery,* vol. 16, no. 4, p. e2106, 2020.

[7] A. Sakes, I. A. Van de Steeg, E. P. De Kater, P. Posthoorn, M. Scali, and P. Breedveld, "Development of a novel wasp-inspired friction-based tissue transportation device," *Frontiers in Bioengineering and Biotechnology,* vol. 8, p. 575007, 2020.

[8] Y. Shi, D. Cheshire, F. Lally, and C. Roffe, "Suction force-suction distance relation during aspiration thrombectomy for ischemic stroke: a computational fluid dynamics study," *Physics in Medicine,* vol. 3, pp. 1-8, 2017.

[9] J. Madjidyar, L. P. Vidal, N. Larsen, and O. Jansen, "Influence of thrombus composition on thrombectomy: ADAPT vs. balloon guide catheter and stent retriever in a flow model," in *RöFo-Fortschritte auf dem Gebiet der Röntgenstrahlen und der bildgebenden Verfahren*, 2020, vol. 192, no. 03: © Georg Thieme Verlag KG, pp. 257-263.

[10] T. D. Long *et al.*, "Novel aspiration catheter design for acute stroke thrombectomy," *Journal of neurointerventional surgery,* vol. 11, no. 2, pp. 190-195, 2019.

[11] Y. Han, Y. Uno, and A. Munakata, "Does flexible small-diameter colonoscope reduce insertion pain during colonoscopy?," *World Journal of Gastroenterology,* vol. 6, no. 5, p. 659, 2000.

[12] X. Yu *et al.*, "Needle-shaped ultrathin piezoelectric microsystem for guided tissue targeting via mechanical sensing," *Nature biomedical engineering,* vol. 2, no. 3, pp. 165-172, 2018.

[13] K. Comley and N. A. Fleck, "A micromechanical model for the Young's modulus of adipose tissue," *International Journal of Solids and Structures,* vol. 47, no. 21, pp. 2982-2990, 2010.

[14] K. Arda, N. Ciledag, E. Aktas, B. K. Arıbas, and K. Köse, "Quantitative assessment of normal soft-tissue elasticity using shear-wave ultrasound elastography," *American journal of roentgenology,* vol. 197, no. 3, pp. 532-536, 2011.

[15] R. G. Barr, R. Memo, and C. R. Schaub, "Shear wave ultrasound elastography of the prostate: initial results," *Ultrasound quarterly,* vol. 28, no. 1, pp. 13-20, 2012.

[16] S. R. Driessen, E. A. Arkenbout, A. L. Thurkow, and F.-W. Jansen, "Electromechanical morcellators in minimally invasive gynecologic surgery: an update," *Journal of minimally invasive gynecology,* vol. 21, no. 3, pp. 377-383, 2014.

[17] A. Karimi and M. Navidbakhsh, "Material properties in unconfined compression of gelatin hydrogel for skin tissue engineering applications," *Biomedical Engineering/Biomedizinische Technik,* vol. 59, no. 6, pp. 479-486, 2014.

[18] M. A. Martínez-Zamora, C. Castelo-Branco, J. Balasch, and F. Carmona, "Comparison of a new reusable gynecologic laparoscopic electric morcellator with a disposable morcellator: a preliminary trial," *Journal of Minimally Invasive Gynecology,* vol. 16, no. 5, pp. 595-598, 2009.

[19] E. Halliday and A. George, "Quantifying the shrinkage of laryngeal laser excisions: a case control study," *The Journal of Laryngology & Otology,* vol. 136, no. 12, pp. 1265-1270, 2022.

[20] S. Ferlito *et al.*, "High definition three-dimensional exoscope (VITOM 3D) in ENT surgery: a systematic review of current experience," *Journal of Clinical Medicine,* vol. 11, no. 13, p. 3639, 2022.

11

CHAPTER 12

DESIGN OF A TOROIDAL TRANSPORT MECHANISM

ABSTRACT

In the medical field, it is essential to remove delicate tissues from the body without damaging them or disturbing the surroundings. Current tissue transport mechanisms depend on the tissue composition and shape of the transported tissue, which results in problems such as clogging. This study presents a soft transportation mechanism for tissues inspired by the longitudinal muscles associated with the peristaltic movement of the gastrointestinal tract. The mechanism is designed as a conveying toroid that turns itself inside out in a continuous motion. A fabrication method was developed to manufacture a small-sized silicone toroid, filled with lubricating liquid. Comparable to the peristaltic movement, the silicone toroid adapts its shape to the transported tissue which results in a soft seal around the tissue.

Published as:
Kortman, V. G., Jovanova, J., & Sakes, A. (2023). Design of a soft bio-inspired tissue transport mechanism. *In 2023 IEEE International Conference on Soft Robotics (RoboSoft)* (pp. 1-6). IEEE.

12.1 Introduction

The transport of delicate objects from confined environments is an urging topic in many industries, especially when manipulating an object remotely. Applications that require this type of transport are exploration and delicate object collection, such as deep sea mining, rescue operations, or surgery [1-3]. The field of soft robotics shows potential solutions for sustainable transportation of these delicate or valuable objects by gentle picking them from their surroundings and transporting them without any damage or disruption to their environment [4]. This is in contrast to rigid robotic transport systems. They are often associated with negative environmental impact and transport damage, as they lack an adaptive feature to real-world environments [5].

In the medical field, a soft transportation mechanism for tissues would be of great benefit. Treatment in many medical fields involves tissue removal from the human body. Disturbances, such as tumorous tissue or thrombus, are removed from the operational field in different surgical procedures [6, 7]. Also, suspicious tissue is removed for diagnostic purposes, which requires undamaged samples for optimal analysis [8].

The current trend is to perform surgeries minimally invasive, where small (5-15 mm) incisions are made to insert slender surgical instruments into the human body. A major downside of Minimal Invasive Surgery (MIS) is the reduced access to the operational field, which requires longer, and sometimes curved, pathways to transport the targeted tissue outside the body. Currently, the 'golden standard' for tissue transportation in MIS is the use of aspiration catheters. These slender and flexible catheters are able to follow curved paths toward the target tissue, where they apply a suction force to remove the tissues from the body. The main issue with these catheters is their vulnerability to clogging [9]. Clogging occurs when the friction between the target tissue and the catheter's lumen exceeds the force that can be applied by the generated negative pressure. Research has shown that the ability to transport tissues with these devices is highly dependent on the length of these devices and the tissue composition. Furthermore, the suction force affects not only the target tissue but also the surrounding tissue, which can result in unwanted damage to delicate structures. Previous research showed alternative tissue transportation mechanisms, but their functionality was again influenced by the tissue composition [2]. A major improvement in this field would be a flexible tissue transport mechanism whose transportation success is independent of the friction between the tissue and the transporting shaft. Therefore, this study aims to develop a soft tissue transport mechanism that transports tissue along while being unaffected by tissue composition or shape.

12.2 Design and Prototyping

12.2.1 Bio-Inspiration: Peristalsis

Inspiration for our novel transport mechanism is taken from the peristaltic movement of the gastrointestinal tract. Figure 12.1 shows a schematic overview of the peristaltic movement, highlighting the circular and longitudinal muscles in the tract's wall. It is relatively easy to understand how a propelling wave of circular muscles' contractions behind the bolus pushes the bolus forward. However, this type of transport has as downside that it needs to overcome

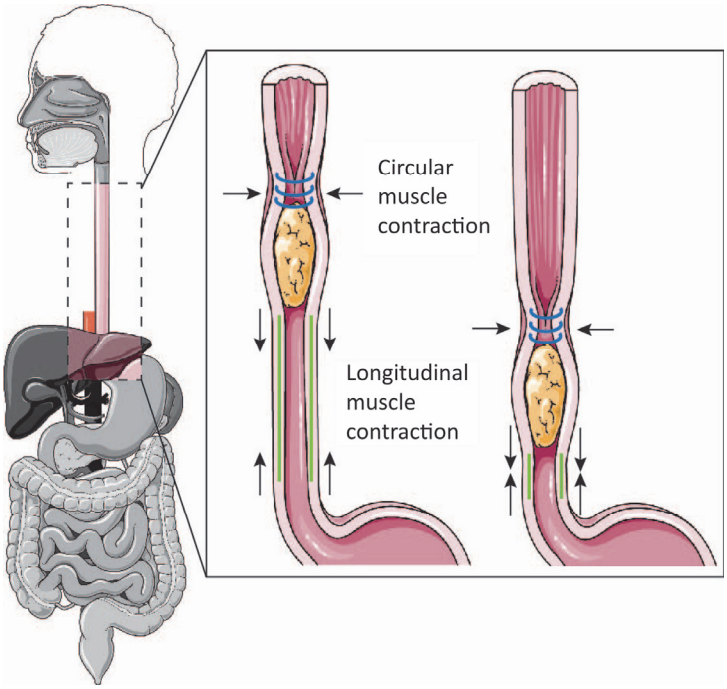


Figure 12.1: Schematic overview of the peristaltic movement in the gastrointestinal tract. The circular muscles (blue) and longitudinal muscles (green) highlighted. Contracting the circular muscles seals the bolus at a fixed spot while contracting the longitudinal muscles shortens the tract before the bolus approaches. Figure adapted from Servier Medical Art, provided by Servier licensed under a Creative Commons Attribution 3.0 unported license.

the friction between the tract's wall and the bolus. More interesting is the contribution of the longitudinal muscles, which is often overlooked [10]. The contraction of these muscles precedes the circular muscle contractions. They shorten the tract gradually before the bolus approaches [11]. The circular muscle contraction acts as sealing of the tract behind the bolus, preventing the escape of the bolus [12]. Prior studies hypothesized different functions for this longitudinal muscle contraction, among which are slipping the tract's wall over the bolus, increasing the density of circular muscle fibers, or rigidifying the tract's wall [10]. Given is that shortening of the longitudinal muscles in front of the bolus 'pulls' the bolus towards the stomach [12]. This means that the bolus translates relative to its original position without shearing along the tract's wall. The bolus is taken along within the longitudinal movement of the tract while being sealed at a stationary spot. This transport method allows for transport without having to overcome the friction between the object and the tract's wall. This, together with the tract's ability to move the bolus in curved pathways and to shape-lock the bolus without damaging, makes the peristaltic movement promising to serve as inspiration for a flexible tissue transport mechanism.

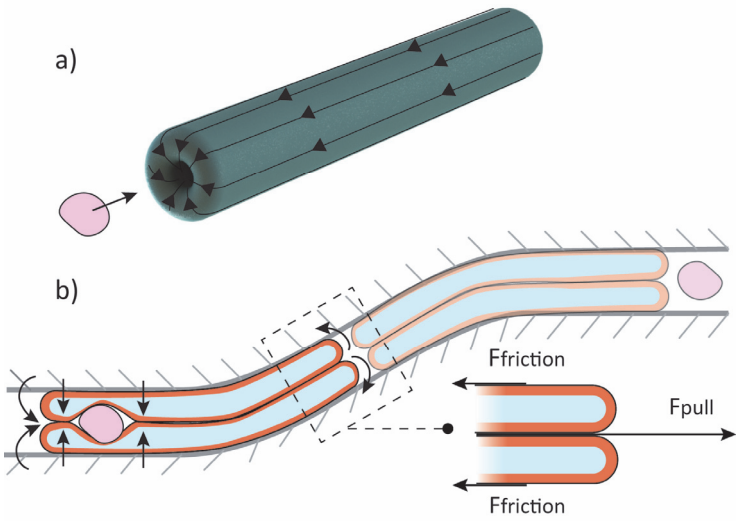


Figure 12.2: Schematic overview of the design of a conveying toroid as transport mechanism. a) The geometry of a conveying toroid. b) Tissue transport by the soft conveying toroid, translating through an outer shaft. Friction forces ($F_{friction}$) are generated between the outer shaft and the outer membrane of the toroid. The toroid's enveloping movement is actuated by a pull force (F_{pull}) acting on the inner membrane.

12.2.2 Design Requirements

Some requirements should be met by our tissue transport mechanism to incorporate similar benefits as the peristaltic movement. In terms of reliability, the transported object should be fixated at a stationary spot to avoid movement relative to the shaft's wall. Illustrated by the peristaltic movement, this fixation can be realized by a shape-lock formed by the adaptation of the wall to the object's shape. In terms of versatility, the transport mechanism should be able to transport objects independently of their composition or shape. The peristaltic movement shows that this can be realized by fixating the object at a spot and moving this spot along the shaft's axis without shearing it along the shaft's wall. Additional requirements are related to the mechanism's application in MIS. In terms of dimensions, the transport mechanism should fit through the small incisions (5-15 mm) made during a procedure. In terms of flexibility, the transport mechanism should be able to transport in curved pathways to enable tissue transport from hard-to-reach regions.

12.2.3 Design conveying toroid

We propose a design for a flexible tissue transport mechanism in the shape of a conveying toroid. A toroid geometry is created by extruding a doughnut shape Figure 12.2a. When filling a toroid with a lubricating liquid, it is able to turn itself inside out in a continuous motion. This is the main principle behind the tissue transport mechanism, where the inside of the toroid functions as transporting lumen. The toroid moves forward by everting its membrane. While doing this, the enveloping motion of the membrane transports an object through its inner lumen. When manufacturing the membrane from an elastic material, the toroid adapts to the object inside the lumen. This ability to self-adapt its shape to the transported object makes this mechanism suitable for the universal transport of tissues. Comparable to the peristaltic

movement, the conveying toroid shape-locks the object in the transporting lumen by forming a soft seal around the object. Similarly, the object is translated along the longitudinal axis of the lumen while being shape-locked at a stationary spot. This makes the conveying toroid transportation independent from the tissue composition and shape.

The idea of a soft conveying toroid is proposed in earlier literature as a promising soft robot locomotion method to squeeze through holes [13], as a universal soft gripping method [14, 15], or as object transportation method [16]. In these studies, the functionality of the conveying toroid was proved by the use of commercial toys, the so-called 'water snakes'. These toys act like conveying toroids on a hand-size scale, showing the capabilities of a conveying toroid as preliminary prototypes. Additionally, a first attempt was made to fabricate a conveying toroid on roughly the same hand-size scale as a water snake, filled with water or air [16]. This prototype showed the potential of a toroid as a universal gripper, but the fabrication method was not yet designed to be down-scaled or up-scaled, nor with object transportation in mind. Concluding, the current preliminary prototypes of a conveying toroid show the potential for this mechanism, mainly focused as a universal gripping method, but are not yet designed for customization for specific applications.

To function as tissue transport mechanism, the conveying toroid is placed inside an outer shaft to translate the tissue in the desired direction (Figure 12.2b). The toroid starts conveying when a pulling force is applied to its inner membrane. The toroid acts as a roller in contact with the outer shaft. Slip should be avoided to perform an optimal rolling contact. This means that it is essential that the pulling force is not larger than the friction forces between the outer shaft and the toroid. Interestingly, this results in contradictory material properties of the toroid's elastic membrane, as the outside requires high friction forces to avoid slip, while the inside requires low friction forces for smooth conveying. A material should be chosen that maintains the toroid's functionality while allowing small-scale manufacturability.

12.2.4 Fabrication

The fabricating process is divided into two parts; (1) fabricating a thin-walled elastic toroid, and (2) filling the toroid leak-free with lubricating liquid. It was chosen to fabricate the toroid's membrane using silicone due to its easy manufacturability, high friction coefficient and elastic

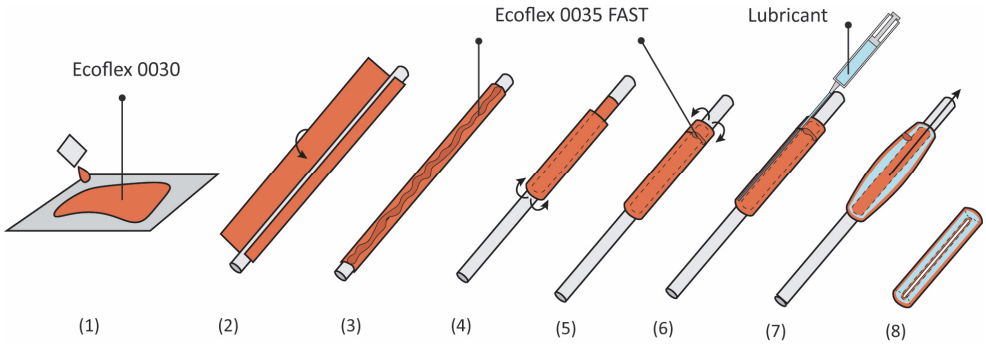


Figure 12.3: Schematic fabrication steps of the conveying toroid. Steps 1-5 focus on fabricating a thin-walled elastic toroid, whereas steps 6-8 focus on filling the toroid with liquid.

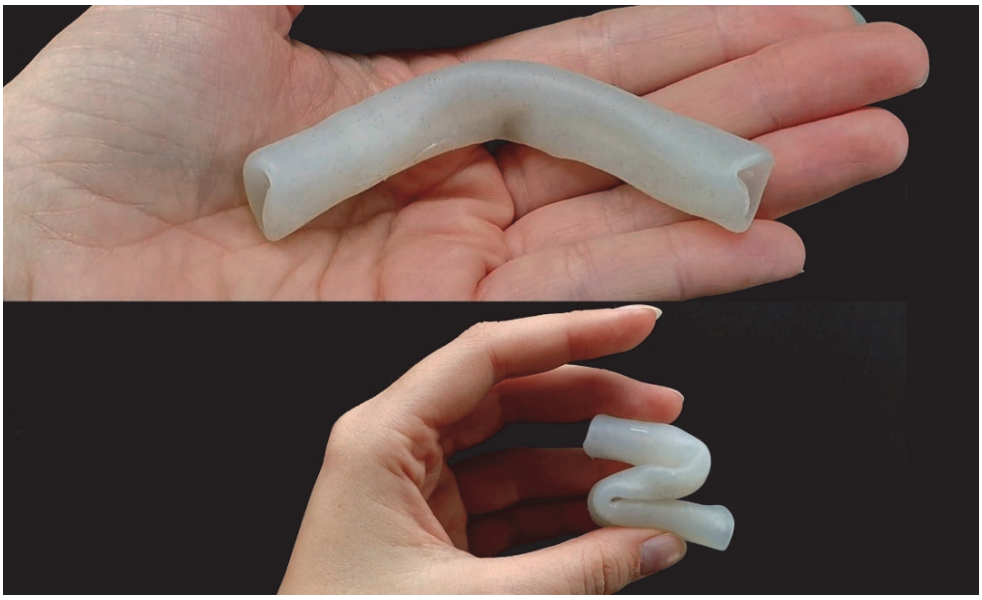


Figure 12.4: Final prototype of the soft conveying toroid.

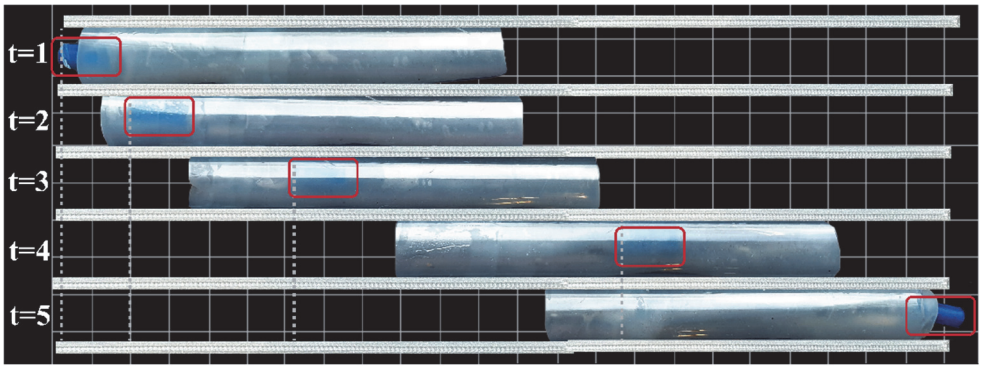


Figure 12.5: Final prototype of the conveying toroid transporting a blue cylinder.

properties. Figure 12.3 shows the fabrication steps schematically. First, the uncured silicone (Ecoflex 00-30, Smooth-On) is smeared on a flat surface to create a thin and highly elastic membrane. After being cured, this membrane is wrapped around a 10 mm diameter tube with the ends joined by fast-curing silicone (Ecoflex 00-35, Smooth-On). This results in a highly flexible, thin-walled silicone tube. Subsequently, the lower end of the tube is flipped over and moved towards the top, where the top is flipped over to meet the lower end. The ends are again joined by fast-curing silicone (Ecoflex 00-35, Smooth-On). The toroid is filled with water-based lubricant to ensure low friction at the inside for smooth conveying. This lubricant is injected by a syringe, where after the injection inlet is closed by fast-curing silicone (Ecoflex 00-35, Smooth-On). Finally, the conveying toroid is rolled from the tube.

12.2.5 Final Prototype

The final prototype, with a diameter of 12 mm and a length of 100 mm, is shown in Figure 12.4. The transported object is conveyed from the inlet to the outlet of the toroid, while the toroid travels its own length at the same time. This means that the object travels two times the length of the toroid, which is in this case 200 mm. Figure 12.5 shows how a random object was transported through the conveying toroid.

12.3 Experimental Validation

The main goal of the experiments was to investigate if the designed transport mechanism was able to transport reliably by assessing its transport efficiency ($\eta_{transport}$) for different curved pathways. The experimental setup is shown in Figure 12.6. In this setup, the conveying toroid moved through a PVC outer shaft. This shaft was fixated in different angles by three shaft holders fixed to a baseplate. The conveying toroid was actuated by a pull force generated by a fiber-reinforced PVC belt driving through the inner lumen of the toroid. This type of belt was chosen because of its stiff properties to minimize elastic deformation of the belt. The belt was driven by an actuation wheel, which was again fixated to the baseplate. The actuation wheel was coated with a silicone strip to create sufficient grip with the belt. A circle of degrees was placed beneath the actuation wheel to measure the number of rotations of the wheel. A tensioning rod was added to ensure sufficient tensioning of the belt during rotation. A 3d-printed cylindrical shape with a diameter of 5 mm and a length of 15 mm acted as target object. A camera mounted on a tripod filmed the setup from above.

The transport efficiency ($\eta_{tranport}$) [%] is the main performance variable of this experiment. This efficiency is affected by the slip between the belt and toroid, the slip between the target object and the toroid, and sub-optimal rolling contact between the toroid and the outer shaft. The transport efficiency was calculated by dividing the theoretical propelled belt length ($t_{theoretical}$) [mm] by the measured propelled belt length ($t_{measured}$) [mm] used to transport the target object from the inlet to the outlet of the conveying toroid, multiplied by 100% (12.1). The efficiency is scaled by the elongation coefficient $\mu_{elongation}$ [-], which counteracts the effect of the toroid's elastic deformation in its longitudinal length while transporting.

$$\eta_{transport} = \frac{t_{theoretical}}{t_{measured}} \cdot \mu_{elongation} \cdot 100\% \qquad (12.1)$$

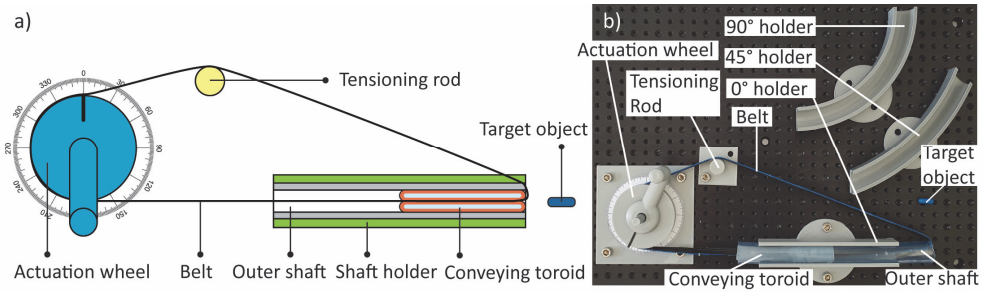


Figure 12.4: Experimental setup. a) Schematic overview of the experimental setup to measure the transport efficiency of the conveying toroid for different curved pathways. b) Experimental setup.

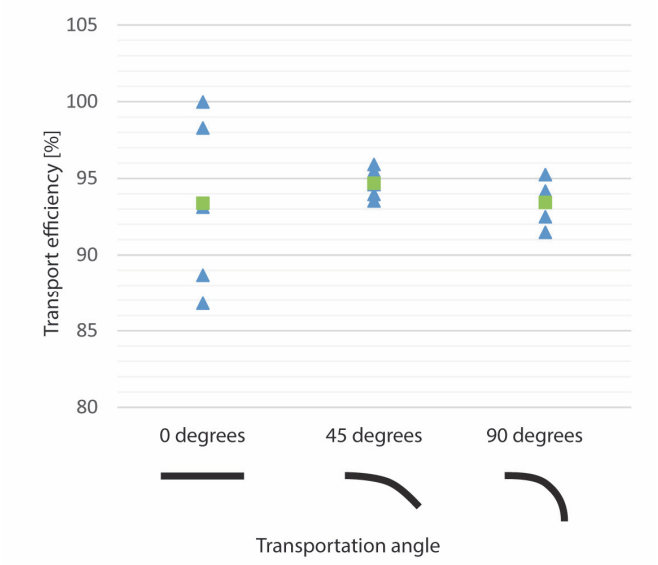


Figure 12.7: The transport efficiency of the conveying toroid per transportation angle. The blue triangles represent the individual measurements and the green boxes represent their average.

The measured propelled belt length ($t_{measured}$) is determined by dividing the perimeter of the actuation wheel (P_{wheel}) [mm] by the number of degrees of one rotation, multiplied by the number of degrees the actuation wheel has rotated during transportation $N_{degrees}$ [-] (12.2).

$$t_{measured} = \frac{P_{wheel}}{360} \cdot N_{degrees} \qquad (12.2)$$

The theoretical propelled belt length $t_{theoretical}$ [mm] is defined as two times the length of the conveying toroid L_{toroid} (12.3).

$$t_{theoretical} = 2 \cdot L_{toroid} \qquad (12.3)$$

The transport efficiency was measured for a straight pathway, a 45° curved pathway, and a 90° curved pathway. For every pathway, five measurements were performed. To obtain an equal start position for every measurement, the target object was inserted at the tip for its full length before the start of a measurement. The wheel was rotated to pull the belt through the conveying toroid. The measurement was terminated when the tip of the target object reached the proximal end of the conveying toroid. A camera filmed the measurements from above. Analyzing the video footage gave the number of degrees the actuation wheel had rotated during every measurement.

The transport efficiency for the three different pathways is visualized in Figure 12.7. The average transport efficiency with its standard deviation for a straight pathway, 45° curved pathway, and 90° curved pathway were 93 ± 5.6%, 95 ± 0.8%, and 93 ± 1.6%, respectively.

A one-way analysis of variance (ANOVA) test shows no significant difference in transport efficiency between the three pathways ((F(2,12)=0.33, p=.7263). The statistical significance was set at an α value of less than 0.05. It should be noted that the object transportation was successful for all measurements.

12.4 Discussion

This study shows the idea of a soft conveying toroid as a transport mechanism for tissues in MIS. This toroid transports tissue through its inner lumen by turning itself inside out in a continuous motion. The toroid is made of a silicone membrane and filled with a lubricating liquid to facilitate a self-adaptable inner lumen that deforms to the transported tissues. The tissue is fixated at a stationary spot in the lumen, while the conveying motion of the toroid brings the tissue forward. This makes this mechanism independent of the tissue composition and shape of the tissue. On this small scale, it is essential to fill the toroid with lubricating liquid instead of another type of liquid or gas. Transporting large objects might push the inner membranes onto each other, which should generate only minimal friction to maintain smooth continuous rotation.

A prototype was developed to evaluate the transporting performance of the conveying toroid in curved and straight pathways. Transporting in curved pathways would be essential during its use in MIS, as the target tissue is often hard to reach from the incision side. The experiments showed no significant difference in the transport efficiency using a straight pathway, a 45° curved pathway or a 90° curved pathway. Moreover, all transportation attempts were successful. Noticeably, the toroid appeared to stretch during transportation (Figure 12.8a). This phenomenon was only observed in transportation over a straight pathway, which could be explained by the potentially larger friction forces between the outer shaft and the toroid during curved transportation. As shown in Figure 12.8b, the toroid's membrane is pushed into a smaller radius at the inner side of the curve. This results in the toroid experiencing larger grip in these curved outer shafts, counteracting stretching forces. The stretching of the toroid during transportation is undesirable as this lowers the predictability of the transportation path of the conveying toroid. Another undesirable event observed during the experiments is the formation of inclinations in the outer membrane of the toroid (Figure 12.8c). These inclinations hinder the continuous rolling motion of the toroid, which makes the belt slip inside the inner lumen of the toroid. Both events could be solved by pouring uncured silicone on top of a fiber mesh during the fabrication process. This would result in a fiber-reinforced thin-walled silicone sheet as the base for the silicone toroid. The integrated fiber mesh makes the toroid stiff in the longitudinal direction while maintaining its flexibility in the radial direction.

The experimental setup gave only preliminary insights into the transportation performance of the conveying toroid. A larger amount of measurements is needed to provide

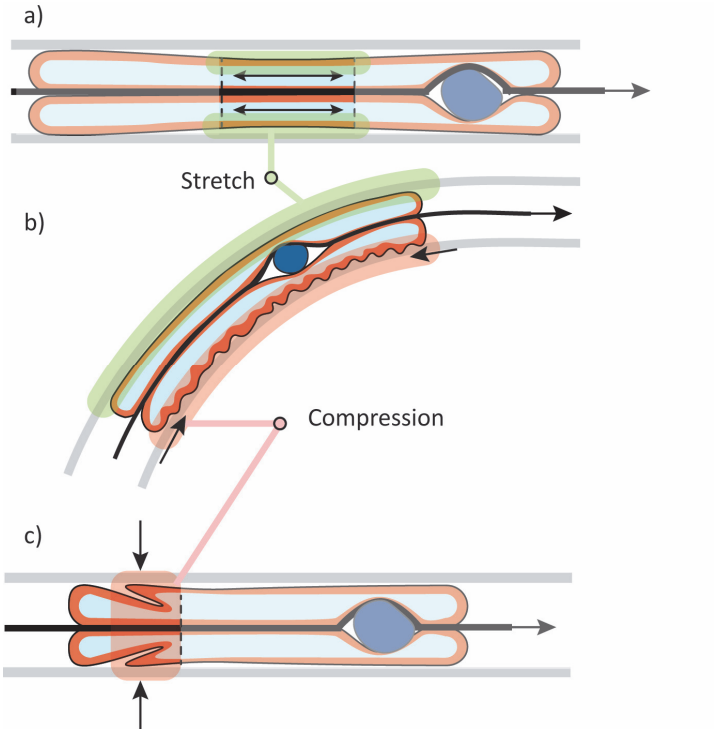


Figure 12.8: Observations impeding the predictability of the tissue transportation of the conveying toroid. Parts of the membrane in stretch are highlighted in green, where parts of the membrane in compression are highlighted in red. a) Elongation of the conveying toroid. b) Higher grip between the curved outer shaft and the conveying toroid by smaller inner radius. c) Inclination of the toroid's outer membrane hinders the continuous rolling motion.

definite conclusions. The performance measurements could have been influenced by uneven actuation velocities. Although it was tried to maintain an equal velocity for every measurement, the manual actuation could have caused deviations. Also, the manual fabrication of the toroid could have introduced irregularities in the membrane, which might influence the interaction between the toroid and outer shaft.

The performance validation of the conveying toroid should be further evaluated by the influence of different actuation speeds on transportation efficiency. This also provides the possibility to determine the ultimate flow rate of this tissue transport mechanism, which can be compared to commercially available aspiration catheters. Additionally, the transportation performance should be evaluated using ex-vivo tissue samples with different shapes and elasticity.

The manufacturing method of the conveying toroid is suitable for fabrication in small dimensions, but also allows fabrication in large dimensions. The scalability of this soft transport mechanism opens possibilities for many applications that require delicate object transport. The outer diameter could be changeable for applications in different regions of the body. Another application could be the deep seabed mining of mineral-containing nodules, which is currently associated with a negative environmental impact. The hydraulic machines

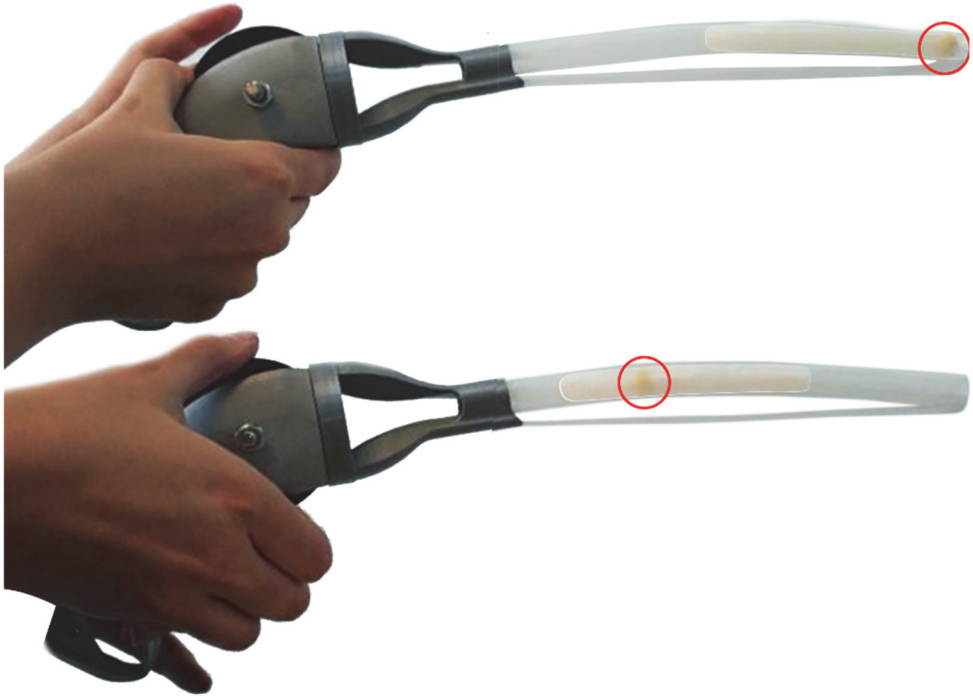


Figure 12.9: A preliminary prototype of the conveying toroid integrated into a handheld device.

used to retrieve the nodules create turbidity in the water column, crush the seabed and deposit sediments [1]. The soft conveying toroid would adapt its shape to the nodule without disturbing the surrounding sea bed fauna.

Figure 12.9 shows a preliminary prototype of the conveying toroid integrated into a handheld device, featuring a future view of this tissue transport mechanism in practical use.

12.5 Conclusion

In this study, a novel solution was presented as a tissue transportation mechanism in MIS. A small-scale conveying toroid was fabricated that transports tissue through its inner lumen when translating through an outer shaft. Contrary to existing solutions, this transport mechanism works independently of tissue composition and tissue shape.

In future work, we want to develop the toroid's ability to grip the tissue before transportation. Although this study focused on the transportation mechanism of the conveying toroid, the toroid intrinsically incorporates a gripping mechanism. As described in previous research [14-16], the conveying toroid swallows an object inside when its tip is in contact with the object. Additionally, steerability should be added as extra functionality of the conveying toroid to bend the mechanism actively in curved pathways. As the outer shaft forces the conveying toroid in its transport direction, this feature could be added by focusing on the steerability of the outer shaft. These additional functionalities contribute to revealing the full potential of the conveying toroid. The simple design of the manufactured prototype shows the

potential for large-scale implementation of the conveying toroid as a soft transport mechanism for tissues in MIS.

References

[1] R. Sharma, "Environmental issues of deep-sea mining," *Procedia Earth and Planetary Science,* vol. 11, pp. 204-211, 2015.

[2] A. Sakes, I. A. Van de Steeg, E. P. De Kater, P. Posthoorn, M. Scali, and P. Breedveld, "Development of a novel wasp-inspired friction-based tissue transportation device," *Frontiers in Bioengineering and Biotechnology,* vol. 8, p. 575007, 2020.

[3] P. A. der Maur *et al.*, "Roboa: Construction and evaluation of a steerable vine robot for search and rescue applications," in *2021 IEEE 4th International Conference on Soft Robotics (RoboSoft)*, 2021: IEEE, pp. 15-20.

[4] E. Brown *et al.*, "Universal robotic gripper based on the jamming of granular material," *Proceedings of the National Academy of Sciences,* vol. 107, no. 44, pp. 18809-18814, 2010.

[5] B. Mazzolai, L. Margheri, M. Cianchetti, P. Dario, and C. Laschi, "Soft-robotic arm inspired by the octopus: II. From artificial requirements to innovative technological solutions," *Bioinspiration & biomimetics,* vol. 7, no. 2, p. 025005, 2012.

[6] M. Meissner, "Rationale and indications for aggressive early thrombus removal," *Phlebology,* vol. 27, no. 1_suppl, pp. 78-84, 2012.

[7] J. F. Buell *et al.*, "Experience with more than 500 minimally invasive hepatic procedures," *Annals of surgery,* vol. 248, no. 3, pp. 475-486, 2008.

[8] G. Hong *et al.*, "Usefulness of endobronchial ultrasound-guided transbronchial needle aspiration for diagnosis of sarcoidosis," *Yonsei medical journal,* vol. 54, no. 6, p. 1416, 2013.

[9] G. Rioufol *et al.*, "Large tube section is the key to successful coronary thrombus aspiration: findings of a standardized bench test," *Catheterization and cardiovascular interventions,* vol. 67, no. 2, pp. 254-257, 2006.

[10] P. Pouderoux, S. Lin, and P. J. Kahrilas, "Timing, propagation, coordination, and effect of esophageal shortening during peristalsis," *Gastroenterology,* vol. 112, no. 4, pp. 1147-1154, 1997.

[11] R. K. Mittal, "Regulation and dysregulation of esophageal peristalsis by the integrated function of circular and longitudinal muscle layers in health and disease," *American Journal of Physiology-Gastrointestinal and Liver Physiology,* vol. 311, no. 3, pp. G431-G443, 2016.

[12] W. J. Dodds, E. T. Stewart, D. Hodges, and F. F. Zboralske, "Movement of the feline esophagus associated with respiration and peristalsis. An evaluation using tantalum markers," *The Journal of clinical investigation,* vol. 52, no. 1, pp. 1-13, 1973.

[13] V. Orekhov, M. Yim, and D. Hong, "Mechanics of a fluid filled everting toroidal robot for propulsion and going through a hole," in *International Design Engineering Technical Conferences and Computers and Information in Engineering Conference*, 2010, vol. 44106, pp. 1205-1212.

[14] D. Sui *et al.*, "A bioinspired soft swallowing gripper for universal adaptable grasping," *Soft Robotics,* vol. 9, no. 1, pp. 36-56, 2022.

[15] H. Zang, B. Liao, X. Lang, Z.-L. Zhao, W. Yuan, and X.-Q. Feng, "Bionic torus as a self-adaptive soft grasper in robots," *Applied Physics Letters,* vol. 116, no. 2, 2020.
[16] S. E. Root *et al.*, "Bio-inspired design of soft mechanisms using a toroidal hydrostat," *Cell Reports Physical Science,* vol. 2, no. 9, 2021.

CHAPTER 13

13

DISCUSSION

13.1 Findings of this thesis

13.1.1 Mechanical Intelligence

As robots increasingly become part of our daily lives, collaborating more closely with humans and being employed in unstructured environments, their expected range of abilities continues to grow. This also means that the computational demand placed upon them is increasing. Traditional approaches to robotic design have often focused on enhancing control architectures, sensing capabilities and computational intelligence. Yet, to operate effectively and safely in the real world, robots can benefit from forms of intelligence that emerge naturally from their physical embodiment, complementing computational control.

This perspective leads to a growing emphasis on the robot's embodiment as a source of intelligence. Nature offers a powerful source of inspiration for such ideas. Across ecosystems, organisms have evolved body structures that exploit environmental interactions to achieve adaptive behavior. These biological phenomena highlight the potential of designing robots whose intelligence emerges not only from computation, but also from their morphology. In this thesis, we called this perspective on intelligence *mechanical intelligence*. It is defined as the ability of a robot to respond to external conditions through its physical design. *Chapter 2* described how this perspective compares to existing perspectives on intelligence that were found in literature. Whereas the well-established framework of embodied intelligence highlights how morphology and material properties can exploit interaction with the environment, mechanical intelligence goes further by explicitly shaping these properties to meet environmental demands and preserve functional performance.

Building on this perspective, **the main goal of this thesis was to investigate mechanical intelligence in soft robots, inspired by nature, with the potential to enhance functionality beyond structured environments**. The question of how to design for mechanical intelligence in soft robots, rather than only adding softness, remains insufficiently understood. Constrained and hard-to-reach environments were used throughout this thesis as motivating and representative application domains, as they place strong demands on robotic systems. To investigate this idea, this thesis focused on three fundamental robotic interactions: (1) intelligent gripping, (2) intelligent movement and (3) intelligent transport (Figure 13.1). These are the basic ingredients of almost any higher-order task a robot might perform. In each case, the aim was to design bodies that behave intelligently by design.

13.1.2 Part I: Intelligent Gripping

Main findings

The thesis first investigated how mechanical intelligence can be embedded into soft robotic end effectors to enable adaptive gripping. The work focused on understanding how compliance and geometry can be exploited to reduce dependence on precise sensing and control, especially in situations where object properties and interaction conditions are unknown or variable.

Chapter 3 drew inspiration from organisms such as the octopus, to understand how compliant bodies and material properties can enable reliable manipulation in unstructured environments. This analysis highlighted suction-based attachment as a promising strategy for operation in constrained and hard-to-reach spaces. Suction enables rapid grasping without

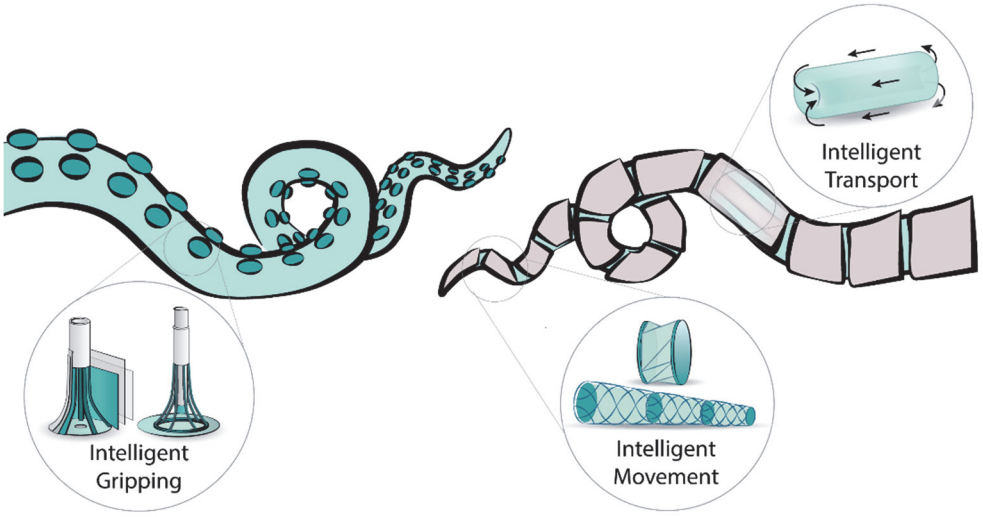


Figure 13.1: Overview of mechanically intelligent soft robotic functionalities developed in this thesis. The three functional domains are demonstrated through suction grippers (Chapters 3-5), soft actuators for localized movement (Chapters 6-9), and (soft) conveying systems (Chapters 10-12). The figure highlights how responsive behaviour emerges from physical design across different robotic functions.

needing precise gripper finger placement, as long as it can form a seal, and it avoids the need to squeeze slippery substrates for sufficient grip. Because suction forces are limited by the applied pressure (theoretically maximally 100 kPa) and suction area, suction inherently embeds a safety mechanism that prevents excessive loading. These insights led to the design of a soft suction gripper, developed and evaluated within the context of Minimally Invasive Surgery (MIS) as a representative and demanding application domain. MIS imposes strict constraints on access, size, and allowable forces, making it a suitable context to expose the advantages of mechanically intelligent gripping. The suction tip consists of five distinct layers, each tailored for a specific function: foldability for insertion, airtightness, slideability for smooth transition, seal formation, and friction magnification. With these layers, the gripper allows for different functional states depending on the demands of the environment, from a compact folded configuration to a deployed state, conforming the required suction surface. The design demonstrated strong and versatile attachment across phantom, liver, and muscle tissues, outperforming existing suction-based grippers in both force and substrate versatility.

Beyond pneumatic actuation, *Chapters 4 and 5* expanded this exploration by investigating magnetic actuation as an embedded shape-change mechanism. Magnetic stimulation allows rapid, remote deformation, enabling transitions between programmed states in the gripper's body, such as attachment and detachment. This led to the development of a magnetically actuated deployable suction gripper composed of silicone mixed with carbonyl iron particles and reinforced with superelastic nitinol. The gripper can fold to small dimensions to access confined spaces and reliably attach to flat, single-curved and double-curved surfaces in both air and water. The gripper's attachment forces were sufficient to lift objects around 350 grams in both air and water, demonstrating versatility across environments.

Taken together, these results reveal several strategies for embedding mechanical intelligence into soft robotic grippers. First, the gripper's morphology can be designed to encode multiple functional states, such as folded and unfolded configurations. This allows the physical structure itself to determine how the gripper responds to spatial constraints, enabling appropriate behavior without requiring additional sensing or control. Second, material composition plays a crucial role in enabling environment-responsive behavior: compliant silicones conform naturally to irregular surfaces, while magnetically responsive composites allow rapid, remote deformation. This gives the gripper multiple response modes without the need for external reprogramming. Third, distributing functions across layered or hierarchical substructures allows each layer to address a specific requirement, so that overall gripping performance emerges from the coordinated behavior of these specialized layers. Finally, passive safety can be directly embedded into the mechanism: suction inherently limits applied forces through pressure limits and suction area, ensuring safe interaction with delicate substrates. Together, these embedded design principles create a gripper whose adaptive capacity and safety emerges from its physical embodiment, illustrating the usefulness of mechanical intelligence for gripping.

Future pathways

A next step toward embedding mechanical intelligence into robotic suction grippers is the integration of multi-functionality within the same physical structure. An illustrative demonstration of multifunctionality in suction-based end effectors is provided in collaboration with the Autonomous Matter Department at AMOLF, where we incorporated their fluidic sensing technology into our MIS suction cup [1]. The suction cup uses its own deformation during contact as information, allowing environmental interaction to serve directly as sensing. The suction cup is attached to a pressurized air reservoir, after which the equilibrium pressure is measured. Because more compliant substrates are drawn further into the cup during suction, reducing the internal volume, the resulting equilibrium pressure serves as an indication for substrate stiffness. This enables the suction cup not only to attach but also to sense mechanical properties of the contacted tissue [1]. A next step would be to examine if this response is accurate enough for reliable stiffness-based tissue discrimination during MIS. In this way, multifunctional sensing and gripping become co-encoded within the same embodiment of the robot, enabling suction-based end effectors to attach to various tissues and to discriminate the type of tissue at the same time.

Another way to enhance the mechanical intelligence of suction-based grippers is by incorporating redundancy. This feature is clearly demonstrated in the original biological inspiration of these grippers. Octopus arms are densely covered with suction cups, of which the appropriate suction cups are recruited when attaching to an object. This means that if one suction cup fails to maintain a seal, attachment is not immediately lost. Also, more suction cups can be recruited for a larger payload capacity. In a preliminary study [2], we explored this principle through a multi-chamber suction gripper and found that it consistently outperformed a single-chamber design on phantom tissues with varying curvature and stiffness. Initial leakage tended to occur at the outer contact boundaries, making designs with multiple independent suction areas more resilient to these primary leaks. Future research should investigate how structural redundancy can be optimally exploited for different target objects. In particular, it would be valuable if interaction alone can passively activate or

deactivate distinct suction areas depending on the target object's properties. This way, redundancy enhances mechanical intelligence by enabling context-dependent selection of functional suction areas.

13.1.3 Part II: Intelligent Movement

Main findings

Next, we explored how mechanical intelligence can be embedded into soft robotic actuators to enable adaptive movement. The work focused on understanding how actuator compliance and geometry can enable diverse and coordinated movement patterns to emerge from simple actuation inputs, reducing reliance on complex actuator combinations. McKibben artificial muscles (AMs) are among the most widely used actuators in soft robotics, yet they still fall short of the versatility and responsiveness observed in biological muscle systems. *Chapter 6* reviewed the state-of-the-art in artificial muscles and classified them according to architectural principles found in natural muscle morphologies. Dependent on their architecture, biological muscles can reorient their fibers and modulate force output a wide variety of tasks. Their internal architectures allow them to combine high force generation with large variety in deformation. Most artificial muscles lack these sophisticated arrangements, and as a result, their adaptability remains limited. Generating more complex motions, such as bending, twisting, or caterpillar-like locomotion, typically requires combining multiple McKibben AMs, often resulting in complex multi-actuator systems.

Chapter 7 focused on simplifying multi-actuator systems by demonstrating how a single actuation input can result in complex motions within a single McKibben AM. Instead of relying on external control algorithms, the study showed that the interaction between the braided sleeve and the inner bladder of the McKibben AM can be designed to predefine the actuator's motion. By encoding local mechanical cues into the muscle's morphology, the actuator can generate contraction, extension, bending, or twisting. This means a single McKibben AM can produce advanced motions that would otherwise require multi-actuator arrays or sophisticated controllers, potentially simplifying the robotic system. Importantly, this approach maintains the simplicity of conventional McKibben manufacturing methods, ensuring low-cost and scalability.

Chapter 8 further expanded the capabilities of McKibben AMs by introducing branched architectures. These branched designs allow a single AM to produce even more complex deformation patterns while still operating on a simple, single pressure input. By deploying complex architectures, these designs move artificial muscles one step closer to the adaptability of natural muscle systems. Together, *Chapters 7* and *8* show how a complex motion can be encoded directly into actuator morphology and material behavior.

Beyond pneumatic systems, the thesis also examined alternative actuation methods that support localized and responsive movement through embedded physical mechanisms. *Chapter 9* introduced a set of design guidelines for integrating electromagnets directly into a robotic body, enabling precise, segment-level control without relying on external compressors or pressure lines. In this study, a Kresling origami structure was chosen as the actuator's body. The Kresling structure was particularly useful because it combines high bending resistance in its unfolded state with smooth transitions between folded and deployed configurations, increasing load-bearing capacity while maintaining flexibility. Electromagnets were added to

the Kresling structure to actuate the origami structure, inducing effective contraction and extension. Unlike alternative systems, such as pneumatic continuum arms, the electromagnetic Kresling actuator avoids fragile airtight components or slow response times. This makes the actuator especially suitable for dynamic, remote, or spatially restricted environments where lightweight, rapid, and localized actuation is essential.

Taken together, these findings reveal several strategies for embedding mechanical intelligence into movement systems. First, complex motion can be encoded directly into an actuator's morphology through local mechanical interactions. By designing the internal architecture and local material interactions of an actuator, such as the braid–bladder coupling in McKibben muscles or the crease patterns in Kresling origami, the global motion emerges from the body itself. Contraction, extension, twisting, and bending become programmed states of the structure, allowing a single actuator to achieve movements that otherwise require multi-actuator assemblies or sophisticated control systems. Second, embedding bistable or state-dependent behavior within actuator architectures expands this responsiveness; the Kresling cylinder, for example, shifts between a stiff, load-bearing configuration and a compliant, deformable state, enabling actuators to shift between stability and flexibility as required by the task.

Future pathways

A next step towards embedding mechanical intelligence for movement is enabling a soft actuator to adjust its motion path real-time, depending on the task or environment at hand. This would imply more motion freedom instead of relying solely on a pre-defined motion encoded in its morphology. This direction aims to bring continuum robots closer to the biological capabilities of an octopus arm. The octopus' arm can shift between a floppy, compliant state and a stiff, load-bearing configuration, forming temporary joints along its length. Such an adaptive reconfiguration simplifies control, allowing the arm to behave like an articulated structure exactly where environmental interaction demands it. Moving towards this level of adaptability suggests the need for a reconfigurable building block that supports multiple deformation modes. Previous work explored the Kresling origami actuator as a candidate. However, alternative origami geometries may offer additional opportunities. In a side study [3], we identified the legged waterbomb origami structure as a potentially interesting building block (Figure 13.2a-b). This structure has an open architecture, providing space for integrating local electromagnets, and exhibits compliance along multiple axes. Depending on which leg is actuated, the structure can bend, contract, or extend, indicating a versatile motion repertoire. These characteristics suggest that the legged waterbomb origami structure could act as a promising building block for future research into mechanically intelligent continuum arms (Figure 13.2c). This strategy can be extended to McKibben artificial muscles. If their braiding angle can be altered in real time, a single McKibben muscle could likewise behave as a continuum arm in which joints emerge dynamically (Figure 13.2c). This could be achieved by embedding responsive materials into the braid, such as magnetically active fibers or thermally adaptive shape-memory wires. This way, a McKibben artificial muscle could take the role of the Kresling-based origami structure as the core of a highly reconfigurable actuator, with local electromagnets similarly enforcing targeted shape shifts. In both cases, the actuator's body enables the creation of temporary joints and

task-dependent motion modes, demonstrating mechanical intelligence where movement adaptability is encoded directly into the actuator's body.

13.1.4 Part III: Intelligent Transport

Main findings

Lastly, we explored how mechanical intelligence can be embedded into soft robotic systems to enable adaptive transport. The work focused on understanding how the robot's body itself can contribute to the transport of objects through physical interaction rather than relying on external grasping or intricate control strategies. Robotic systems often move objects externally, meaning transport outside the robotic body, which makes transport generally more sensitive to disturbances and challenges performance in cluttered or hard-to-reach environments. In contrast, internal transport, meaning transport through the robotic body, has the potential to inherently enhance stability. In this approach, objects will be protected within the robot's body, reducing exposure to external forces and enabling navigation through tight or constrained spaces. To study the challenges of internal transport under severe spatial and safety constraints, the work focused on surgical applications as a representative application domain. Medical instruments used in these procedures must operate through narrow holes and pathways while safely handling fragile tissue, placing strong demands on robotic embodiment. Within this context, *Chapter 10* reviewed existing aspiration catheters used for removing blood clots from the body as a widely adopted internal transport solution. The review concludes that these internal transport mechanisms have as drawback their sensibility to clogging and low adaptability when confronted with variable tissue consistency.

Chapter 11 addressed this challenge by introducing a cable-driven transport mechanism that moves tissue through a cylindrical conveyor-like system. The device uses friction between continuously rotating cables to pull material through its lumen. A proof-of-principle prototype demonstrated successful transport of phantom tissues with different stiffnesses, and the measured mass-transport rates fell within the range of clinically used devices. This showed that internal transport can be achieved through a mechanically simple mechanism embedded directly into the robot's structure.

Building on this, *Chapter 12* explored a biologically inspired direction based on the longitudinal muscles used during the peristaltic motion of the esophagus. We developed a soft conveying toroid that turns itself inside out in a continuous motion. A silicone toroid filled with lubricating liquid was fabricated to enable smooth inversion and tight shape adaptation around various objects. Unlike traditional suction-based transport mechanisms, the toroid forms a shape grip, locking onto an object and conveying it forward even when its geometry, stiffness, or surface properties vary widely. Preliminary experiments showed that the toroid transported objects effectively through curved pathways, demonstrating adaptability.

Together, these studies reveal how mechanical intelligence for transport can be embedded directly into a robot's morphology. In these designs, the robot's body itself becomes the transporting agent by relocating the external object internally. This means the transported object is inherently protected from environmental disturbances. At the same time, passive shape-adaptive gripping emerges from the interplay between geometry and material compliance, allowing the transport mechanism to conform around objects of varying shapes,

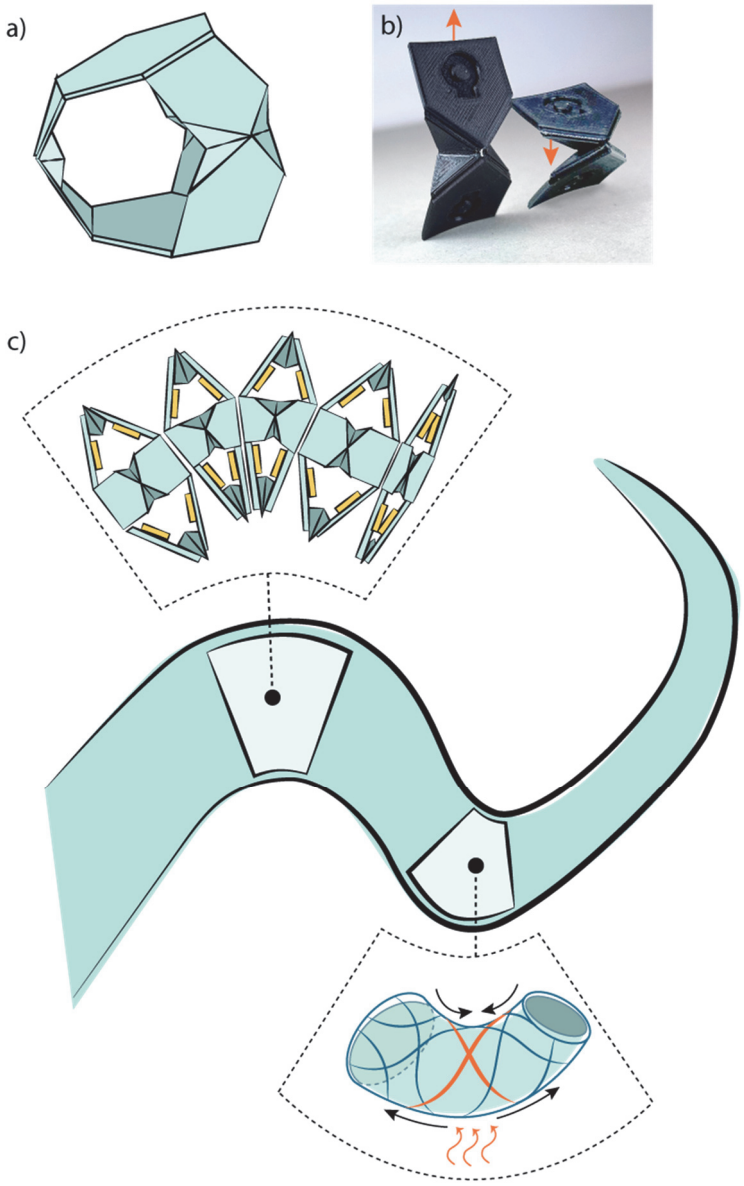


Figure 13.2: Future vision of a continuum arm able to adjust its movement characteristics real-time. a) Schematic visual of a legged waterbomb origami structure. b) 3D-printed waterbomb origami leg, showcasing contraction and extension. c) Top: Origami building blocks with embedded electromagnets (yellow) to adapt the local state of the continuum arm [3]. Bottom: A single McKibben AM adjusting its braiding angle by locally responsive braid materials, such as magnetically active fibers or thermally adaptive shape-memory wires (orange).

stiffnesses or surface textures. In both the cable-driven conveyor and the inverting toroid, transport is generated by how the structure physically engages with the object, not by precise

coordination. This shape-grip principle makes the mechanism largely independent of surface properties and enables reliable internal transport through curved or constricted pathways. These embedded design strategies illustrate how soft robots can achieve safe and versatile transport by encoding responsiveness directly into their body.

Future pathways

The main limitation of the developed toroidal transport mechanism is that it functions as a discrete transporter, delivering objects one at a time. A logical next step is to transform it into a continuous transport system, which would reduce transport time. Achieving continuous transport requires the toroid to remain stationary while its membrane everts, which is a fundamentally different type of motion. In a side study [4], we developed a preliminary prototype consisting of an actuation system that generates both a driving force for membrane eversion and an anchoring force to keep the toroid stationary (Figure 13.3). The toroid is driven from its distal end using wheels connected to a gearbox, while magnetic anchors keeps the toroid in place. Preliminary experiments with objects of different shapes, sizes, and stiffnesses revealed no significant differences in transport efficiency. The latter describes whether the movement of the toroid's outer membrane corresponds with the traveled distance of the transported object. The experiments indicate that the mechanism shows potential to remain reliable under varying conditions [4]. A next step towards enhanced mechanical intelligence would be to give the toroid the same adaptive deformation capability as seen in octopus arms, similar to the intelligent movement strategies described earlier. This would allow the toroid to deform its body around obstacles and dynamically reshape its transport pathway in response to the environment.

13.2 Implementation challenges

13.2.1 Scalability and robustness

For soft robots to achieve effective societal impact, challenges related to scalability, robustness, and long-term reliability must be addressed. One of the key challenges in bringing soft robots into real-world applications is the lack of scalable fabrication strategies. Many soft-robotic components rely on silicone molding with intricate internal geometries, leading to fragile structures and variability between batches. This challenges reliable series manufacturing. Alternatively, advanced 3D printing techniques enable highly detailed designs but are often slow, costly, and difficult to scale. These 3D printing techniques frequently require specialized facilities, custom-made manufacturing equipment, and high-performance materials. Additionally, the large structural variability between different soft robotic designs hinders standardization for large scale production [5].

A promising direction towards scalable soft robots is to build on the artificial muscles explored in this thesis. Their simple architecture and reliance on established braiding principles make them well suited for existing industrial braiding machinery. Basic pneumatic McKibben muscles are already commercially available, demonstrating practical viability. Although the fabrication of branched muscular networks is challenging for conventional continuous braiding machines, automated 3D braiding technologies capable of branching and

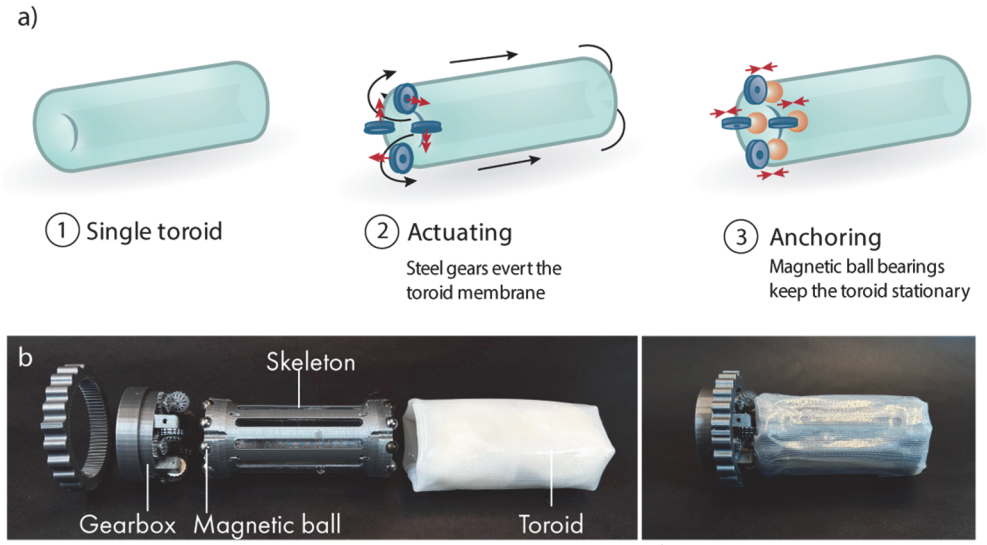


Figure 13.3: Future vision of the continuous toroidal transport mechanism. a) In blue the driving wheels embedded in a gearbox and in orange the anchoring system consisting of magnetic ball bearings. b) Left: exploded view of the preliminary prototype. Right: assembly of the preliminary prototype [4].

splicing already exist in cable manufacturing and textile engineering [6-10]. These technologies are already commercialized for use in medical device development, indicating a possible pathway toward automated fabrication of intricate artificial muscular networks. With targeted machinery adaptations, intelligent McKibben actuators could transition from laboratory prototypes to industrially manufactured components. In terms of size, commercially available braided tubes already span diameters from 1 mm to 100 mm and lengths of several meters, paving the way for large-scale deployment of mechanically intelligent soft robotic systems.

In addition to manufacturing scalability, the long-term robustness of soft robotic systems remains a significant challenge for real-world deployment. Soft robots are often vulnerable to material fatigue and degradation by environmental factors. As fluidic actuation remains one of the most commonly used actuation approaches in soft robots, soft robotic systems are inherently vulnerable to leakage and pressure losses. For real-world deployment, soft robots must maintain consistent and predictable over extended operational timespans. To address these limitations, substantial research effort has been directed towards alternative actuation strategies, including stimuli-responsive actuation methods [11, 12]. Further investigation into the potential of these approaches, as well as other strategies to improve long-term reliability, remains essential for enabling robust real-world operation.

13.2.2 Inclusivity, equality and diversity in robotics

As robotic technologies move toward real-world deployment, increasingly interacting with people and society, issues of inclusivity, equality, and diversity across STEM (Science, Technology, Engineering and Mathematics) fields become an important implementation challenge. In particular, the field of robotics is notably affected by gender imbalance [13]. Future advances in robotics may have a substantial impact on society and everyday life,

making this underrepresentation especially pressing. Broad representation among both designers and users becomes increasingly relevant for effective implementation of robotics, especially when pursuing mechanical intelligence, to ensure that systems perform effectively across a wide range of contexts. Within the broader robotics landscape, soft robotics has been identified as a welcoming subfield, due to its accessibility. Its interdisciplinary nature, spanning disciplines such as biology, material science, textile engineering, mathematics, mechanical engineering and control, attracts researchers from a wide range of backgrounds. Bao *et al.* [11] and Sadati *et al.* [14] presented maps of research collaborations within the soft robotics community revealing a highly interconnected research field. In addition, soft robotics research often employs accessible materials and comparatively low-cost, simple fabrication methods. This helps lower barriers to entry. Its accessibility also makes soft robotics a suitable field for outreach activities aimed at introducing young students to STEM. A survey that is yearly conducted through the IEEE Diversity Working Group shows a promising gender balance within the soft robotics field [15]. While this does not imply that soft robotics is uniquely inclusive, these results highlight how young and interdisciplinary research fields may provide opportunities to improve representation while robotics continue to evolve and enter daily life.

13.3 Perspective

This thesis demonstrates that soft robots can embed mechanical intelligence by adopting design strategies inspired by the adaptive physical principles found in nature. Through the development of soft robotic systems for gripping, movement, and transport, we showed how functionality can be encoded directly into the robot's embodiment, allowing each system to respond to its environment through its morphology and material composition.

A next question is whether we can go one step further. Can we move beyond bio-inspiration and explore forms of soft robotic intelligence that are not directly observed or inspired by living organisms? Doing so would mirror the way mythical creatures combine capabilities that span multiple environments. While nature offers many examples of multi-modal and adaptable systems, evolution is constrained by ancestry and survival. Therefore, certain combinations of functions or living environments may be uncommon in natural organisms, yet feasible in engineered systems. If we strip away this evolutionary history and instead initiate an artificial evolution cycle for (soft) robotic systems, new design spaces may emerge, in which morphology, material properties, and mechanical intelligence co-develop. In such a process, mechanical intelligence would not only imitate biological strategies but would become an intrinsic driver of evolution, allowing soft robotic bodies to embed functionalities that are optimized for engineered environments, hybrid tasks, or entirely novel modes of operation.

13.4 Scientific contribution

While the concept of mechanical intelligence has existed in the field of engineering for a longer time [16], its role within soft robotics has remained insufficiently understood. Due to the soft materials employed in soft robotic systems, they are often described as being embodied intelligent, as their compliant structures passively conform to the environment. However, passive compliance alone does not guarantee functional performance. For example, a soft

gripper may adapt its shape to an object but suffer from reduced payload capacity. Therefore, this thesis formulated a more precise definition of mechanical intelligence tailored to soft robotics: the ability of an artificial agent to respond to external conditions through programmed states embedded in its body [17]. Here, external conditions refer to task-dependent requirements imposed by the operating environment, such as surface properties, load conditions or spatial constraints. This means that not every physical response to the environment results in mechanical intelligence. In this thesis, a system is considered mechanically intelligent only if its responses preserve or extend its intended functionality. Building on this definition, the thesis demonstrated how mechanical intelligence can be embedded into soft robots through geometry, material composition, local mechanical interactions, and integrated actuation. Through various studies on gripping, movement and transport systems, mechanical intelligence is shown to enhance the capabilities of soft robots. These capabilities include safe, adaptive gripping across various substrates, artificial muscles that generate complex motions with one simple input and transport mechanisms that function independently of stiffness or geometry. These examples collectively illustrate that mechanical intelligence can be a powerful way to achieving reliable, scalable and context-aware soft robotic behavior. Taken together, these contributions position mechanical intelligence as a promising direction to bring future soft robotic designs into our daily lives.

References

[1] S. Zou, S. Picella, J. De Vries, V. G. Kortman, A. Sakes, and J. T. Overvelde, "A retrofit sensing strategy for soft fluidic robots," *Nature communications,* vol. 15, no. 1, p. 539, 2024.

[2] V. G. Kortman, L. van Loo, J. Jovanova, and A. Sakes, "Design of an expandable multi-chamber suction gripper for minimally invasive surgery " presented at the The 16th Hamlyn Symposium on Medical Robotics, Londen, 2024.

[3] J. Cuijpers, "Design and Experimental Evaluation of an Origami-inspired Robotic Arm with Octopus-like Functionalities," Master thesis, Delft University of Technology, 2025.

[4] F. van Erp, "Development of a Continuous Toroidal Tissue Transporter for Minimal Invasive Surgery," Master thesis, Delft University of Technology, 2024.

[5] H. Zhang, Z. Wang, and Z. Fan, "Standardizing structure design of soft robots through origami," *Nature Reviews Electrical Engineering,* vol. 2, no. 3, pp. 145-146, 2025.

[6] R. Miksch and F. Ficker, "Multi bifurcation branch braided structures on a herzog variation braiding machine," in *Recent Developments in Braiding and Narrow Weaving*: Springer, 2016, pp. 15-20.

[7] X. Yang *et al.*, "Rotary Three-Dimensional Braider Design Method Based on the Average Cutting Circle Strategy," *Engineering,* vol. 49, pp. 260-271, 2025.

[8] C. Emonts *et al.*, "Innovation in 3D braiding technology and its applications," *Textiles,* vol. 1, no. 2, pp. 185-205, 2021.

[9] A. Bogdanovich, "An overview of three-dimensional braiding technologies," *Advances in braiding technology,* pp. 3-78, 2016.

[10] M. Lengersdorf and T. Gries, "Three-dimensional (3D)-maypole braiding," in *Advances in braiding technology*: Elsevier, 2016, pp. 89-105.

[11] G. Bao *et al.*, "Soft robotics: Academic insights and perspectives through bibliometric analysis," *Soft robotics,* vol. 5, no. 3, pp. 229-241, 2018.

[12] Q. Chen, T. Kalpoe, and J. Jovanova, "Design of mechanically intelligent structures: Review of modeling stimuli-responsive materials for adaptive structures," *Heliyon,* 2024.

[13] L. Graesser, A. Faust, H. Kress-Gazit, L. Tapia, and R. Ulinski, "Gender diversity of conference leadership [Women in Engineering]," *IEEE Robotics & Automation Magazine,* vol. 28, no. 2, pp. 126-130, 2021.

[14] S. Hadi Sadati, M. ElDiwiny, S. Nurzaman, F. Iida, and T. Nanayakkara, "Embodied intelligence & morphological computation in soft robotics community: Collaborations, coordination, and perspective," in *IOP Conference Series: Materials Science and Engineering*, 2022, vol. 1261, no. 1: IOP Publishing, p. 012005.

[15] S. Aracri *et al.*, "Soft robotics: A route to equality, diversity, and inclusivity in robotics," *Soft Robotics,* vol. 11, no. 6, pp. 903-910, 2024.

[16] A. Khaheshi and H. Rajabi, "Mechanical intelligence (MI): a bioinspired concept for transforming engineering design," *Advanced Science,* vol. 9, no. 32, p. 2203783, 2022.

[17] V. G. Kortman, B. Mazzolai, A. Sakes, and J. Jovanova, "Perspectives on intelligence in soft robotics," *Advanced Intelligent Systems,* vol. 7, no. 1, p. 2400294, 2025.

Acknowledgements

I am grateful to everyone who contributed to my phd journey, both professionally and personally.

Jovana and Aimée, you introduced me not only to the world of soft robotics, but also to the broader international research community. One of my earliest highlights was attending RoboSoft in Singapore together. Being welcomed into the soft robotics community in such an inspiring way was incredibly motivating and shaped how I experienced the start of my PhD. **Jovana**, I am grateful for the international perspective you brought, your curiosity towards people and cultures, and the way you continuously encouraged me to look beyond my own horizon. Your talent for connecting people has made the JAM group a very welcoming place. **Aimée**, thank you for the many adventures we had together. What started as a graduation project six years ago continued through a research project and eventually into this PhD. The research stay in Tokyo was one of the highlights of my PhD, giving me the opportunity to experience research in a completely different setting.

Paul, thank you for your guidance and support throughout this journey. Having worked together since my graduation project, I have always appreciated our creative brainstorming sessions and your ability to look at challenges from a totally different perspective. Your ideas and feedback have contributed greatly to my development as a researcher.

I would also like to thank my paranymphs, **Jette and Robin**. Since the bridging program, we have been an incredible power team. **Jette**, thank you for always being there. Working together has always been effortless. You have been a constant source of support, both professionally and personally. I miss sharing an office and working every day together. **Robin,** thank you for being a partner-in-crime during our house renovations. I have always admired how quickly you can dive into a topic and make it completely your own. I could not wish for a better paranymph team.

A special thank you goes to all my office mates for turning the office into such a welcoming place every day. **Jette**, I have to mention you again because you were simply impossible to leave out. You were a constant factor in the office and someone everyone could rely on. **Esther**, thank you for always being a listening ear and inspiring us with all your great adventures. **Merle**, thank you for the many enjoyable moments in and outside the office, and for hosting the three of us during such a great weekend in Freiburg. **Kirsten**, thank you for your contagious enthusiasm and creativity and for sharing so much valuable senior-phd wisdom. **Mostafa**, thank you for your enthusiasm in creating new memories and saving them in photos. **Fabian**, thank you for inspiring us with your 3d-printing wisdom. **Indra**, thank you for your creativity and enthusiasm, whether it involved sewing, 3D-printing amazing lampshades, or any of the many other projects you manage to bring to life. **Nynke**, thank you for your positive energy and motivating us for lunch walks, running, and gentle reminders that we should occasionally stretch. **Haymi**, thank you for the many interesting conversations and for teaching me so much about Ethiopia. **Dina**, thank you for always looking out for everyone

and for your sharp observations. **Nianlei**, thank you for sharing your sporting adventures, including introducing us to badminton. **Jean**, thank you for being one of the calm and steady presences in the office. **Karin**, thank you for your endless energy and the many conversations. **Giacomo**, thank you for being such a social and welcoming person.

I would also like to thank all PhDs and colleagues within the BMD department for creating such a friendly, relaxed, and supportive working environment. The daily coffee breaks, lunches, and conversations made the department a great place to work. Thank you **Abhijeet, Anneke, Anton, Benjamin, Bob, Christoph, Dirk, Ebrahim, Edwin, Federica, Gabriele, Guiomar, Giovanni, Hassan, Iris, Jenna, Jonathan, Karien, Kasra, Katerina, Kim, Koen, Lennart, Lizelotte, Ludovica, Maria, Marin, Marit, Mauricio, Monika, Nasim, Pascal, Pier, Rogier, Rick, Sara, Shibo, Suzanne, Vahid, and Judith**. **Remi** and **David**, thank you for all the nice conversations and your interest in my project. Also, thanks to **Angelique**, **Amanda**, and **Marjolijn** for making everything run smoothly.

Momo, thank you for your enthusiasm for every activity, no matter how questionable the weather conditions. The run in pouring rain remains a memorable example. **Niko**, thank you for your positivity, your social nature, and the many fun moments at X. To the **running crew**, thank you for the motivation to keep on running, with the Kopjesrun and Singelloop as highlights.

Of course, I would also like to thank the entire JAM group: **Aaron, Adam, Ana, Christof, Chamod, Hao, Jimmy, and Tom**. Thank you for the support, the weekly lunches, and the many enjoyable trips and conferences. From Leuven during a heatwave in a car without air conditioning to Keulen, Enschede, Italy, and the highlight of all, our trip to Macedonia.

I also had the opportunity to work together with a lot of great bachelor and master students: **Rajae, Rodrigo, Jelle, Jules, Floortje, Mike, Sjoerd, Pieter, Jouke, Suzanne, Coen, Ellen, Yinte, Lars, Kai, David, Kasper, Boris, Mats, Julian, Lauren and Christiaan.** Thank you for the trust you gave me to supervise your projects.

And of course, a big thank you for my family and friends. Thank you for offering a listening ear, distraction and the interest you showed in my work. A special thank you to **Coco, Sharda, Loulou, and Tessa**, for your steady support throughout this journey.

Last but not least, I want to thank my **parents**, I want to thank **Jelle and Robbin** and, of course, I want to thank **Ruben**. Thank you for your support, listening and understanding. You made this journal the amazing experience it has been.

Curriculum Vitae

Vera Kortman, born 13-06-1996 in Rotterdam, the Netherlands

Work Experience

- *Postdoctoral researcher* — 2026-present, TU Delft, Departments of Sustainable Design Engineering (IDE) & Maritime & Transport Technology (ME)
- *Ph.D. in Mechanical Engineering* — 2022-2026, TU Delft, Departments of Maritime & Transport Technology & BioMechanical Engineering
- *Visiting researcher Endo-Suzumori Lab* — Dec 2023- Mar 2024, Institute of Science Tokyo
- *Researcher Bio-Inspired Technology Group* — 2021-2022, TU Delft, Department of BioMechanical Engineering

Education

- *Master of Science in Mechanical Engineering (cum laude)* — 2018-2021, TU Delft
- *Bridging program* — 2017-2018, TU Delft
- *Bachelor of Science in Industrial Design Engineering (cum laude, honors program)* — 2014-2017, TU Delft
- *Gymnasium (cum laude)* — 2008-2014, Emmauscollege Rotterdam

Awards

- *Best poster award* — International conference on adaptive structures and technologies (ICAST) 2025
- *Best pitch award* — BioMechanical Engineering Symposium 2024
- *KNAW Young Talent Philips graduation award* — 2021

Invited talks

- *SHErobot café* — TU Delft library 2024
- *Robots in business* — Robohouse 2024
- *'Inflatable actuators'* — Animated Materials course 2024 & 2025, IDE, TU Delft

- *Bio-inspired soft robotics'* — Biomimetics course 2024 & 2025, Biology, Wageningen University
- *'Intro to soft robotics'* — Integration Project course 2023, ME, TU Delft

Academic Service

- *Associate Editor* — BioRob 2026
- *Member* — Diversity & inclusivity working group, RAS IEEE Soft Robotics TC
- *Co-organizer* — Dutch soft robotics summerschool, TU Delft, 2022
- *Reviewer* — Materials & Design 2026, Journal of Mechanisms and Robotics 2025, RA-L 2025, ICRA 2024, AIM 2024, Soft Robotics 2023, Robosoft 2022-2023, Journal of the Brazilian Society of Mechanical Sciences and Engineering 2023-2025

Public Outreach

- *Visibility assistant High Tech research theme* — Mechanical Engineering, TU Delft, 2026, science communication
- *Speaker Opening of the Academic year* — TU Delft, 2026, recording
- *Soft Robotics Exhibition* — NEMO Science Museum, 2023-present, recording
- *Research & Design high school course* — Christelijk Lyceum Delft, 2026, coaching
- *Girls day* — TU Delft, 2022, 2023, 2024, 2025, 2026, workshops
- *Teknowlogy Day* — DeFabrique Utrecht, 2025, demonstrations
- *Science Day* — TU Delft, 2025 & 2026, workshops
- *High School PWS inspiration day* — TU Delft, 2024, talks
- *'Nacht van de ontdekkingen'* — Boerhaave museum, Leiden, 2023, exhibition

Supervising

- *Master students*

Rajae Atahiri	Adaptive 3D-Printed Cushion for Wheelchairs
Rodrigo Vega Covelo	Electro-Magnetic Variable Stiff Unrolling Octopus Arm
Jelle Cuijpers	Electro-Magnetic Origami Joints for Distributed Actuation
Jules de Ruiter	Wasp-Inspired Needle with Mechanical Stroke Adjustment
Floortje van Erp	Soft Conveying Tissue Transporter

Mike van der Zelm	Compliant Conveying Tissue Transporter
Sjoerd van der Voort	Breast Stabilization Device for Biopsies
Pieter d'Hont	Variable Stiff Vacuum Delivery Device
Jouke Hompes	Electro-Magnetic Origami Actuator
Suzanne van Wees	Wasp-Inspired Propulsing and Transporting Needles
Coen Overvliet	Earthworm-Inspired Self-Borrowing Robot
Ellen de Vries	Magnetically-Actuated Suction Gripper
Yinte Verberne	Rigid Conveying Tissue Transporter
Lars van Loo	Multi-Chamber Tissue Suction Gripper

- *Bachelor students*

David Wolfrat, Kasper Stavenga, Boris Ullrich, Mats Kerver	Suction Needle Stabilization Device for Laparoscopic Liver Surgery
Julian van den Bos, Lauren Jonk and Christiaan Oosterom	3D-Printed Bellow Actuator for Leg Prosthetics

- *Internship*

Kai Cussen	Customized Silicone 3D Printer

Teaching

• *Bio-Inspired Design (MSc course) 2021, 2022, 2023, 2024, 2025*	Mechanical Engineering, TU Delft, lectures and assignments
• *Product Futures (MSc course) 2025*	Industrial Design Engineering, TU Delft, assignments
• *Designing Medical Technology (BSc course) 2024*	Clinical Technology, TU Delft, Q&A sessions
• *General introduction to biomedical engineering (BSc course) 2023*	Minor Biomedical Engineering, TU Delft, assignments
• *Lecture: 'Finding biological information'*	Bio-Inspired Design 2023, Mechanical Engineering, TU Delft

List of publications

Publications as part of this thesis

- **Kortman, V. G.**, Jovanova, J., Nabae H., Endo G., Suzumori K., & Sakes, A. (2026). Designing McKibben Muscles: A Critical Review for Practical Implementation. *Bioinspiration & Biomimetics*, *21*(3), 031002.
- **Kortman, V. G.**, Sakes, A. & Jovanova, J. (2026). Advancing McKibben Artificial Muscles: Bio-Inspired Design for Complex Motion. *Journal of Intelligent Material Systems and Structures*, 1045389X261484720.
- **Kortman, V. G.**, Jovanova, J., & Sakes, A. (2025). Adaptable by design: encoding complex deformation profiles in mckibben artificial muscles. *Materials & Design*, 115188.
- **Kortman, V. G.**, Hompes, J. T., Sakes, A., & Jovanova, J. (2025). Kresling origami actuator with embedded electromagnetic actuation. *Smart Materials and Structures*, *34*(6), 065018.
- **Kortman, V. G.**, Mazzolai, B., Sakes, A., & Jovanova, J. (2025). Perspectives on intelligence in soft robotics. *Advanced Intelligent Systems*, *7*(1), 2400294.
- **Kortman, V. G.**, de Vries, E., Jovanova, J., & Sakes, A. (2024). Unlocking versatility: magnetic-actuated deployable suction gripper for complex surface handling. *Soft Robotics*, *11*(6), 1020-1031.
- **Kortman, V. G.**, Verberne, Y., Atalla, M. A., & Sakes, A. (2024). Advancements in aspiration catheter tip design for thrombectomy: A comprehensive patent review. *Frontiers in Medical Technology*, *6*, 1388638.
- **Kortman, V. G.**, De Vries, E., Jovanova, J., & Sakes, A. (2024). Magnetic Stimulation for Programmed Shape Morphing: Review of Four-Dimensional Printing, Challenges and Opportunities. *3D Printing and Additive Manufacturing*, *11*(3), 977-993.
- **Kortman, V. G.**, Verberne, Y., Jovanova, J., & Sakes, A. (2023). Advancing minimally invasive surgery: a cutting-edge cable-actuated conveying mechanism for reliable tissue transportation. *Plos one*, *18*(12), e0295585.
- **Kortman, V. G.**, Jovanova, J., & Sakes, A. (2023). Design of a soft bio-inspired tissue transport mechanism. In *2023 IEEE International Conference on Soft Robotics (RoboSoft)* (pp. 1-6). IEEE.
- **Kortman, V. G.**, Sakes, A., Endo, G., & Breedveld, P. (2023). A bio-inspired expandable soft suction gripper for minimal invasive surgery—an explorative design study. *Bioinspiration & Biomimetics*, *18*(4), 046004.

Other publications

- Bloemberg, J., van Wees, S., **Kortman**, **V. G**., & Sakes, A. (2025). Design of a wasp-inspired biopsy needle capable of self-propulsion and friction-based tissue transport. *Frontiers in Bioengineering and Biotechnology*, *12*, 1497221.
- Aracri, S., Hughes, J., Della Santina, C., Jovanova, J., Hoh, S., Garcia Morales, D.S., Barcaro, R., Tan, Y.J., **Kortman**, **V.G**., Sakes, A. and Partridge, A.J. (2024). Soft robotics: A route to equality, diversity, and inclusivity in robotics. *Soft Robotics*, *11*(6), pp.903-910.
- Zou, S., Picella, S., De Vries, J., **Kortman**, **V. G**., Sakes, A., & Overvelde, J. T. (2024). A retrofit sensing strategy for soft fluidic robots. *Nature communications*, *15*(1), 539.
- Breedveld, P., **Kortman**, **V. G.**, & Sakes, A. Essentials of instrument manipulation. *The Technical Principles of Endoscopic Surgery*, 215.

Conference contributions

- **Kortman V.G**., Sakes A., Jovanova J. (2025). Complex-shaped bio-inspired McKibben artificial muscles for advanced robotic systems. 34th International conference on adaptive structures and technologies (ICAST). May 19-21, Capua, Italy, 1 p.
- **Kortman V.G.**, van Erp F., Jovanova J., Sakes A. (2025). Soft Conveying Toroidal System for Continuous Tissue Transportation. 2025. IEEE International Conference on Soft Robotics (RoboSoft), April 23-26, Lausanne, Switzerland, 2 p.
- **Kortman V.G.**, Sakes A., Jovanova J. (2024). Embodied Intelligence in Soft Robotics. Soft robotics PhD conference, Nov 22, Leuven, Belgium, 1 p.
- **Kortman V. G**., van Loo L., Jovanova J., Sakes A. (2024). Design of an expandable multi-chamber suction gripper for minimally invasive surgery. The Hamlyn Symposium on medical robotics, June 25-28, Londen, United Kingdom, 2 p.
- **Kortman V.G.** Jovanova J., Sakes A. (2024). Deployable suction grippers for small-scale applications. Dutch soft robotics symposium, May 28-29, Eindhoven, The Netherlands, 1 p.
- **Kortman**, **V. G.**, Jovanova, J., & Sakes, A. (2023). Design of a soft bio-inspired tissue transport mechanism. In *2023 IEEE International Conference on Soft Robotics (RoboSoft)* (pp. 1-6). IEEE.
- **Kortman V.G**., Bloemberg, J., Sakes A. (2022). Design of an octopus-inspired, double-walled suction disc for upper abdominal biopsy stabilization. 44th International Engineering in Medicine and Biology Conference (EMBC), July 11-15, Glasgow, United Kingdom, 1 p.

